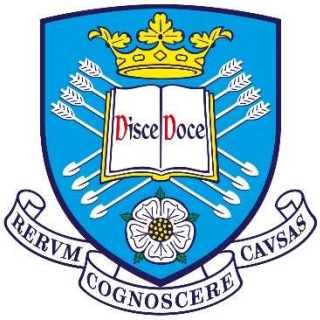


The University Of Sheffield.

An Investigation on the Stability and Resilience of Engineered Slopes Under Simulated Climate Conditions.

Muna A ALFERGANI

A thesis submitted in partial fulfilment of the requirement for the degree of Doctor of Philosophy

School of Mechanical, Aerospace and Civil Engineering

The University of Sheffield

November 2024

Declaration

I, Muna Alfergani, hereby affirm that the content of this PhD thesis, titled "Investigating the Stability and Resilience of Engineered Slopes Under Simulated Climate Conditions." is entirely original and has not been submitted, either in full or in part, for consideration towards any other academic qualification at this or any other university or institution. The research and findings presented in this thesis are the result of my own independent work, except where due acknowledgement is given to the contributions or work of others.

Muna A Alfergani

November, 2024

Acknowledgements

I wish to express my heartfelt gratitude to my supervisor, Dr. Elisabeth Bowman, for her invaluable guidance, encouragement, and unwavering support throughout this research. It has been both a privilege and a pleasure to be part of the Geotechnical group and to benefit from her mentorship. I am also deeply grateful to Dr. Tiago Gaspar for his insightful advice and steadfast assistance during this journey. My sincere thanks extend to Holly for her academic and social support, as well as her valuable guidance. Additionally, I would like to express my gratitude to Dr. Colin Smith for his insightful feedback and contributions, which have greatly enriched my research and enhanced its depth and clarity.

I am profoundly thankful to the technical staff in the Department of Civil and Structural Engineering, particularly Mark Foster, whose exceptional technical expertise and tireless assistance during the centrifuge testing phases were instrumental to this research. This PhD would not have been possible without his dedication and support.

This journey has been marked by numerous challenges. Alongside the global disruption caused by the COVID-19 pandemic, I faced significant personal health struggles during my PhD. These included battling COVID-19, enduring an extended illness, and grappling with the lingering effects of post-COVID-19. Additionally, I was diagnosed with an autoimmune condition, which brought further challenges, and I recently underwent a major surgical operation. Despite these adversities, my determination remained steadfast. The unwavering support of my supervisor, husband, colleagues, and loved ones enabled me to persevere and successfully complete this research.

Finally, I wish to express my deepest gratitude to my beloved husband, my children, and my brothers and sisters for their unconditional love, encouragement, and unrelenting support. They have been my constant source of strength and inspiration. I

also take this moment to honour the memory of my parents, who passed away before they could witness this milestone. Their absence is deeply felt, and I pray for their eternal peace and mercy.

شكروتقدير

الحمد لله عز وجل على النعمة التي أنعم بها علينا في إتمام هذا البحث العلمي القدير والصلاة والسلام على سيد المرسلين وعلى آله وصحبه أجمعين، قال تعالى:

بسم الله الرحمن الرحيم

" وَأَلْقَىٰ فِي الْأَرْضِ رَوَاسِيَ أَن تَمِيدَ بِكُمْ وَأَنْهَارًا وَسُبُلًا لَّعَلَّكُمْ تَهْتَدُونَ "

صدق الله العظيم (النحل - 15)

أود أن أستغل هذه اللحظة لتكريم ذكرى والديّ، اللذين وافتهما المنية قبل أن يتمكنا من رؤية هذا الإنجاز. لقد ترك غيابهما فراغًا عميقًا في حياتي، وأدعو الله أن يرحمهما ويسكنهما فسيح جناته.

أتوجه بخالص شكري وامتناني إلى مشرفتي، الدكتورة إليزابيث بومان، على توجيهها القيّم، وتشجيعها المستمر، ودعمها الذي لا ينقطع طوال فترة البحث. لقد كان من دواعي الشرف والسرور أن أكون جزءًا من مجموعة الجيوتكنيك وأن أستفيد من خبرتها وإرشاداتها. كما أعرب عن امتناني العميق للدكتور تياغو على نصائحه الثاقبة ومساندته الدائمة طوال هذه الرحلة. ويمتد شكري الصادق إلى هولي على دعمها الأكاديمي والاجتماعي، بالإضافة إلى توجيهاتها القيّمة. كما أود أن أعبر عن امتناني للدكتور كولين سميث على ملاحظاته القيّمة ومساهماته التي أثرت أبحاثي بشكل كبير وعززت من عمقها ووضوحها. أعرب عن امتناني العميق للطاقم الفني في قسم الهندسة المدنية والهيكلية، وخاصة مارك فورست، الذي لعبت خبرته التقنية الاستثنائية ومساعدته المستمرة خلال مراحل اختبار جهاز الطرد المركزي دورًا أساسيًا في نجاح هذا البحث. لم يكن من الممكن إتمام هذا الدكتوراة بدون تفانيه ودعمه.

لقد تميزت هذه الرحلة بالعديد من التحديات. إلى جانب الاضطراب العالمي الناجم عن جائحة كوفيد-19، واجهت صعوبات صحية شخصية كبيرة أثناء الدكتوراة. وكان الدعم الذي لا يتزعزع من مشرفتي وزوجي وزملائي وأحبائي هو العامل الأساسي الذي مكّنني من المثابرة وإكمال هذا البحث بنجاح. وأخيرًا، أود أن أعرب عن أعمق امتناني لزوجي الحبيب، وأطفالي، وإخوتي وأخواتي، على حبهم غير المشروط، وتشجيعهم، ودعمهم المستمر لقد كانوا مصدر قوتي وإلهامي الدائم.

ABSTRACT

This thesis investigates the stability of soil slopes subjected to climate scenarios involving rainfall, flooding, and drawdown through experimental and numerical methods. Centrifuge modelling of scaled soil slopes was employed to simulate the effects of seasonal variations and extreme hydrological events, including cycles of wetting, drying, and rapid water level changes. These experiments revealed how rainfall infiltration, surface ponding, and drawdown influence slope deformation and failure mechanisms.

Physical models of the slopes were constructed using sandy kaolin clay mixtures. Pore pressures were monitored in detail during the experiments and pore pressure contours were subsequently mapped. Particle Image Velocimetry (PIV) was used to monitor sidewall displacements, shear strain, and volumetric strain. The results showed the evolution of shear strains, localised displacements, and erosion patterns. These evaluations indicate that wetting-drying cycles and subsequent flooding significantly affect slope stability along with localised erosion near the slope and toe.

Numerical modelling using GeoStudio (Slope/W and Seep/W) was conducted to replicate experimental conditions during flooding and drawdown. Key soil parameters, including permeability, effective cohesion (c'), angle of friction (φ') were derived from laboratory tests such as permeameter and triaxial. The soil-water characteristic curve (SWCC) was determined from dewpoint and pressure plate tests and fitted using the van Genuchten model. These simulations predicted hydraulic responses and slope behaviour reasonably well, generally aligning with experimental results. Discrepancies appear to be related to choice of strength parameters and issues associated with a lack of pore-fluid coupling in simplified numerical approaches.

Wetting-drying cycles and rapid water level changes are found to destabilise slopes, highlighting the importance of cyclic climate conditions. This research provides a

framework for analysing slope behaviour under dynamic hydraulic conditions, helping design and manage slopes in seasonal rainfall and flooding zones.

Table of Contents

DECLARATION I

ACKNOWLEDGEMENTS II

ABSTRACT III

TABLE OF CONTENTS 1

LIST OF FIGURES 8

LIST OF TABLE 26

1 CHAPTER 1: INTRODUCTION 28

1.1 INTRODUCTION & MOTIVATION FOR RESEARCH 28

1.2 IMPACTS OF FLOODING AND DRAWDOWN ON SLOPE STABILITY AND INFRASTRUCTURE RESILIENCE. 33

1.2.1 UK Flood Embankments and Global Infrastructure Resilience. *33*

1.3 RESEARCH AIM AND OBJECTIVES 44

1.4 THE OUTLINE OF THE THESIS 45

2 CHAPTER 2: LITERATURE REVIEW 48

2.1 INTRODUCTION 48

2.2 UNSATURATED SOIL 48

2.2.1 Shear strength behaviour and stress state variable of unsaturated soil. *48*

2.2.2 Extended Mohr-Coulomb Failure Envelope *50*

2.2.3 Relationship between tan ϕ^b and χ. *51*

2.2.4 Measurements of pore water pressure. *52*

2.2.5 Stress profiles, moisture content and pore pressure of unsaturated soil. *54*

2.2.6 Soil-Water Characteristic Curve (SWCC). *55*

2.2.7 Flow of water within unsaturated soil. *57*

2.3 INSTABILITY OF SLOPES IN UNSATURATED SOIL. 58

2.3.1 Rainfall infiltration mechanism. *58*

2.3.2 Profiles of pore water pressure in the soil during rainfall events. *62*

2.3.3 Mechanism of rainfall-induced landslides *64*

2.3.4 Field Investigations of slope instability due to rainfall and flooding *66*

2.3.5 Full scale tests of slope instability due to rainfall and flooding *66*

2.3.6 Numerical models of cyclic loading due to rain and flood 66

3 CHAPTER 3 71

3.1 CENTRIFUGE MODELLING 71

3.1.1 Scaling laws 71

3.1.2 Scaling laws of seepage and rainfall specifications. 73

3.1.3 Stress variation error. 74

3.1.4 Coriolis effect 77

3.1.5 Droplet trajectories in a centrifugal rotating frame. 78

3.2 CENTRIFUGE MODELLING OF RAINFALL-INDUCED SLOPE INSTABILITY. 79

3.3 KNOWLEDGE GAPS, NOVEL CONTRIBUTIONS, AND LITERATURE INTEGRATION 90

4 CHAPTER 4 94

4.1 SOIL CALIBRATION AND PREPARATION OF SLOPE MODEL. 94

4.1.1 Particle size distribution. 94

4.1.2 Consistency and Atterberg limits. 98

4.1.3 Standard Proctor Compaction test. 104

4.1.4 Rowe cell testing of the soil. 106

4.1.5 Oedometer experiments 108

4.1.6 Shear strength 111

4.1.7 Triaxial test (Consolidated Drained or CD Test). 116

4.1.8 Falling head permeability test 123

4.1.9 Soil Water Retention Curve (SWCC). 125

5 CHAPTER 5 136

5.1 INTRODUCTION 136

5.1.1 Centrifuge facility at university of Sheffield. 137

5.1.2 Scaling laws considerations 138

5.1.3 Strong box 138

5.2 CLIMATE CHAMBER 139

5.2.1 Principles of climate chambers and rainfall simulation 139

5.2.2 Rainfall distribution system 140

5.2.3 Procedure for simulating rainfall in the centrifuge 141

5.2.4 Nozzle selection criteria 142
5.3 NOZZLE CALIBRATION 143
5.4 RAINFALL INTENSITY 146
5.4.1 Calculation of rainfall intensity from test data 146
5.5 MEASUREMENT OF DEFORMATION. 151
5.5.1 GeoPIV 151
5.5.2 Calibration 154
5.6 TENSIOMETERS AND PORE PRESSURE TRANSDUCERS 155
5.6.1 Saturation and calibration 157
5.6.2 Key Observations: 158
5.6.3 Surface modelling and contour generation using the GRIDFIT method for pore water pressure distribution. 160
5.7 HUMIDITY AND TEMPERATURE SENSORS 161
5.8 HUMIDITY MEASUREMENT 162
5.8.1 Temperature Measurement 164
6 CHAPTER 6 166
6.1 INTRODUCTION 166
6.2 MODEL SLOPE EXPERIMENTS 166
6.3 PREPARATION OF SOIL MODELS. 168
6.3.1 Methodology for model M-T3a test. 168
6.3.2 Testing procedures for M-3a test. 175
6.3.3 Methodology for model M-T3r test. 177
6.3.4 Testing procedure for M-T3r. 179
6.3.5 Methodology for model M-T4 test. 180
6.3.6 Testing procedure of M-T4 test. 183
6.3.7 Methodology for model M-T5 test. 185
6.3.8 Testing procedure for model M-T5. 192
6.3.9 Methodology for model M-T6 test. 194
6.3.10 Testing procedure for model M-T6 test. 196
6.3.11 Methodology for model M-6r test. 197
6.3.12 Testing procedure for models M-T6r. 199

7 CHAPTER 7 200

7.1 INTRODUCTION 200

7.2 TEST M-T3 200

7.3 TEST M-T3R. 206

7.4 TEST M-T4 210

7.4.1 Gravity increase effect 211

7.4.2 Test M-T4: Deformations 217

7.4.3 Seasonal cycles effect 220

7.4.4 Flooding effect M-T4 test. 221

7.5 TEST M-T5 226

7.5.1 Hydrostatic calibration during flood stage in M-T5 centrifuge test. 227

7.5.2 Gravity increase effect 228

7.5.3 Test M-T5: Deformations 234

7.5.4 Seasonal cycles effect 237

7.5.5 Flooding and drawdown effects M-T5 test. 243

7.5.6 Slope failure after centrifuge test. 248

7.5.7 Shear strength reduction due to drawdown failure 250

7.5.8 Factor of safety reduction and numerical validation 251

7.5.9 Failure Mechanism and Theoretical Comparison 251

7.6 TEST M-T6 253

7.6.1 Hydrostatic calibration during flood stage in M-T6 centrifuge test 254

7.6.2 Gravity increase effect. 254

7.6.3 Seasonal cycle effect for M-T6 test. 261

7.6.4 Flooding and drawdown effects for M-T6. 261

7.6.5 Stability interpretation and theoretical insights 264

7.7 TEST M-T6R. 264

7.7.1 Gravity increase effect 266

7.7.2 M-T6r: Auto balance and consolidation deformations 274

7.7.3 Seasonal cycle effect for M-T6r test 274

7.7.4 Flooding and the drawdown effect for M-T6r. 277

7.7.5 Failure mechanisms of the M-T6r test 287

7.8 COMPARISON OF FAILURE BEHAVIOUR IN M-T5, M-T6, AND M-T6R. 290
7.8.1 Overview of Seasonal (Cyclic Weather) Response 290
7.8.2 Seasonal (Cyclic Weather) Displacement and Strain Distribution Insights.....291
7.8.3 Overview of Flooding and Drawdown Response 293
7.8.4 Influence of Boundary Conditions, Slope Inclination, and Soil Preparation on Failure Behaviour. 294
7.9 RAINFALL INTENSITY SELECTION AND EXPECTED FAILURE BEHAVIOUR 296
7.9.1 Comparison of experimental results with existing literature.....297
7.10 CONCLUSIONS: 301
8 CHAPTER 8 303
8.1 INTRODUCTION 303
8.2 MATERIAL PROPERTIES 304
8.3 ANALYSIS SEQUENCE 305
8.4 M-T5 TEST 307
8.4.1 Steady-State Analysis for M-T5 Test. 307
8.4.2 M-T5 Test: Gradual Drawdown Condition. 310
8.4.3 Slope Stability Analysis for M-T5 Test: Rapid Drawdown Condition.....315
8.5 M-T6 TEST 318
8.5.1 Steady-State Analysis for M-T6 Test using ϕ'=26.6°. 318
8.5.2 Stability Analysis for M-T6 Test: Gradual Drawdown Condition using ϕ'=26.6°. 319
8.5.3 Steady-State Analysis for M-T6 Test using ϕ'=31°. 320
8.5.4 Stability Analysis for M-T6 Test: Gradual Drawdown Condition using ϕ'=31°. .321
8.5.5 Pore water pressure at different heights over time.....322
8.6 M-T6R TEST. 325
8.6.1 Steady-State Analysis for M-T6r Test.....325
8.6.2 Slope Stability Analysis for M-T6r Test: Gradual Drawdown Condition. 326
8.6.3 Slope Stability Analysis for M-T6r Test: Rapid Drawdown Condition. 332
8.7 COMPARISON BETWEEN NUMERICAL MODELS AND EXPERIMENTS 332
8.8 SUMMARY: 334
9 CONCLUSION 336

9.1 KEY CONTRIBUTIONS AND NOVEL ASPECTS OF THE STUDY 336

9.2 LINKING FINDINGS TO THE KNOWLEDGE GAP 338

9.3 MAIN RESULTS AND THEIR RELATION TO SLOPE FAILURE MECHANISMS 338

9.4 EXPERIMENTAL CHALLENGES AND DATA INTERPRETATION..... 339

9.5 SUMMARY AND PRACTICAL IMPLICATIONS 340

9.6 RECOMMENDATIONS AND FUTURE WORK 341

9.7 FUTURE WORK 342

10 REFERENCES..... 343

A APPENDIX A 1

A.1 TEST M-T4 1

A.1.1 Deformations 1

A.1.2 Seasonal cycles effect..... 3

A.1.3 Flooding effect M-T4 test. 4

A.2 TEST M-T5 5

A.2.1 Seasonal cycles effect..... 5

A.2.2 Flooding and drawdown effects M-T5 test. 9

A.3 TEST M-T6 13

A.3.1 Hydrostatic calibration during flood stage in M-T6 centrifuge test 13

A.3.2 Deformations 14

A.3.3 Seasonal cycle effect for M-T6 test. 15

A.3.4 Flooding and drawdown effects M-T6. 27

A.4 TEST M-T6R 36

A.4.1 Hydrostatic calibration during flood stage in M-T6r centrifuge test. 36

A.4.2 M-T6r: Autobalance and consolidation deformations..... 38

A.4.3 Seasonal cycle effect for M-T6r test..... 40

A.4.4 Flooding and the drawdown effect for M-T6r. 48

A.5 METHODOLOGY FOR MODEL M-T1 TEST. 57

A.6 METHODOLOGY FOR MODEL M-T2 TEST. 62

A.6.1 Testing procedure for M-T2 65

B PUBLICATIONS 66

List of Figures

Figure 1-1 Monthly rainfall and earthwork events on Network Rail infrastructure in England & Wales. Rail (2021) 29

Figure 1-2 Annual average rainfall distribution across the United Kingdom (1981–2010). Kendon et al. (2021) 30

Figure 1-3 Ladybower Reservoir Overflow Spillway. Photo by Muna Alfergani, 2024. 36

Figure 1-4 (a) Aerial view of flood-affected areas in Wainfleet, Lincolnshire. (b) Military helicopters dropping sandbags along breached riverbanks to contain flooding. Source: Sun Reporter (2019). 38

Figure 1-5 Left: Aerial view of the Mississippi River levee; Right: Cross-sectional diagram illustrating the historical evolution of the Mississippi River levee. (n.d.) (2017) 39

Figure 1-6 Levee failures along the mississippi river due to rapid drawdown and high-water events. Pinyol et al. (2008) 40

Figure1-7 Aerial view showing the locations of Dam 1 and Dam 2 breaches along the Wadi Derna River, with images of the extensive urban destruction in Derna, Libya. (Alkomaty.J,2023). https://www.aljazeera.com/ 42

Figure 1-8 Left: Remains of the Wadi Bu Mansur Dam, after its collapse due to catastrophic floods, September 2023. Right: Devastated low-lying areas near the coast in Derna, severely impacted by the flooding. (Gazzini, 2023) & https://www.bbc.co.uk/news/world-africa-66785466 (BBC News, 2023). 43

Figure 2-1 Degree of saturation and Bishop's effective stress χ after (Lu&Likos,2004). 49

Figure 2-2 Extended Mohr-Coulomb failure envelope for unsaturated soils (Fredlund and Rahardjo, 1993) 50

Figure 2-3 Comparison between both methods b and x to specify shear strength, after Fredlund (2006). 51

Figure 2-4 Surface tension at the interface of the water and air conceptual pressure distribution with depth from the interface Likos et al. (2019). 53

Figure 2-5 Stress patterns that occur in sandy soil for both saturated and unsaturated situation Lu and Likos (2004).....54

Figure 2-6 demonstrates desaturation zones of a typical soil water characteristic curve Vanapalli et al. (1999).....56

Figure 2-7 Soil-water Characteristic Curves for different soil types Fredlund et al. (2012)...56

Figure 2-8 Green Ampt model.....59

Figure 2-9 Transient infiltration in an unsaturated soil Sun et al. (1998).....60

Figure 2-10: Typical of pore water pressure in an unsaturated soil with the different flow of ground surface; where (a) is steady state case, (b) is transient case when q/ksat <1 and (c) transient flow at q/ksat≥1 Rahardjo et al. (1995).....63

Figure 2-11 The comparison between stress trajectories for slope failure induced by rainfall and Triaxial tests Brand (1982).....64

Figure 2-12: Slope failure with different stages (Leroueil, 2001). 65

Figure 2-13 Geometry of the Princeville levee section and a discretised mesh Jadid et al. (2020) 68

Figure 2-14 Shear strain rises at elements A and B during storm cycles Jadid et al. (2020)..68

Figure 3-1 Self-weight stress in both scale of prototype and model at condition of centrifugal acceleration. 72

Figure 3-2 The distribution of vertical stress in a soil model under g, that includes under and over-stress, along with its prototype Taylor (2018).....77

Figure 3-3 The impact of changing the centrifuge's acceleration in in droplet trajectories, at an initial velocity of 20m/s and rotation radius 1.4m:(a) 3D view, (b) lateral view and (c) top view (Caicedo et al., 2015).....79

Figure 3-4 Setup test for test cases of the rainfall infiltration experiment (Kimura, 1991).....80

Figure 3-5 Climate chamber for rainfall simulation on slopes (Take, 2003).....82

Figure 3-6 Response of embankment WAT5 to first wet season (a) Relative humidity boundary condition, and (b) observed seasonal pore water pressure cycles, (c) direction of seasonal movement (d) total maximum shear strain, (f) total volumetric strain and (e) failed slope Take (2003).....83

Figure 3-7: Model slope test in centrifuge to investigate slide-to-flow landslide triggering mechanism , PPT: pore pressure and tension transducer, PIV: Particle image velocimetry Take et al. (2004b).....85

Figure 3-8 : Model slope geometry PPT: pore pressure transducer Lee et al. (2008).....85

Figure 3-9 Threshold curves: The relationship between rainfall duration and rainfall intensity Ling et al. (2009).....87

Figure 3-10 Deformation and failure surfaces in silty sand slopes under rainfall conditions Jayakody et al. (2023).....89

Figure 3-11 Effect of rainfall gap durations on pore water pressure (PWP) response in silty sand slopes Jayakody et al. (2023).....90

Figure 4-1 Particle size distribution of HST95 sand fraction E.....95

Figure 4-2 Sedimentation test for E-grade kaolin clay.....97

Figure 4-3 Particle size distribution curve for gap-graded soil (sand and kaolin).....98

Figure 4-4 Consistency and Atterberg limits (Das and Sivakugan, 2017).....99

Figure 4-5 Results of liquid limit testing for several soil mixtures.....100

Figure 4-6 Modified Casagrande plasticity chart for all soil mixtures tested excluding 100% bentonite. Note that PImax has been used for the majority of mixtures (denoted as small stars) while PI has been used for 100% kaolin and 90% kaolin + 10% bentonite (denoted as circle).
.....104

Figure 4-7 Standard proctor compaction test results of various soil mixtures. 106

Figure 4-8 Rowe cell apparatus for consolidation testing. 107

Figure 4-9 Void ratio and log applied pressure in Rowe cell tests. 108

Figure 4-10 Oedometer void ratio and log applied pressure graph. 109

Figure 4-11 Example of square-root/settlement curve analysis.....110

Figure 4-12 Results of shear box tests. 113

Figure 4-13 Normalised shear Stress Ratio (τ/σ) with shear strain ($\varepsilon s\%$). 113

Figure 4-14 Volumetric strain ($\varepsilon_v\%$) with shear strain ($\varepsilon_s\%$) for different normal stresses. .114

Figure 4-15 Mohr-Coulomb failure envelope for shear strength vs. normal stress for sand fraction E.....115

Figure 4-16 Setup of Triaxial test apparatus for soil testing.....117

Figure 4-17 Deviator stress with axial strain for CD Triaxial tests at different confining pressures.....119

Figure 4-18 Mohr circles and failure envelope for triaxial test. 120

Figure 4-19 The relationship between volumetric strain and axial strain for different levels of confining pressure.....121

Figure 4-20 Stress ratio (q/p') vs. axial strain for Triaxial tests.....122

Figure 4-21 Shear failure of soil sample in Triaxial test apparatus showing bulging deformation. 123

Figure 4-22 (a): The general setup for the falling head permeability test. (b): Datum measurement. 124

Figure 4-23 Pressure plate apparatus for determining soil-water retention characteristics. ..127

Figure 4-24 Dewpoint potentiometer and soil sample measurement setup 130

Figure 4-25 Soil-Water Characteristic Curve (SWCC) for the mixture 65 % sand and 35% kaolin.....131

Figure 4-26 Soil-water characteristic curve (SWCC) for drying fitted with van Genuchten Model. 133

Figure 4-27 Permeability against suction for drying using van Genuchten-Mualem Model.134

Figure 5-1 Centrifuge facility at the University of Sheffield.....137

Figure 5-2 Plane strain window environmental test chamber.....139

Figure 5-3 The rainfall simulator showing the unsealed lid set up.....141

Figure 5-4 Schematic Diagram of Rainfall Simulation Setup with M1 Nozzles.....142

Figure 5-5 Layout of spraying nozzle, type M1 (a) schematic diagram showing nozzle dimensions and spray cone angle, adapted from manufacturer's data sheet, (b) photograph of nozzle M1 photo taken by Alfergani. 143

Figure 5-6 M1 nozzle manufacturer calibration (Take, 2003).....144

Figure 5-7 Nozzle calibration at 1g. 145

Figure 5-8 (a) Rainfall intensity distribution. (b): Water distribution at 400 kPa. 146

Figure 5-9 Rainfall simulation setup within a centrifuge apparatus. 148

Figure 5-10 The distribution of water volume with top plate and position n1 for the nozzle at various g levels (Khan et al., 2018) 150

Figure 5-11 The distribution of water volume without top plate and position n1 for the nozzle at various g levels (Khan et al., 2018). 150

Figure 5-12 The changing of image during Particle Image Velocimetry (PIV) analysis (White et al., 2003) 152

Figure 5-13 GoPro 7 hero black camera setup with locked exposure time during tests.....154

Figure 5-14: (a) physical appearance of the EPB transducer; (b) schematic diagram illustrating the components of the EPB transducer (Matziaris, 2019). 157

Figure 5-15 Left: PPTs under raised water. Right: PPTs under applied vacuum. 159

Figure 5-16 Left: Automatic Pressure Controller. Right: LabVIEW collecting data. 159

Figure 5-17 PPTs calibration data..... 160

Figure 5-18 Example of PWP contours generated using the GRIDFIT method during the flooding phase of the M-Tr6 test. 161

Figure 5-19 Variation of relative humidity (RH%) over time during a one-week rain and one-week no-rain in the M-T6 test. 163

Figure 5-20 Zoomed-in view of RH% during a one-week rain and one-week no-rain cycle. 163

Figure 5-21 Humidity and temperature sensors (HM1500LF and LM35) used in experiments. 165

Figure 5-22Temperatures variation over time during the first spin of the M-T6 test. 165

Figure 6-1 Consolidated Slope Model (M-T3a) Preparation:(a): The initial consolidation process. (b): The consolidated block. 169

Figure 6-2 Shaping the consolidated soil Block: Left: Positioning the plastic template. Right: Cutting the level ground model..... 170

Figure 6-3 (a): Application of Black Seeds. (b): The model of M-T3a test and moisture control layers. 171

Figure 6-4 Schematic diagram of M-T3a test and PPTs locations. 172

Figure 6-5 Left: Drilling holes for PPTs installation. Right: Inserting PPTs at different heights in the soil block. 173

Figure 6-6 Left: Applying soil pasta. Right: Organizing and routing wires. 174

Figure 6-7: (a) LED light, camera and top plate connecting. (b): final adjustment and model setup in the centrifuge platform. 175

Figure 6-8 Slope model prepared for M-T3r test with sensor array and protective covering. 177

Figure 6-9 Detailed view of the rainfall simulation system and sensor setup on the centrifuge apparatus. 178

Figure 6-10 The final adjustment and setup of the centrifuge M-T3r test. 179

Figure 6-11 Cutting of the consolidated soil block to form a 26° slope using a template. 181

Figure 6-12 Installation of pore pressure transducers (PPTs) from previous test M-T3r to the slope model in M-T4 182

Figure 6-13 Cutting the 5-cm drainage part in the slope model using a metal plate. 183

Figure 6-14 Left: Dry soil mixing. Right: Water adding to the mixture 186

Figure 6-15 Mixing of soil mixture using mechanical mixer. 186

Figure 6-16 Left: Using a vibrating machine to compact soil layers. Right: sieving soil mixture to break up clumps. 187

Figure 6-17 Compaction of soil layers and precision measurement using laser tool in the strong box 188

Figure 6-18 Shaping the slope with plastic templates and steel wire. 189

Figure 6-19 (a) drawing reference points on Perspex viewing window and (b) preparing slope surface with black seeds for PIV analysis 190

Figure 6-20 Experimental design of the centrifuge model and rainfall simulator. 192

Figure 6-21 (a) The initial cutting of the soil using steel wire.(b) The completed slope profile. 195

Figure 6-22 Lift: Adjustments for slope angle modification in model M-T6r.Right: Removal of PPT2 to accommodate the new slope geometry. 198

Figure 7-1 PIV Analysis of Displacement and Strain Distributions During Flooding Phase in the M-T3 test. 202

Figure 7-2 Soil model with flood water level indicated in test M-T3. 202

Figure 7-3Drainage valves and PPT (Pore Pressure Transducer) Locations for M-T3a Test. 204

Figure 7-4 Pore water pressure response over time during flooding phase in M-T3 test (first configuration). 205

Figure 7-5 Pore water pressure response over time during flooding and sequential drainage phases in M-T3 test (second configuration). 206

Figure 7-6 Initial Failure Observed in the M-T3r Trial Test under Centrifuge Loading. 207

Figure 7-7 Soil model subjected to continuous rainfall and flooding phase M-T3r. 208

Figure 7-8 Pore water pressure response during continuous rainfall and flooding phase in M-T3r test. 208

Figure 7-9 PIV analysis during flood phase in M-T3r Test. 209

Figure 7-10 Slope dimension and PPTs locations. 211

Figure 7-11 Changes in pore water pressure during the consolidation and flood1 stages of the M-T4 test. 212

Figure 7-12 Pore water pressure at the end of auto balance. 213

Figure 7-13 Pore water pressure at the end of consolidation. 214

Figure 7-14 Pore water pressure and relative humidity variations during auto-balance, consolidation, winter 1, and summer 1 stages in the M-T4 test. 216

Figure 7-15 Pore water pressure and relative humidity variations during auto-balance, consolidation, winter 2, and summer 2 stages in the M-T4 test. 216

Figure 7-16 Erosion at the end of Winter 1 stage. 218

Figure 7-17 Erosion at the end of Winter 2 stage. 218

Figure 7-18 Erosion at the end of Summer 2 stage. 219

Figure 7-19 Erosion at the end of the test. 219

Figure 7-20 Displacements and strain at the end of the first winter (M-T4) test. 220

Figure 7-21 Displacements and strain at the end of the second winter (M-T4) test. 221

Figure 7-22 Water level at the end of Flood 1 in M-T4 test. 222

Figure 7-23 Pore water pressure during flood1. 223

Figure 7-24 Post-test slope failure in M-T4 centrifuge experiment. 225

Figure 7-25 View of slope failure and erosion features. 225

Figure 7-26 Slope dimension and PPTs locations. 226

Figure 7-27 Soil slope model with hydrostatic calibration during flood (M-T5 test). 227

Figure 7-28 Changes in pore water pressure during the consolidation stage of the M-T5 test. 229

Figure 7-29 Pore water pressure at the end of auto balance. 230

Figure 7-30 Pore water pressure at the end of consolidation phase. 231

Figure 7-31 Pore water pressure and relative humidity variations during different climate scenarios. 232

Figure 7-32 Pore water pressure and relative humidity variations during second spin. 233

Figure 7-33 Pore water pressure and relative humidity variations during third spin for flooding and drawdown stages. 234

Figure 7-34 Crest settlement during auto balance phase. 235

Figure 7-35 Displacements and strain at the end of auto balance phase (M-T5) test. 236

Figure 7-36 Volumetric strain at the end of auto balance. 236

Figure 7-37 Displacements and strain at the end of consolidation phase (M-T5) test. 237

Figure 7-38 PIV analysis at the end of Winter 2 (M-T5) test. 238

Figure 7-39 Pore water pressure contours at the end of Winter 2 for M-T5 test. 239

Figure 7-40 soil deformation at the end of Summer 2. 240

Figure 7-41 Pore water pressure at the end of second consolidation (M-T5) test. 241

Figure 7-42 Soil deformation at the end of Winter 3. 242

Figure 7-43 Pore water pressure at the end of Winter 3 (M-T5) test. 243

Figure 7-44 Gradual reduction of water level from above the crest to the toe surface. 245

Figure 7-45 Soil deformation at the end of Drawdown 1 246

Figure 7-46 Pore pressures at the end of Drawdown 1 at Y=195mm (when the water reaches the toe). 246

Figure 7-47 Soil deformation at the end of Drawdown 2. 247

Figure 7-48 Pore pressures at the end of Drawdown 2. 248

Figure 7-49 Crack formation and slope failure in M-T5 model. 249

Figure 7-50 Top view of cracks and toe erosion after centrifuge test for M-T5 slope. 250

Figure 7-51 Front view of slope failure and cracking in M-T5 slope model after centrifuge test. 250

Figure 7-52 Slope dimension and PPTs locations. 253

Figure 7-53 Changes in pore water pressure during the consolidation stage of the M-T6 test. 254

Figure 7-54 Pore water pressures at the end of auto balance phase (M-T6) test. 255

Figure 7-55 Pore water pressure contours at the end of consolidation phase (M-T6 test). ...256

Figure 7-56 Variation of pore water pressure (PWP) and relative humidity (RH) during the first spin in the M-T6 test. 257

Figure 7-57 variation of pore water pressure (PWP) and relative humidity (RH) during the second spin in the M-T6 test. 258

Figure 7-58 Variation of pore water pressure (PWP) and relative humidity (RH) during flood 1 and drawdown stages in the third spin of the M-T6 test. 259

Figure 7-59 Variation of Pore Water Pressure (PWP) and Relative Humidity (RH) during Flood 2, Flood 3, and associated Drawdown stages in the Final Spin of the M-T6 Test. 260

Figure 7-60 Displacements and strain at the end of auto balance phase (M-T6 test). 261

Figure 7-61 Soil deformation analysis at the end of the Drawdown 3 for M-T6 test..... 263

Figure 7-62 Pore water pressure distribution at the end of Drawdown 3 in M-T6 test. 264

Figure 7-63 Slope dimension and PPTs locations. 266

Figure 7-64 Changes in pore water pressure during the consolidation stage of the M-T6r test. 267

Figure 7-65 The contours of (PWP) during auto balance phase (M-T6r) test. 268

Figure 7-66 The contours of (PWP) during consolidation phase (M-T6r) test..... 268

Figure 7-67 Pore Water Pressure (PWP) and Relative Humidity (RH) Variations During the First Spin of the M-T6r Test. 270

Figure 7-68 PWP and RH variations during the second spin of the M-T6r test. 271

Figure 7-69 Pore water pressure (PWP) and relative humidity (RH) variations during the Third Spin of the M-T6r test with flood-drawdown attempt. 272

Figure 7-70 Pore water pressure (PWP) and relative humidity (RH) variations during multiple flood and drawdown stages in the final spin of the M-T6r test. 274

Figure 7-71 PIV analysis at the end of the second winter cycle for the M-T6r test. 275

Figure 7-72 Pore water pressure distribution at the end of winter 2 in the M-T6r slope test. 276

Figure 7-73 PIV analysis at the end of the third winter cycle for the M-T6r test.....276

Figure 7-74 Pore water pressure distribution at the end of winter 3 in the M-T6e slope test. 277

Figure 7-75 PIV analysis at the end of the first drawdown for the M-T6r test.....279

Figure 7-76 Pore water pressure distribution at the end of drawdown 1 in the M-T6r slope test. 280

Figure 7-77 PIV analysis at the end of the second drawdown for the M-T6r test.....281

Figure 7-78 Pore water pressure distribution at the end of the second drawdown in the M-T6r test. 282

Figure 7-79 PIV analysis at the end of the third drawdown for the M-T6r test. 283

Figure 7-80 Pore water pressure distribution at the end of the third drawdown in the M-T6r test. 284

Figure 7-81 PIV analysis at the end of the fourth drawdown for the M-T6r test. 285

Figure 7-82 Pore water pressure distribution at the end of the fourth drawdown in the M-T6r test. 286

Figure 7-83 (a) Cracking at the crest of the slope after failure;(b) Slope failure at the end of the M-T6r test. 287

Figure 7-84 Comparison of vectorial displacements for M-T5, M-T6, and M-T6r at the end of Drawdown 3.....292

Figure 7-85 Comparison of shear strain for M-T5, M-T6, and M-T6r at the end of Drawdown 3.....293

Figure 7-86 Comparison of Rainfall Intensity-Duration Thresholds with data from this thesis and length of rainfall at prototype (note that "DNF" denotes did not fail). Note: At first winter (1-week rain and 1-week dry) there is no failure in any test (M-T5, M-T6 and M-T6r).....299

Figure 7-87 Comparison of vectorial displacements and shear strain distributions at the end of Winter 2 and Winter 3 for the M-T5 test. 300

Figure 7-88 Comparison of vectorial displacements and shear strain distributions at the end of Winter 2 and Winter 3 for the M-T6r test. 301

Figure 8-1 Steady state flooding condition for M-T5 test. 309

Figure 8-2 Critical slip surface and factor of safety of steady-state flooding condition for M-T5 test.....309

Figure 8-3 Gradual drawdown condition with critical slip surface and factor of safety for M-T5 test.....310

Figure 8-4 Factor of safety over time during gradual drawdown scenario for M-T5 test. 312

Figure 8-5 Pore water pressure monitoring locations in slope model during drawdown scenario for M-T5 test. 313

Figure 8-6 Pore water pressure dissipation at different heights in slope during gradual drawdown for the M-T5 test. 314

Figure 8-7 Comparison of Pore Water Pressure Distribution at the End of Drawdown between Centrifuge Test (PPT Readings) and SEEP/W Numerical Model for M-T5 (Prototype Scale). 315

Figure 8-8 Pore pressure distribution and critical slip surface at 0.58 day during rapid drawdown.....316

Figure 8-9 Factor of safety vs. time during rapid drawdown condition. 317

Figure 8-10 Pore water pressure during rapid drawdown (MT5 Test). 317

Figure 8-11 Steady-State Flooding Condition for M-T5 Test. 318

Figure 8-12 Gradual drawdown condition with critical slip surface and factor of safety for M-T6 test using ϕ'=26.6°.....319

Figure 8-13 Steady-State Flooding Condition for M-T6 Test. 320

Figure 8-14 Gradual drawdown condition with critical slip surface and factor of safety for M-T6 test.....321

Figure 8-15 Factor of safety over time during gradual drawdown scenario for M-T6 test. ..322

Figure 8-16 Pore water pressure monitoring locations in slope model during drawdown scenario for M-T6 test.....323

Figure 8-17 Pore water pressure dissipation at different heights in slope during gradual drawdown for the M-T6 test. 323

Figure 8-18 Comparison of Pore Water Pressure Distribution at the End of Drawdown between Centrifuge Test (PPT Readings) and SEEP/W Numerical Model for M-T5 (Prototype Scale). 325

Figure 8-19 Steady state flooding condition for M-T6r.....326

Figure 8-20 Gradual drawdown condition with critical slip surface and factor of safety for M-T6r test. 327

Figure 8-21 Factor of safety over time during gradual drawdown scenario for M-T6r test. .328

Figure 8-22 Pore water pressure monitoring locations in slope model during drawdown scenario for M-T6r test. 329

Figure 8-23 Pore water pressure dissipation at different heights in slope during gradual drawdown for the M-T6r test.....329

Figure 8-24 Comparison of Pore Water Pressure Distribution at the End of Drawdown between Centrifuge Test (PPT Readings) and SEEP/W Numerical Model for M-T6r (Prototype Scale). 331

Figure 8-25 Comparison of numerical in the left and experimental shear strain patterns for M-T5, M-T6, and M-T6r right.....334

Figure A-1 Displacements and strain at the end of auto balance phase (M-T4) test. 2

Figure A-2 Displacements and strain at the end of consolidation phase (M-T4) test.....2

Figure A-3 Displacements and strain at the end of the first summer (M-T4) test. 3

Figure A-4 Displacements and strain at the end of summer 2 phase (M-T4) test. 4

Figure A-5 Displacements and strain at the end of flood1 phase (M-T4) test.....5

Figure A-6 End of the Winter 1 for M-T5 test.....6

Figure A-7 Pore water pressure contours at the end of Winter 1.....7

Figure A-8 PIV analysis at the end of summer 1 (M-T5) test. 8

Figure A-9 Pore water pressure contours at the end of summer 1 for M-T5 test. 9

Figure A-10 Soil deformation during Flood 1. 10

Figure A-11 Flood 1 phase of the M-T5 test in a centrifuge model. 10

Figure A-12 Pore water pressure (adjusted to theory) during Flood 1 (M-T5 test).....11

Figure A-13 Soil deformation during Flood 2. 12

Figure A-14 Pore pressures at the end of Flood2. 13

Figure A-15 Displacements and strain at the end of consolidation phase (M-T6) test.....15

Figure A-16 PIV Analysis results for the M-T6 Slope model at the end of Winter 1. 16

Figure A-17 Pore water pressure distribution at the end of winter 1 in the M-T6 slope test. .17

Figure A-18 Deformation and strain analysis of the slope at the end of summer 1 in M-T6 test. 18

Figure A-19 Pore water pressure distribution at the end of summer 1 in M-T6 test. 19

Figure A-20 Soil deformation analysis at the end of Winter 2 for M-T6 test. 20

Figure A-21 Pore water pressure distribution at the end of winter 2 in M-T6 test.....21

Figure A-22 Soil deformation analysis at the end of summer 2 for M-T6 test.....22

Figure A-23 Pore water pressure distribution at the end of summer 2 in M-T6 Test.....23

Figure A-24 Soil deformation analysis at the end of winter 3 for M-T6 test 24

Figure A-25 Pore water pressure distribution at the end of winter 3 in M-T6 Test. 25

Figure A-26 Soil deformation analysis at the end of summer 3 for M-T6 test.....26

Figure A-27 Pore water pressure distribution at the end of second consolidation in M-T6 Test. 26

Figure A-28 Soil deformation analysis during flood 1 for M-T6 test.....27

Figure A-29 Pore water pressure distribution during flood 1 in M-T6 Test.....28

Figure A-30 Soil deformation analysis at the end of drawdown 1 for M-T6 test.....29

Figure A-31 Pore water pressure distribution at the end of drawdown 1 in M-T6 Test.....30

Figure A-32 Soil deformation analysis during second flood for M-T6 test. 31

Figure A-33 Physical condition of soil slope model during second flood of M-T6 Test. 31

Figure A-34 Pore water pressure distribution during second flood in M-T6 Test.....32

Figure A-35 Soil deformation analysis at the end of drawdown for M-T6 test.....33

Figure A-36 Pore water pressure distribution at the end of second drawdown in M-T6 Test.34

Figure A-37 Soil deformation analysis during flood 3 for M-T6 test.....35

Figure A-38:The progression of water levels during Flood 3 as the water rises from the middle section of the slope (a) to the crest (b).....35

Figure A-39 Pore water pressure distribution during third flood in M-T6 Test. 36

Figure A-40 Soil slope model with hydrostatic calibration during Flood 4 of M-T6r. 38

Figure A-41 Displacements and strain at the end of auto balance phase (M-T6r) test.....39

Figure A-42 Displacements and strain at the end of consolidation phase (M-T6r) test. 40

Figure A-43 Visualisation of settlement magnitude during the consolidation phase of the M-T6r Test. 40

Figure A-44 PIV analysis at the end of the first winter cycle for the M-T6r test. 41

Figure A-45 Pore water pressure distribution at the end of winter 1 in the M-T6r slope test. 42

Figure A-46 PIV analysis at the end of the first summer cycle for the M-T6r test. 43

Figure A-47 Pore water pressure distribution at the end of summer 1 in the M-T6r slope test. 44

Figure A-48 PIV analysis at the end of the second summer cycle for the M-T6r test.....45

Figure A-49 Pore water pressure distribution at the end of summer 2 in the M-T6r slope test. 46

Figure A-50 PIV analysis at the end of the second consolidation for the M-T6r test. 47

Figure A-51 Pore water pressure distribution at the end of summer 3 in the M-T6r slope test. 48

Figure A-52 PIV analysis at the end of the first flood for the M-T6r test. 49

Figure A-53 First flooding event for the M-T6r Test. 49

Figure A-54 Pore water pressure distribution at the end of flood 1 in the M-T6e slope test. .50

Figure A-55 PIV analysis at the end of the second flood for the M-T6r test. 51

Figure A-56 Pore water pressure distribution at the end of the second flood in the M-T6e test. 52

Figure A-57 Flooded slope model at the end of the second flood event (M-T6r Test). 52

Figure A-58 PIV analysis at the end of the third flood for the M-T6r test. 53

Figure A-59 Pore water pressure distribution at the end of the third flood in the M-T6r test. 54

Figure A-60 PIV analysis at the end of the fourth flood for the M-T6r test. 55

Figure A-61 Pore water pressure distribution at the end of the fourth flood in the M-T6r test. 56

Figure A-62 Compaction procedure for M-T1 58

Figure A-63 Slope construction using wood template. 59

Figure A-64 Setup of the M-T1 kaolin slope model in the Centrifuge Box and black seeds application. 60

Figure A-65 Final adjustment and setup with rainfall simulator for M-T1test. 62

Figure A-66 (a) Initial construction phase and (b) Slope shaped and PPTs installation. 63

Figure A-67 The setup of centrifuge model and rainfall simulator for M-T2. 64

List of Table

Table 3-1 Scaling laws for rainfall parameters Askarinejad et al. (2015). 74

Table 3-2 : The experiment of rainfall infiltration: test conditions and results for case 1 (Kimura, 1991). 81

Table 3-3 : The experiment of rainfall infiltration: test conditions and results for case 2 (Kimura, 1991). 81

Table 4-1 Characteristics parameters of HST95 fraction E sand. 95

Table 4-2 Atterberg limit testing results of several soil mixtures. 102

Table 4-3 Results of standard compaction tests for different mixtures. 105

Table 4-4 Oedometer consolidation test calculation of cell 1 111

Table 4-5 consolidation parameters determined from the Rowe cell. 111

Table 4-6: Analysis of peak and critical shear stresses in shear box tests at different normal stress limits 112

Table 4-7 Fitting parameters for soil-water characteristic curve (SWCC). 132

Table 5-1: Summary of spinning tests with g levels and water pressures. 148

Table 7-1PPTs coordinate in model scale for M-T3 test 203

Table 7-2 : PPTs coordinates in model scale. 211

Table 7-3: PPTs coordinates in model scale. 226

Table 7-4 : Hydrostatic pressure calibration during flood 3 in the M-T5 test. 228

Table 7-5 Shear strength reduction at different PPT locations in the M-T5 Test. 251

Table 7-6: PPTs coordinate in model scale 253

Table 7-7: PPTs coordinates in model scale. 265

Table 7-8 Shear strength reduction and stress variation at different depths at the end of drawdown. 288

Table 7-9 Comparison of Failure Behaviour Due to Weather cycling in M-T5, M-T6, and M-T6r 290

Table 7-10 Summary of Failure Behaviour at end of Drawdown 2 for M-T5 and Drawdown 3 across M-T6, and M-T6r. 293

Table A-1 Hydrostatic pressure calibration during Flood 2 in the M-T6 test. 14

Table A-2: Calculated offsets for PPT sensors during the Flood 4 stage in the M-T6r centrifuge test. 38

CHAPTER 1: Introduction

1.1 Introduction & Motivation for Research

Infrastructure embankments are a vital part of the transport network, and it is therefore important to assess the stability of these structures. Long and/or intense rainfall events that occur in many parts of the world cause significant serviceability problems in this infrastructure via a number of mechanisms. Climate change has been known to affect the earth infrastructure performance such as clay embankments, where wet periods are associated with a higher number of slope failures. Higher average temperatures, wetter winters and drier summers, variable rainfall patterns, and temperature variations are expected to be among the effects of changing climate conditions in the UK. The performance of the UK's infrastructure slopes is changing, and more effort is needed to evaluate the potential implications of changing climate conditions in order to develop effective asset management strategies to improve the resilience. According to a preliminary estimate of the spatial distribution of unstable slopes, over 20% of the UK is classed as having a moderate to considerable hazard of slope instability. During periods of intense or continuous rainfall, this potential for slope instability can be triggered.

Pasley (1842) outlines that landslides are widespread in clay cuttings/embankments during rainy seasons during construction and in operational service some years later, because compacted clay lumps can be softened by rainfall absorption. In some cases, it is stated that slopes may be prone to slipping for up to 50 years or more after construction, depending on soil conditions and location. Flood defences generally consist of earth embankments, needing to withstand both wetting and drying as well as flooding and drawdown. Earth embankments are also an important part of road and rail networks since they serve as a basis for these crucial transportation infrastructure systems. In the context of changing climate conditions and the raised operational demand, there is significant concern about the current and future resilience of constructed slopes. Extreme rainfall or repeated seasonal cycles of pore water pressure from frequent smaller rainfall events are commonly acknowledged as some of the key driving mechanisms for slope deterioration, softening, or catastrophic failure. The Rail Accident Investigation Branch (RAIB 2014) has established a link between increasing incidences of landslides and rainfall events, and this is illustrated in Figure 1-1.

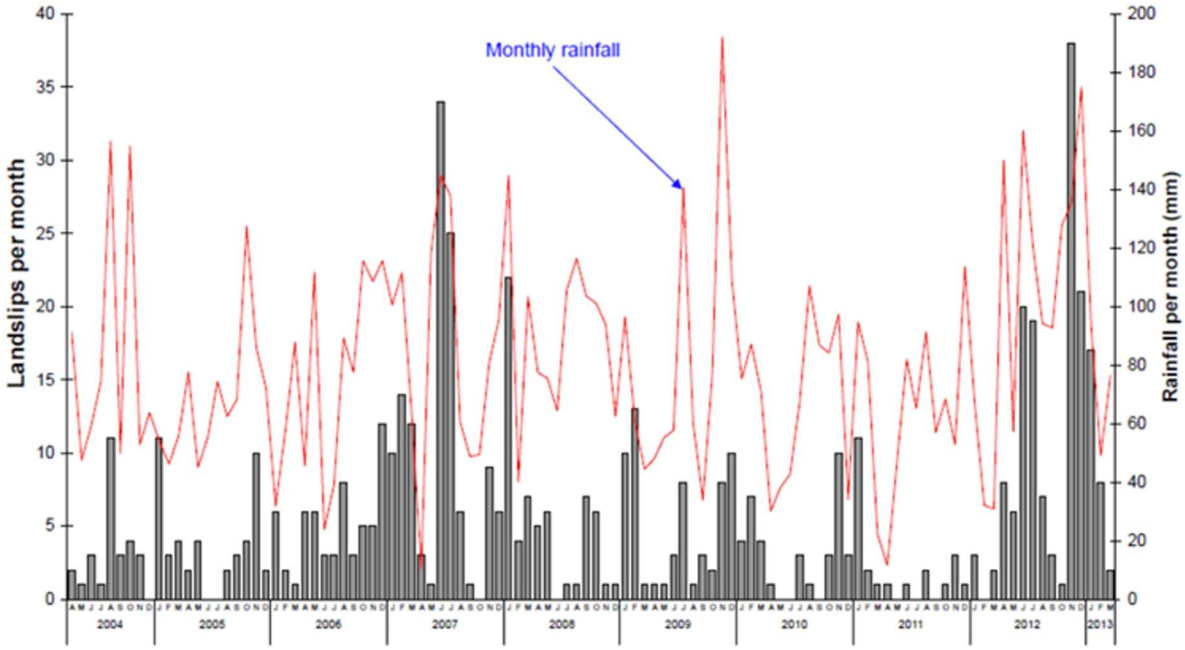


Figure 1-1 Monthly rainfall and earthwork events on Network Rail infrastructure in England & Wales. Rail (2021)

Since future climate conditions in the UK are expected to include higher average temperatures, wetter winters, and drier summers (UKCP18), thus the UK's infrastructural slopes are anticipated to become more subject to further deterioration and failure Dixon et al. (2006).

UK climate conditions & global climate change

The UK experiences diverse climate conditions, with annual average rainfall and relative humidity (RH) data from 1981 to 2010 highlighting regional variations as shown in. Rainfall ranges from approximately 600 mm in south eastern England to over 3000 mm in north western Scotland (Met Office, n.d.). The average RH is generally between 80 and 85%, fluctuating seasonally from about 70% in the summer months to over 90% in the winter. Climate change refers to long-term alterations in the statistical distribution of weather patterns, including changes in average conditions or the frequency and intensity of extreme weather events (IPCC, 2021). The observed acceleration of climate change in recent decades is primarily linked to human activities, notably the burning of fossil fuels, which has significantly increased the concentration of greenhouse gases in the atmosphere (Met Office, n.d.). Future climate projections are modelled based on three greenhouse gas emission scenarios: low, medium, and

high. At present, global greenhouse gas emissions continue to rise, aligning with medium or high emission trajectories. If these trends persist, global temperatures could increase by up to 3°C by 2050, accompanied by substantial changes in precipitation patterns, further emphasising the need for mitigation and adaptation strategies (IPCC, 2021; UKCP18).

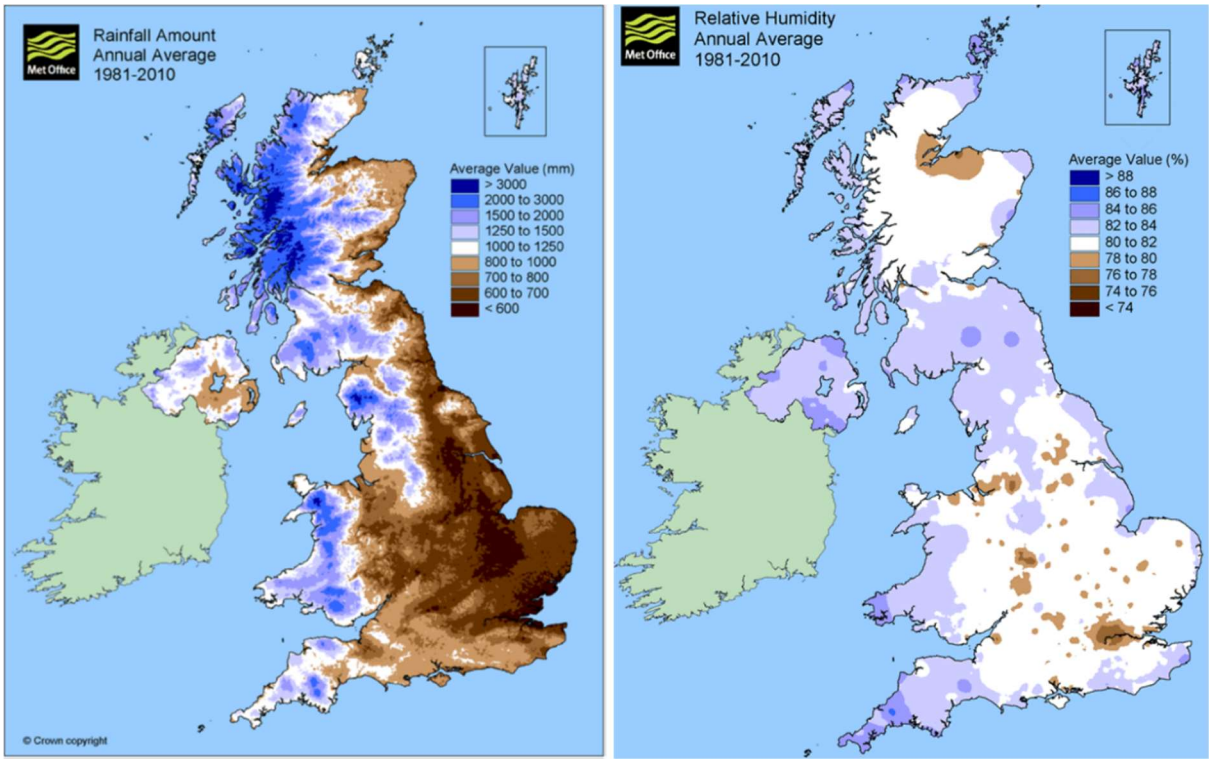


Figure 1-2 Annual average rainfall distribution across the United Kingdom (1981–2010). Kendon et al. (2021)

The relationship between rainfall, slope failure, and climate change in the UK has been extensively studied, highlighting the significant impact of changing precipitation patterns on slope stability. Increased rainfall intensity and frequency, as projected under climate change scenarios, can elevate pore water pressures within slopes, reducing their stability and increasing the likelihood of landslides. Conversely, prolonged dry periods may cause soil desiccation and cracking, potentially leading to slope failures upon rewetting Dixon and Brook (2007).

Liu and Wang (2024) developed a probabilistic framework to assess how climate change-induced precipitation scenarios affect the annual probability of rainfall-triggered landslides on specific slopes. Their methodology integrates statistical downscaling of global climate model outputs using the generalised extreme value (GEV) distribution with slope stability analysis.

By applying this approach to a case study, they demonstrated that projected increases in rainfall intensity and frequency could significantly elevate the likelihood of slope failures. This research underscores the necessity of incorporating climate projections into landslide risk assessments to inform effective mitigation strategies

The ACHILLES project, funded by the UK's EPSRC (2018-2023), focused on enhancing the resilience of geotechnical infrastructure, focusing on clay slopes, under changing climate conditions. A key aspect of the project was understanding the impact of extreme weather events, including prolonged rainfall and dry periods, on slope stability. This aligns closely with this PhD research, which investigates the effects of climate scenarios on engineered slopes, particularly under conditions of flooding and drawdown. By employing advanced numerical modelling and experimental techniques, ACHILLES examined how variations in pore water pressure and soil properties contribute to slope failure. Related to this, ACHILLES project also investigated how variations in precipitation and temperature affect slope stability. For instance, increased heavy rainfall can lead to higher pore water pressures within clay slopes, reducing their stability. Conversely, prolonged dry periods may cause soil desiccation and cracking, potentially leading to slope failures upon rewetting. These findings align with studies indicating that climate change-induced alterations in rainfall patterns significantly impact slope stability Powrie and Smethurst (2019).

The project employed advanced numerical modelling to simulate slope behaviour under various climate scenarios. These models incorporated factors such as soil properties, vegetation effects, and hydrological changes to predict slope responses to different weather patterns.. ACHILLES also explored mitigation strategies to enhance slope resilience. These include improved drainage systems, vegetation management, and the use of advanced materials to reinforce slopes.

Bračko et al. (2022) investigates the impacts of anticipated climate change on slope stability, focusing on a landslide in Slovenia triggered in 2021. The authors employed the GeoStudio SEEP/W module to model rainfall infiltration and conducted a parametric stability analysis to assess the influence of climate change on slope stability. The study emphasises that increased net infiltration due to intensified rainfall is a critical factor leading to slope instability. This aligns with findings from the ACHILLES project, which also highlights the role of extreme weather events in slope failures. The analysis reveals that low soil permeability results in a decreased factor of safety during and after rainfall events, whereas higher permeability can lead

to increased safety post-rainfall. Bračko et al. (2022) found that a linear relationship was observed between reduced soil cohesion and slope stability, with the factor of safety decreasing by approximately 0.1 for every 1 kPa reduction in cohesion. This research underscores the necessity of incorporating climate change projections into slope stability assessments. It suggests that implementing measures to reduce net water infiltration, such as vegetation planting and proper surface water management, can be cost-effective strategies to mitigate landslide risks.

Wong et al. (2022) examines how climate change influences slope stability, focusing on temperature and precipitation variations. It highlights that increased rainfall can elevate pore water pressure in slopes, reducing their stability, while higher temperatures can lead to permafrost thawing, destabilising slopes in cold regions. The authors emphasise the need for predictive models that incorporate climate variables to assess future slope stability accurately. They also discuss the importance of developing mitigation strategies, such as improved drainage systems and vegetation management, to enhance slope resilience against climate-induced instability.

Psarropoulos et al. (2024) highlighted that climate change leads to more intense precipitation events, even in regions with decreasing average rainfall. This escalation in precipitation intensity can elevate groundwater levels and induce soil erosion, both of which compromise slope stability. Changes in precipitation patterns directly influence groundwater table fluctuations, affecting pore water pressures within slopes. Elevated pore water pressures reduce the effective stress in soils, diminishing their shear strength and increasing the likelihood of slope failures. The authors emphasize the importance of understanding soil properties, such as cohesion and internal friction angle, in assessing slope stability under changing climatic conditions. They advocate for integrating hydrological data with geotechnical analyses to accurately predict slope behaviour.

This PhD research presents an experimental investigation that takes advantage of centrifuge accelerated time-scaling for seepage flow, and in order to study the behaviour of infrastructure earthworks (clay embankments) over several "years" of seasonal rainfall occurrences and flooding, and subsequent cycles of pore pressure within an atmospheric chamber that controls the boundary of climatic conditions. The project investigates how slope infrastructure responds to seasonal moisture changes and extreme flooding, in order to assess the performance and how resilient slopes are designed due to climate change conditions.

From the previous literature various factors such as the soil properties, rainfall intensity (boundary conditions), initial water table location, and slope geometry have all been shown to affect and contribute to instability of slopes during rainfall. While these studies have contributed to our general understanding of slopes, many studies have not fully replicated in-situ conditions and thus it is often difficult to translate the observations into meaningful guidance for prototype slopes. Shortcomings in model testing currently limit the application of the work to provide a useful framework on which to inform effective slope resilience strategies.

1.2 Impacts of Flooding and Drawdown on Slope Stability and Infrastructure Resilience.

1.2.1 UK Flood Embankments and Global Infrastructure Resilience.

Flood embankments play a critical role in protecting infrastructure and communities from flooding events, particularly in the United Kingdom, where extreme rainfall and rising river levels have become increasingly common due to climate change. The UK's network of flood embankments is subject to significant hydrological stress, particularly during high-water events and rapid drawdown scenarios. These events elevate pore water pressures within embankments, reducing effective stress and compromising structural stability. Study such as the ACHILLES project demonstrate the progressive failure mechanisms in embankments during such events, emphasising the need for robust design and maintenance strategies to enhance resilience.

Globally, flood embankments face similar challenges, with varying climatic and hydrological conditions influencing their performance. For instance, in Southeast Asia, regions such as the Mekong Delta frequently experience flooding due to monsoonal rains and typhoon events. Embankments in these areas often fail due to overtopping and prolonged saturation, exacerbated by inadequate maintenance and increased sedimentation. Research by Hackney et al. (2020) highlights that the interplay of river dynamics, sediment transport, and embankment material properties is critical to understanding failure mechanisms in these regions.

Similarly, in the United States, flood embankments along the Mississippi River have been subjected to extreme hydrological events, such as Hurricane Katrina in 2005. These events exposed vulnerabilities in ageing infrastructure, including under-designed embankments that were unable to withstand the combined effects of high water levels, seepage, and rapid drawdown. The American Society of Civil Engineers (ASCE) highlighted that approximately

169 miles of the 284-mile federal levee system were damaged during Katrina, underscoring the need for modernization Soga et al. (2019). Additionally, the U.S. Army Corps of Engineers admitted that faulty design specifications and substandard construction contributed to the levee failures Amjad et al. (2018). These studies emphasise the importance of modernising embankments with advanced materials and incorporating real-time monitoring systems to detect early signs of instability.

The catastrophic flooding event in Derna, Libya, in September 2023 serves as a stark reminder of the devastating consequences of extreme weather events on human settlements and infrastructure. Triggered by Storm Daniel, this disaster resulted in the unprecedented failure of two upstream dams, releasing a massive surge of water that overwhelmed the city. Reports indicate that over 11,000 people lost their lives, with thousands more displaced, highlighting the severity of the event Jazeera (2023).The failure of the Derna dams exemplifies the vulnerabilities of ageing and poorly maintained infrastructure in the face of extreme weather conditions. The floodwaters, exacerbated by climate change-induced intensification of storms, caused significant erosion and destabilisation of embankments, further magnifying the damage.

Comparative studies of embankment performance globally underscore the need for a multi-faceted approach to infrastructure resilience. These approaches include adopting advanced design techniques, such as incorporating geosynthetics for reinforcement, and leveraging numerical and physical modelling to predict performance under varying climatic scenarios. Furthermore, integrating global experiences provides valuable lessons for regions like the UK, where the impacts of climate change are becoming more pronounced.

Overview of Flood Embankments in the UK

The United Kingdom maintains an extensive network of flood embankments totalling around 35,000 kilometres, strategically located along estuaries and riverbanks. These embankments play a critical role in safeguarding infrastructure, farmland, and densely populated urban areas from the risk of flooding. Due to ongoing wear and tear, as well as the increasing challenges posed by climate change such as more frequent and intense storms these flood defences require significant upkeep. The government allocates an annual budget of approximately £450 million to cover both the maintenance of existing embankments and the construction of new flood defences. This investment ensures that embankments remain resilient against rising water levels and storm surges, thereby reducing the risk of costly flood damage and enhancing long-

term protection for communities and key economic asset. Most of these embankments are constructed using materials that are acquired from the immediate area. The resilience of these materials varies depending on the soil composition, construction methods, and maintenance procedures that have been used in the past Dyer (2004).

In the United Kingdom, the population density within floodplains is approximately three times higher than the global average, rendering urban areas, agricultural lands, and transportation networks particularly vulnerable to flooding. Recent data indicates that about one-third of urban regions experience frequent flooding, one-fourth of croplands are situated in flood-prone zones, and one-fifth of roads traverse areas susceptible to flooding. This heightened exposure has prompted increased investment in flood defences, especially in high-risk areas such as England and Wales. Cottam (2018) https://geographical.co.uk/science-environment/why-do-we-live-on-floodplains

A largescale example, the Ladybower Reservoir, with its dam and distinct overflow spillway, as shown in Figure 1-3, is a key component in managing water supply and excess water during high rainfall events, helping to mitigate potential flooding downstream. The spillway design ensures that water release is carefully controlled to prevent sudden surges, which could otherwise cause scour effects on the reservoir embankments, posing a risk of slope instability. In addition to managing day-to-day water levels, these spillways are vital for flood resilience, allowing the reservoir dam to adapt to seasonal weather patterns and extreme weather events that are becoming more common due to climate change.

The historical engineering of Ladybower and other UK reservoir dams reflects a deep commitment to provide clean potable water as well flood risk management, achieved through rigorous design standards and structural / geotechnical durability. These dam structures are maintained with regular inspections, updates to design based on modern hydrological data, and reinforcements where necessary to meet evolving safety and resilience standards.

For broader flood defence strategies in the UK, infrastructure is increasingly designed not only to withstand high water events but also to reduce the impacts of sudden drawdowns, bank erosion, and overflow. This commitment ensures that such embankments can continue to protect surrounding communities, ecosystems, and agricultural lands from the escalating threats posed by climate change while sustaining water resources critical for the UK's infrastructure.



Figure 1-3 Ladybower Reservoir Overflow Spillway. Photo by Muna Alfergani, 2024.

Historical Flood Events and Their Impact on Embankments.

The UK has a long-standing history of significant flooding from diverse sources, including coastal surges, intense rainfall, storms, and snowmelt, extending back thousands of years. In recent decades, the frequency and severity of flood events have increased considerably. Since 1998, the UK has been in what is often referred to as a "flood-rich" period, characterised by an elevated occurrence of high-impact flooding events Bruen and Gebre (2001). Between 1998 and 2009, flood events increased by 70% Penning-Rowsell (2021), marking the beginning of an unusually wet period that extended through the prolonged flooding of 2013/14 and the record-breaking rainfall and flooding of 2015/16. These intense weather events impacted numerous regions, leading to significant damage, service disruptions, and substantial economic losses for businesses Marsh et al. (2016). In the UK, surface water flooding accounts for over 50% of all flood events Penning-Rowsell (2021). The Joseph Rowntree Foundation estimates that coastal flooding represents 40% of the overall flood risk, though some researchers consider this figure to be overestimated (Penning-Rowsell, 2021). Over nearly a century, the UK has experienced severe coastal flooding on only three occasions—on the East Coast in 1953, in Towyn in 1990, and across extensive areas in 2013/14. These events were classified as coastal floods due to their primary cause being storm surges and coastal inundation. In contrast, the

country has faced at least eight significant fluvial flooding events, with major incidents recorded in 1947, 1968, 1998, 2000, 2007, 2012, 2013/14, and 2015/16. Notably, while the 2004 Boscastle flood was a significant event, it is categorised as a fluvial flood caused by intense rainfall and river overflow, which explains its exclusion from the coastal flood records. Coastal flooding has a very low annual probability (under 0.1%) of causing extreme damage; however, when it occurs, it can lead to economic losses amounting to billions of pounds Penning-Rowsell (2021).

Notable floods in 2007, 2013, 2014, and 2019 caused extensive damage across the country, highlighting vulnerabilities in infrastructure and prompting ongoing improvements in flood management strategies. These floods resulted in substantial damage to flood defenses and embankments, exposing vulnerabilities in existing infrastructure, especially along critical waterways like the River Thames and River Severn. In response, each event prompted a review and improvement of embankment design, construction standards, and maintenance practices. The repeated failures highlighted the need for more durable construction materials and enhanced slope stability measures, particularly as climate change continues to increase the frequency and intensity of severe weather events. In June 2019, Wainfleet experienced an exceptionally prolonged rainfall event, with an unprecedented 132 mm—equivalent to two and a half months' worth of rain—falling between June 10 and June 12 and continuing into June 13. This heavy rainfall caused the River Steeping and its relief channel to overflow (Figure 1-4 (b)), flooding numerous properties in Wainfleet and nearby Thorpe St. Peters (Figure 1-4(a)). By Monday, June 17, water levels in the River Steeping and its relief channel had notably decreased, but further heavy rainfall persisted until June 19. By June 21, evacuated residents began returning, only to find that 59 properties had been flooded Bang and Burton (2021).

Bang and Burton (2021) examined flood risk perceptions (FRP) in England with a case study focusing on Wainfleet in Lincolnshire, a community that suffered greatly from floods in June 2019. The research underscores the growing frequency and intensity of floods in England, exacerbated by climate change. Findings reveal that community members affected by the flood faced both physical and psychological impacts, with challenges including insufficient funding, low risk awareness, and a lack of preparedness. Despite a multi-agency response to the 2019 floods, the study identified gaps in climate risk management (CRM), particularly regarding public awareness and community involvement in flood risk mitigation.



(a) (b)

Figure 1-4 (a) Aerial view of flood-affected areas in Wainfleet, Lincolnshire. (b) Military helicopters dropping sandbags along breached riverbanks to contain flooding. Source: Sun Reporter (2019).

The Mississippi River Levee System: Engineering Adaptations and Historical Developments in Flood Control.

The Mississippi River and Tributaries (MR&T) project relies heavily on levees for flood control, protecting the alluvial valley from Mississippi River overflows. The levee system stretches from Cape Girardeau, Missouri, to Venice, Louisiana, covering about 3,787 miles, with significant improvements since the Great Flood of 1927. Technological advancements have enhanced the levee's integrity with features like landside berms and drainage systems. The levee system is designed with freeboard to prevent overtopping during floods, with specific provisions for areas like New Orleans due to coastal storm surges. Additional measures, such as floodways and reservoirs, are employed to manage floodwater during extreme conditions Tide (1997).

Historically, the levee system dates back to 1717, with the French constructing the first levee in New Orleans. Over time, the system expanded with contributions from landowners, states, and eventually federal involvement, especially after the devastating floods of 1927. The Mississippi River Commission, formed in 1879, played a crucial role in coordinating levee construction and maintenance. The 1928 Flood Control Act marked a pivotal shift, authorising

comprehensive flood control measures and federal funding for levee improvements without requiring local financial contributions.

The Mississippi River levee system has undergone extensive modifications since its inception, adapting to the demands of flood control and infrastructure resilience in the Mississippi River and Tributaries (MR&T) Project. The cross-sectional diagram (Figure 1-5) demonstrates the levee's structural evolution across key periods, reflecting legislative and engineering advancements. Initially modest in scale, the levees have been systematically enlarged—first under the 1914 guidelines, with significant height increases in 1928 following the Great Flood, and further expansions between 1942 and 1972 to accommodate growing flood control needs. The addition of a roadway in more recent years also highlights the levee's multifunctional role, providing both flood protection and logistical support for maintenance and inspection. This progressive enhancement underscores the system's ongoing adaptation to regional hydrological challenges, incorporating freeboard for high water stages and integrating new materials and engineering techniques for improved durability Kemp et al. (2014).

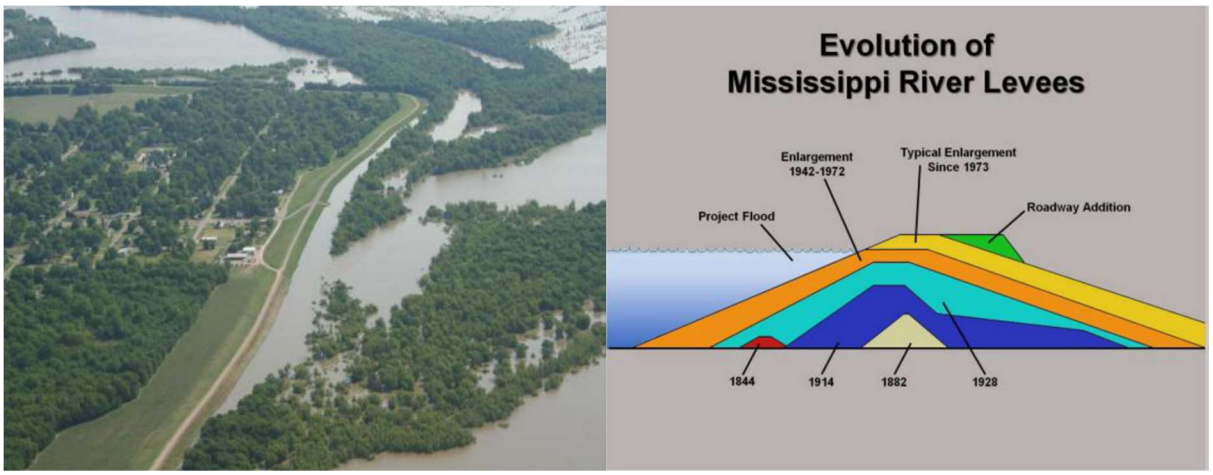


Figure 1-5 Left: Aerial view of the Mississippi River levee; Right: Cross-sectional diagram illustrating the historical evolution of the Mississippi River levee. (n.d.) (2017)

Drawdown-Induced Failure: Mississippi River Case Study

The failure of a 250-meter section of levee along the Mississippi River, Louisiana, USA, on August 8, 2023, provides a striking example of the risks associated with rapid drawdown scenarios in major river systems. The levee failed on the riverside shortly after high water levels

receded, exposing critical vulnerabilities in the embankment's design and maintenance. This failure underscores the significant impact of transient hydrological conditions, where rapid reductions in water pressure on the riverside create destabilising forces within the embankment. The drawdown-induced failure mechanism is characterized by a mismatch in hydraulic gradients, leading to increased seepage forces and pore water pressure reductions, which in turn compromise the levee's structural integrity. This event is consistent with findings from studies such as Pinyol et al. (2008) which emphasize the importance of accounting for rapid water level changes in slope and levee stability assessments. The Mississippi case highlights the role of aging infrastructure and insufficient real-time monitoring systems in exacerbating the failure risk during extreme hydrological events.

This event further illustrates the need for proactive management strategies, such as improving seepage control measures, upgrading levee materials to withstand fluctuating pressures, and incorporating advanced numerical modelling techniques to predict the embankment's response to drawdown conditions. The Mississippi River drawdown failure serves as a critical global example, demonstrating the urgent need for resilient infrastructure to mitigate the increasing risks posed by climate change-induced hydrological extremes.



Figure 1-6 Levee failures along the mississippi river due to rapid drawdown and high-water events. Pinyol et al. (2008)

The Failure of the Derna Dams in Libya and the Impact of Hurricane Daniel

The catastrophic failure of the Derna dams in Libya highlights the devastating impact of extreme weather events on ageing infrastructure, particularly in regions vulnerable to climate change. In September 2023, Hurricane Daniel, a powerful Mediterranean tropical-like cyclone,

brought unprecedented rainfall and severe flooding to northeastern Libya, significantly affecting the city of Derna. This intense rainfall overwhelmed the two main dams situated above the city, the Derna and Mansour dams leading to their collapse. Figure1-7 illustrates the aftermath of the catastrophic flooding in Derna, Libya, showing the extensive damage to the city and the locations of Dam 1 and Dam 2 collapses along the Wadi Derna River, which contributed to widespread devastation across the region. The breaches in these dams released an overwhelming volume of water, which cascaded through the valley with force, inundating neighbourhoods, collapsing buildings, and rendering essential services inoperable. The impact on the low-lying areas of Derna near the coast was particularly severe, with floodwaters completely submerging homes, businesses, and roadways, leaving an indelible mark on the landscape.



Figure1-7 Aerial view showing the locations of Dam 1 and Dam 2 breaches along the Wadi Derna River, with images of the extensive urban destruction in Derna, Libya. (Alkomaty.J,2023). https://www.aljazeera.com/

The Derna dam system, originally constructed in the 1970s to manage seasonal floods and provide water storage, had not received adequate maintenance over the years. Despite their importance to the region's flood control infrastructure, both dams suffered from prolonged neglect, which left them structurally vulnerable. As Hurricane Daniel unleashed extraordinary rainfall, the reservoirs quickly reached critical levels. The dams were unable to withstand the pressure, ultimately failing and releasing an overwhelming surge of water downstream.

It is estimated that thousands of people lost their lives, with many more injured or displaced. The disaster has drawn attention to Libya's infrastructure challenges, exacerbated by years of conflict and political instability, which have hindered the upkeep and modernisation of critical flood protection structures Gazzini (2023). Figure 1-8 illustrates the severe impact of the September 2023 floods in Derna, Libya. The left image shows the remains of the Wadi Bu Mansur Dam, located 13 km south of Derna, which collapsed under the unprecedented floodwaters. The right image highlights the extensive damage in the low-lying coastal areas of Derna, where the floodwaters caused widespread destruction, devastating infrastructure and residential areas.



Figure 1-8 Left: Remains of the Wadi Bu Mansur Dam, after its collapse due to catastrophic floods, September 2023. Right: Devastated low-lying areas near the coast in Derna, severely impacted by the flooding. (Gazzini, 2023) & https://www.bbc.co.uk/news/world-africa-66785466 (BBC News, 2023).

Imran et al. (2024) provided an in-depth analysis of the catastrophic flooding in Derna, Libya, following the failure of the Derna and Bu Mansour dams. The study combines hydrological and hydraulic modelling to explore various scenarios, including dam breaches and their cascading effects on downstream areas. Key findings highlighted that the extreme runoff from Storm Daniel was far beyond the design capacity of the dams, suggesting that even if the dams had survived, they would have offered minimal protection against such extreme events. However, the dams' structural failure generated a devastating flood wave, resulting in significant loss of life and infrastructure destruction Imran et al. (2024). The authors recommend moving away from over-reliance on structural measures alone, advocating for

better flood management practices, evacuation plans, and public awareness to mitigate the impact of future extreme weather events.

1.3 Research Aim and Objectives

Research Aim

The overarching aim of this project is to investigate the performance and resilience of engineered slope infrastructure under changing climate conditions. This study seeks to assess how climate-induced factors, such as rainfall intensity, prolonged wet-dry cycles, and extreme weather events like flooding and drawdown, affect embankment slope stability. By understanding these influences, the project aims to contribute valuable insights toward enhancing the durability and operational lifespan of flood embankment infrastructure.

Research Objectives

To achieve the research aim, the specific objectives are as follows:

1. Development of Climate Chamber Testing Protocols

    - Characterise a highly non-plastic gap-graded sandy clay soil used in centrifuge testing to simulate realistic embankment materials.
    - Develop and calibrate a climate chamber to replicate controlled non-extreme wetting and drying cycles for embankment slopes under laboratory conditions.

2. Investigation of the Impact of Non-Extreme Wetting and Drying Cycles on Slope Performance
    - Evaluate the influence of repeated wet-dry cycles on soil strength, permeability, and deformation characteristics.
    - Assess the implications of these changes on long-term slope performance and stability.

3. Analysis of Flooding and Drawdown Effects on Slope Stability

- Examine the effects of flooding and drawdown scenarios on pore pressure distribution, slope deformation, and failure mechanisms.
- Investigate the role of rapid drawdown and gradual drawdown rates in initiating slope failure under centrifuge-scale conditions.

4. Numerical Analysis and Validation
    - Use numerical modelling techniques (e.g., GeoStudio) to simulate the effects of wet-dry cycles, flooding, and drawdown on slope stability.
    - Validate numerical results with experimental findings to improve model reliability for predicting slope performance under climate scenarios.

5. Contribution to Slope Infrastructure Design and Resilience
    - Synthesise findings to provide practical insights into slope resilience under changing climate conditions.
    - Identify key vulnerabilities and recommend strategies to enhance the operational service life of engineered slope infrastructure.

1.4 The Outline of the Thesis

Chapter 1: Introduction

- Background and significance of slope infrastructure in civil engineering.
- Motivation for studying climate impacts on slope stability.
- Objectives of the research.

Chapter 2: Literature Review:

- Overview of slope stability analysis and challenges under changing climate conditions.
- Review of relevant works, including Kumar (1996) and Take (2003) insights.
- Understanding slope failure mechanisms, pore pressure behaviour, and seepage.
- Establishes a foundation in unsaturated soil mechanics, rainfall infiltration, and climate-induced slope instability.

Chapter 3: Centrifuge Modelling in the Literature

- Fundamentals of centrifuge modelling, including scaling laws for stress, seepage, and rainfall simulation.
- Previous studies on centrifuge modelling for slope stability under rainfall, flooding, and drawdown.
- Identified gaps in the literature addressed by this research.

Chapter 4 to 6: Soil Characterisation and Model Preparation

- Chapter 4 describes the soil mixture composition, geotechnical characterisation, and the laboratory tests conducted to determine key soil properties, including plasticity, permeability, and strength parameters.
- Chapter 5 details the experimental setup, including the centrifuge modelling configuration, instrumentation, and applied climate scenarios. The methodology for simulating rainfall events, flooding, and drawdown processes is also outlined.
- Chapter 6 presents the specific test procedures, highlighting the variables considered in the experiments, such as rainfall intensity, flooding durations, drawdown rates, and g-level adjustments. The instrumentation setup for monitoring slope deformation, pore water pressures, and failure mechanisms is also discussed.

Chapter 7: Experimental Results

- Centrifuge test results and slope failure observations under climate-driven conditions.
- Displacement and crack formation analysis using Particle Image Velocimetry (PIV).
- Pore pressure measurements, vectorial displacement patterns, and seepage effects.
- Experimental challenges, including solenoid valve malfunctions, leakage issues, and optical reflections affecting PIV analysis.
- Performance of slope models under different climate scenarios:
    - Impact of rainfall intensity and duration.
    - Flooding phases and their effect on slope deformation.
    - Comparison of gradual vs. rapid drawdown behaviours.

Chapter 8: Numerical Analysis

- Numerical modelling in GeoStudio:
- Steady-state seepage, gradual drawdown, and rapid drawdown stages.
- Factors of safety for each condition.
- Discussion on slope-parallel and angled pore pressure contours.
- Insights into the numerical results and comparison with experimental findings.
- Correlation between experimental and numerical results.

Chapter 9: Conclusions and Recommendations

CHAPTER 2: Literature Review

2.1 Introduction

Occurrences of slope failures induced by long and/or intense rainfall events that occur in many parts of the world lead to significant serviceability issues in infrastructure embankments via a number of mechanisms. It is widely known that performance of clay embankments is affected by weather, particularly during or following wet periods of intense or lengthy rainfall. However, possibly the most important factor contributing to slope instability is changing of pore water pressure and shear strength of the soil due to rainfall infiltration that causes increase in the ground water level and rapid development of pore water pressure under a flood scenario. This Chapter provides a foundational understanding of the principles of unsaturated soil mechanics and their relevance to slope stability. Key topics include the role of pore water pressure, soil-water retention behaviour, and the factors influencing slope performance under variable climatic conditions. Specific principles related to centrifuge modelling, such as scaling laws and test setup considerations, will be discussed in detail in Chapter 3. By establishing these principles, this chapter sets the stage for analysing the effects of climate-induced factors such as rainfall infiltration, flooding, and drawdown on slope stability in subsequent chapters.

2.2 Unsaturated soil

2.2.1 Shear strength behaviour and stress state variable of unsaturated soil.

It is known that the unsaturated soil consists of three phases, that are particles of soil, pore water and pore air. Understanding the behaviour of unsaturated soil for example, seepage, volume change and shear strength can deal with many unexpected failures that may occur in engineering structures and slope stability is an example of such a problem. Generally, it is important to determine the shear strength of the unsaturated soil and any change in shear strength that may occur as a result of water infiltration into the soil Fredlund et al. (2012).

The stress state in unsaturated soil has been described as a function of the net normal stress (σ - u_a) with matric suction (u_a - u_w). Hence the matric suction is considered to be the most important parameter for describing unsaturated soil. However, the two independent stress state variables were introduced in Equation *2-1* that was proposed by Bishop (1959).

$$\sigma' = (\sigma - u_a) + \chi(u_a - u_w) \qquad 2\text{-}1$$

Bishop's equation referred to the relationship between the effective stress (σ') in an unsaturated state with net normal stress (σ - u_a) and matric suction (u_a - u_w). Where χ is known as an effective stress parameter which is related to the degree of soil saturation and varies between 0 to 1. Several studies have shown experimental results that demonstrate the relationship between the effective stress parameter and saturation degree for different soils.

Figure 2-1 illustrates the parameter χ in Bishop's equation assumed to be unity when the soil is fully saturated which reverts to the effective stress given by Terzaghi's equation. In other words, Bishop's equation used these two independent stress state variables to formulate the fundamental equations in assessing the shear strength and volume change behaviour of unsaturated soil.

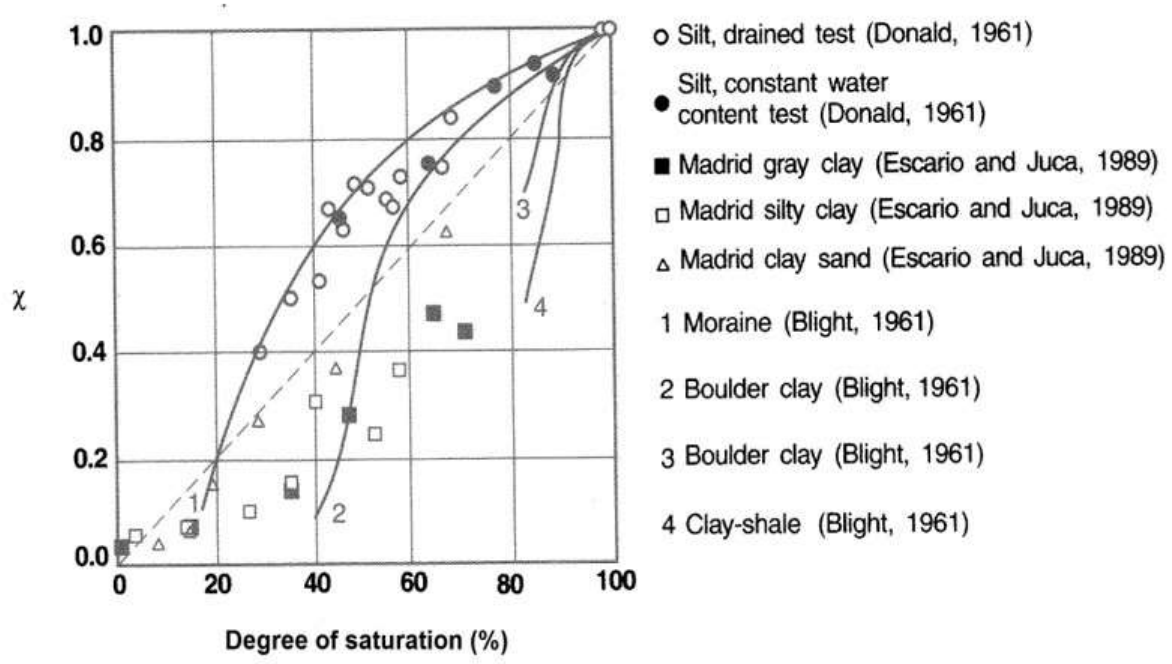


Figure 2-1 Degree of saturation and Bishop's effective stress χ after (Lu&Likos,2004).

2.2.2 Extended Mohr-Coulomb Failure Envelope

Fredlund et al. (1978) presented an extended Mohr-Coulomb failure envelope for unsaturated soil. A new variable, $ø^b$ is introduced in this criterion that ranges from 0 to $ø^b$ and clarifies the impact of soil suction on the shear strength of the soil. Sheng et al. (2011) reported $ø^b$ values of approximately 15° for a sandy clay and 10° for a silty clay, highlighting the variability of this parameter. Determining $ø^b$ through laboratory testing is essential for accurately analysing the stability of slopes under unsaturated conditions. The shear strength of an unsaturated soil is then presented in relation to two stress-state variables *:$(\sigma - u_a)$* and *$(u_a - u_w)$* as written in *2-2*.

$$\tau_f = c' + (\sigma - u_a)_f tan ø' + (u_a - u_w)_f \, tan ø^b \qquad 2\text{-}2$$

Where τ_f is the shear strength of the unsaturated soil, $(\sigma - u_a)_f$ is the net normal stress on the failure plane at failure c' is the cohesion at zero matric suction, ø' is the internal angle of friction that relates to the net normal stress variable, $(u_a - u_w)$ is the matric suction at failure phase and $ø^b$ is the strength parameter used to relate shear strength to the stress state variables. The failure envelope for unsaturated soil is illustrated as a surface on a shear stress - net normal stress - matric suction graph, as shown in Figure 2-2.

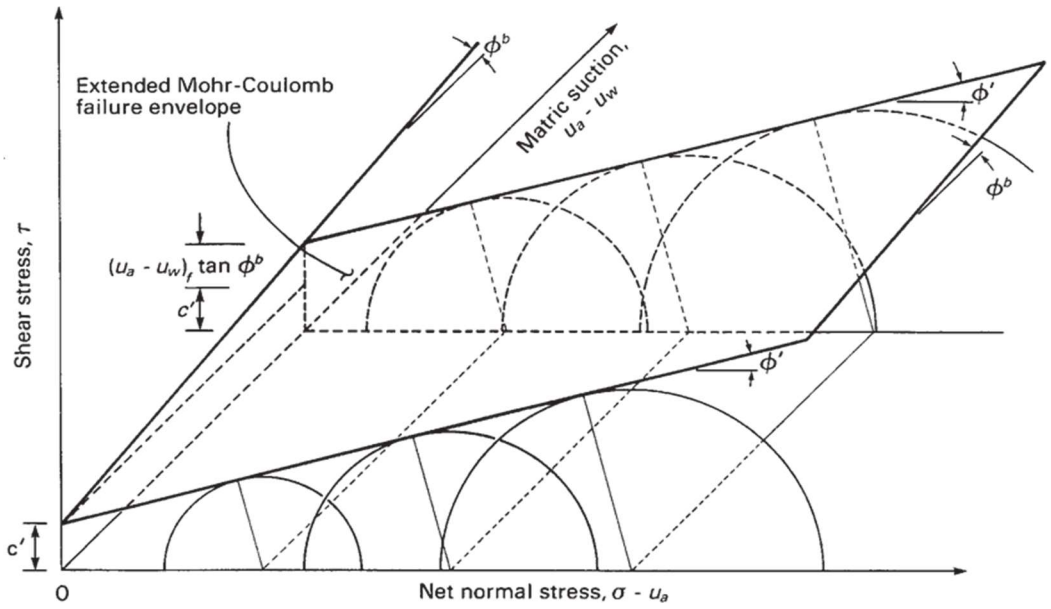


Figure 2-2 Extended Mohr-Coulomb failure envelope for unsaturated soils (Fredlund and Rahardjo, 1993).

2.2.3 Relationship between tan $ø^b$ and χ.

Bishop et al. (1960) and Fredlund et al. (1978) established shear strength equations that appear to be similar in form. Thus, Equation *2-3* shows the relationship of the shear strength obtained by equating the linear shear strength form of Fredlund et al. (1978)'s equation and the yield equation of Bishop et al. (1960). Therefore, the parameter χ in Equation *2-3* can be solved as written in Equation *2-4*.

$$(u_a - u_w)_f tanø^b = \chi(u_a - u_w)_f \ tanø' \qquad 2\text{-}3$$

$$\chi = tanø^b / tanø' \qquad 2\text{-}4$$

Figure 2-3 illustrates the relationship between shear strength and shear strength parameters $ø^b$ and χ. When utilizing Fredlund et al. (1978) and due to matric suction, shear strength increase is represented as an upward translation of the saturated failure envelope. The upward translation amount is equivalent to (u_a - u_w *tan* $ø^b$); point A in the figure.

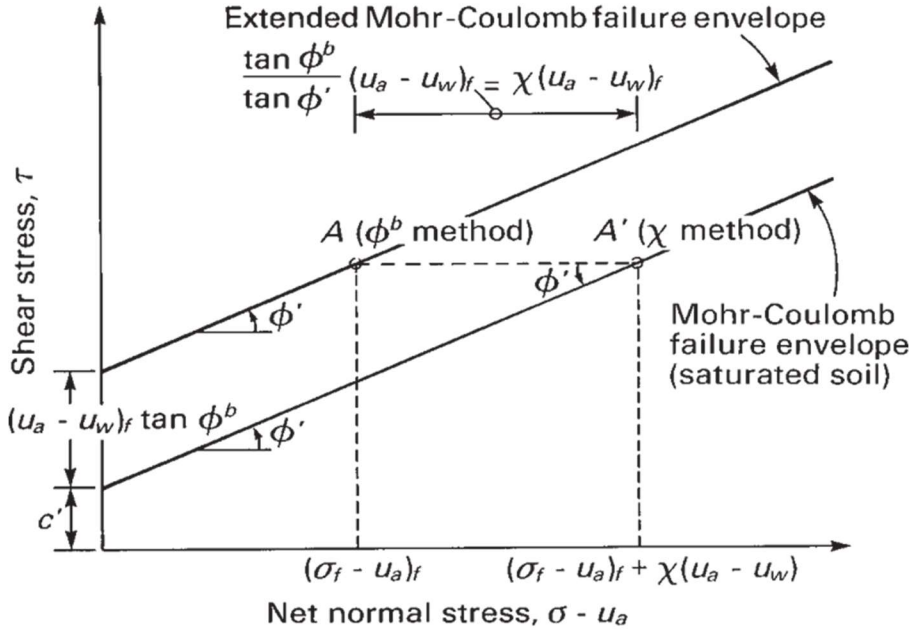


Figure 2-3 Comparison between both methods b and x to specify shear strength, after Fredlund (2006).

According to the equation proposed by Bishop et al. (1960) using the χ parameter, saturated and unsaturated states share the same failure envelope, while the net normal stress increases due to matric suction. According to the Bishop et al. (1960) equation using the χ parameter, saturated and unsaturated states have the same failure envelope, while the net normal stress increases as a result of matric suction. The net normal stress increases by a fraction of the matric suction at failure as presented in Figure 2-3. The shear strength at point *A* using the ϕ^b method is the same as the shear strength at point *A'* found by the χ parameter method.

2.2.4 Measurements of pore water pressure.

Under both saturated and unsaturated conditions, the existence of negative pore water pressures can be found within the soil above the ground water level. The applied tension on the air - water interface due to negative pore water pressure participates in the shear strength of the soil. The increase of soil saturation degree as a result of infiltration during rainfall events leads to increase in pore water pressure (from negative) within the soil. Therefore, this has an effect on the reduction of soil strength, and consequently has an impact on slope stability.

2.2.4.1 The role of matric suction on slope stability.

The volumetric and mechanical responses of soil elements are influenced by the presence of soil suction in unsaturated soil. All theories and design approaches for unsaturated soil have relied on soil matric suction.

Matric suction is defined as the difference in pressure between the pore air pressure u_a and the pore-water pressure u_w Fredlund and Rahardjo (1993). A water molecule at the air-water interface is subjected to unbalanced molecular forces, resulting in a "tensile pull" along the interface. A meniscus forms at the air-water interface resulting from surface tension which causes reduction of vapour pressure in the water (surface tension is typically described as the maximum amount of energy that a fluid has to hold before breaking apart). The vapour pressure decreases and trends to a more negative value so that the matric suction pressure increases as the radius of curvature of the meniscus decreases, Likos et al. (2019).

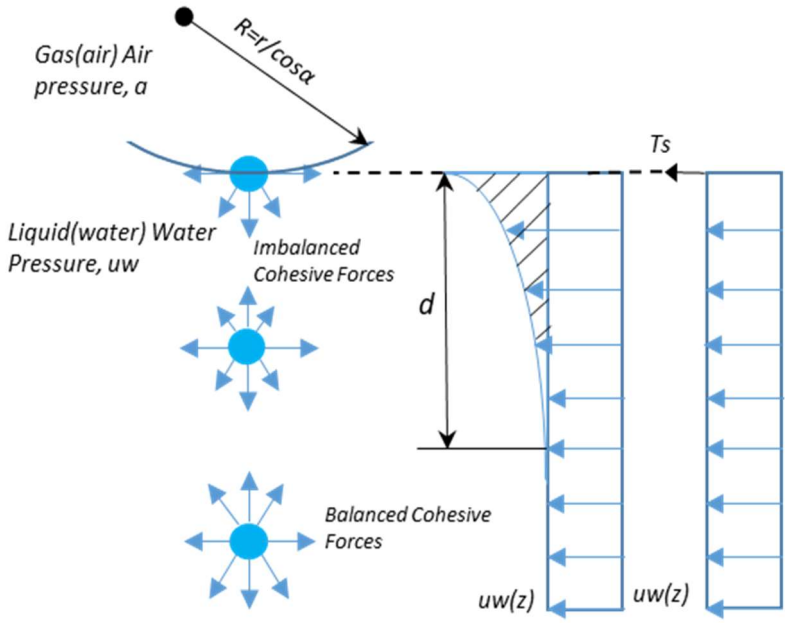


Figure 2-4 Surface tension at the interface of the water and air conceptual pressure distribution with depth from the interface Likos et al. (2019).

The intermolecular cohesive forces at the surface containing polar molecules, such as water, and the associated surface tension are relatively high. Since the pressure on the water side is lower than the pressure on the air side, the interface takes on a concave shape. The angle of contact is dependent on the radius (pores in the soil), and the membrane curvature radius. However, the contact angle varies depending on the type of soil grains. The difference of pressure between the two sides is controlled by the membrane's shape. The determination of pressure difference depends on force equilibrium:

$$u_a - u_w = {}^{2T_s \cos \alpha}/_{R} \qquad 2\text{-}5$$

In which the difference between air pressure and water pressure represents the value of the matric suction, (*Ts)* is the tension force of the surface and α refers to the membrane's contact angle with the container wall (the grains of soil). According to Equation *2-5* the smaller value of meniscus radius leads to larger increase of matric suction. As a consequence, soils which have smaller pores space and/or hold less moisture content produce greater suction values.

2.2.5 Stress profiles, moisture content and pore pressure of unsaturated soil.

The profiles of subsurface moisture, suction, and stress are affected by soil and pore water characteristics, including the climate condition. The balance distribution and pore water flow inside the soil profile are all affected by the type of soil, particle size distribution, and the distribution of pore size. The changes of flow and pore water subsurface distribution are affected by atmospheric factors such as relative humidity, the degree of temperature, wind speed, and rainfall. Lu and Likos (2004) provides an illustration of stress patterns that occur in sandy soil for both saturated and unsaturated situations as shown in Figure 2-5.

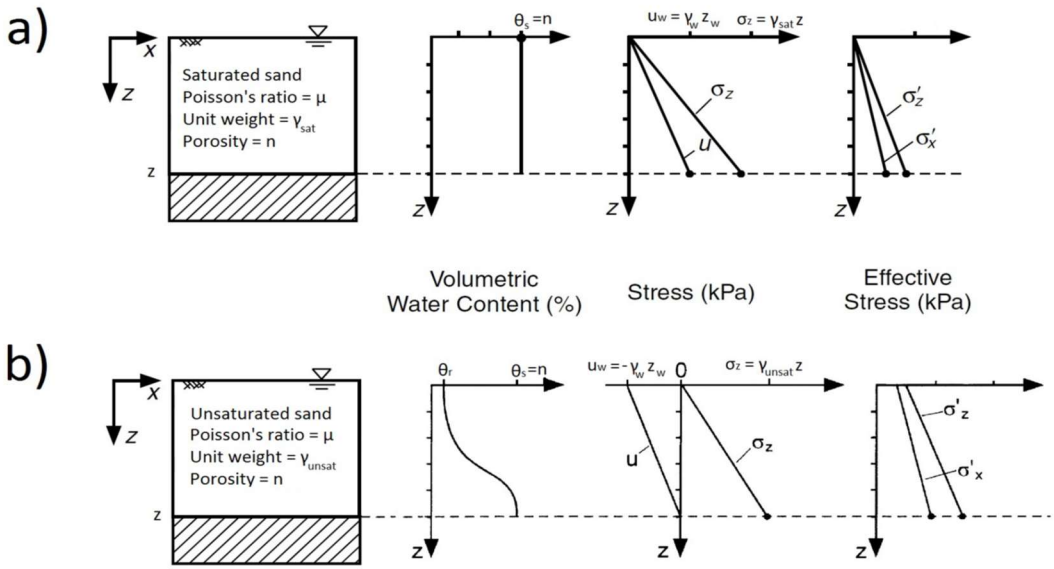


Figure 2-5 Stress patterns that occur in sandy soil for both saturated and unsaturated situation Lu and Likos (2004).

The level of the water table in the first example (a) is situated at the soil surface, whereas in (b) at depth z. In a saturated situation the volumetric water content *(θ)* stays stable ($\theta = \theta_s$), whereas in unsaturated cases (θ) may range from the residual value (θ_r) near the surface of the soil to the saturated value (θ_s) at the the water table. Pore water pressures above the level of the water table are negative in the case of a low groundwater level (Figure 2-5(b)), and distributed linearly with depth under the state of hydrostatic equilibrium below and above the water table, until air entry is reached (see below).

2.2.6 Soil-Water Characteristic Curve (SWCC).

The Soil Water Characteristic Curve (SWCC) defines the relationship between water content and suction Williams and Shaykewich (1970). The SWCC is illustrated in Figure 2-6, and has been extensively used to estimate properties such as shear strength, permeability, pore size distribution and volume change Vanapalli et al. (1996). It is known that the gravimetric, volumetric, and saturation degree are three methods to determine the amount of water in the soil Tuller et al. (2004). Accordingly, a typical SWCC illustrates the essential features of the soil water characteristic (such as the air entry value and residual state of saturation). The suction value range is plotted on a semi-log scale from 0 to 10^6 kPa and is correlated with the degree of saturation. The most essential parameters that determine the amount of moisture content within soil pores that correspond to the required suction are demonstrated in this curve.

The typical soil water characteristic curves demonstrate three main stages of desaturation which are known as the saturation zone, the transition zone and the residual zone. In the first stage, pores between soil particles are largely filled with water and suction increases considerably inside the saturation zone once the soil loses a small quantity of moisture. The capillary zone is represented by this segment of the curve, which illustrates a state when the soil remains almost saturated while the matric suction increases. The Air Entry Value (AEV) is the point at which matric suction is sufficient to enable the air to enter into the mass of the soil. In the second part, the SWRC curve turns nearly linear after the AEV, which indicates a smooth increase in suction and corresponding a reduction in the saturation of soil. Considering this segment of the curve, the slope in the transition zone is influenced by the kind of soil, and increases when the soil grains become coarser. Concerning the residual zone which begins when the soil becomes saturated or at residual water content where at this stage the suction increases considerably the soil saturation decreases slightly.

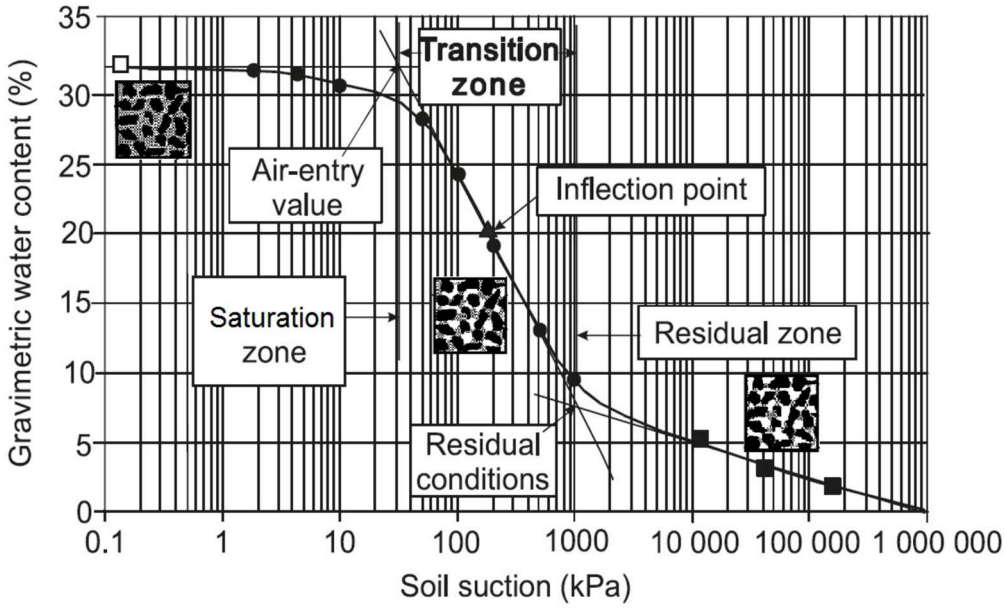


Figure 2-6 demonstrates desaturation zones of a typical soil water characteristic curve Vanapalli et al. (1999).

Considering several types of soil, the SWCC has been illustrated in terms of suction value, which corresponds to a volumetric water content. Figure 2-7 shows a typical SWCC of various types of soil. Noticeably, there is a rapid change in the degree of saturation for the coarse-grained soil, that contains wide and interconnected pores, with a significant increase in suction value. The specific suction value corresponds to the soil storage capacity of water, in particular for the soil that has a high percentage of fine particles. Likewise, for finer soils, the air-entry value is higher. Consequently, the residual state of saturation increases with the increase of fine grains in the soil.

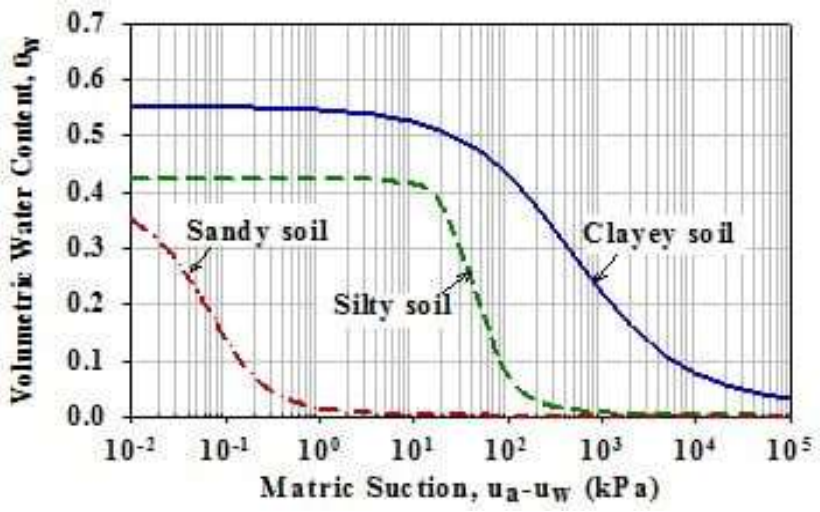


Figure 2-7 Soil-water Characteristic Curves for different soil types Fredlund et al. (2012).

2.2.7 Flow of water within unsaturated soil.

The prediction of movement of water through unsaturated soil has been assessed using a range of approaches. For instance, the gradient in water content, suction matric, and the gradient of hydraulic head have each been proposed as the driving force that causes water to flow through the pore spaces in the soil.

The gradient of water content method considers water to flow from a point that has higher water content to a point with a lower water content through the layers of unsaturated soil. However, water might move from a zone that has lower water content to a region of higher water content because of differences in the soil type or state. Thus, the essential concepts of water content gradient cannot describe the driving force for water flow. Alternatively, a matric suction gradient has been utilised as the driving force of water movement. However, water flow is not completely dependent on a matric suction gradient because of the differences of pressure gradient for the individual phases of unsaturated soil such as, water and air. As a consequence, even though the suction gradient may be equal to zero, water movement is likely due to the changing of air and water pressure gradients. Hence, water does not always flow from a point of low suction to a point of higher suction, even if the height of head remains constant. Therefore, hydraulic head gradient is the most suitable term used for describing water flow in unsaturated soil Fredlund (2006). The pressure head gradient in the water phase, as well as a gradient due to the differences of head elevation control the water flow within any soil. The gradient is given to the hydraulic head, which constitutes the basic process of water movement within the soil, by combining the pressure and height gradient in a linear manner.

In conclusion, the hydraulic head is considered to be the essential driving potential that causes the water flow in both saturated and unsaturated soils Fredlund et al. (2012). Most numerical models follow this approach, meaning that numerical modelling of both the strength of soil and of flow in soils where there may be an unsaturated condition requires a knowledge of the SWCC.

2.3 Instability of slopes in unsaturated soil.

2.3.1 Rainfall infiltration mechanism.

The slope instability and landslides caused by rainfall are natural tragedies that occur all over the world, especially in regions of residual soil that are subject to heavy rainfall. It is widely acknowledged that the change in pore water pressure and seepage forces are the main cause of slope instability Gerscovich et al. (2006). As a result of the increase in pore water pressure caused by infiltration, effective stresses are reduced and, which decrease the soil shear strength along the potential failure surface. The changes that occur in soil behaviour which include the volumetric increase of water content (θ), the degree of saturation (S_r), permeability coefficient (k) and bulk density (γ), due to rainfall infiltration inside the slopes, are factors that contribute to slope failure. The capacity of water infiltration into the soil also varies, which can be described as the maximum rate that water can enter the soil during rainfall incidents.

Many significant studies have been conducted on rainfall infiltration into slopes and its impact on slope stability. Generally, the seepage impacts in slope stability analyses are studied by determining a safety factor and critical depth of failure of those slopes, which are subject to infiltration into the surface of the slope. It is frequently assumed that the phreatic surface elevates to correspond with the surface of slope, and that the slope is totally saturated, in order to address the analysis simply as a worst scenario for infiltration Collins and Znidarcic (2004). In 1911 the analysis of rainfall seepage through slopes was investigated by Green and Ampt Chen et al. (2008). Through these researches, it becomes possible, based on the Green-Ampt infiltration model Green and Ampt (1911) and Richard's equation Richards (1931), to address and solve problems of infiltration and slopes stability in partially saturated soils under conditions of rainwater infiltration. According to Darcy's law, the initial suggestion to illustrate the rainfall infiltration into unsaturated soil beneath ponded water was the Green–Ampt infiltration model which is presented in Figure 2-8. The soil above the wetting front is assumed to be fully saturated, whereas the initial water content below the front wetting remains constant. In the wetted zone, the permeability coefficient is assumed to remain constant with time and there is a soil suction just above the wetting front that has constant value. The required time to saturate the soil to a depth of (Z_w), based on the Green–Ampt model, is:

$$T_w = \frac{\theta_1 - \theta_0}{K_w}\left[Z_w - C_s\, ln\left(\frac{C_s + Z_w}{C_s}\right)\right] \qquad 2\text{-}6$$

Where (θ_0) and (θ_1) are the initial and final volumetric water content before wetting respectively, K_w is the permeability coefficient of the soil in the wetted zone and (C_s) capillary suction in the wetting front as well. The soil infiltration rate when the water can enter the surface of soil is:

$$v_i = k_w\,\frac{Z_w + C_s}{Z_w} \qquad 2\text{-}7$$

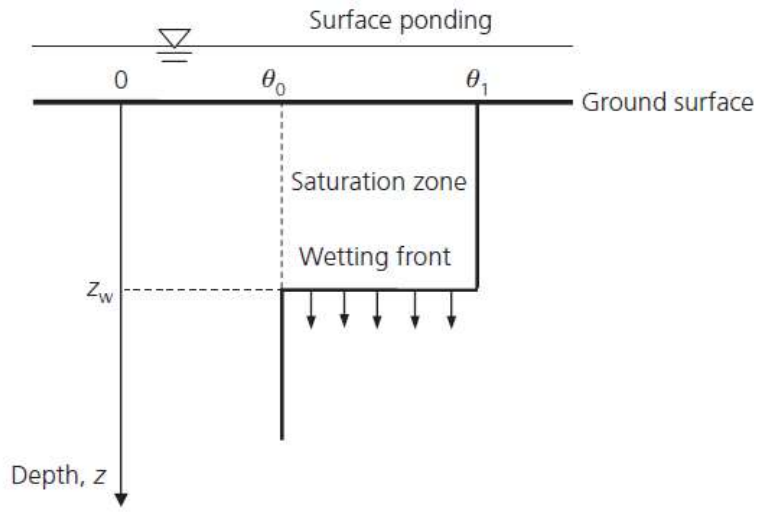


Figure 2-8 Green Ampt model.

Mein and Larson (1973) modified the Green–Ampt model to account for conditions in which the intensity of rainfall initially is less than its ability to infiltrate into the soil, producing a simple two-stage model has been developed which shows the prediction of soil infiltration before and after surface ponds. Lumb (1962) introduced the concept of wetting front related with the analysis of slope failures. The depth of wetting front Z during continuous and heavy rainfall is determined as:

$$Z_w = \frac{K_{sat}\,T}{n(S_f - S_0)} \qquad 2\text{-}8$$

The permeability coefficient of saturated condition is K_{sat}, whereas S_f and S_o are the final and initial saturation degree of the soil respectively, the porosity of soil is defined by n, and T is known as filtration time. The water flow of ground surface q and according to Lumb's equation of the wetting front is equivalent to k_{sat}. The process of the wetting front will be slower than that suggested by Equation *2-8* in the scenario where the rainfall is less intense.

Following on Lumb's (1962) equation, Sun et al. (1998) suggested a general wetting region equation. The difference of soil suction is illustrated in Figure 2-9 with depth in partially saturated soil.

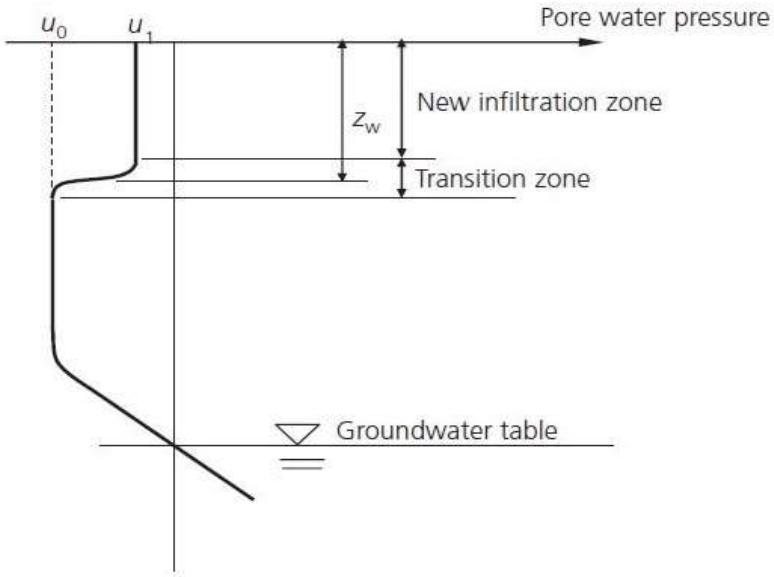


Figure 2-9 Transient infiltration in an unsaturated soil Sun et al. (1998).

Assuming steady-state conditions, the soil pore water pressure is u_0 for a certain soil flow q_0 that is less than k_{sat}. A new region of infiltration is created by the pore water pressure when the flow rises in the soil surface, which gradually increases downward over time. Thus the calculation of wetting front depth by using Equation 2-9. Whereas $K_0 = q_0$; $K_1 = q_1$; θ_0 , θ_1 are initial and final volumetric water content and correspond to the value of pore water pressure u_0 and u_1 respectively.

$$Z_w = \frac{(K_1 - K_0)t}{\theta_1 - \theta_0} \qquad 2\text{-}9$$

Equation *2-9* is simplified to Lumb's equation when $k_1 = k_{sat}$ and is considerably larger than Equation *2-8*. There are significant limitations when applying concepts of infiltration models, associated with the topography of inclined ground, the flow in lower slopes, in addition to the change in the intensity of precipitation, but the most crucial of all is the dependence of the permeability on soil moisture content Ng and Shi (1998). Under the complicated boundary conditions of slopes, the water flow equation through the unsaturated and saturated soil must be solved in order to obtain a more stringent pore water pressure distribution. Fredlund and Rahardjo (1993) introduced the water flow equation through soils with consideration of Darcy's law and the water conservation mass.

$$\partial/\partial x\left(k\frac{\partial h}{\partial x}\right) + \partial/\partial y(k\frac{\partial h}{\partial y}) + \partial/\partial z\left(k\frac{\partial h}{\partial z}\right) = \frac{\partial \theta w}{\partial t} \qquad 2\text{-}10$$

Where θ_w is the volumetric water content and, conductivity or permeability of unsaturated soil is k and the total height which in 3D Cartesian coordinates (x,y,z). In the situation of shallow soil and rainfall times less than the required transmission time of lateral water pressure, Iverson (2000) evaluated the governing equation of a local coordinate system in for soil slope due to rainfall infiltration. The analytical pressure head has been determined by using the assumption that the soils are initially fully saturated ($k = k_{sat}$).

The infiltration of rainfall into the soil is assumed to take place completely when the intensity of rainfall is less than or equal to the permeability in the state of saturation. When the intensity of rainfall exceeds the soil permeability in the saturated case, it is assumed that the permeability will equal the infiltration rate, and thus the excess rainwater flows over slopes and appear as surface flow. Also the Green-Ampt and Mein-Larson models have used this assumption to predict the capacity of rainfall infiltration in soil Mein and Larson (1973).

In Hong Kong 2001 and during the rainfall season, the rate of infiltration through a totally decomposed granite slope was investigated by Li et al. (2005). It was found that the permeability in saturated conditions ranged from 1×10^{-6} to 1×10^{-5} m/s which corresponded to

the intensity of rainfall during the test and valued between 2.8×10^{-7} to 2.3×10^{-6} m/s. According to the study, runoff occurred before near-surface soils started to be totally saturated. Rahardjo et al. (2005) conducted experimental tests to find out the infiltration capacity of rainwater in the slope by applying artificial rain with a density of 13×10^{-6} m/s on an initially partially saturated slope with permeability (k_{sat} = 5.18×10^{-6} m/s) and it has been found that the infiltration capacity converges to 2×10^{-6} m/s which mean ~$0.4k_{sat}$.

In any case, it is not possible to obtain the analytical solutions for the problem of infiltration except after making some assumptions that include some initial and boundary conditions, due to the high nonlinearity of hydraulic parameters in the equation that controls the partially saturated flow Zhan and Ng (2004). As a result of this, numerous computer simulations for soil slopes have been conducted in terms of seepage and infiltration, under precipitation scenarios Rahardjo et al. (2007) .

2.3.2 Profiles of pore water pressure in the soil during rainfall events.

The concept of wetting front is one of the simplified approaches that helps to understand changes that occur in soil saturation under precipitation conditions. The pore water pressure profiles in soil slopes, including determining slope instability criteria under rainfall conditions, have been conducted by several theoretical and simulation analyses. Figure 2-10 illustrates the typical distribution of pore water pressure under different flow conditions. The pore pressure gradient under conditions of steady-state can be written according to Kisch (1959).

$$\frac{duw}{dy} = \gamma_w \left[\left(\frac{q}{k}\right) - 1\right] \qquad 2\text{-}11$$

Where γ_w is water unit weight.

Figure 2-10(a) demonstrates the pore water pressure gradient under hydrostatic conditions, expressed in Equation *2-11*. The pressure gradient is zero just when the value of ground surface flow (q) reaches the permeability coefficient of unsaturated soil, k, at a given amount of matric suction. In the condition of transient seepage, the profiles of pore water pressure in the cases where $q/k_{sat} < 1$ and $q/ksat > 1$, are illustrated in Figure 2-10 (b) & (c), respectively. Under transient seepage conditions, infiltration can be considered as a transitional stage between the

initial state and final state of steady seepage. Figure 2-10 (b) & (c) (left) illustrate the condition of hydrostatic seepage from the initial states when q=0. Figure 2-10 (b) & (c) (right) demonstrate stable seepage in the initial condition and when the flow of the ground surface is greater than zero. The time required to reach the steady state depends on the flow of ground surface, the coefficient of permeability and water storage capacity of the soil. Figure 2-10 (b) shows a reduction of matric suction in unsaturated soil but does not disappear when the saturated coefficient of permeability is greater than ground flow. In the case when the rainfall duration is long term, matric suction can be reduced only if the ground surface flow is similar or greater than the coefficient of permeability in saturated soil as described in Figure 2-10 (c).

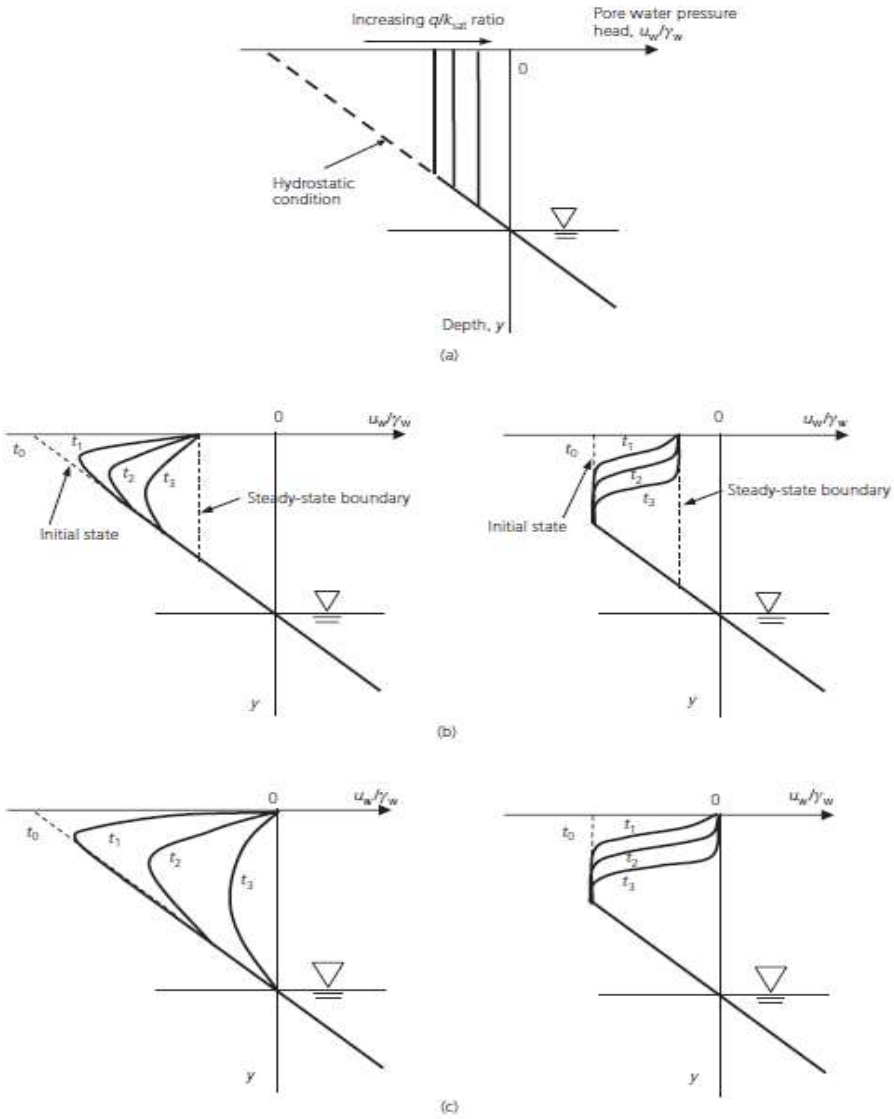


Figure 2-10: Typical of pore water pressure in an unsaturated soil with the different flow of ground surface; where (a) is steady state case, (b) is transient case when q/ksat <1 and (c) transient flow at q/ksat≥1 Rahardjo et al. (1995).

2.3.3 Mechanism of rainfall-induced landslides

Changes in pore water pressures and seepage forces due to rainfall events are recognized as the most important causes of landslides Zhu and Anderson (1998), Gerscovich et al. (2006). For rainfall-induced landslides, two different failure mechanisms have been identified. For the first mechanism, a significant cumulative increase of positive pressures was observed during the rainfall infiltration into the soil, specifically below the surface layer of slope and on the expected failure surface Collins and Znidarcic (2004). Soil movements along the failure surface can cause liquefaction phenomena along the sliding surface, potentially leading to rapid movements which result in slope collapse Wang and Sassa (2001). It has been found that the static shear stress path can be used to characterize the stresses at the site Anderson and Sitar (1995). Brand (1982) emphasized that the change in stress caused by water infiltration that corresponds to the field stress can differ significantly from the stress pathway developed during a triaxial compression stress test (Figure 2-11).

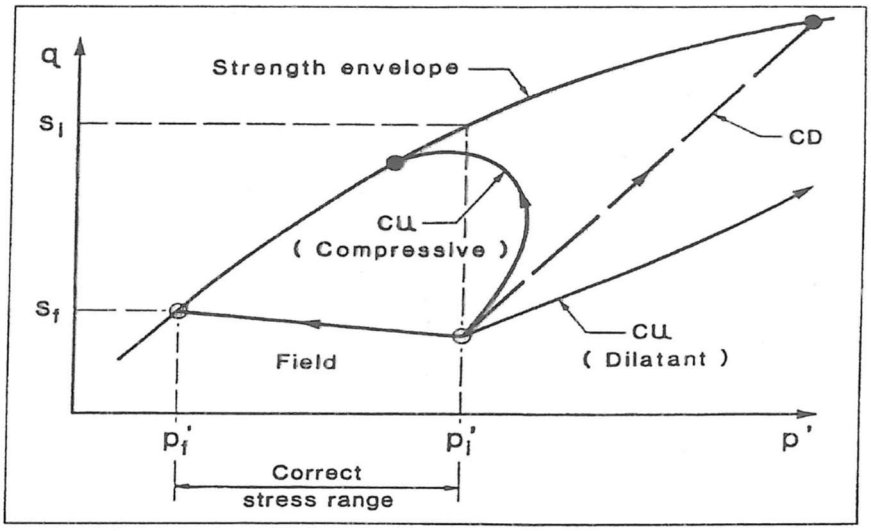


Figure 2-11 The comparison between stress trajectories for slope failure induced by rainfall and Triaxial tests Brand (1982).

In the second mechanism, slope failure results foremost from the rainfall infiltration through the soil that is in an unsaturated state, and thus the soil loses its resistance to shear due to the reduction of soil suction. Additional rainfall infiltration produces near-saturation conditions in the soil, which reduces suction and consequently decreases effective stresses along the possible failure surface of slope Fredlund and Rahardjo (1993).

Generally, slope instability is a complicated phenomenon and in order to simplify the analysis, four failure stages were proposed by Vaunat et al. (1994) and Leroueil et al. (1996)

1- the pre-failure stage, this stage contains all failure reasons due to deformation processes. Deformations that occur as a result of changes in pressure, creep and increasing failure are dominant in this stage.
2- the onset of failure, regarding this stage the development of a continuous shear surface throughout the entire soil mass, indicating the beginning of failure.
3- The post-failure stage, immediately after failure until the landslide effectively ends, the post-failure stage includes movement of the soil mass participating in the landslide. It's typically described by the increment of displacement rate due to a progressive reduction in velocity.
4- The reactivation stage, this stage known when a mass of soil moves along one or more preexisting shear surfaces.

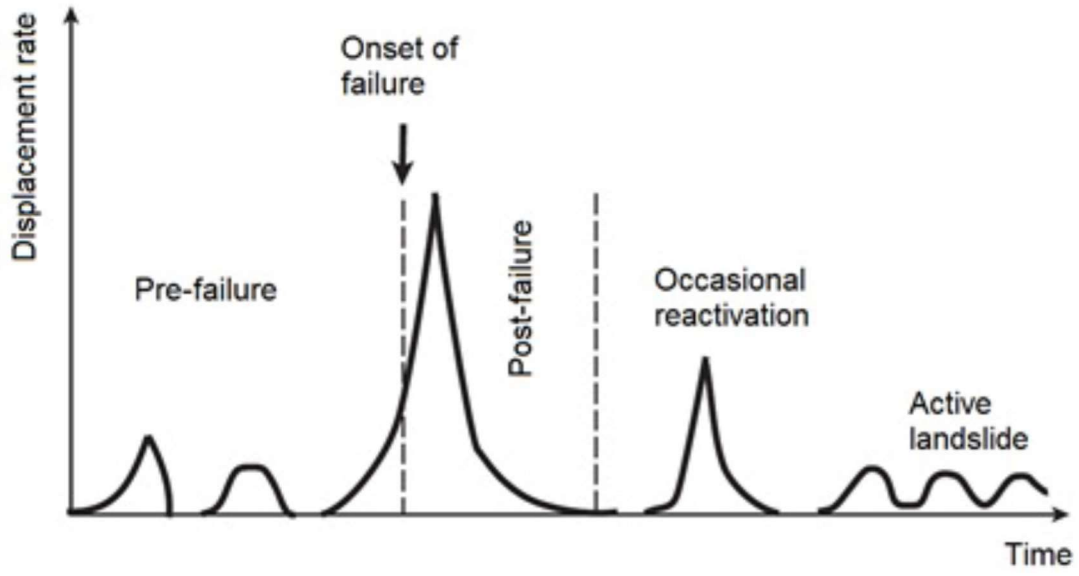


Figure 2-12: Slope failure with different stages (Leroueil, 2001).

More recently combining these concepts, Cascini et al. (2010), categorized shallow landslides induced by rainfall according to failure stages, as: slide, slide to flow or flow slide, which depends on the acceleration of the failed soil mass. The failure stage of a slope has been defined as the formation of a continuous shear surface due to rainfall infiltration throughout the mass of soil. The post-failure flow phase occurs as a result of rapid production of significant plastic strains, which leads to a sudden acceleration of the failed soil mass.

2.3.4 Field Investigations of slope instability due to rainfall and flooding

Several investigations have been carried out to determine how pore water pressure varies in slopes in response to annual and heavy rainfall events. Three tests on natural slopes were conducted by Harp et al. (1990) in order to investigate how the slope responded to wetness in terms of pore water pressure distribution during failure. The space pores in the soil plays an essential role for understanding the effect of fluid pressure inside these pores and its effects on soil behaviour, and thus its impact on the stability and performance of engineering facilities, whether built on or inside the soil. It has been observed that water infiltration typically flows through porous structures such as animal burrows and root casts, and the discharge varies depending on time and location. The rapid reductions in pore water pressure were recorded between 5 and 50 minutes before collapse at several points on the slopes. They suggested that the increase of pore water pressure and flow rate resulted in fine particle redistribution and removal (piping), which could contribute to increased pore diameters and degradation of the soil structure near the sliding surface.

2.3.5 Full scale tests of slope instability due to rainfall and flooding

The phenomena of stress redistribution have been noticed at the pre-failure stage and on the onset of failure in landslide triggering tests conducted by Ochiai et al. (2004) and Moriwaki et al. (2004b) in sandy soil slopes. The artificial rainfall that has an intensity of 78 mm/hr over a 5 m wide and 30 m long with an average gradient of slope 33°, induced a fluidized landslide that has a maximum depth 1.2 m, according to Ochiai et al. (2004). Moriwaki et al. (2004a) found that bending stresses within the soil layers, along with a significant rise in pore water pressure, were detected simultaneously by soil-strain probes 4.83 hours after the rainfall began. These bending stresses were caused by internal deformation within the slope material as water infiltration weakened the soil, leading to differential movement and strain. The slope failure was observed 6.83 hours after the onset of rainfall. It is important to clarify that the bending stresses refer specifically to the deformation of the soil layers, as they responded to increased pore water pressure and shear stress during the rainfall-induced failure.

2.3.6 Numerical models of cyclic loading due to rain and flood

Recent research has highlighted the limitations of traditional factor-of-safety approaches in assessing the stability of levee structures subjected to cyclic hydraulic loading. Jadid et al.

(2020) investigated the effects of repeated rises and falls in water levels on the Princeville levee in North Carolina, which has historically endured severe storm impacts, including Hurricanes Floyd and Matthew. Using both finite element modelling (Plaxis 2D) and limit equilibrium analysis (Slope/W), the authors compared strain-based and strength reduction methods to understand the cumulative impact of storm cycles on levee stability.

Their findings reveal a significant accumulation of plastic shear strain as storm cycles increase, indicating a progressive degradation of the levee's structural integrity. The strain-based analysis showed that from the first to the sixth storm cycle, the shear strain increased by 3.5 times. This suggests that there was a higher risk of failure than what was shown by standard factor-of-safety assessments. This discrepancy underscores the limitations of traditional approaches, which generally fail to capture the incremental damage associated with cyclic loading.

Jadid et al. (2020) also emphasise the need for rate-dependent analyses to model the effects of rapid drawdown realistically, as the assumption of instantaneous drawdown can lead to overly conservative or inaccurate safety estimates. Their study advocates for the integration of strain-based methodologies in levee performance assessments, particularly under conditions of repeated hydraulic loading. Such an approach not only provides a more comprehensive evaluation of levee stability but also offers critical insights for managing flood defence infrastructure in regions vulnerable to severe storm cycles.

In their study of the Princeville levee, Jadid et al. (2020) identify critical monitoring points within the levee cross-section, specifically Element A and Element B, to analyse the distribution and accumulation of shear strain under repeated hydraulic loading conditions as shown in Figure 2-13. Element A, located near the blanket toe on the landside, experiences the highest concentration of plastic deformation due to cyclic water level fluctuations, which makes it a primary indicator of potential slope instability. By contrast, Element B, positioned closer to the crest, serves as an additional monitoring point, allowing the authors to capture strain and stress variations across different sections of the levee.

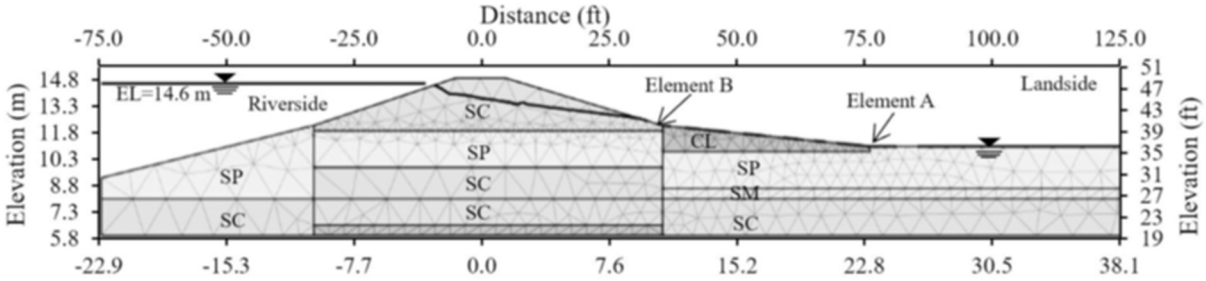


Figure 2-13 Geometry of the Princeville levee section and a discretised mesh Jadid et al. (2020)

Figure 2-14 illustrates the increase in shear strain at two key locations (elements A and B) within the Princeville levee over multiple storm cycles. This graph demonstrates how the cumulative effect of repeated storm loading cycles significantly increases shear strain, particularly at the blanket toe (element A). This buildup of plastic shear strain is linked to a higher chance of reaching critical limit states, which shows how the levee becomes more unstable over time when it is loaded and unloaded repeatedly.

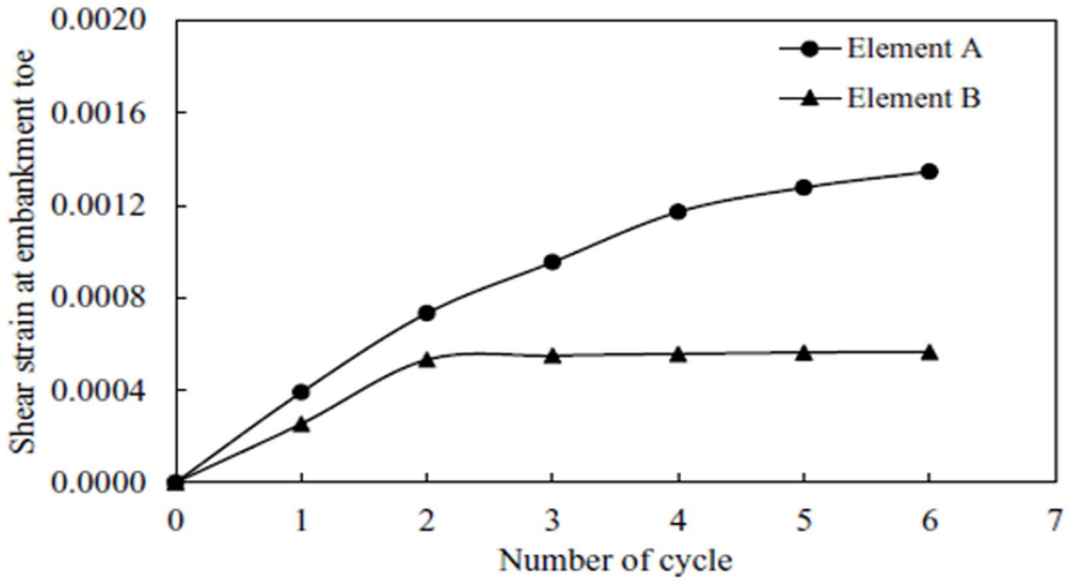


Figure 2-14 Shear strain rises at elements A and B during storm cycles Jadid et al. (2020).

Jayakody et al. (2023) explore the behaviour of unsaturated soil slopes subjected to intermittent antecedent rainfall patterns, a crucial factor in understanding rainfall-induced landslides. The study examines how varying rainfall gaps influence landslide initiation on slopes composed of silty sand. The researchers used a centrifuge model (discussed in Chapter 3) to test three different types of pre-rainfall patterns: uniform, decreasing, and increasing gaps. After these

patterns, it rained nonstop until the slope gave way. The experimental results were analysed using a coupled hydro mechanical finite element model, which successfully replicated pore water pressure, displacement, and strain distribution observed in physical tests.

Findings indicate that the decreasing gap rainfall pattern led to the quickest landslide initiation, followed by the uniform and increasing gap patterns. This outcome suggests that not only the cumulative rainfall but also the timing and frequency of antecedent rainfall events significantly affect slope stability. Pore water pressure analyses revealed that shorter gaps between rainfall events hindered the dissipation of pore water pressure, accelerating failure. The study highlights the importance of incorporating antecedent rainfall patterns in early landslide warning systems. Where traditional approaches focused solely on cumulative rainfall may overlook critical pre-failure conditions in slopes.

Postill et al. (2020) investigates the long-term deterioration of high-plasticity clay slopes due to seasonal wetting and drying cycles. These cycles lead to the accumulation of outward and downward deformations, resulting in plastic strain accumulation and progressive failure, a phenomenon known as seasonal ratcheting. The authors utilized advanced hydro-mechanical coupling techniques for unsaturated soil behaviour and nonlocal strain-softening regulatory models to replicate this mechanism within a numerical framework. Their model was validated against physical measurements from centrifuge experiments, demonstrating its accuracy in simulating seasonal ratcheting. This research underscores the importance of considering environmental stress cycles in slope stability assessments and provides a validated numerical tool for predicting the progressive failure of clay slopes under such conditions.

A recent study by Kim et al. (2023) explores the instability of embankment slopes under conditions of overtopping and rapid drawdown, providing critical insights relevant to slope failure mechanisms in engineered infrastructure. The authors utilise probabilistic modelling to assess the effects of initial water levels, derived from historical rainfall data, on the probability of slope collapse. Their findings reveal that rapid drawdown significantly destabilises slopes by reducing effective stress and increasing pore water pressures, leading to potential failures.

Using a Limit Equilibrium approach and Bishop's Simplified Method, the authors investigate the influence of flooding and drawdown events on slope stability under varying climate scenarios. The study underscores the importance of transient seepage analyses and the need for incorporating probabilistic approaches when assessing the vulnerability of slopes to extreme

weather events. Additionally, the focus on critical periods for embankment collapse highlights the necessity of adaptive risk management strategies, such as enhancing drainage systems or optimising drawdown rates, to mitigate failure risks in slope infrastructure.

CHAPTER 3

Centrifuge Modelling of Climate-Induced Slope Instability

3.1 Centrifuge modelling

The developments in geotechnical centrifuge technology have provided a fundamental understanding of slope instability modelling with considering soil parameters and boundary conditions due to rainfall scenarios. The centrifuge modelling test is based on the following principle: a model is created with geometric dimensions that are N times smaller than the prototype, and centrifugal acceleration is applied by N times Earth's gravity. Accordingly, it has been hypothesized that the stress gradient within the model, which includes similar effective pressures and groundwater pressures, are similar to the prototype at the same depths Schofield (1980). For simplified analysis, the Earth's gravity g has been used to normalize with the centripetal acceleration, so from Newton's equation $N = \omega r^2/g$ as the quantity expressing the acceleration field and how much it is greater than Earth's gravity. The scaling laws are one of the most important requirements in centrifuge modelling tests. The basic concept in the scaling laws are those relationships that determine the behaviour of the tested model in the centrifuge compared with the prototype. These scaling laws can be obtained through dimensional analysis or through the differential equations that control scaling laws Taylor (2018).

3.1.1 Scaling laws

The application of centrifugal modelling is crucial in the field of geotechnical engineering, where stress simulation is the essential concept, and based on scale self-weight of prototype, as shown in Figure 3-1. Stresses of self-weight in prototype scale at depth H is giving by Equation 3-1:

$$\sigma_p = \gamma H = \rho g H \qquad 3\text{-}1$$

Where: -

σ_p = self-stress of prototype.

γ = Soil unit weight.

ρ = Soil density.

g = gravity acceleration.

At any position self-weight stresses in an N times scaled model under centrifugal acceleration are:

$$\sigma_m = \frac{\gamma H}{N} = \frac{\rho g N H}{N} = \rho g H = \sigma_p \qquad 3\text{-}2$$

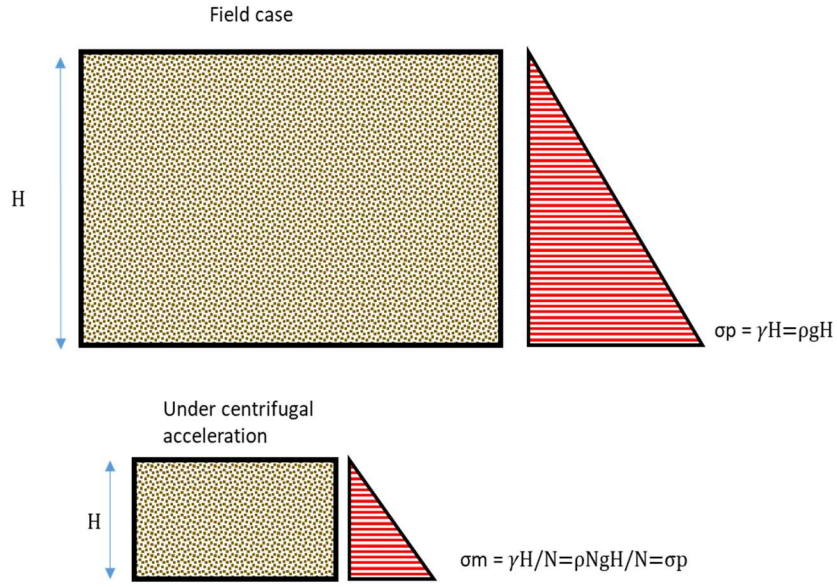


Figure 3-1 Self-weight stress in both scale of prototype and model at condition of centrifugal acceleration.

Because of the same self-weight stresses that are applied at two equal position of the model and prototype at depths H/N in the model and H in the prototype, the following conclusions can be obtained:

$$H_p = N H_m \qquad 3\text{-}3$$

When a soil model is subjected to a centrifugal acceleration Ng, the basic scaling principles of centrifuge modelling indicate that it experiences the same self-weight stresses within its mass as a corresponding prototype with N times higher.

3.1.2 Scaling laws of seepage and rainfall specifications.

The seepage of rainfall during slope model tests under centrifuge conditions is one of the most crucial factors that controls the flow process through the soil layers Kimura (1991). The velocity of seepage in the centrifuge experiments is N times that in the gravitational field of Earth, as long as the material used to create the model is known and classified and identical to prototype soil Garnier et al. (2007). Since the seepage velocity and rainfall intensity have the same dimension, thus in the Ng field rainfall intensity is N times that of rain in the Earth's gravitational. Darcy's law states that between two points in a porous material (soil), the seepage velocity (v) will be proportional of the hydraulic gradient (i) between these points as shown in Equation*3-4*. Hydraulic conductivity k is the constant that governs this proportionality.

$$v = \frac{q}{A} = -ki \qquad 3\text{-}4$$

The coefficient of soil permeability, k, is written as follows in terms of intrinsic permeability, K, which is affected by soil grain size and shape.

$$k = \frac{K\rho g}{v} \qquad 3\text{-}5$$

Where: -

ν is dynamic viscosity.
ρ is fluid density.
g is gravitational acceleration.

If the model and prototype contain the same pore fluid, the soil permeability coefficient will be affected by gravitational acceleration, and thus:

$$k_p = \frac{1}{N} k_m \qquad 3\text{-}6$$

Since the hydraulic gradient (i) has no dimensions, it means that:

$$i_p = i_m \qquad 3\text{-}7$$

Thus:

$$v_m = i_m k_m = i_p N k_p = N v_p \qquad 3\text{-}8$$

Schofield (1980) found that the velocity of seepage in the model is N times higher when the centrifugal acceleration is Ng. As a result, the rainfall duration in the model is scaled down to be N^2 times smaller under Ng than the prototype. The equivalent length of the total precipitation in the model will be less than the prototype by N times so that the rain intensity is N times higher in the model, and the rain intensity is expressed as the ratio between the total amount and duration of rainfall Askarinejad et al. (2012). For instance, consider a 24-hour simulation for rainfall event of a prototype that has rainfall intensity of 24mm/hr thus, a period of $24\times3600/70^2$ =17.6s is required for a rainfall intensity of 1600 mm/h in the model at 70g centrifugal acceleration. Table 3-1 shows the scaling of rainfall parameters during centrifuge modelling.

Table 3-1 Scaling laws for rainfall parameters Askarinejad et al. (2015).

Term	Prototype	Model
Length(L)	1	1/N
Seepage velocity (L/T)	1	N
Seepage time (T)	1	$1/N^2$
Total rain	1	1/N
Rain duration	1	$1/N^2$
Hydraulic gradient	1	N
Rainfall intensity (L/T)	1	N

3.1.3 Stress variation error.

It is recognized that the stress distribution within soil layers in the centrifuge model is not uniform as it appears in the prototype. It has been considered that the evaluation of small centrifuges models in the gravitational field is a linear function of the model's distance from the rotation centre. However, the centrifuge model's variable acceleration generates a non-

linear stress distribution. Consequently, the field of gravity changes linearly with radius r from the rotation centre and as a square of the centrifuge's angular velocity (ω). The radius from the rotation centre to the upper surface of the centrifuge model is R_t, as shown in *3-9*. According to Taylor (1994) in the centrifuge model and at a depth of z the vertical stress is determined by following equation by

$$(\sigma_v)_m = \int_D^z \rho\omega^2 (R_t + z)dz = \rho\omega^2 z(R_t + \frac{z}{2}) \qquad 3\text{-}9$$

The distribution of gravity stress in the prototype and in the centrifuge, model is demonstrated in *3-10*. The dashed line in this diagram presents the linear relation for the vertical stress increment in the prototype horizontal soil layer. The vertical stress will increase as a quadratic equation in the identical centrifuge model, as represented by the solid line shown in Figure 3-2. The contrast between these two curves illustrates two featured states that can be observed in the centrifuge soil model. As described, the horizontal soil layer is under-stressed when inertial stresses are smaller than gravity stresses. Whereas in the second state is overstress in which the model's stresses are higher than in the prototype. In addition, three different depths might be determined, namely maximum under-stress at depth (h_u), the depth at the maximum over-stress (h_o), and the two stresses coincide at the depth (h_i).

As presented in the figure at a depth of *hi* below the surface of the centrifuge model these two lines intersect, when the vertical stresses in the prototype and the centrifuge model are equal. At a depth of (h/2), the maximum under-stress occurs. Likewise, the highest level of over-stress is found near the bottom of the centrifuge model, at a depth of (H). It is essential to understand the relative magnitudes of the over-stress and under-stress in the centrifuge model, so that could reduce the stress distribution error. The maximum error of under-stress that occurs in the model at depth of (h_i/2) and expressed by R ratio is calculated as follows:

$$R_u = R_0 = \frac{H}{6r_e} \qquad 3\text{-}10$$

Here:

R_u: The ratio representing the maximum under-stress error at depth $h_i/2$.

r_e: The effective radius from the centrifuge axis of rotation to the centre of mass of the soil layer.

H: The total height of the soil layer in the centrifuge model.

The effective radius re is calculated using the following relationship:

$$r_e = r_t + \frac{2H}{3} \qquad 3\text{-}11$$

Where:

r_t: The distance from the axis of rotation to the base of the soil layer.

H: The height of the soil layer in the centrifuge model.

In the centrifuge model, the stresses vary due to the effects of rotation, with stress increasing quadratically rather than linearly, as in the prototype. The depth $hi/2$ represents the location where the maximum under-stress error occurs as a result of this stress distribution difference. The parameter (r_e) accounts for the geometry of the centrifuge setup, incorporating both the base distance (r_t) and the contribution of the soil layer height ($2H/3$), Schofield (1980).

It can be seen that the model and prototype have an equivalent stress relationship at two-thirds model depth, and that the effective radius must be determined from the central axis to one-third above the model's base using these equations. Most geotechnical centrifuges have a maximum error in the stress profile of less than 3% in the prototype stress and according to Taylor (1994) this is considered to be insignificant. In a centrifuge model, the error magnitude must be maintained low; nevertheless, there is no clear standard for the level of unacceptable error.

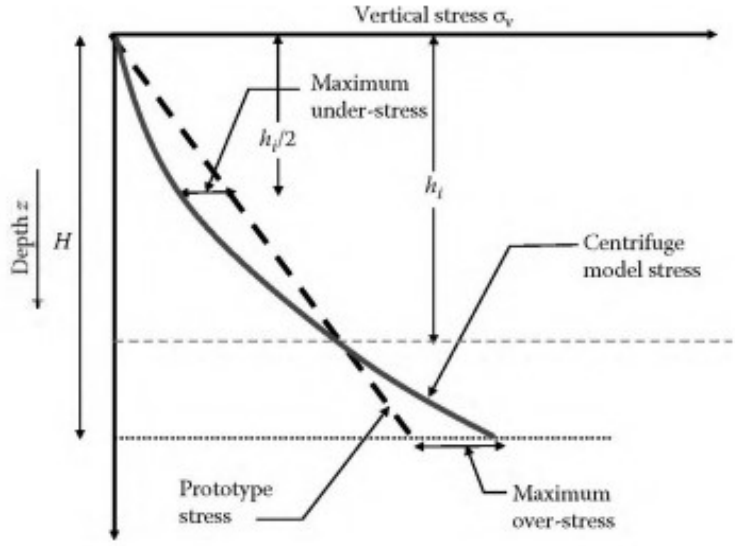


Figure 3-2 The distribution of vertical stress in a soil model under g, that includes under and over-stress, along with its prototype Taylor (2018).

3.1.4 Coriolis effect

Coriolis effect is one of the most important phenomena in centrifuge modelling when dealing with objects moving in any orientation with a velocity v, for instance simulations of rainfall Schofield (1980). The Coriolis acceleration, a_c, is proportional to the model's angular velocity, and velocity v, and is calculated using the following equation:

$$a_c = 2\omega v \qquad 3\text{-}12$$

The inertial acceleration of the model is determined as follows:

$$a = \omega^2 R = \omega V \qquad 3\text{-}13$$

where (V) is the model's velocity in the centrifuge flight.

The inaccuracy induced by the Coriolis effect is measured as the ratio between the Coriolis acceleration and the model's inertial acceleration. In general, an error rate of less than 10% is considered to be acceptable, which implies $v < 0.05V$. However, the effect of Coriolis and other

features should be calibrated to achieve a sufficient distribution over the soil surface. The vertical distance between the surface of the model and the spraying nozzles must be precisely investigated to reduce the Coriolis effect and to avoid surface erosion that is caused by rainfall influence. In order to minimize the impacts of Coriolis an appropriate stand-off was determined by Askarinejad et al. (2012), and it was found that the distance of 70 to 100 mm is appropriate, but that was subject to the intensity of the rainfall and the nozzle type. A theoretical framework of Coriolis and rainfall simulation was presented by Caicedo et al. (2015), which included parameters such as droplet size, initial velocity, the evaporation rate, air velocity with its direction, and relative speed between air and rainfall droplet.

3.1.5 Droplet trajectories in a centrifugal rotating frame.

When performing rainfall simulations in a centrifugal rotating frame, Coriolis acceleration significantly affects the trajectory of water droplets. Parameters such as centrifuge acceleration, initial droplet velocity, and droplet size influence droplet deviation. Caicedo et al. (2015) applied conservation principles to estimate the deviation of droplets injected under Ng compared to 1 g. Their simulations demonstrated that droplets ejected at a 45-degree angle with varying horizontal plane angles deviated toward the centrifuge axis, opposite the rotational movement, due to Coriolis forces. Smaller droplets, with a diameter of 100 μm and an initial velocity of 20 m/s, were found to be more affected by the combined Coriolis and centrifugal forces, resulting in fewer droplets reaching the model surface as acceleration increased. To address this, Askarinejad et al. (2012) experimentally calibrated the minimum distance between nozzles and the soil surface to minimise erosion and Coriolis effects in centrifuge tests at 50 g. They determined this distance should be 70–100 mm for a droplet size of 40 mm. These findings emphasise the importance of nozzle positioning and droplet characteristics in achieving accurate rainfall simulation in centrifuge experiments.

Figure 3-3, as described by Caicedo et al. (2015), illustrates the significant impact of Coriolis and centrifugal forces on droplet trajectories during rainfall simulation in a centrifuge. As the centrifuge acceleration increases from 1 g to 50 g, the trajectories deviate more toward the centrifuge axis, opposing the direction of rotation. This deviation, influenced by an initial velocity of 20 m/s and a rotation radius of 1.4 m, becomes evident in the lateral, top, and 3D views, showing asymmetry in droplet paths. At higher accelerations, fewer droplets reach the intended surface, highlighting the importance of precise nozzle positioning and design to

counteract these forces for effective rainfall simulation. Figure 3-3 as presented by Caicedo et al. (2015), highlight that both the initial velocity and droplet size significantly influence droplet trajectories in centrifuge rainfall simulations. Higher velocities and larger droplet sizes help counteract the Coriolis and centrifugal forces, ensuring more droplets reach the model surface effectively. These findings underscore the importance of optimising these parameters for accurate rainfall simulation in centrifuge experiments.

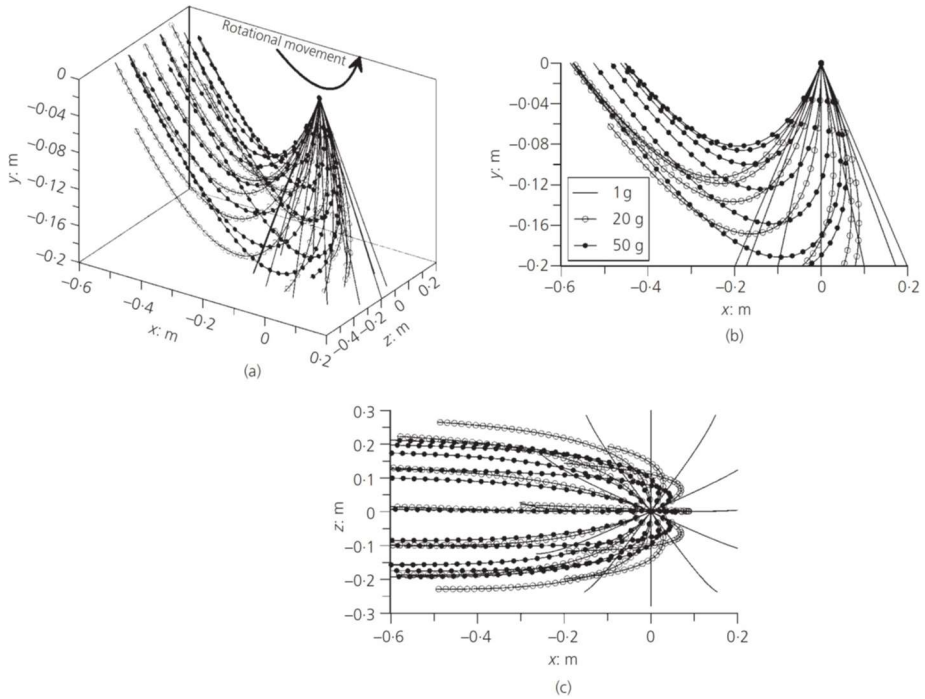


Figure 3-3 The impact of changing the centrifuge's acceleration in in droplet trajectories, at an initial velocity of 20m/s and rotation radius 1.4m:(a) 3D view, (b) lateral view and (c) top view (Caicedo et al., 2015).

3.2 Centrifuge modelling of rainfall-induced slope instability.

Kimura (1991) conducted a series of centrifuge experiments to evaluate a slope's stability due to intense rainfall. They used an SM-classified artificial mixture of 50% Kanto loam, 33% Toyoura sand, and 17% crushed Toyoura sand. In some cases, the initial conditions of the soil were considered priorities during experiments, such as the initial void ratio and water content, whereas other tests focused on the consequences of rainfall intensity and slope inclination. All experiments were carried out at a centrifugal acceleration of 50g as shown in Figure 3-4.

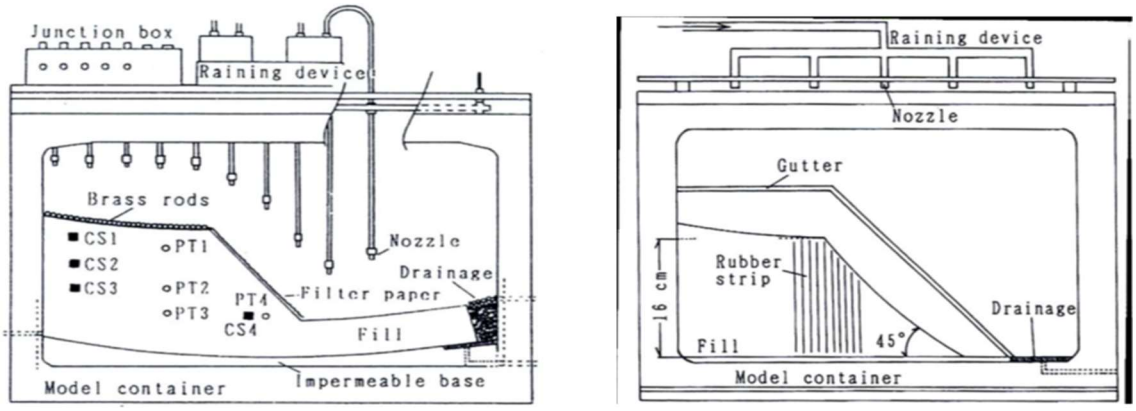


Figure 3-4 Setup test for test cases of the rainfall infiltration experiment (Kimura, 1991).

Two kinds of slope failure were found when the model was exposed to intense rainfall: -

1- In regions where the wetting front is infiltrated into the soil, failure along a well-defined deep slip surface occurred.
2- When the groundwater was reached to the top layer of an impervious base, failure in the toe areas occurred.

Table 3-2 illustrates how variations in initial void ratio and water content influence the occurrence and type of failure. Tests with higher initial void ratios (e.g., C-1, C-2, D-1, D-2) generally experienced faster failure times and were more susceptible to Type 1 failures. In contrast, samples with lower void ratios (A-1, A-2, B-1) exhibited greater stability with no observed failures. This trend suggests that increased porosity and moisture content reduce soil strength, aligning with the failure mechanisms examined in this study. It was noticed that the wetting front moves downward during rainfall and had a shape that corresponded to the slope's geometry. When void ratios were similar, more rainfall was required to produce failure in the soil with lower initial water content, and when void ratios were similar, more rainfall was required to cause failure in the soil with lower initial water content.

Table 3-3 summarises the failure times and modes under varying slope angles and rainfall intensities based on Kimura's tests. The results show that steeper slopes (60°) with high rainfall intensities tend to fail more quickly (e.g., 35 seconds at 2250 mm/hr), exhibiting primarily Type 1 failures. In contrast, gentler slopes (30°) demonstrated longer failure times (up to 97 seconds) and were more prone to Type 2 failures. These trends emphasise the combined influence of slope geometry and rainfall intensity on slope stability.

Table 3-2 : The experiment of rainfall infiltration: test conditions and results for case 1 (Kimura, 1991).

Test No.	Initial condition		Time of failure(s)	Type of failure
	e_o (-)	w (%)		
A-1	1.75	27.9	--	No failure
A-2	1.81	27.3	--	No failure
A-3	1.86	25.5	--	Type 2
A-4	1.86	24	--	Type 2
B-1	1.66	36.2	--	No failure
B-2	1.72	36.6	44	Type 1
B-3	1.81	38.3	48	Type 1
C-1	2	25.5	50	Type 1
C-2	2.02	27.6	42	Type 1
D-1	1.94	37.1	30	Type 1
D-2	2	33.2	13	Type 1

Table 3-3 : The experiment of rainfall infiltration: test conditions and results for case 2 (Kimura, 1991).

Test No.	Slope Angle (°)	Rainfall intensity (mm/hr)	Failure time(s)	Type of failure
E-60(1)	60	2250 (45) *	35	Type 1
(2)	60		36.8	
E-45(1)	45		66	
(2)	45		50.5	
E-30(1)	30		97	Type 2
(2)	30		90	
F-45	45	1400(28) *	58	Type 1
G-60	60	700 (14) *	61.5	Type 1
G-45	45		250	Type 2
G-30	30		400	
Figures in brackets (*) are at prototype. Average initial void ratio e_0 = 1.87 water content w = 28.5%				

In a geotechnical centrifuge, Take (2003) conducted a series of centrifuge tests into the progressive failure of slopes due to rainfall and to investigate seasonal pore pressure cycles of over-consolidated clay embankments. Tests were carried out on model embankments that consolidated from grade E Kaolin clay slurry. One model embankment was formed at a height of 140 mm high (equivalent to an 8.4-meter high slope in the prototype) and 200 mm wide, with a 36-degree slope angle where the model was tested at 60 g. As shown in Figure 3-5, the rainfall and drying were simulated using an environmental chamber with louvered vents that could be opened to simulate drying. The lengths of the wet and dry seasons were divided into

a 5 month/7month ratio to obtain a full calendar year of flow in the field in 2.43 h of seepage flow.



Figure 3-5 Climate chamber for rainfall simulation on slopes (Take, 2003).

The relative humidity and temperature in the test chamber were not controlled and changed as air passed through. Two major achievements in this research were the digital image correlation development techniques and customized tensiometers in order to monitor suction levels in the soil. Figure 3-6 (a) shows the applied boundary condition of seasons to the model surface as a time history of relative humidity, with Figure 3-6 (b) showing the pore water pressure. Swelling and shrinkage sequences were found to be irreversible, resulting in creep in the form of down-slope ratcheting as shown in Figure 3-6 (c & d), accompanied by seasonal moisture fluctuations followed by progressive regional softening. Slope failures have been observed as a result of regional softening, with segments of soil separating from the mass through the emergence of tension cracks and the formation of a localized shear rupture Figure 3-6 (e & f). Clay slopes that temporarily produce an average stress ratio in excess of the critical state stress ratio for any section of a normal year, according to back-analyses, and thus seasonal changes in pore pressure, may finally bring the system to a long-term breakdown.

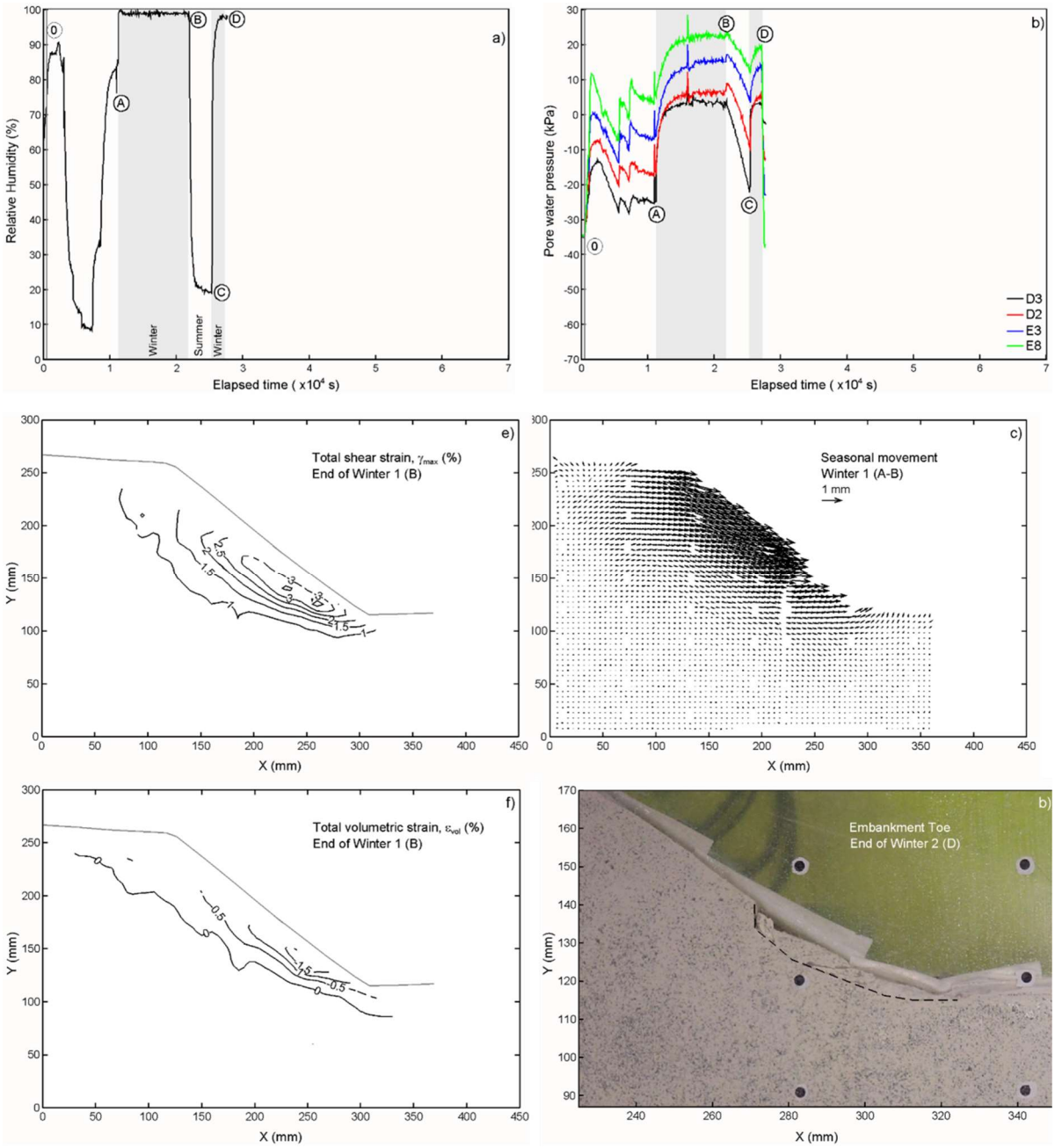


Figure 3-6 Response of embankment WAT5 to first wet season (a) Relative humidity boundary condition, and (b) observed seasonal pore water pressure cycles, (c) direction of seasonal movement (d) total maximum shear strain, (f) total volumetric strain and (e) failed slope Take (2003).

Hudacsek et al. (2009) investigated the behaviour of a compacted clay embankment during cycles of climate condition in a similar way as Take (2003). Glacial till was compacted to produce small-scaled embankments that were tested in a geotechnical centrifuge. In this research the climate chamber was used and it was able to simulate wet (winter) and dry (summer) seasons by controlling rainfall and evaporation. Despite the fact that the initial

seasonal cycles resulted in cumulative displacements of around 17 mm (at prototype), the rate of deformation dropped considerably after eight simulated seasons. The reasons for this refers to the stress history and mechanical behaviour of the model.

Tamate et al. (2012) used centrifuge modelling to investigate the behaviour of sand slopes during rainfall events. In order to simulate rainfall, a comparison was performed between using water and a viscous liquid. The slope models had inclinations of 30° and 45°. According to the results of a conducted tests, failure was caused by the advance of the wetting front in the slope profile, thus shear strength was reduced as a result of the soil's saturation. Different types of failure were observed during centrifuge experiments in terms of the liquid viscosity that was used on rainfall simulation, although the conditions of permeability were equivalent and maintained during tests. The conclusion that reached from this study, using water caused shallow flow failures, whereas viscous liquid appeared to cause bigger instabilities with deeper slide failures.

The heterogeneity effect of slope layering, which might cause a reduction in groundwater flow and the creation of elevated pore pressures, was investigated by Take et al. (2004b), Lee et al. (2008). The failure mechanisms of static liquefaction and slide to flow was simulated in this study in a completely decomposed granite. Decomposed granite has been classified as clayey, silty, and highly gravelly sandy. Two rows of five mist nozzles located near to the soil surface were used to apply rainfall events to the slopes. Figure 3-7 and Figure 3-8 represent the geometry of the models for these two series of experiments, respectively. Water was infiltrated into the higher permeability soil layers; they formed ponds at the layer's edge. It was observed that when the velocity of seepage into the upper layer in slope was less than the infiltration rate, the ponded water developed high pore pressures. Consequently, the suction was reduced due to the ponded water seepage, which led to a rapid failure. The cause for this is that the air in unsaturated voids is very compressible and movable, allowing the slope to tolerate wetness collapse without causing undrained failure.

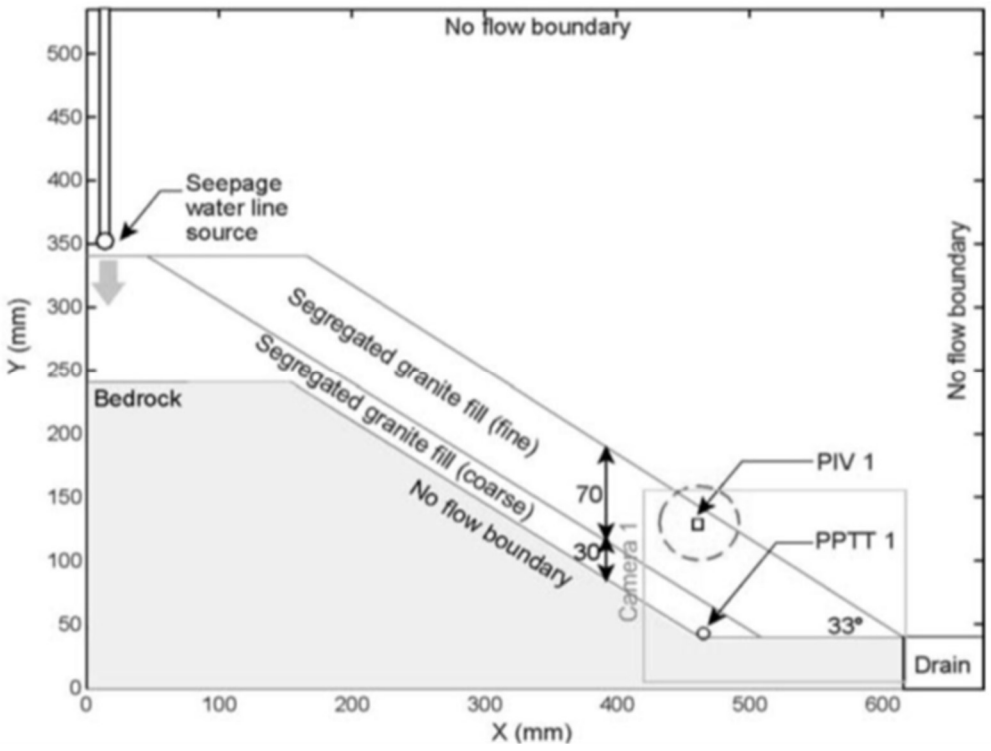


Figure 3-7: Model slope test in centrifuge to investigate slide-to-flow landslide triggering mechanism , PPT: pore pressure and tension transducer, PIV: Particle image velocimetry Take et al. (2004b).

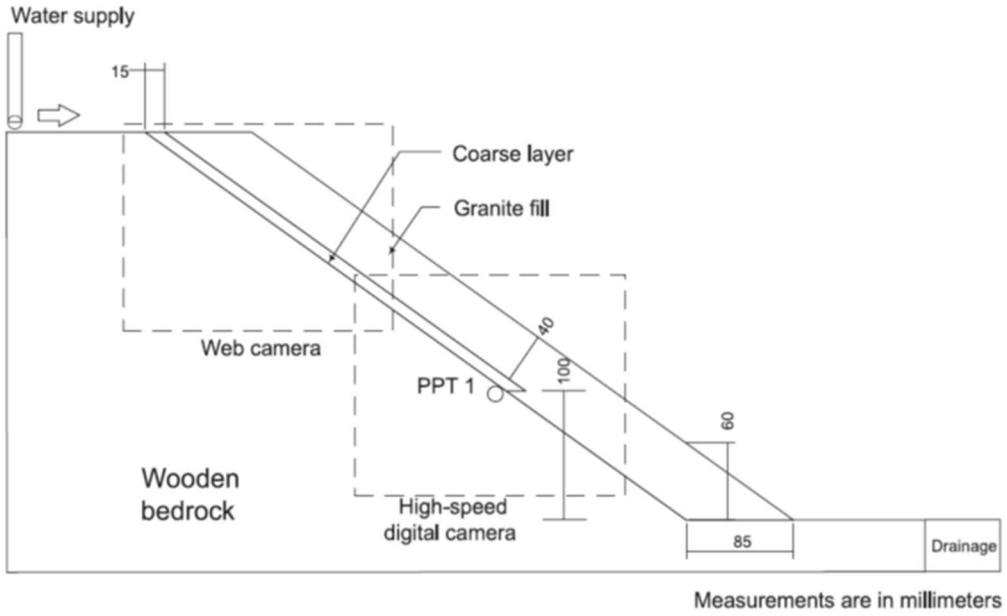


Figure 3-8 : Model slope geometry PPT: pore pressure transducer Lee et al. (2008).

However, in their centrifuge modelling tests, Askarinejad et al. (2012) observed that only a liquid that had more viscosity than water could cause static liquefaction. In this experiment a

slide-to-flow triggering mechanism was investigated, where the slope model was constructed from loose and dense soil with fine fraction soil overlying the coarse layer. The simulation of rainfall infiltration in this test was applied by providing the water at the crest of the slope as a line source, where a thin seepage layer is formed which follows the weak lines of the low permeable layers. It was noticed from the experiment, the high-speed, low-angle run-outs in the model slopes were easily triggered and slow-moving slips were created by localized transient pore pressures caused by restricted seepage through soil layers.

Silty sand soil was used by Wang et al. (2010) in order to form slope models that have heterogeneous layers which contain weak montmorillonite layers and high-permeability filter paper scrap mixes. The purpose from this study was to assess the stability of slopes that were created from heterogeneous materials and exposed to rainfall events, particularly when compared to homogeneous slopes, when these contain highly permeable weak layers. According to experiments results, the wetting front proceeds rapidly when it enters the weak layers, resulting in rapid suction dissipation and shear zones production on the slope. Thus, due to the deformation development the zone at weak layers becomes discontinuous and expanded, and when the rainfall continues, a quick localization of the zone occurs which leads to failure.

Centrifuge tests were conducted by Ling et al. (2009) to investigate slope stability induced by rainfall using sand and clay mixtures with a 60° slope model. In terms of rainfall simulation system, mist spray nozzles were used to simulate the rain event, and rainfall intensities ranged from 5.3 to 11.8 mm/h at a centrifuge acceleration of 80g, whereas rainfall intensities varied between 6.1 mm/h and 13.6 mm/h when centrifugal acceleration was 60g. It was observed that the reduction of matric suction, which accompanies decreased apparent cohesion, caused slope instability during rainfall. The slope instability occurred due to the slight decrease in the apparent cohesion, as a consequence, slip surfaces caused by the rainfall were very close to each other when the model was exposed to rains of different intensity. Threshold curves were created that show the relationship between rainfall intensity against duration, which were very near to the recorded global threshold as shown in Figure 3-9.

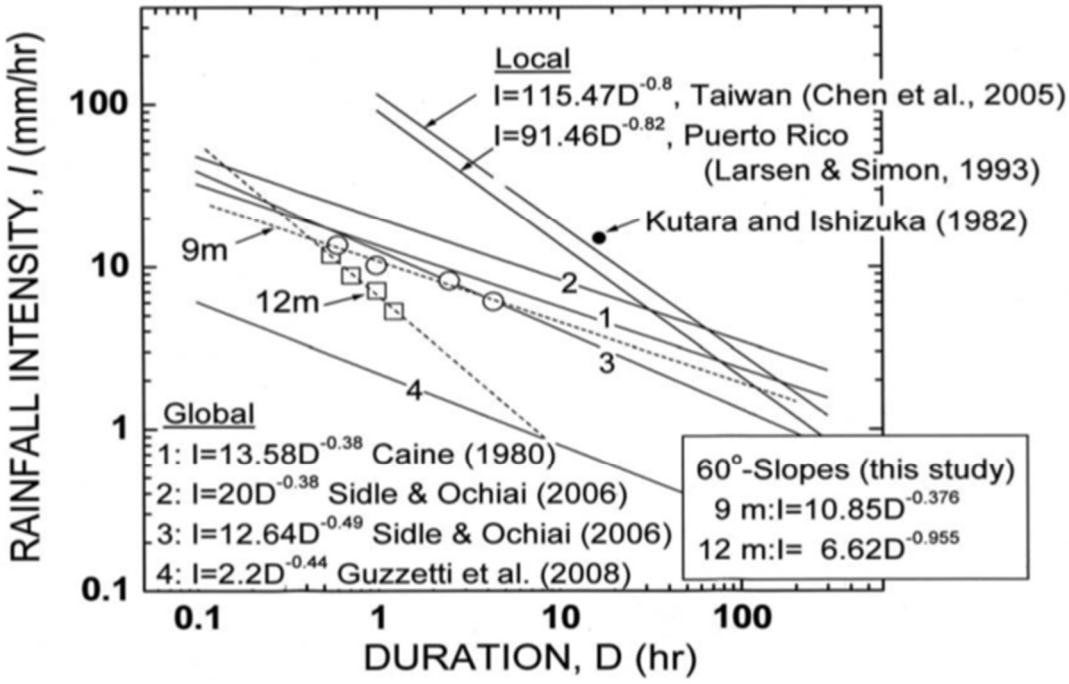


Figure 3-9 Threshold curves: The relationship between rainfall duration and rainfall intensity Ling et al. (2009)

Centrifuge model experiments were conducted by Askarinejad et al. (2012) using silty sand mixture to simulate the same boundary conditions on a natural slope in Switzerland which functioned as a test of full-scale. The bottom-up saturation mechanism caused the collapse of a natural slope when subjected to precipitation after several hours. Furthermore, a simulation of the static liquefaction failure mechanism was carried out by using a viscous liquid and reducing the velocity of seepage.

Zhang (2005) investigated the mechanism of static liquefaction failure on loose fill slopes using centrifuge testing. The loose fill slopes were formed using a mixture of sand and completely decomposed granite (CDG). The groundwater level rise and the simulation of precipitation events were among the boundary conditions of the groundwater. The rainfall simulation system that was applied to the slope models had an outlet plate which consisted of four small chambers, where the bottom plate contained 220 holes with a diameter of 0.5mm. This setup was created with the intention of just supplying water to the crest of the slope. In the sandy slope case, a cover consisting of an iron fine mesh placed on the top of slope, was added in order to prevent erosion due to droplets impact on the surface, rather than reducing droplets size. Alternatively, in the case of slopes generated by CDG, a 5 mm layer of coarse CDG was applied on top of

the crest surface. A rapid flow failure at elevated groundwater level was seen in the 24° sand slope model, which was caused by static liquefaction under undrained conditions. However, when precipitation was applied, a failure event at the crest edge of the model occurred due to seepage flow under drained conditions.

Caicedo et al. (2010) conducted experiments on physical modelling in relation to the interaction of soil with the atmosphere in centrifuges, focusing on the evaporation process. They evaluated the evaporation scaling factor and found that in order to maintain the same equilibrium between the soil and the atmosphere, the potential evaporation had to be increased by a factor of N in both the prototype and the model.

Jayakody et al. (2023) investigated the influence of intermittent antecedent rainfall patterns on landslide initiation in silty sand slopes, emphasising the significance of rainfall patterns beyond cumulative totals in landslide risk assessments. In this study, the authors conducted four centrifuge model tests, three of which examined slopes exposed to similar cumulative rainfall but varying antecedent rainfall patterns namely, uniform, decreasing, and increasing gap intervals between rainfall events. These experimental results were then compared with a three-phase, two-dimensional coupled hydromechanical finite element method (FEM) analysis, providing a robust framework to assess both hydraulic and mechanical slope responses under different conditions.

In Figure 3-10, the authors present a detailed visual representation of the deformation and failure surfaces observed in centrifuge model tests on silty sand slopes. This figure includes three key components: (a) the physical model showcasing the observed failure surface, delineated by a distinct line that highlights the zones of detachment and material slippage; (b) a schematic showing the initial slope geometry, including the development of tension cracks and the primary failure surface; and (c) numerical simulation results that displays incremental velocity fields across the slope, with colour-coded indicators that reveal varying degrees of displacement and areas of heightened instability.

The study focused on a 225-second antecedent rainfall period, applying each rainfall pattern (uniform, decreasing, and increasing gaps) before transitioning to continuous rainfall until slope failure occurred. Results indicated that the decreasing gap pattern produced the most rapid landslide initiation, while the increasing gap pattern led to the delayed failure. Notably, despite identical cumulative rainfall levels, the variation in timing significantly influenced the

initiation of failure. These findings suggest that early warning systems for landslides should account not only for cumulative rainfall but also for the specific patterns of antecedent rainfall, as these can greatly impact porewater pressure dynamics and slope stability.

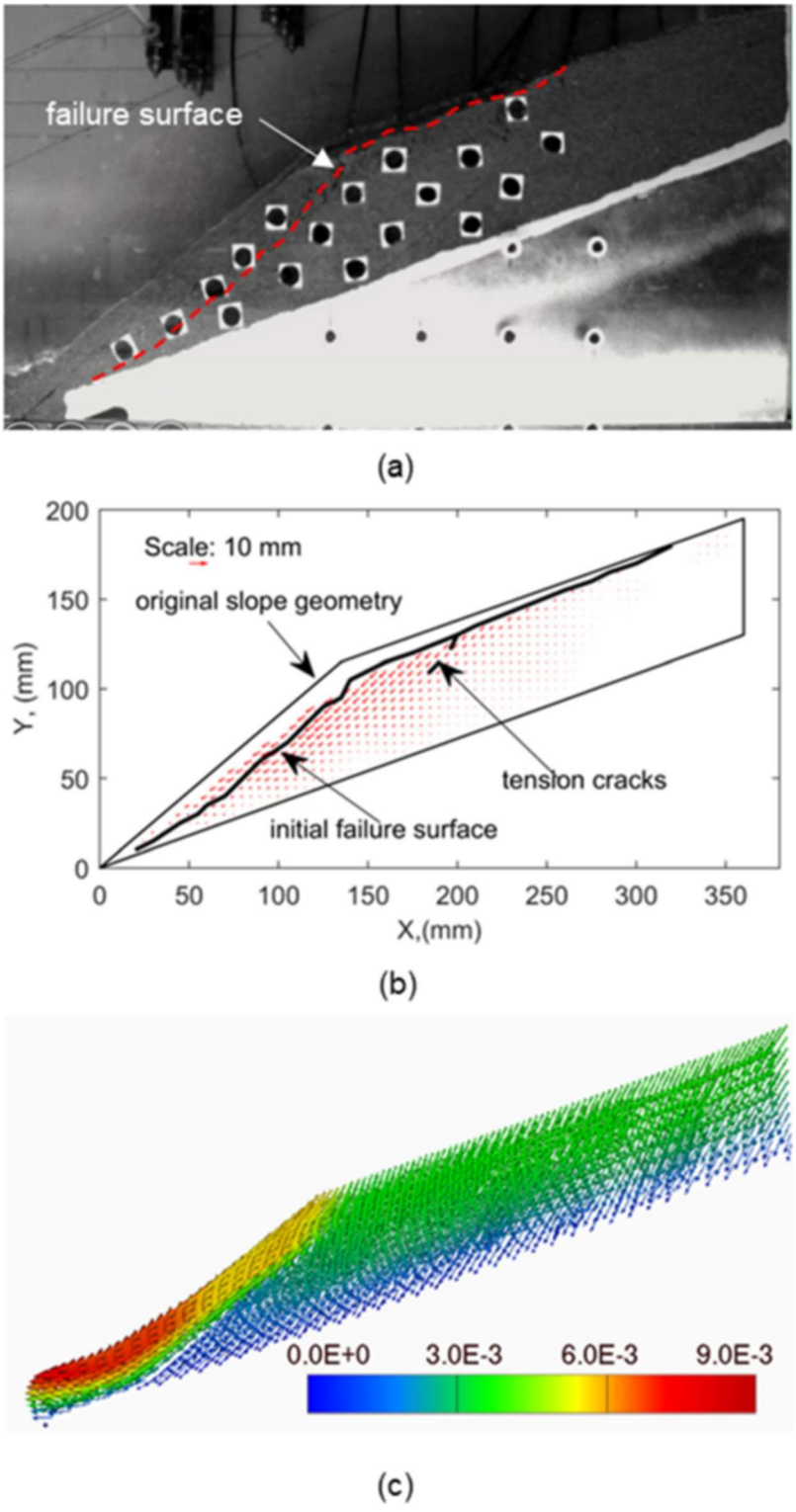


Figure 3-10 Deformation and failure surfaces in silty sand slopes under rainfall conditions Jayakody et al. (2023).

Figure 3-11 in the study by Jayakody et al. (2023) illustrates the impact of varying rainfall gap durations on pore water pressure (PWP) fluctuations. Shorter gaps lead to higher pore water pressure increases compared to longer gaps, which exhibit reduced PWP buildup, even reaching negative values. The buildup of positive Porewater pressure correlated with the wetting front's progression and slope instability, demonstrating that shorter gaps between rainfall events limit pore pressure dissipation and accelerate failure.

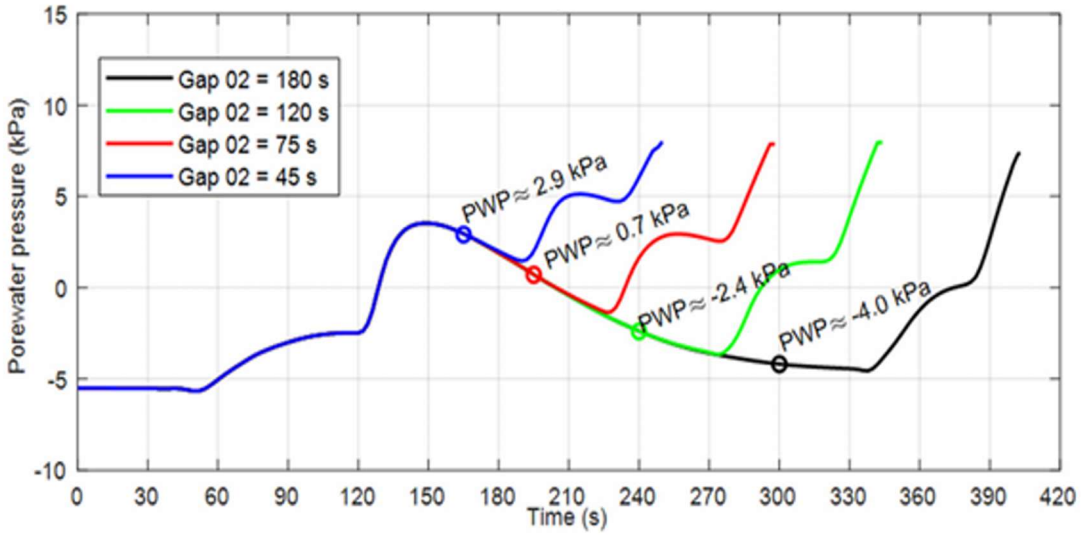


Figure 3-11 Effect of rainfall gap durations on pore water pressure (PWP) response in silty sand slopes Jayakody et al. (2023).

3.3 Knowledge Gaps, Novel Contributions, and Literature Integration

Chapters 2 provides an examination of the general literature and understanding of the behaviour of flood embankments and related slopes under weather cycles. Focusing on centrifuge studies, Chapter 3 provides an in-depth examination of the knowledge gaps, novel contributions, and integration of relevant literature. The key focus areas include the lack of studies on drawdown effects in centrifuge modelling, cyclic effects on mixed soils, and comparative analyses with similar studies.

1. **Drawdown Effects in Centrifuge Modelling**

Current research extensively explores slope stability under rainfall conditions and wetting-drying cycles, but limited studies focus on flooding combined with drawdown scenarios. Take

(2003) examined the effects of cyclic wetting and drying on pure kaolin slopes using centrifuge modelling, highlighting cumulative deformations under seasonal moisture variations but without investigating flooding or drawdown conditions. Hudacsek et al. (2009) conducted centrifuge modelling to investigate climatic effects on clay embankments, focusing on moisture variations and their influence on slope stability; however, their work did not explore flooding or drawdown scenarios. Ling et al. (2009) explored slope stability under varying rainfall intensities and different soil mixtures (sand-clay), focusing on infiltration behaviour rather than drawdown effects. Lee et al. (2008) investigated seepage mechanisms in layered fill slopes subjected to rainfall but did not address drawdown scenarios or cyclic loading effects.

Miao et al. (2018) investigated the stability and failure mechanisms of retrogressive landslides subjected to reservoir water level fluctuations using centrifuge model testing and numerical simulations. The results indicate that vertical displacement dominates during water level rise, while horizontal displacement is more significant during drawdown, leading to instability. Cracks first form at the slope toe and propagate towards the middle and rear, resulting in a retrogressive failure mode. The factor of safety initially increases during water level rise but decreases gradually when the water level remains stable. During drawdown, stability declines due to hydrodynamic pressure before recovering. Additionally, the study highlights that repeated reservoir water level fluctuations progressively weaken slope stability over time. These findings are closely related to this study, which examines the impact of hydrological changes on slope stability, particularly during drawdown. The results support the need for long-term monitoring and mitigation strategies to improve the resilience of engineered slopes under fluctuating water conditions.

Despite these contributions, the complexity of rapid versus gradual drawdown and its role in slope instability remains underexplored, especially when combined with preceding rainfall or flooding events. This research addresses these gaps by examining how different drawdown rates influence slope failure mechanisms under centrifuge conditions, particularly in gap-graded mixed soils. The integration of sequential flooding, cyclic wetting-drying, and drawdown phases provides valuable insights into slope behaviour under realistic hydrological conditions, offering practical implications for reservoir management and flood defence infrastructure.

2. Cyclic Effects on Mixed Soils

Previous research has predominantly explored cyclic loading in pure soils, such as kaolin or sandy materials (Jayakody et al., 2023; Ling et al., 2009). Jayakody et al. (2023) investigated the influence of intermittent antecedent rainfall patterns on landslide initiation in silty sand slopes, highlighting how variations in rainfall timing and frequency can significantly affect pore water pressure dissipation and slope stability. While valuable, their work did not explore the combined effects of cyclic wetting-drying and drawdown or the behaviour of gap-graded soil mixtures under such conditions. These mixtures, like the sand-kaolin mixture used in this study, are more representative of field conditions where heterogeneity affects seepage behaviour, volumetric strain, and slope deformation. Notably, the sand-kaolin mixture represents a gap-graded soil, a type that has not been extensively studied under cyclic loading and drawdown conditions. Gap-graded soils exhibit unique hydraulic and mechanical behaviours due to the presence of both coarse and fine particles, which influence water retention, infiltration, and deformation patterns under repeated hydrological cycles.

Take et al. (2004a) examined the impact of wetting-drying cycles on kaolin slopes using centrifuge modelling, demonstrating cumulative deformation under cyclic conditions. However, their research did not consider mixed or gap-graded soil compositions or the added influence of drawdown. This study builds on these findings by investigating how combined cyclic wetting-drying and drawdown phases affect slope stability in gap-graded mixed soils, addressing a critical gap in the literature and providing more field-relevant insights into slope failure mechanisms.

3. Comparative Analysis with Similar Studies and Validation Gaps

Few studies have systematically compared experimental centrifuge results with numerical simulations to validate predictive models. While in the ACHILLES project, Bračko et al. (2022), and Wong et al. (2022) have used numerical modelling tools like GeoStudio to analyse slope stability, they often lack physical validation under cyclic hydrological loadings. Take et al. (2003) investigated seepage and infiltration in unsaturated slopes but did not extend the work to encompass cyclic loading with drawdown. Ling et al. (2009) emphasized initial failure conditions in centrifuge tests, overlooking the progressive deterioration caused by multiple hydrological cycles. This research bridges these gaps by integrating Particle Image Velocimetry (PIV) for high-resolution displacement measurements and pore pressure transducers (PPTs) for internal stress monitoring against a numerical model of failure. The combination of experimental and numerical approaches not only enhances the accuracy of

predictive models but also provides a deeper understanding of the long-term performance of slopes subjected to realistic climatic variations.

4. Novel Contributions of This Study

This research presents an integrated experimental and numerical approach to evaluate slope stability under cyclic climatic conditions, including rainfall infiltration, flooding, and drawdown. Unlike previous studies that focused on isolated hydrological events or pure soil models, this work incorporates mixed soil compositions under multi-cycle testing, offering more realistic insights into field conditions. The findings demonstrate that slopes subjected to combined cyclic wetting-drying and drawdown events exhibit more pronounced deformations and lower factors of safety compared to single-event analyses. By validating numerical simulations with experimental data, this study contributes to the development of robust predictive models and practical design guidelines for infrastructure exposed to varying hydrological conditions.

5. Practical Implications for Engineering Practice

The results of this research have direct implications for the design and maintenance of flood embankments, reservoir slopes, and transportation infrastructure. Traditional design methods often underestimate the cumulative effects of repeated climatic loading, potentially compromising long-term stability. By highlighting the destabilizing influence of rapid drawdown and cyclic wetting-drying in mixed soils, this study underscores the need to revise current design standards (Dixon et al., 2006; UKCP18; Powrie and Smethurst, 2019). Incorporating the combined effects of these processes into slope stability assessments ensures that infrastructure remains resilient under increasing climatic variability, improving safety and extending service life.

CHAPTER 4

4.1 Soil calibration and preparation of slope model.

Laboratory soil classification testing is important to fully understand the soil conditions and also to enable back analysis of slope performance. Properties such as shear resistance, density, compressibility are fundamental to understanding and connecting observations of slope performance. This chapter gives details about the soil classification used in this research including experimental tests according to the British Soil Classification System. Various laboratory tests were carried out in the soil mechanics laboratory of the University of Sheffield in order to classify the soil. Key tests carried out include particle size distribution, triaxial shear, and oedometer testing, as well as relative density testing, falling head permeability testing and Atterberg limits.

A number of initial trials of clay-sand mixtures was conducted. These were first checked for plasticity (Atterberg) limits and Proctor compaction. From this, a soil mixture that was 35% HST95 Fraction E sand and 65% E-grade kaolin clay was chosen for subsequent model making. Most other characterisation tests were then carried out on this mixture.

4.1.1 Particle size distribution.

Given that the soil used was artificially manufactured from sand and clay, the particle size distribution, PSD, was determined by combining the PSDs from the individual components.

For the Fraction E sand (HST95) used in this study, a process of sieving was conducted to determine the particle size distribution of the coarse-grained soil. The soil sample was sieved through a series of standard test sieves with mesh sizes based on *BS1377: Part2: 1990 :9.3*. The soil mass remaining in each sieve was computed, along with the cumulative percentage of mass passed through each sieve.

The soil categorization parameters, such as effective diameter D_{10}, mean diameter D_{50}, and D_{60}, which represents the particle size of which 60% of the soil is coarser were obtained from particle size distribution curve as shows in Figure 4-1. Therefore, the soil is classified as gap graded where:

C_u (coefficient of uniformity) = D_{60} / D_{10}, which measures the range of particle sizes in the sample. C_c (coefficient of curvature) = $(D_{30})^2$ / (D_{10} × D_{60}). Table 4-1provides information about the shape of the particle size distribution curve.

Table 4-1 Characteristics parameters of HST95 fraction E sand.

Sand fraction E	
D10	90
D30	160
D60	180
Cu	2
Cc	1.58

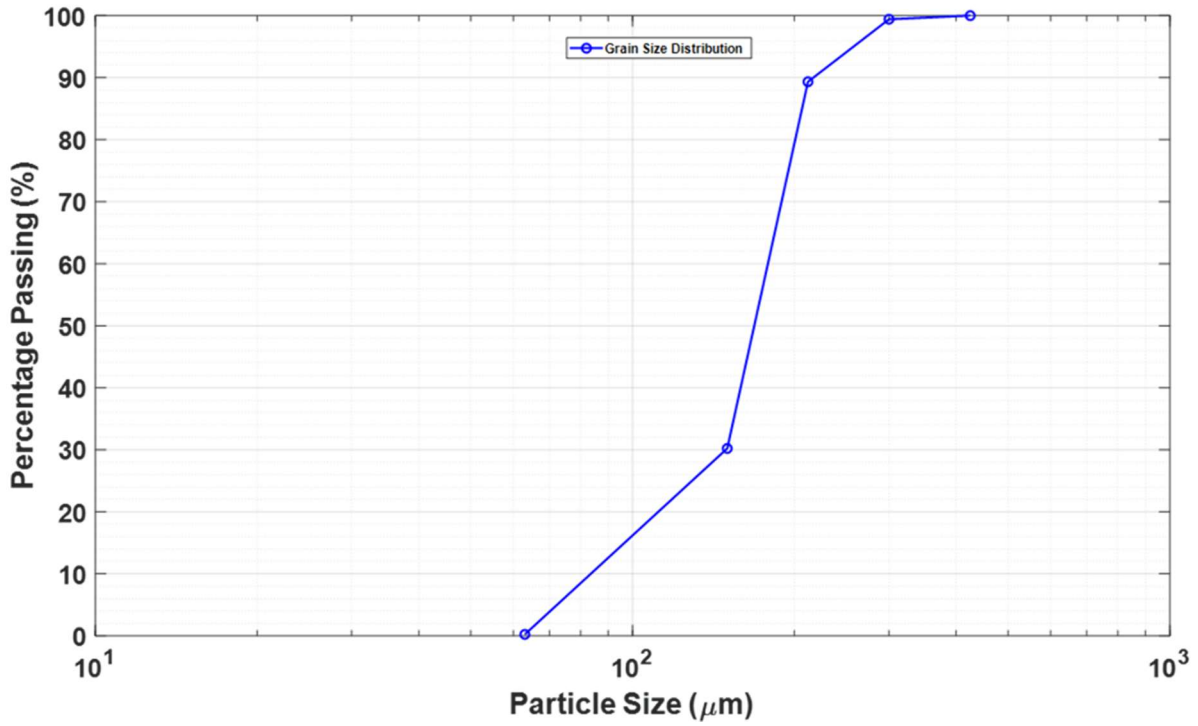


Figure 4-1 Particle size distribution of HST95 sand fraction E.

For the clay component, *BS1377: Part2: 1990: 9.5* describes the hydrometer analysis using sedimentation test. Hydrometer tests were conducted on fine material passing through the 0.063 mm sieve and clayey soil. The sedimentation test is based on Stokes' Law which states the velocity of falling particles that have smooth spherical shape suspended in a fluid, will settle at a certain speed due to gravity as shown in the following equation:

$$v = \frac{d^2}{18\eta}(\rho_s - \rho_f) \qquad 4\text{-}1$$

Where: -

d = Particle diameter

ρ_s = Density of particle

g = gravitational acceleration =9.81 m/s^2

ρ_f = Fluid density

η = Fluid viscosity

In practice, this indicates that particles of larger size are a quicker to settle out of suspension. In this research the hydrometer analysis method was conducted to determine the grain size distribution of the fine material.

According to the requirements of *BS1377: Part2: 1990: 9.5.2.1* a hydrometer was calibrated and used to determine the density of the solution at various time intervals. A 1000 ml glass measuring cylinder was used to prepare the suspension. The solution of fines or kaolin and water was shaken up until the particles were evenly distributed throughout the liquid and this is at the beginning of the test (t=0). All the large and coarse-sized particles settle to the bottom of the fluid when 1000 seconds has passed. When the time approaches 3000 seconds all coarse the particles of clay have settled and only the fine particles are left suspended. After 48 hours, the test procedure ends from the start of the mixture initial shaking. The distribution of grain size from the hydrometer test was obtained (conducted twice to determine the mean value) to plot the final curve. Figure 4-2 illustrates the results of a hydrometer test conducted on E-grade kaolin.

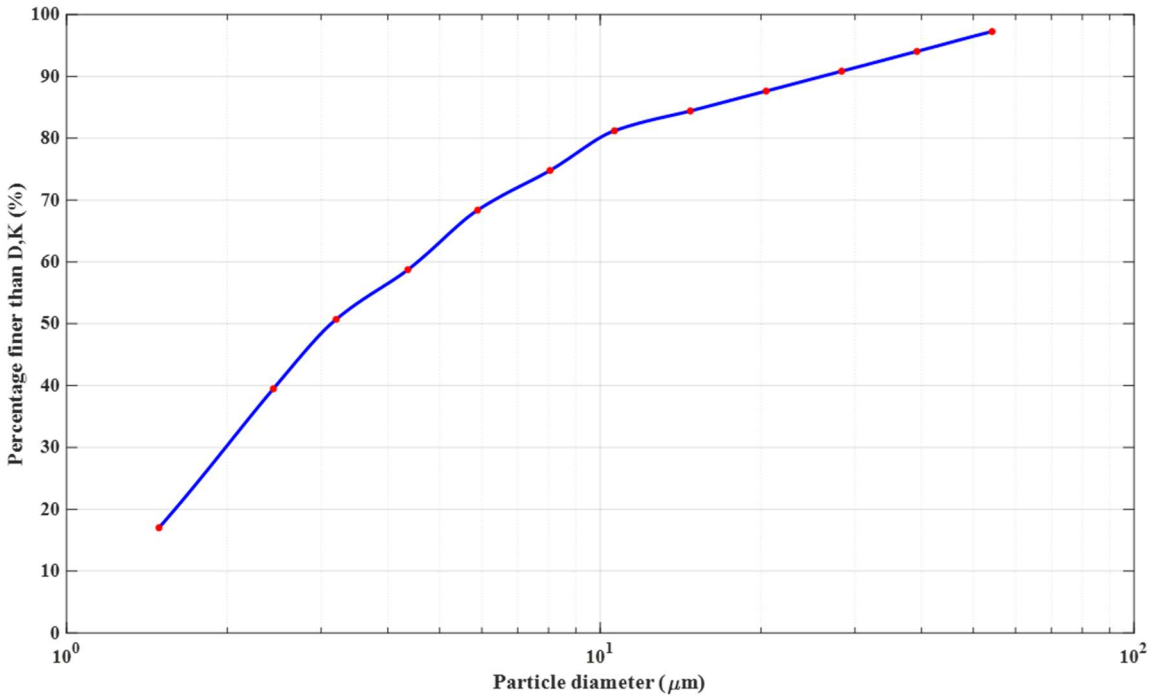


Figure 4-2 Sedimentation test for E-grade kaolin clay.

Final PSD Characteristics:

The results from both the sieve analysis and hydrometer test are combined to produce a comprehensive PSD curve that covers the entire range of particle sizes in the soil sample. The combined data ensures an accurate representation of the soil's gradation, from the finest kaolin particles to the coarser sand particles.

Figure 4-3 represents the particle size distribution (PSD) of a soil sample, which is a mix by mass of 35% sand and 65% kaolin. The distribution curve was generated using data obtained from both sieve analysis and hydrometer testing.

The combined soil is classified as gap-graded, a term used to describe the lack or limited occurrence of specific particle sizes within its distribution. In this graph, the relatively flat sections in the middle portion (approximately 3 µm to 50 µm) suggest a gap or deficiency in certain intermediate particle sizes.

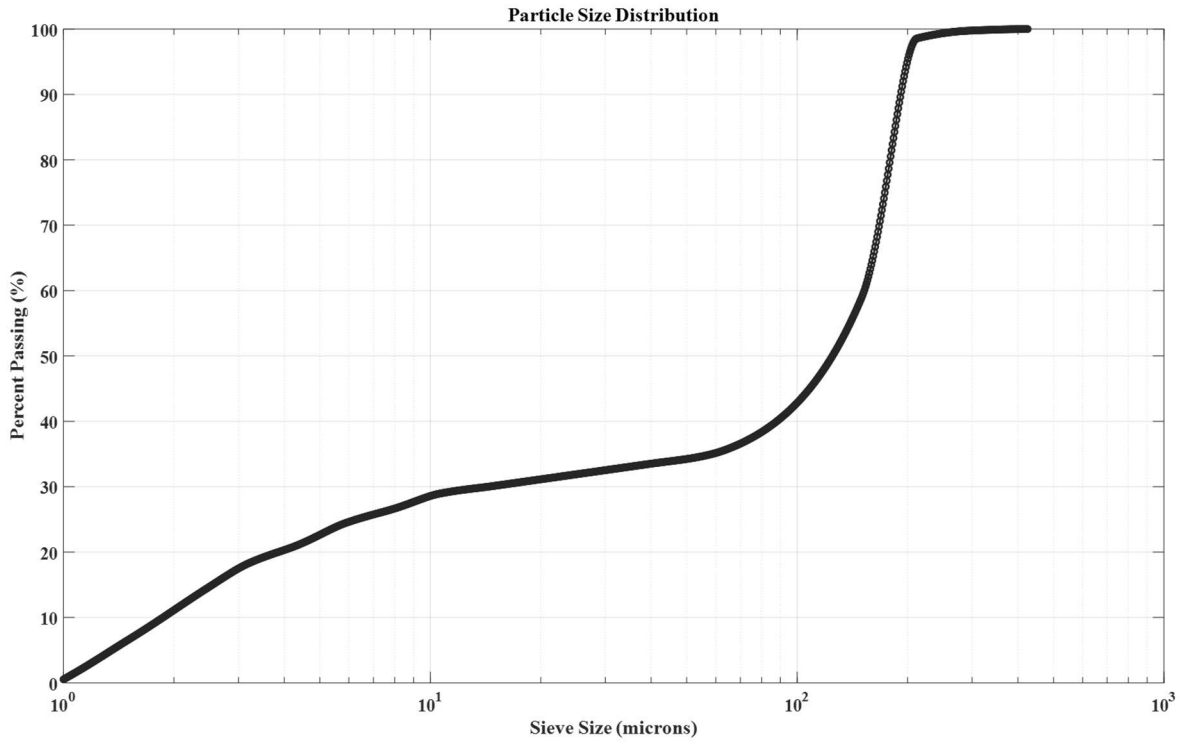


Figure 4-3 Particle size distribution curve for gap-graded soil (sand and kaolin).

4.1.2 Consistency and Atterberg limits.

Atterberg limit tests were also determined for kaolin-sand mixtures according to BS 1377:1999. While the focus was on kaolin and fraction E sand, the possible addition of bentonite was considered in order to evaluate the impact of plasticity of the soil mixture base and to alter the soil mineralogy to generate greater volumetric response due to changing moisture conditions.

Figure 4-4 shows boundaries that mark transitions from a liquid to a plastic state (liquid limit, LL or w_L), from a plastic to a semisolid state (plastic limit, PL or w_P), and from a semisolid to a solid state of a fine-grained soil (shrinkage limit, SL or w_S).

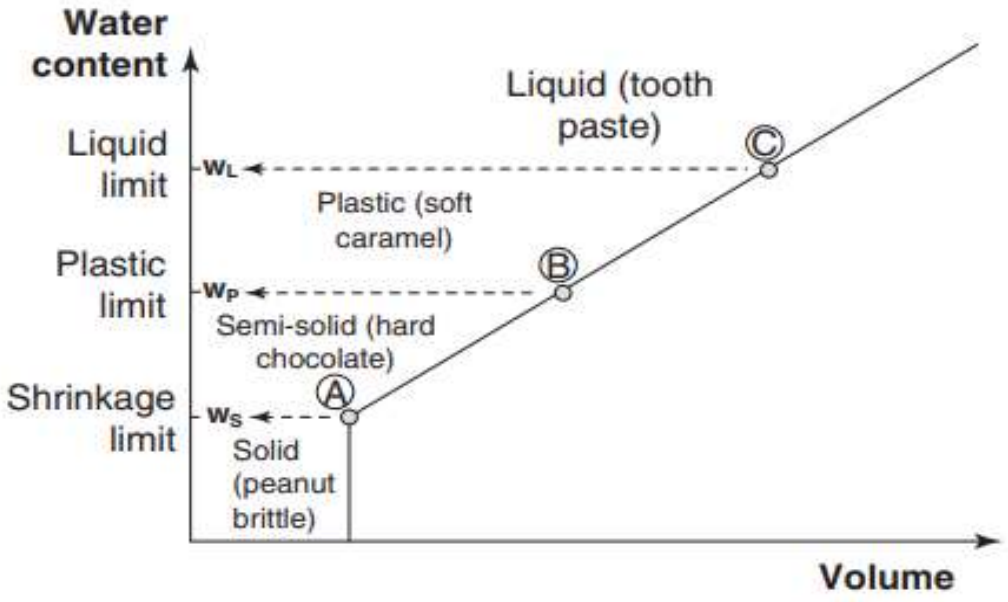


Figure 4-4 Consistency and Atterberg limits (Das and Sivakugan, 2017).

All tests were carried out with soil samples prepared by drying sieving finer than 0.425 mm. The initial of gravimetric water content was added that was expected to be lower than the liquid limit of samples and after that allowed for mature in a sealed container for 24 hours. The amount of water was controlled before being added to the soil each test and properly mixed to create a homogenous specimen. Therefore, all specimens were produced to a known gravimetric water content.

Liquid Limit

The liquid limit (LL) test identifies the water content at which the soil transitions from a plastic state to a liquid state. A falling cone test was used (BS 1377:1999). Five specimens of each mixture with various water content were examined to obtained the Liquid Limit (LL). The results are displayed in Figure 4-5. As the water content (%) increases, the penetration (mm) also increases for each mixture, indicating that the soils become more fluid-like (less stiff) as more water is added. This is expected in fine-grained soils like clays, where water softens the soil structure, causing higher penetration under the cone.

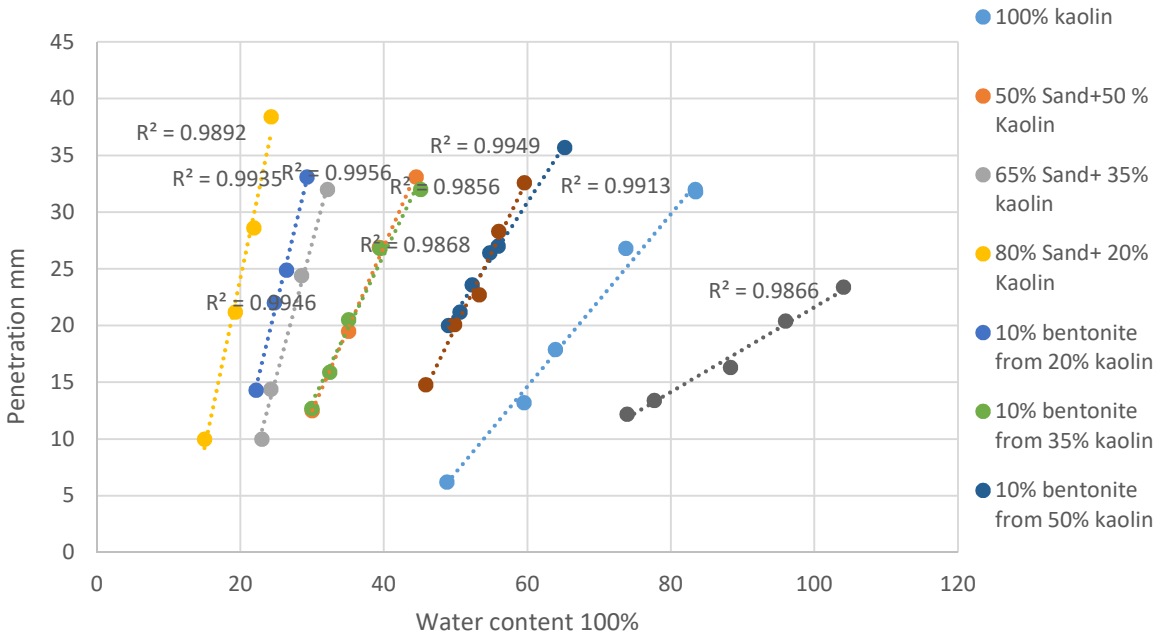


Figure 4-5 Results of liquid limit testing for several soil mixtures.

Plastic Limit

The plastic limit was determined for several mixtures using the procedure outlined in *BS 1377-2:1990*. According to this standard, the plastic limit is the water content at which soil threads rolled to a diameter of approximately 3 mm begin to crumble.

During the experiments:

1. Preparation: Soil samples were first air-dried and sieved to remove particles larger than 425 microns as per the standard specifications.

2. Procedure: The samples were then moistened and carefully rolled into threads until they reached a consistent diameter of 3 mm. This process was repeated for each mixture to ensure uniformity.

For several of the mixtures, the plastic limit was successfully obtained. These soils displayed enough plasticity to be rolled into threads without breaking prematurely, allowing for the measurement of moisture content at the point where the threads crumbled, indicating the plastic

limit. However, for certain mixtures, the test could not be completed successfully. These mixtures displayed a tendency to cut or crumble immediately upon rolling, making it impossible to form the required threads for a valid plastic limit test. This behaviour suggests that these mixtures have very low plasticity, or they may have already been in a semisolid or solid state at the tested moisture content, indicating that they could not retain enough water to exhibit plastic behaviour as per the BS 1377 standard.

In summary, the mixtures that crumbled immediately could not be tested for plastic limit using the BS 1377 procedure due to their inability to remain cohesive at the 3 mm thread diameter. This could imply that the clay content in these mixtures is too low or that the materials are inherently non-plastic. In contrast, the mixtures that allowed for successful rolling demonstrated sufficient plasticity and yielded reliable plastic limit values.

Shrinkage Limit

The shrinkage limit was measured in the lab for all the mixtures using procedures outlined in the British Standard *BS 1377-2:1990*. Specifically, it is performed using:

1. A soil specimen at its liquid limit (or natural moisture content),

2. Dried in a controlled environment,

3. The volume change is monitored as the soil dries, until no further shrinkage occurs.

The shrinkage limit is calculated as shown in following equation:

$$SL = \frac{W_s}{W_d} \times 100 \qquad 4\text{-}2$$

Where:

- W_s is the weight of the soil at the shrinkage limit.
- W_d is the weight of the dry soil.

Plasticity Index

The Plasticity Index (PI) is determined as the difference between Liquid and Plastic Limits, that is:

$$PI = LL - PL \qquad 4\text{-}3$$

Results

Different liquid and plastic limits were obtained from different soil mixtures in order to evaluate volumetric moisture response. The averages of liquid, shrinkage limits and plastic index for some of these mixtures are presented in Table 4-2.

Table 4-2 Atterberg limit testing results of several soil mixtures.

Soil types	LL	SL	PL	PI	PI^*_{max}
100% kaolin E	67	11.9	34.2	32.8	55.1
50% Sand & 50% Kaolin	35	11.4	NA	NA	23.6
80% Sand & 20% Kaolin	18	6.9	NA	NA	11.1
65% Sand & 35% Kaolin	27	8.5	NA	NA	18.5
100% Bentonite	380	16.2	84.7	295.3	364.1
90% kaolin +10% Bentonite	97	15.9	45.7	51.3	81.1
90% Sand + 10% Bentonite	50	5.7	NA	NA	44.3
5% bentonite + 45% Kaolin + 50%Sand	49	13.3	NA	NA	35.7
2% Bentonite + 18% Kaolin + 80%Sand	25	6.3	NA	NA	18.7
3.5% Bentonite + 31.5% Kaolin + 65%Sand	36	9.3	NA	NA	26.7

Casagrande plasticity chart:

The Casagrande Plasticity Chart is a graphical tool used in geotechnical engineering to classify fine-grained soils based on their Liquid Limit (LL) and Plasticity Index (PI). It helps engineers determine the behaviour and suitability of soils for construction projects by providing insight into the soil's plasticity characteristics. This chart allows visualisation of where soil types fall in terms of plasticity and liquid limit, to classify them accordingly.

Since the shrinkage limit (SL) was able to be measured but not the plastic limit (PL) for some soils, it is difficult to directly calculate the plasticity index (PI). However, since the shrinkage limit must be less than or equal to the PL, this was used for plotting purposes. In the absence

of measured plastic limit values, we can use the shrinkage limit to obtain an upper bound on the plasticity index PI. The plasticity index bound (PI^*_{max}) would then be:

$$PI^*_{max} = LL - SL \qquad 4\text{-}4$$

This equation gives an approximation to plot the data on the Casagrande Plasticity Chart.

Figure 4-6 shows the relationships between the liquid limit (LL) and plasticity index (PI) for different soil mixtures. The legend displays the various types of soil mixtures, each with a different colored marker. The A-line (shown red) on the Casagrande Plasticity Chart indicates the transition from clay to silt behaviour – with clays plotting below and silts above. The U-line (shown green) represents the upper boundary of typical natural soils. Soils that plot above the U-line are generally not considered natural soils. The data points in the figure represent the Plasticity Index (PI) values calculated for each soil sample. The Plasticity Index provides insight into the range of moisture content over which the soil maintains plastic behaviour. This characteristic is crucial in understanding the soil's mechanical properties, as it defines the extent to which the soil can deform without fracturing.

For some soil samples, however, obtaining the plastic limit was impossible because the soil threads broke easily. In such cases, the max Plasticity Index PI^*_{max} was determined using the shrinkage limit (SL) as an alternative. By incorporating the shrinkage limit, it was possible to approximate the outer limit of plasticity of the soils for mixtures where obtaining a consistent plastic limit proved impractical. This approach allowed for a more comprehensive assessment of the soil's plasticity characteristics, providing insights into the behaviour of materials that could not be accurately tested using traditional methods for determining the plastic limit due to their propensity to cut or crumble during testing.

The mixtures include combinations of kaolin, sand, and bentonite in varying proportions. Each data point represents a specific soil mixture tested, providing insights into how different combinations of materials impact soil plasticity properties. While it may appear from the plot that the soil mixture of 65% sand and 35% kaolin is classified as CL (clay with low plasticity), this is an upper limit (as the Shrinkage Limit SL will be lower than the PL). This means the soil has low to very low plasticity, which impacts its behaviour under loading and its suitability

for engineering applications. It is also interesting to note that the use of the SL rather than PL for the PImax puts the soils upper limit of plasticity along the U line.

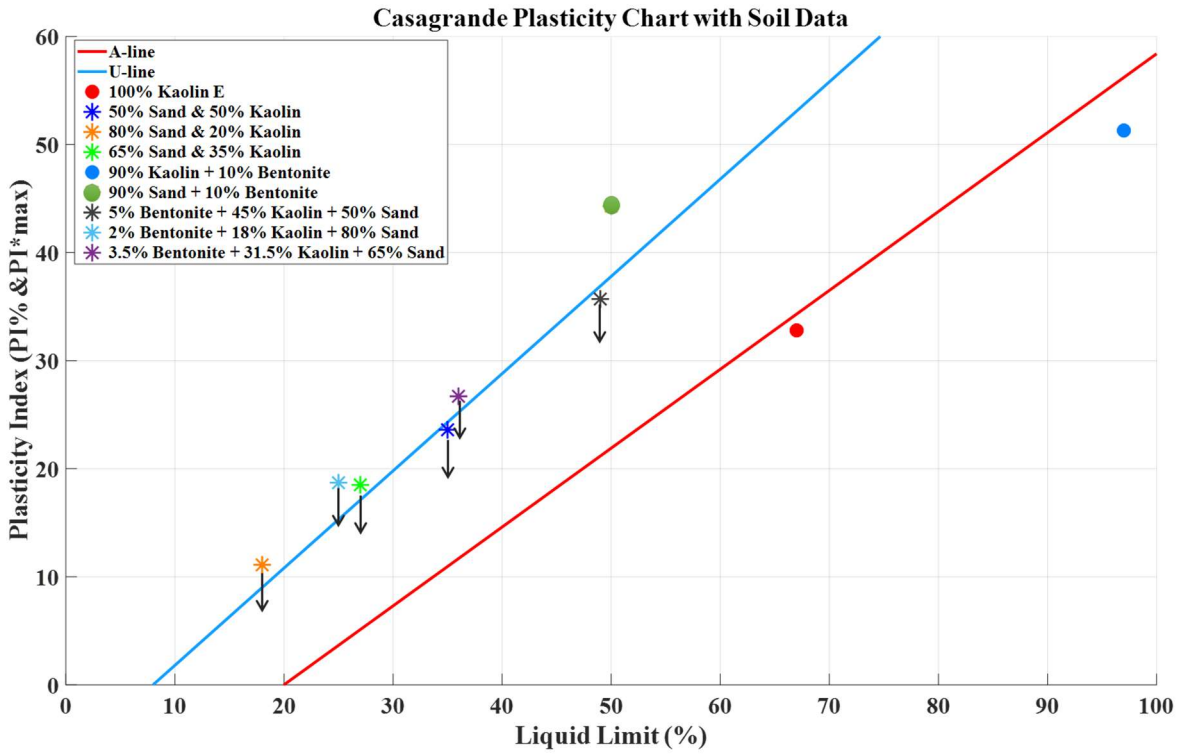


Figure 4-6 Modified Casagrande plasticity chart for all soil mixtures tested excluding 100% bentonite. Note that PImax has been used for the majority of mixtures (denoted as small stars) while PI has been used for 100% kaolin and 90% kaolin + 10% bentonite (denoted as circle).

4.1.3 Standard Proctor Compaction test.

Tests were conducted on pure kaolin and sand-kaolin mixtures to determine the optimum placement density. The dry densities for various kaolin-sand mixtures ranged between 1700 to 1800 kg/m³, aligning well with typical field compaction values. Additionally, the optimum moisture content for all the mixtures was found to be approximately 12%.

In accordance with BS 1377: Part 4: 1990: 3.3, a series of standard compaction tests were performed to identify the maximum dry density and optimum moisture content for each mixture. presents the data collected from these tests, where each mixture was subjected to compaction at varying water contents to determine the best compaction characteristics. Among

the mixtures tested, the combination of 65% sand and 35% kaolin exhibited the highest dry density of 1840 kg/m³, achieved at an optimum moisture content of 12.4%. This mixture demonstrated the most favorable compaction properties and was, therefore, selected as the most suitable material for constructing slope models.

Table 4-3 Results of standard compaction tests for different mixtures.

Type of mixtures	**w/c (%)**	**γ_d (kg/m^3)**
50% sand + 50% kaolin	9.1	1620
	11.57	1700
	13.41	1710
	19.33	1620
80% sand + 20% kaolin	8.5	1710
	10	1760
	11.88	1790
	15.7	1700
65% sand +35% kaolin	6.5	1680
	8.5	1760
	12.4	1880
	18.2	1690
100% kaolin	5	900
	15	1200
	21.26	1320
	36.11	1210
	54.16	1020

Four mixes tests were conducted based on the standard compaction test BS1377: Part 4: 1990: 3.3 in order to identify the maximum dry density and optimal moisture content. As illustrated in Figure 4-7, the mixture of 65 % sand and 35 % kaolin produced the highest dry density (1840 kg /m^3 at an optimum water content of 12.4%), so that it was considered to be the most appropriate mixture for creating slope models.

$$\rho_d = \frac{\left(1 - \frac{V_a}{100}\right)\rho_w}{\frac{\rho_w}{\rho_s} + \frac{w}{100}} \qquad 4\text{-}5$$

Where:

ρ_d is the dry density.

V_a is the percentage of air void.

ρ_s is the particle density.

ρ_w is the density of water.

w is water content of the soil.

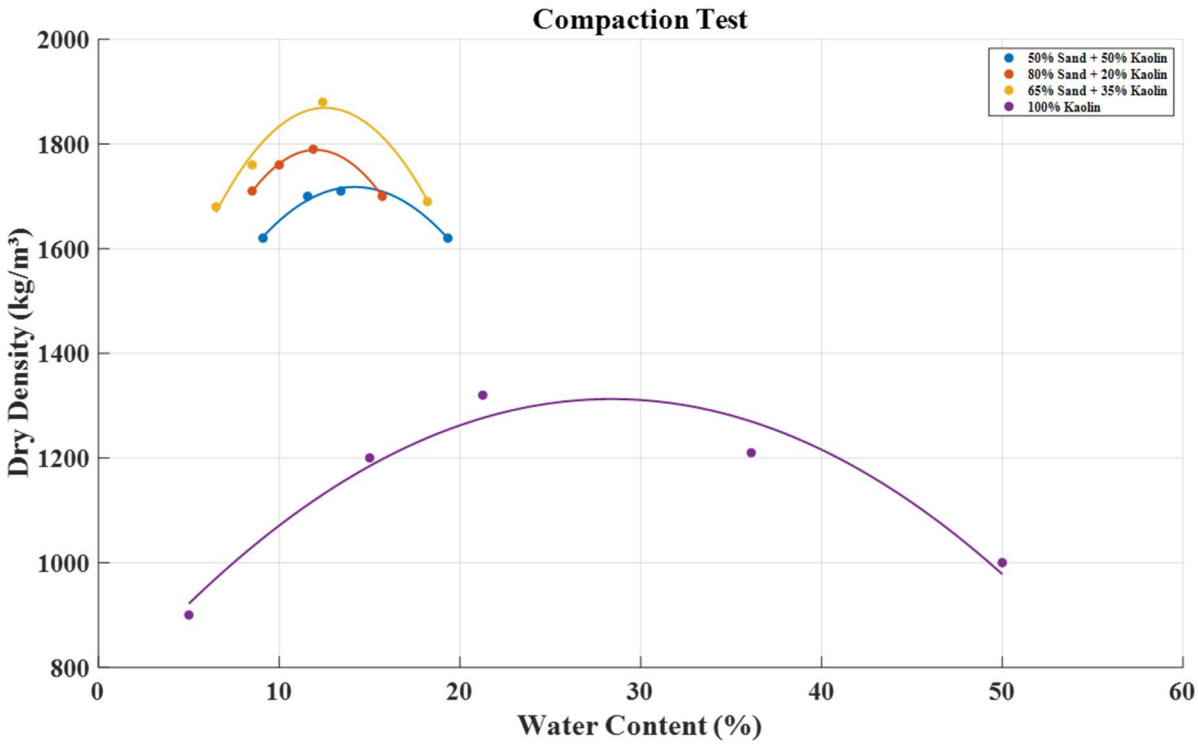


Figure 4-7 Standard proctor compaction test results of various soil mixtures.

4.1.4 Rowe cell testing of the soil.

Rowe consolidation tests were conducted to generate initial understanding of the consolidation characteristics of the chosen soil mixture via the coefficient of consolidation c_v. Also from this data, permeability, k and coefficient of compressibility, m_v were estimated to enable selection of suitable infiltration rates for the rainfall simulation. The test setup involved placing a sample of the soil mixture into a Rowe cell apparatus shown in Figure 4-8, which allows for controlled vertical loading and drainage. The soil sample was first prepared by mixing 65% sand and 35% kaolin with a water content of 34% to produce slurry. After that, the slurry was placed in the apparatus, ensuring uniformity and avoiding disturbance to the sample structure. Incremental loads were applied to the soil sample using a pressurised system in the Rowe cell. Each load

increment was maintained for a specific duration until the consolidation of the soil sample reached equilibrium. The settlement of the soil was recorded over time, providing data for calculating the coefficient of consolidation (c_v). The coefficient of compressibility (m_v) was derived from the consolidation curves, which relate the applied stress to the resulting strain (change in volume or settlement). This parameter provides insight into how compressible the soil mixture is under load.



Figure 4-8 Rowe cell apparatus for consolidation testing.

The compression index (Cc) was obtained from the e-log p graph that represents the experimental results of the consolidation test. In this study the average of Cc that calculated from Rowe cell testing is 0.027 and the coefficient of volume change is 0.00048 per kPa. The e-log P for the Rowe cell can be seen in Figure 4-9.

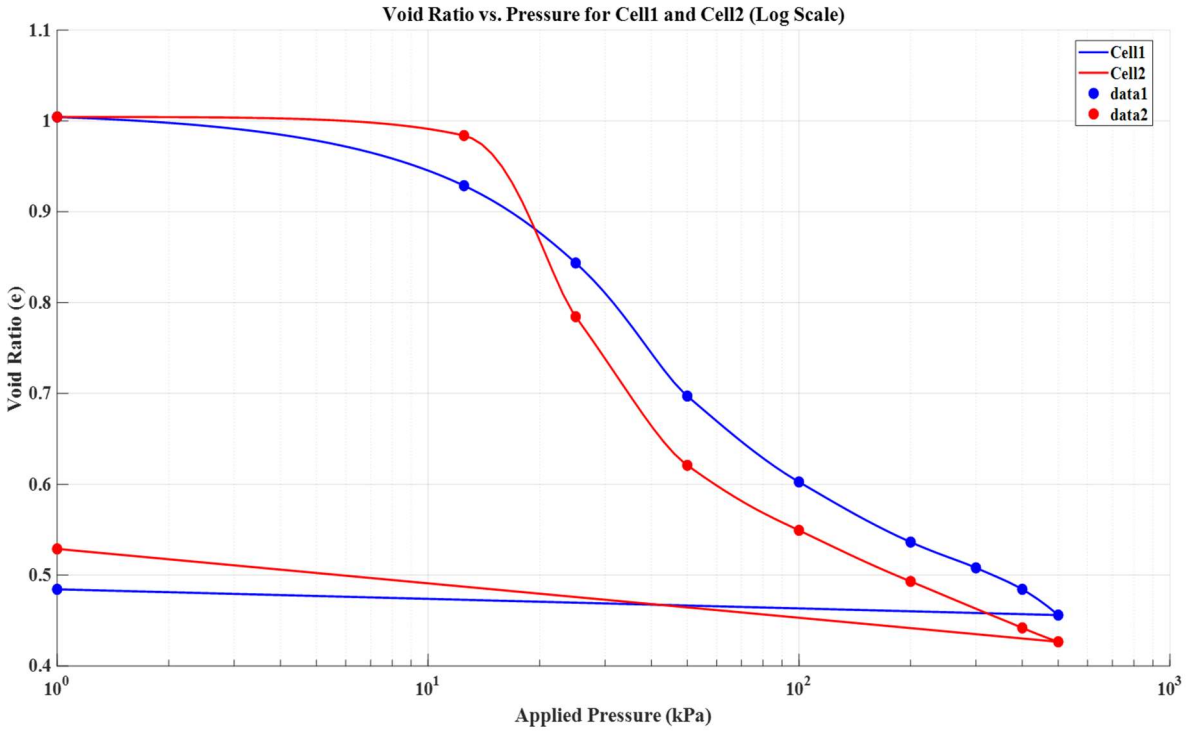


Figure 4-9 Void ratio and log applied pressure in Rowe cell tests.

4.1.5 Oedometer experiments

A series of oedometer experiments was conducted on samples that were taken from the Rowe cell, by inserting the metal oedometer ring with a 75mm inner diameter and 20mm high into the Rowe cell sample. After that the soil that surrounding the top and bottom of the lower ring was trimmed samples were prepared for testing. These had an average initial water content (w_0) of 16.6% and void ratio (e_0) of 0.44.

The samples were set to equilibrate for 24 hours, then the loads were applied to the soil samples, which was always submerged in water. Loads were applied as 50, 100, 200, 400 and 800 kPa, then unloaded in a reverse sequence. On a semi-logarithmic chart, the deformation with load increment, recorded during the test, is plotted as shown in Figure 4-10.

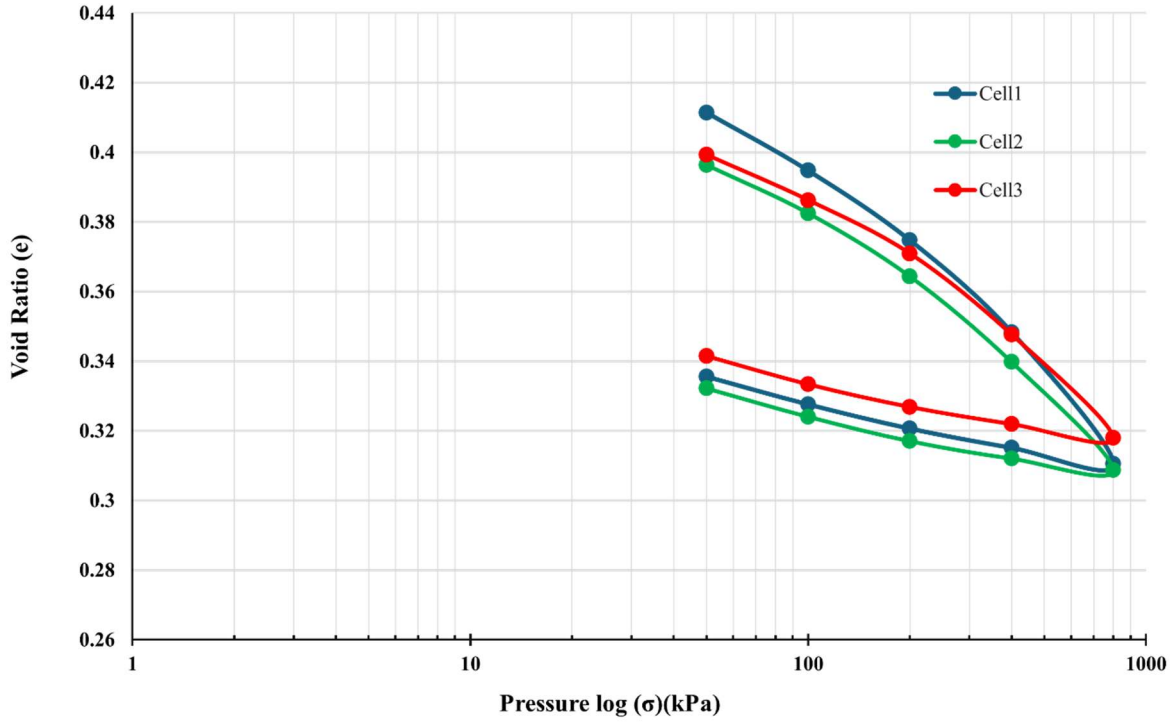


Figure 4-10 Oedometer void ratio and log applied pressure graph.

Swelling parameters from the oedometer test for all specimens were calculated according to the measured initial void ratio and the initial value of water content. Figure 4-11 shows a typical plot of settlement-time graphs for a given loading step on a square root-time basis, The following equation, which is used to calculate the value of the consolidation coefficient (c_v). was used to calculate the consolidation coefficient for a specific load increment of the test when the actual time (t) for a given percentage of primary consolidation is known.

$$Cv = \frac{0.848}{t90} h^2 \qquad 4\text{-}6$$

Where (h) is the maximum drainage path length and is equal to (H/2), (H) is height of the specimen that measured in mm during period of loading increment, t_{90} was obtained from square root graph in min.

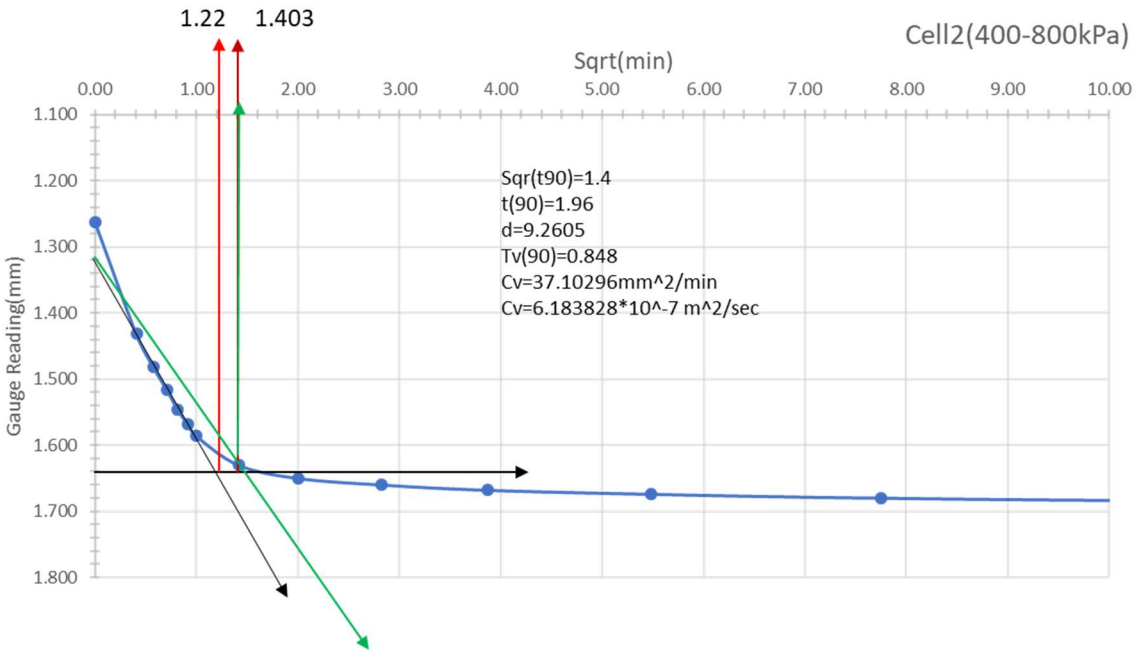


Figure 4-11 Example of square-root/settlement curve analysis.

Four coefficients were determined from consolidation experiments that describe soil compressibility and can be used to predict the amount of settlement due to primary consolidation.

1- Consolidation coefficient *(c_v)*
2- Compressibility coefficient *(m_v)*.
3- Compression index *(C_c)*.
4- Swelling index (C_s)

The following equation was used to obtain the coefficient of permeability, k, when the parameters c_v and m_v were calculated.

$$C_v = \frac{k \cdot m_v}{\rho_w} \cdot g \qquad 4\text{-}7$$

Table 4-4: Summarises the consolidation parameters determined from swelling curve from Oedometer test results while =

Table 4-5:Summarises the consolidation parameters determined from the Rowe cell.

Table 4-4 Oedometer consolidation test calculation of cell 1.

Pressure increment (kPa)	m_v (m^2/kN)	C_v (m^2/s)	k (m/s)	C_s
100-50	0.00016	3.82×10^{-7}	5.99×10^{-10}	0.020
200-100	7.4×10^{-5}	6.0×10^{-7}	4.36×10^{-10}	
400-200	3.2×10^{-5}	5.95×10^{-7}	1.86×10^{-10}	
800-400	1.1×10^{-5}	4.37×10^{-7}	4.71×10^{-11}	

Table 4-5 consolidation parameters determined from the Rowe cell.

Initial void ratio, e_0	1.098
Initial water content, w_0	41 %
Final water content, w_f	18.27 %
Compression index (C_c)	0.207

4.1.6 Shear strength

The accurate estimation of the shear strength parameters of the soils used in this study is required for the evaluation of the stability of slope models. The results of a number of laboratory studies to determine the shear strength parameters of various soils are included in this section. Strength tests have been undertaken to evaluate the shear strength of the sand and kaolin clay, individually and combined. Tests include shear box tests on Fraction E sand alone and consolidated-drained triaxial tests on sand-clay mixtures. The tests involve allowing water to drain out of the soil sample while it is being sheared, so replicating the conditions that soils would encounter in real-world situations characterised by gradual adjustment and settling in reaction to environmental loads and stresses. This form of testing is necessary to precisely ascertain the effective stress parameters and cohesive strength of the soil. These factors are vital for the design and analysis of engineering projects, including slope stabilisation, earthworks, and foundation engineering.

Direct shear tests on Fraction E sand

The direct shear test was conducted to evaluate the shear strength of the sand alone to identify the maximum and peak friction angles. The shear box test procedure was conducted based on BS 1377:1990-7. The maximum void ratio of the sand was determined to be 0.756, and the minimum void ratio was 0.508. The sand tested had a dry density of 1710 kg/m³, corresponding to a relative density of 80%. These values provide context for the sand's compaction state during testing, which has a direct impact on its shear strength and deformation behaviour. A relative density of 80% and a dry density of 1710 kg/m³ indicate that the sand was in a dense state, which typically results in higher peak shear strength, lower compressibility, and enhanced resistance to deformation.

The test was carried out on dry specimens using three different normal stresses: 25 kPa, 50 kPa, and 100 kPa until failure occurred. Each curve corresponds to a test with a different normal load applied to the sample. Figure 4-12 presents the shear box results for fraction (E) sand. In all three tests, shear stress increases sharply at the beginning as the sample undergoes initial deformation. The higher the normal stress applied, the higher the peak shear stress observed. After the peak, the shear stress decreases in all tests, indicating strain softening behaviour. The material then approaches a residual shear stress level, where the shear stress remains relatively constant as displacement continues The peak shear stress is reached at different displacements for each test, with the 100 kPa test reaching its peak at around 2 mm, while the other tests reach their peaks slightly later, around 3 mm.The average peak friction angle was found to be 42° while the critical friction angle was found to be 33°. These results are shown in Table 4-6.

Table 4-6: Analysis of peak and critical shear stresses in shear box tests at different normal stress limits.

	Peak (kPa)		Peak angle	Critical (kPa)		Critical angle
	Normal (X)	Max shear (Y)	(°)	Normal (X)	Shear @ ε = 25% (Y)	(°)
Test1	100	88	41.3	100	63	32.2
Test2	50	40	38.7	50	34	32.6
Test3	25	25	45.0	25	19	37.2
Average / mode	-	-	42	-	-	33

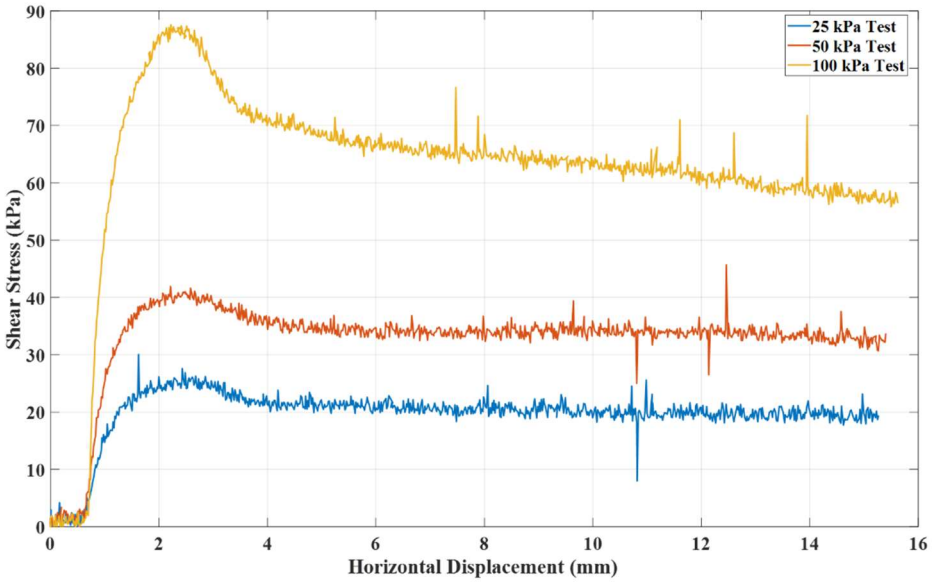


Figure 4-12 Results of shear box tests.

Figure 4-13 presents the relationship between the shear stress ratio (τ/σ) and the shear strain (ε_s%) for the three tests. The shear stress ratio is a normalised representation of the shear stress divided by the corresponding normal stress (τ/σ), allowing for comparison across different loading conditions. All three tests exhibit an initial rapid increase in the shear stress ratio as shear strain increases from 0% to around 5%. The normalised stress ratio (τ/σ) facilitates comparison between the tests by eliminating the effect of different normal loads, focusing on the relative shear resistance of the sand.

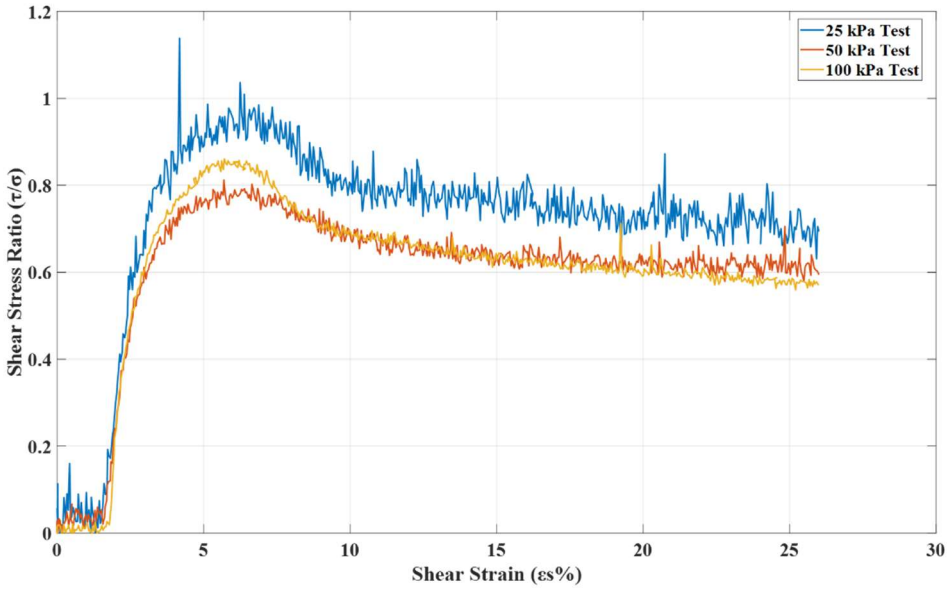


Figure 4-13 Normalised shear Stress Ratio (τ/σ) with shear strain (εs%).

Figure 4-14 illustrates the sand volumetric behaviour during shear loading, with an initial contraction followed by dilation. Dilation is most significant in the 25 kPa test, where the sand reaches a maximum volumetric strain of around 1.6%, indicating a greater degree of expansion. In comparison, the 50 kPa and 100 kPa tests exhibit maximum volumetric strains of approximately 1.1% and 0.9%, respectively. The maximum volumetric strain is reached at around 10% shear strain in all three tests, after which the rate of dilation slows and the volumetric strain levels off. The lower peak volumetric strains in the 50 kPa and 100 kPa tests show that as the normal stress increases, the amount of dilation decreases. This suggests that the higher normal stress compresses the particles more effectively, limiting their ability to expand during shearing.

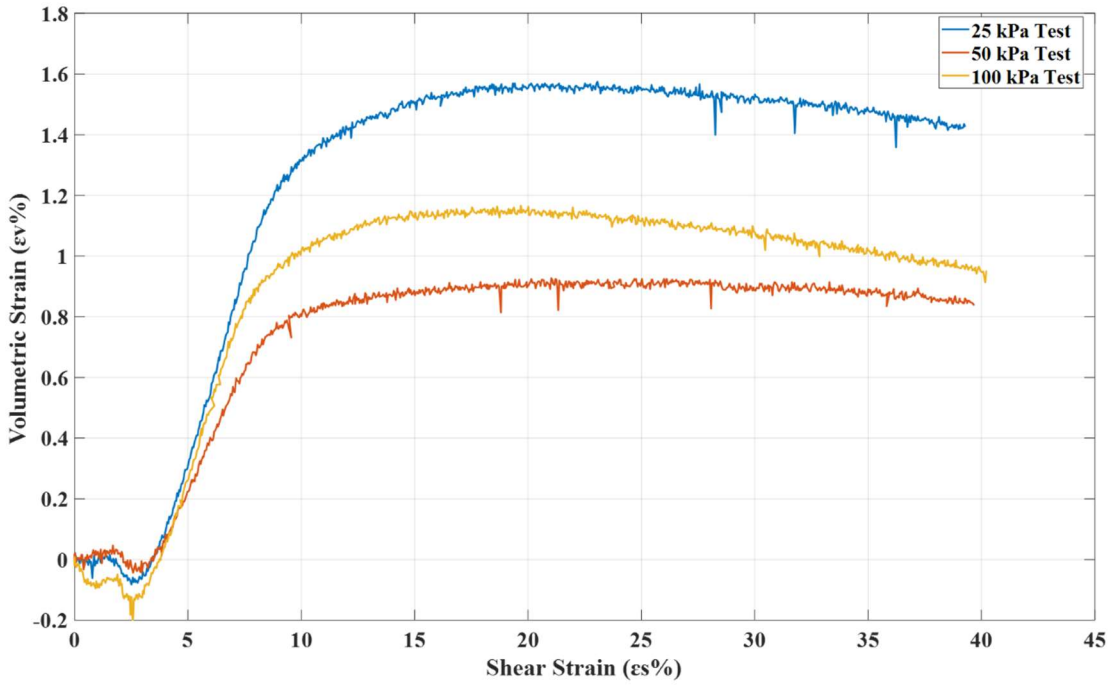


Figure 4-14 Volumetric strain (ε_v%) with shear strain (ε_s%) for different normal stresses.

Error! Reference source not found. presents the shear stress versus normal stress data along with the failure envelope for a series of shear tests. The failure envelope is a straight line representing the relationship between the peak shear stress and the normal stress, which helps to determine the shear strength parameters of the material, such as the cohesion and friction angle. The blue data points represent the peak shear stress values obtained from the tests at different normal stresses. The shear stress increases linearly as the normal stress increases, indicating that higher normal loads result in higher shear strength, consistent with typical soil behaviour. The red line is the failure envelope, which is fitted through the peak shear stress

data points. This line represents the Mohr-Coulomb failure criterion, which is used to describe the shear strength of the material:

$$\tau = c + \sigma.\tan(\varphi) \qquad 4\text{-}8$$

Where:

(τ) is the shear stress.

(σ) is the normal stress.

(*C*) is the cohesion of the material (y-intercept of the line).

(φ) is the friction angle (slope of the line).

From the plot, the cohesion is near zero (since the y-intercept is very small), which is typical for non-cohesive materials like sand. The friction angle is derived from the slope of the failure envelope, indicating the material's resistance to sliding under normal stress. A steeper slope indicates a higher friction angle.

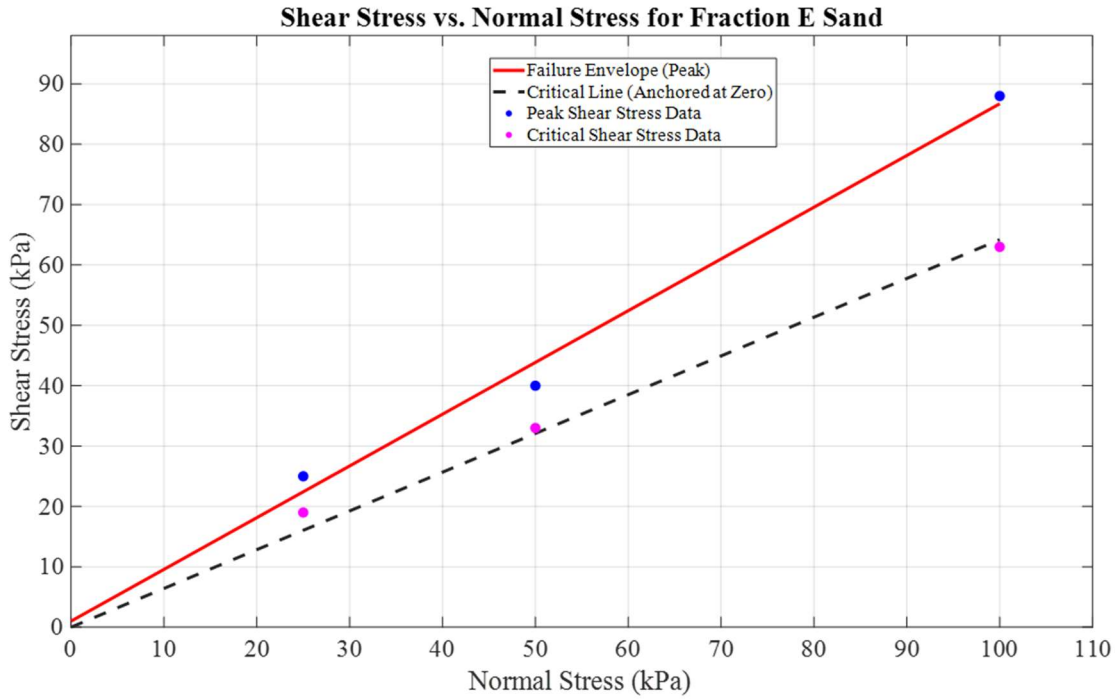


Figure 4-15 Mohr-Coulomb failure envelope for shear strength vs. normal stress for sand fraction E.

4.1.7 Triaxial test (Consolidated Drained or CD Test).

The triaxial test is one of the most common and important tests in geotechnical engineering used to evaluate the mechanical properties of soils, particularly their strength and deformation characteristics under controlled stress conditions. The Consolidated Drained (CD) Triaxial Test is a specific type of Triaxial test where the soil sample is allowed to drain during both consolidation and shearing, making it ideal for analysing the long-term stability of soils under drained conditions.

In the Consolidated Drained (CD) Test, the goal is to:

1. Allow the sample to fully consolidate under the applied confining pressure with the drainage lines open, so any excess pore water pressure is dissipated.
2. Slowly apply the axial load while continuing to allow drainage, ensuring that the soil behaves in a fully drained manner during shearing.

By applying different confining pressures and axial loads, the triaxial test can be used to determine the shear strength, stress-strain behaviour, and volume change characteristics of soils under controlled conditions.

Test setup and procedure:

Consolidated Drained traixial tests were conducted on the sand-clay mixture of 65% Fraction E sand and 35% kaolin clay. The British Standard (BS) that specifies the method for conducting the Triaxial compression test on soils, including the CD Triaxial test, is: **BS 1377-8:1990**

1. Specimen preparation:

The soil sample used in this experiment was cylindrical, with a height-to-diameter ratio of 2:1, while having dimensions of 50 mm in diameter and 100 mm in height. The specimen was placed inside a triaxial cell and surrounded by a radial rubber membrane to isolate it from the confining water. The full setup is shown in

Figure 4-16.The sample was extracted from a previously residual consolidated soil before testing in the centrifuge – i.e. from the soil block removed to construct the slope.

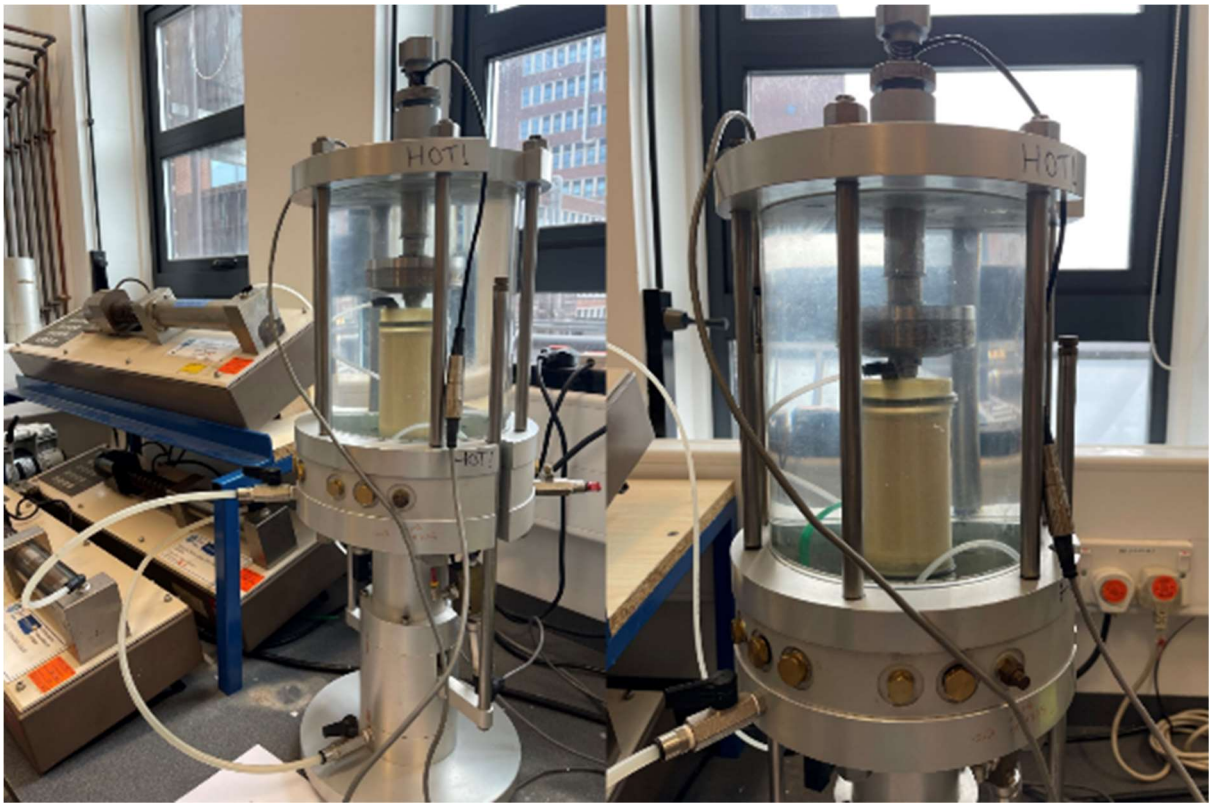


Figure 4-16 Setup of Triaxial test apparatus for soil testing.

2. Consolidation stage.

The soil specimen was subjected to an initial confining pressure, σ_3, which was applied by the fluid surrounding the sample within the triaxial cell. This confining pressure simulates the in-situ stresses that soil typically experiences under field conditions. Within this investigation, 3 tests were conducted, one for each confining pressure: 100 kPa, 200 kPa, and 300 kPa. Throughout this stage, drainage valves were left open to facilitate the escape of pore water. Complete consolidation of the soil occurred when all surplus pore water pressures had dissipated, resulting in a change in soil volume as it approached equilibrium under the applied confining pressure.

3. Shearing stage:

Once the consolidation process was finished, the sample was subjected to axial loading by the application of a vertical load or stress (σ_1) via the compression piston. During this phase, the drainage valves were maintained in an open position, facilitating the unrestricted drainage of pore water. The axial load was incrementally increased, resulting in the induction of shear stresses within the soil of the model. The soil deformed, and the applications of stress persisted

until the soil either failed due to shear or reached the desired level of strain. The axial load (σ_1) was gradually applied to prevent the accumulation of pore water pressure, ensuring that the soil demonstrated behaviour consistent with drained conditions.

Investigation of stress-strain reaction and strength characteristics

1. Shear strength

In order to construct the Mohr-Coulomb failure envelope, several samples are subjected to varying confining pressures during testing. The equation that represents this envelope of soil shear strength is as follows:

$$\tau = c' + \sigma' \tan(\varphi') \qquad 4\text{-}9$$

Where:

τ= Shear strength

c' = Effective cohesion

σ' = Effective normal stress

φ' = Effective angle of internal friction

2. Effective stress

Due to the drainage-facilitated dissipation of pore water pressures, the CD test obtains effective stress parameters. Analysing the long-term behaviour of soils is crucial, as the majority of field conditions provide adequate drainage.

Triaxial test results

The deviator stress versus axial strain for three different confining pressures (100, 200, and 300 kPa) is depicted in Figure 4-17. With an increase in deviator stress, the axial strain initially rises, reaches a maximum value, and then either stabilises or partially decreases, suggesting strain hardening followed by softening behaviour in certain instances. As the confining pressure increases, there is a corresponding increase in the deviator stress at the stage of failure.

The failure point for each confining pressure is identified when the deviator stress reaches its maximum value. These peak values correspond to the shear strength of the soil under the respective confining pressures applied during the test. Subsequent to the peak, the stress exhibits a slight reduction or achieves a stable state, indicating the features of post-peak behaviour. The Mohr circles are constructed, and the shear strength parameters are determined using the failure points (deviator stress at peak) for each confining pressure.

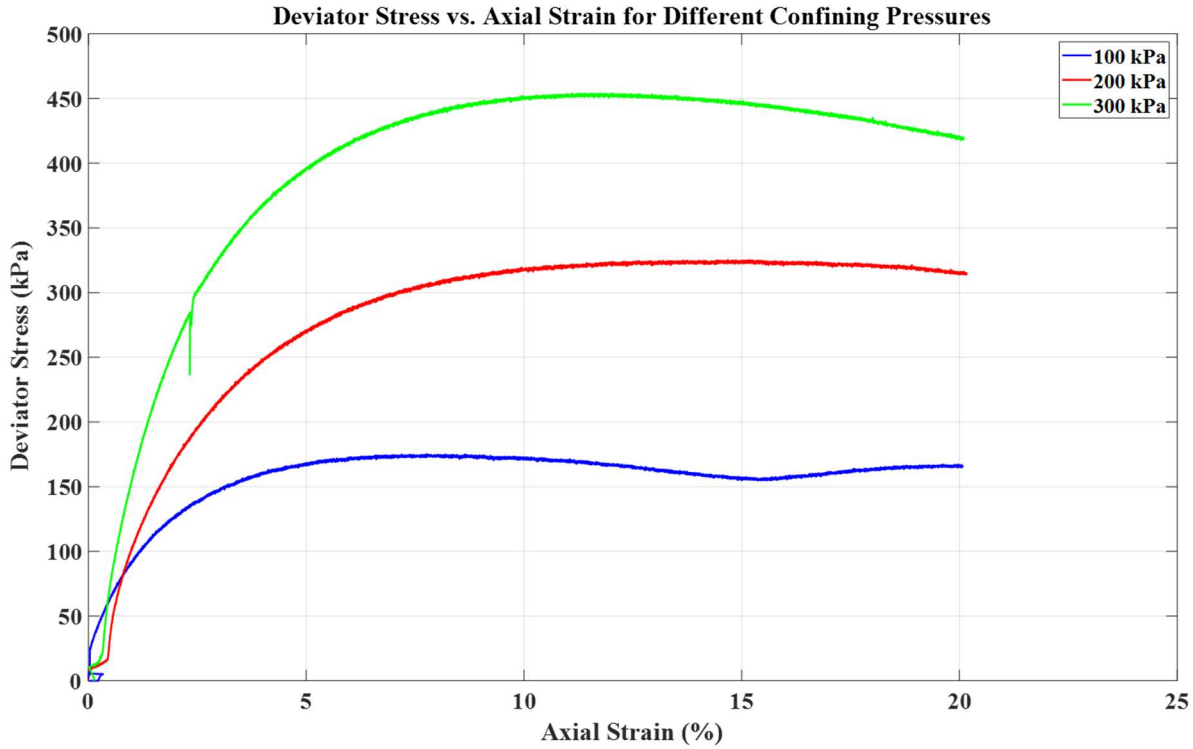


Figure 4-17 Deviator stress with axial strain for CD Triaxial tests at different confining pressures.

Mohr circles for three Triaxial tests conducted at various confining pressures (σ_3) are depicted in Figure 4-18. A failure envelope is constructed to determine the shear strength parameters of the soil by representing the stress states of the soil samples at failure under various conditions. The dashed line passing tangentially through all three Mohr circles is the Mohr-Coulomb failure envelope. The slope of this line indicates the friction angle (φ'), which is represented as 26.51° in the figure.

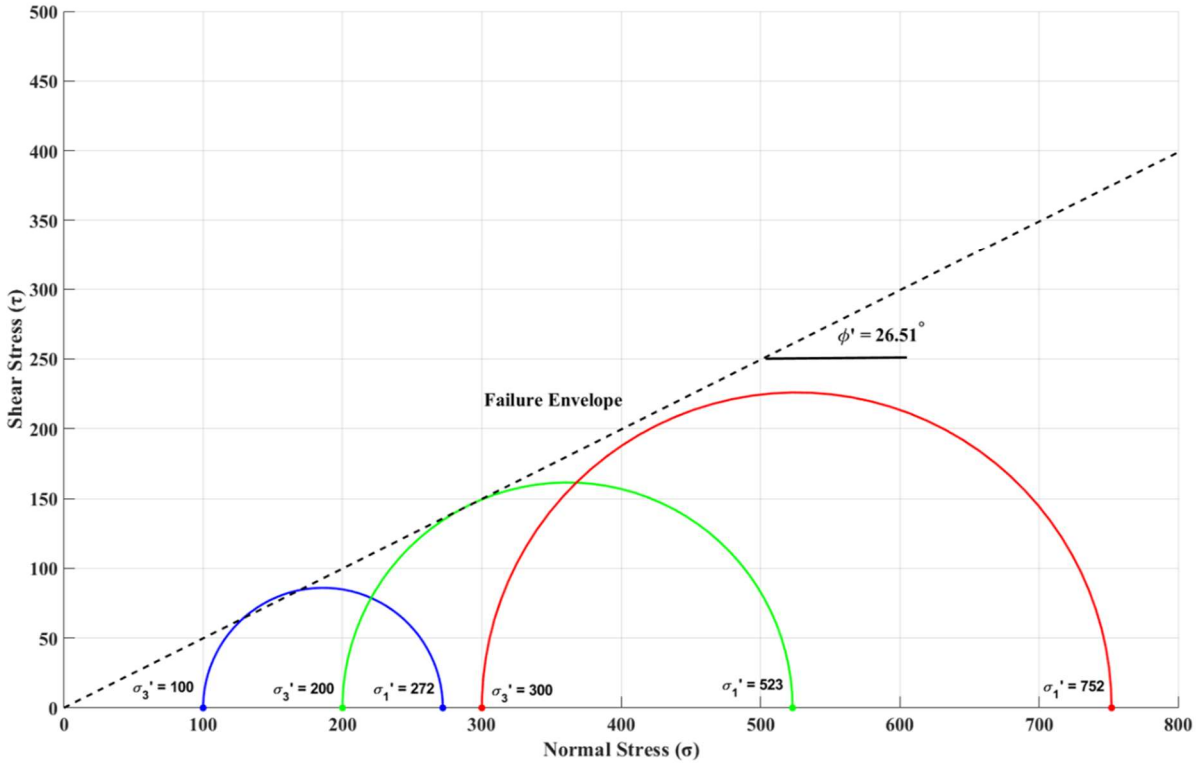


Figure 4-18 Mohr circles and failure envelope for triaxial test.

The relationship between volumetric strain and axial strain in soil samples subjected to three different confining pressures is demonstrated in Figure 4-19. With increasing axial strain, the soil undergoes initial contraction (negative volumetric strain) under all confining pressures, indicating compression and volume loss in the soil sample. The volumetric strain decreases rapidly at the beginning, which is characteristic of the soil adjusting to the axial load as voids between the particles reduce under increasing confining pressure. Subjected to higher confining pressures of 200 kPa and 300 kPa, the samples demonstrate more pronounced volumetric contraction compared to the sample at 100 kPa. Where the axial strains exceed around 10%, the curves start to stabilise and the rate of volumetric contraction reduces. By the end of the test (at around 20% axial strain), the volumetric strain values for 200 kPa and 300 kPa are closer together, while the 100 kPa sample exhibits much less volumetric strain.

The graph suggests that the soil exhibits contractive behaviour for all confining pressures, meaning that the volume decreases without any apparent dilatancy (volume expansion). This behaviour is typical in loose or normally consolidated soils where particles move closer together during shearing.

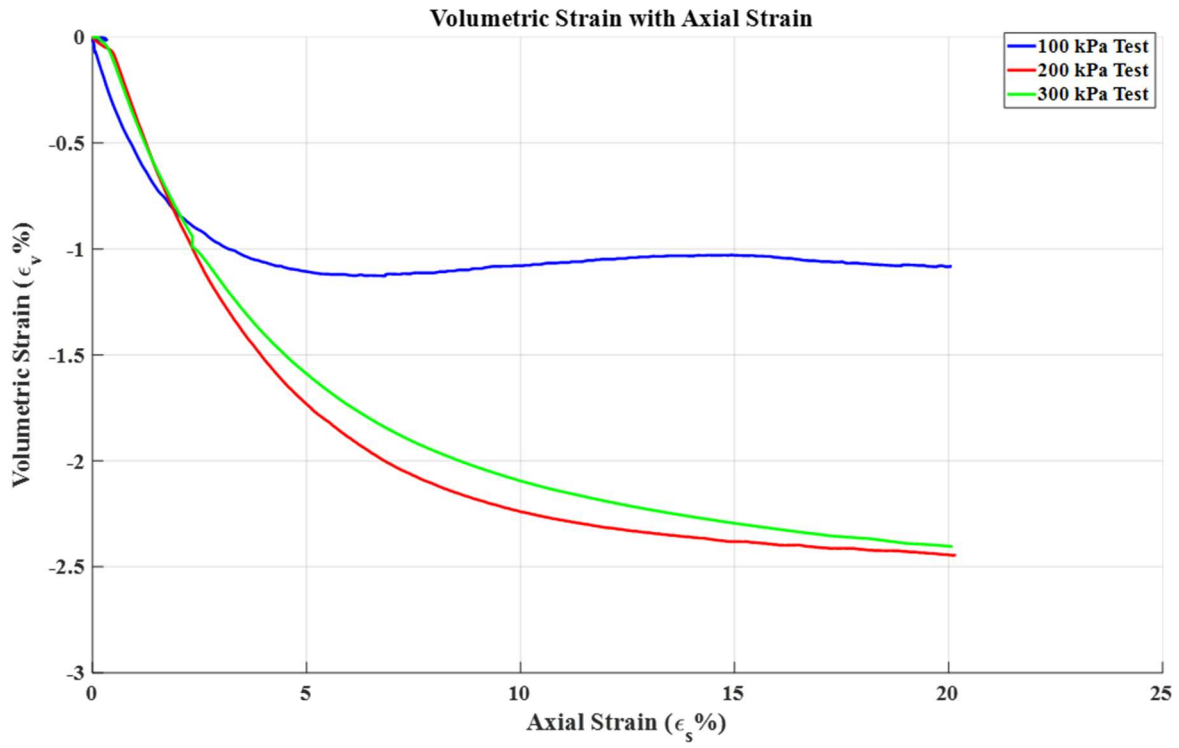


Figure 4-19 The relationship between volumetric strain and axial strain for different levels of confining pressure.

The plot of axial strain (%) against the ratio of q/p' is shown in

Figure 4-20 , where q represents the deviator stress (difference between the major and minor principal stresses, $(\sigma_1-\sigma_3)$ and p' represents the mean effective stress, which is the average of the principal effective stresses, typically calculated as $p' = (\sigma'_1+2\sigma'_3)/3$.

The ratio q/p', which is an indicator of the normalised deviator stress relative to the mean effective stress. This ratio helps in understanding the mobilised shear strength of the soil and is commonly used in critical state soil mechanics. The peak of each curve represents the maximum mobilised shear strength of the soil before it begins to soften. This peak is particularly notable in dense or over-consolidated soils, which exhibit a distinct peak strength followed by strain-softening behavior.

As the curves progress, they begin to converge or reach a plateau, representing the critical state. At the critical state, the soil deforms at a constant volume and stress ratio, implying that it has reached a stable condition where additional deformation occurs without an increase in stress.

The effect of confining pressure is evident in the Figure 4-20**Error! Reference source not found.** but it is also evident that the test conducted at 100kPa behaves with slightly more stiffness steeper initial slope and higher peak (q/p').

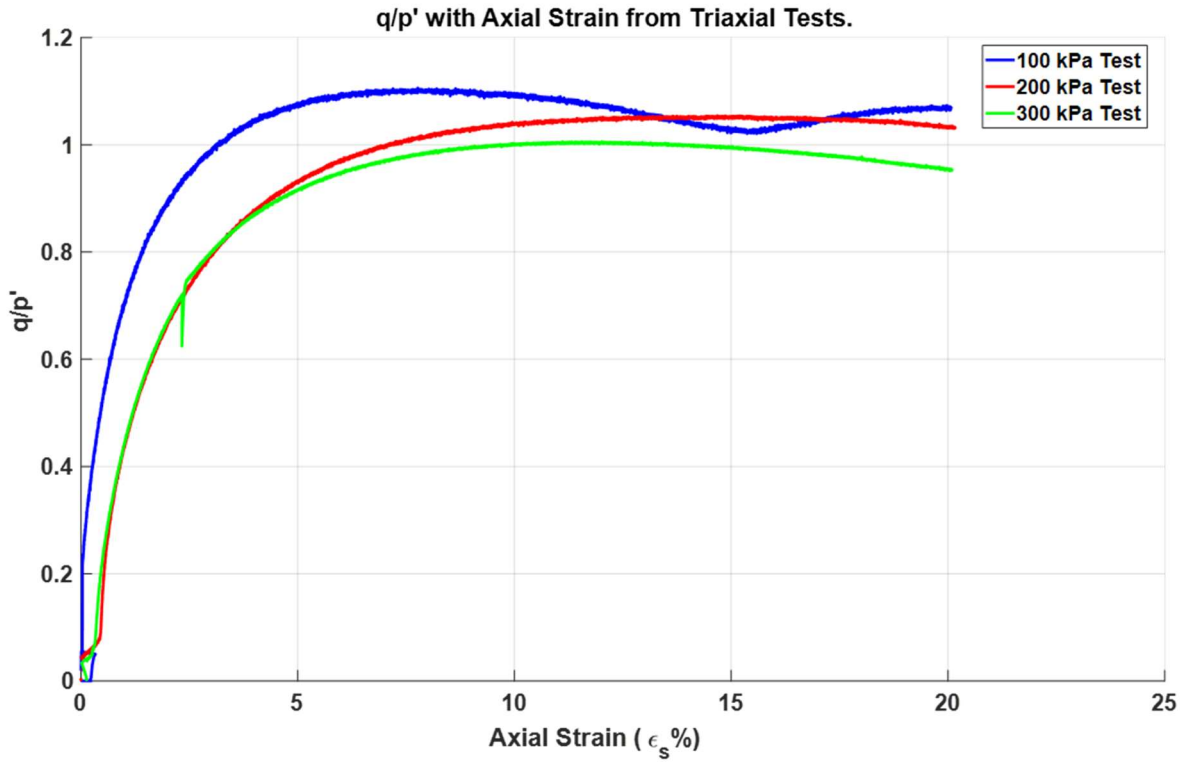


Figure 4-20 Stress ratio (q/p') vs. axial strain for Triaxial tests.

Triaxial test failure

The triaxial test sample depicted in Figure 4-21 exhibits a classical ductile shear failure marked by bulging in the central region. There is not a clearly defined shear plane or failure surface except towards the end. Instead, the deformation is distributed across a broader area, leading to the observed bulging. The latex membrane surrounding the sample shows some wrinkling, particularly around the bulged area. This occurs as the membrane stretches and conforms to the deformed shape of the soil.

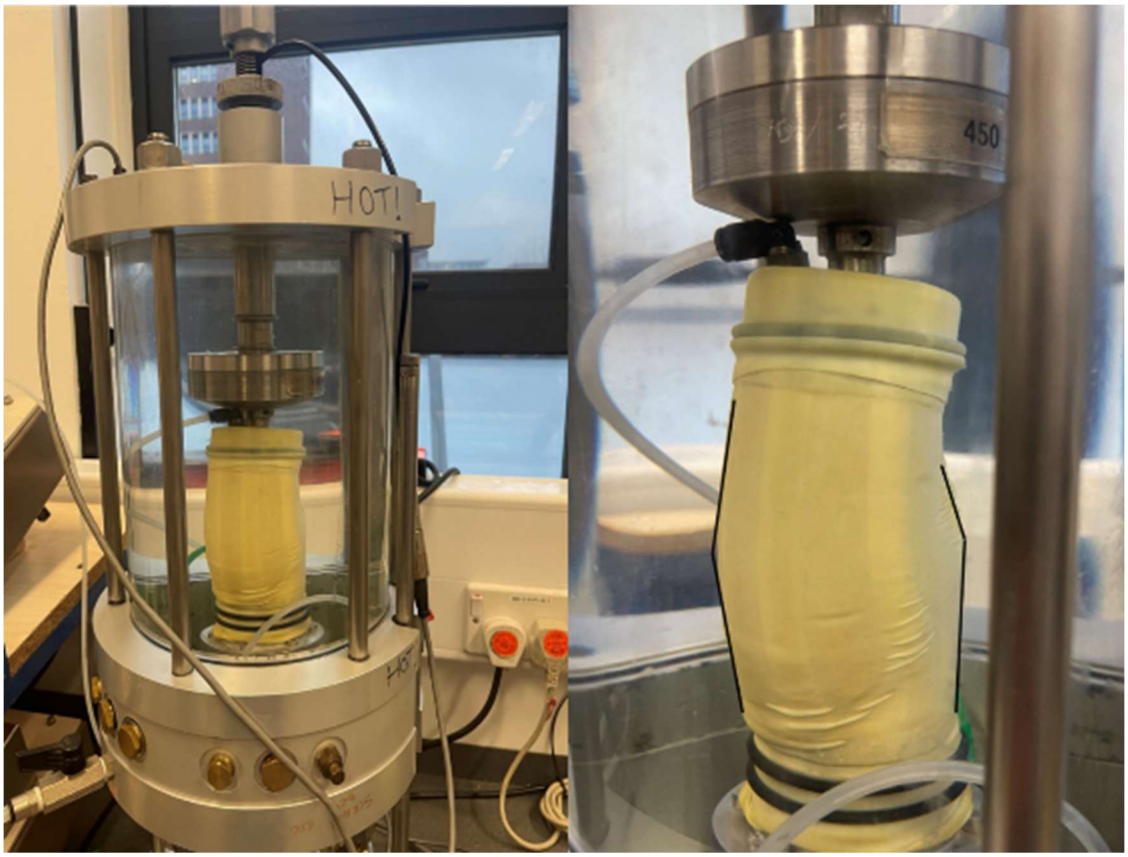


Figure 4-21 Shear failure of soil sample in Triaxial test apparatus showing bulging deformation.

4.1.8 Falling head permeability test

The study of soil permeability or hydraulic conductivity, k, used in the construction of the model is required in order to understand and control the rainfall infiltration during centrifuge testing, and to understand the drainage characteristics of the soil. In the laboratory, there are two methods to measure the hydraulic conductivity of soils, which are based on the grain size distribution. The laboratory tests for determining the soil permeability include:

1- Constant head test for high-permeability soils, such as sands.
2- Falling head test for soils that have intermediate and low permeability, for example clay and silty soil.

The falling head permeability test was conducted to determine the permeability of the soil mixtures used in the slope model. The test procedure followed the guidelines specified in BS 1377:1990 (Part 5) and is also discussed in the Head's Manual of Soil Laboratory Testing. The

setup for the test is shown in Figure 4-22, which illustrates the apparatus and methodology used during the testing process.



(a) (b)

Figure 4-22 (a): The general setup for the falling head permeability test. (b): Datum measurement.

A permeameter cell with a diameter of 100 mm and a length of 125 mm was used to test the mixture of sand and kaolin. The falling head permeability test works on the basis of calculating the difference of height between the inlet and outflow levels at any given time which is equal to (h-h0). The water quantity that flow through the specimen during specific time was calculated by multiplying the cross-section area of standpipe by the drop of water level.

$$\tau = dQ = adh \qquad 4\text{-}10$$

Based on Darcy's law and from the data collected from falling head test, the permeability of the sample was determined using following equation.

$$k = 2.3\frac{aL}{At}\log_{10}\left(\frac{h_1}{h_2}\right) \times 10^{-5} \qquad 4\text{-}11$$

Where is:

k = Permeability coefficient.

a = The cross-section area of standpipe in square millimetre.

A = The cross-section area of the sample in square millimetre.

L = Sample length in millimetre.

T = Time of water flow through the sample in second.

(h_1) and (h_2) = Water Heights in standpipe in millimetre.

The saturated permeability average of the 65% sand & 35% kaolin mixture from laboratory testing was measured to be 9.8×10^{-10} m/s. In comparison, based on (Kumar, 1996), the permeability characteristics of pure kaolin were evaluated to be 6.37×10^{-10} m/s. In that study, it was noted that when the clay content exceeded 30-40%, the permeability was predominantly controlled by the clay phase, meaning that sand particles in mixtures acted primarily as volume fillers without significantly increasing permeability. This result is in line with that of Kumar (1996) in that the mixture permeability appears to be very similar to that of pure kaolin.

4.1.9 Soil Water Retention Curve (SWCC).

The Soil Water Retention Curve is an important feature that describes the relationship of water content and suction in the soil, which play a key role in the behaviour of unsaturated soil. The moisture condition of unsaturated soils is described by soil suction, which is one of the most essential characteristics. It is well known that rainfall infiltration reduces the unsaturated shear strength of soil slopes due to matric suction decreases and through the wetting front movement. Numerous studies have been carried out for the estimation the permeability coefficient and shear strength for several types of soils using the SWCC.

Pressure Plate Test

The pressure plate test is a widely used experimental method to determine the water retention characteristics of soils. This method is commonly applied to measure the soil-water retention curve (SWCC), which is essential for understanding how soil retains and releases water at varying suction levels. The test is particularly useful for analysing mixtures like sand-kaolin and other relatively fine-grained soils that exhibit both drainage and capillarity effects under unsaturated conditions.

Overview of the pressure plate apparatus:

The pressure plate apparatus consists of a porous ceramic plate that allows the application of controlled suction (negative pore-water pressure) to the soil sample. The apparatus is housed inside a sealed pressure chamber, where a defined air pressure is applied to force water out of the sample while maintaining a water-air interface at the boundary of the soil. In this setup, matric suction (the difference between the pore-air pressure, u_a, and pore-water pressure, u_w) is applied to the soil, simulating field conditions where soils experience varying levels of suction due to natural drying or wetting cycles. By maintaining the pore-air pressure (u_a) at atmospheric pressure (i.e., zero), and adjusting the pore-water pressure (u_w), matric suction (ψ_m) is induced, which is given in following equation:

$$\psi_m = u_a - u_w = -u_w \qquad 4\text{-}12$$

Methodology:

1. **Soil sample preparation:**

The soil samples, in this case, a sand-kaolin mixture, are carefully prepared from the consolidated sample to the desired density. They are then placed on the porous ceramic plate inside the pressure chamber. It is essential that the samples are in complete contact with the air-water interface to ensure proper testing conditions as shown in the Figure 4-23.

2. **Air-water interface and high air entry value (HAEV):**

The High Air Entry Value (HAEV) of the ceramic plate is a critical parameter in the test. The HAEV ensures that free air does not enter the soil during testing, allowing only water to pass

through. This ensures that the pore-water pressure is controlled while maintaining atmospheric pore-air pressure. The soil sample is allowed to either absorb or drain water based on the suction applied, and the HAEV ceramic plate prevents air from entering the soil sample, ensuring that only water movement occurs. This provides a clear measurement of the water content at different suction values.



Figure 4-23 Pressure plate apparatus for determining soil-water retention characteristics.

3. **Application of Suction:**

A controlled air pressure is applied to the pressure chamber, and the corresponding negative pore-water pressure (u_w) is applied to the sample. This negative pore-water pressure induces matric suction in the soil. The air pressure is incrementally increased, allowing the soil to progressively drain as the matric suction increases. At each pressure increment, the amount of water retained in the soil sample is measured, and equilibrium is allowed to establish at each stage before proceeding to the next increment.

4. **Drainage and water retention:**

The soil retains water through capillarity and the attraction of water to its particles, which diminishes as the applied suction increases. The soil-water retention curve (SWCC), also called the moisture characteristic curve, is generated by measuring the water content at each applied matric suction. The SWCC represents the relationship between soil water content (volumetric or gravimetric) and matric suction. It shows the soil's capacity to hold water at different levels of drying (or wetting) and is critical for understanding unsaturated soil behaviour in engineering applications.

Dewpoint potentiometer method for measuring soil suction.

The Dewpoint potentiometer is a precise instrument used to measure the soil-water potential, especially in soils that have high suction, like fine-grained soils (e.g., clays or clay-rich mixtures). This method is commonly used in geotechnical engineering, agriculture, and environmental science to understand the moisture characteristics of soil, particularly in unsaturated conditions. This method was chosen in addition to the Pressure Plate test because the soil may exhibit high suction, which means the soil has a strong ability to hold onto water even under dry conditions.

Principle of the Dewpoint potentiometer

The Dewpoint potentiometer works based on the chilled mirror Dewpoint technique, where the water potential (suction) of the soil is determined by measuring the relative humidity above a soil sample. The key parameter measured is the Dewpoint temperature, which is the temperature at which the water vapour in the air above the soil sample condenses into liquid water. This temperature is related to the water potential of the soil.

Steps of the Dewpoint potentiometer method

1. Soil sample preparation:

Extract small soil samples from the consolidated soil mixture and bring them to different moisture contents. This can be done by gradually adding or removing water from the soil samples to create a range of moisture states from saturated to near dry. Apply a precise and measured quantity of distilled water to each soil sample using a sprayer. It is important to let the sample reach equilibrium after each addition of water. To achieve uniform moisture distribution, the samples were placed in sealed containers for a few hours. After equilibration, the sample was weighted to determine the wet mass (*Wwet*). This helps in calculating the gravimetric water content after each step. The soil sample was carefully placed in a small container, which was then introduced into the dewpoint potentiometer for analysis, as illustrated in Figure 4-24. It is important that the soil is homogenized and properly compacted to ensure accurate readings. For high-suction measurements, the soil sample is typically quite dry, as high suction values indicate strong attraction between soil particles and water.

2. Dewpoint measurement of water potential:

The dewpoint potentiometer operates by cooling a mirror until condensation appears on its surface, occurring at the dewpoint temperature. This temperature is recorded by the instrument's sensors, identifying the precise point at which water vapour condenses. For this experiment, an equilibrated sample was initially placed in the dewpoint potentiometer chamber, and measurements were taken as the sample was gradually dried. After each drying increment, the system was allowed to reach equilibrium, and the matric suction (water potential in MPa) was recorded once the reading stabilised. The mass of the sample was also measured at each stage, allowing calculation of the water potential throughout the drying process. This method was continued, incrementally drying the sample, until it reached a range of moisture contents, spanning from near-saturation to relatively dry conditions

3. Determine the gravimetric water content:

Following the last addition and measurement of water, the sample was dried in an oven set at 105°C to find the ultimate dry weight. The gravimetric water content was calculated for each stage using following equation.

$$w = (w_{wet} - w_{dry})/w_{dry} \qquad 4\text{-}13$$

4. Measurement of Suction:

The Dewpoint temperature is used to calculate the relative humidity of the air in equilibrium with the soil sample. The matric suction (soil water potential) is determined using the relationship between relative humidity and water potential, which is based on the Kelvin Equation:

$$\psi = \frac{RT}{V_w}\ln(\frac{P}{P_0}) \qquad 4\text{-}14$$

Where:

Ψ = water potential (matric suction)

R = universal gas constant

T = temperature (in Kelvin)

V_w = molar volume of water

P = partial vapor pressure of water in the soil sample

P_0 = saturated vapor pressure of water

The potentiometer calculates the suction (in MPa) based on this dewpoint value. The instrument is highly sensitive and can measure suction values in the range of 0 to -300 MPa.

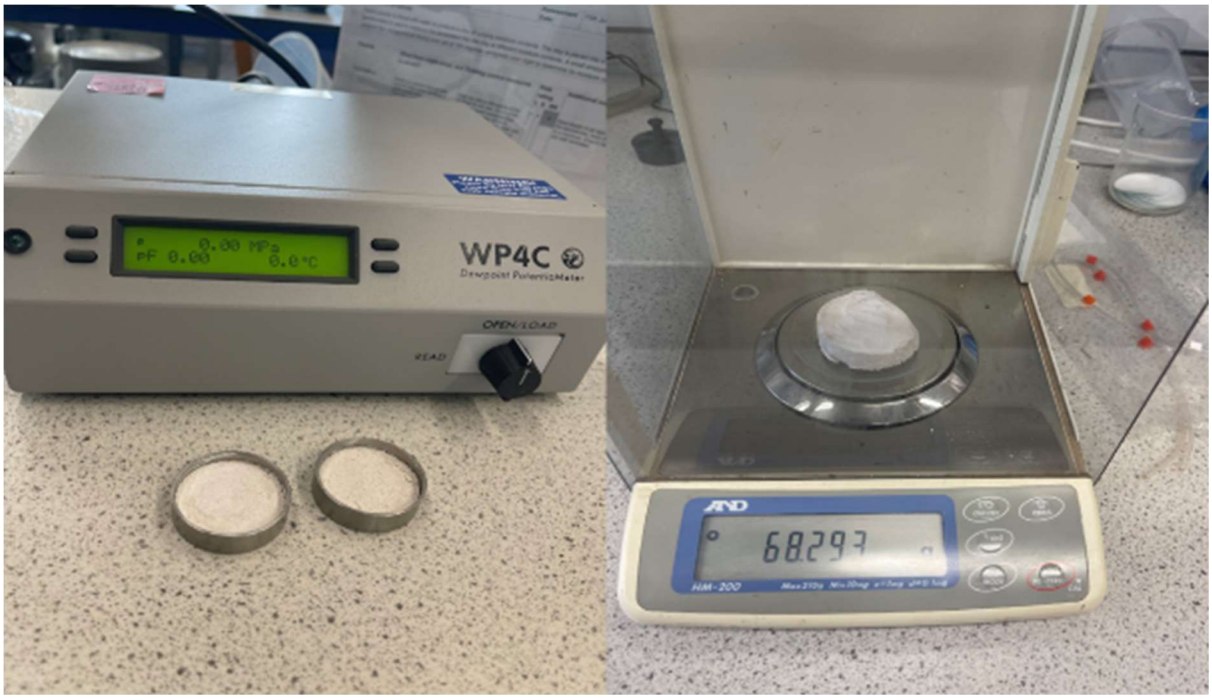


Figure 4-24 Dewpoint potentiometer and soil sample measurement setup

5. Plotting the Soil-Water Characteristic Curve (SWCC):

The SWCC can be generated by plotting the matric suction (y-axis) against the corresponding gravimetric or volumetric water content (x-axis). Figure 4-25 demonstrates the correlation between soil moisture and matric suction for the kaolin-sand mixture, illustrating the variability in water retention by the soil at various moisture levels.

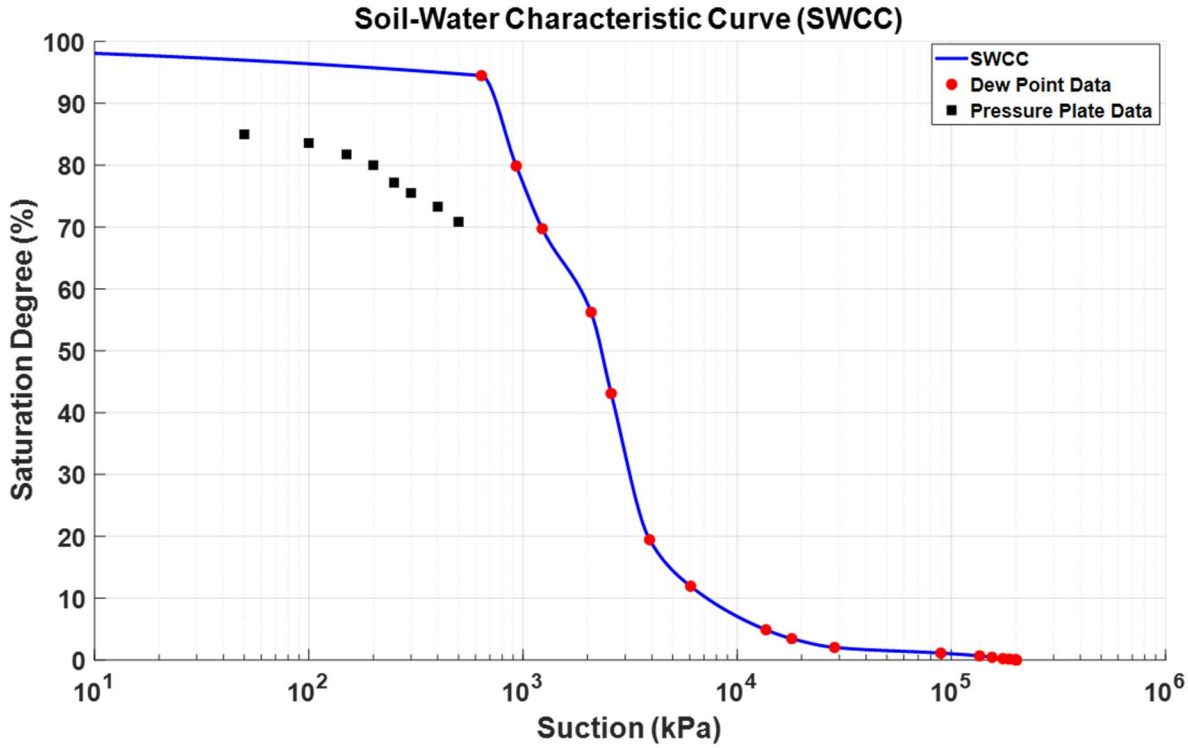


Figure 4-25 Soil-Water Characteristic Curve (SWCC) for the mixture 65 % sand and 35% kaolin.

Fitting the soil-water characteristic curve (SWCC) using the van Genuchten Equation:

In unsaturated soil mechanics, the van Genuchten (1980) equation is a general model used to describe the Soil-Water Characteristic Curve (SWCC). This empirical model is designed to describe the correlation between soil suction (matric potential) and the water content or level of saturation. The equation generates a smooth curve to represent the water retention in soil pores during the drying process. The van Genuchten equation for the SWCC is expressed as:

$$S_e = 1/(1 + (\alpha\psi)^n)^m \qquad 4\text{-}15$$

Where:

S_e = Effective saturation degree and defined as:

$$S_e = \frac{\theta - \theta_r}{\theta_s - \theta_r} \qquad 4\text{-}16$$

θ = Volumetric water content

θ_r = Residual water content

θ_s = Saturated water content

ψ = Soil matric suction (kPa)

α, n, and m = Empirical fitting parameters

$m = 1-1/n$

The following fitting parameters were determined for the van Genuchten model to represent the soil-water characteristic curve (SWCC) of the tested soil sample as displayed in Table 4-7. The model parameters were optimised to achieve a target residual suction of 20,000 kPa, which indicates the suction level at which the soil reaches its residual moisture content. This point signifies the stage where further increases in suction result in minimal water loss from the soil.

Table 4-7 Fitting parameters for soil-water characteristic curve (SWCC).

a	2186.3
n	2.4
m	2.1
Suction-residual (kPa)	20000

The data presented in Figure 4-26 demonstrates the drying properties of the soil by showing a decrease in its water retention capacity as suction increases. The van Genuchten model provides a good fit to the experimental data, offering a smooth and continuous representation of the SWCC. The blue line corresponds to the van Genuchten model estimated based on the experimental data points (red dots). The model represents the overall pattern of the SWCC, encompassing the phases of initial saturation, transition, and residual saturation.

Three stages in a soil-water characteristic curve (SWCC)

For the tested soil (65% sand and 35% kaolin), the degree of saturation remains close to 100% until suction reaches approximately 100 kPa, indicating the saturated stage. In the transition stage, between 100 kPa and 10,000 kPa, saturation drops rapidly from 100% to around 10%. Finally, in the residual stage, beyond 10,000 kPa, the degree of saturation stabilises near 0% as the soil retains minimal water.

1. Saturation zone:

Under low suction conditions, the soil on the left side of the graph is nearly completely saturated, with a saturation level close to 100%. From 100% saturation, the soil remains fully saturated until around 100 kPa.

2. Transition stage:

As suction rises, the curve starts to sharply decline. This region represents the transition from a saturated to an unsaturated state. Between suctions of 100 kPa to around 10,000 kPa, the soil rapidly loses water. Saturation decreases from 100% to around 5-10%. During this phase, water is progressively removed from the soil pores, and the degree of saturation decreases significantly.

3. Residual phase:

At higher suction values, the curve flattens out, indicating that most of the easily extractable water has been removed. The soil reaches a residual saturation state, where further increases in suction result in minimal changes in saturation. Beyond 10,000 kPa, the soil retains very little water, and the saturation is nearly 0%.

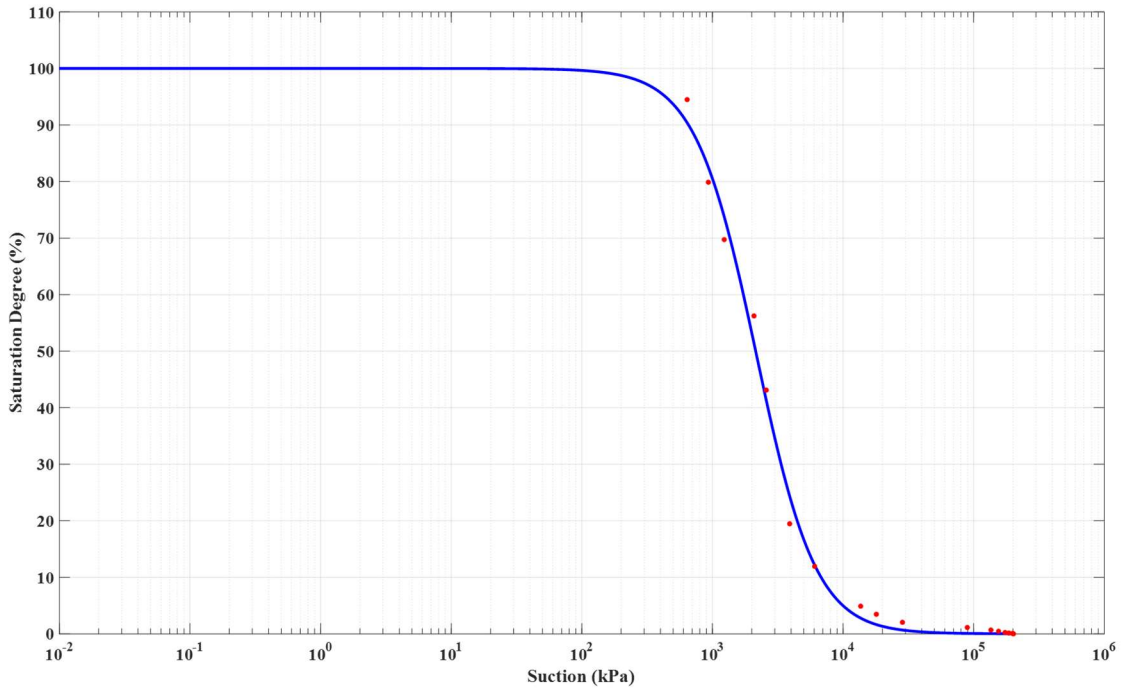


Figure 4-26 Soil-water characteristic curve (SWCC) for drying fitted with van Genuchten Model.

To plot permeability as a function of suction using the van Genuchten-Mualem model, the permeability was computed using the fitted van Genuchten parameters and then plotted against the measured suction values. The relationship between suction and permeability using the van Genuchten-Mualem model is illustrated in Figure 4-27. The blue curve represents the fitted model, while the red dots are the original data points for permeability. The blue curve closely corresponds to the data points falling within the range of permeability that significantly declines as suction increases (about 10^2 to 10^4 kPa). The red dots indicate the measured or calculated permeability values from the experimental data. Most data points fall along the predicted curve, supporting the validity of the van Genuchten-Mualem model for this soil.

The van Genuchten-Mualem model relates the unsaturated hydraulic conductivity (K) to the saturation degree (S_e):

$$K(\psi) = K_{sat}.S_e^{\frac{1}{2}}.(1-\left(1-S_e^{\frac{1}{m}}\right)^{m})^2 \qquad 4\text{-}17$$

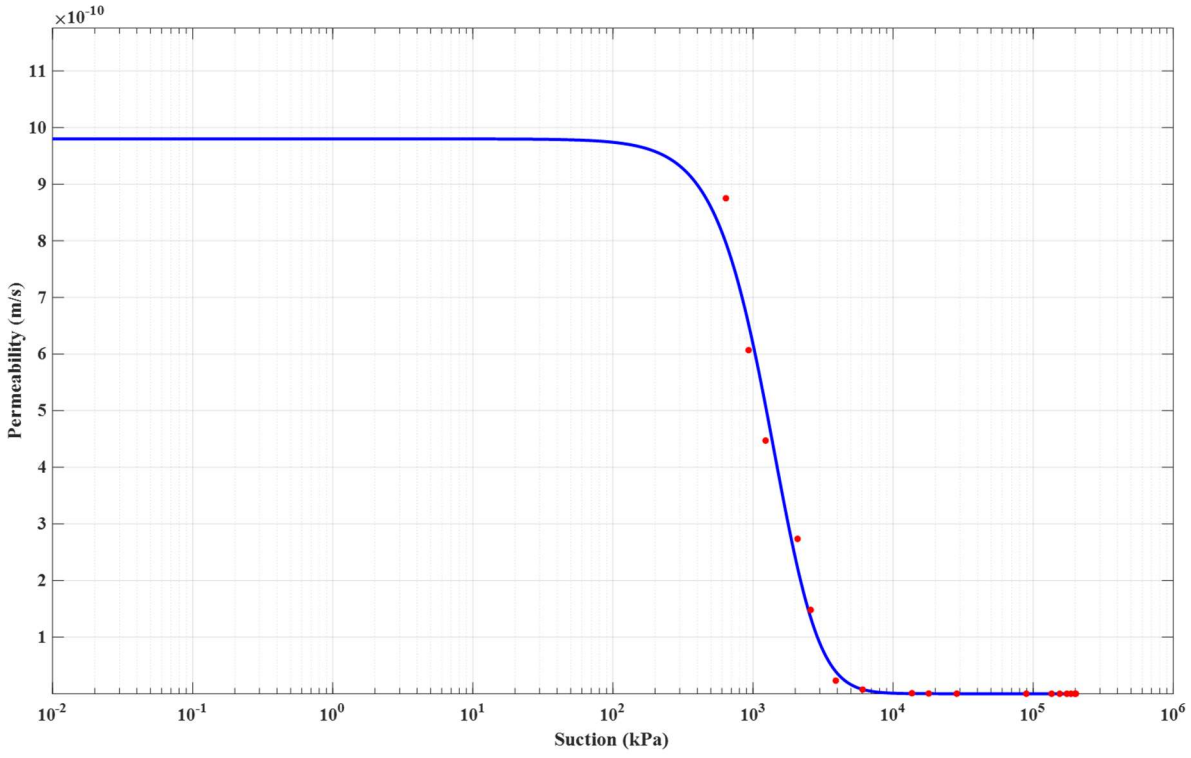


Figure 4-27 Permeability against suction for drying using van Genuchten-Mualem Model.

Summary:

This chapter provides a comprehensive overview of the process of preparing and calibrating soils for use in slope modelling. It begins by detailing the laboratory tests conducted to classify soil types according to the British Soil Classification System, which includes particle size distribution, Atterberg limits, compaction, and consolidation tests. These tests were essential for selecting a mixture of 65% sand and 35% kaolin for the slope model based on the results from compaction and plasticity tests.The 65% sand and 35% kaolin mixture exhibited notable properties, particularly its behaviour in terms of plasticity and compaction. Based on the Casagrande Plasticity Chart, the mixture was classified as low to very low plasticity. The Liquid Limit (LL) for this mixture was around 27%, while its Plasticity Index (PI) was around 18.5% that calculated frm shrinkage limit.

The chapter further highlights the significance of moisture content, consolidation characterist cs, and mechanical properties for understanding soil behaviour under stress and its application in slope stability. The discussion also incorporates various test results to ensure the accuracy of the soil model and refine the understanding of its behaviour under field conditions, ultimately preparing the model for experimental simulations.

CHAPTER 5

Slope model instrumentation and centrifuge modelling.

5.1 Introduction

While significant efforts have been dedicated to understanding rainfall- or climate-induced slope failures through full-scale monitoring and instrumentation, this approach is often time-consuming and may not provide comprehensive insights. The challenges arise from the inherent isolation and variability of full-scale field conditions, which can limit the generalisability of findings. Additionally, replicating such problems under controlled laboratory conditions at full scale is impractical due to the extensive resources, space, and time required to monitor slope performance over extended periods. These limitations highlight the need for alternative approaches, such as scaled-down physical models or advanced numerical simulations, which allow for the systematic investigation of slope behaviour under controlled and repeatable conditions, offering a more efficient and insightful path to understanding these complex problems. While small-scale modelling is attractive, model simulations at 1g (earth's gravitational acceleration) do not scale the soil self-weight body forces that cause downward slope movements effectively. As a consequence, the variation in stress levels comparing to full size is the most difficult aspect to scale modelling these phenomena. A centrifuge is able to overcome this obstacle as testing a small scale model in elevated gravity conditions increases self-weight body stresses to levels observed at full scale; hence, prototype behaviour can be replicated in the accelerated gravity environment provided by centrifuge modelling. Furthermore, centrifuge tests allow the hastening of certain time dependent processes that require a long time in reality to occur (i.e. movement of fluid through porous media); for example, 10 years of rainfall infiltration/seepage in the field can be achieved in a centrifuge model lasting approximately 20 hours when tested at 70g. Hence, using scale relationships it is possible to observe and detect the onset of progressive slope failure due to seasonal moisture variations in realistic prototype simulations or simulate rapid failure triggered by an extreme event. This capability offers unique potential to evaluate infrastructure deterioration for a variety of predicted climate scenarios and the development of well-informed intervention mitigation strategies to de risk infrastructure investment and boost future infrastructure resilience.

5.1.1 Centrifuge facility at university of Sheffield.

Thomas Broadbent and Son Limited designed and manufactured the centrifuge at the University of Sheffield and it was commissioned in 2014 as shown in Figure 5-1. The 50g-ton geotechnical beam drum centrifuge has a radius of 2 m and is capable of generating a maximum acceleration of up to 150 g at a payload of 330 kg and 100g at 500 kg.



Figure 5-1 Centrifuge facility at the University of Sheffield.

During experiments described in this thesis, a range of electronic equipment including sensors and cameras was located on the centrifuge centre at the arm side to allow for experimental

control, image capture and data acquisition of experimental tests. The system of data acquisition contains channels of pore water pressure sensors, strain gauge and connection power supply of load cell slots to solenoid valves. All channels are inserted into the electronics rack in the DAS cabinet and then connected to the computer network via optic fibre links. During each test procedure, all channels and instrumentation must be completely connected, ensuring that there is no relative movement. On the other hand, data acquisition takes place on board, while experiment monitoring and controlling is performed by two PCs that run LabVIEW in the control room. For this work, a climate chamber with rainfall simulation was designed and manufactured in the Department of Civil and Structural Engineering at the University of Sheffield, to investigate the stability of slopes with a soil mixture of 65% sand & 35% kaolin under different rainfall and flooding events.

5.1.2 Scaling laws considerations

The application of scaling laws was crucial to ensure that the centrifuge model tests accurately represented prototype conditions. A detailed discussion of the scaling relationships applied in this study, including those for length, time, and seepage processes, can be found in Chapter 3, Section 3.1.1.

5.1.3 Strong box

A plane strain strong box was fabricated to deliver this work. The chamber, designed from EN485 T6061-T6 Aluminium, is capable of accommodating a sample 600mm (L) x 400mm (H) x 200mm (W). The viewing window enables full field observations of slope performance during testing. The chamber is designed to enable operation within a sealed environment whereby suitable ‘O’-rings work in conjunction with a sealed lid. The lid can interface with the rain distribution nozzles and other external control systems. Drainage tapping points in the side and base are provided to enable control of the ground water table. An overview of this designed system is shown in Figure 5-2.

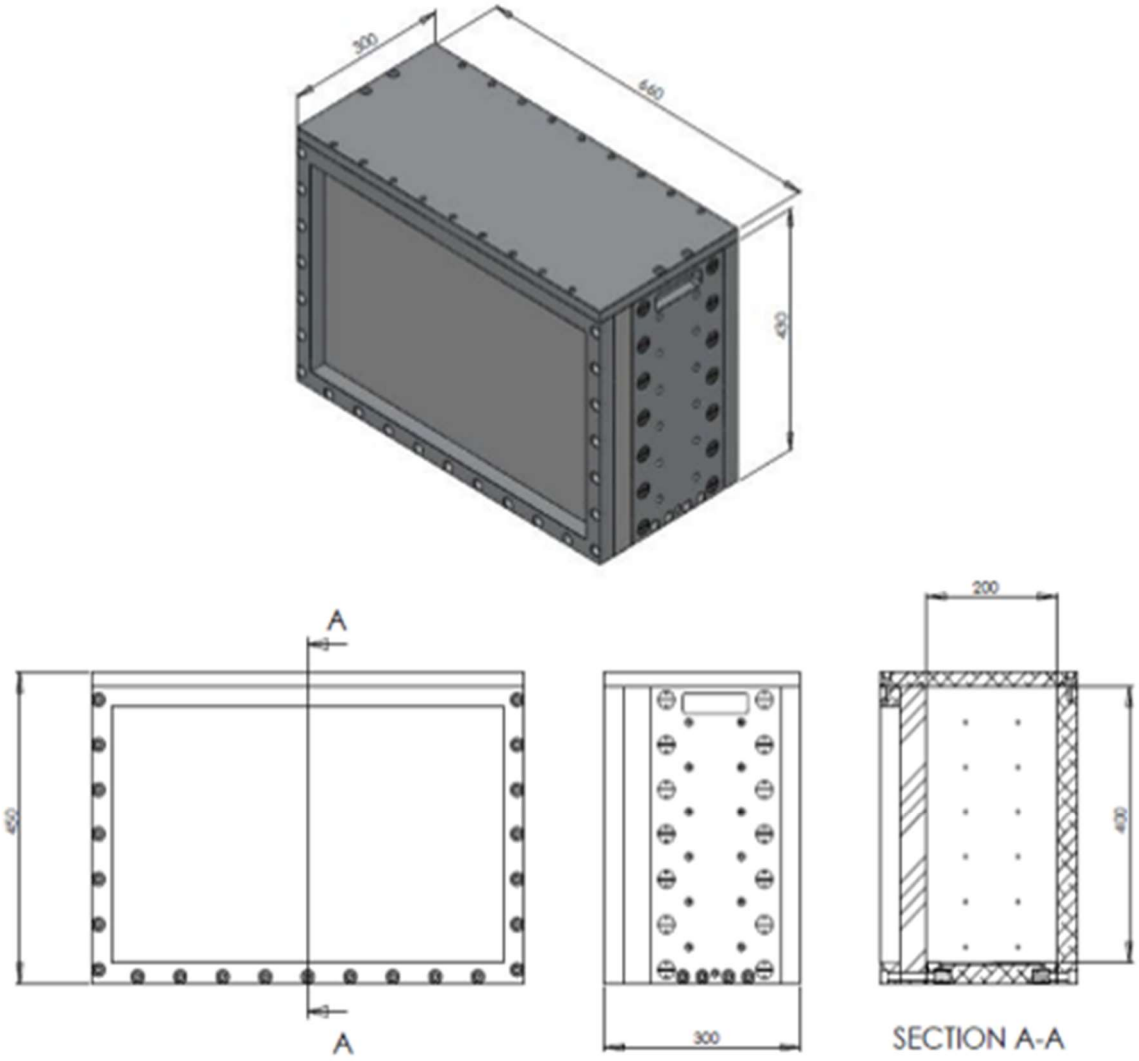


Figure 5-2 Plane strain window environmental test chamber.

5.2 Climate chamber

5.2.1 Principles of climate chambers and rainfall simulation

Simulating rainfall in a centrifuge is a mainstream method for assessing the influence of infiltration and cyclic pore pressures on constructed earth structures. Rain simulation in the centrifuge environment was achieved using nozzles that generate dispersed water droplets. An important factor is that the droplets are influenced by Coriolis and drag forces as they freefall toward the soil surface. The design of the nozzle system plays a crucial role in achieving a consistent and uniform rainfall simulation within the centrifuge environment. The selected nozzles needed to meet several key requirements:

- Uniform Rainfall Distribution: Ensuring even infiltration across the soil surface.
- Steady Flow Conditions: Maintaining a continuous flow without clogging or pulsation.
- Adequate Droplet Size: Controlling droplet dispersion while considering the Coriolis and drag forces within the centrifuge.

5.2.2 Rainfall distribution system

This section provides a description of rainfall simulation on centrifuge slope models. The rainfall system consists of several components, which include the water distribution system, spraying nozzles, a solenoid valve, and a pressure regulator as shown in Figure 5-3. Rainfall was simulated using a series of spraying/misting nozzles affixed to aluminium rods, positioned beneath a lid that was either sealed (initial experiments) or not (later experiments). To ensure that the Coriolis effect did not significantly influence the rainfall distribution, the nozzles needed to be placed very close to the model surface. However, placing the nozzles too close can result in soil erosion due to the high-pressure impact of the water droplets. Based on previous research by (Askarinejad et al., 2012, Caicedo et al., 2015, Tamate et al., 2012) , the nozzles were installed at an optimal distance of 70 to 100 mm from the model surface. These nozzles were connected to a network of pipes that distributed the water for the rainfall simulations. The water supply tank, located outside the centrifuge, was connected to the nozzles via a hydraulic rotary joint, with a pressure regulator sensor and an on/off solenoid valve situated between the tank and the nozzles. The solenoid valve can be opened to allow water to flow from the supply tank, through the hydraulic rotary joint, and into the distribution network of pipes leading to the spraying/misting nozzles. The pressure regulator continuously monitors the water volume delivered to the nozzles, ensuring a consistent flow rate and rainfall intensity.

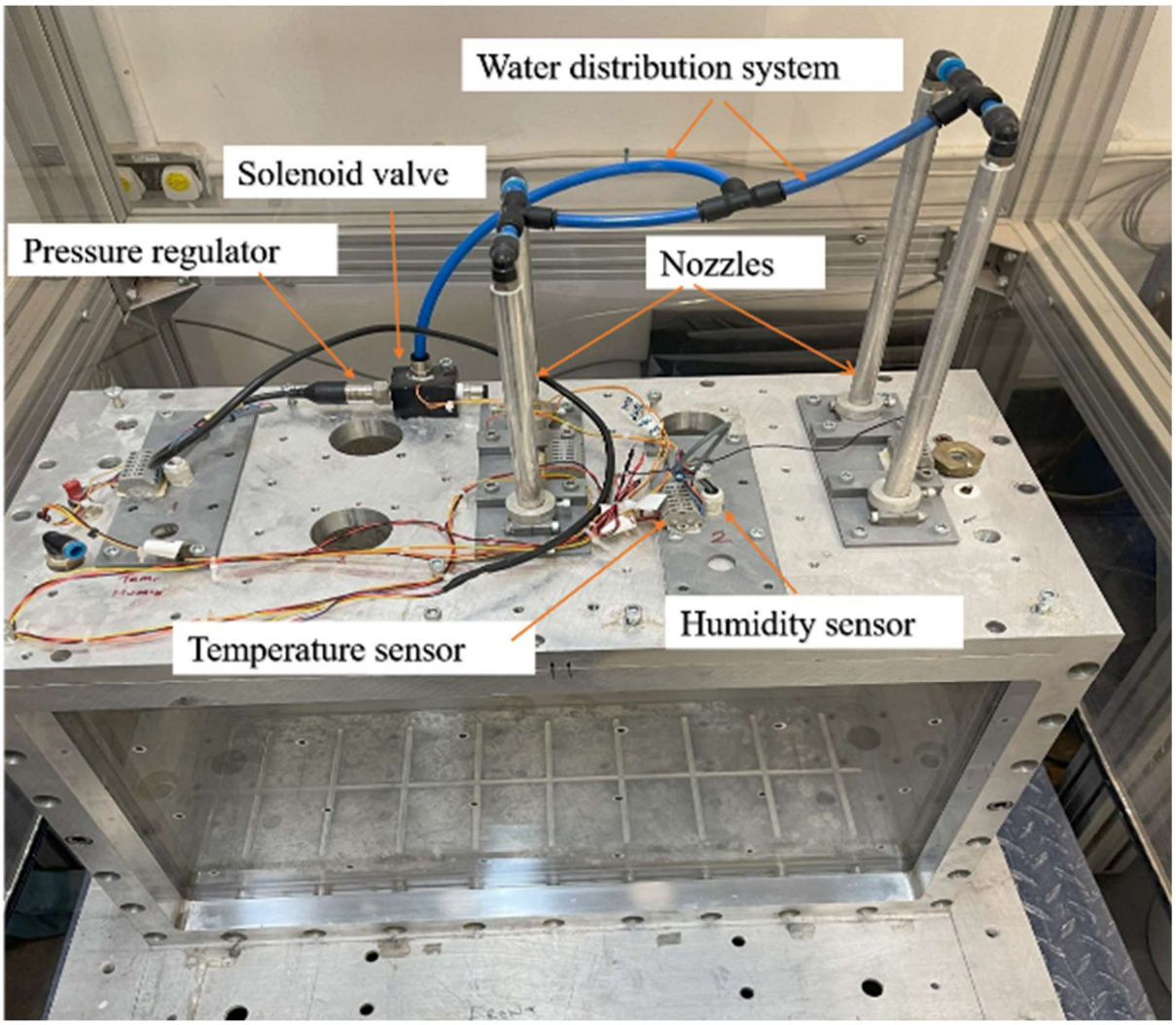


Figure 5-3 The rainfall simulator showing the unsealed lid set up.

5.2.3 Procedure for simulating rainfall in the centrifuge

Water was sourced from the main supply tap and delivered to the testing setup through the centrifuge slip rings. A flow regulator was connected to the main supply to limit the flow rate to the maximum value recorded by the pressure regulator. The initial water pressure from the main supply was 600 kPa at the maximum flow rate. However, this pressure was decreased to a maximum of 50 kPa before entering the centrifuge system. The water line is connected from the mains supply tap and routed through the centrifuge slip rings to the testing box using a pipe with an internal diameter of 10 mm. This pipe is mounted securely on the centrifuge arm. Despite the reduction in water pressure near the mains, a significant increase in pressure occurred as a result of centrifugal acceleration. The slope centrifuge tests were conducted at an

acceleration of 70g, resulting in a water pressure of more than 300 kPa at the nozzle delivery system. A pressure regulator was installed at the rainfall system so as to measure accurately the water pressure delivered to the nozzles during testing. Pore pressure transducers or PPTs were also installed within the soil model. Figure 5-4 presents a schematic diagram of the slope model, indicating the area where the PPTs were installed before each centrifuge test. It also shows the relative positions of the spraying nozzles in relation to the PPT installation areas. The precise locations of the PPTs for each test are detailed in Chapter 7.

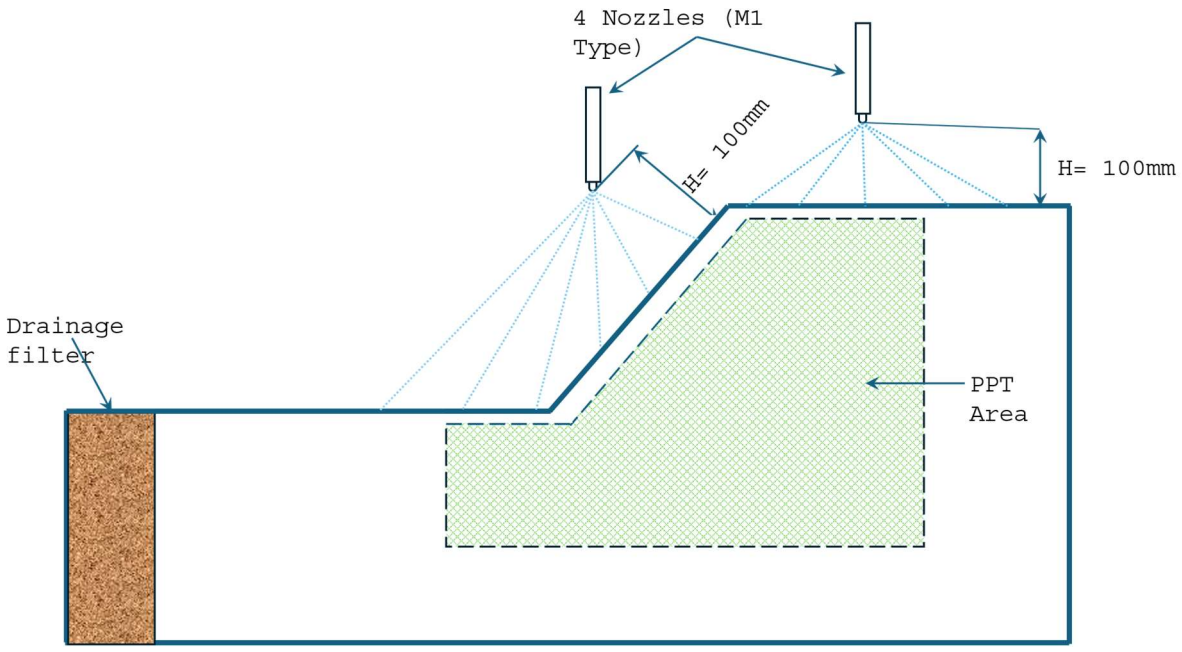


Figure 5-4 Schematic Diagram of Rainfall Simulation Setup with M1 Nozzles.

5.2.4 Nozzle selection criteria

M1 spraying nozzles, manufactured by Hago Manufacturing Co., were utilized in these experiments. A schematic illustration of the nozzles is depicted in Figure 5-5. The nozzles are manufactured using either stainless steel or brass materials and are equipped with a finely woven mesh filter at the inlet to prevent any blockage of the outlet opening. Their compact size makes them well-suited for simulating precipitation patterns in centrifuge models. Their spraying pattern forms a solid cone shape, ensuring a relatively uniform distribution of water across the entire spray area. When simulating rainfall in centrifuge models, it is important to consider two primary characteristics of the spraying nozzles: the flow rate and the average size

of the water droplets. The flow rate directly correlated to the prototype rainfall intensity simulated in the centrifuge testing. As described in Section 3.1.2, the ratio of the scale factor for rainfall intensity in the prototype (I_p) to that in the model (I_m) is equal to 1/N. Four M1 nozzles were used for this study, as the M1 nozzle type provides a low flow rate.

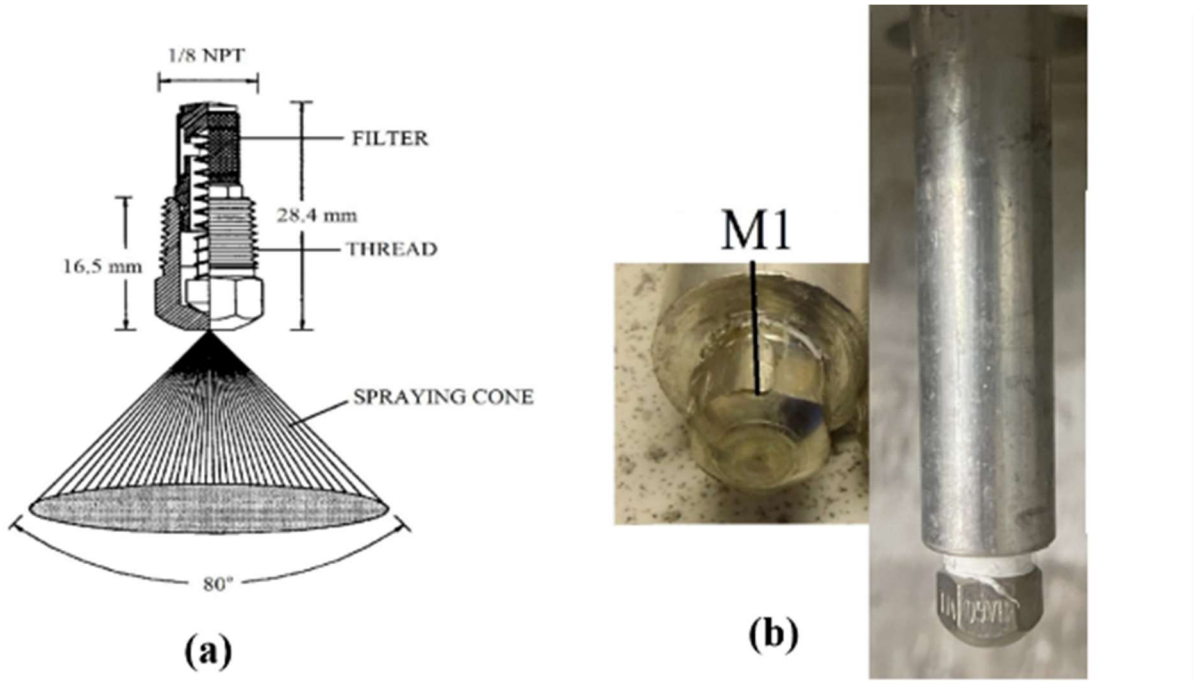


Figure 5-5 Layout of spraying nozzle, type M1 (a) schematic diagram showing nozzle dimensions and spray cone angle, adapted from manufacturer's data sheet, (b) photograph of nozzle M1 photo taken by Alfergani.

5.3 Nozzle calibration

The flow rate of the spraying nozzles depends on the applied water pressure. At pressures below 200 kPa, the nozzles malfunction, causing dripping instead of spraying. This occurs because the water fails to atomize effectively, forming larger droplets and an inconsistent flow, which results in uneven water distribution across the soil surface. To maintain a continuous and uniform spray, the manufacturer recommends a minimum operating pressure of 300 kPa. At pressures above this threshold, the nozzle produces a steady, dispersed spray pattern with controlled droplet size and velocity. Figure 5-6 displays the calibration test results for the M1 nozzle, illustrating the relationship between flow rate and operating pressure.

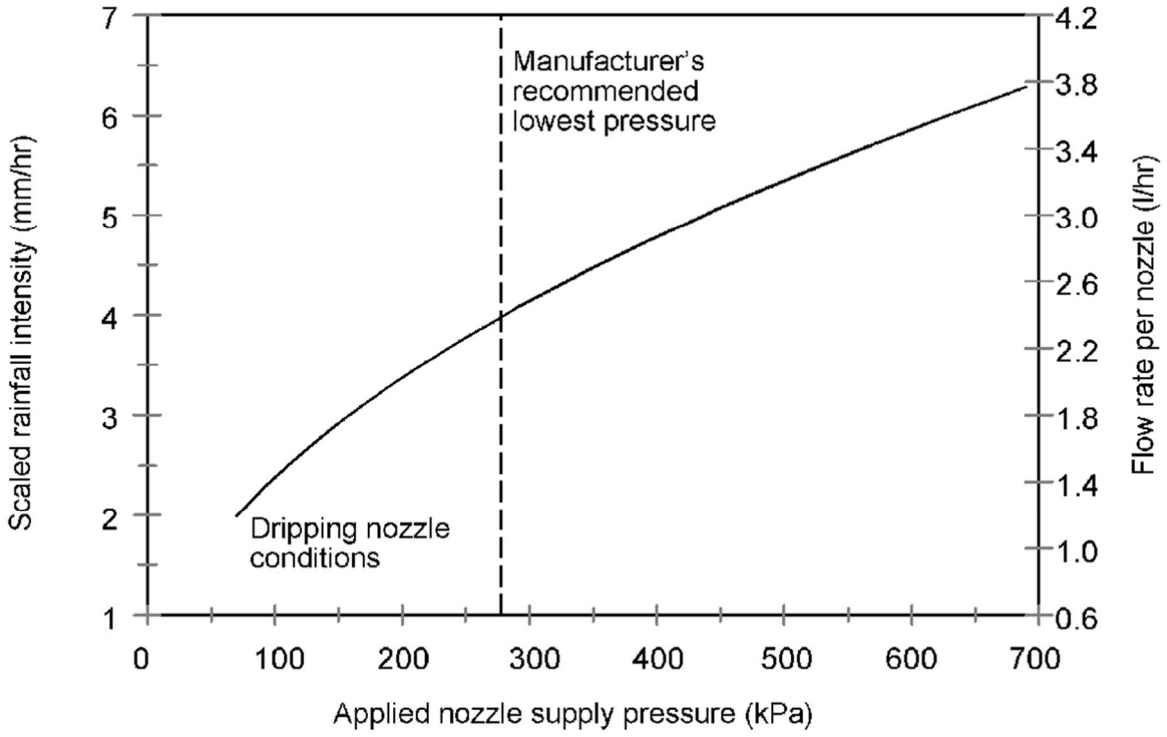


Figure 5-6 M1 nozzle manufacturer calibration (Take, 2003).

Accurate control of nozzle flow rate is essential for maintaining consistent rainfall intensity in centrifuge tests.Figure 5-7 shows the relationship between the applied water pressure and the average flow rate for the nozzles at 1g, providing key insights into nozzle performance across different pressure levels. This is useful for understanding how the nozzles perform under different pressures, which is critical for applications requiring precise control of water flow. The data can be used to calibrate the nozzles and set the desired pressure to achieve specific flow rate during the centrifuge tests. The data suggests a nearly linear relation between pressure and flow rate, indicating that an increase in pressure results in a proportional increase in flow rate.

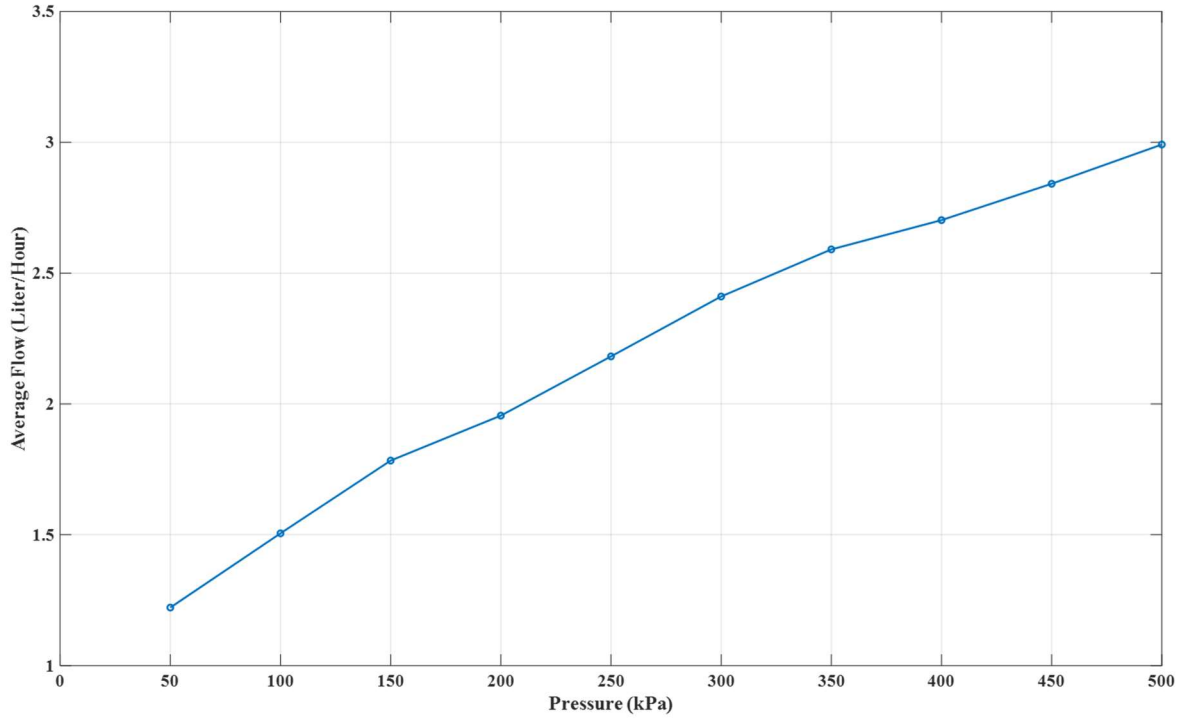


Figure 5-7 Nozzle calibration at 1g.

A series of initial rainfall simulation tests was conducted at 1g to evaluate nozzle performance and optimize the rainfall distribution pattern. Supply pressures ranging from 50 kPa to 450 kPa (in 50 kPa intervals) were tested at varying nozzle heights (50, 100, 150, and 200 mm) to determine the optimal flow characteristics. Figure 5-8 presents the results of a calibration test at 400 kPa supply pressure and 100 mm nozzle height. The left plot illustrates the rainfall intensity distribution, peaking at the centre and gradually decreasing outward. The right plot shows the water distribution contours, confirming that 400 kPa at 100 mm height provides effective ground coverage with minimal concentration imbalances. These calibration tests provided critical insights into how nozzle configuration, pressure settings, and fall height influence rainfall uniformity in the centrifuge environment. The results demonstrated that a 400 kPa supply pressure at 100 mm nozzle height yielded the most uniform distribution, ensuring consistent and controlled rainfall conditions for subsequent centrifuge tests.

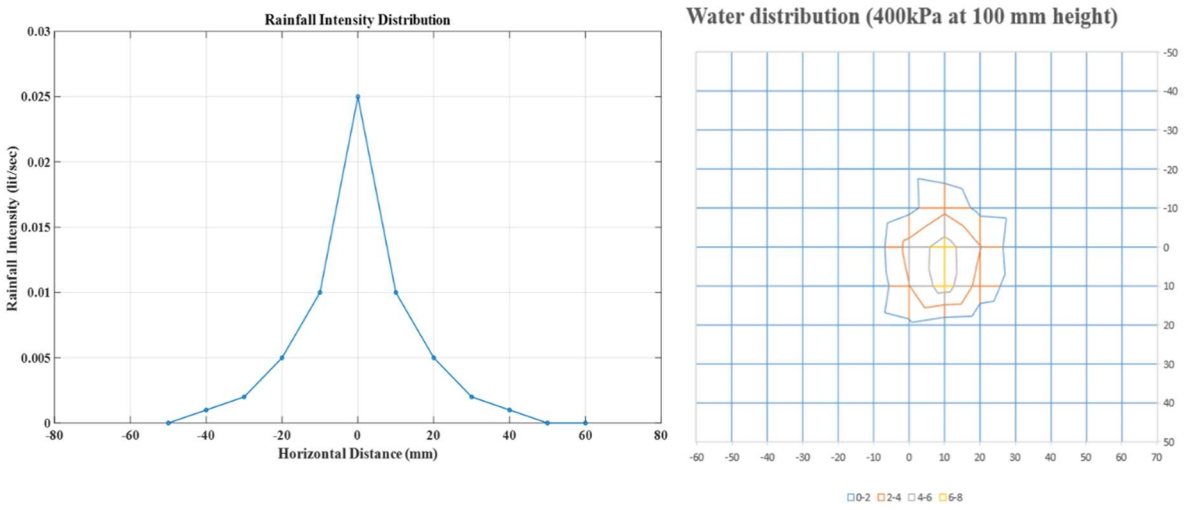


Figure 5-8 (a) Rainfall intensity distribution. (b): Water distribution at 400 kPa.

5.4 Rainfall intensity

As discussed in Section 3.1.3 of Chapter 3, the model rainfall intensity must be N times greater than the prototype intensity to achieve similitude. This adjustment ensures that infiltration and hydrodynamic effects in the model accurately represent those in the full-scale prototype. The Figure 5-9 shows a detailed view of a rainfall simulation setup used for experiments. Inside the chamber, a vertical measurement scale is marked on the transparent wall, which allows for the observation and recording of water levels during the experiment.

5.4.1 Calculation of rainfall intensity from test data

To determine the rainfall intensity in the prototype from the collected water volume in the model at 70g, the following steps were undertaken:

1. Measurement of water volume and flow rate:

For each test, the total water volume collected over a specific period was measured. The flow rate was then calculated by dividing the collected water volume by the time in seconds.

Box dimension = (L × H × W) = 60 × 40 × 20 cm^3

2. Calculation of rainfall intensity in the model:

The catchment area for the model was assumed to be a specific value (e.g., 0.2 m × 0.6 m), and the time was adjusted constant for all tests. All tests were conducted at 70g over a 30- minute rainfall period.

3. Scaling to prototype rainfall intensity:

To achieve similitude and scale the model rainfall intensity to the prototype, a scaling factor of N was applied. The prototype rainfall intensity was then calculated by multiplying the model rainfall intensity by the factor N = 24 (hours / day) × 365 (days / year) / 70 (N scale-value).

Given:

Height of water (h) = 40 mm = 0.04 m over 30 minutes.

i.e. Which is 40 mm over 30 mins= 80 mm over 60 mins

Prototype rainfall intensity = Model rainfall intensity/g = (80mm/h)/70 =1.14mm/h, which aligns with moderate natural rainfall rates in the UK. (Typical moderate rain in the UK generally ranges from 1 to 4 mm/h). (Office, 2023)

Table 5-1 summarizes the results of a series of spinning tests conducted at different G levels and water pressures. It includes the corresponding pressure readings from the sensor, duration of spinning, and water level heights. The tests were performed over a 30-minute duration, with a focus on capturing sensor readings and observing water levels. Special attention is given to the minimum pressure test noted in Test 1, where the water pressure was 0.5 bar. Although the pressure applied to the water line, which simulates rainfall via the nozzles, varied across the tests, it is noteworthy that the height of the water level remained relatively consistent. This observation suggests that, despite the differing pressures used to produce the rainfall, the water level reached during the experiments showed minimal variation, particularly between tests 1 and 3, where the water pressures were 0.5 bar and 2 bar, respectively. The sensor readings captured further underscore this trend, except in Test 4, where the pressure sensor failed to register data.

Table 5-1: Summary of spinning tests with g levels and water pressures.

Test number	G level, N	Pressure from water line (bar)	Pressure reading from the sensor (kPa)	Duration of spinning (min)	Water level (mm)	Notes
1	70	0.5	401-418	30	40	Minimum pressure
2	70	1	440-462	30	43	
3	70	2	577-588	30	46	
4	70	4	not	30	56	
5	1	4	370	30	38	



Figure 5-9 Rainfall simulation setup within a centrifuge apparatus.

In 2018, a study was conducted in collaboration with (Khan et al., 2018) on the development of a rainfall simulator for geotechnical modelling, with a particular focus on mitigating the Coriolis effect. This work was critical to ensure that the rainfall coverage over the slope was uniform and realistic within the centrifuge environment. Extensive nozzle calibration tests were conducted at different g-levels and heights to optimise the position and reduce the impact of the Coriolis effect, which could otherwise distort rainfall trajectories. By addressing challenges such as uneven rainfall distribution and potential soil erosion caused by raindrop impact, this work identified the ideal nozzle configurations for effective simulation. To investigate the Coriolis effect on rainfall simulators, a series of experimental tests were conducted at varying levels of gravity (1 g, 25 g, 50 g, and 75 g). In all tests, the nozzle pressure was maintained at 400 kPa, with a consistent flow rate of 8.05×10^{-7} m^3/s, and the rainfall duration was fixed at 5 minutes. It was observed that, in the absence of airflow within the testing package, the Coriolis effect had a negligible impact on the droplets' movement. The droplet trajectories under different g-levels were compared to their positions at 1 g, with the centrifuge rotating in a clockwise direction.

The experiments also examined the influence of nozzle positions (n1, n2, n3, and n4), with a top plate installed to minimise the effect of airflow windage, as shown in Figure 5-10. Subsequently, a second series of tests was conducted with airflow introduced into the system to simulate drag forces on the water droplets. This additional drag resulted in a noticeable translation of the water distribution position, as illustrated in Figure 5-11. These findings highlighted the interplay between gravity levels, nozzle positioning, and airflow in determining the effectiveness of rainfall distribution in centrifuge-based simulators. This comprehensive testing approach contributed to a deeper understanding of the Coriolis effect and its mitigation in geotechnical rainfall simulations.

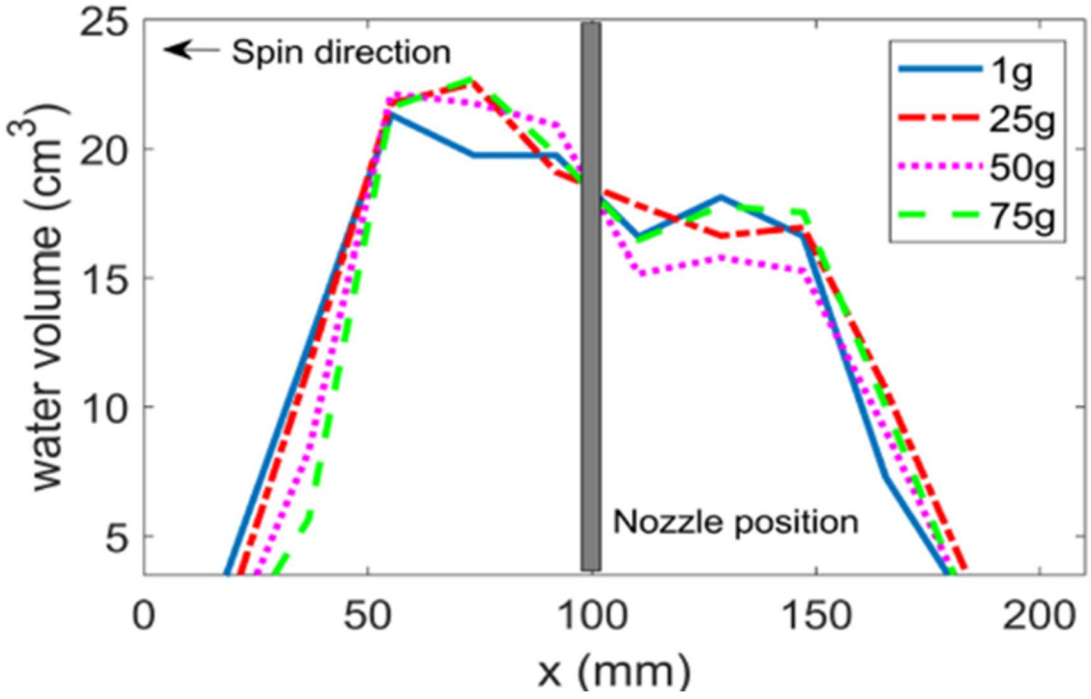


Figure 5-10 The distribution of water volume with top plate and position n1 for the nozzle at various g levels (Khan et al., 2018)

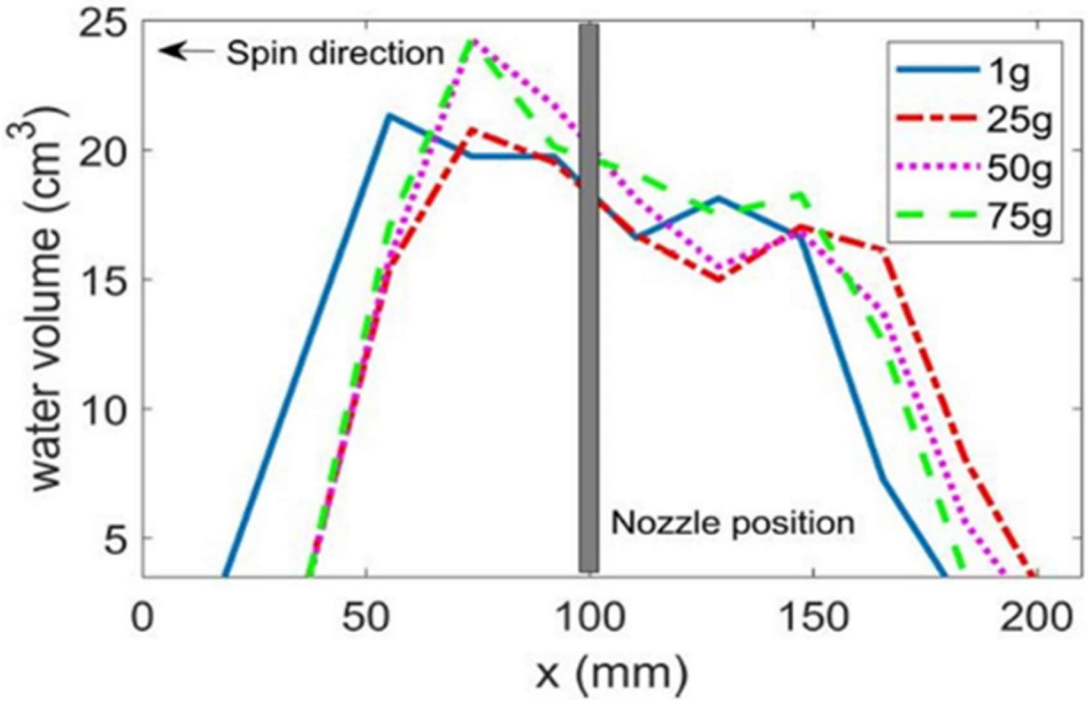


Figure 5-11 The distribution of water volume without top plate and position n1 for the nozzle at various g levels (Khan et al., 2018).

5.5 Measurement of deformation.

Reliable evaluation of the soil deformation is necessary for understanding how the behaviour of the slope model changes during rainfall events at various phases. The slope models created have plane strain behaviour, enabling monitoring through the transparent Perspex window. In consequence, strain fields can be estimated at any point throughout the test by carefully examining soil displacement fields. Scaling in the centrifuge causes slope movements of models to deform 1/N times less than in the prototype. As a result, slope stability analysis typically is necessary to measure soil movement smaller than 0.1 mm in the model. In this research, the slope deformation was measured using Geotechnical Particle Image Velocimetry (PIV) at the side wall.

5.5.1 GeoPIV

For soil deformation, (White et al., 2003) and (Take, 2003) created an effective PIV system called GeoPIV. The GeoPIV measurement technique operates by analysing a series of images captured throughout an experimental test. In this context, each monochrome image, once digitized, is represented as a matrix comprising intensity values corresponding to individual pixels. This matrix serves as a foundational dataset for subsequent image processing tasks. The technique leverages these intensity matrices to track and quantify displacements or deformations in the material or structure under investigation. By comparing sequential images, GeoPIV identifies shifts in pixel intensities that correlate with physical movements, enabling precise measurement of strain, displacement, or other relevant mechanical properties within the tested material. This method is particularly valuable in geotechnical engineering and materials science, where understanding subtle changes over time is critical for assessing the behaviour and integrity of materials under various conditions (White et al., 2003). The intensity values in a digitized image range from 0 to 255, where 0 represents black and 255 represents white. The intensity matrix, denoted as $I(U)$, is a function of the pixel coordinates $I(U) = (u, v)$, where (u) represents the horizontal coordinate and (v) the vertical coordinate (White et al., 2003). In the case of colour images, there are three separate intensity matrices, each corresponding to one of the colour channels: red, green, and blue. The GeoPIV applies a patch-based approach to track the displacement of pixels across a sequence of images, enabling the determination of their movement relative to their initial positions in the first image.

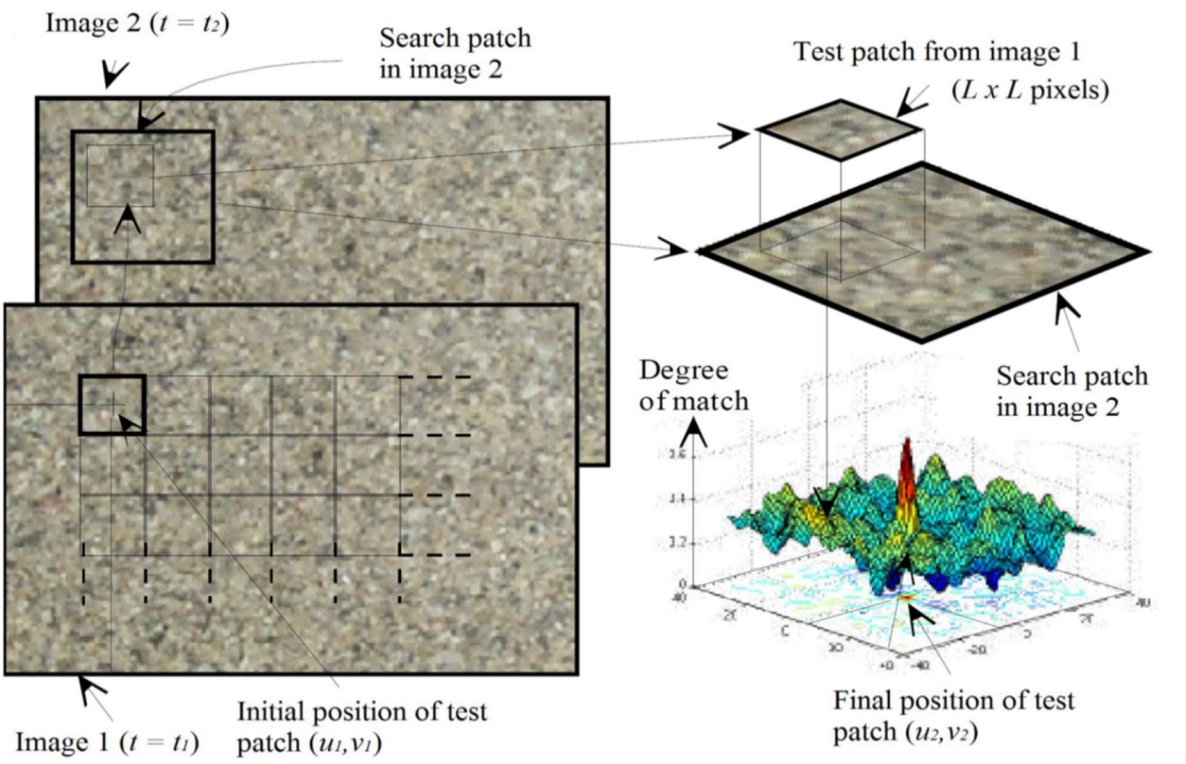


Figure 5-12 The changing of image during Particle Image Velocimetry (PIV) analysis (White et al., 2003)

Validation experiments conducted by (White et al., 2003) demonstrated that the accuracy of PIV analysis is highly dependent on the patch size (L), and that this precision can be notably enhanced when the soil exhibits a random texture, as this leads to the formation of well-defined correlation peaks. In the current study, the patch size was determined through a process of trial and error. For each analysis, L was adjusted to minimize the occurrence of anomalous vectors, thereby optimizing the reliability of the results.

In this research, the slope models for the centrifuge tests were constructed using a mixture consisting of 65% sand fraction E and 35% kaolin. This silty sand mixture was chosen for its broad particle size distribution, which made it particularly well-suited for GeoPIV analysis by providing a natural texture that enhanced image tracking. Additionally, black seeding was applied to the face of the slope to further enhance surface texture, ensuring improved accuracy and reliability in the displacement tracking during GeoPIV analysis. This combination of material selection and surface preparation optimised the quality of the experimental data.

The precision of PIV analysis is also influenced by the intensity levels, which are determined by the varying pixel intensities within each patch. Enhancing the texture in the captured images can be achieved by selecting an optimal exposure time for the digital camera. To identify the exposure time that yields the most accurate PIV results, an evaluation of the intensity distribution in the captured images was conducted prior to the experiments. The assessment of image quality and its suitability for PIV analysis is primarily determined by the range of intensity levels. Each patch consists of numerous pixels, which ideally should exhibit distinct grey levels that are easily identifiable by GeoPIV. When this condition is met, a broad intensity distribution pattern is formed, facilitating effective tracking across successive images. The optimal scenario would involve a uniform distribution across the entire range of intensities. Exposure time plays a critical role in the accuracy of Particle Image Velocimetry (PIV) by influencing the clarity of particle displacement within the flow. Here is how it affects PIV accuracy:

1. Motion blur: If the exposure time is too long, the particles may move significantly during the exposure, causing motion blur. This makes it difficult to accurately track the movement of individual particles and can reduce the precision of velocity measurements. The particles will appear as streaks instead of distinct points, making displacement harder to quantify.

2. Particle visibility: On the other hand, if the exposure time is too short, the particles might not be illuminated sufficiently, resulting in low-intensity images. Poorly visible particles can be harder for the PIV software to detect, also reducing accuracy.

3. Image sharpness: Optimal exposure time ensures that particles move just enough between frames to provide clear and detectable shifts, without causing excessive blurring. This balance allows for clear velocity vector fields to be computed with minimal error.

4. Flow speed: The effect of exposure time also depends on the speed of the flow. For fast flows, shorter exposure times are generally needed to prevent motion blur, while slower flows can tolerate longer exposure times without sacrificing accuracy.

In summary, selecting the appropriate exposure time is a balance between ensuring particle visibility and minimising motion blur. Optimal exposure time provides distinct particle images, allowing for precise tracking and accurate velocity measurements in PIV analysis. An exposure time of 1/10 second was manually selected through a process of trial and error to ensure the best possible image quality. This duration provided the optimal balance between motion blur

and sharpness, resulting in a wider distribution of intensities. The chosen exposure time allowed for clearer tracking of particle movement, enhancing the accuracy of velocity calculations and ensuring precise analysis. This calibration was conducted to determine the optimal exposure time using the GoPro 7 Hero Black camera. PIV analyses of these trials at 1 g and 70 g were completed prior to conducting the actual test. Figure 5-13 shows the setup of a GoPro 7 Hero Black camera used during an experiment. The display screen indicates a locked exposure setting, which was part of the calibration process to ensure the optimal exposure time for capturing high-quality images.



Figure 5-13 GoPro 7 hero black camera setup with locked exposure time during tests.

5.5.2 Calibration

The initial outcomes produced by the GeoPIV analysis are presented in pixel units, which correspond to measurements in the image-space. While these pixel-based measurements are necessary for the analysis process, they are not directly applicable in the context of geotechnical engineering, where precise, real-world measurements are required. Therefore, to ensure the data is meaningful and useful for engineering applications, it is necessary to convert these pixel

units into real units, such as millimetres, within the object-space. The conversion from pixel units to millimetres is achieved by utilizing fixed reference points marked on the inner surface of the Perspex window. These reference points, referred to as calibration targets, are designed as circular black dots with a diameter of 4 mm. Each dot is encircled by a slightly larger circular area coated with white paint, measuring 8 mm in diameter. These calibration targets provide a consistent and precise basis for the spatial transformation, enabling the accurate scaling of measurements from the image-space to real-world dimensions. In addition to the transformation from image-space to object-space coordinates, the calibration process also compensates for image distortion, commonly known as the fish-eye lens effect. While (White et al., 2003) thoroughly describe the sources of this distortion, the experiments conducted for this research incorporated the "linear" mode of the GoPro Hero 7 Black camera to significantly reduce fish-eye distortion. To ensure a high level of precision in the calibration process, 24 reference points were employed, surpassing the minimum requirement and thereby enhancing the accuracy of the spatial transformation. This approach not only mitigated distortion but also provided a robust calibration framework, accounting for any potential displacement of the camera due to the increased gravitational forces experienced during centrifuge testing, which could otherwise cause deviations from its initial position.

5.6 Tensiometers and Pore Pressure Transducers

Tensiometers are extensively utilized in geotechnical centrifuge experiments due to their ability to directly and continuously measure matric suction as well as positive pore fluid pressure (Askarinejad et al., 2015, Hudacsek et al., 2009, Take et al., 2004a, Tamate et al., 2012, Take and Bolton, 2022). This capability provides real-time insights into the soil's hydraulic properties, allowing for more accurate modelling and prediction of soil responses to various stresses.

The fundamental operation of tensiometers relies on the exchange of water between the soil and the instrument, aiming to balance the difference between the pore water pressure in the soil and the internal water pressure within the tensiometers. In recent decades, several advanced tensiometers have been developed, capable of measuring suctions exceeding 100 kPa. These innovations have expanded the applicability of tensiometers in geotechnical research, allowing for more accurate assessments of soil moisture dynamics under higher suction conditions. (Mair, 1979) employed a comprehensive saturation method along with a high air-entry filter

element to quantify suctions exceeding 100 kPa in soils during the process of unloading from elevated pressures. (Ridley and Burland, 1993) devised an apparatus capable of quantifying suctions exceeding 1500 kPa. These devices are commonly referred to as High Capacity Tensiometers.

Pore Pressure Transducers (PPTs) can function as tensiometers for direct matric suction measurement when equipped with a ceramic porous stone. A typical PPT comprises the main body, a transducer (diaphragm), a small water reservoir, and the ceramic porous stone, which acts as a filter. The porous stone must remain saturated to maintain effective contact between the pore water and the PPT reservoir. When properly saturated, the water pressure is transmitted to the reservoir and measured by the diaphragm deformation. The strain-gauged diaphragm allows for the measurement of both positive and negative pressures. The performance of PPTs in measuring suction is influenced by three factors: the permeability of the porous stone, the sensitivity of the pressure gauge, and the saturation ratio. The permeability is quantified by the Air Entry Value (AEV), which represents the negative water pressure at which air begins to infiltrate the pores. The AEV, determined by the Soil Water Retention Curve (SWRC), indicates the point at which soil desaturation starts. Consequently, the AEV of the porous stone also defines the upper limit for accurate suction measurement using the PPT, as contact between the pore water and the water within the porous stone may be compromised at this pressure. Higher suction levels can lead to the desaturation of the porous stone and potentially cause cavitation within the instrument. A high degree of saturation of the porous stone is crucial for the tensiometers performance. The maximum measurable suction may be constrained by the expansion of trapped air bubbles into the porous stone or by the nucleation and release of vapour bubbles from crevices within the tensiometers body (Take and Bolton, 2003). These factors limit the accuracy and effectiveness of suction measurements under high suction conditions.

In the current study, the EPB-PW pressure transducers, equipped with porous stones, were utilized to measure both positive and negative pore water pressures as shown in Figure 5-14. These transducers had a full-scale capacity of 1500 kPa and could measure up to 100 kPa of suction. Each transducer was fitted with a porous stone, often referred to as a filter, which was attached at the top of the sensor. Epoxy was used to seal the junction between the porous stone and the steel casing, ensuring a secure and effective measurement setup.

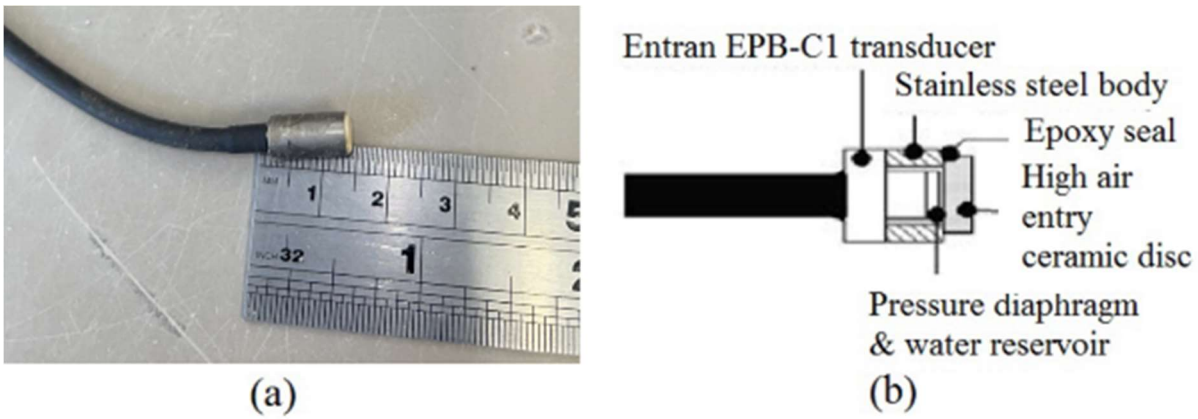


Figure 5-14: (a) physical appearance of the EPB transducer; (b) schematic diagram illustrating the components of the EPB transducer (Matziaris, 2019).

5.6.1 Saturation and calibration

The saturation and calibration of the Pore Pressure Transducers (PPTs) were carried out as shown in Figure 5-15.

1. Initial Saturation: The process began by raising the water level around the PPTs. A vacuum was applied to remove any trapped air within the system. This vacuum was maintained while the PPTs were submerged in water, ensuring that all air pockets were eliminated.
2. Extended Saturation: After submersion, the vacuum was applied for two hours, which facilitated deeper saturation of the porous stone within the PPTs. The system was then left overnight, allowing the sensors to achieve full saturation, which is critical for accurate measurement.
3. Calibration: Once the PPTs were fully saturated, the calibration process commenced. This involved applying incremental pressure using the centrifuge at specific intervals (50, 100, 150, 200, 250, 300, 350, 400 kPa). Throughout this stage, de-aired water was used to prevent the introduction of air bubbles, which could affect the accuracy of the readings. The device shown in the Figure 5-16 is an Automatic Pressure Controller, which was used during the calibration phase of the Pore Pressure Transducers (PPTs). This controller allows for precise regulation and application of pressure during the calibration process. The pressure was incrementally applied to the PPTs in steps of 50

kPa, ranging from 50 kPa to 400 kPa, ensuring accurate calibration across the entire pressure range. The controller display shows the current pressure values being applied by the two pistons, ensuring that the calibration is carried out with high precision.

4. Data Collection: During calibration, data were collected through a data acquisition system, allowing for precise monitoring of the PPTs' response to the applied pressures. This step ensures that the PPTs are correctly calibrated to measure both positive and negative pore water pressures accurately.

5.6.2 Key Observations:

1. Linear Relationship: The calibration results for the Pore Pressure Transducers (PPTs) are presented in Figure 5-17.
2. Each PPT exhibits a generally linear relationship between the applied pressure and the corresponding voltage output. This linearity indicates that the PPTs are functioning correctly, providing consistent and predictable responses to changes in pressure.
3. Slopes of the Calibration Curves: The slope of each calibration curve represents the sensitivity of the PPT to pressure changes. A steeper slope indicates a higher sensitivity, meaning the PPT produces a larger voltage change for a given pressure increase. Conversely, a flatter slope suggests lower sensitivity.
4. Intercepts: The intercepts of the calibration lines represent the voltage output when no pressure is applied (0 kPa). These values should ideally be close to zero, but minor variations can occur due to manufacturing differences or baseline shifts in the PPTs.
5. Consistency Across PPTs: While most PPTs show similar slopes and intercepts, some variation is expected due to slight differences in individual sensor characteristics. However, the consistency across the PPTs suggests that they are well-calibrated and should provide reliable measurements during experiments.
6. Linear Fit: The fitted lines on the calibration plot closely match the actual data points, further confirming the accuracy and reliability of the calibration process. The tight fit indicates that the PPTs' response to pressure is primarily linear, which is crucial for accurate pressure measurements.

Overall, the calibration results demonstrate that the PPTs were functioning as expected, providing a reliable basis for their use in subsequent experimental procedures.



Figure 5-15 Left: PPTs under raised water. Right: PPTs under applied vacuum.



Figure 5-16 Left: Automatic Pressure Controller. Right: LabVIEW collecting data.

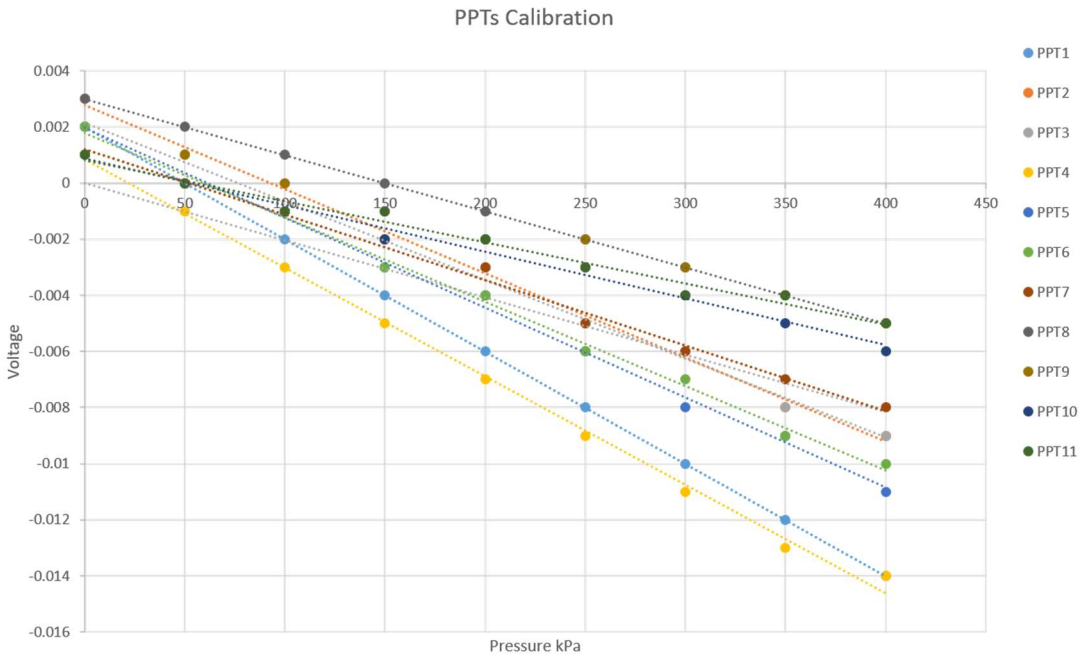


Figure 5-17 PPTs calibration data.

5.6.3 Surface modelling and contour generation using the GRIDFIT method for pore water pressure distribution.

The pore water pressure (PWP) contours for all tests were generated using the GRIDFIT method, as described by (D'Errico, 2006). GRIDFIT is a surface modeling tool designed to approximate smooth surfaces, z (x, y), from scattered or gridded data points. It is particularly useful for handling geotechnical data where noise and irregularities are present. In this approach, a grid of nodes was established across the slope model, and the PWP values from the pore pressure transducers (PPTs) were used as input data. Unlike traditional interpolation methods that enforce exact matching of the data, GRIDFIT approximates the surface while balancing two key factors: fidelity to the data and smoothness of the surface. This balance is controlled through the "plate stiffness" parameter, which determines the extent to which the surface smooths out noise or irregularities in the measurements. The method involves solving a sparse linear least-squares problem to generate a smooth surface that best fits the input data. Bilinear interpolation was employed to estimate values between grid nodes, and regularisation techniques ensured a smooth and well-behaved surface, even in regions with sparse data. For areas outside the data bounds, GRIDFIT assumed local planarity, resulting in realistic

extrapolation of PWP values. This methodology allowed for accurate visualization and interpretation of pore water pressure distributions across the slope, ensuring that the contours represented the hydraulic conditions effectively. The smooth and reliable output of GRIDFIT made it a robust choice for processing the PWP data from the tests. As part of the methodology, the GRIDFIT method was used to generate pore water pressure (PWP) contours for each stage of the test. Figure 5-18 illustrates an example of the PWP contours during the flooding phase of the M-Tr6 test. The GRIDFIT method enabled the smooth approximation of PWP values based on measurements from pore pressure transducers (PPTs) installed within the slope. The contours demonstrate a slope-parallel distribution of pore pressures, with values increasing downslope as water infiltrates the soil during the flooding phase.

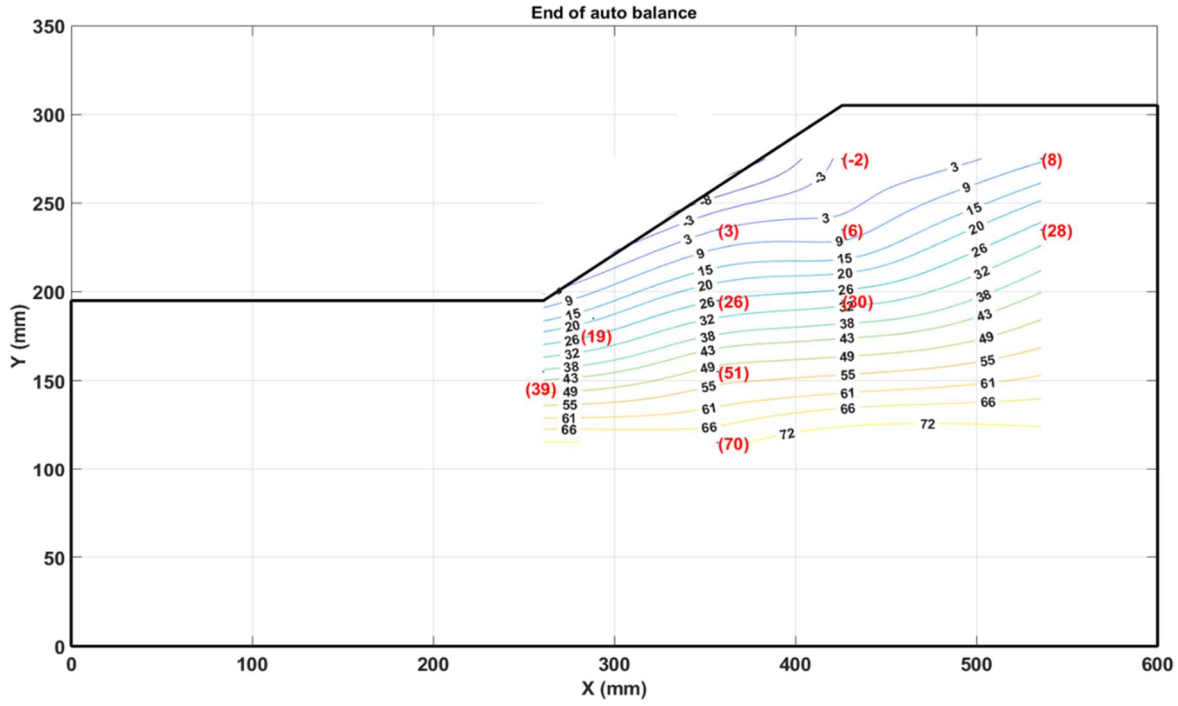


Figure 5-18 Example of PWP contours generated using the GRIDFIT method during the flooding phase of the M-Tr6 test.

5.7 Humidity and temperature sensors

In the experiments aimed at assessing slope stability under varying environmental conditions, particularly during rainfall application and subsequent drying periods, a precise monitoring system was essential. To achieve accurate control and data collection throughout the centrifuge

tests, a combination of sensors was utilised. Specifically, two HM1500LF humidity sensors were employed to measure humidity, while two LM35 temperature sensors were used to monitor temperature as shown in Figure 5-21. These sensors provided data on environmental parameters during the experiments. This monitoring was important to understand the influence of these factors on slope stability and for ensuring the reliability of the experimental results.

5.8 Humidity Measurement

0.1% RH, which means it can detect very small changes in relative humidity (as small as 0.1%). This sensor played a critical role in monitoring the moisture levels during the experiment, particularly during the rainfall simulation, where accurate humidity data was essential for understanding the interaction between water and soil. Figure 5-19 shows the variation in relative humidity (RH%) over time during the first spin of the M-T6 test, specifically during the first winter period. The climate scenario involves one week of rain followed by one week of no rainfall. The test simulates winter conditions in the prototype model, where the alternation of wet and dry phases influences the environmental humidity. Dataset 1 (red): RH% fluctuates between 65% and 70%, exhibiting smaller and more stable oscillations. The stability of this dataset may indicate that the sensor is located in an area less exposed to direct environmental changes, such as rainfall. Dataset 2 (Blue): RH% oscillates between 65% and 80%, with much larger swings than Dataset 1. This indicates a stronger response to environmental changes, likely driven by direct exposure to rainfall. In summary, the oscillations in both datasets are likely linked to the alternating periods of one week of rain followed by one week of no rainfall during the test. The larger variations in Dataset 2 could be due to the fact that sensor 2 is located closer to the rainfall nozzle, resulting in more direct exposure to moisture during the rain period. This location difference accounts for the greater RH% swings observed in Dataset 2, as compared to the more stable humidity levels recorded by sensor 1. The humidity sensor (HM1500LF) used was a robust and reliable model, designed to provide precise measurements of relative humidity within the test environment. The sensor has a range of 0 to 100% RH and an accuracy of ±2% RH. Typically, the HM1500LF sensor has a sensitivity of about 0.4 mV/%RH, ensuring precise and reliable humidity measurements within the test environment.

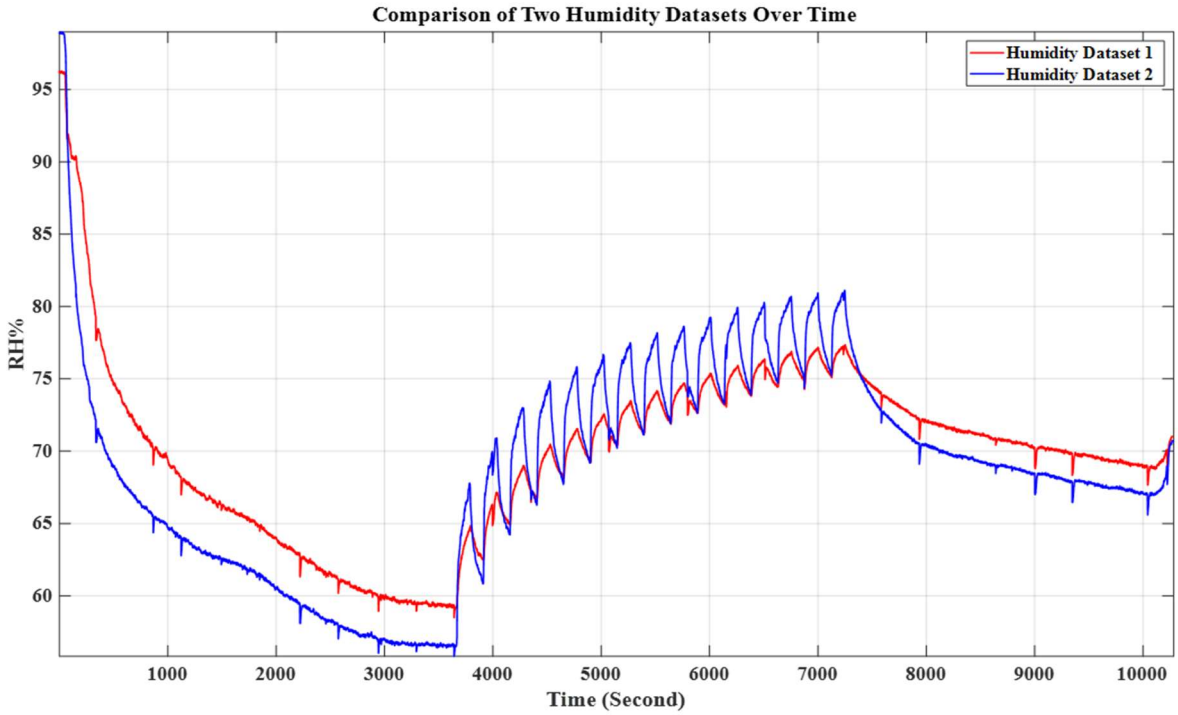


Figure 5-19 Variation of relative humidity (RH%) over time during a one-week rain and one-week no-rain in the M-T6 test.

This zoomed-in view in Figure 5-20 provides a closer look at the behaviour of RH% during the transition phases of the test.

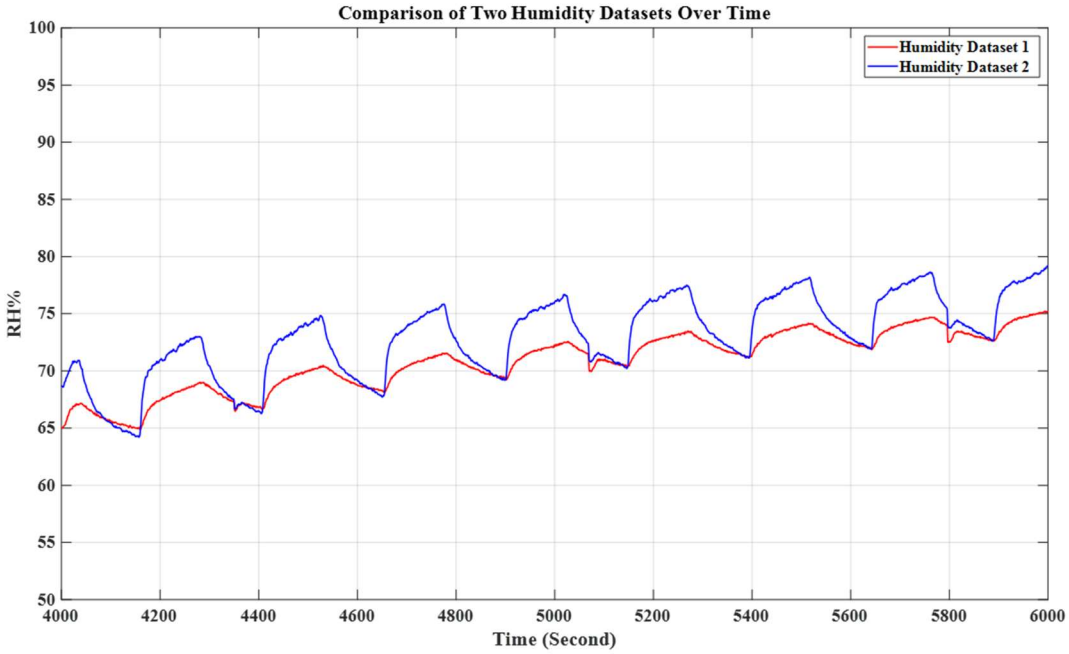


Figure 5-20 Zoomed-in view of RH% during a one-week rain and one-week no-rain cycle.

5.8.1 Temperature Measurement

The LM35 V3 Temperature Sensor is known for its high accuracy and stability. This sensor was used to continuously monitor the temperature during both the rainfall application and the dry periods. The LM35 sensor outputs a voltage proportional to the temperature, allowing for easy integration with data acquisition systems. These sensors were strategically placed within the testing setup, specifically attached to the top of the plate as shown previously in Figure 5-3, to capture real-time data on humidity and temperature, providing a comprehensive understanding of the environmental conditions throughout the experiment. Figure 5-22 shows the temperature variation of 2 sensors over time during the first spin of the M-T6 test. This test simulates winter by having one week of rain and one week of no rain. Dataset 1 (Red): The temperature starts from around 20.5°C and rises gradually, reaching a maximum of approximately 23.5°C towards the end of the test. This dataset shows fewer fluctuations and exhibits a more stable increase in temperature compared to Dataset 2.

Dataset 2 (Blue): This dataset starts from a similar value of 20.5 °C but experiences more pronounced fluctuations throughout the test period. The temperature reaches approximately 24°C at its peak, exhibiting more dynamic behaviour with frequent temperature oscillations, especially noticeable between 4000 and 7000 seconds. The difference in temperature profiles between the two datasets could be attributed to the location of the sensors. Similar to the humidity data, Sensor 2 (blue) is closer to environmental influences (e.g., near the rainfall nozzle), which leads to more dynamic temperature changes. Sensor 1 (red) appears to be located in a more sheltered area, where the temperature rises more steadily and remains stable, indicating less exposure to direct environmental changes.

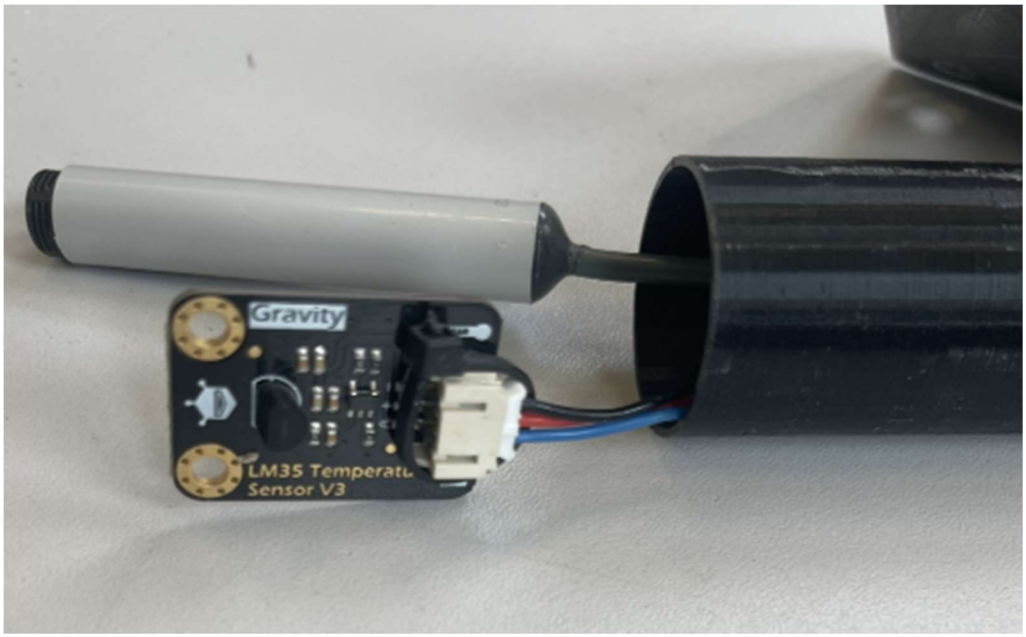


Figure 5-21 Humidity and temperature sensors (HM1500LF and LM35) used in experiments.

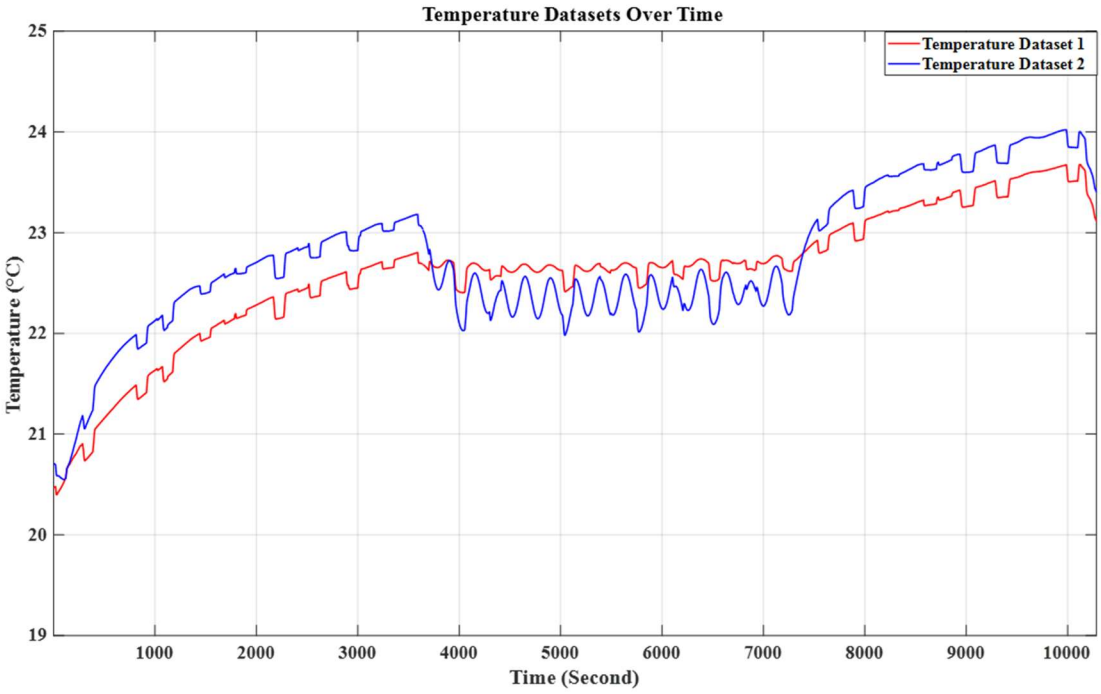


Figure 5-22Temperatures variation over time during the first spin of the M-T6 test.

CHAPTER 6

6.1 INTRODUCTION

This chapter introduces the detailed procedures employed to create and test a series of soil models under controlled centrifuge conditions. The chapter focusses on the development and testing of six distinct model slopes, each subjected to various environmental conditions designed to simulate slope behaviour, particularly under cycles of wetting and drying caused by rainfall and/or flooding. The use of the centrifuge provides a crucial scaling advantage, replicating gravitational forces and stress conditions found in natural slopes, but within a more accelerated timeframe, allowing for quicker observation of soil behaviour.

The slopes were carefully constructed with specific angles, soil compositions, and boundary conditions to ensure that each model effectively represented typical geotechnical scenarios. In some cases, the slopes were further steepened to replicate increased stress conditions or simulate progressive failure mechanisms. The variation in slope angles allowed for a more comprehensive analysis of how slope geometry interacts with moisture content and saturation levels to influence slope stability, deformation, and potential failure.

A key aspect of this study is the role of wetting and drying cycles, which were applied across the different tests to observe how rainfall infiltration and subsequent drying affect pore water pressures, soil structure, and displacement within the slope. Flooding events were also simulated in later tests, where water levels were intentionally raised to observe how the slopes responded to extreme hydrological conditions, including the effects of rapid drawdown on slope stability. These flooding and drawdown events aimed to mimic real-world scenarios such as heavy rainfall, seasonal flooding, or rapid water level changes.

6.2 MODEL SLOPE EXPERIMENTS

Table 6.1 provides an overview of the centrifuge model tests. The first two tests (M-T1 and M-T2, a pure compacted kaolin clay slope and a compacted slope of the chosen sand-clay 35-65 mixture, respectively) were conducted in 2018. There was period of no testing then in late 2022, testing began again with a level-ground consolidated clay situation (M-T3) to examine

the response of new PPTs, and a new camera set up for imaging. The last three tests and their slope variants were all conducted on the 35-65 sand-kaolin mixture in 2023.

Table 6.1 Experimental arrangements of the model test slopes

Model Test	Slope Angle	Slope material	Fabrication Type	Notes
M-T1	26^{o}	E-Grade kaolin	Compaction	No PPTs installed
M-T2	26^{o} (1:2)	Mixture of 65 % sand+35% kaolin	Very dense compacted (unsaturated)	Poor PPT data. Model eroded due to heavy rainfall
M-T3a	Level Ground	Mixture of 65 % sand+35% kaolin	Consolidated pressure 600 kPa	PPT calibration + camera & LED lighting location and reflection reduction
M-T3r	60^{o} (1:0.6)	Mixture of 65 % sand+35% kaolin	Re-graded this model from M-T3	Failure by Surface Erosion Slope failure occurred imm ediately during spin-up.
M-T4 May-23	26^{o} (1:2)	Mixture of 65 % sand+35% kaolin	Consolidated pressure 600 kPa	Erosion Poor surface cover Accidental flooding through stuck solenoid valve and slope movement during auto balance.
M-T5 June-23	33^{o} (1:1.5)	Mixture of 65 % sand+35% kaolin	Compacted using Vibrocompactor	Auto balance movement Seasonal cycles Continuous rainfall failure Flooding Drawdown continuing movement of failed slope
M-T6 July-23	29^{o} (1:1.75)	Mixture of 65 % sand+35% kaolin	Consolidated pressure 600 kPa	Auto balance movement Seasonal cycles Flooding Drawdown No failure
M-T6r August-23	33^{o} (1:1.5)	Mixture of 65 % sand+35% kaolin	Re-graded this model M-T6 from 29^{o} to 33^{o}	Auto balance movement Seasonal cycles Flooding failure Drawdown continuing movement of failed slope

6.3 Preparation of soil models.

The accurate preparation of soil models is vital for investigating the performance of slopes under various environmental influences. This section provides an overview of the steps taken to prepare each model, emphasising the methodologies used to ensure accurate simulation of environmental conditions. The preparation techniques outlined here aim to replicate real-world challenges, offering valuable data on how slopes behave under combinations of rainfall, drying cycles, flooding, and drawdown.

The M-T1 and M-T2 tests, conducted in 2018, were preliminary experiments designed to evaluate slope behaviour under specific conditions: M-T1 involved a saturated pure kaolin slope, while M-T2 utilised an unsaturated sand-kaolin mixture (65% sand and 35% kaolin). However, due to the disruptions caused by the COVID-19 pandemic, much of the data from these tests, which were stored on the university's centrifuge lab computers, could not be retrieved subsequently. Furthermore, the testing system at the time was still under development and encountered several operational challenges. Specifically, in the M-T2 test, excessive rainfall was applied, resulting in significant erosion at the very beginning of the experiment and rendering it unfeasible to proceed further. Given these limitations and the incomplete nature of the data, the results of these preliminary tests are not included in this chapter.

6.3.1 Methodology for model M-T3a test.

Soil Slurry Preparation.

In preparing the soil slurry for the M-T3a preliminary test, a mixture of kaolin, sand, and deaired water was used. The components were mixed to achieve a moisture content approximately twice the liquid limit, specifically 120% moisture content for a mixture consisting of 65% sand and 35% kaolin. The total weight of the mixture required for the slope was approximately 100 kg. This substantial quantity necessitated the use of a large electric mixer. To minimize air entrainment, the slurry was carefully transferred from the mixer to the consolidation rig or consolidometer immediately after mixing.

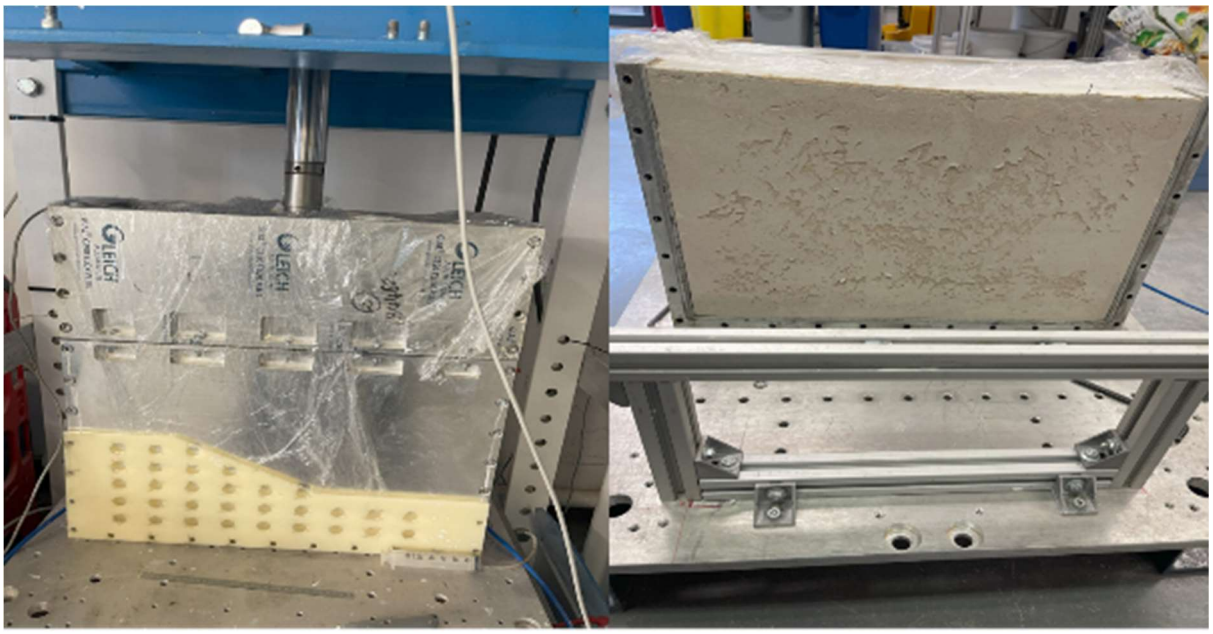
Consolidation of Soil Block.

The consolidation of the soil block was conducted in a separate consolidometer, distinct from the atmospheric chamber. This method offers several advantages, including reduced risk of

damaging the observation window and avoiding prolonged confinement of the atmospheric chamber during consolidation. The soil slurry was gradually poured into the consolidometer, ensuring an even distribution from the bottom of the chamber upwards. A drainage layer, comprising filter paper, was placed on top of the slurry. Following this, the consolidation ram was positioned on the soil slurry, and an initial load of approximately 21 kPa was applied. Subsequent loading increments were introduced in stages, with each stage allowing time for primary consolidation to complete. The load increment history typically followed a sequence of stresses: 21, 42, 84, 168, 336, 500, and 600 kPa. Unloading was performed in 58 kPa increments to prevent soil particle formation, with a typical unloading history of 500, 442, 384, 326, 183, and 125 kPa, before the final unloading stage from 125 kPa to 0 kPa.

Figure 6-1 Consolidated Slope Model (M-T3a) Preparation:(a): The initial consolidation process. (b): The consolidated block.

(b) shows the soil block after the consolidation process within the strong box, illustrating the uniform compaction achieved through the preparation and loading procedures.



(a) (b)

Figure 6-1 Consolidated Slope Model (M-T3a) Preparation:(a): The initial consolidation process. (b): The consolidated block.

The ground level model cutting.

In this stage of the M-T3a preliminary test preparation, the consolidated soil block is being precisely shaped to achieve the desired model profile as illustrated in the Figure 6-2. The ground level model is carefully cut using a plastic template to ensure accuracy and uniformity. The left figure shows the consolidated soil block securely positioned and ready for shaping. The plastic template is affixed to the side of the soil block, serving as a guide for the cutting process. This template ensures that the cut follows the exact model dimensions and profile required for the test. The right figure shows the process of cutting the soil block. The cutting wire was used and guided by the plastic template to shape the soil block accurately.

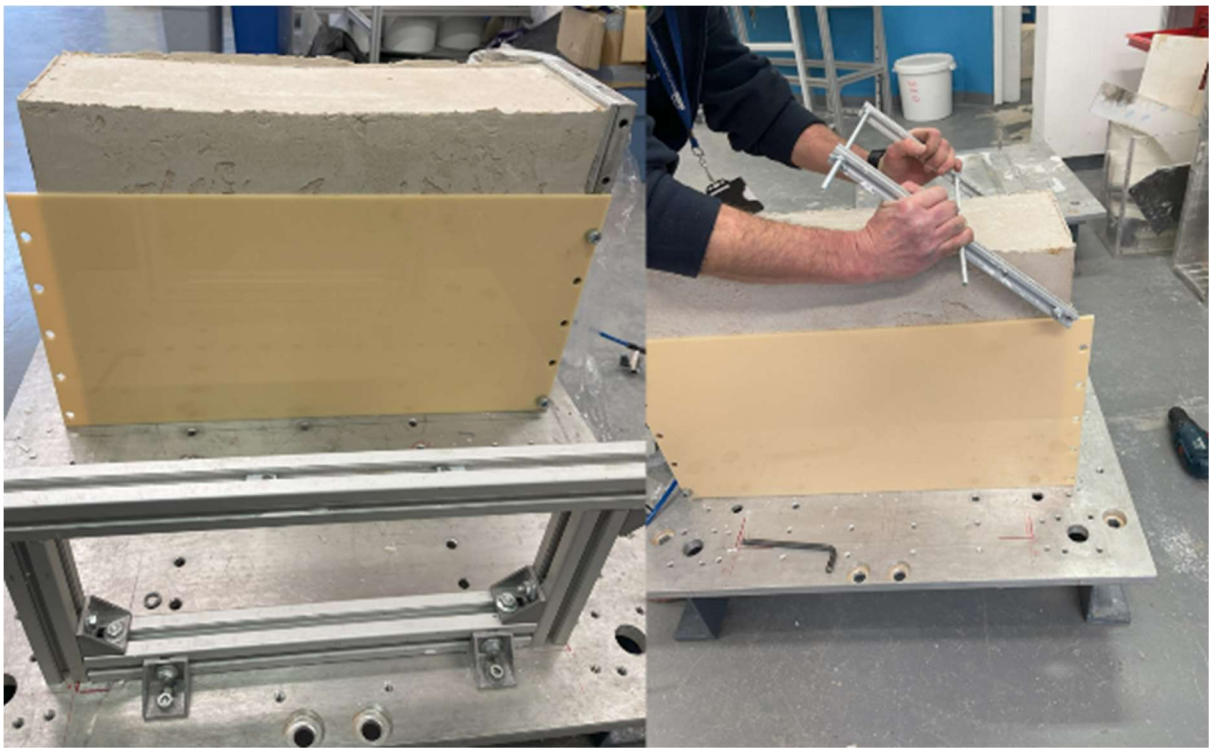
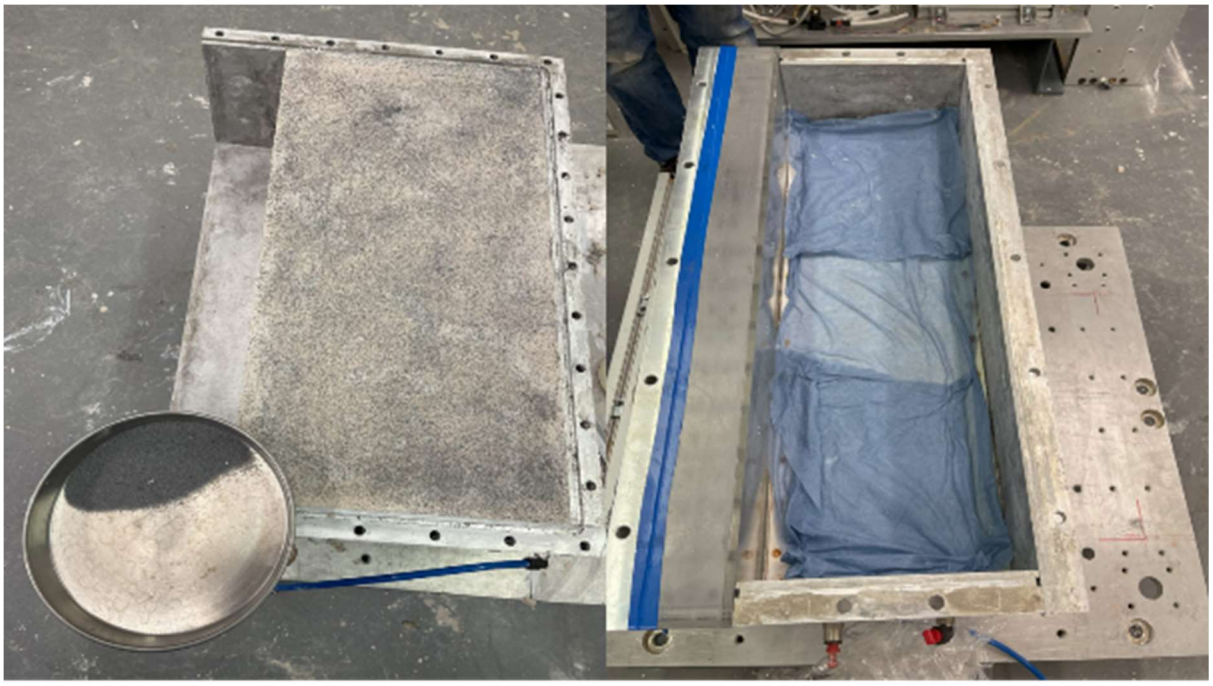


Figure 6-2 Shaping the consolidated soil Block: Left: Positioning the plastic template. Right: Cutting the level ground model.

M-T3a ground level test preparation stage.

At this stage of the M-T3a ground-level test, black seeds were applied to the front face of the consolidated soil block, similar to the M-T1 test as shown in the Figure 6-3 (a). The Perspex window was then securely bolted into place, providing an unobstructed view of the internal soil structure during testing. To maintain consistent moisture levels and facilitate uniform water

distribution, the model was covered with a permeable layer and wet blue tissue, as illustrated in Figure 6-3 (b).



(a) (b)

Figure 6-3 (a): Application of Black Seeds. (b): The model of M-T3a test and moisture control layers.

Pore Pressure Transducers (PPTs) Locations.

The Figure 6-4 illustrates the placement of 12 pore pressure transducers (PPTs) within the soil model to monitor pore water pressure at various depths and positions. The dual vertical array of PPTs provides detailed information on the horizontal distribution of pore water pressure across different depths. The diagram indicates the maximum water level, providing a reference for the highest expected pore water pressure conditions during the test.

Water Supply Levels (A, B, C):

- Point A: Located 375 mm above the base, indicating a high water level scenario.
- Point B: Located 220 mm above the base, representing an intermediate water level scenario.
- Point C: Located at the base level, representing the lowest water level scenario.

These water supply levels help simulate different hydrological conditions within the horizontal soil block, allowing for a comprehensive analysis of pore water pressure dynamics under varying water table scenarios.

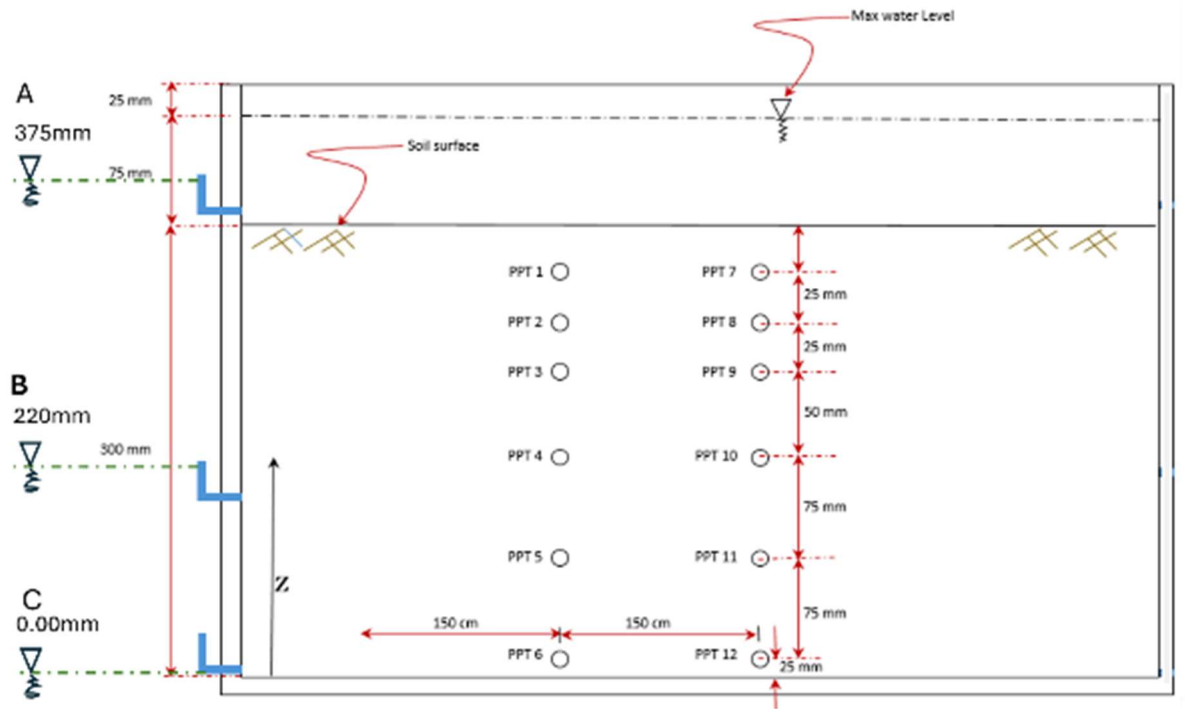


Figure 6-4 Schematic diagram of M-T3a test and PPTs locations.

Installation of the PPTs.

In this stage of the M-T3a test preparation, 12 pore pressure transducers (PPTs) were installed at different heights within the consolidated soil block to monitor pore water pressure throughout the experiment as shown in Figure 6-5.

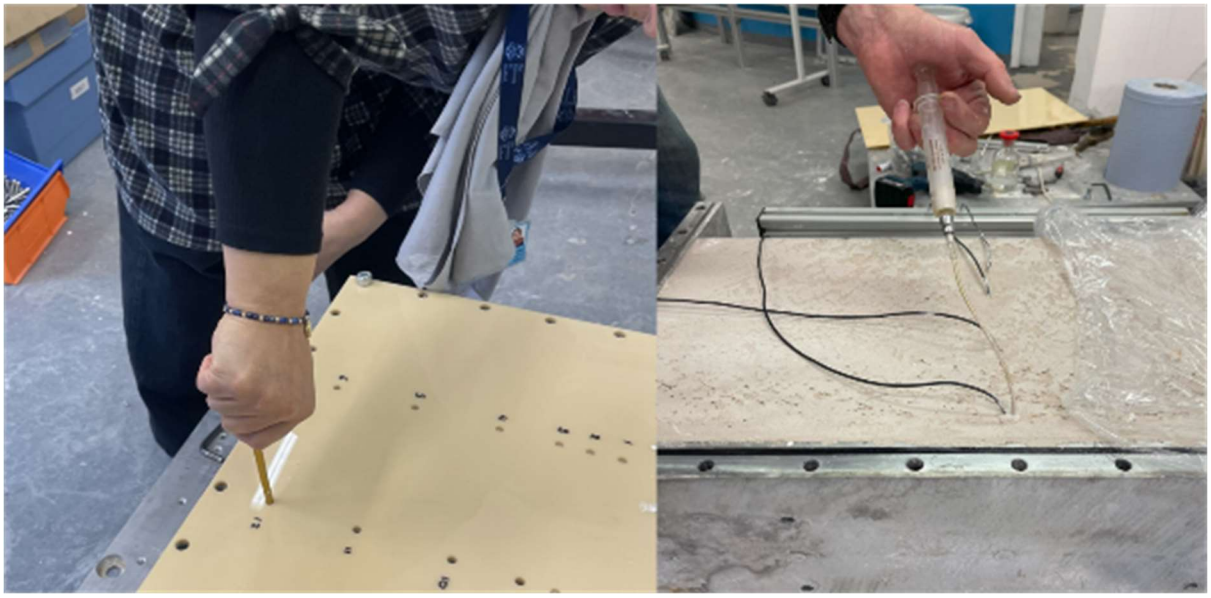


Figure 6-5 Left: Drilling holes for PPTs installation. Right: Inserting PPTs at different heights in the soil block.

The front face of the soil block, covered with a plastic template, was marked with specific locations for the transducers. Holes were drilled precisely at these marked positions to ensure accurate placement of the PPTs at desired heights. The transducers (PPTs) were inserted into the pre-drilled holes within the soil block. The slurry from the same mixture was injected into the soil using a syringe, ensuring that all PPTs were properly positioned and adhered to the soil block.

After inserting the PPTs, a soil paste was applied around each transducer. This step in the left of the Figure 6-6 is crucial to ensure that no air can enter the holes, which could cause the PPTs to dry out and potentially lead to inaccurate readings. The soil paste acts as a sealant, maintaining consistent moisture levels around the sensors. In the right of the Figure 6-6, grooves were carefully created in the soil to accommodate the wires from the PPTs. This organizational step helps in neatly routing the wires, preventing them from interfering with the soil surface and ensuring they remain in place during the testing phase. The image shows the top view of the soil block with the wires neatly arranged in the grooves, ready for the final setup and testing. Applying the soil paste and creating grooves for the wires ensures that the PPTs remain functional and accurately measure pore water pressure throughout the experiment.

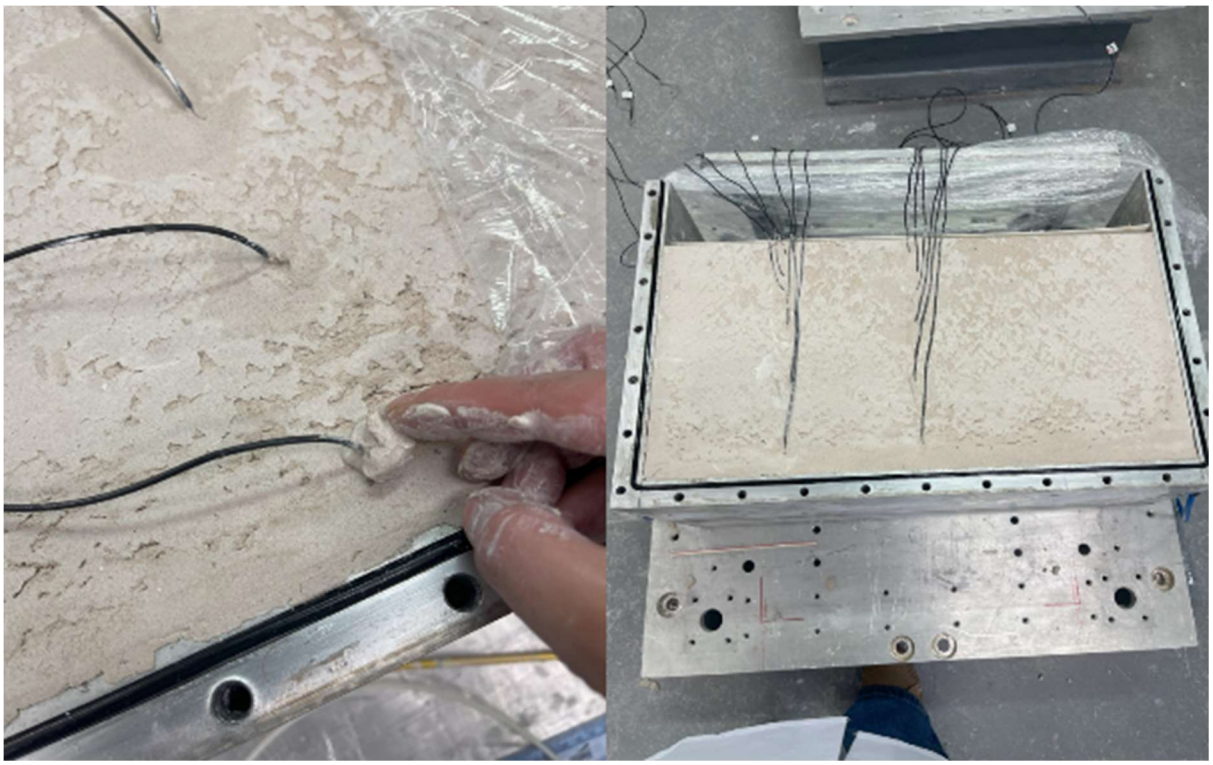
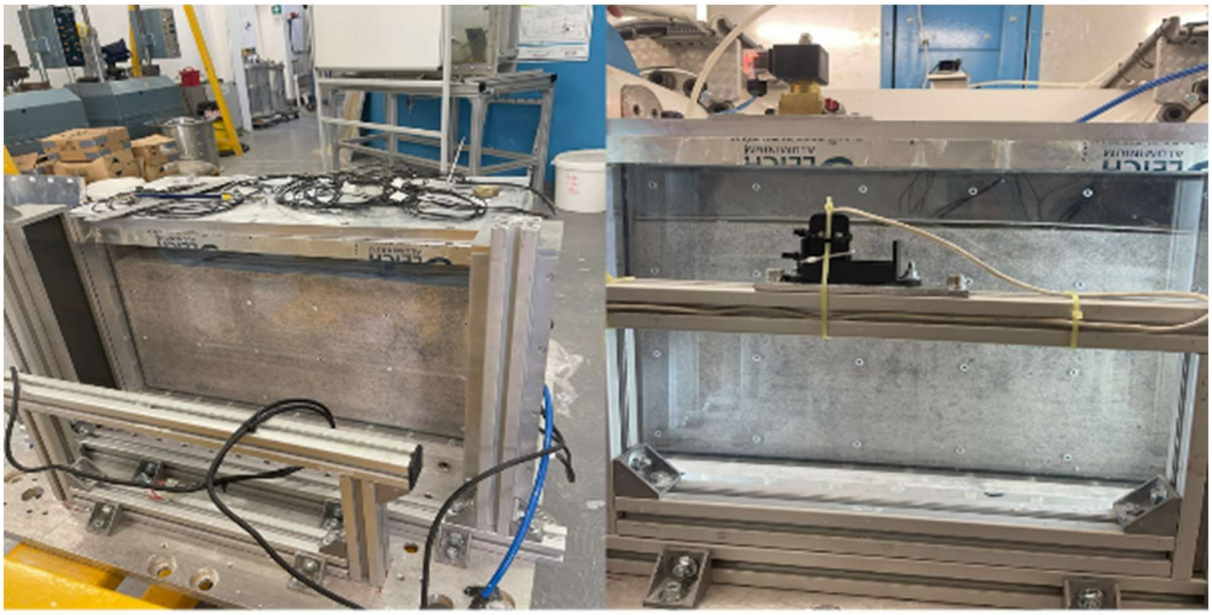


Figure 6-6 Left: Applying soil pasta. Right: Organizing and routing wires.

Final Setup of the M-T3a Test.

At this stage, the final components of the M-T3a test setup were assembled, including the LED light and camera frame, the top plate, and the connection of all sensors. The LED light and camera frame, along with the top plate, were securely mounted to the testing rig, as illustrated in Figure 6-7 (a). After installing these components, the model was weighed to ensure proper calibration before proceeding with the test. Following the weighing process, the model was mounted onto the centrifuge arm, and all sensors, such as the pore pressure transducers (PPTs), were connected to the data acquisition system. These sensors were routed and organised through a central duct to ensure accurate measurement and data recording during the experiment. The setup, with the sensors firmly attached and the wiring neatly arranged, is shown in Figure 6-7(b), ready for the centrifuge testing to commence.



(a) (b)

Figure 6-7: (a) LED light, camera and top plate connecting. (b): final adjustment and model setup in the centrifuge platform.

6.3.2 Testing procedures for M-3a test.

The testing procedures for the M-T3a centrifuge test are designed to systematically evaluate the behavior of the soil model under varying hydrological conditions at an acceleration of 70g. The methodology involves adjusting the water level at different stages to simulate real-world scenarios and gather comprehensive data on pore water pressure and soil movement.

1. **Initial Equilibrium and Spin-Up.**

Equilibrium Establishment: Before initiating the water level adjustments, the centrifuge is spun up to 70g to allow the soil model to reach initial equilibrium under the increased self-weight stresses. This phase ensures that any initial settlements or adjustments in the soil structure occur due to the gravitational forces.

2. **Water level adjustments.**

The height of the water level is adjusted at three distinct stages to replicate different hydrological conditions:

(a) Above the soil surface (2 cm):

Procedure: The water level is raised to 2 cm above the soil surface. This stage simulates conditions of surface water infiltration, which could occur due to heavy rainfall or flooding.

Objective: To observe the impact of surface water on pore water pressure distribution and potential surface erosion or infiltration processes.

(b) Mid-drainage point:

Procedure: The water level is adjusted to the mid-drainage point, aligning with an intermediate height of 220 mm above the base of the soil block. Although the soil model is initially saturated due to the consolidation process, this adjustment simulates a condition where water is partially drained to an intermediate level.

Objective: To assess the behavior of the already saturated soil model as the water level drops. This stage is critical for understanding the soil's response to decreasing water levels and the associated changes in pore water pressure and soil stability.

(c) Base level:

Procedure: The water level is lowered to the base of the soil block, indicating full drainage or the lowest possible water table condition (0 cm).

Objective: To analyses the soil response under fully drained conditions. This stage helps in evaluating the soil's stability when the pore water pressure is minimized, replicating scenarios such as post-rainfall drainage or drought conditions.

3. Data Collection and Monitoring

Throughout each stage of water level adjustment:

(a) Pore Pressure Transducers (PPTs): The PPTs installed at various heights within the soil model continuously monitor the pore water pressure. This data is crucial for understanding the internal water pressure dynamics and their influence on soil stability.
(b) Particle Image Velocimetry (PIV) System: The PIV system captures high-resolution images to analyses soil movement and deformation. The visual data obtained from the PIV system is used to correlate soil behavior with changes in pore water pressure.

6.3.3 Methodology for model M-T3r test.

Objective

The primary objective of Test M-T3r was to evaluate the stability and failure mechanisms of a re-cut 60° slope under centrifugal acceleration and flooding conditions, using a new rainfall simulation system as shown in Figure 6-8. Despite initial issues with the centrifuge equipment, the findings contributed to a better understanding of slope behaviour under extreme conditions, while also ensuring the proper functioning of the new rainfall simulator.

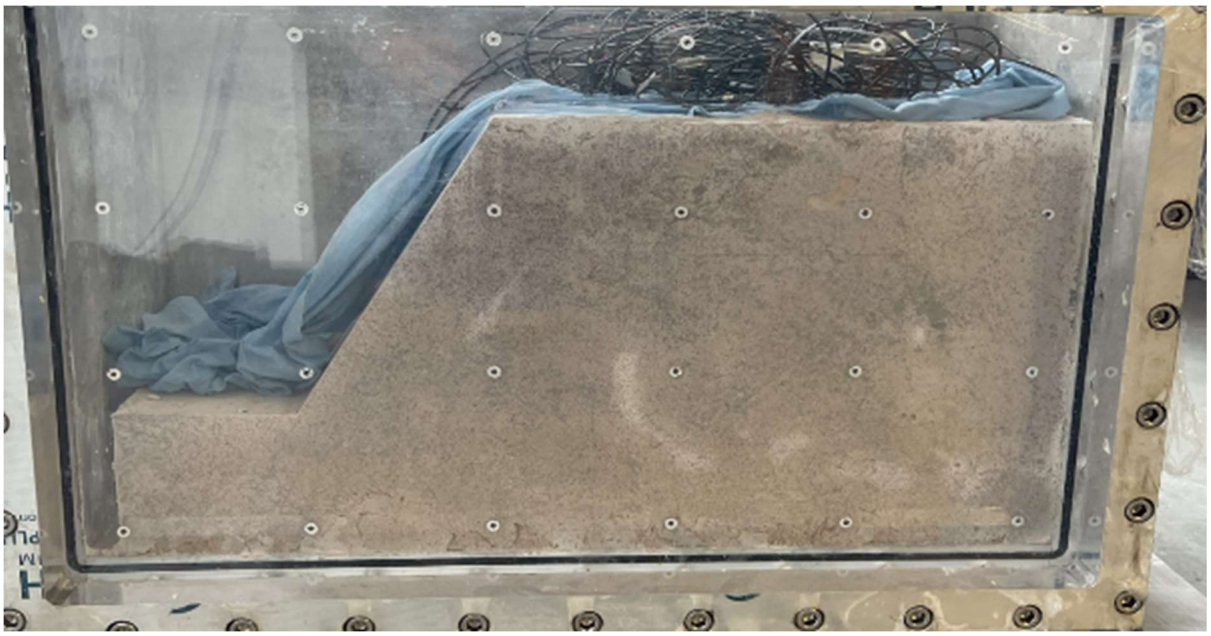


Figure 6-8 Slope model prepared for M-T3r test with sensor array and protective covering.

Model preparation.

The slope model was re-cut from the previous M-3a test block to form a new slope with a 60° angle. The model was carefully adjustment in the centrifuge container, ensuring stability and proper alignment.

Rainfall simulator.

A newly designed rainfall simulator equipped as illustrated in Figure 6-9 with:

- 4 nozzles for uniform water distribution (placed as two pairs across the width of the box).
- 2 humidity sensors to monitor atmospheric moisture levels.
- 2 temperature sensors to observe temperature variations.
- 1 A pressure regulator to observe and measure the water pressure during testing.

The rainfall intensity was calculated based on nozzle calibration and catchment area measurements, which are detailed in Chapter5.

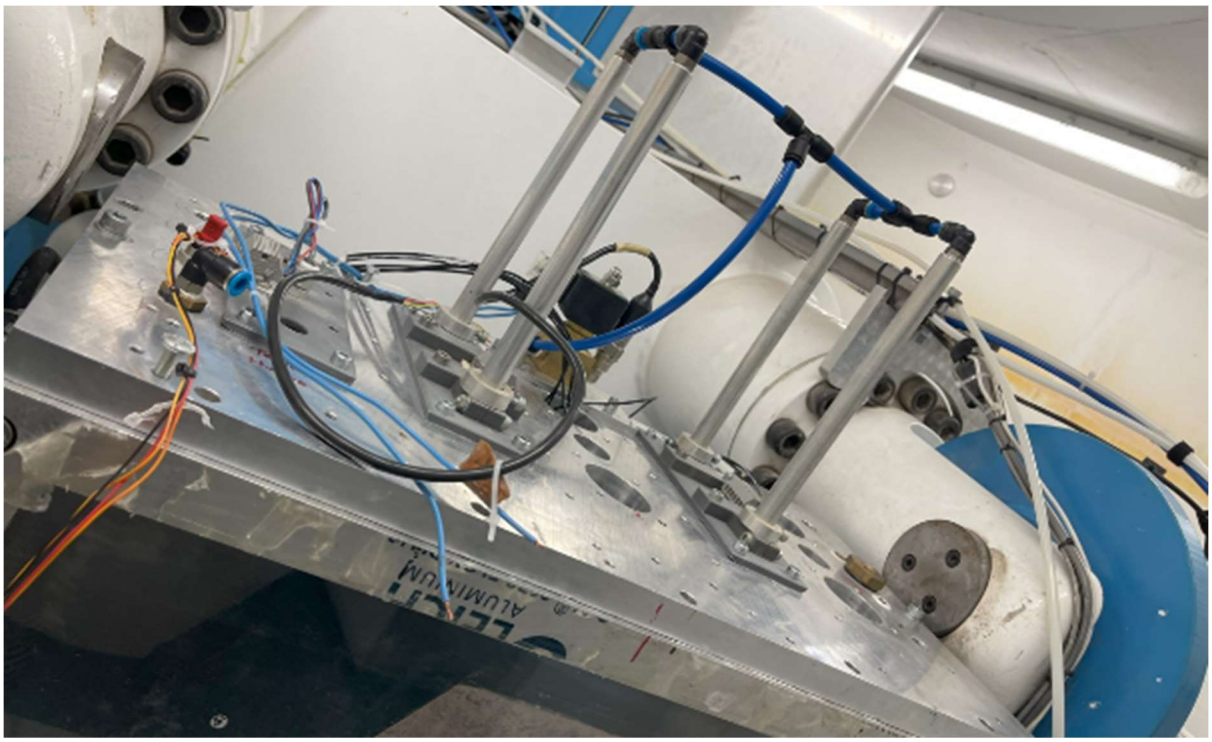


Figure 6-9 Detailed view of the rainfall simulation system and sensor setup on the centrifuge apparatus.

Data acquisition.

The installation of (PPTs) was done from the M-T3a to collect data on pore water pressure during the all-testing stages.

Imaging equipment.

A GoPro 7 black camera was used to capture a set of images for Particle Image Velocimetry (PIV) analysis to observe soil movement but after the initial failure. The GoPro camera was

positioned at the known distance chosen during camera calibration to capture high-resolution images of the slope surface for subsequent PIV analysis (Figure 6-10).

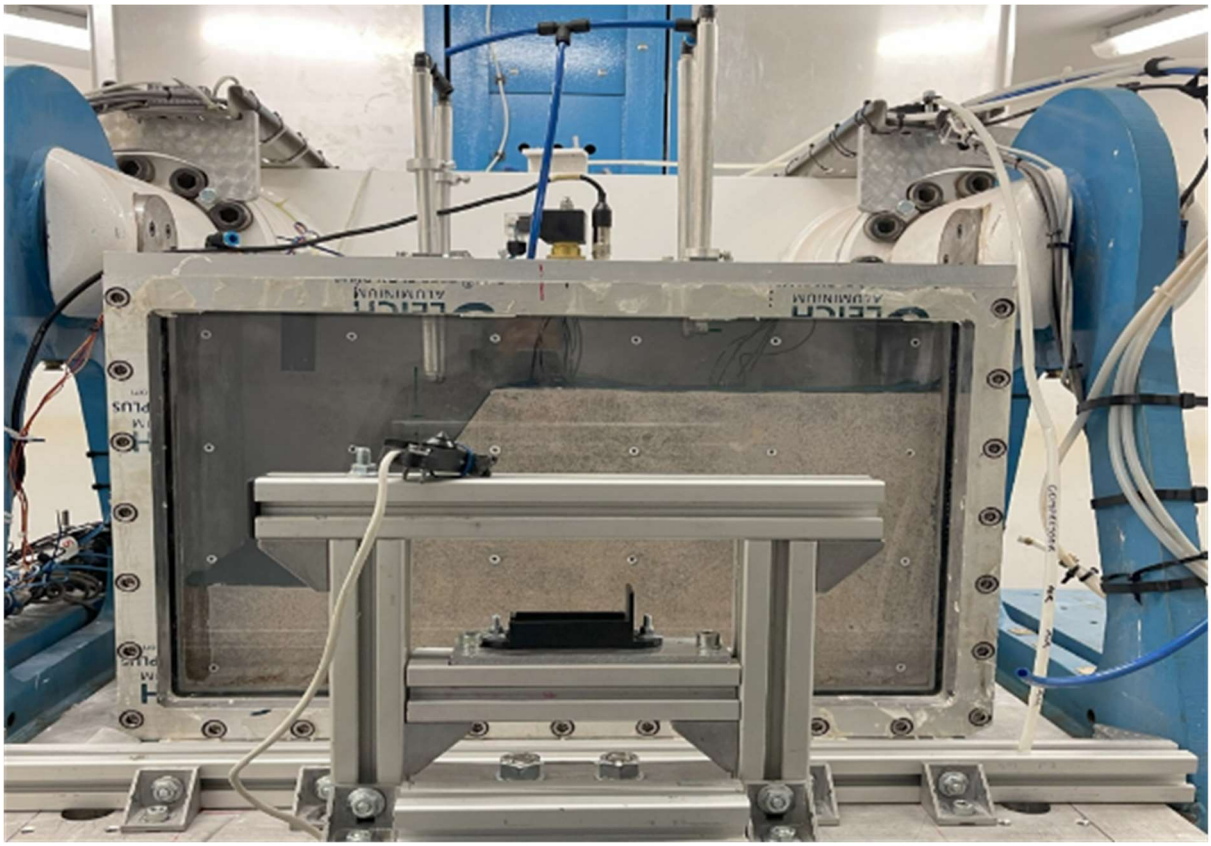


Figure 6-10 The final adjustment and setup of the centrifuge M-T3r test.

6.3.4 Testing procedure for M-T3r.

1. **Centrifuge Spin-Up.**

The centrifuge was gradually accelerated to 70g to simulate the enhanced gravitational conditions. An initial equilibrium phase allowed the model to adjust to the increased gravitational force.

2. **Flooding and Rainfall Simulation.**

Once the centrifuge reached the target acceleration, the rainfall simulation commenced. Water was evenly distributed over the slope using the four nozzles, with the rainfall intensity calculated based on previous calibrations. Throughout the test, humidity and temperature levels were continuously monitored and recorded. The performance of the new rainfall simulator was closely monitored to ensure it was functioning properly and delivering the expected rainfall intensity and distribution.

3. **Issue encountered and resolution.**

During the initial phase, issues with the centrifuge auto-balance and oil leakage were encountered. The test was temporarily halted to fix these issues. After addressing the issues, the test was resumed to verify proper functionality. However, the camera was not set back into its position. and unfortunately, during this trial the slope failed, and no images were captured for PIV analysis.

4. **Subsequent testing and data collection.**

Following the initial failure, the model was spun again with the camera set up to capture images for PIV analysis. Continued rainfall was applied to create conditions of flooding and drawdown. During this period, the slope experienced additional failures and movements, with visible cracks developing near the crest. High-resolution images captured by the GoPro camera were analysed using (PIV) to quantify soil displacement and movement patterns. Pore water pressure data from the PPTs were recorded and analysed to understand the pressure changes during the flooding phase. Results are presented in Chapter 7, detailing the failure mechanisms and providing insights into the behaviour of the re-cut slope under the given test conditions.

6.3.5 Methodology for model M-T4 test.

The soil slurry preparation for M-T4 followed the same procedural steps as M-T3a, ensuring consistency in consolidation. The methodology for M-T3a has already been detailed in Section 6.3.1, where the slurry composition, liquid limit determination (27%), and preparation process at 1.2 times the liquid limit was explained.

Consolidation of the soil block

The consolidation process for M-T4 followed the same procedure as previously described for M-T3a (Section 6.3.1). The same loading and unloading sequence, drainage setup, and consolidation apparatus were used, as detailed in the M-T3a methodology.

Cutting the Consolidated Block to a Slope

Following the consolidation process, the soil block was prepared for the next phase: cutting the slope at a precise angle. Using a specially designed template, the block was carefully cut to form a slope with an angle of 26°. Figure 6-11shows the initial setup with the template in place, then the finished cut, which reveals a clearly defined slope. The cutting process is executed using a cutting wire, which allows for precise and clean cuts through the consolidated soil block.

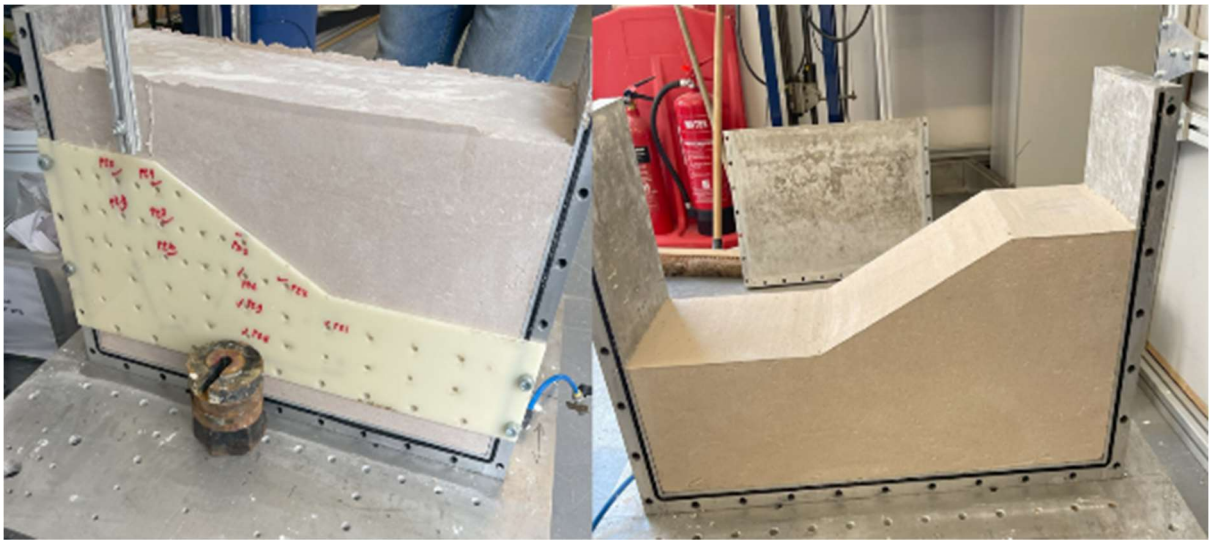


Figure 6-11 Cutting of the consolidated soil block to form a 26° slope using a template.

PPTs installation.

Following slope cutting, PPTs were installed using the same procedure as in previous tests to ensure consistent and reliable data collection. Precise holes were drilled at strategic locations based on the experimental design to capture pore water pressure variations across the slope. To prevent water leakage and ensure accurate readings, the PPTs were embedded in saturated slurry before placement. An important aspect of this stage was the decision to reuse PPTs from the previous test, M-T3r. Each PPT was carefully removed from the M-T3r setup with some slurry around it in an effort to maintain saturation and minimize the risk of air entering the sensors, as shown in Figure 6-12. This immediate transfer helped reduce the risk of water evaporating from the pore stone, aiming to keep the PPTs as saturated as possible for reliable readings. While full saturation could not be guaranteed by the end of the test, this process was intended to limit the introduction of air bubbles, which are known to affect the responsiveness and accuracy of pore pressure measurements.



Figure 6-12 Installation of pore pressure transducers (PPTs) from previous test M-T3r to the slope model in M-T4

Cutting the drainage part.

Following the installation of the PPTs, the next step involved preparing the drainage section of the slope model. The 5-cm drainage section is critical for simulating realistic drainage conditions within the slope model, allowing for accurate monitoring and analysis of water flow and pore pressure behavior during testing. This involves cutting a 5-cm wide drainage part using a metal plate, as depicted in Figure 6-13. To create the drainage section, a precise cut was made along the slope model using a sharp metal plate. The metal plate was carefully positioned and pressed into the soil to achieve a clean and accurate cut. After cutting the drainage part, aggregate was added to the newly created section. The aggregate helps facilitate effective drainage by allowing water to flow freely through the slope, preventing water buildup and simulating natural drainage conditions.



Figure 6-13 Cutting the 5-cm drainage part in the slope model using a metal plate.

Centrifuge platform loading and final adjustments.

After shaping the slope, blue tissue paper was placed on the surface to minimize erosion during simulated rainfall at 70g. The strongbox and rainfall simulator lid were weighed to adjust the centrifuge counterweight for balance. The model was securely placed on the centrifuge platform, with all sensors connected to a junction box for integration with the data acquisition system. The precipitation system was connected to the water supply via a 10 mm conduit through the centrifuge slip rings, completing the final setup adjustments.

6.3.6 Testing procedure of M-T4 test.

1. **Initial Equilibration Phase**

The experimental procedure for M-T4 commenced with a gradual increase in centrifuge acceleration, initially reaching 50g during the auto-balance phase, which lasted approximately 25 minutes. Following this, the acceleration was increased to the target level of 70g. The model then entered a stabilisation phase, where it spun for 40 minutes at 70g. Although the actual consolidation time was about one minute, equivalent to 82 hours at the

prototype scale, which aligning with theoretical expectations, the model continued to spin for 40 minutes to ensure thorough stabilization. This extended spinning period can be considered a dry period, effectively simulating a short 'summer' of 4.5 months at the prototype scale, where the system achieved equilibrium and the pore water pressures within the slope stabilized quickly, typically within one minute. This setup established the baseline conditions for the subsequent testing phases.

2. Seasonal Simulation Phase

After the initial equilibration, the model was subjected to annual cycle simulations to study the impact of variable rainfall durations on deformation and slope stability. The first climate scenario began with a 'winter' phase, lasting seven months at the prototype scale. This phase included alternating week-long periods of rainfall and dry conditions. However, due to an issue with the drainage valve at 70g, water accumulated on the slope during Winter 1 until it reached the middle of the slope, initiating the condition referred to as Flood 1. This situation persisted throughout the remainder of Winter 1. To address this, the centrifuge acceleration was reduced to 50g, allowing the drainage valve to be opened and all the accumulated water to be drained. Once the water was completely drained, the centrifuge acceleration was increased back to 70g to commence the summer phase. The subsequent 'summer' phase, equivalent to five months at the prototype scale, was characterized by the total absence of rainfall.

On the second day, the 'Winter 1' and 'Summer 1' scenarios were repeated, with the drainage valve manually opened before testing to prevent flooding. After repeating these phases, the model underwent the 'Winter 2' phase, which consisted of two weeks of rainfall followed by one week of dry conditions, extending over seven months at the prototype scale. This variation aimed to assess the effects of different precipitation patterns on slope stability. This scenario was implemented during the third spin of the centrifuge tests. Following the winter phase, the model entered 'Summer 2,' characterised by an absence of rainfall, simulating dry conditions. This sequence allows for a comprehensive analysis of how alternating precipitation patterns and extended dry periods impact the deformation and stability of the slope.

6.3.7 Methodology for model M-T5 test.

The following methodology outlines the process for creating slope models in the centrifuge strong box using a mechanical compaction process. The soil was compacted in controlled layers using vibration machine, with each layer reaching a thickness of (30 mm) before the next was added, ensuring uniform density and minimizing air voids. Note that, while the soil was the same mixture, the test preparation was different from M-T2, since mechanical compaction was used for M-T5 while hand compaction was used for M-T2.

Preparation of soil mixture

The dry soil mixture was prepared by mixing it with water at the optimum moisture content (w/c = 12.4%), as determined by compaction tests obtained in Chapter 4. The process of soil mixing was carried out using a mechanical mixer.

Soil mixing procedure steps:

1- Initial Dry Mixing: The dry soil components were first mixed thoroughly to ensure a homogeneous base mixture as shown in Figure 6-14 (left). This initial mixing step is crucial to avoid segregation of the soil particles.
2- Water Addition: Water was then added to the dry soil mixture at the determined optimum moisture content. The addition was done gradually to allow even distribution and absorption of moisture by the soil particles. These steps are shown in Figure 6-14.
3- Mechanical Mixing: The soil-water mixture was then mixed using an electric mechanical mixer.
4- Figure 6-15 Figure 6-15 depicts the use of a powerful mixer to ensure a uniform and consistent mix to achieve the desired moisture content uniformly throughout the soil.
5- Batch Division: To facilitate the mixing process and ensure uniformity, the soil mixture was divided into manageable batches. Each batch was mixed separately, allowing for better control over the moisture distribution and ensuring that all soil particles were adequately coated with water.

   Moisture Equilibration: After mixing, the soil was placed in sealed containers and stored for more than 24 hours. This storage period allows the moisture to equilibrate within the soil mixture, ensuring homogeneity in soil moisture content.

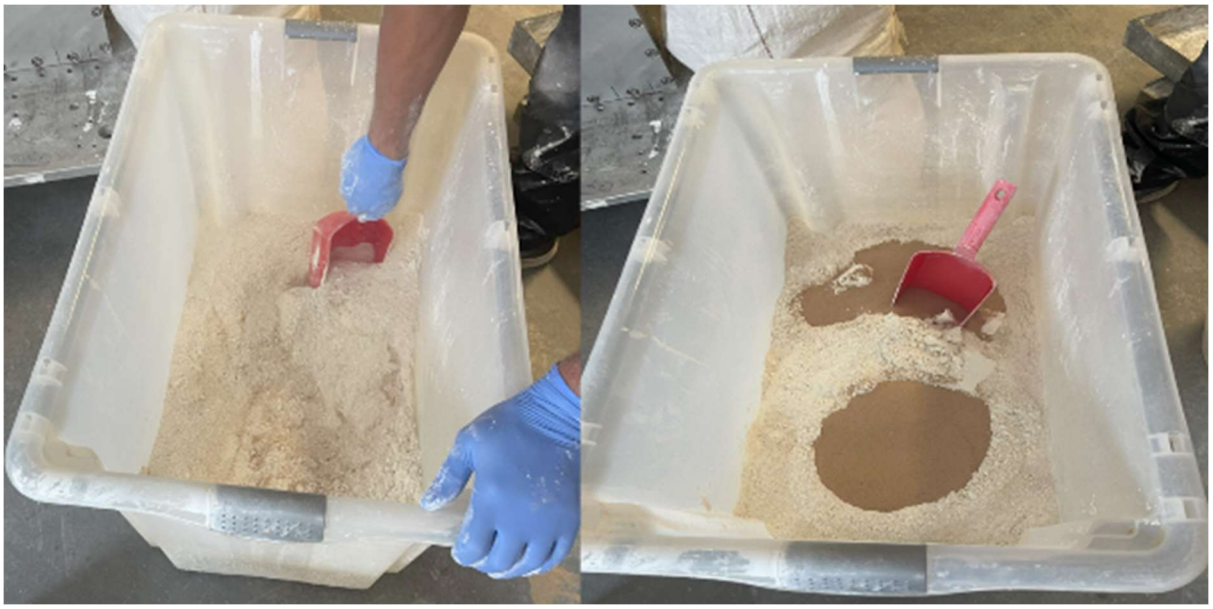


Figure 6-14 Left: Dry soil mixing. Right: Water adding to the mixture.

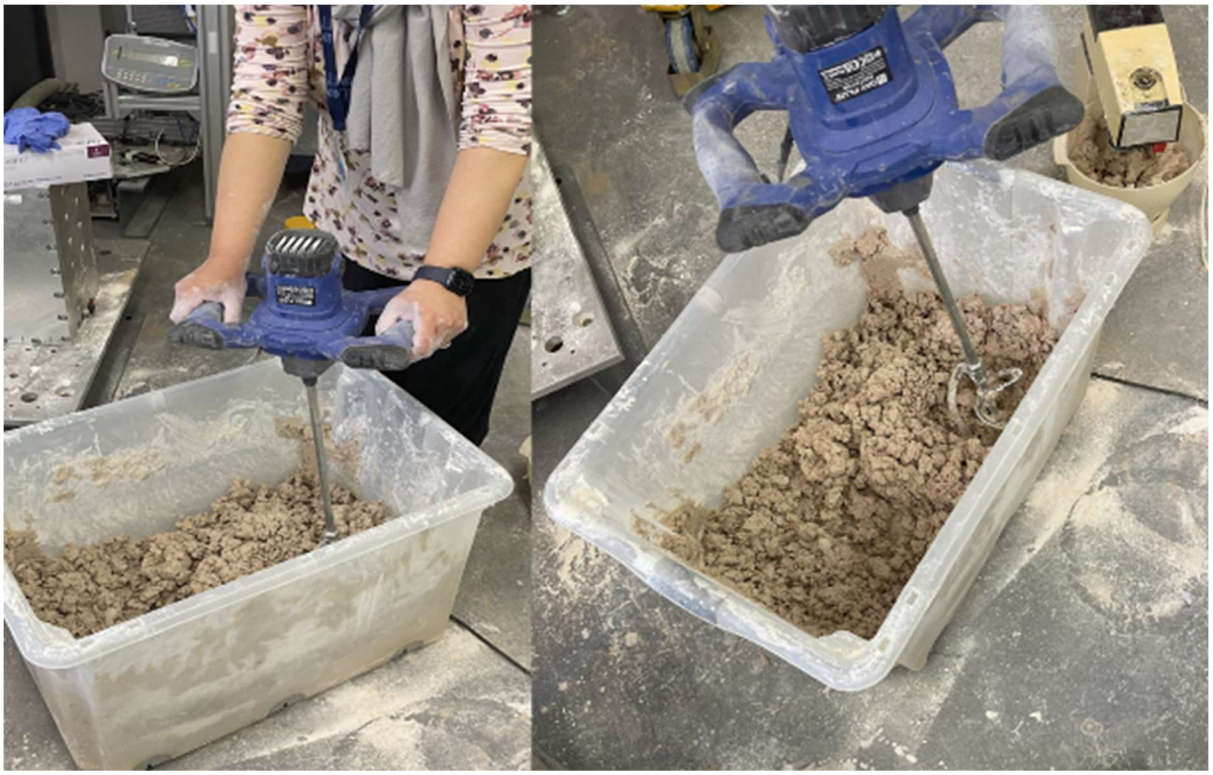


Figure 6-15 Mixing of soil mixture using mechanical mixer.

Layering and compaction

The soil mixture was then layered and compacted inside the strong box in ten layers, each with a thickness of 30 mm. The objective was to achieve a final height of 300 mm for the compacted soil. Uniform compaction of each layer was crucial to maintaining consistent density and structural integrity throughout the soil profile. The compaction of the soil was achieved by employing a vibrating machine that was equipped with a steel plate. This steel plate generated the required compactive effort, ensuring the uniform compaction of the soil in every layer and ensured that the compaction energy was evenly distributed, preventing any variability in soil density that could affect the experimental results. When the soil was placed in the strong box, it was passed through a sieve. This step was essential to break up any clumps and prevent particles from sticking together, ensuring a more uniform mixture. The sieving process helped to achieve a consistent particle size distribution, which is crucial for uniform compaction.

Figure 6-16 Figure 6-16 illustrates the detailed steps of the layering and compaction process.



Figure 6-16 Left: Using a vibrating machine to compact soil layers. Right: sieving soil mixture to break up clumps.

To ensure precise and consistent layer thickness, a laser measurement tool was employed during the compaction process. The use of laser technology ensured that each layer met the specified thickness of 30 mm. This meticulous and controlled approach to layering and compaction guaranteed that the soil model was prepared to the highest standards, establishing a robust foundation for the subsequent stages of the experiment. The process of soil layering using laser measurement is illustrated in the Figure 6-17.



Figure 6-17 Compaction of soil layers and precision measurement using laser tool in the strong box.

Shaping the slope

To shape the slope, two plastic templates were secured on both sides of the soil block, serving as guides to define the desired slope shape, which was precisely set to an angle of 33.7°. A sharp steel wire was employed to accurately trim the excess soil and create the slope profile. Samples were then extracted from the region of the soil block above the plastic template for triaxial testing, which provided data on the shear strength of the soil. Additionally, samples of the removed soil were oven-dried to determine the initial gravimetric moisture content. The final slope profile was refined using the sharp cutting wire, ensuring the top surface conformed precisely to the template. This step maintained consistent slope dimensions across all tests, as shown in Figure 6-18.



Figure 6-18 Shaping the slope with plastic templates and steel wire.

Surface preparation and Perspex viewing window installation.

Once the construction of the slope was completed, black seeds were evenly distributed onto the slope surface to achieve optimal texture. This step is essential to creating a textured surface, enhancing the contrast and facilitating the Particle Image Velocimetry (PIV) analysis by maximising the standard deviation of pixel intensities across the image patch. Following the surface preparation, the Perspex viewing window was fixed onto the strong box. Unlike previous setups, the thin plate containing reference points was excluded from this test due to issues with increased light reflection, which negatively impacted the PIV analysis. Instead, reference points were directly drawn on the thick Perspex window. This adjustment was made to reduce light reflection and improve the accuracy and quality of the visual data collected during the experiment.

Figure 6-19 illustrates the distribution of black seeds on the slope surface and the careful drawing of reference points on the thick Perspex window.



a b

Figure 6-19 (a) drawing reference points on Perspex viewing window and (b) preparing slope surface with black seeds for PIV analysis.

Installation of the PPTs.

The PPT installation procedure for M-T5 followed the same methodology as described in M-T3a (Section 6.3.1), where sensors were installed using a plastic template and augured through the back face to ensure precise positioning. The same slurry backfilling technique was applied to prevent voids and ensure proper contact between the PPTs and the soil matrix.

Erosion protection from applied rainfall scenarios.

The application of a fine mist onto the soil surface without proper control has the potential to cause runoff that could lead to significant erosion of the top layer of the model embankment. In order to mitigate the potential for erosion that occurs during extended periods of seasonal moisture cycles, a surficial erosion control layer was introduced in the form of filter paper strips. The filter paper was sliced into strips of 50 x 205mm and systematically positioned along the slope, extending from the crest to the toe, with a slight overlap similar to that of roof shingles. The filter paper was divided into 50-mm segments in order to prevent it from functioning as a means of reinforcing slopes. The width of 205mm of the filter paper is

marginally greater than the plane-strain width of 200mm, resulting in a small fillet at the boundaries. This fillet served the purpose of ensuring that the paper effectively captured the precipitation that had accumulated on the boundaries.

Climate chamber installation with the model.

With all the required instruments in place, including pore pressure transducers (PPTs), temperature sensors, and humidity sensors, the model embankment was prepared for installation into the atmospheric chamber. When positioning the liner containing the model embankment on the base of the atmospheric chamber, special care was taken to ensure that the PPTs leads were oriented vertically upwards. This orientation was vital to prevent any potential damage to the leads and to facilitate unobstructed data transmission. Additionally, the placement of the atmospheric chamber was conducted with great precision to maintain the integrity of the embankment structure and to avoid any disturbances to the instrumentation. allowing for reliable experimental results. To further enhance the quality of the experimental setup, one of the LED lights was repositioned to the right top of the model. This adjustment was made to improve the illumination of the model, ensuring good-quality images and reducing reflections, as illustrated in the accompanying image. By optimising the lighting conditions, the visual data captured during the experiment was of higher clarity, contributing to more accurate observations and analyses.

The centrifuge platform loading and final adjustments.

The centrifuge platform setup and final adjustments followed the same procedure as in previous tests, ensuring balance, sensor integration, and proper system functionality before testing. The strongbox and rainfall simulator lid were weighed, and counterweight adjustments were applied to maintain equilibrium. The final adjustment and slope model setup on the centrifuge beam is shown in Figure 6-20

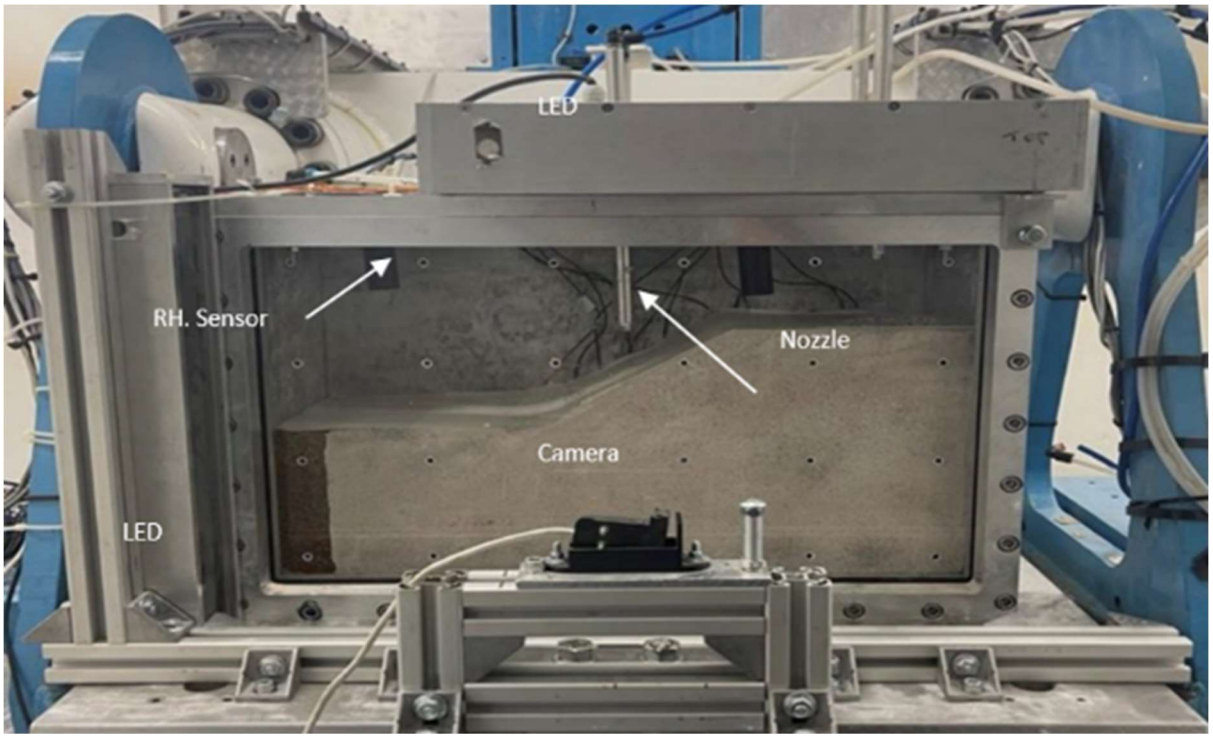


Figure 6-20 Experimental design of the centrifuge model and rainfall simulator.

6.3.8 Testing procedure for model M-T5.

The testing programme for model M-T5 was meticulously designed to investigate the effects of flooding, drawdown, and prior rainfall events on slope failure initiation. The experiments were conducted following a standardised protocol to ensure consistency and comparability across tests.

1. **Initial Equilibration Phase**

The testing procedure for M-T6 followed the same steps as M-T4 (Section X.X). The centrifuge acceleration was gradually increased to 50g for auto-balancing over 25 minutes, ensuring system stability. Once balanced, the acceleration was raised to 70g, initiating a 40-minute consolidation period (equivalent to 136 prototype days). Pore water pressures stabilized within one minute, consistent with theoretical predictions.

2. **Seasonal Simulation Phase**

Following consolidation, the model underwent simulated seasonal cycles designed to reflect annual climate variations, allowing an assessment of the effects of different rainfall patterns on slope deformation and stability.

a. First climate scenario (Winter 1): The first winter phase spanned seven months at the prototype scale. It involved alternating weekly cycles of rainfall and dry periods. A five-month period known as "Summer 1" followed this phase, during which there was no rainfall.
b. Second climate scenario: The second winter phase (Winter 2) lasted for seven months as well, but it differed in that there were two weeks of rain and then a week of dry weather. Following this, there was a five-month dry spell known as "Summer 2."
c. Third climate scenario: The "half-winter" scenario used three weeks of rain in a row, then one week of dry weather. Continuous rainfall was then applied until the end of the winter period, and drainage was introduced at the embankment toe to evaluate the effect of prolonged wet conditions on slope stability.

3. **Flooding and drawdown phase**

After completing the seasonal simulations, a flooding event was simulated by temporarily closing the drainage outlet, causing the water level to rise above the embankment crest, followed by a drawdown. However, during the tests, an issue arose with the valve becoming stuck, which required the centrifuge acceleration to be reduced to 50g in order to restart continuous rainfall and generate the flood. The flooding was carried out in three stages, each followed by a drawdown. In the first flood (Flood 1), the water level rose above the crest, while in the second and third floods (Flood 2 and Flood 3), the water reached the crest but did not exceed it.

4. **Extended dry period:**

Following the flooding and drawdown cycles, the models entered a summer period lasting 310 days with no precipitation. This phase was designed to observe the effects of prolonged dry conditions following the simulated flooding events.

5. **Rainfall intensity**

During the rainfall experiments, a steady rainfall intensity of 1.14 mm/h (in prototype scale) was applied throughout. The precipitation cycles were carefully managed and manually adjusted at specific intervals to maintain accurate control over the experimental conditions. By adhering to this systematic and well-structured testing procedure, the experiments yielded valuable insights into how different climatic and hydrological conditions affect slope stability and the onset of failure.

6.3.9 Methodology for model M-T6 test.

The soil slurry preparation and consolidation process for M-T6 followed the same methodology as M-T3a (Section 6.3.1), with a 65% sand, 35% kaolin mixture prepared at 1.2 times the liquid limit (27%). For consolidation, the soil block was formed in a separate consolidometer to protect the observation window. A U-shaped aluminium liner with a drainage system was used for transferring the block. The loading and unloading sequence followed the same staged increments as in M-T3a.

Shaping the slope after consolidation

After consolidation, the soil block was shaped into a 30° slope using plastic templates as guides, ensuring accuracy and consistency. A sharp steel wire was used for precise trimming, following the template contours as depicted in Figure 6-21. Soil samples from above the template were extracted for triaxial testing, while additional samples were oven-dried to determine the initial moisture content.



Figure 6-21 (a) The initial cutting of the soil using steel wire.(b) The completed slope profile.

Installation of PPTs

The PPT installation for M-T6 followed the same methodology as previous tests, with eleven sensors inserted through the back face using a plastic template for positioning. The key difference in M-T6 was that the same PPTs from M-T5 were reused, requiring careful handling to maintain saturation. To prevent desaturation, the PPTs were kept submerged in water after removal from M-T5 and coated with a saturated slurry paste before insertion. Slurry backfilling was performed using a syringe to ensure complete contact with the soil. All PPTs were pre-calibrated and verified for accurate suction and positive pressure measurement before testing.

The application of black seed texture and erosion mitigation measures on the model slope.

The application of black seeds for GeoPIV analysis and the 50 mm saturated gravel drainage layer at the slope base followed the same methodology as previous tests. The key difference in M-T6 was the addition of overlapping strips of filter paper from the crest to the toe to mitigate erosion during prolonged seasonal moisture cycles.

Model installation and final adjustment.

The installation and adjustment process followed the same methodology as previous tests, with the model and climate chamber positioned on the centrifuge platform alongside the necessary sensors.

6.3.10 Testing procedure for model M-T6 test.

The M-T6 test followed the same structured approach as M-T5 (Section 6.3.8) to assess the impact of flooding, drawdown, and preceding rainfall on slope stability. A standardized protocol ensured consistency and comparability between tests.

1. **Initial Equilibration Phase**

Centrifuge acceleration was gradually increased to 50g for auto-balancing over 25 minutes, then raised to 70g. A 40-minute consolidation period (136 prototype days) allowed the system to reach equilibrium, with pore water pressures stabilizing within one minute as expected.

2. **Seasonal Simulation Phase**

The model underwent simulated seasonal cycles, mimicking climatic fluctuations to assess rainfall-induced deformation and stability changes. Three climate scenarios were applied, featuring alternating rainfall and dry periods over winter and summer phases, with drainage introduced at the embankment toe in the final scenario.

3. **Flooding and Drawdown Phase**

Following the seasonal simulations, three flooding and drawdown events were conducted:

- Flood 1: Water reached just below the crest; drawdown initiated immediately.
- Flood 2: Water exceeded the crest for 41 minutes, followed by rapid drawdown in 2 minutes.
- Flood 3: Water exceeded the crest for 46 minutes, followed by rapid drawdown in 2.3 minutes

4. **Rainfall Intensity**

A consistent rainfall intensity of 1.14 mm/h (prototype scale) was applied, following the same controlled sequences as in M-T5 to maintain precise experimental conditions.

Note: The model was subjected to centrifuge testing on four separate spins over the course of three days. All times mentioned correspond to the model scale.

6.3.11 Methodology for model M-6r test.

Initial setup and background

The model embankment M-T6 underwent three years of prototype-scale wet and dry seasonal cycles, as well as three flooding and drawdown events. Despite experiencing increased pore water pressures due to prolonged rainfall, the slope exhibited only minor deformations. These minor deformations were generally recoverable, even after multiple stress cycles from repeated gravity applications during auto-balance events.

Objective and rationale for reconstruction

To increase the likelihood of slope failure, the slope inclination was increased after the third flooding and drawdown event. The objective was to simulate more severe conditions that could potentially lead to slope failure.

Slope angle adjustment

The embankment was removed from the centrifuge and reshaped to a new slope angle of 33.7°. This newly adjusted model was designated as embankment M-T6r, where 'r' indicates its reconstruction from M-T6. The increased slope angle required several modifications to the model setup.

Modifications and adjustments

- **Slope Cutting and Shaping**: The slope was accurately reshaped using a sharp wire and templates to achieve the desired angle of 33.7° as shown in the Figure 6-22 (a) .

- **PPT adjustment**: Due to the new slope geometry, one PPT (PPT2) located beneath the toe of the embankment had to be excavated and removed. The remaining PPTs near the toe were repositioned slightly to fit within the new slope geometry, as shown in the Figure 6-22.

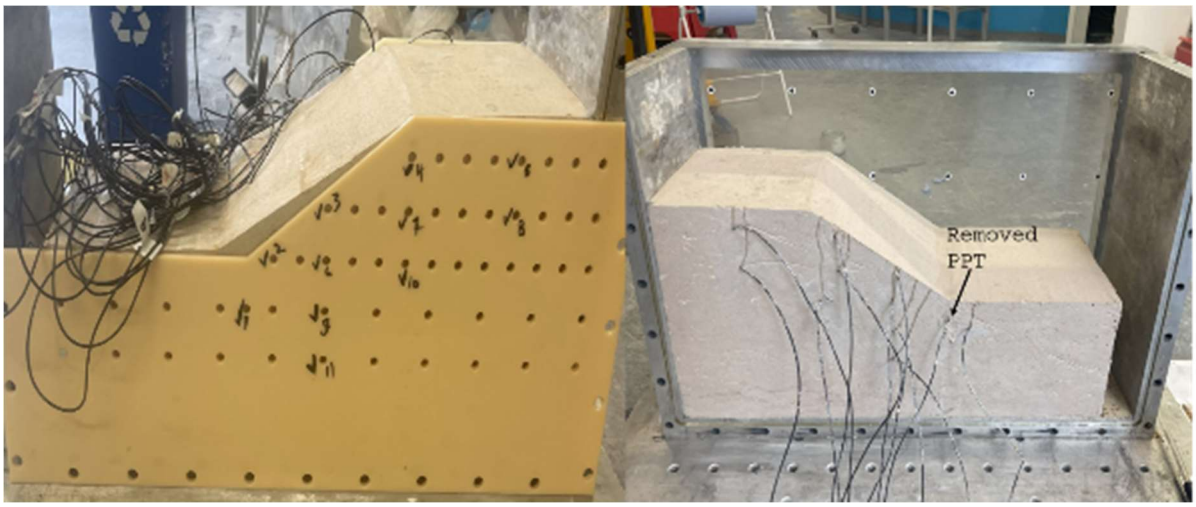


Figure 6-22 Lift: Adjustments for slope angle modification in model M-T6r.Right: Removal of PPT2 to accommodate the new slope geometry.

Reconstructing the slope.

The reconstruction process involved several steps:

1. **Excavation and removal**: The soil is carefully excavated to remove the identified PPT without damaging the embankment's structural integrity.
2. **Repositioning PPTs**: Some of remaining PPTs near the toe were therefore situated in a slightly different location within the new slope geometry. Adjusting the remaining PPTs was unnecessary as they were already positioned in locations suitable for the new slope geometry.
3. **Cutting and shaping**: Sharp steel wires and templates were used to reshape the slope to the new angle, ensuring precise cutting to maintain consistent slope dimensions.
4. **Smoothing and texture application**: After reshaping the slope, the old texture was removed and the slope surface smoothed to ensure uniform application of the new texture.
5. **Black seed texture application**: Black seeds were applied to the front face of the model slope to enhance PIV / DIC analysis using GeoPIV software.
6. **Drainage gravel placement**: At the base of the slope, a layer of saturated gravel was reapplied with a thickness of 50 mm to facilitate free drainage. This layer helps to mitigate potential erosion caused by prolonged seasonal moisture cycles.

6.3.12 Testing procedure for models M-T6r.

The M-T6r testing programme followed the same structured protocol as M-T5 and M-T6 (Section 6.3.7). After gradual centrifuge acceleration to 70g, a 40-minute consolidation phase (equivalent to 136 prototype days) was conducted, simulating a 4.5-month dry period. The model then underwent three seasonal climate scenarios, each lasting seven months in prototype scale:

1. Winter 1: Alternating weekly rainfall and dry periods, followed by a five-month dry summer.
2. Winter 2: Two weeks of rainfall, one week dry, followed by five-month summer.
3. Winter 3: Three weeks of rainfall, one week dry, repeated until the end of the phase.

Flooding and Drawdown Phase.

The M-T6r test experienced challenges due to a persistent leak, requiring adjustments to the flooding procedure.

- Flood 1: Took 60 minutes to reach the slope (below the crest), with drawdown lasting 14 minutes. Despite reducing to 20g, the leak persisted.
- Flood 2: Water reached mid-slope, requiring a pause before additional water was added at 1g. The test was then spun back to 70g.
- Floods 3 & 4: Conducted at 1g, followed by spinning to 70g for 11 minutes before drawdown, which lasted 13 minutes.

Rainfall Intensity

Throughout the rainfall experiments, a consistent intensity of 1.14 mm/h (prototype scale) was maintained. The precipitation sequences were manually regulated at predetermined intervals to ensure precise control over the experimental conditions.

CHAPTER 7

Centrifuge results of the slope models.

7.1 Introduction

This chapter provides the results obtained from a series of experiments on slope stability conducted on sandy clay models. The experiments were conducted at 70g, with a specific focus on understanding the behaviour and characteristics associated with slope failure within a controlled environment. The main aim of these tests was to evaluate the key conditions that contribute to slope instability and to assess the impact of different factors on the stability of slopes composed of sandy clay.

The centrifuge slope experiments can be generally divided into preliminary tests (Tests M-T1 to M-T3) and multi-stage tests (M-T4 to M-T6r), each based on different applied boundary conditions, to comprehensively assess their individual effects on slope stability. Unless specified otherwise, all distances and timings discussed in this chapter related to the centrifuge test results are presented at a model scale.

7.2 Test M-T3

In the M-T3 test, a consolidated soil block (under a horizontal ground condition) was employed to study the pore pressure response and stability behaviour under controlled flooding conditions. This test aimed to capture essential data on the pore water pressure (PWP) evolution within the soil block during flooding events and to investigate the effects of different drainage configurations on pore pressure dissipation and overall stability.

The M-T3 test was conducted using two distinct configurations:

First configuration: -

In the first configuration, the soil block was subjected to flooding without drainage adjustments. The model was filled with water up to 75 mm above the soil surface, as depicted in Figure 7-2. The centrifuge was then spun to 70 g to replicate increased gravitational forces. This high-gravity environment allowed for an accelerated observation of the soil behaviour,

enabling insights into how rapid inundation might affect internal pore pressures and structural integrity within a short period.

The challenges encountered with PIV analysis due to the reflection in the Perspex window indicated that this setup required adjustment. These reflections created image distortions that affected PIV accuracy within certain regions, particularly near the edges. Despite the challenges, PIV data was able to be obtained during the flooding phase. To maintain data integrity, all reference points in these reflective zones were excluded from the analysis. The PIV results, as shown in

Figure 7-1, present four key aspects of displacement and strain distribution in the model. The PIV analysis reveals that during flooding, the slope experiences uniform downward displacement, primarily indicating settlement (a). The highest displacements are observed in the upper portion of the slope (b), likely due to increased pore pressure and soil softening. Shear strain remains low and evenly distributed across the model, with values below 0.2%, suggesting minimal internal deformation (c). Volumetric strain shows slight compression with alternating zones of expansion and contraction, potentially due to local variations in soil structure and drainage conditions (d). Overall, the slope remains stable with no significant deformation.

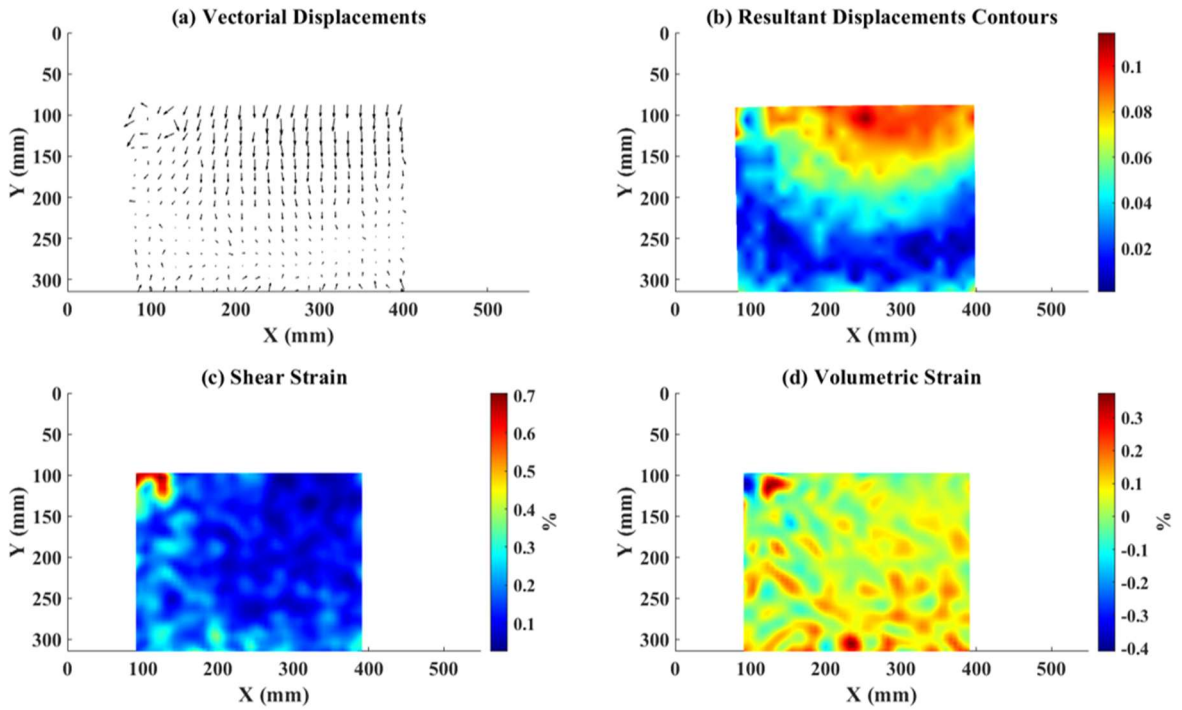


Figure 7-1 PIV Analysis of Displacement and Strain Distributions During Flooding Phase in the M-T3 test.

Despite this limitation, the level-ground M-T3 test contributes valuable data on the internal behaviour of consolidated soil blocks under extreme hydrological conditions, providing a foundation for understanding the mechanical responses of slopes and soil structures subjected to repeated flooding events.

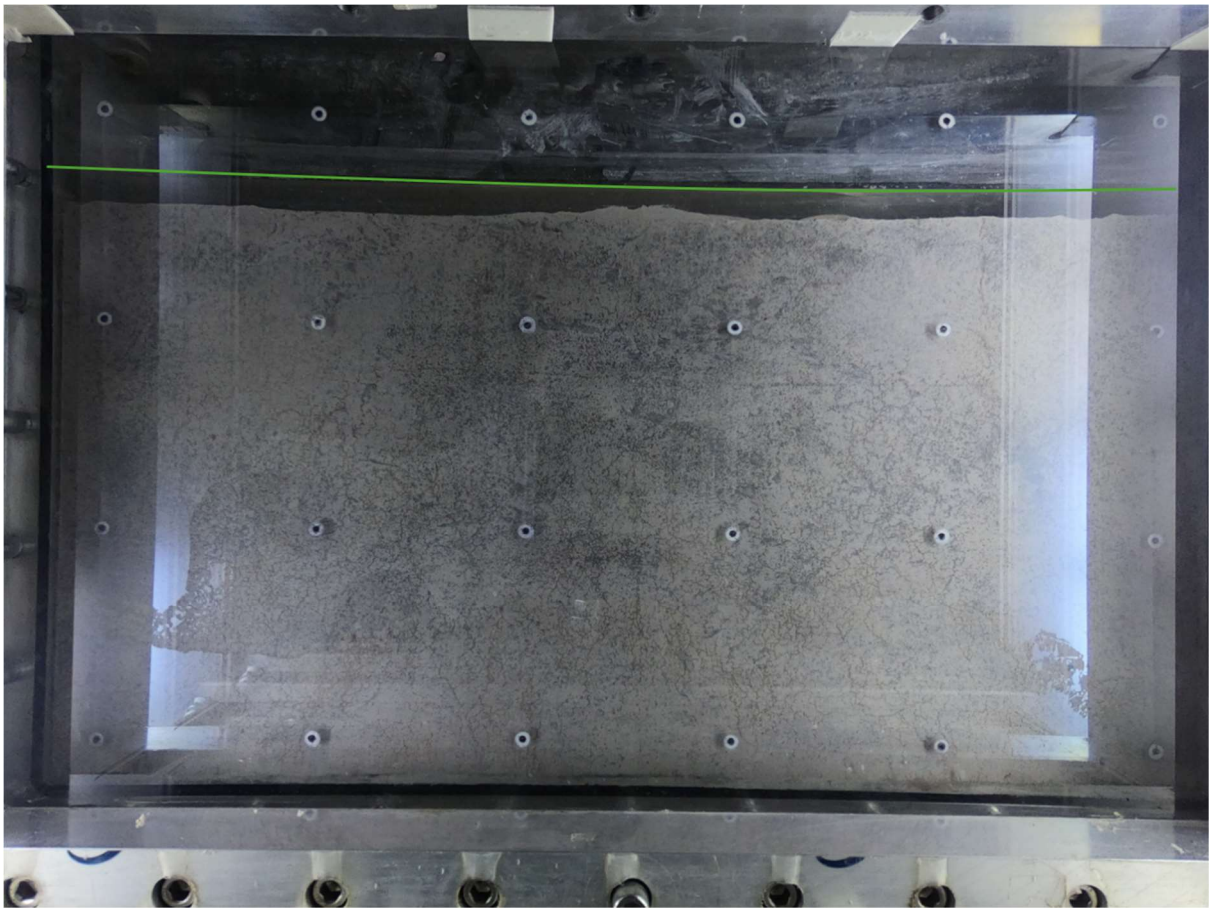


Figure 7-2 Soil model with flood water level indicated in test M-T3.

Pore Water Pressure Analysis during First Configuration of M-T3 Test.

In the first configuration of the M-T3 test, pore water pressure (PWP) data was recorded using multiple PPT sensors positioned throughout the soil model to capture the response to flooding conditions. The positions of these sensors are shown in Figure 7-3. Table 7-1 presents the locations of the PPTs in the M-T3 slope model.

Table 7-1PPTs coordinate in model scale for M-T3 test

PPT No.	X Coordinate (mm)	Y Coordinate (mm)
PPT1	300	275
PPT2	300	250
PPT3	300	225
PPT4	300	175
PPT5	300	100
PPT6	300	25
PPT7	450	275
PPT8	450	250
PPT9	450	225
PPT10	450	175
PPT11	450	100
PPT12	450	25

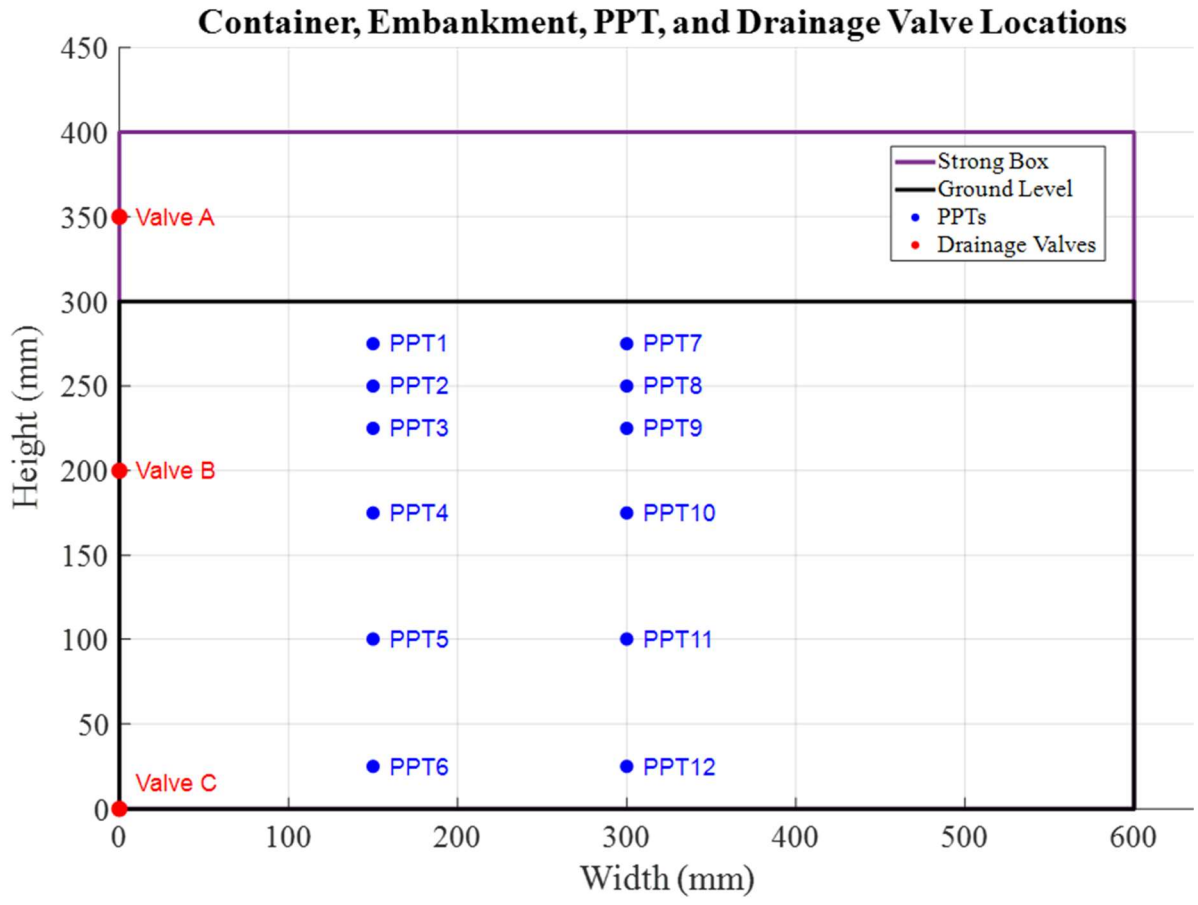


Figure 7-3Drainage valves and PPT (Pore Pressure Transducer) Locations for M-T3a Test.

The flooding event was initially created at 1 g, and then the centrifuge acceleration was increased to 70 g. As the g-level increased, the pore pressures rose significantly and eventually stabilised as the soil reached a pseudo-equilibrium state under the higher gravitational force. This stabilisation indicates the model's adaptation to both the flooding conditions and the increased g-level. The data obtained from only the upper level of PPTs in the two vertical arrays that had good saturation throughout the testing phase, while some PPTs were removed due to poor response as presented in Figure 7-4. The remaining sensors exhibited consistent readings, allowing for an accurate analysis of the PWP response. The two arrays should, in theory, have had the same result for sensors placed at the same height (e.g. PPT1 & PPT7; PPT2 & PPT8, etc.) but there was typically a 5-15 kPa difference between them (representing up to 30% difference for the lowest PWPs but more typically around 10% at 70g). Given that there is no systematic difference, this suggests that either there were slight positioning differences when being placed or the PWP offsets of the PPTs were not accurate. This has ramifications for PPTs placed shallow in the slopes in particular.

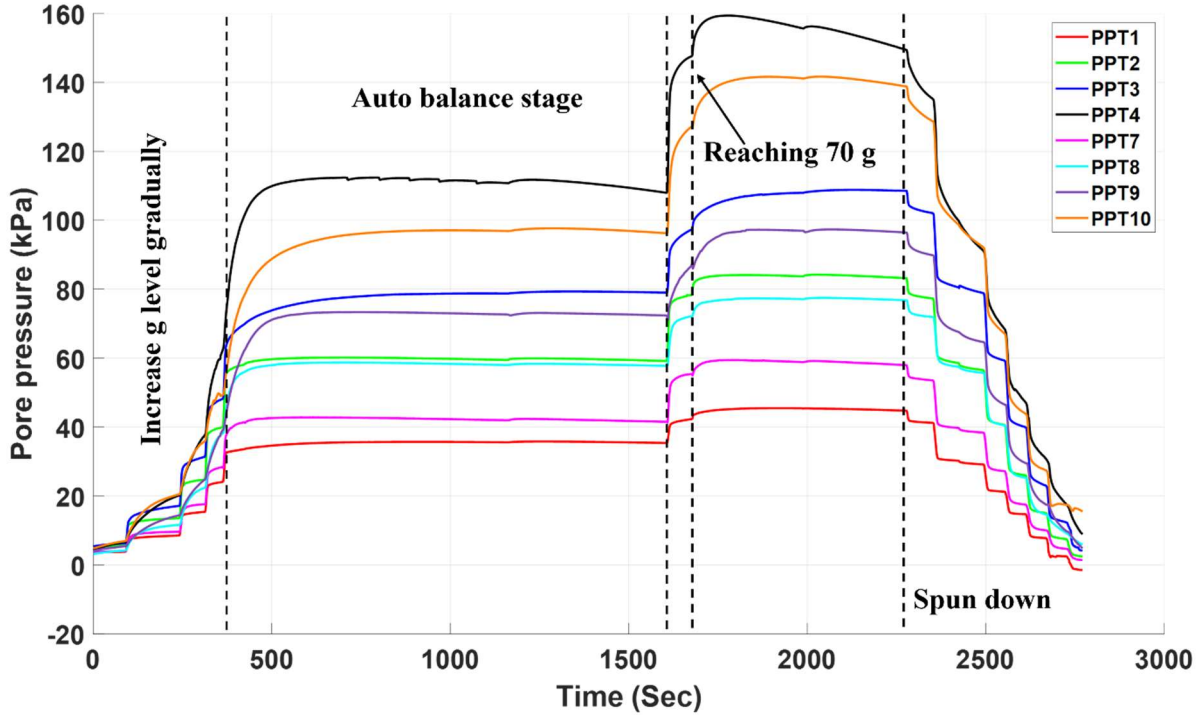


Figure 7-4 Pore water pressure response over time during flooding phase in M-T3 test (first configuration).

Second configuration

In the second configuration of the M-T3 test, the procedure involved initially filling the model with water until the water level reached approximately 2 cm above the model surface. The model then gradually spun up to reach the auto-balance stage, ensuring stability before further acceleration. Once the auto-balance was achieved, the centrifuge acceleration was increased to the target of 70 g. Once the model reached the desired level of acceleration, the middle valve was opened for a duration of 1200 seconds. This phase allowed partial drainage from the mid-depth of the soil, creating a pathway for water to escape and reducing pore pressures in the upper layers of the model. The purpose of this step was to simulate a controlled, intermediate drainage event, which mimics situations such as partial slope dewatering.

After 1200 seconds of mid-level drainage being opened, the lower drainage valve was activated to further reduce the water level. This allowed more complete drainage, facilitating the removal of residual water until no visible water remained on the soil surface.

Pore Water Pressure Analysis during Second Configuration of M-T3 Test.

In the second configuration of the M-T3 test, the model was first flooded at 1 g until the water reached a specified level. Pore water pressure (PWP) data was used to observe the soil response to a controlled flooding scenario, followed by a drainage phase. As shown in Figure 7-5, PWP readings increased sharply at the start of the flood, indicating a rapid buildup of pressure within the soil. The pore pressures rose until reaching a peak, suggesting the soil reached a temporary balance under the applied water level at 70 g. Following this, partial drainage was initiated by opening the mid-level valve for 1250 seconds, which allowed the pore pressures to gradually decrease. Finally, the lower drainage valve was opened, allowing water to drain fully from the soil surface and completing the drawdown phase. Again, some lower PPT sensors have been removed from the data set. The PPTs at the deepest depths showed the greatest change in PWP when the mid drainage was opened, while there was no step change in behaviour when the low drainage was opened, suggesting the drainage was simply cumulative.

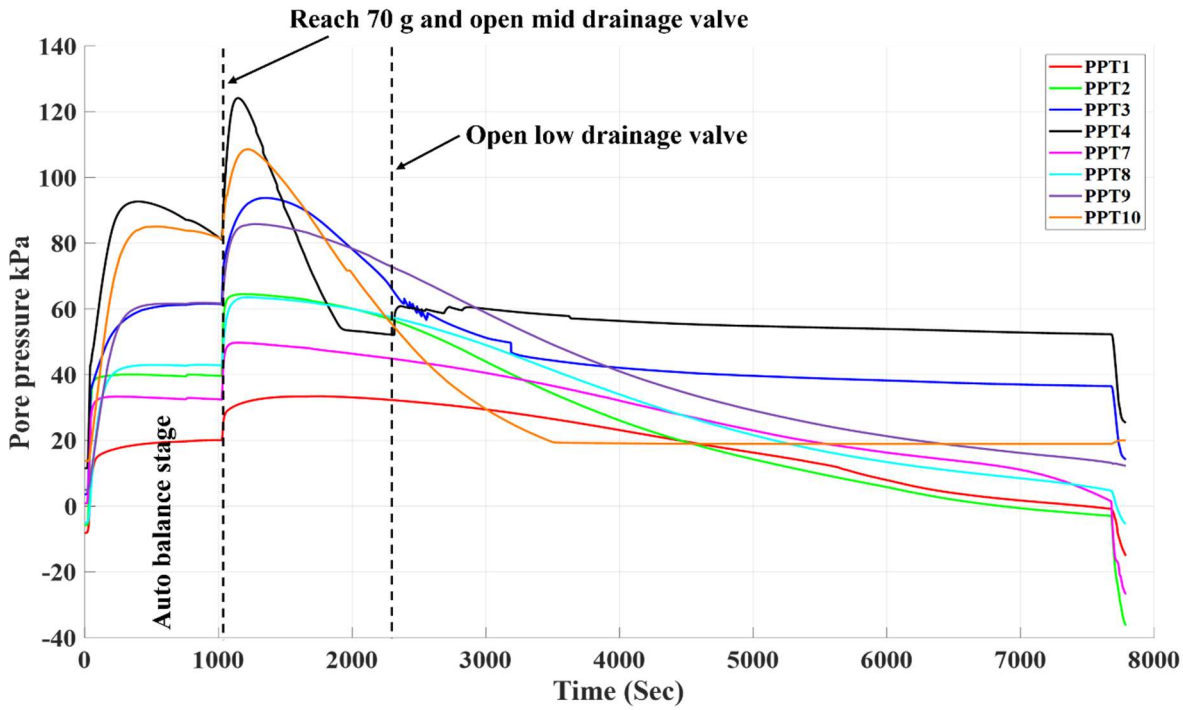


Figure 7-5 Pore water pressure response over time during flooding and sequential drainage phases in M-T3 test (second configuration).

7.3 Test M-T3r.

In the M-T3r test, the soil model was reconstructed by cutting away the soil to simulate a 60-degree slope for further investigation under centrifuge loading. However, during the initial trial spin intended to verify the centrifuge setup and auto-balance configuration, the model failed before the full test sequence could be initiated. This trial was primarily conducted to ensure the correct balance and alignment of the model in preparation for high-speed centrifuge testing, but the slope's stability proved insufficient under the spinning conditions. The early failure showed that the soil was did not have sufficient suction to hold the over steepened slope.

The cracks and fissures on the slope surface, indicating structural weakness in the model under simulated gravitational stress is shown in Figure 7-6. This outcome emphasises the critical importance of preliminary trials to evaluate setup and balance before recording data, as well as the need to refine the model preparation to prevent such failures in future tests.



Figure 7-6 Initial Failure Observed in the M-T3r Trial Test under Centrifuge Loading.

After observing the initial failure in the M-T3r trial test, further testing was conducted by applying continuous rainfall to the soil model, followed by a flooding phase. This approach aimed to evaluate the pore pressure response under simulated prolonged rainfall conditions and subsequent inundation, assessing the model's stability and response to additional water infiltration. As the test progressed, the model experienced further failure, with visible erosion developing along the slope surface, as seen in Figure 7-7. The continuous rainfall and subsequent flooding intensified the failure, highlighting the vulnerability of the model to water-induced weakness and surface erosion.

Figure 7-8 illustrates the pore water pressure (PWP) data collected from multiple PPT sensors during the continuous rainfall and subsequent flooding phase of the M-T3r test. At the beginning of the infiltration phase, most PPT sensors show a slight increase in PWP. The fluctuations in pressure may indicate both issues around desaturation of the PPTs and transient responses as water moves through different layers and the soil adapts to the moisture levels. In

the latter part of the test, the flooding phase was introduced. This caused another noticeable rise in PWP for most sensors, particularly those located deeper in the soil profile.

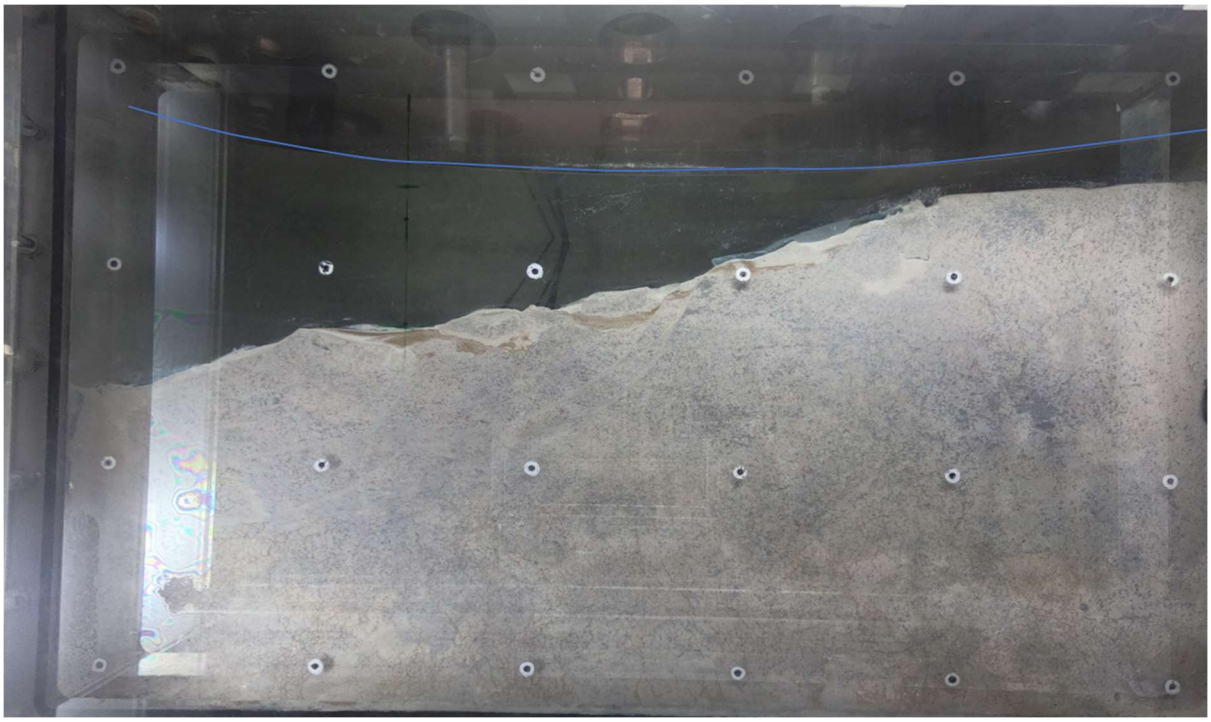


Figure 7-7 Soil model subjected to continuous rainfall and flooding phase M-T3r.

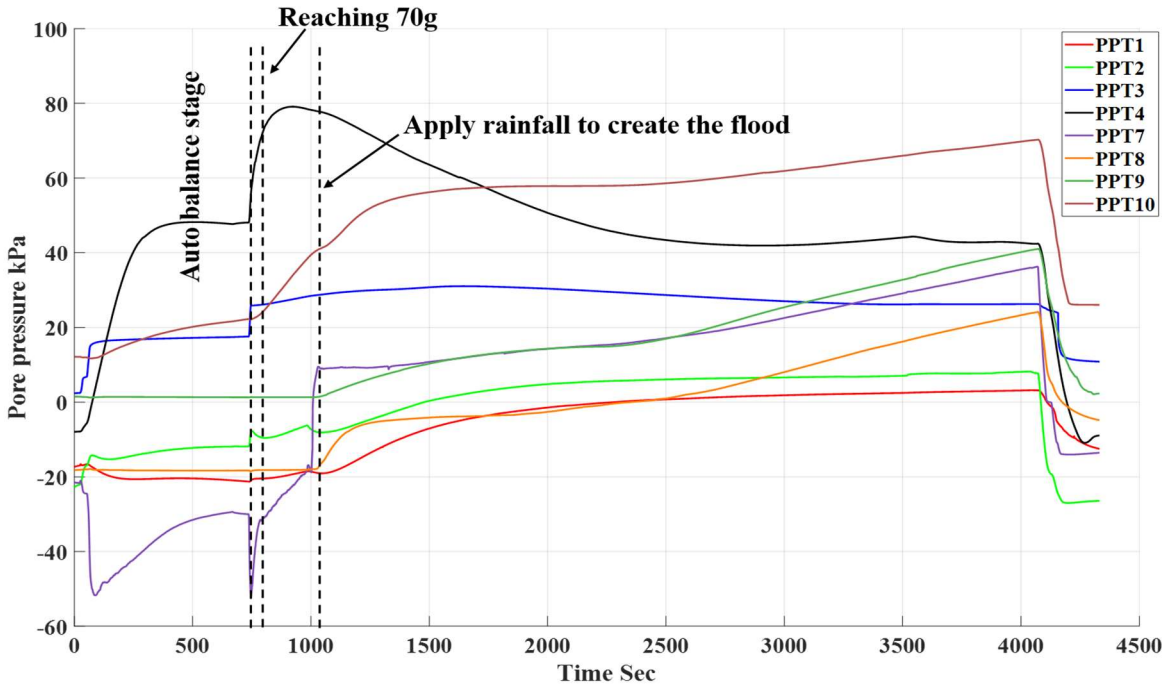


Figure 7-8 Pore water pressure response during continuous rainfall and flooding phase in M-T3r test.

Figure 7-9 illustrates the PIV analysis results during the flood stage, showing minimal soil movement and strain, indicating slope stability under flood conditions. Vectorial displacements (a) and resultant displacement contours (b) reveal no significant movement, suggesting the slope remained structurally intact. Shear strain (c) is low, with minor surface effects near the crest likely due to erosion rather than deep-seated instability. Volumetric strain (d) shows negligible volume change, reinforcing that the flood-induced loading was insufficient to cause significant deformation or shear within the slope.

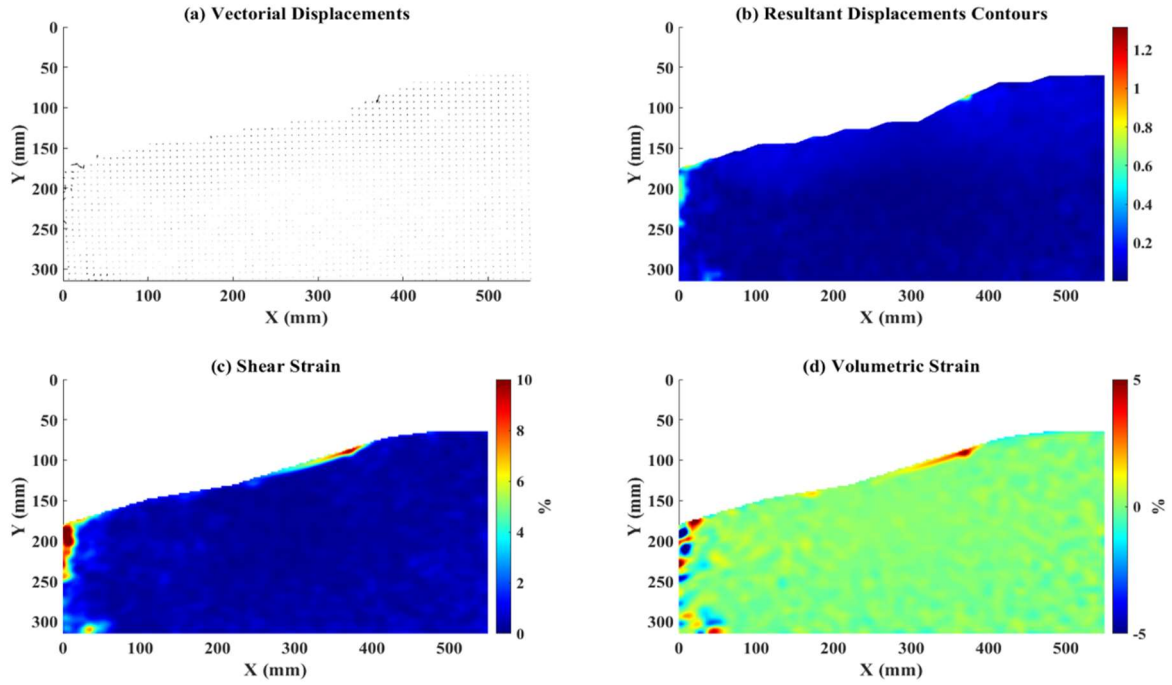


Figure 7-9 PIV analysis during flood phase in M-T3r Test.

7.4 Test M-T4

The M-T4 test was conducted to evaluate the mechanical response and deformation behaviour of a slope model under controlled conditions. The simulation involved the effects of rainfall across two distinct winter scenarios. The first scenario involved one week of rain and one week of dry weather, while the second involved two weeks of rain and one week of dryness. Additionally, two summer seasons were applied after each winter scenario to further assess the model's response to fluctuating moisture conditions. Although the aim of the test was to evaluate the impact of these conditions on pore water pressure, soil displacement, and strain, the model unfortunately experienced significant erosion during the testing phases. As a result, the planned flooding and drawdown phases could not be executed. Despite the challenges encountered, the M-T4 test provides valuable insights into the factors contributing to slope failure under wetting and drying cycles.

In preparation for the M-T4 test, a soil model was constructed with specific dimensions and material properties designed to replicate typical geotechnical conditions. Initially, the slope was designed with a gradient of 1:2 (vertical: horizontal), and the test involved simulating two winters and two summers. During the first winter phase, an issue arose when the drainage valve failed to open at the target centrifuge acceleration of 70 g. Consequently, the floodwaters rose above the middle of the slope but remained below the crest, leading to a situation where there was no opportunity for drawdown. The water was removed after spin down, at an acceleration of 1g. These challenges were addressed in subsequent tests, ensuring a more controlled environment for evaluating the slope response.

The Pore Pressure Transducers (PPTs) were strategically placed throughout the slope model to measure pore water pressure at various critical locations. Table 7-2 presents the locations of the PPTs in the M-T4 slope model. The positions of these PPTs are depicted in Figure 7-10, ensuring comprehensive monitoring of pore pressure distribution across different zones of the embankment. These PPTs play a vital role in providing insights into the internal dynamics of the slope, particularly during varying hydrological and gravitational conditions.

Table 7-2 : PPTs coordinates in model scale.

PPT No.	X Coordinate (mm)	Y Coordinate (mm)
PPT1	261	155
PPT2	309	195
PPT3	366	235
PPT4	481	275
PPT5	538	275
PPT6	366	195
PPT7	481	235
PPT8	538	235
PPT9	366	155
PPT10	481	195
PPT11	366	115

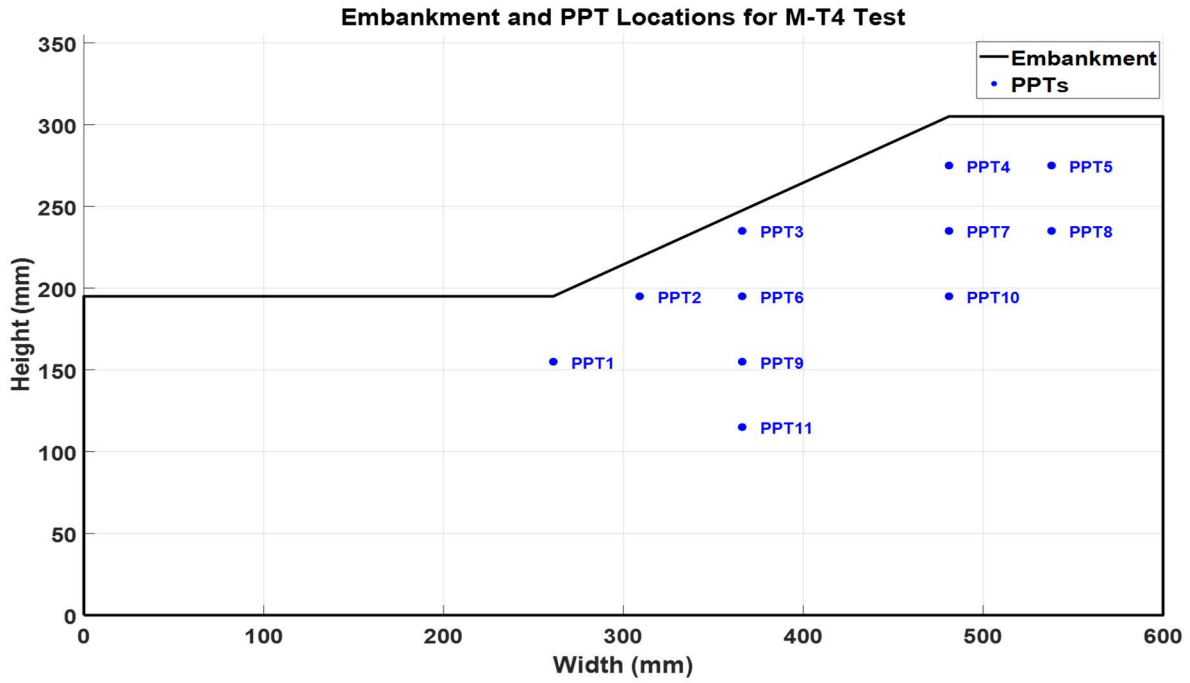


Figure 7-10 Slope dimension and PPTs locations.

7.4.1 Gravity increase effect

The pore water pressure (PWP) data from the PPTs showed irregularities during the consolidation stage of the M-T4 test as shown in Figure 7-11. This was especially true for the

readings from PPT1, PPT2, and PPT3, which are close to the slope's surface. These PPTs demonstrated inconsistencies likely due to insufficient saturation. This issue arose because the PPTs were carried over from a previous test, which may have affected their ability to provide reliable measurements in this configuration. Additionally, due to the lack of a large enough cylinder to contain all 11 PPTs for simultaneous saturation, we could only saturate the sensors in batches, with four PPTs being saturated at a time. This staged saturation approach may have led to incomplete or uneven saturation, especially among the surface PPTs, further contributing to the observed inconsistencies.

Despite these limitations, the deeper PPTs (e.g., PPT6, PPT7, and PPT10) showed more stable and reliable readings, which captured the general trend of pore pressure changes as consolidation progressed. A noticeable increase in PWP signalled the start of the consolidation phase at around 1500 seconds, and it lasted until pore pressures levelled off at around 4000 seconds, indicating its conclusion. While these readings provide valuable insights into the internal pressure response of the slope under applied loads, caution must be taken when interpreting data from the surface layer due to the saturation limitations.

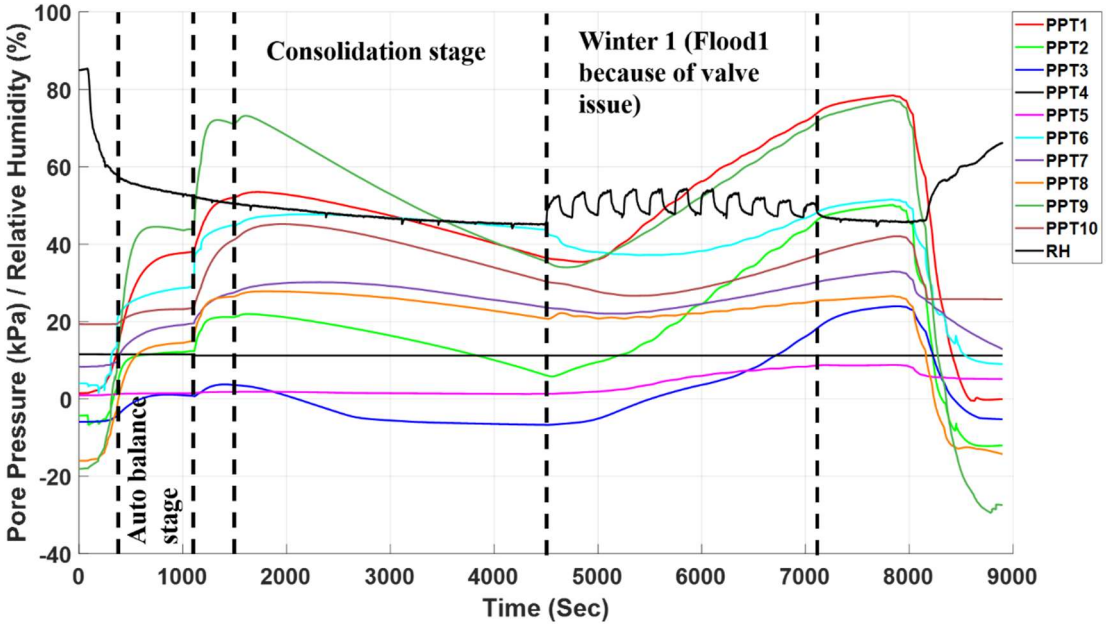


Figure 7-11 Changes in pore water pressure during the consolidation and flood1 stages of the M-T4 test.

Analysis of PWP distribution.

At the end of the auto balance stage in the M-T4 test (Figure 7-12), PWP distribution showed a downward gradient, with higher values near the toe (up to 44 kPa) and lower values towards the crest. The steeper PWP gradient near the toe, indicated by denser contour lines, suggests rapid pressure changes and initial water accumulation in the lower slope due to gravitational effects and drainage pathways. During the consolidation stage in the M-T4 test (Figure 7-13), PWP increased, particularly near the lower slope, reaching up to 70 kPa. The more uniform contour distribution suggests the slope approached a stable pore pressure profile, achieving quasi-equilibrium. A suction zone (-20 kPa) was observed along the surface, transitioning to positive values with depth, indicating balanced pore pressures under sustained gravitational forces.

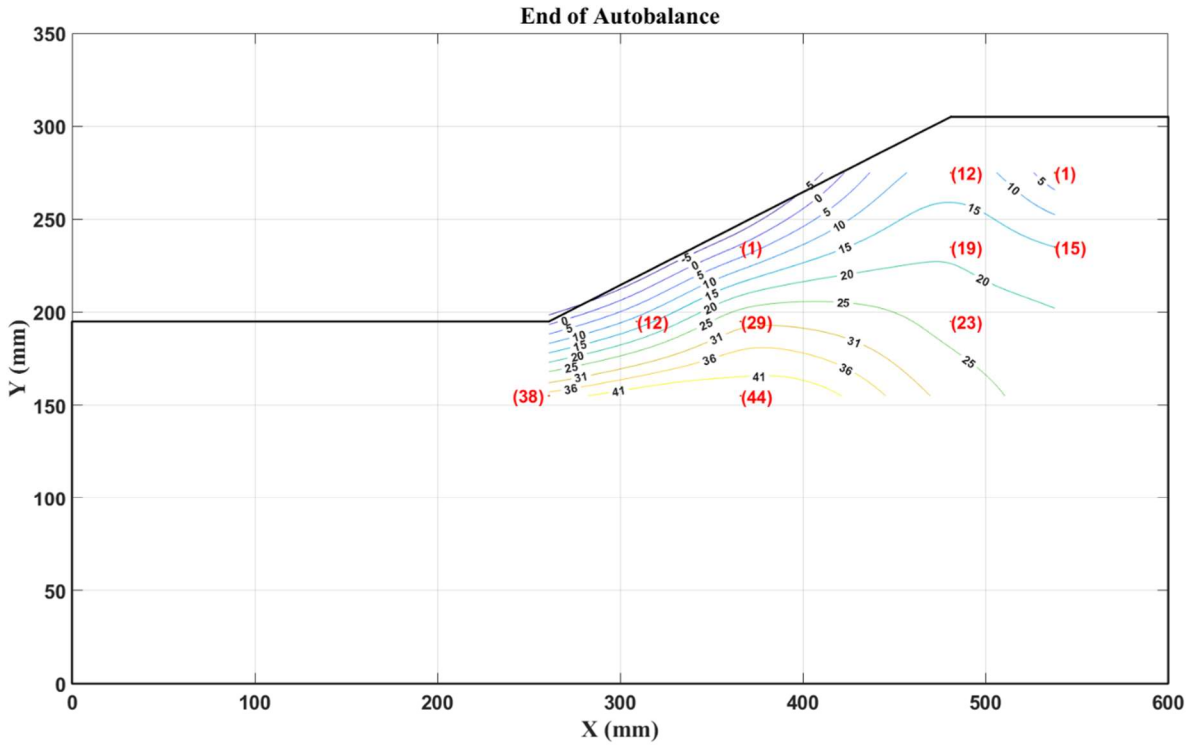


Figure 7-12 Pore water pressure at the end of auto balance.

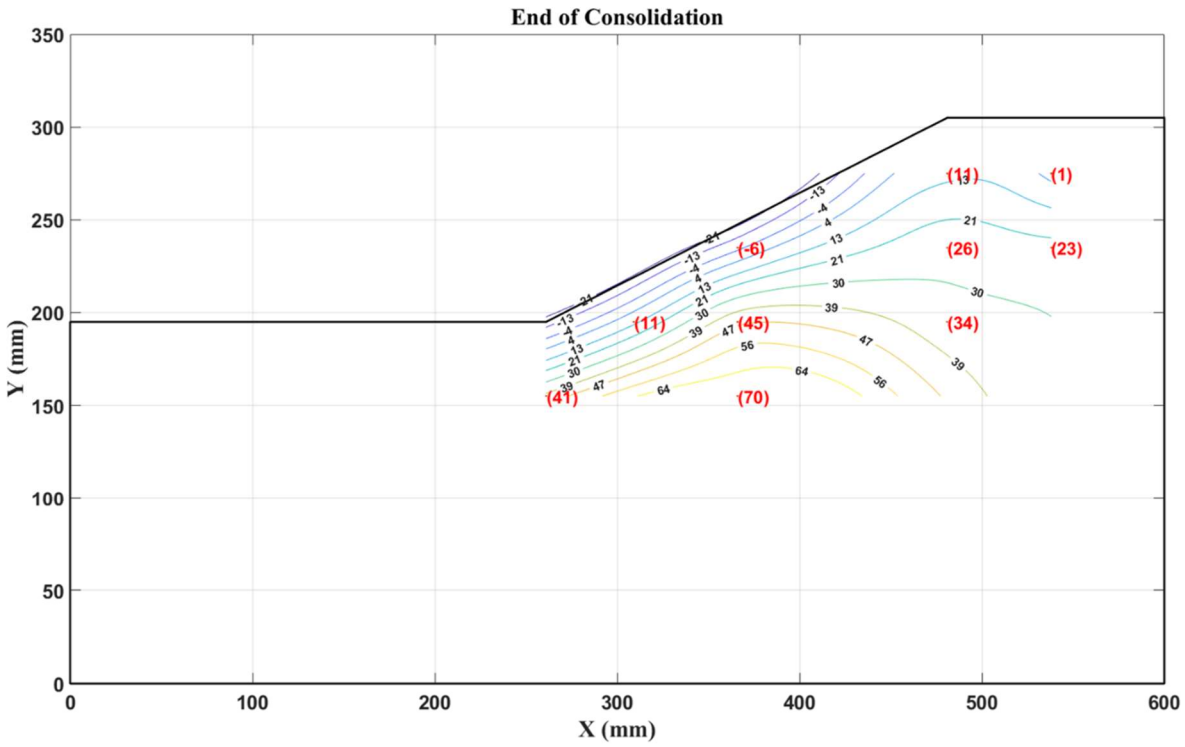


Figure 7-13 Pore water pressure at the end of consolidation.

The data presented in Figure 7-14 and Figure 7-15 corresponds to the second and third spins of the M-T4 test. These spins were conducted the day after the first spin, which encountered an issue during the application of Winter 1. During the first spin, a flood was inadvertently created, reaching above the midpoint of the slope but below the crest surface due to a malfunction with the valve. This issue disrupted the planned climate scenario. After identifying and fixing the valve problem, the test was resumed the following day, aiming to correctly apply the intended climate scenario and proceed with the second and third spins.

1. **<u>Auto-balance stage:</u>**

In both graphs, PWP measurements show initial stabilization, though some PPTs exhibit variability, likely due to sensor calibration differences. Relative humidity (RH) remains stable with minimal environmental changes. While the auto-balance stage aims to establish consistency, variations in some PPTs suggest the need for further assessment of sensor saturation.

2. **Consolidation stage:**

PWP increases across most PPTs, showing gradual loading effects during consolidation. RH stabilises further, indicating steady-state conditions after initial adjustments. The consolidation leads to a redistribution of water in the slope, which aligns with expected behaviour as the slope undergoes compression.

3. **Winter conditions (Winter 1 and Winter 2):**

Winter 1:

PWP fluctuations in multiple PPTs correspond to the 1-week rainfall / 1-week no-rain cycle, simulating winter conditions over 7 months (prototype scale). RH oscillates significantly, reflecting moisture variations during alternating phases. These fluctuations highlight dynamic water infiltration and redistribution, crucial for understanding slope response to repeated wetting-drying events.

Winter 2:

In Winter 2, PWP fluctuations follow the 2-week rainfall / 1-week no-rain cycle, similar to Winter 1 but with a greater water load due to extended rainfall. An irregularity occurred due to the "valve stuck" issue, briefly disrupting infiltration. RH trends remained oscillatory, reflecting alternating moisture conditions. The longer rainfall duration intensified PWP and RH responses, influencing slope water retention and redistribution.

4. **Summer conditions (Summer 1 and Summer 2):**

Summer 1:

PWP levels decrease across most PPTs, reflecting drainage and drying effects as rainfall stops. RH reduces significantly, showing drier conditions consistent with the summer climate.

Summer 2:

In Summer 2, PWP and RH did not decrease significantly as expected, instead maintaining a steady state with only slight declines in some PPTs. This suggests that residual moisture from Winter 2's extended rainfall limited drying, making the summer phase less effective in reducing moisture levels.

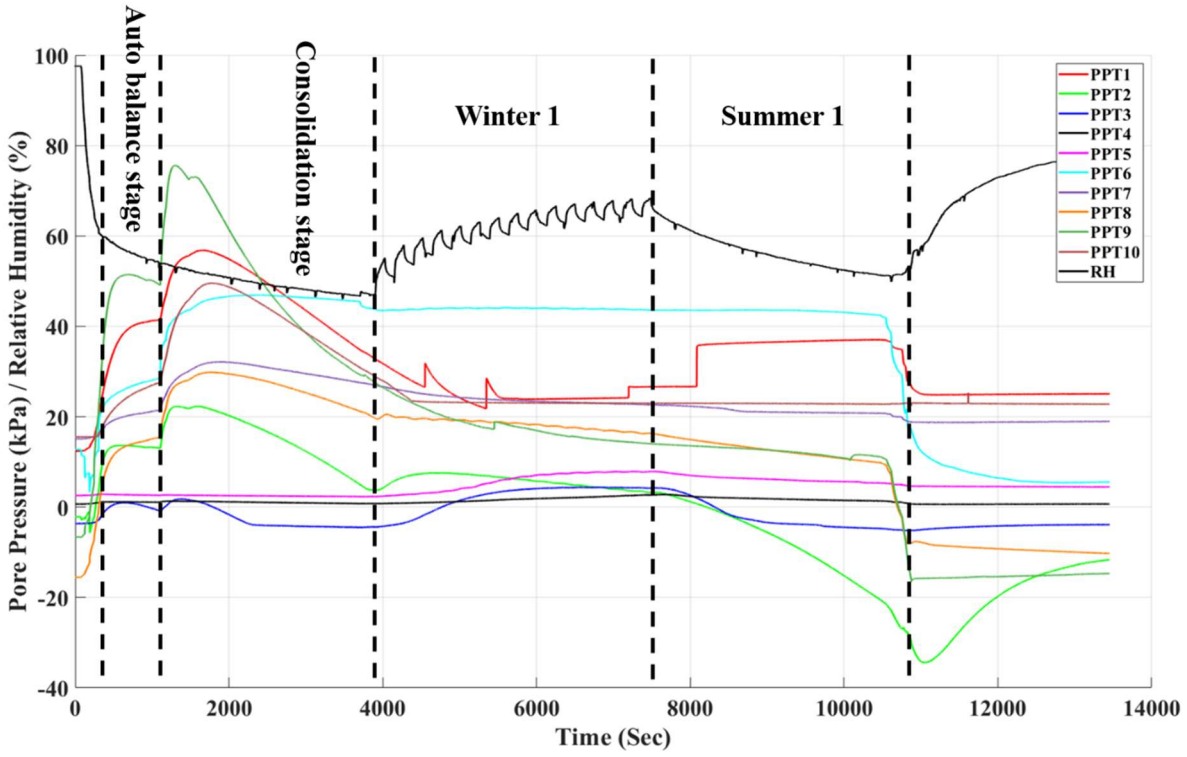


Figure 7-14 Pore water pressure and relative humidity variations during auto-balance, consolidation, winter 1, and summer 1 stages in the M-T4 test.

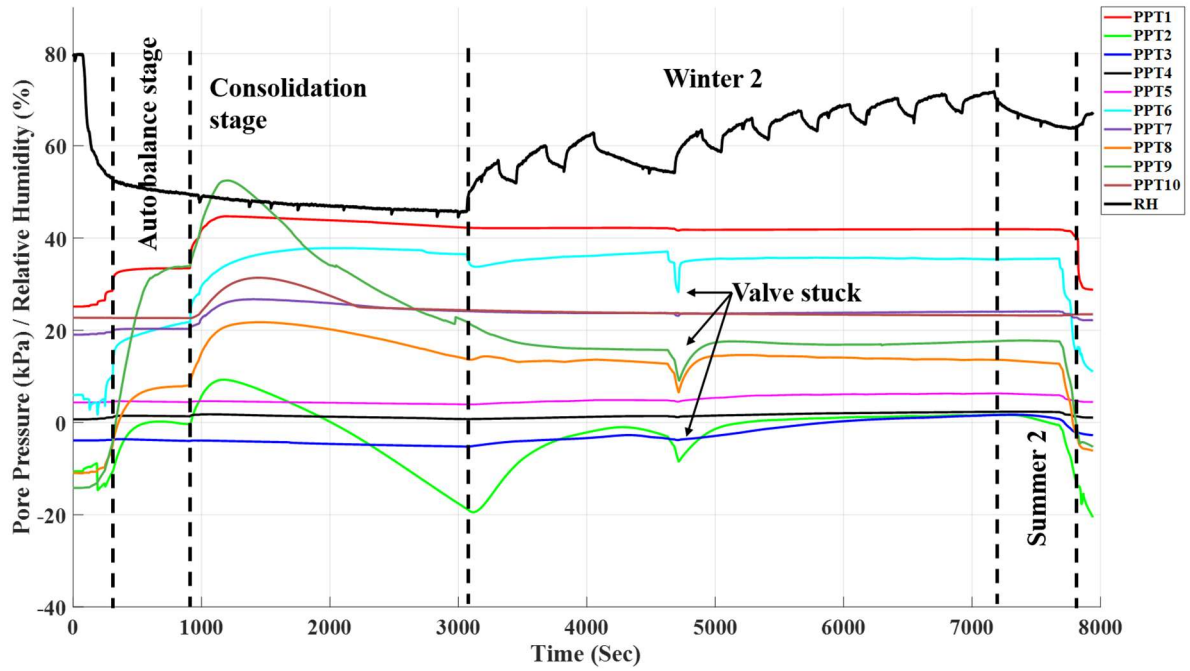


Figure 7-15 Pore water pressure and relative humidity variations during auto-balance, consolidation, winter 2, and summer 2 stages in the M-T4 test.

7.4.2 Test M-T4: Deformations

Auto balance and consolidation stages

The PIV analysis for Test M-T4 (auto balance and consolidation stages) showed negligible displacement and strain, indicating stable slope conditions with no significant deformation or movement. Detailed analysis is provided in Appendix (A.1.1).

Overall behaviour of centrifuge M-T4 test under seasonal cycles

In the M-T4 centrifuge test, progressive erosion and slope degradation were observed, beginning from the end of the first winter and continuing through subsequent seasonal cycles.

1. Winter 1:

After the initial winter cycle, minimal erosion was evident on the slope, primarily confined to the surface layer near the crest (Figure 7-16). This stage was characterised by slight soil displacement, attributed to the repeated wetting and drying cycles.

2. Winter 2:

Following the second winter, which involved an extended rainfall period, the slope exhibited more pronounced erosion as shown in Figure 7-17. The accumulation of water and saturation effects likely weakened the soil structure further, leading to visible slope degradation, especially near the midsection. The soil erosion was more extensive than in Winter 1, indicating an increasing vulnerability of the slope to hydrological changes.

3. Summer 2:

By the end of the second summer cycle, the drying process caused the slope material to contract, consolidating parts of the soil mass but also leaving certain areas more susceptible to erosion. This period accentuated cracks and soil displacements, with continued erosion focusing on lower slope areas as shown in Figure 7-18.

4. End of Test:

At the end of the test, significant erosion had developed, especially in the lower sections of the slope as shown in Figure 7-19, suggesting that the cumulative effects of seasonal cycles

and hydrological forces had destabilised the slope. This final stage of erosion highlighted the impact of prolonged wetting and drying cycles, coupled with gravitational forces, which eventually led to slope instability and failure.

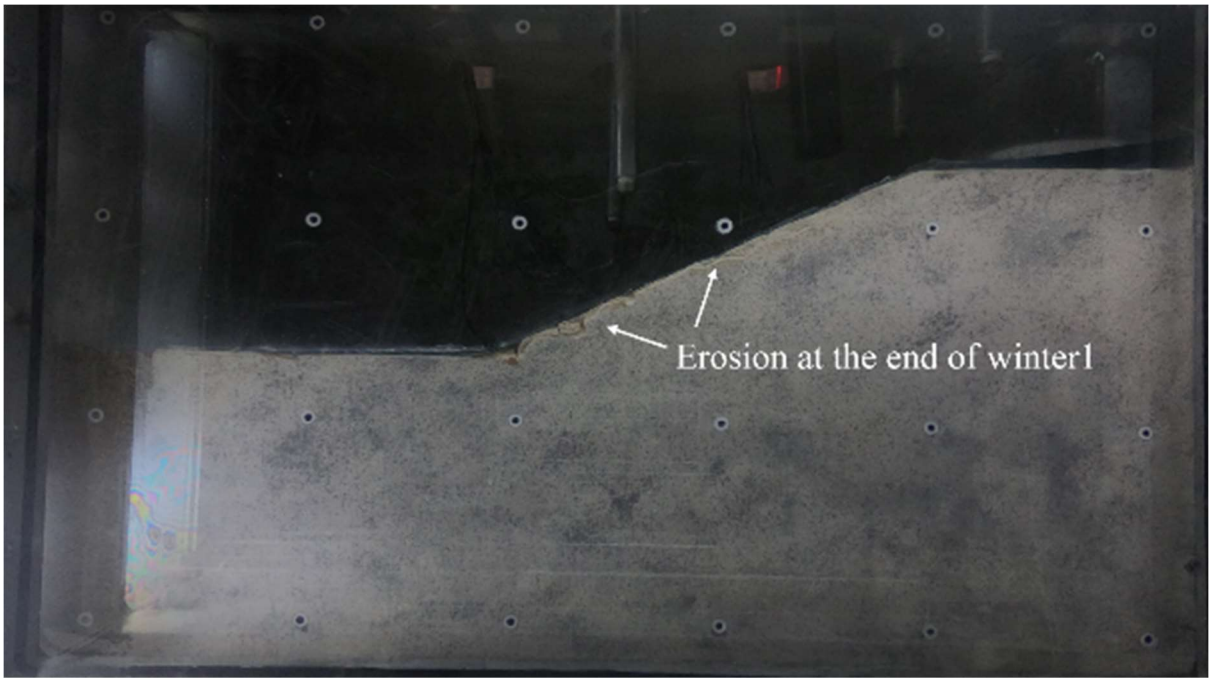


Figure 7-16 Erosion at the end of Winter 1 stage.

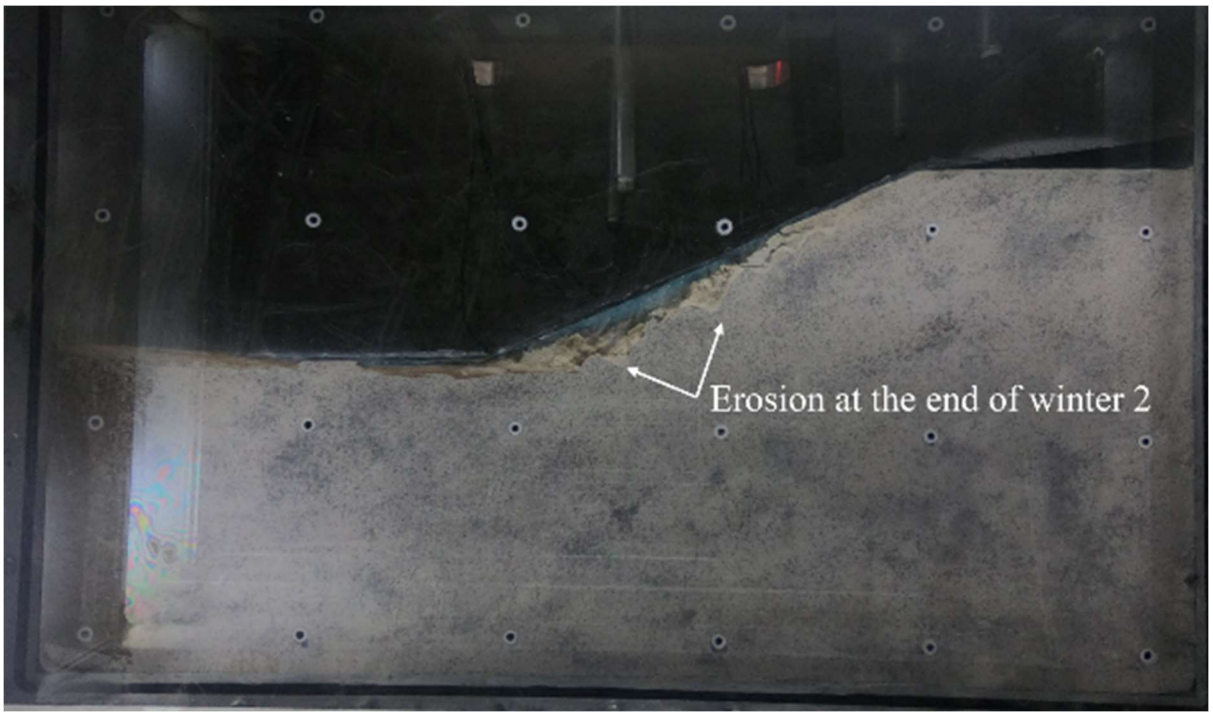


Figure 7-17 Erosion at the end of Winter 2 stage.



Figure 7-18 Erosion at the end of Summer 2 stage.

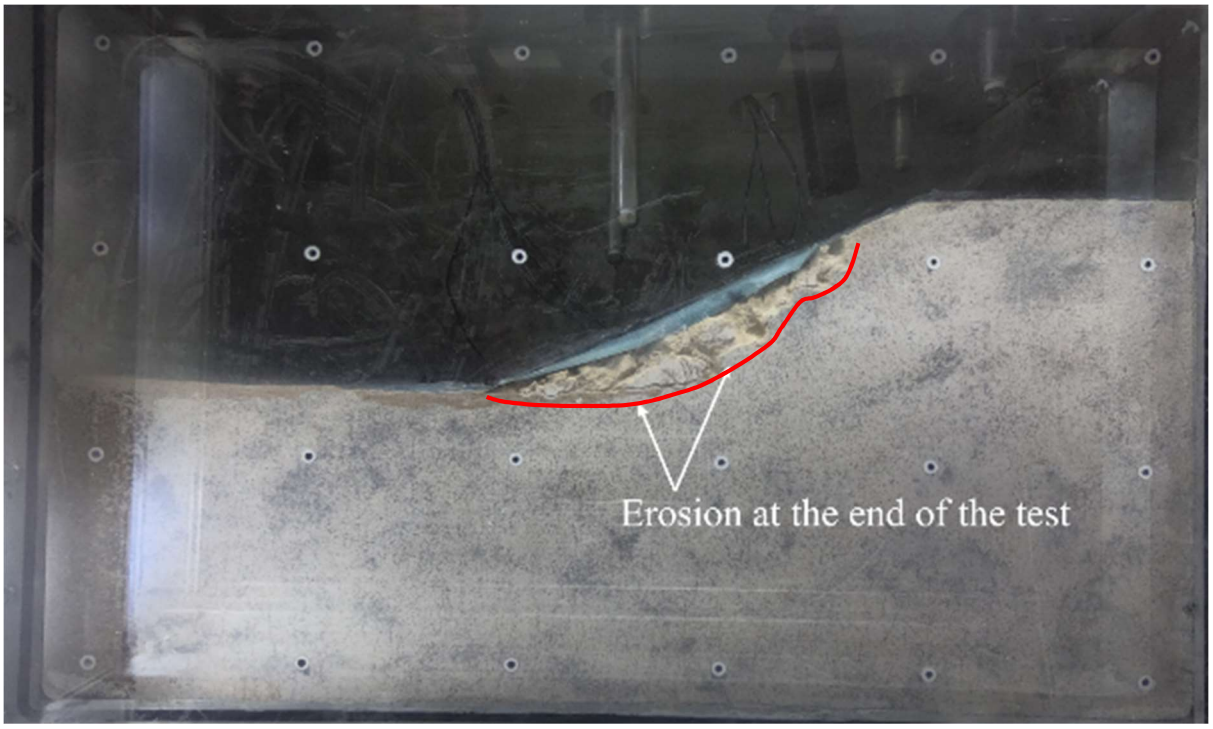


Figure 7-19 Erosion at the end of the test.

7.4.3 Seasonal cycles effect.

Slope movement at the end of first winter / M-T4.

The M-T4 test at the end of Winter 1 showed minimal slope deformation, with slight displacement (up to 3 mm) and minor strain localized mainly near the slope toe. The wetting-drying cycle induced subtle movements potentially related to erosion, but overall, the slope remained stable with negligible internal stresses or significant volumetric changes observed. The PIV data at the end of the first winter cycle is shown in Figure 7-20.

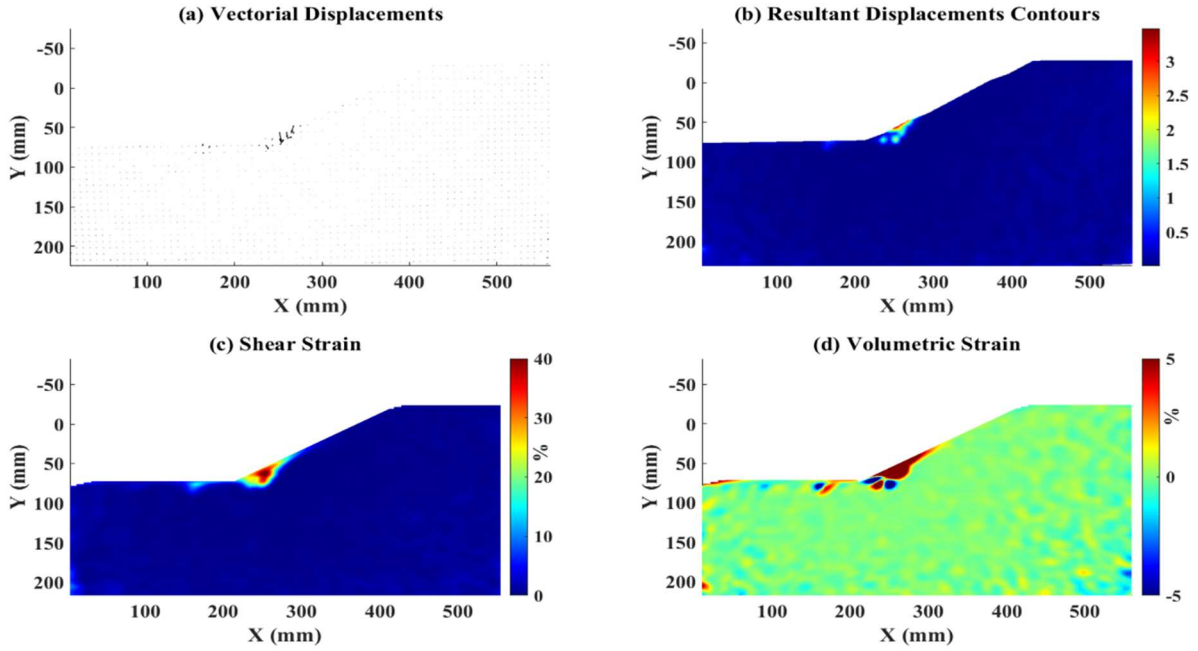


Figure 7-20 Displacements and strain at the end of the first winter (M-T4) test.

Slope movement at the end of Winter 2 / M-T4.

At the end of the second winter in the M-T4 test, the slope remained stable despite localised minor movements (up to 3.5 mm) and concentrated shear strains reaching 60% near the surface and downslope regions. These movements and strains are likely associated with soil erosion and moisture-driven soil expansion/contraction cycles but do not indicate widespread instability. This PIV analysis suggests that while there are localised changes in strain and displacement as depicted in Figure 7-21.

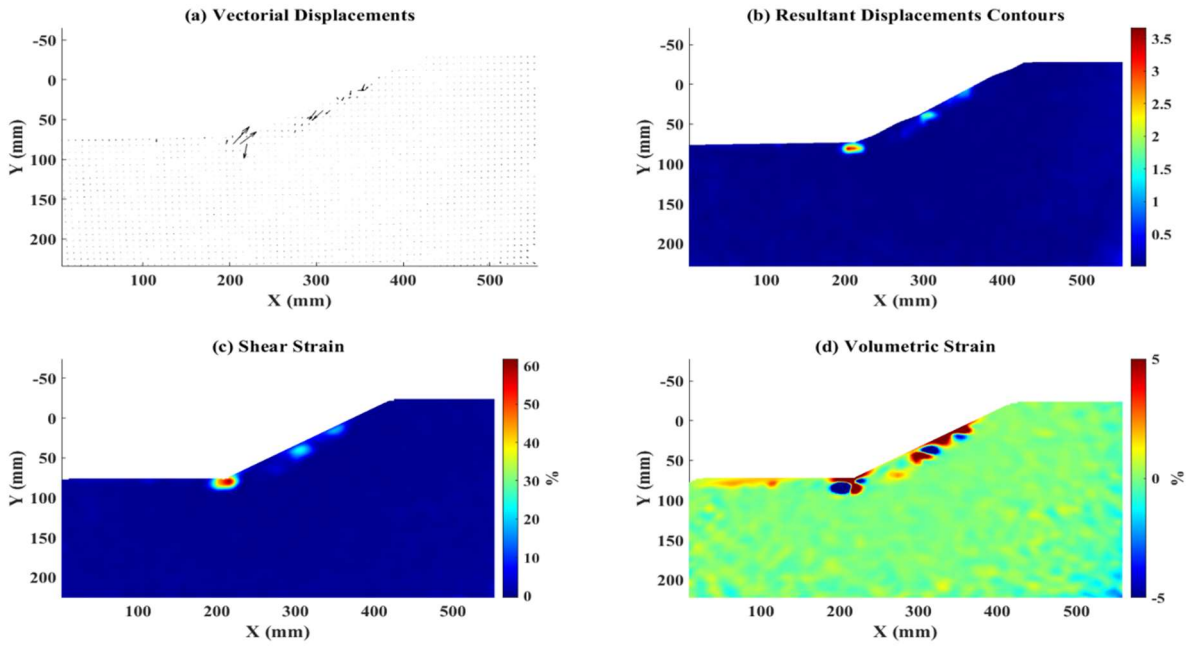


Figure 7-21 Displacements and strain at the end of the second winter (M-T4) test.

7.4.4 Flooding effect M-T4 test.

Slope movement at the end of the flood / M-T4

In the M-T4 test, the first scenario involved an unexpected flooding event, referred to as Flood 1. This occurred due to an issue with the drainage valve, which failed to open at 70 g, causing water to accumulate in the slope model. The blue line in Figure 7-22 shows the water level rising above the midpoint of the slope but remaining below the crest. This initial flooding phase provided critical insights into the slope response to water infiltration without the controlled drawdown initially planned. Following Flood 1, two winter scenarios (alternating rainfall and drying periods) and two summer scenarios (drying conditions) were applied. Over the course of these cycles, significant soil erosion was observed, ultimately leading to the decision to conclude the test. During the transitions between these stages, the centrifuge was swung down to remove excess water, allowing for potential swelling to occur at low effective stress. This swelling, coupled with repetitive wetting and drying cycles, led to surface layer deterioration, highlighting the impact of these cycles on slope stability.

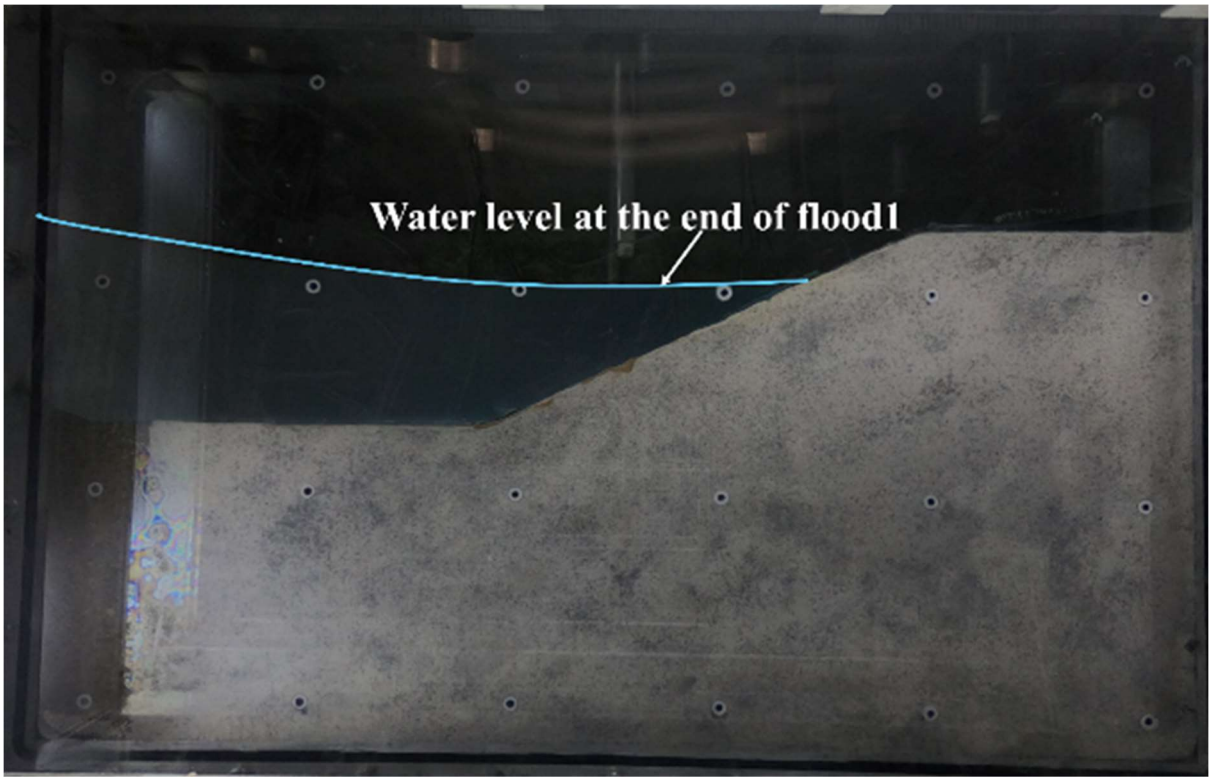


Figure 7-22 Water level at the end of Flood 1 in M-T4 test.

Challenges with PPTs.

To improve pore pressure transducer (PPT) readings which had shifted between centrifuge spins, theoretical hydrostatic pressures were calculated during Flood 1. This adjustment resolved some issues for the PPTs positioned under the water table, allowing more reliable pressure measurements in submerged areas. However, accurately determining the water height for other PPTs, particularly those located under the crest and at the beginning of the slope, remained challenging, possibly due to desaturation of these PPTs. The difficulty in measuring water levels in these areas limited the effectiveness of the correction, leaving some PPTs with inconsistent readings.

Due to the challenges with pore pressure transducer (PPT) saturation and inconsistent readings, it was not feasible to perform a reliable analysis of pore water pressure during the winter and summer cycles. Specifically, the issues in accurately measuring water heights above certain PPTs, along with the partial effectiveness of the hydrostatic pressure correction, compromised the data integrity for these periods.

As a result, the pore water pressure analysis for Winter 1, Winter 2, Summer 1, and Summer 2 cycles are omitted. This limitation underscores the need for improved PPT calibration and saturation procedures to ensure consistent reading, particularly in critical slope regions.

Pore Water Pressure at the end of Flood 1

At the end of Flood 1, the pore water pressure (PWP) distribution, adjusted by applying offsets to specific PPTs submerged underwater, is shown in Figure 7-23. The adjustment process follows the hydrostatic calibration method outlined in Section [7.1.9] for the M-T5 test, where offsets were applied to correct for discrepancies between measured and expected hydrostatic pressures. The pore water pressure (PWP) distribution shows a clear gradient along the slope: high PWP at the lower elevations near the slope toe (PPT1, PPT9, PPT10), moderate PWP with gradual gradients in the mid-slope area, and significantly lower PWP values near the slope crest (PPT4 and PPT5). This pattern directly corresponds with the observed water levels and indicates decreasing pore water pressures with increasing elevation.

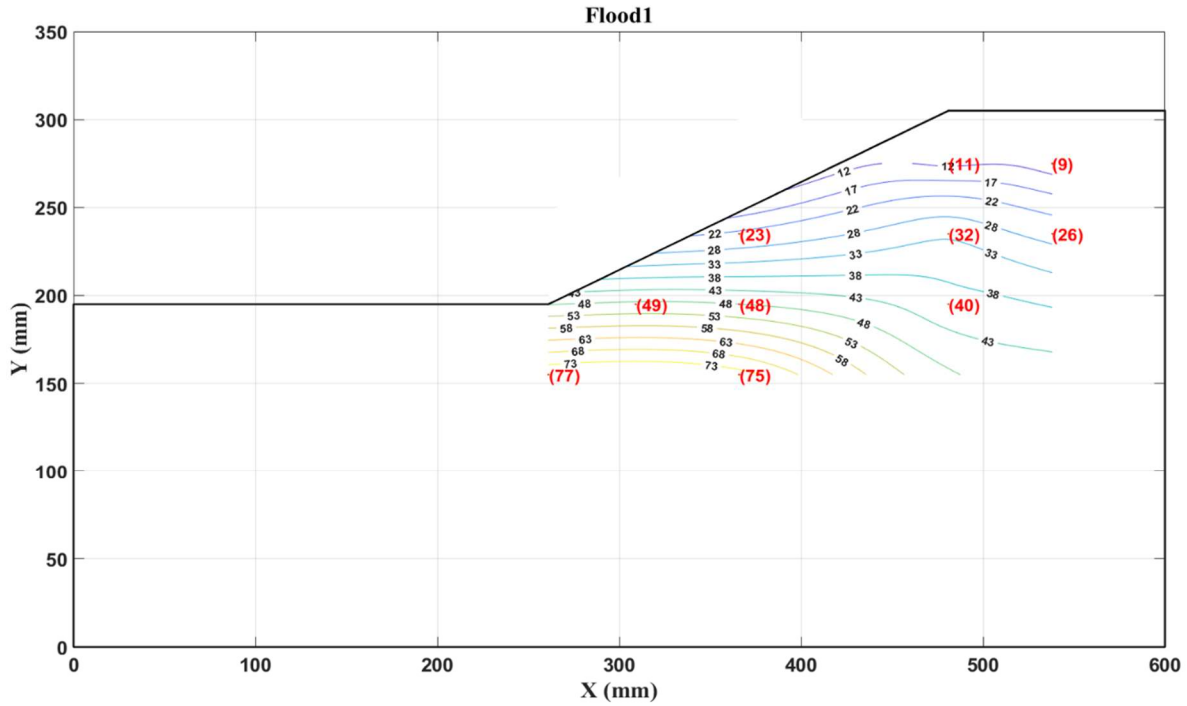


Figure 7-23 Pore water pressure during flood1.

Slope failure in the M-T4 centrifuge test.

Figure 7-24 and Figure 7-25 illustrate the aftermath of a slope failure following the M-T4 centrifuge test. Significant deformation and erosion patterns are evident, indicating the slope's response to the applied loading and environmental conditions during the test. A distinct failure plane is observed along the mid-section of the slope, indicating significant deformation likely caused by shear stresses. Surface erosion is prominent, characterised by the removal of finer particles (kaolin), which can be attributed to water flow and seepage pressures acting on the slope during the test. Although the nozzle was carefully calibrated to ensure even water distribution, the use of blue tissue instead of proper filter paper may have influenced the infiltration process, potentially altering the interaction between rainfall and the slope surface. This could have contributed to localised erosion and increased susceptibility to instability.

The depth of the failure zone is approximately 5 cm, which correlates to significant deformation within the model. The cracks and crevices extend laterally, with lengths exceeding 10 cm, suggesting progressive failure. Secondary cracks are visible along the upper portion of the slope, indicating tensile stresses likely caused by a combination of drawdown and lateral seepage pressures. These cracks are irregular in shape and depth, with some extending towards the slope's crest. The sand-kaolin mixture used in the model appears to have undergone a combination of shear failure and piping erosion, as evidenced by the undermining near the base and the bulging of material in the lower slope regions. This soil mixture is gap-graded, as identified in Chapter 4, which may have contributed to the erosion observed.



Figure 7-24 Post-test slope failure in M-T4 centrifuge experiment.



Figure 7-25 View of slope failure and erosion features.

7.5 Test M-T5

The Pore Pressure Transducers (PPTs) were strategically placed within the slope to monitor the pore water pressure at various locations. Table 7-3 shows the locations of the Pore Pressure Transducers (PPTs) specified in the slope model for the test M-T5. The PPTs were positioned as shown in Figure 7-26.

Table 7-3: PPTs coordinates in model scale.

PPT No.	X Coordinate (mm)	Y Coordinate (mm)
PPT1	261	155
PPT2	288	195
PPT3	343	235
PPT4	426	275
PPT5	508	275
PPT6	343	195
PPT7	426	235
PPT8	508	235
PPT9	344	155
PPT10	426	195
PPT11	343	115

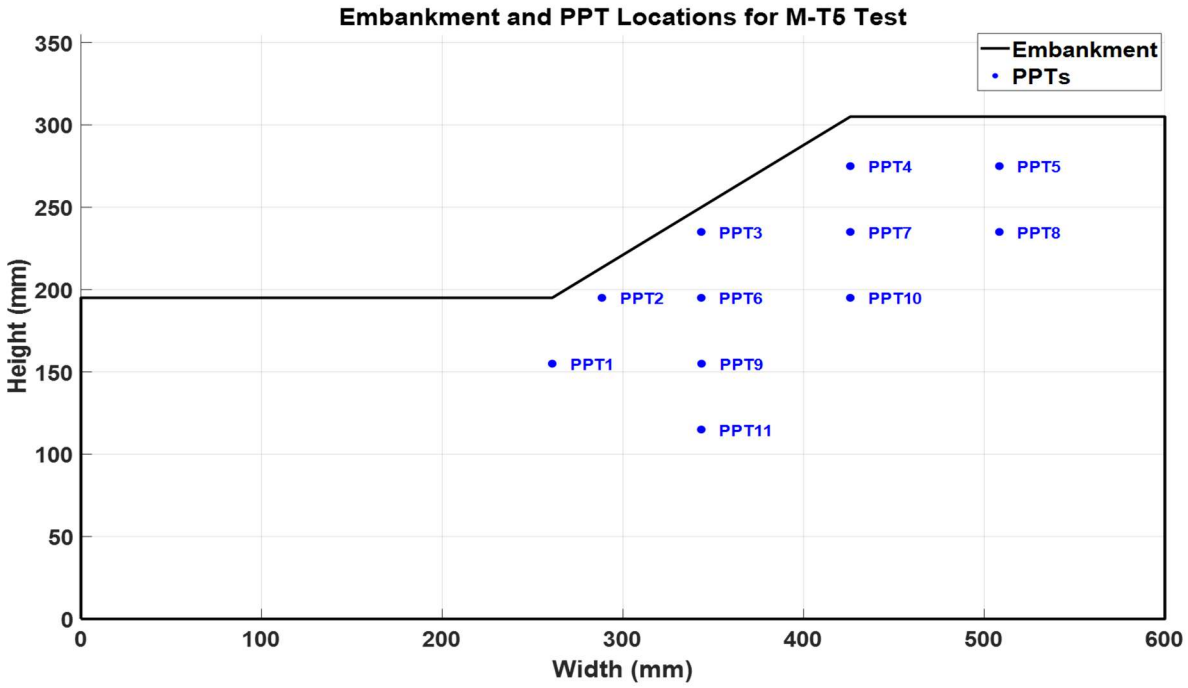


Figure 7-26 Slope dimension and PPTs locations.

7.5.1 Hydrostatic calibration during flood stage in M-T5 centrifuge test.

During the flood stage of the M-T5 centrifuge test, hydrostatic calibration was done to make sure that the pore water pressure (PWP) measurements from the pore pressure transducers (PPTs) were accurate. Images from a GoPro camera was used to capture the flood stage within the model as shown in Figure 7-27. The images were subsequently imported into AutoCAD to precisely measure the water level and various elevations within the embankment.

The calibration process involved careful measurement and calculation of the pore water pressures (PWPs) across various positions within the slope model using pore pressure transducers (PPTs). To achieve this, the locations of each PPT were determined relative to the model geometry, with their vertical positions (Y model) and radial distances (Ri) from the centrifuge center precisely measured. Additionally, the vertical distance from each PPT to the water surface (Zi) during the flood stage was recorded. Using these measurements, the hydrostatic pore water pressures (u_{fl}) were calculated based on the centrifuge rotational acceleration and the specific geometry of the model.

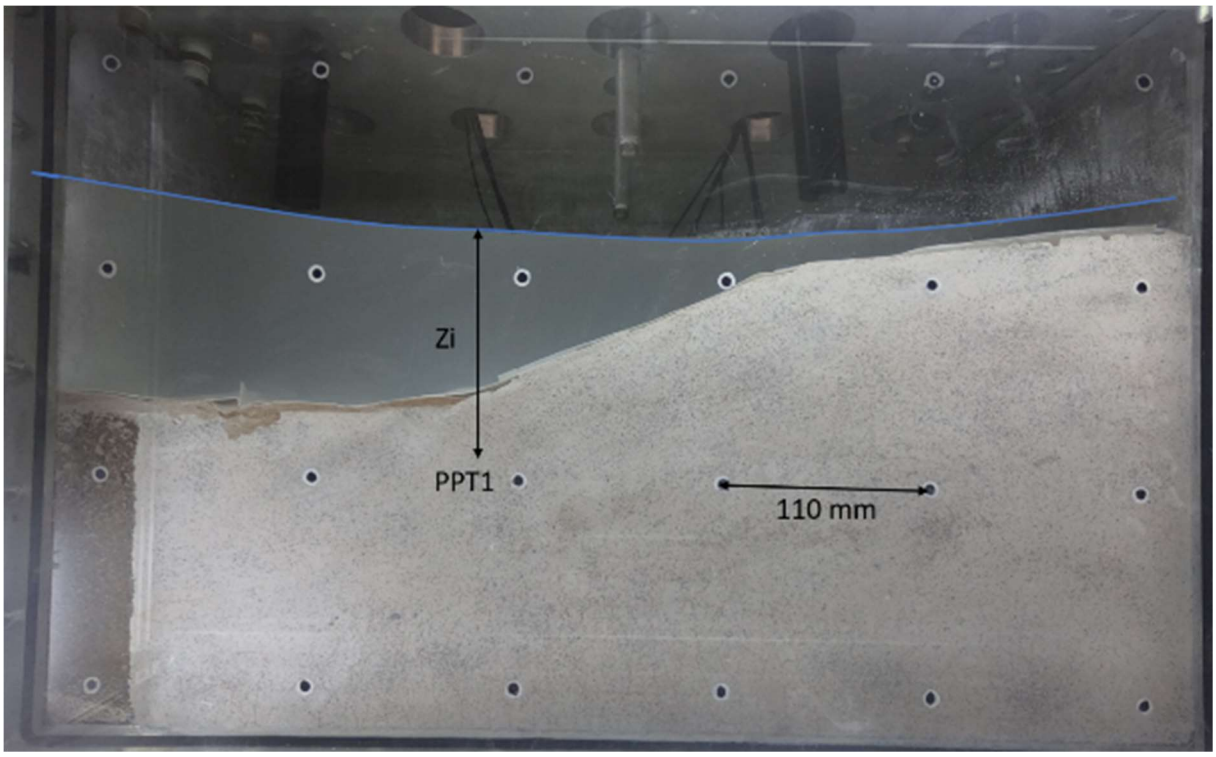


Figure 7-27 Soil slope model with hydrostatic calibration during flood (M-T5 test).

Equation *7-1* was employed to estimate the expected PWPs under hydrostatic flood conditions including curvature, (Schofield, 1980).

$$u_{fl} = \rho_w \times \omega^2/2 \times (2Ri^2 - Zi^2) \qquad 7\text{-}1$$

where ρ_w is the water density, and ω is the angular velocity of the centrifuge.

The directly measured PWPs from the test were then compared to these calculated values. To account for any discrepancies and enhance accuracy, offset values were applied to the measured data. The difference between the recalibrated and initially adjusted PWPs was also computed to highlight any necessary corrections. This calibration process was crucial in verifying the reliability of the pore pressure data collected during the test. By ensuring that the measured pressures align with the expected hydrostatic conditions, the calibration validates the accuracy of the experimental setup and the resulting data. This thorough calibration allows for a more precise interpretation of the soil behaviour and water pressure dynamics within the slope model under the flood conditions simulated in the M-T5 test. The calibration table provides detailed measurements and calculations at various points within the slope model, as summarised in Table 7-4 below:

Table 7-4 : Hydrostatic pressure calibration during flood 3 in the M-T5 test.

PPT	P1	P2	P3	P4	P5	P6	P7	P8	P9	P10	P11
Location (Y)model (m)	0.155	0.195	0.235	0.275	0.275	0.195	0.235	0.235	0.155	0.195	0.115
Ri (from Fug.center to PPT) (m)	1.795	1.755	1.715	1.675	1.675	1.755	1.715	1.715	1.795	1.755	1.835
Zi (from PPT to water surface) (Ht)	0.166	0.125	0.083	0.045	0.050	0.123	0.085	0.090	0.163	0.125	0.203
u _flood	105.554	78.379	51.803	27.426	30.647	77.573	52.602	55.823	103.938	78.372	130.896
PWP(measured) from the test	79.853	63.009	47.174	28.613	19.576	79.108	43.398	45.340	82.374	84.879	103.179
Offset	25.701	15.370	4.629	-1.187	11.071	-1.535	9.204	10.483	21.564	-6.507	27.717

7.5.2 Gravity increase effect

Tensiometers (PPT), which were described in Section 5.1.10, are used as instruments to measure positive and negative pore water pressures in the soil of slopes during a centrifuge

test. Tensiometers are strategically positioned within the soil model in order to observe and record changes in pore water pressures (PWP) as the slope experiences simulated gravity loading. During the acceleration to 70g, at the University of Sheffield, 10g increments in effective g-level are made to 50g, where the centrifuge undergoes an auto-balance phase. For each 10g increment the increase is paused for approximately 60 seconds until 50g is reached, where the centrifuge acceleration is maintained for 660 seconds. At approximately 1440 seconds, the centrifuge acceleration is increased to 70g.

Figure 7-28 shows the changes in pore water pressure (PWP) during the consolidation stage of the M-T5 test, where the PPTs were properly saturated. As time progresses, the pressure in each transducer gradually stabilises. This stabilisation, particularly evident in the mid-range indicates that the pore pressure is equalising throughout the slope as water escapes from the pores and soil particles settle. This gradual balancing of PWP continues until the "Consolidation End" mark, where most PPT readings have reached a near-steady state, indicating that the soil structure has largely consolidated.

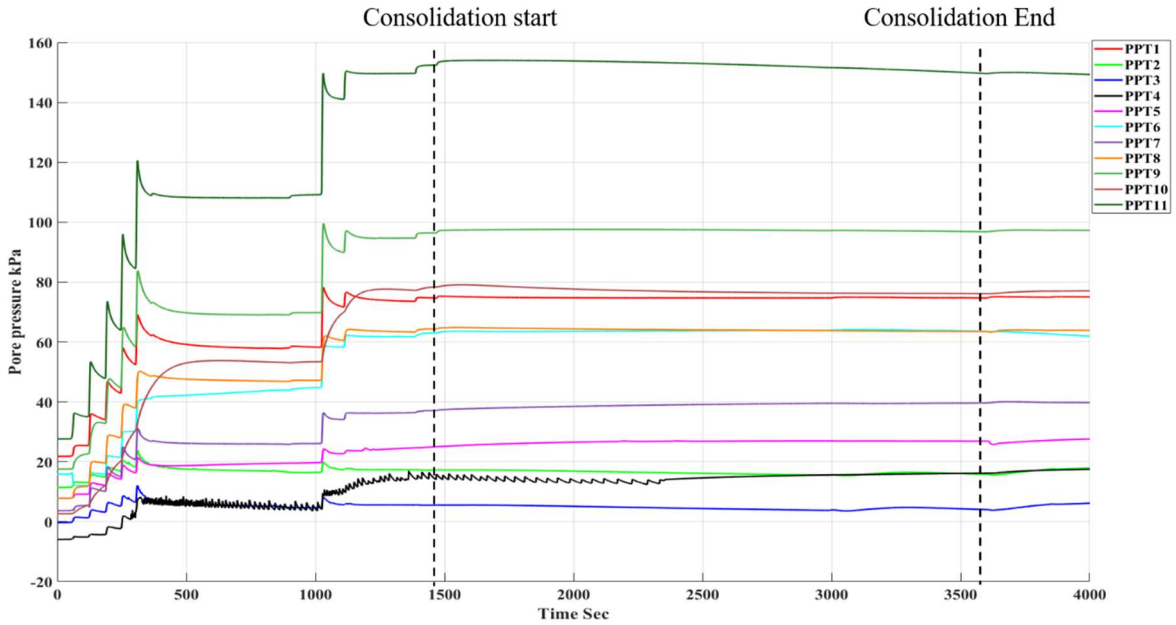


Figure 7-28 Changes in pore water pressure during the consolidation stage of the M-T5 test.

Analysis of PWP distribution.

The evaluation of the PPT data compared to their positions during the M-T5 at the end of the auto balance and consolidation stages is illustrated in Figure 7-29 and Figure 7-30, respectively. The pore pressures measured at each PPT location is given in red. The PPT located near the drainage path capture the combined effect of the soil weight above and any hydraulic gradients caused by water movement. This is observed in the foundation PPTs (1, 9, 11).

PPT2, PPT3, and PPT4: These sensors are at the surface of the slope and show a slight increase of PWP towards the toe. The pressure readings in the lower parts of the model (PPTs 1, 9, and 11) and along the base of the inclined plane are elevated, consistent with hydrostatic pressures resulting from gravity. While pressures increase along the slope, the contour lines exhibit a greater degree of uniform spacing, indicating that the soil response along this trajectory is more consistent.

A poorly saturated PPT can lead to misleading data particularly with respect to rapid changes, affecting the overall interpretation of pore pressure distribution within the slope. The soft response observed in PPT10 suggests that it was not fully saturated. Nevertheless, the long-term output of PPT10 is in line with the others, so that its data is included in the end-stage.

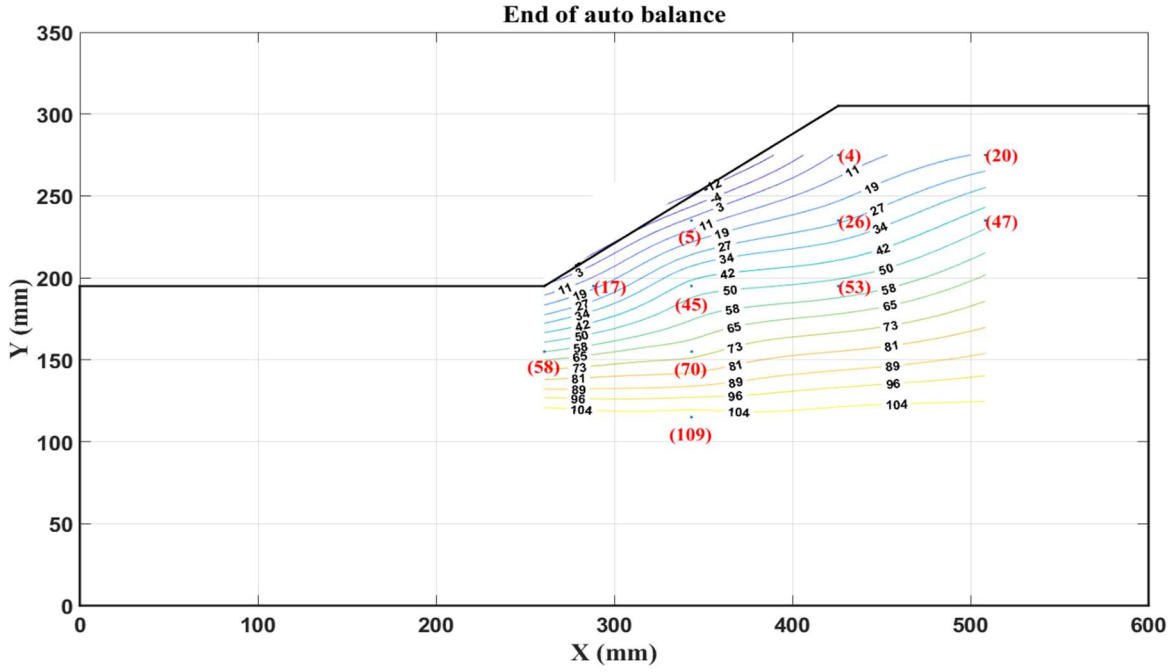


Figure 7-29 Pore water pressure at the end of auto balance.

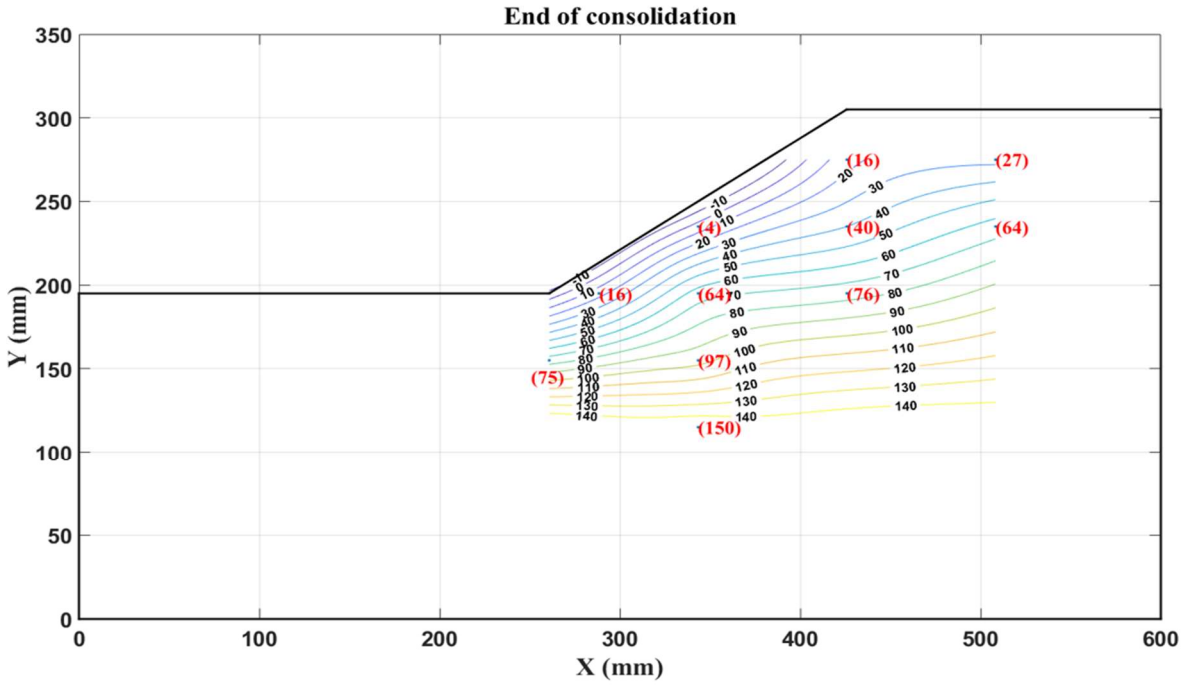


Figure 7-30 Pore water pressure at the end of consolidation phase.

PWP observations across different stages and spins in the M-T5 test.

Figure 7-31 shows PWP and RH in the first spin. Initial stabilisation of PWP sensors is observed during the auto-balance and consolidation phases. RH stabilises, and PWP increases slightly, indicating redistribution of water pressure. Alternating rainfall and drying cycles result in fluctuations in PWP, consistent with the applied climate scenario (1-week rain, 1 week no rain for Winter 1). During Summer 1, PWP decreases gradually, reflecting drainage and drying effects as the slope stabilises under drier conditions. Winter 2 follows a similar alternating rainfall pattern (2 weeks of rain, 1 week of no rain), causing fluctuations in PWP. However, the magnitude of fluctuations is slightly dampened, possibly due to cumulative effects of water retention from the prior winter. Summer 2 exhibits slower PWP reductions compared to summer 1, with residual moisture likely contributing to prolonged drying times. The first half of winter 3 continues the alternating rainfall scenario, with fluctuations in PWP and RH similar to prior winters. The remaining phase transitions into continuous rainfall, resulting in a steady rise in PWP across some sensors. RH reaches near-saturation levels during the continuous rainfall period, indicating persistent wet conditions in the model.

Figure 7-32 shows PWP during a continuous rainfall scenario starting at 70 g in the second spin.

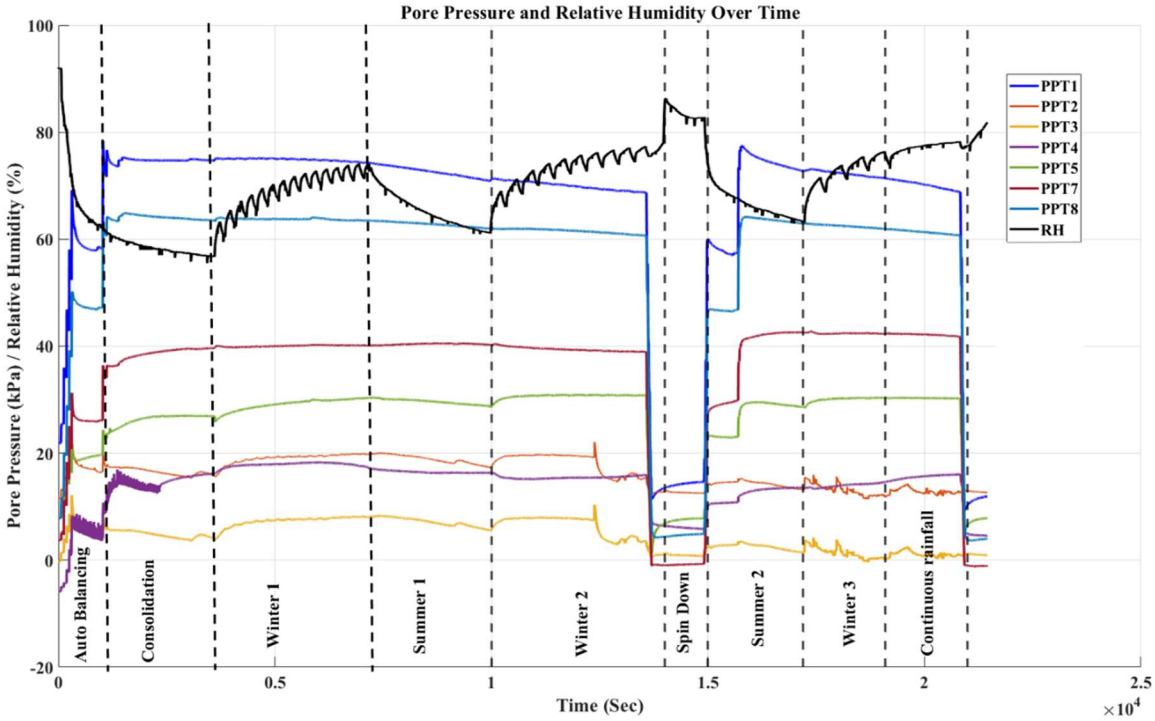


Figure 7-31 Pore water pressure and relative humidity variations during different climate scenarios.

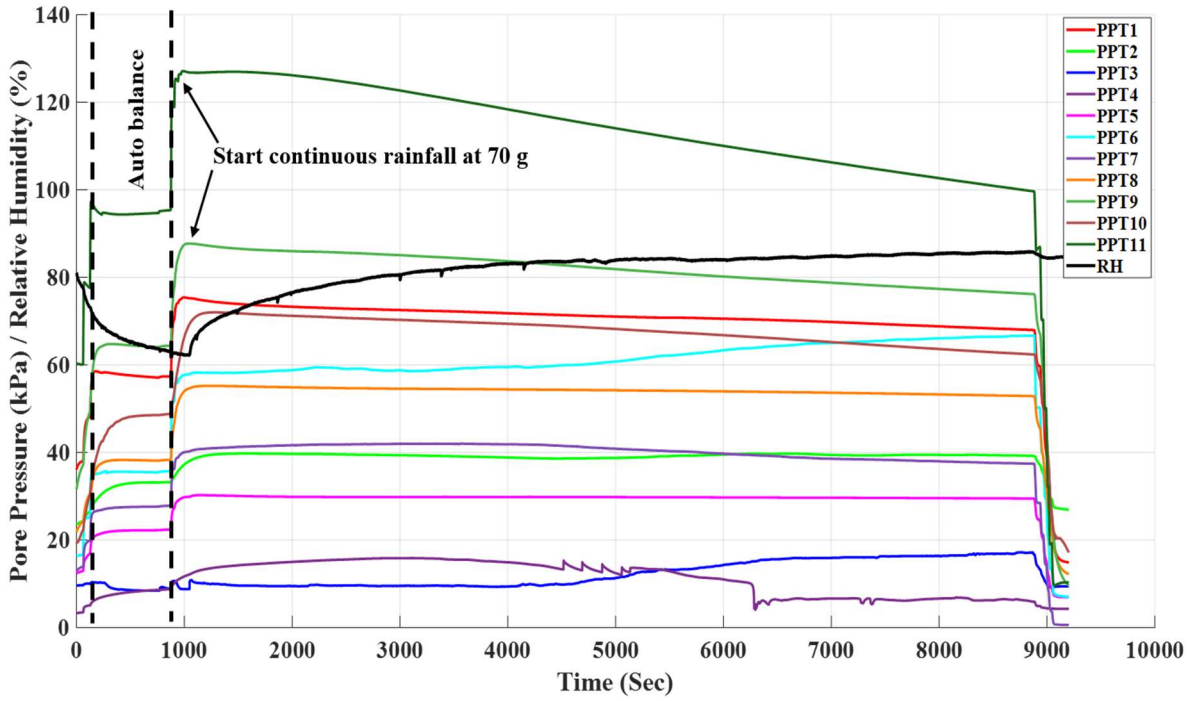


Figure 7-32 Pore water pressure and relative humidity variations during second spin.

The continuous application of rainfall results in steady increases in PWP for most PPTs. RH increases gradually, aligning with the continuous rainfall. No significant anomalies, such as abrupt PWP changes, are observed, indicating stable experimental conditions during this phase.

Figure 7-33 captures multiple flooding and drawdown phases (Flood 1, Flood 2, Flood 3) during third spin. After each flood phase, PWP rises sharply due to water infiltration and decreases during drawdown, reflecting effective drainage mechanisms. Sharp PWP increases correspond to flooding, followed by sharp decreases during drawdown. The valve issue is noted, requiring a reduction in g-level (to 50 g) to operate correctly, followed by an increase back to 70 g.

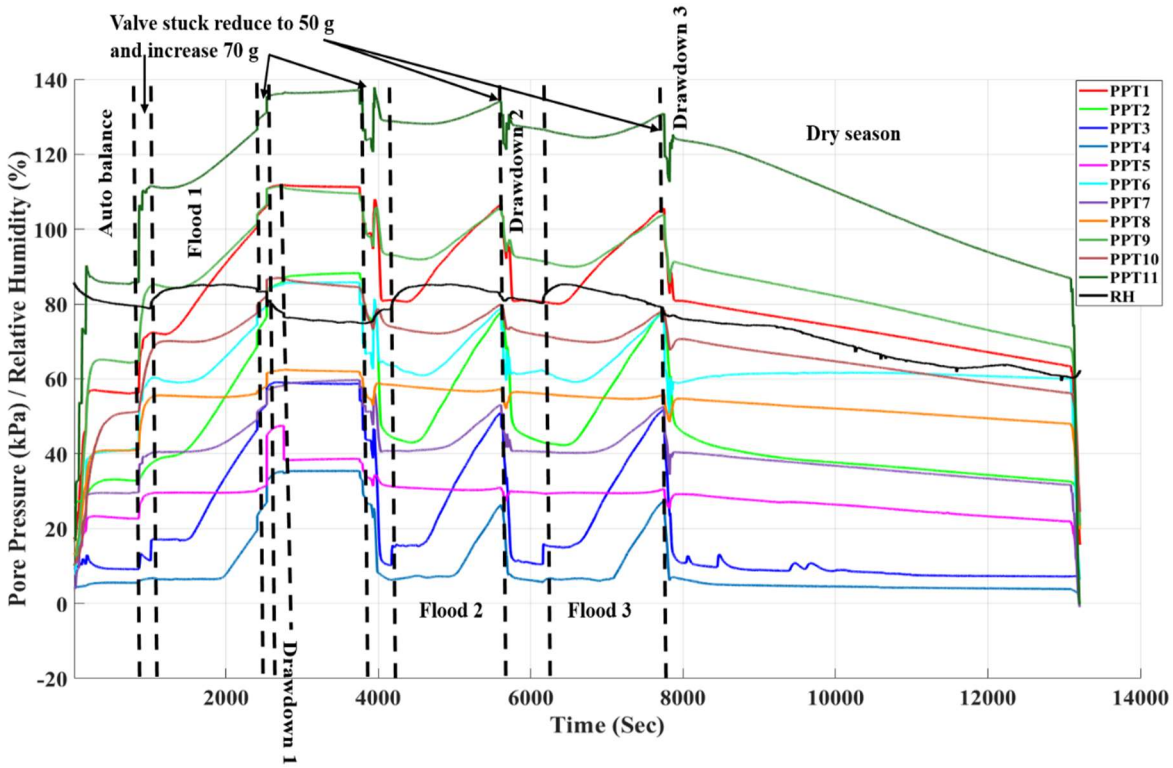


Figure 7-33 Pore water pressure and relative humidity variations during third spin for flooding and drawdown stages.

7.5.3 Test M-T5: Deformations

The horizontal blue line shown in Figure 7-34 serves as a visual reference point to aid in the observation of variation in the slope elevation. The visible settlement during the auto balance stage indicates that the soil has responded to the centrifugal forces, resulting in a clearly discernible reduction in the elevation of the soil mass in relation to the reference line.

Figure 7-35 presents the outcomes at the auto balance phase in terms of (a) vector displacement (b) resultant contours of displacement, (c) shear strain and (d) volumetric strain. The figure, generated using a GeoPIV-RG mesh size of 100×100 pixels with a 50-pixel overlap, demonstrates the progression of strain over a 10-second period in model time. The auto balance phase resulted in noticeable shear strains in the model (≤5%), as depicted in Figure 7-35(c), while the volumetric strain was relatively minor Figure 7-35(d). Furthermore, a minor crack in the slope crest became apparent at the conclusion of this auto-balancing stage and has been labelled in Figure 7-35(c). The presence of elevated shear strains at the crest suggests that the material has reached its limit of shear strength, resulting in the initiation of a crack. The

volumetric strain graph illustrates that the regions close to the crack show distinct strains, with some areas experiencing compression (yellow tones) and others experiencing dilation (light blue tones) as shown in the Figure 7-36. Differential strain behaviour indicates that cracks might form because of complicated interactions between compressive and tensile forces. The soil displacement vectors demonstrate predominantly deep-seated movements towards the toe of the slope. The observed displacements provide strong evidence that the soil is experiencing both horizontal and vertical movements due to the simulated gravitational forces. Despite this, the crack vanished shortly after the auto-balance process, likely due to being filled with fines (kaolin) and did not resurface afterwards. After reaching a centrifugal acceleration of 70g, the model was given an equilibration period of 36 minutes without any precipitation events.

Figure 7-37 illustrates the strain that occurred in the model throughout this time, which was accompanied by the observation of apparent movement through DIC. The magnitude of the strains encountered during this specific time frame was estimated to be around 4%.

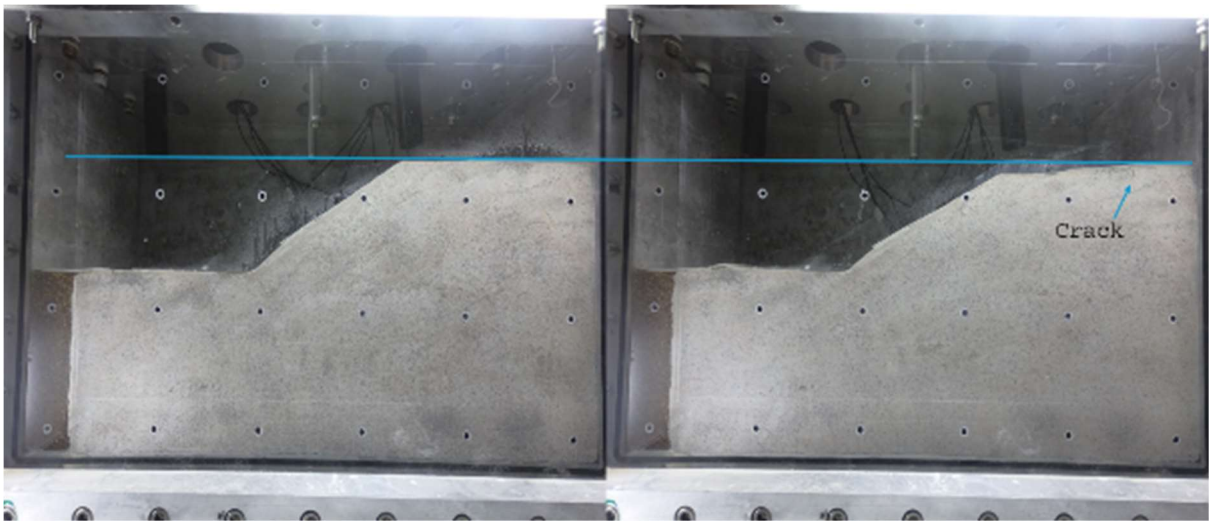


Figure 7-34 Crest settlement during auto balance phase.

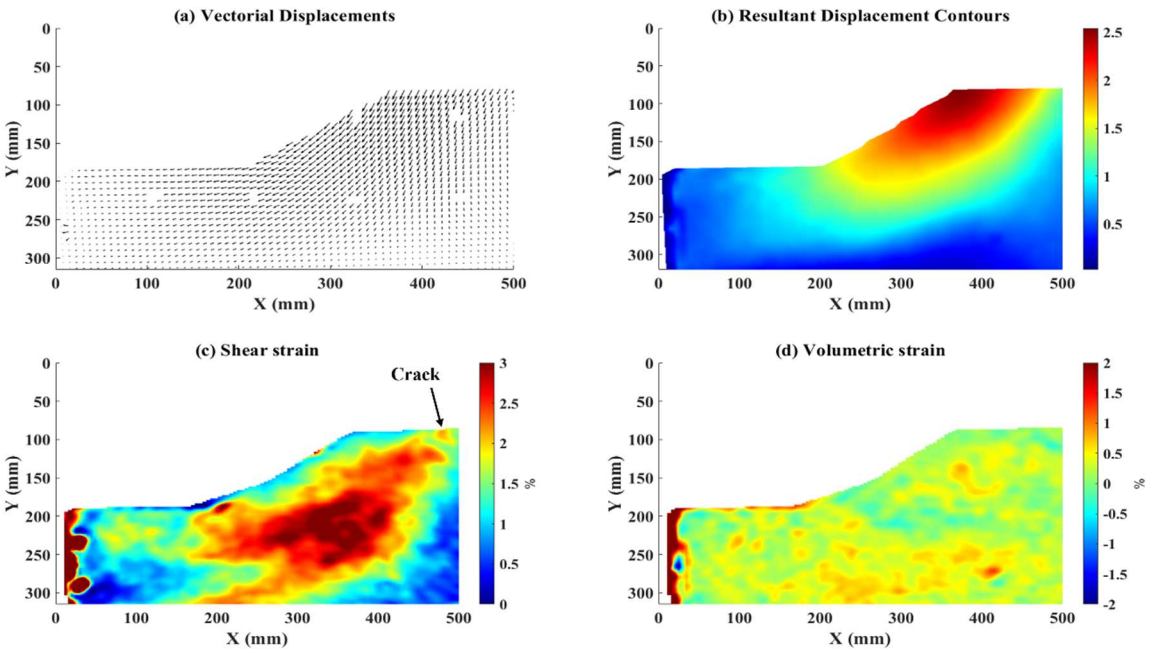


Figure 7-35 Displacements and strain at the end of auto balance phase (M-T5) test.

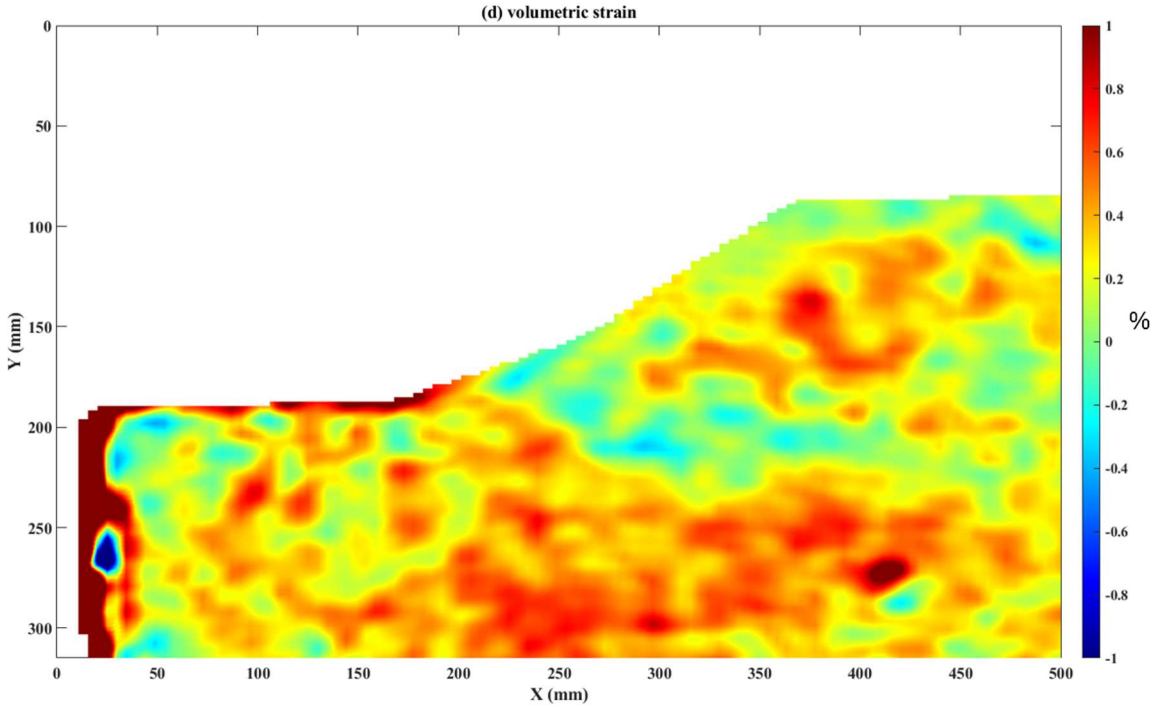


Figure 7-36 Volumetric strain at the end of auto balance.

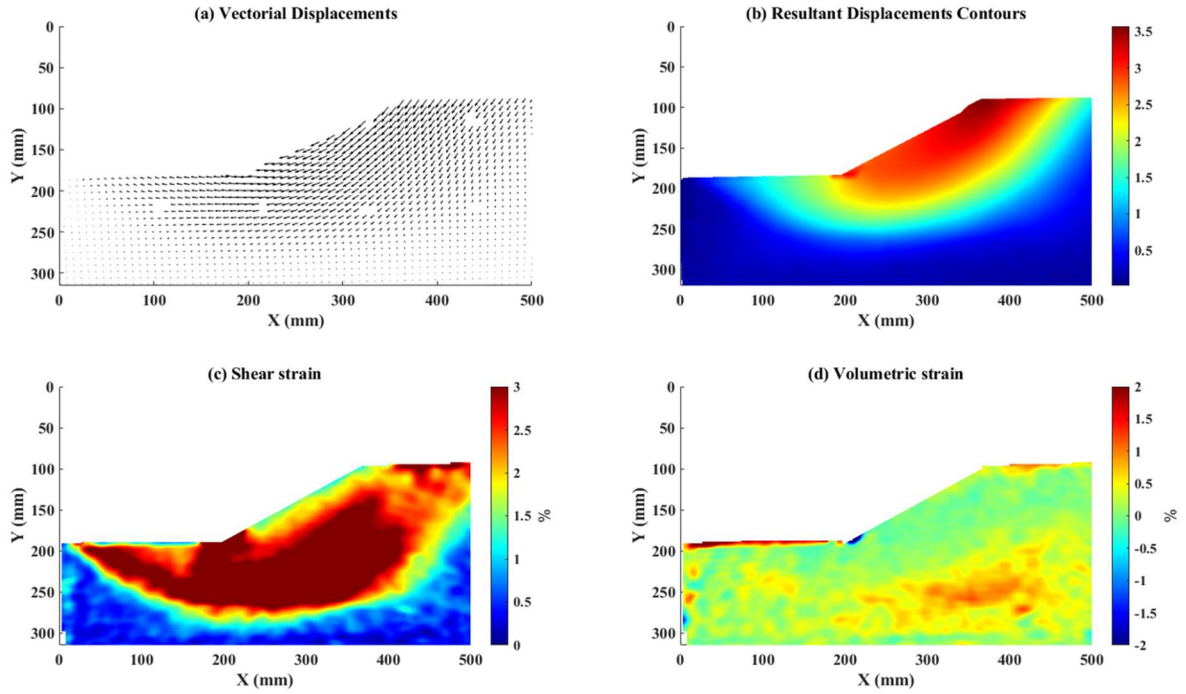


Figure 7-37 Displacements and strain at the end of consolidation phase (M-T5) test.

7.5.4 Seasonal cycles effect.

Across the initial seasonal cycles simulated in the M-T5 test – including the Summer 1 and Winter 1, no significant slope movement or deformation was observed. The applied climatic variations, including wetting and drying cycles, did not induce noticeable displacements or strains, and the slope maintained structural stability throughout. The soil structure appeared to successfully adapt to moisture fluctuations, suggesting that these seasonal changes, within the simulated parameters, did not compromise slope integrity. Detailed displacement and strain analyses are provided in Appendix A.2.1.

Second winter /M-T5.

During the second winter scenario (Figure 7-38), which included two weeks of rainfall followed by two weeks of dryness, the slope remained relatively stable with minimal displacement, shear strain, and volumetric strain. Resultant displacement contours showed low-magnitude movements, primarily in the upper slope – suggesting the possibility of incipient failure. However, shear strain remained negligible, suggesting the soil retained strength without internal stresses or failure.

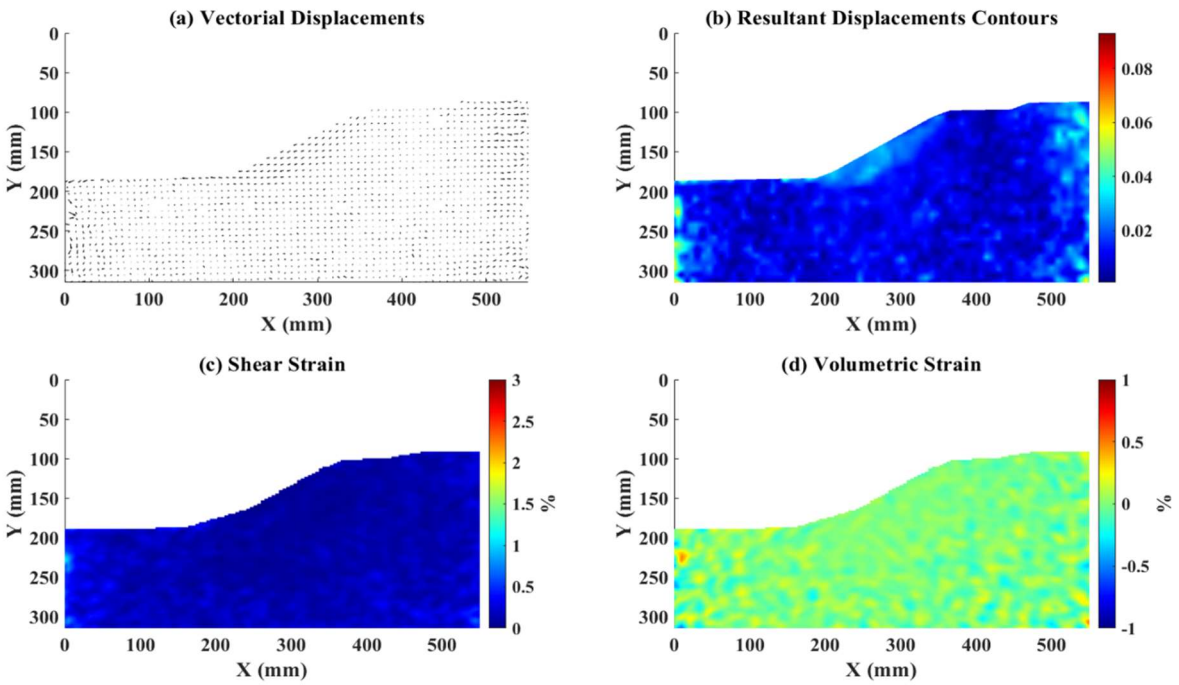


Figure 7-38 PIV analysis at the end of Winter 2 (M-T5) test.

Pore water pressure analysis:

The pore water pressure (PWP) distribution at the end of Winter 2 (Figure 7-39) shows a slope parallel gradient. Moving upward towards the slope surface, pore pressures decrease progressively, reaching slightly negative values (approximately -2 to -3 kPa). Compared to the end of Summer 1, Winter 2 exhibits relatively lower surface suction (-2 to -3 kPa compared to -10 kPa at Summer 1), indicating a wetter slope surface condition during winter due to rainfall infiltration.

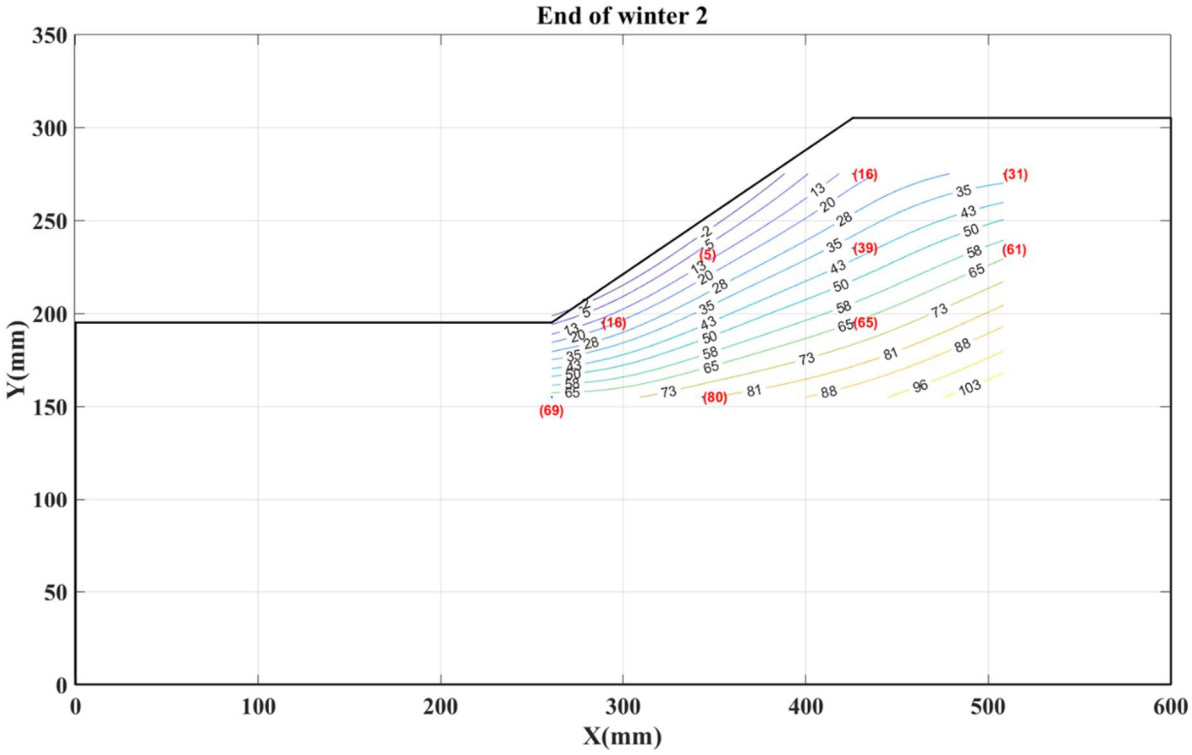


Figure 7-39 Pore water pressure contours at the end of Winter 2 for M-T5 test.

Soil deformation at the end of Summer 2

At the end of Winter 2, the centrifuge was spun down to 1g for the replacement of the camera battery. This temporary interruption in the test sequence affected the displacements very slightly and pore water pressure (PWP) dissipation process and influenced the observed trends at the end of Summer 2 (Second Consolidation Phase).

At the end of the second summer phase (Figure 7-40), PIV analysis shows minor soil movement. Vectorial displacements suggest slight downslope movement due to drying-induced contraction and settlement, though an anomaly in the bottom right corner may be linked to PIV reference calibration or camera movement. Shear strain remains low, with slight increases near the crest, suggesting minor deformation but no structural instability. Volumetric strain contours show little contraction or dilation, reinforcing the stability of the slope under drying conditions.

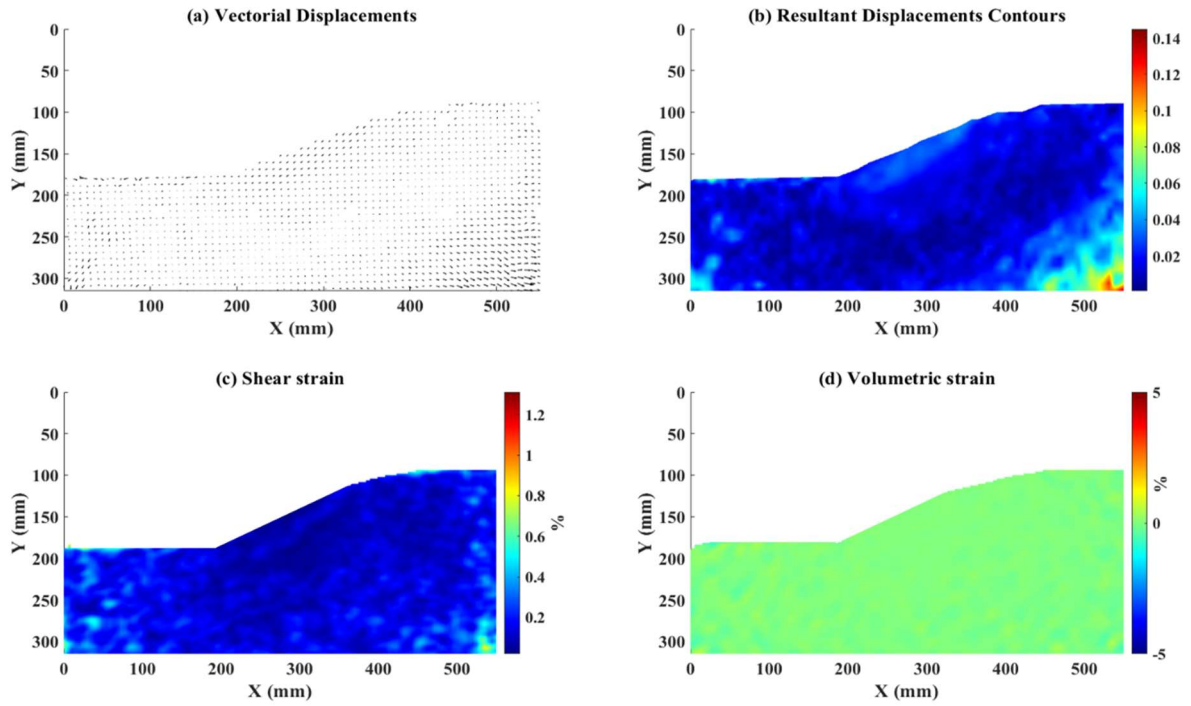


Figure 7-40 soil deformation at the end of Summer 2.

Pore water pressure analysis at the end of second consolidation (Summer 2):

Figure 7-41 illustrates the pore water pressure distribution at the end of second consolidation phase, which was assumed to represent Summer 2 in the testing sequence. The contours illustrate the variation of PWP across the slope, highlighting zones of higher pressure accumulation and potential drainage limitations. Notably, compared to the end of Winter 2, elevated PWP values persist in the lower and mid-slope regions, suggesting incomplete dissipation due to the influence of prior spin-down and the consolidation process during Summer 2.

Influence of spin-down on pore water pressure dissipation

At the end of Winter 2, the centrifuge was spun down to 1g for the replacement of the camera battery. This temporary interruption in the test sequence affected the pore water pressure (PWP) dissipation process and influenced the observed trends at the end of Summer 2 (Second Consolidation Phase). During centrifuge testing, the stress conditions scale with g-level, meaning that at 70g, self-weight stresses and hydraulic gradients are much higher than at 1g. When the centrifuge was spun down, the following effects likely occurred:

1. Reduction in Effective Stress and Drainage Potential
    - Under 70g conditions, the increased effective stress promotes faster pore water dissipation.
    - When the centrifuge was stopped, the effective stress returned to 1g, significantly reducing the drainage gradient and slowing water movement within the soil matrix.
2. Redistribution of Pore Pressure in Fine-Grained Layers
    - The soil mixture used (65% sand, 35% kaolin) contains low-permeability clay, which retains water due to high suction forces.
    - The sudden change from 70g to 1g could have resulted in partial rebound and de-saturation of some fine-grained layers, preventing complete drainage.
3. Lack of Drying Effect During Summer 2
    - Unlike natural summer conditions, where evaporation and surface drying reduce PWP, the centrifuge test environment had limited drying effects, especially for deeper soil layers.
    - This contributed to higher PWP retention compared to Winter 2, even though no additional rainfall was applied.

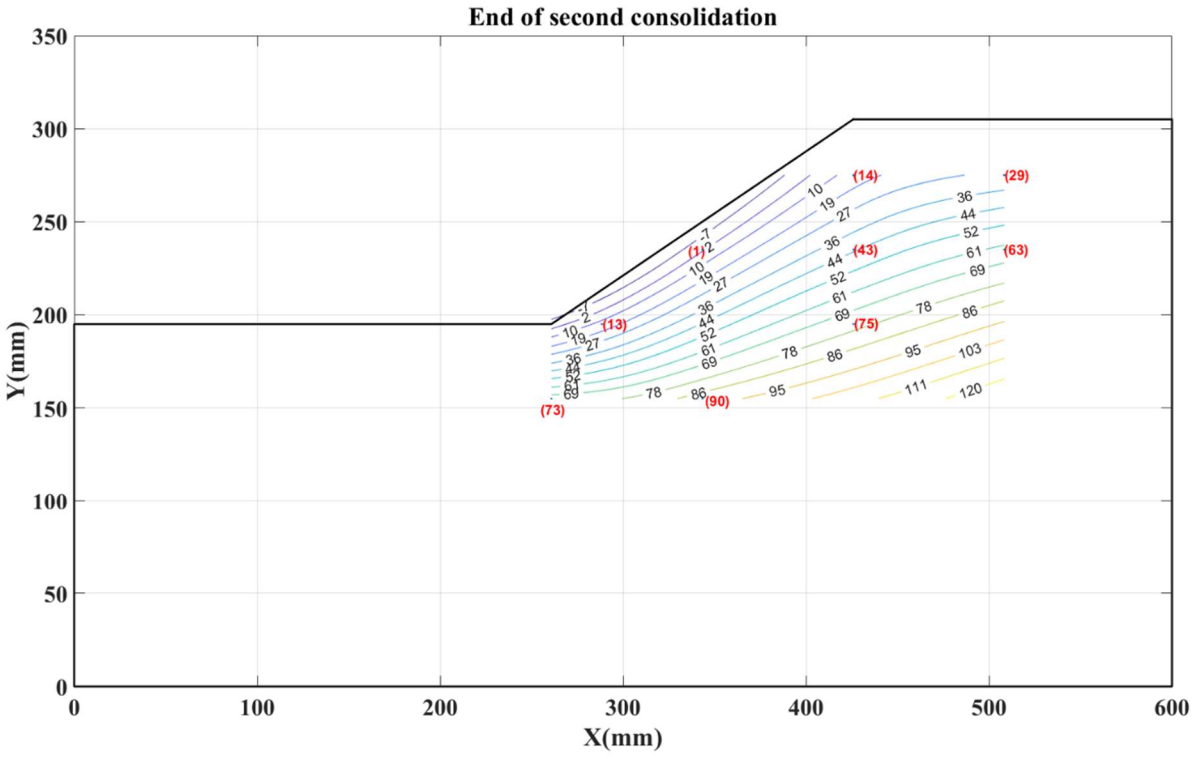


Figure 7-41 Pore water pressure at the end of second consolidation (M-T5) test.

Soil deformation at the end of Winter 3-half season continuous rainfall M-T5

At the end of Winter 3 in the M-T5 test, the slope exhibited noticeable downslope movement, with displacements reaching up to 5 mm near the crest and mid-slope. Shear strain (up to 25%) was concentrated in the upper and middle sections, indicating potential localized deformation. Volumetric strain patterns showed alternating compression and expansion, particularly along the shear surface, suggesting the effects of continuous rainfall on soil stability. Figure 7-42 illustrates the soil deformation at the end of Winter 3, a season characterized by an initial phase of three weeks of rain followed by one week of dryness, and continuous rainfall during the latter part of the season.

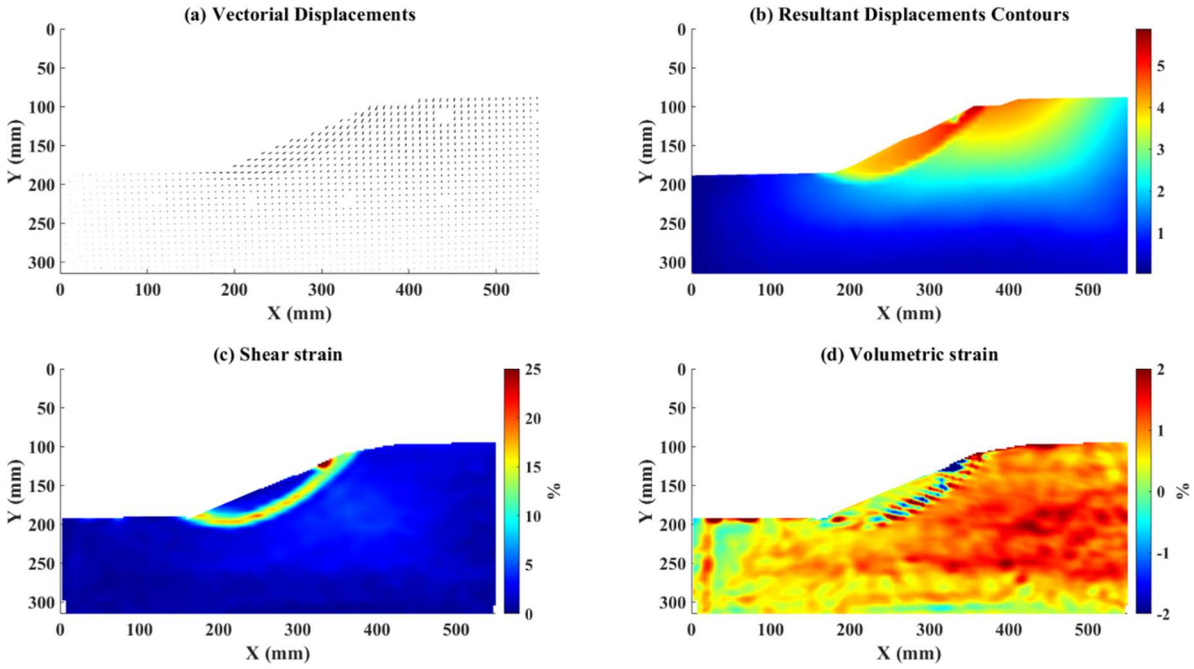


Figure 7-42 Soil deformation at the end of Winter 3.

Pore Water Pressure Analysis at the end of Winter 3:

Figure 7-43 illustrates the pore water pressure (PWP) distribution within the slope at the end of Winter 3, which involved a period of continuous rainfall following an initial phase of three weeks of rain and one week of dryness. he PWP distribution shows a uniform gradient angled to the slope, indicating significant seepage from the slope face. Higher PWP values are concentrated near the slope base, decreasing towards the crest, reflecting the water pressure gradient within the slope.

Impact of continuous rainfall:

Continuous rainfall has caused the soil to reach over-saturation levels. The high PWP values reflect the soil's inability to drain the excess water efficiently, resulting in elevated water pressures that can destabilise the slope. The combination of high PWP and significant shear strain near the slope gradient indicates a failure mechanism driven by pore pressure-induced instability.

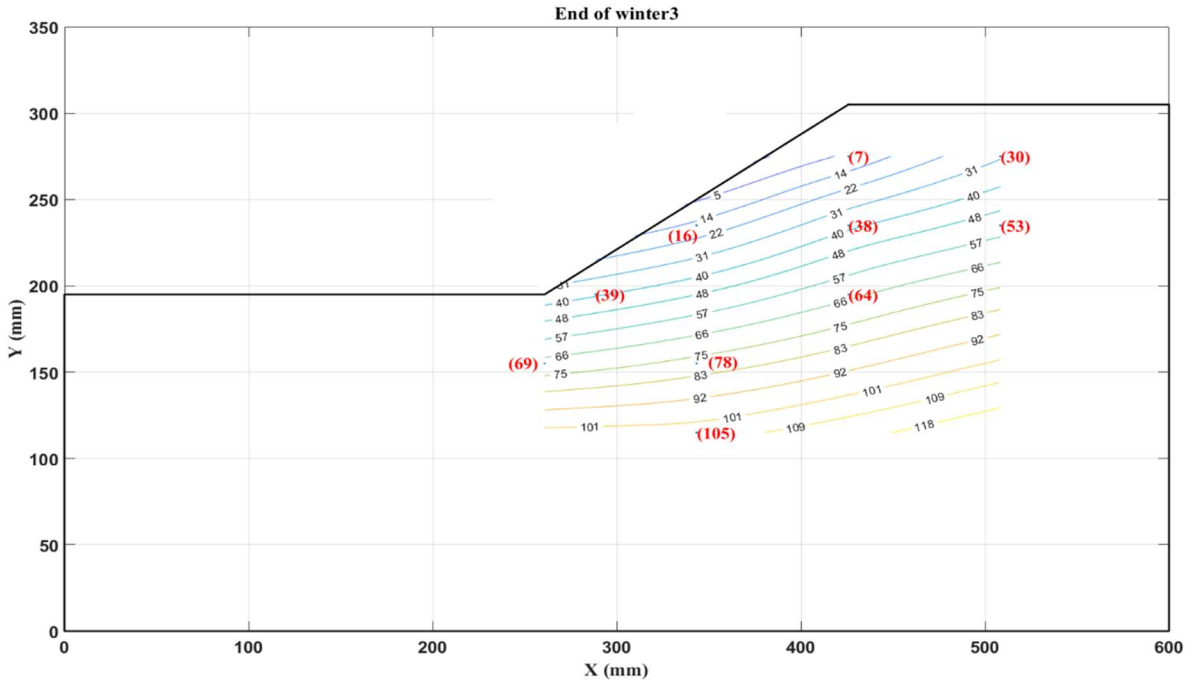


Figure 7-43 Pore water pressure at the end of Winter 3 (M-T5) test.

7.5.5 Flooding and drawdown effects M-T5 test.

During the first flood (Flood 1) of the M-T5 test, water levels rose above the crest of the slope. The process of filling the slope with water took approximately 36 minutes at the model scale. However, an issue occurred with the solenoid valve, which malfunctioned at 70 g. To resolve this, the g-level was reduced to 50 g, and rainfall was initiated to simulate the flooding phase. Once the water levels rose above the slope crest, Flood 1 continued for an additional 24 minutes before the drawdown commenced. The drawdown phase lasted 2.3 minutes, during which the water level receded and eventually reached the surface of the slope toe.

In subsequent floods (Flood 2 and Flood 3), the water surface reached the crest of the slope but did not go beyond it. It took approximately 26 minutes for the water to rise to this level. However, the same issue of solenoid valve reappeared, hindering proper operation at 70 g. After addressing this by resuming rainfall, the drawdown phase began immediately at 70 g for both Flood 2 and Flood 3. The drawdown process in these cases took about 2 minutes for the water to reach the surface of the toe.

These events demonstrate the challenges faced in maintaining precise equipment function during high g-level testing and emphasise the importance of adjusting g-levels to ensure accurate flood simulation.

Soil deformation during Flood 1

No significant deformation was observed during Flood 1, suggesting that the slope maintained stability under the applied flooding conditions. (Appendix A.2.2)

Soil deformation during Drawdown 1

Figure 7-44 illustrates the drawdown process during Drawdown 1, where the water level drops from above the crest to the surface of the toe. This process takes approximately 3 minutes on the model scale, which corresponds to 10 days on the prototype scale. The image (a) shows the initial water level above the crest before the drawdown begins. Image (b) represents the early stage of the drawdown process, where the water level starts to recede gradually, exposing parts of the slope near the crest. Image (c) depicts the intermediate stage of the drawdown, where the water level continues to lower, exposing more of the slope surface. The last image (d) captures the slope conditions after the water level has receded to the surface of the toe.

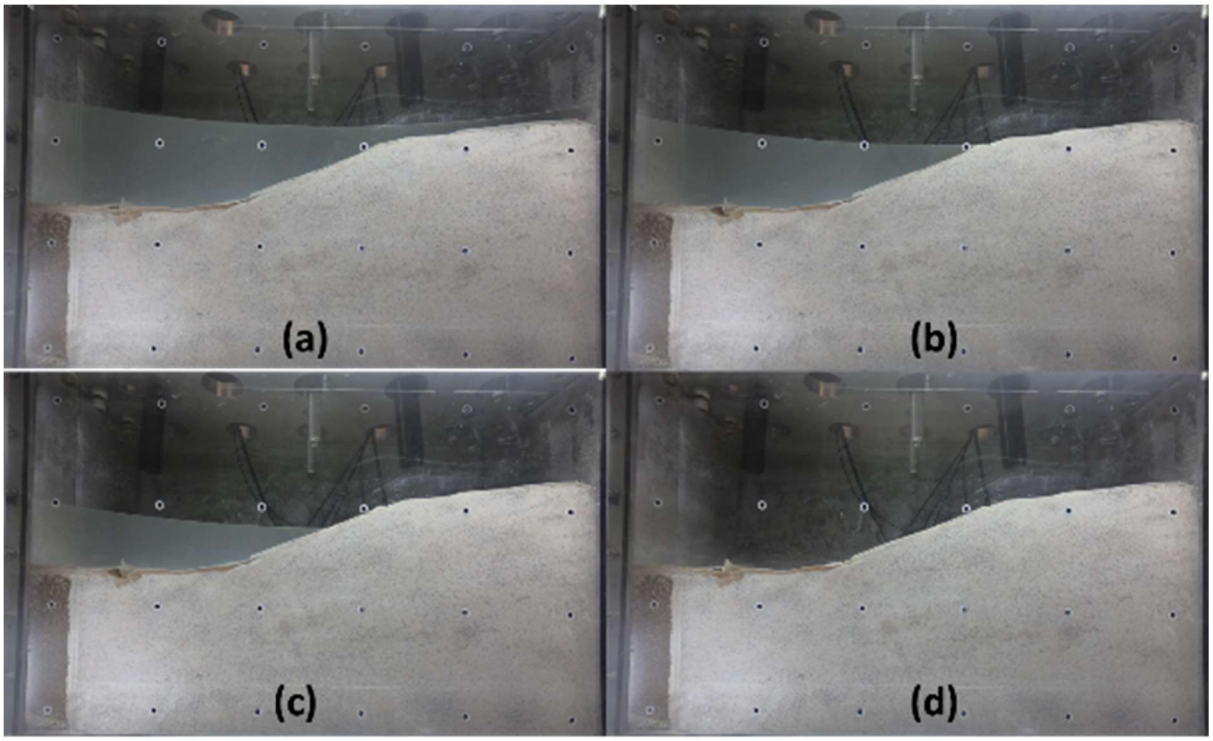


Figure 7-44 Gradual reduction of water level from above the crest to the toe surface.

Figure 7-45 illustrates the soil deformation behavior at the end of the drawdown phase following Flood 1. The PIV analysis indicates clear slope failure movements, with significant displacements concentrated near the crest and downslope. Shear strain and volumetric strain patterns further confirm instability, likely due to pore water pressure reduction during drawdown.

Pore water pressure at the end of Drawdown 1

Figure 7-46 shows the pore water pressure distribution during the first drawdown phase. The contours of pore pressure are not slope parallel, instead exit the slope at an angle, indicating that outward seepage is still occurring. This results in pore pressures above zero at the slope face towards the bottom half, and is more likely to lead to a destabilised slope. The PIV analysis shows significant soil displacement vectors near the slope crest and mid-slope region. These areas correspond with moderate pore water pressures, suggesting that the drawdown process is causing shear deformation as the soil adjusts to the changing pressure conditions due to the removal of water pressure during drawdown on the outside of the slope while there still being elevated pore pressure inside the soil.

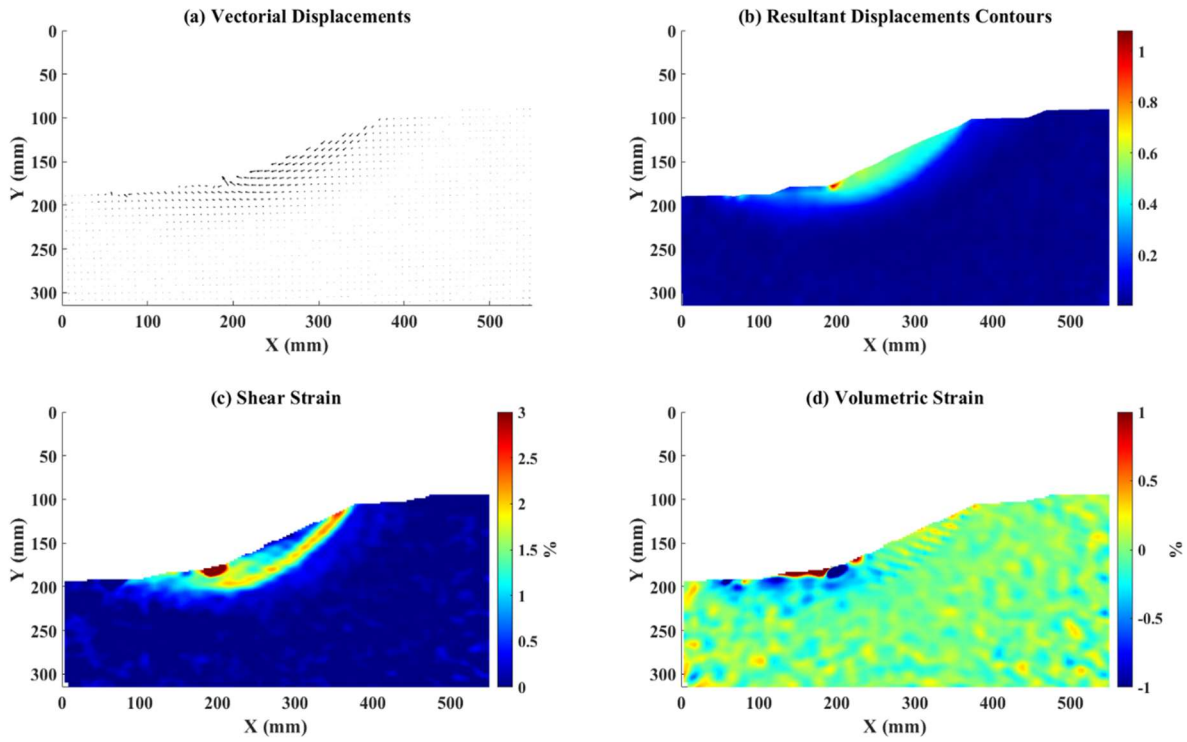


Figure 7-45 Soil deformation at the end of Drawdown 1

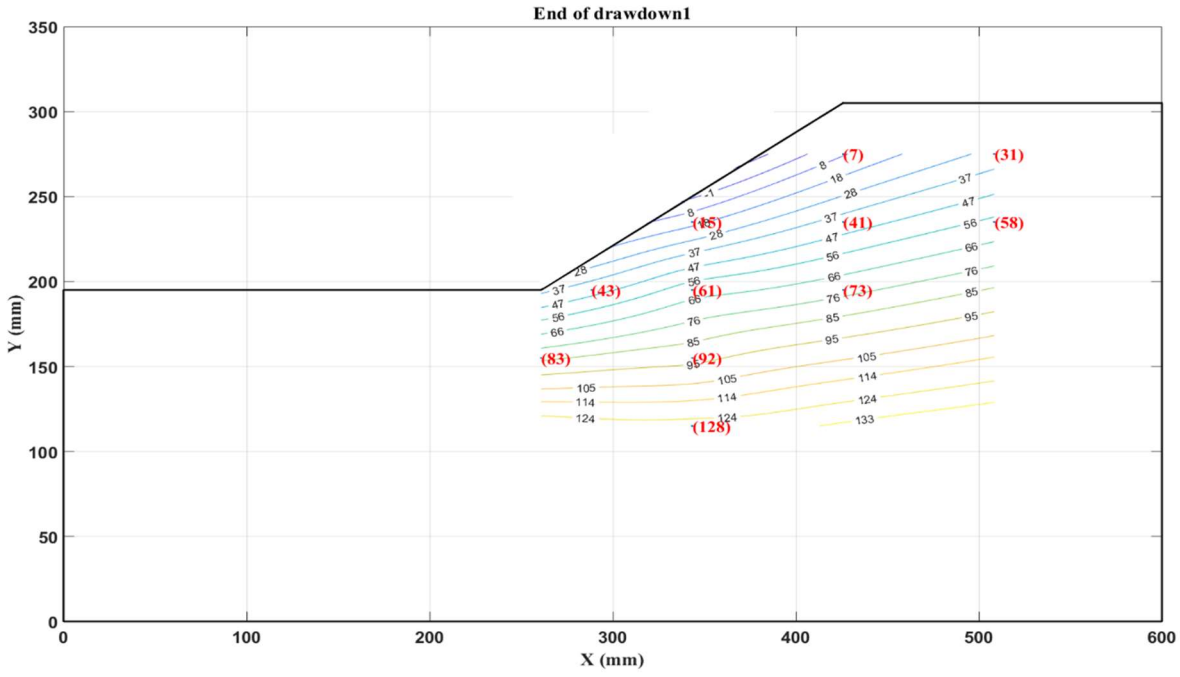


Figure 7-46 Pore pressures at the end of Drawdown 1 at Y=195mm (when the water reaches the toe).

Soil deformation during Flood 2

No significant deformation was observed during Flood 2, suggesting that the slope maintained stability under the applied flooding conditions. (Appendix A.2.2)

Soil deformation at the end of Drawdown 2

Figure 7-47 shows the soil deformation at the end of Drawdown 2. At the end of Drawdown 2, significant slope displacement is observed, with higher movement in the upper layers. Shear strain (up to 10%) is concentrated near the surface, while volumetric strain shows compression near the crest and slight dilation along the failure surface.

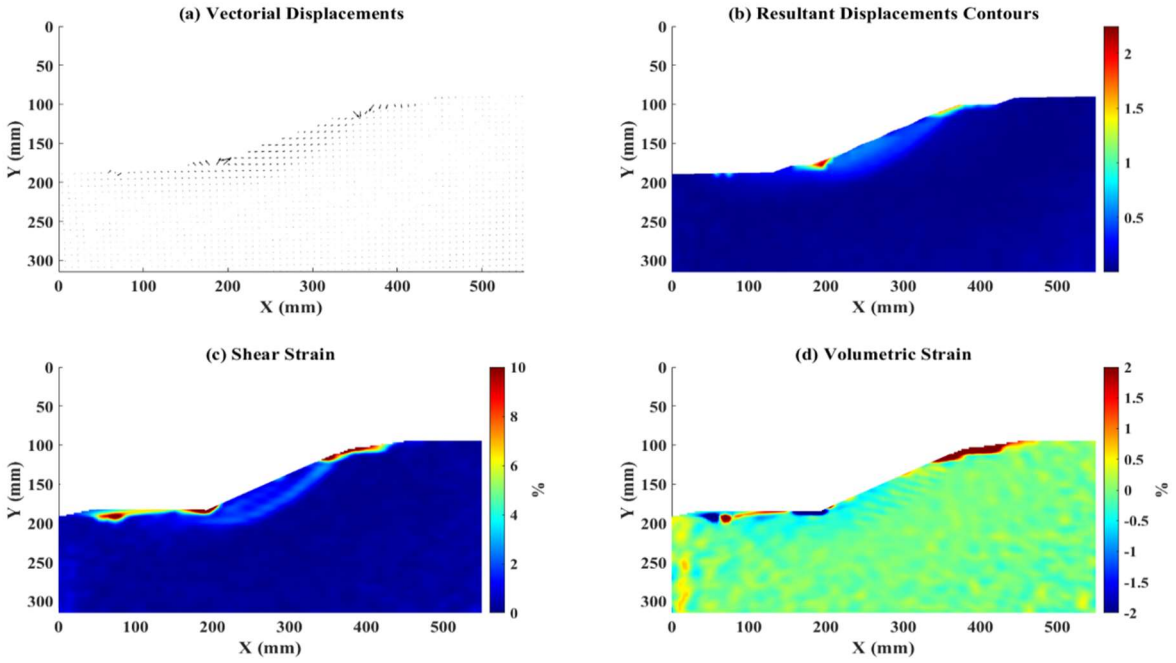


Figure 7-47 Soil deformation at the end of Drawdown 2.

Pore water pressure (PWP) analysis at the end of Drawdown 2

At the end of Drawdown 2, PWP contours exited the slope face at an angle, indicating ongoing seepage as shown in

Figure 7-48 .

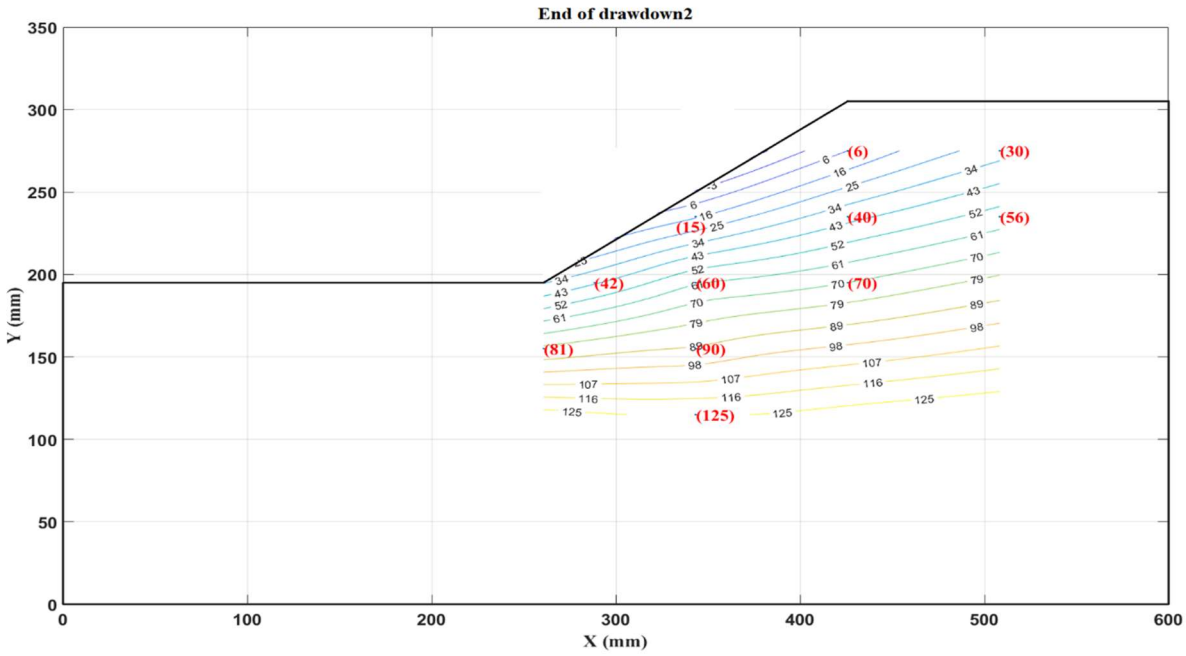
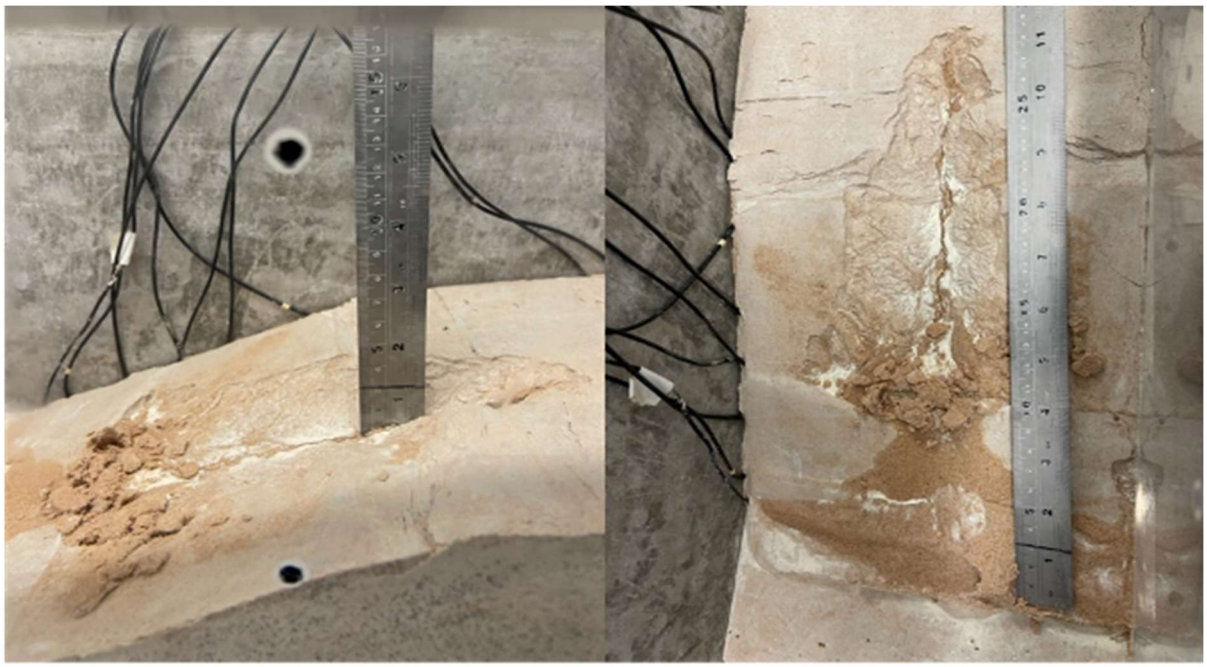


Figure 7-48 Pore pressures at the end of Drawdown 2.

7.5.6 Slope failure after centrifuge test.

The failure observed in the M-T5 test after the centrifuge test and the application of various climate scenarios, including flooding and drawdown, is shown in

Figure 7-49. Cracks near the crest, penetrated approximately 1 cm deep and extended 29 cm in length. Furthermore, the size of the crack confirms that erosion has had an impact on the slope because the upper portions of the slope are more vulnerable to failure under the current loading and moisture conditions. Localised erosion is clearly visible in the left image, most likely as a result of water infiltration and surface runoff that caused the displacement of fine soil particles. Minor sliding or peeling seems to have occurred because of water-induced shear stresses during the drawdown phase. This type of erosion may have contributed to weakening the slope's overall stability, facilitating the formation of cracks. The right image reveals more pronounced erosion, with deeper soil displacement and vertical cracking, likely indicating zones of concentrated water flow. This removal of surface material has led to the formation of localised erosion pits, where water may have accumulated, exerting hydrostatic pressure. These combined processes erosion, infiltration, and water pressure—likely played a critical role in the destabilisation and eventual failure of the slope.



(a) Depth of the crack on the slope (b) Length of the crack on the slope

Figure 7-49 Crack formation and slope failure in M-T5 model.

Figure 7-50 depicts the top view of the M-T5 slope following the multistage centrifuge test. The cracks propagate through the body of the slope. Additionally, toe erosion is visible, which suggests the removal of soil material at the base of the slope due to water flow during the flooding event.

Figure 7-51 displays a front view of the slope failure and shear plane in the soil model after testing. This shear zone, appearing within the body of the slope rather than just at the surface, is indicative of internal stress and strain responses to the test conditions, but would not be observable to an external viewpoint, unlike the cracking and erosion.



(a) The top view of the slope (b): Cracks on the toe

Figure 7-50 Top view of cracks and toe erosion after centrifuge test for M-T5 slope.

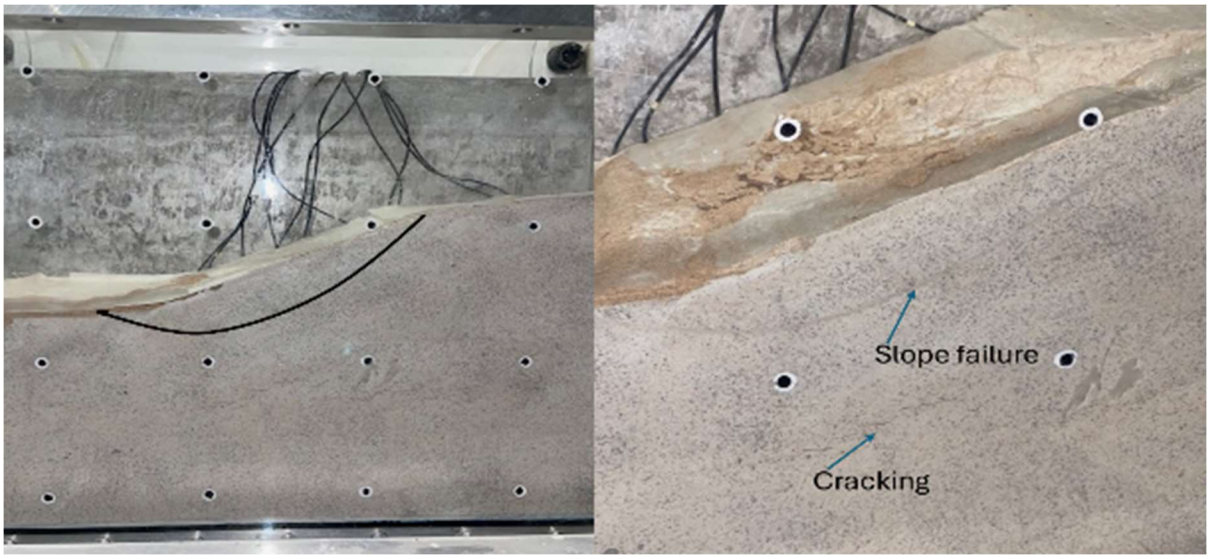


Figure 7-51 Front view of slope failure and cracking in M-T5 slope model after centrifuge test.

7.5.7 Shear strength reduction due to drawdown failure

To further investigate the failure mechanism, the effective stress before and after drawdown was calculated using prototype-scale depths (scaled at 70g). This analysis provides a quantitative understanding of how shear strength was affected by drawdown-induced pore pressure changes. The total stress was determined using the soil unit weight (γ = 18 kN/m^3), and PWP values were obtained from pore pressure transducers (PPTs) at the start and end of drawdown. The Mohr-Coulomb failure criterion was applied to compute shear strength

$$\sigma' = c' + \sigma' \tan(\phi') \qquad 7\text{-}2$$

- c' = 5 kPa (effective cohesion)
- ϕ' = 28° (effective friction angle)
- $\sigma' = \sigma - u$ (effective stress before and after drawdown)

The calculated shear strength reduction in prototype scale is summarized in Table 7-5.These results confirm that shear strength reduction was most significant in the lower and mid-depth layers, particularly at PPT1 (~19.7%) and PPT9 (~16.5%), where pore pressure dissipation was slower and effective stress was significantly reduced. The higher shear strength reductions at PPT1, PPT9, and PPT3 confirm that drawdown effects influenced the entire slope profile, with deeper layers remaining vulnerable due to pore pressure lag. These findings support the pore pressure dissipation theory Wright and Duncan (1987), (Duncan et al., 2014), which states that delayed drainage can temporarily weaken the soil, increasing the likelihood of slope failure.

Table 7-5 Shear strength reduction at different PPT locations in the M-T5 Test.

PPT	Depth in Prototype (m)	Total Stress (kPa)	PWP Start Drawdown (kPa)	PWP End Drawdown (kPa)	Effective Stress Before (kPa)	Effective Stress After (kPa)	Shear Strength Before (kPa)	Shear Strength After (kPa)	Shear Strength Reduction (%)
PPT1	10.85	195.30	83.21	105.25	112.09	90.05	64.6	52.9	19.7
PPT2	13.65	245.7	59.7	78.39	186	167.31	103.9	94	10
PPT3	16.45	296.10	23.63	51.02	272.47	245.08	149.9	135.3	10.01
PPT4	19.25	346.5	6.19	27.32	340.31	319.18	185.9	174.7	6.2
PPT5	19.25	346.5	25.78	30.54	320.72	315.96	175.5	173.3	1.5
PPT7	16.45	296.1	35.34	52.17	260.76	243.93	143.6	134.7	6.5
PPT8	16.45	296.1	48.65	55.72	247.45	240.38	136.6	132.8	2.9
PPT9	13.65	195.30	85.69	103.81	109.61	91.49	63.3	53.6	16.5
PPT10	8.05	245.7	67.67	78.34	178.03	167.36	99.7	94	6

7.5.8 Factor of safety reduction and numerical validation

To further verify the failure mechanism, a numerical slope stability analysis was conducted using GeoStudio (Slope/W) – see Chapter 8.

7.5.9 Failure Mechanism and Theoretical Comparison

The observed failure behavior in M-T5 aligns with several well-established drawdown failure mechanisms:

1. Pore Pressure Lag Model (Wright and Duncan, 1987):
    - The observed failure behavior in M-T5 aligns with several well-established drawdown failure mechanisms. Specifically, the failure began during the drawdown phase, starting approximately on the fifth day and progressively increasing until the end of the drawdown on the 10th day. This progression of failure during the drawdown phase aligns with the Pore Pressure Lag Mode (Wright and Duncan, 1987), which suggests that failure may initiate during drawdown, driven by undrained conditions in the slope. The results from M-T5 confirm this behavior, highlighting the dynamic nature of pore pressure response and failure development as the drawdown progresses.
    - This is supported by the fact that PPT3 and PPT4 showed the highest strength reductions, where pore pressure lag was most significant.
2. Seepage-Induced Instability (Terzaghi, 1943):
    - Seepage forces acted outward, reducing the internal shear resistance of the soil.
    - The presence of visible erosion features and surface displacement confirms that seepage played a key role in the observed instability.
3. Skempton's Effective Stress Concept (Skempton, 1954):
    - The gradual decrease in effective stress due to delayed pore pressure dissipation explains why failure developed progressively rather than instantaneously.

These mechanisms reinforce the observation that the delay in pore pressure dissipation significantly reduced effective stress, leading to localised failure at mid-depth layers, which progressively worsened as the drawdown continued. This resulted in surface cracking towards the end of the drawdown phase.

7.6 Test M-T6

The M-T6 test was designed to investigate slope stability under controlled flooding, drawdown, and seasonal rainfall. M-T6 featured a gentle slope angle (29.7°) compared to M-T5 and M-T6r, to assess how reduced inclination influences stability. Additionally, M-T6 was constructed using a pre-consolidated soil block, whereas M-T5 was created through compaction. Pore Pressure Transducers (PPTs) were placed throughout the slope to monitor PWP distribution as illustrated in Figure 7-52. The locations of the PPTs are detailed in Table 7-6:

Table 7-6: PPTs coordinate in model scale.

PPT No.	X Coordinate (mm)	Y Coordinate (mm)
PPT1	261	155
PPT2	288	195
PPT3	357	235
PPT4	426	275
PPT5	536	275
PPT6	357	195
PPT7	426	235
PPT8	536	235
PPT9	357	155
PPT10	426	195
PPT11	357	115

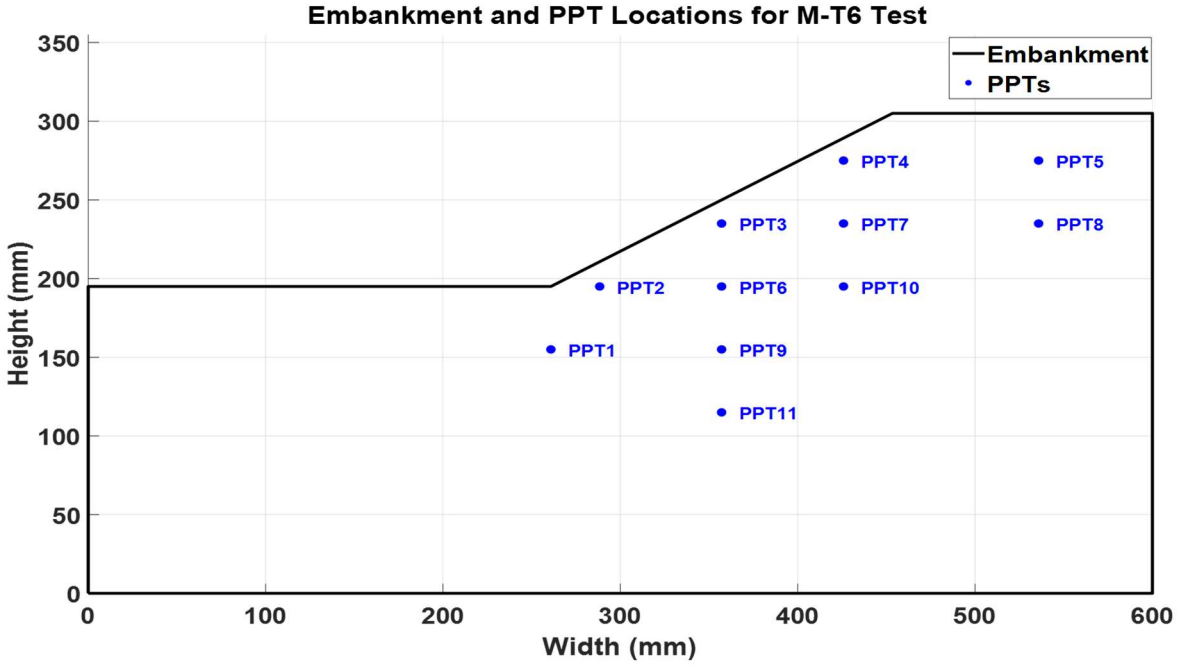


Figure 7-52 Slope dimension and PPTs locations.

7.6.1 Hydrostatic calibration during flood stage in M-T6 centrifuge test

A hydrostatic calibration was performed during the flood phase of test M-T6 to ensure accurate pore pressure measurements, with considerations for potential sensor saturation issues. Detailed calibration procedures and calculated PPT offsets are provided in Appendix A.3.1.

7.6.2 Gravity increase effect.

During the initial phase of the centrifuge test M-T6, the sensors indicated an elevation in pore water pressure (PWP). However, the magnitude of this response was lower compared to the observations in the M-T5 test. The softer reaction can be mainly attributed to the sensors not being completely saturated at the start of the test due them being transferred from the previous test without resaturation. The sensors located near the slope surface, namely PPT1, PPT2, and PPT3, displayed the highest initial responses. The final response in pore water pressure results from an acceleration in gravitational forces to 70g, subsequently followed by the consolidation of the soil. The consolidation phase begins at 1440 seconds and concludes at 3600 seconds during the test, as depicted in Figure 7-53.

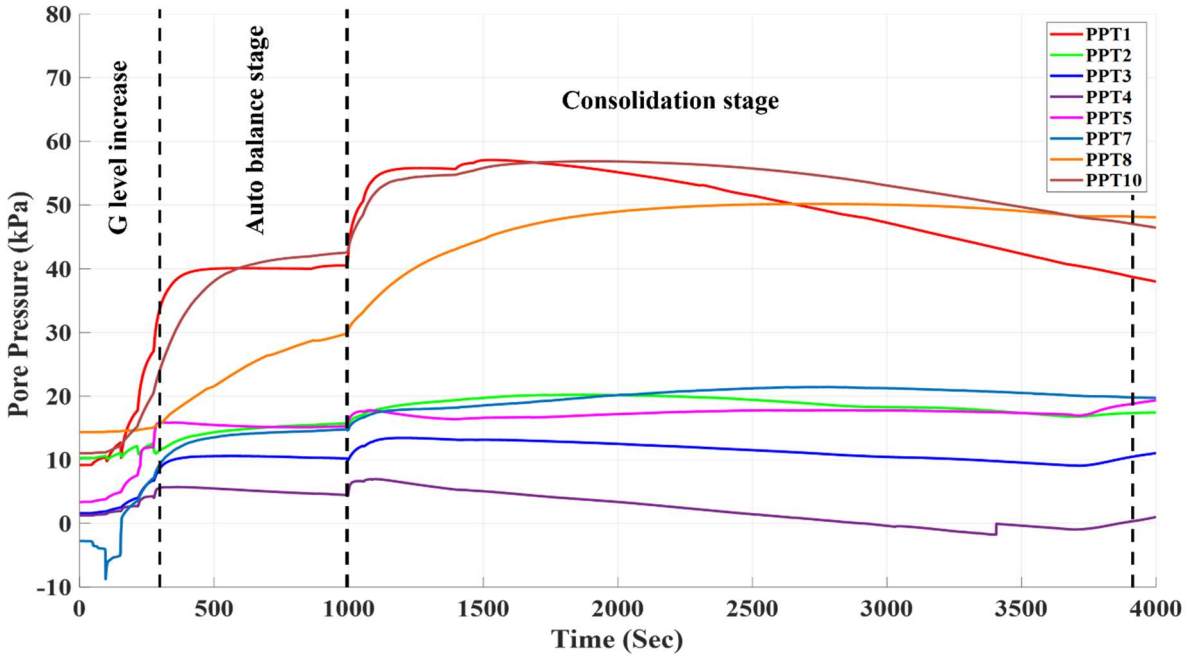


Figure 7-53 Changes in pore water pressure during the consolidation stage of the M-T6 test.

During the consolidation phase, there is a noticeable decrease in pore water pressure (PWP) values observed across all sensors. Following an initial decline, the pressures in most PPTs

begin to stabilise. At the end of the consolidation period, most PPTs demonstrate stable PWP levels, suggesting that the soil has largely reached a state of equilibrium under the imposed load.

Analysis of PWP distribution:

Figure 7-54 and Figure 7-55 show the pore water pressure at the end of the auto-balance stage and the corresponding locations of these PPTs in the slope model. Three PPTs (6, 9, and 11) were identified as malfunctioning during the consolidation stage and were subsequently excluded from further analysis. The remaining PPTs showed reliable readings, enabling the generation of PWP contours. From the remaining PPTs, the contours of pore pressure follow the slope, in a similar manner to M-T5. PWPs are seen to be slightly positive at the surface during auto balance, but then pore pressure redistributes during consolidation so that the pore pressure is near zero at the slope surface. It may also be that the pore pressures are slow to respond due to their poor saturation so that they read "correct" values at the end of the consolidation phase.

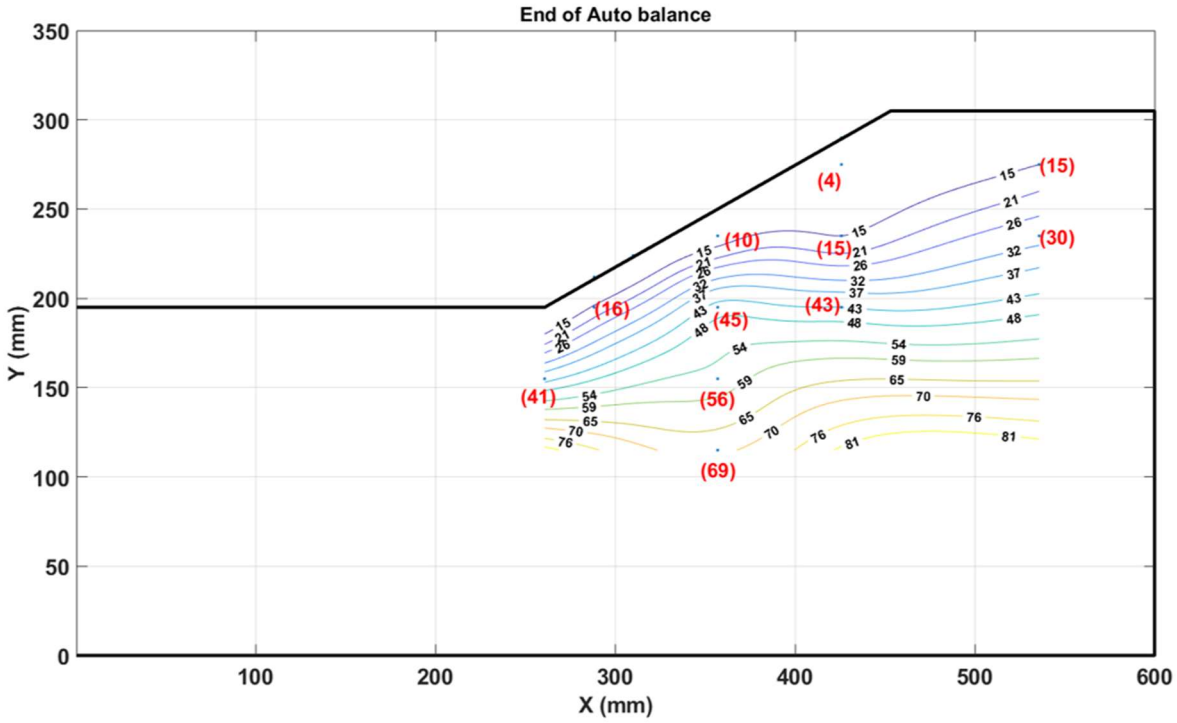


Figure 7-54 Pore water pressures at the end of auto balance phase (M-T6) test.

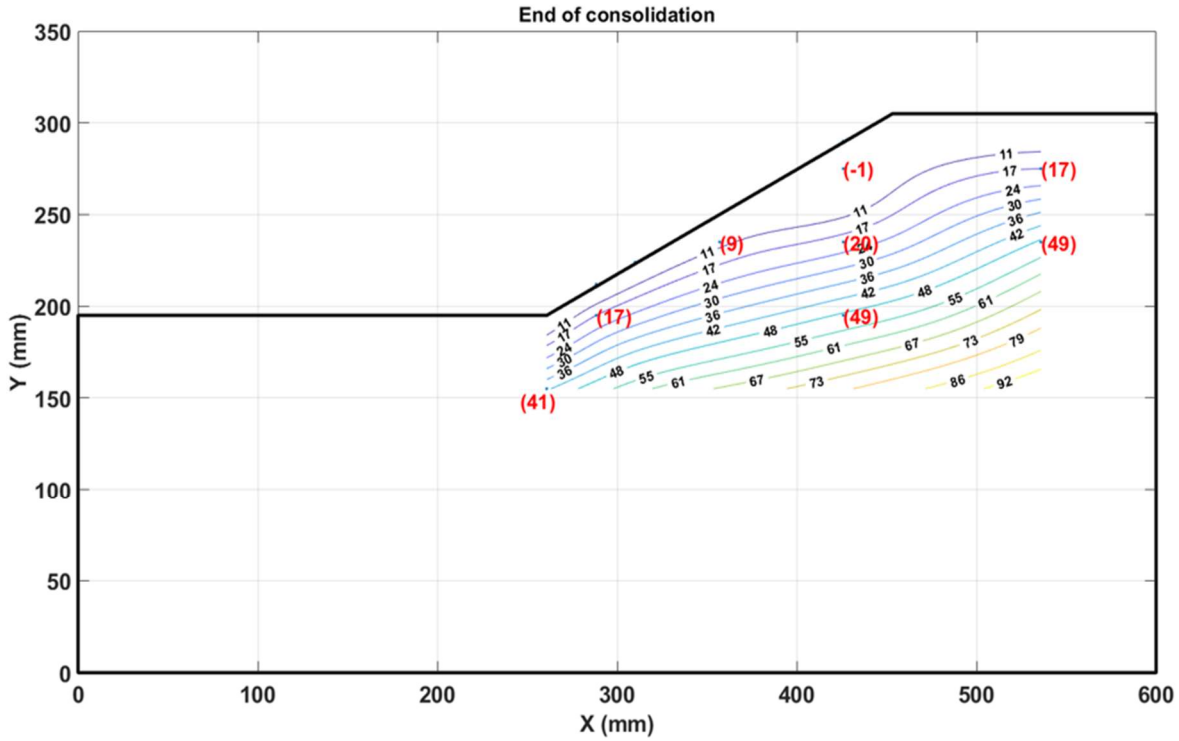


Figure 7-55 Pore water pressure contours at the end of consolidation phase (M-T6 test).

PWP observations across different stages and spins in the M-T6 test.

The pore water pressure (PWP) data during the consolidation, Winter 1, and Summer 1 stages are presented in Figure 7-56 . Some sensors such as PPT1, PPT8 and PPT10 show a clear initial increase in pore pressure at the start of consolidation stage, followed by a rapid decline during the Winter and Summer stages, without pronounced cyclic fluctuations typically associated with direct infiltration responses. The lack of clear cyclic responses is likely due to incomplete initial saturation of these sensors. Sensors (e.g., PPT3, PPT4, and PPT5) show a similar pattern, though show a more gradual decline during summer 1 and consolidation stages.

Figure 7-57 shows the PWP and RH data recorded during the second spin in the M-T6 test, encompassing Winter 2, Summer 2, and Winter 3 phase. During the auto-balance stage, PWP sensors stabilise, and RH decreases before equilibrating. In Winter 2, despite cyclic rainfall reflected in RH, PWP sensors show no distinct cyclic fluctuations; crest and surface sensors (PPT2, PPT3, PPT4, PPT5, PPT7) remain stable, while deeper sensors (PPT1, PPT10)

gradually decline, indicating drainage rather than direct infiltration. In Summer 2, PWP decreases more slowly than in Summer 1, with prolonged drying near the toe (PPT1, PPT2) and residual moisture retention. At the start of Winter 3, RH fluctuations persist, but PWP sensors remain stable or decline gradually, indicating limited infiltration response. Overall, cumulative water retention increases residual PWP, especially in deeper regions and near toe.

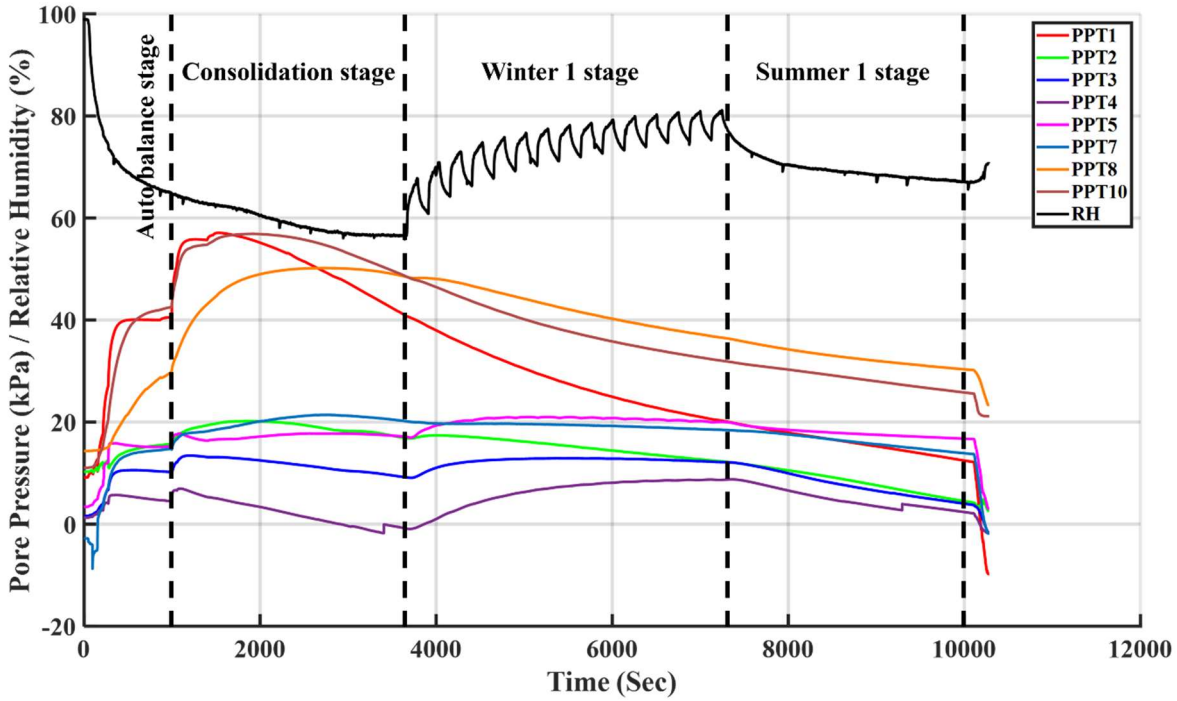


Figure 7-56 Variation of pore water pressure (PWP) and relative humidity (RH) during the first spin in the M-T6 test.

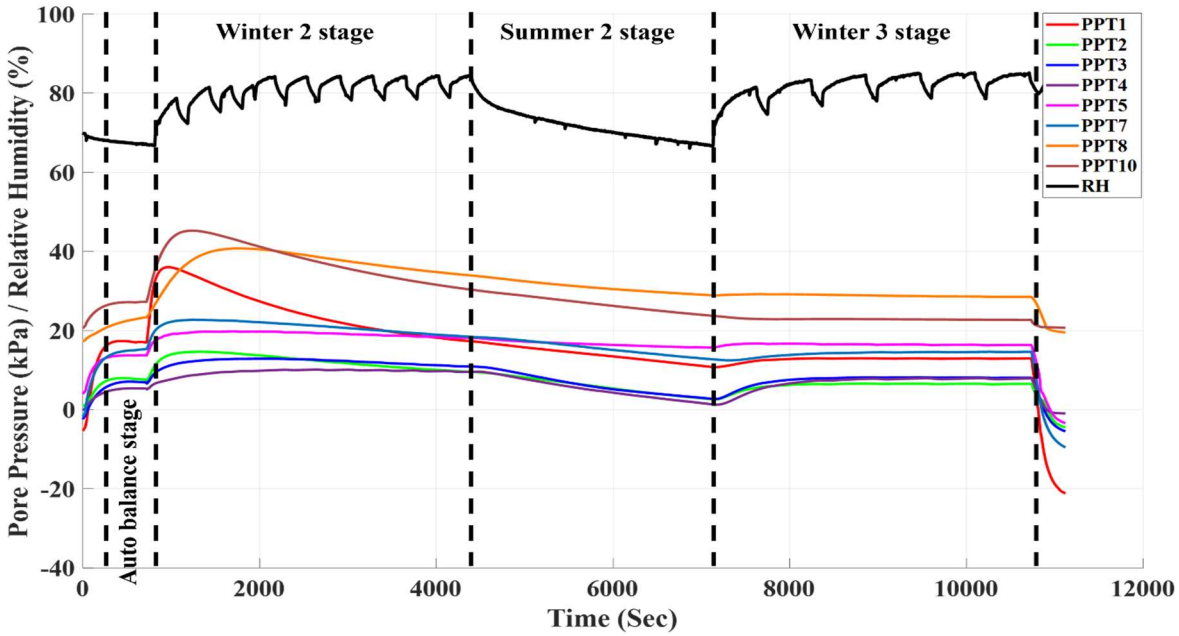


Figure 7-57 variation of pore water pressure (PWP) and relative humidity (RH) during the second spin in the M-T6 test.

Figure 7-58 shows the PWP and RH data recorded during the third spin, focusing on the flooding and drawdown stages. This test was conducted two days after the second spin. During the auto-balance stage, everything proceeded as expected, similar to other tests, with no issues observed. The g-level was maintained at 70 g to stabilise the model during this phase. To initiate the flooding stage, the valve was operated to produce continuous rainfall. However, the valve failed to open, requiring the g-level to be reduced to 50 g. Once the valve was successfully opened, the g-level was spun back up to 70 g to continue the flooding stage. Flood 1 caused a sharp rise in PWP across all sensors, particularly those near the toe (e.g., PPT1 and PPT2) and mid-slope (e.g., PPT3 and PPT10). Sensors near the crest (e.g., PPT4 and PPT5) showed slightly delayed responses due to the time required for water redistribution across the slope. During the drawdown stage, the g-level was again reduced to 50 g to operate the valve before spinning the model back up to 70 g. The drawdown phase resulted in a rapid decline in PWP across all sensors. The drawdown took approximately 3 minutes (model scale) to reach the toe surface.

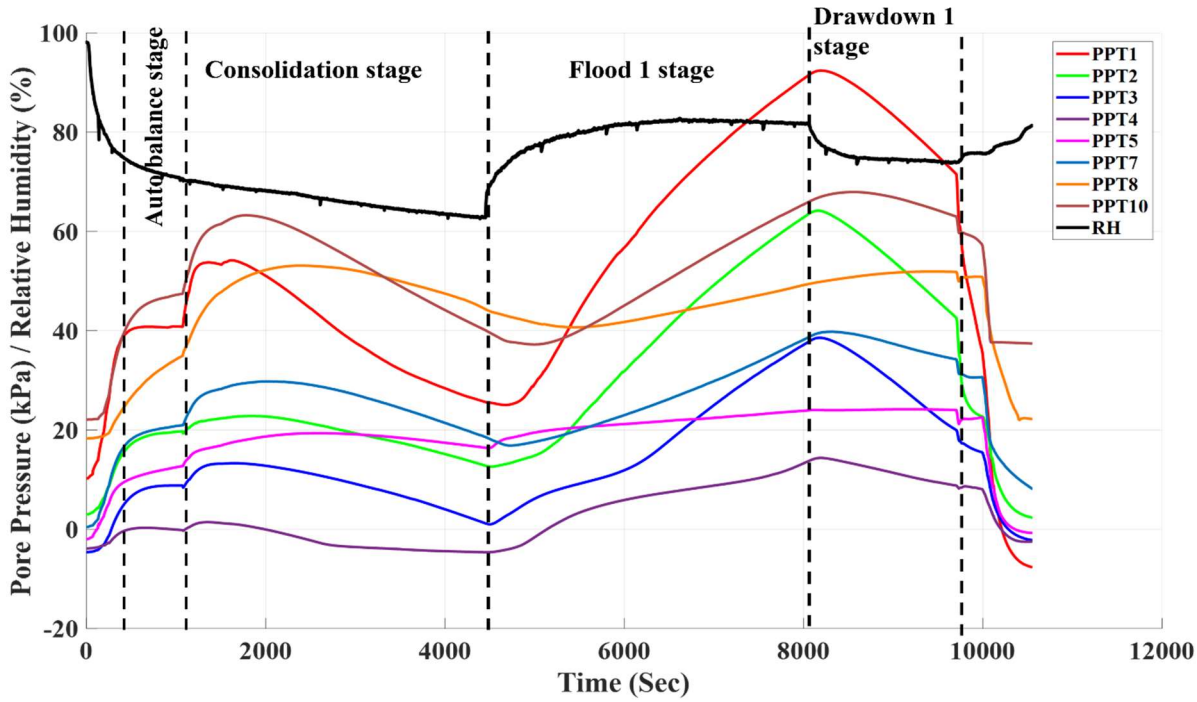


Figure 7-58 Variation of pore water pressure (PWP) and relative humidity (RH) during flood 1 and drawdown stages in the third spin of the M-T6 test.

Despite the operational challenges with the valve, the PWP behaviour during flooding and drawdown stages showed consistent trends, with sharp rises during flooding followed by steep declines during drawdown. The cyclic nature of the PWP fluctuations and the differences in response times across the slope highlight the influence of sensor location and slope hydrodynamics. Figure 7-59 shows the PWP and RH data recorded during the last spin of the M-T6 test, focusing on Flood 2, Flood 3, and the associated drawdown stages (Drawdown 2 and Drawdown 3). This phase aimed to simulate the combined effects of flooding and rapid drawdown under successive conditions. During the auto-balance stage, the g-level was maintained at 70 g, and initial stabilisation of PWP sensors was observed, consistent with earlier phases of the test.

Flood 2 triggered a sharp PWP increase, with the highest and fastest response observed at the toe (PPT1, PPT2), while mid-slope sensors (PPT3, PPT7 and PPT8) showed a moderate rise. Crest sensors (PPT4, PPT5) exhibited a delayed but gradual increase, reflecting the time required for water infiltration and redistribution across the slope. Drawdown 2 caused a sharp PWP drop, though valve issues required reducing g-level to 50 g before resuming at 70 g. Crest sensors exhibited slower drainage, and drawdown reached the toe in ~3 minutes (model scale). Flood 3 followed a similar pattern. Drawdown 3 led to a steep PWP drop, particularly at the

toe and mid-slope, indicating effective drainage. Despite ongoing valve issues, requiring adjustments in g-level, PWP patterns remained consistent, with sharp increases during floods and steep declines during drawdowns, confirming the slope's rapid drainage response.

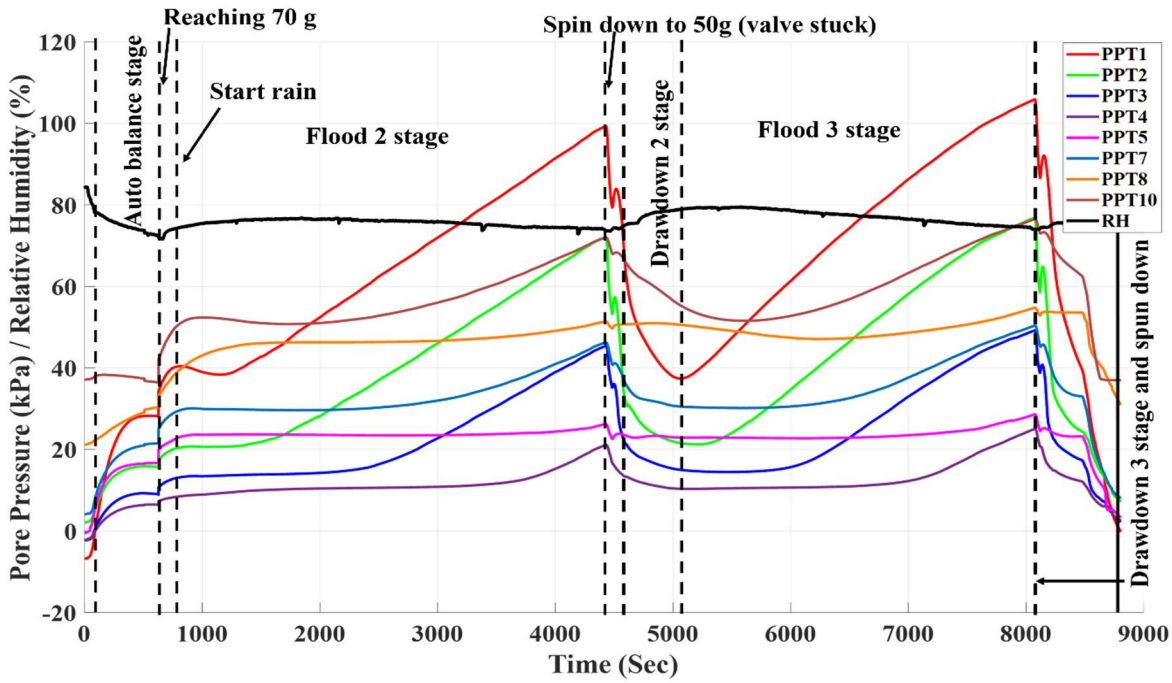


Figure 7-59 Variation of Pore Water Pressure (PWP) and Relative Humidity (RH) during Flood 2, Flood 3, and associated Drawdown stages in the Final Spin of the M-T6 Test.

Test M-T6: Deformations

During the auto balance phase of test M-T6, displacement was more pronounced in the upper slope, particularly near the crest, indicating potential instability. Shear strain reached up to 3% in deeper regions below the crest, while volumetric strain showed contraction near the base (-2%) and slight expansion near the crest (1%). After reaching 70g, the model equilibrated for 40 minutes, during which minimal displacement and low strain values were observed.

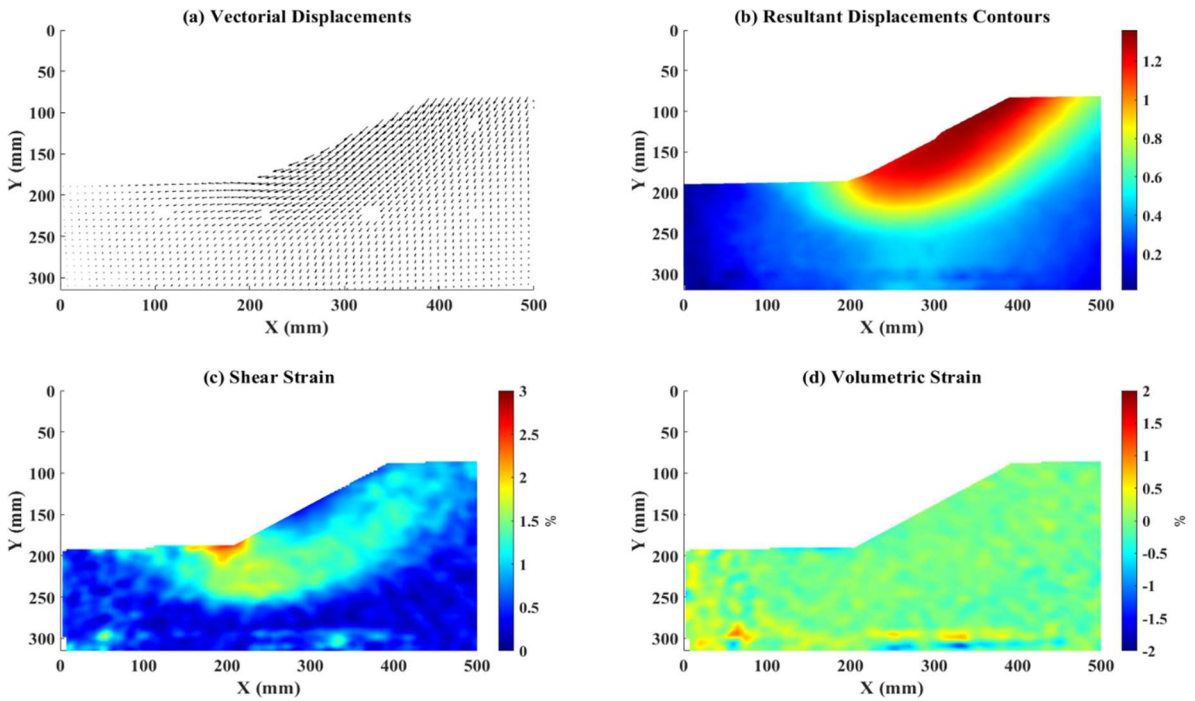


Figure 7-60 Displacements and strain at the end of auto balance phase (M-T6 test).

7.6.3 Seasonal cycle effect for M-T6 test.

Throughout the seasonal cycles in the M-T6 test, the slope exhibited high stability with no significant deformation observed during the first and second summer phases, indicating resilience under drying conditions. Minor soil movements and strain variations were noted at the end of the first and second winters, though these were limited and did not affect overall slope stability, as detailed in Appendix 11.3.3. Similarly, the slope remained stable at the end of Winter 3, despite prolonged wetting, demonstrating its capacity to withstand repeated seasonal climate variations without substantial deformation.

7.6.4 Flooding and drawdown effects for M-T6.

For the M-T6 test, the flooding and drawdown cycles presented some challenges and unique characteristics across the different flood events. The flooding and drawdown times in the model scale:

Flood 1: This flood event took approximately 60 minutes to reach the crest of the slope, which indicates a steady infiltration process. However, a persistent issue with the solenoid valve became apparent. The valve malfunctioned under the high-g conditions (70 g), requiring the g-level to be reduced to 50 g to open or close the valve properly. This prolonged the flooding process, and the subsequent drawdown took significantly longer than anticipated, around 27 minutes to reach the surface of the toe. This unusually long drawdown time suggests a possible blockage or drainage issue that hindered efficient water removal from the slope.

Flood 2: During the second flood event, the water level rose above the crest, taking approximately 52 minutes. Once again, the solenoid valve issue persisted, necessitating the reduction of the g-level from 70 to 50 g. The drawdown was completed in 2.2 minutes, a more expected duration in comparison to the extended time observed in Flood 1. This suggests that the drainage system was functioning better for Flood 2.

Flood 3: For the third flood, the water took around 46 minutes to reach the crest, a faster rate than in the previous floods. The drawdown, similar to Flood 2, occurred in a shorter and expected timeframe, taking approximately 2.3 minutes to complete. Each time the g-level adjustment from 70 to 50 g was necessary to operate the valve effectively.

The variability in flooding and drawdown times reflects both operational challenges (with the valve under high-g conditions) and potential environmental factors affecting drainage efficiency, particularly in the case of Flood 1, where drawdown was unexpectedly delayed.

Soil deformation

Throughout the flood and drawdown phases in the M-T6 test, the slope generally remained stable during flooding, with no significant deformation observed in Floods 1, 2, or 3. In contrast, drawdown phases triggered noticeable soil movement. During Drawdown 1, displacement was primarily directed downslope, with the highest movement (0.1–0.25 mm) near the toe and shear strain (0.5%–1.5%) concentrated in the mid to lower slope; volumetric strain showed contraction near the toe and slight swelling elsewhere. Drawdown 2 caused the most significant deformation at the crest and upper slope, with displacements of 0.5–0.7 mm, shear strain up to 2%, and volumetric expansion in shallow areas due to water loss. Detailed analysis for each phase is provided in Appendix 11.3.4.

Soil deformation at the end of the Drawdown 3 for M-T6.

At the end of the third drawdown in the M-T6 test, the highest displacement (up to 0.3 mm) occurred near the crest, with moderate movement downslope. Shear strain (1.5%) was concentrated under the crest and mid-slope, while volumetric strain ranged from -1% (compression) near the toe to +1% (expansion) near the crest, indicating localized deformation due to the rapid reduction in water levels. Figure 7-61 presents the PIV analysis at the end of the third drawdown in the M-T6 test.

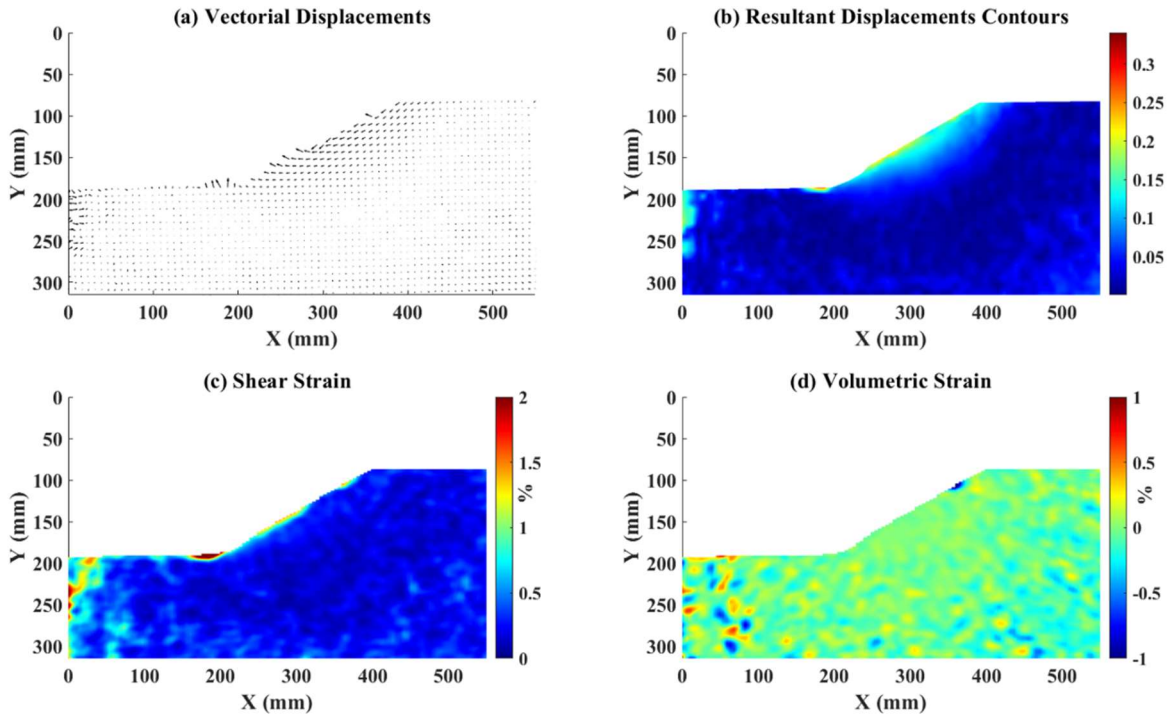


Figure 7-61 Soil deformation analysis at the end of the Drawdown 3 for M-T6 test

Pore water pressure analysis at the end of the Drawdown 3 for the M-T6 test.

At the end of the third drawdown in the M-T6 test, pore water pressure (PWP) significantly decreased at the crest (14–24 kPa) due to rapid drainage, while mid-slope values ranged from 31–36 kPa. Higher PWP persisted at the lower slope and toe (57–86 kPa), indicating slower drainage in these regions. The data suggests a gradual water table decline, with faster drainage near the surface and slower drainage at the slope base. The correlation between PWP and PIV data (Figure 7-62) shows that pore pressure reduction during drawdown contributes to slope deformation, with high displacement occurring in areas of reduced PWP. Elevated pore

pressures in the mid-slope coincide with significant shear and volumetric strain, indicating internal stress buildup that may lead to instability

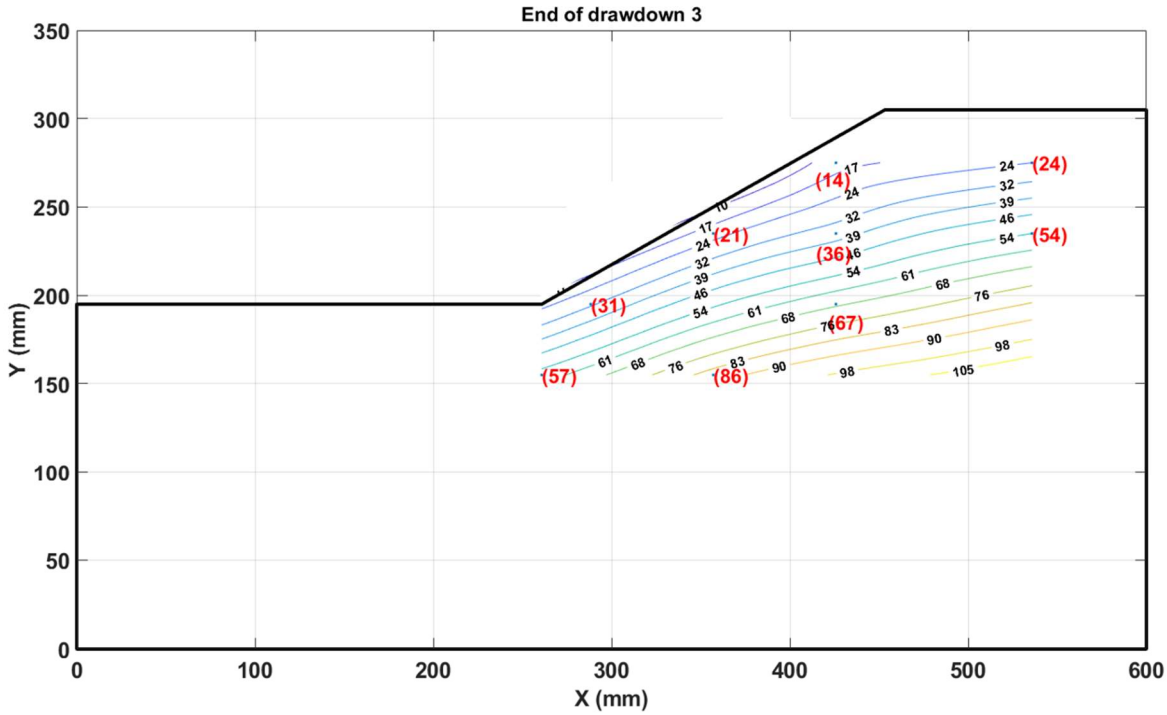


Figure 7-62 Pore water pressure distribution at the end of Drawdown 3 in M-T6 test.

7.6.5 Stability interpretation and theoretical insights

In the M-T6 test, failure was not visually observed during drawdown. Only minor movement was detected at the end of drawdown, indicating that while significant instability did not occur, changes in stress and pore pressure dynamics influenced the slope behaviour. The significant reduction in PWP at PPT1, PPT2, PPT3, and PPT11 suggests drainage and reduction in excess pore pressures, which would generally increase effective stress and stabilise the slope. Despite these changes, no major slope failure was detected, suggesting that the drawdown rate or initial slope conditions may have prevented significant instability. The minor movement at the end of drawdown could be attributed to a temporary imbalance between effective stress recovery and residual seepage forces.

7.7 Test M-T6r.

The embankment M-T6r was removed from the centrifuge and modified to achieve a revised slope angle of 33 degrees. One of the PPTs that was positioned beneath the embankment's toe

had to be excavated and removed due to the higher slope angle. Consequently, certain PPTs locations in the toe area have shifted to different positions due to the new slope design as shown in the Figure 7-63. The new locations of the (PPTs) in the M-T6e are provided in Table 7-7.

Table 7-7: PPTs coordinates in model scale.

PPT No.	X Coordinate (mm)	Y Coordinate (mm)
PPT1	260.85	155
PPT2	288.35	185
PPT3	357.10	235
PPT4	425.85	275
PPT5	535.85	275
PPT6	357.10	195
PPT7	425.85	235
PPT8	535.85	235
PPT9	357.10	155
PPT10	425.85	195
PPT11	357.10	115

Regarding the M-T6r test, there is an increase in pore water pressure in all PPTs from time 0 to 500 seconds, specifically in PPT1, PPT2, PPT8, and PPT9 as shown in the Figure 7-64. As the test progresses, certain PPTs, particularly PPT4 through PPT7 and PPT10, start showing a tendency towards stability. There are minor fluctuations after the consolidation ends, and some PPTs still show minor fluctuations in pressure, indicating possible variations in saturation levels.

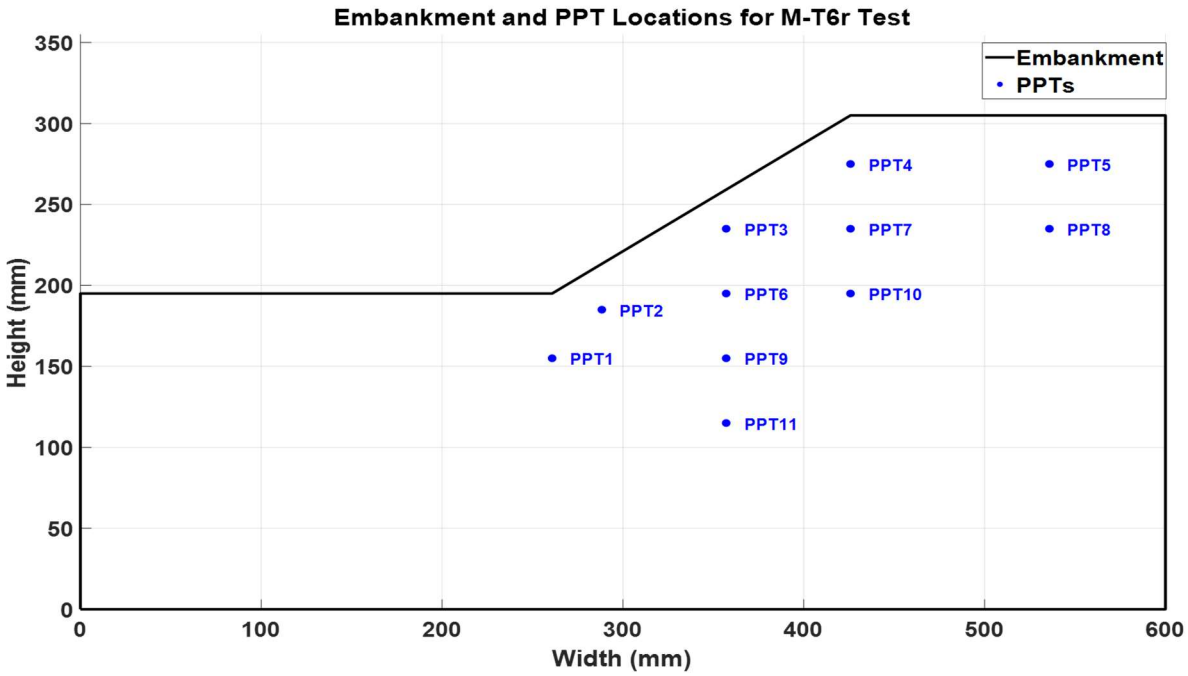


Figure 7-63 Slope dimension and PPTs locations.

Hydrostatic calibration during flood stage in M-T6r centrifuge test.

The hydrostatic calibration during the flood stage in the M-T6r test followed the same methodology as M-T6, ensuring accurate PWP measurements by accounting for PPT offsets. Theoretical PWP values were calculated based on radial distance, water height, and centrifuge velocity to replicate prototype conditions. Detailed calibration procedures are provided in Appendix section A.4.1.

7.7.1 Gravity increase effect

During the initial stages of the M-T6r centrifuge test, a significant increase in gravitational forces (up to 70 g) was applied to simulate prototype conditions. This rise immediately changed the pore water pressures (PWP) across the different sensors (PPT1 to PPT11). The gravity increases in the M-T6r test produced a comparable but slightly softer response in PWP to that seen in the M-T6 test, mainly due to incomplete saturation in the sensors. The stabilisation of PWP levels towards the end of the consolidation phase further indicates that the soil model had reached equilibrium phase.

Key observations:

As gravity increased in the M-T6r test, PWP rose across most sensors, though some showed a softer increase due to incomplete saturation, as illustrated by Figure 7-64 . The consolidation phase (1440–3700 seconds) led to a significant drop in PWP, particularly in PPT1, PPT9, PPT10, and PPT11, as excess water dissipated and the soil stabilised. After consolidation, most sensors reached equilibrium, with minor fluctuations in PPT11 likely due to its proximity to drainage paths.

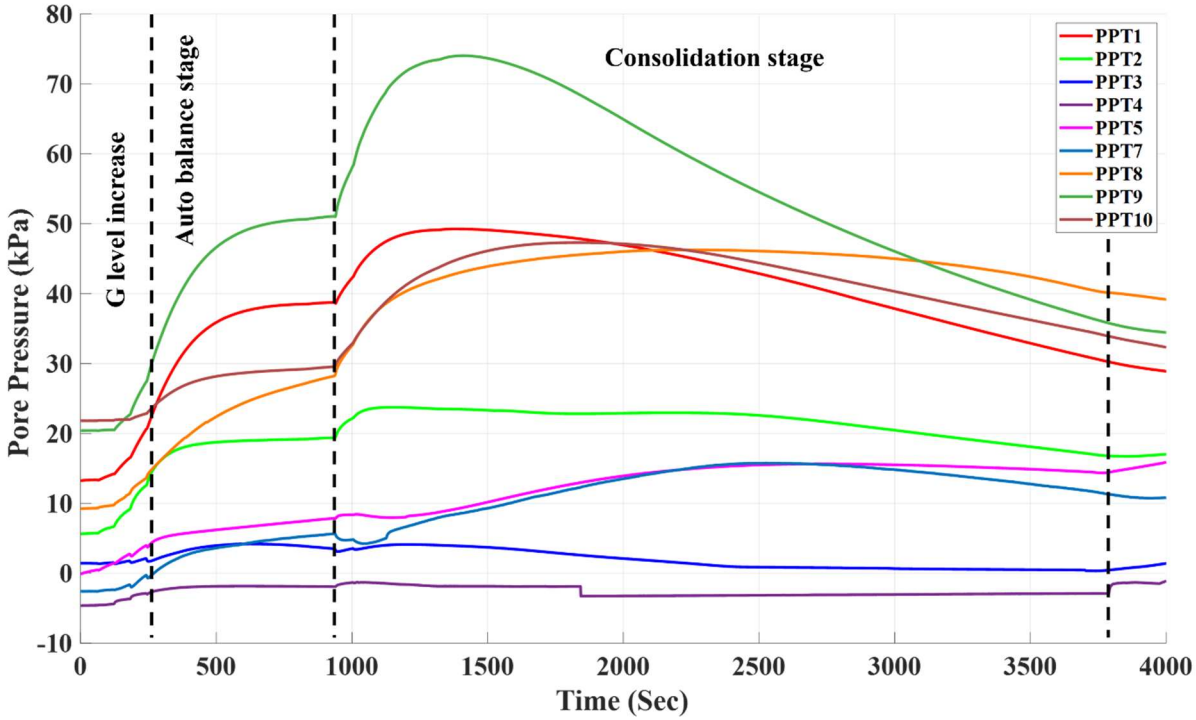


Figure 7-64 Changes in pore water pressure during the consolidation stage of the M-T6r test.

The contours of PWP are shown at the end of auto balance in Figure 7-65 and the end of consolidation in Figure 7-66 . At the end of auto balance, high PWP (70–73 kPa) was observed at the slope toe near PPT11 due to the overlying soil weight, while moderate PWP (26–50 kPa) occurred in the mid-slope (PPT6, PPT9, PPT10). The crest (PPT4, PPT5, PPT8) showed low PWP (~-2 kPa), reflecting drainage. By the end of consolidation, PWP significantly decreased across the slope, particularly at depth, with PPT1 and PPT9 stabilizing at 30–36 kPa. Mid-slope PWP also dropped (31–44 kPa), indicating substantial consolidation and soil stabilisation.

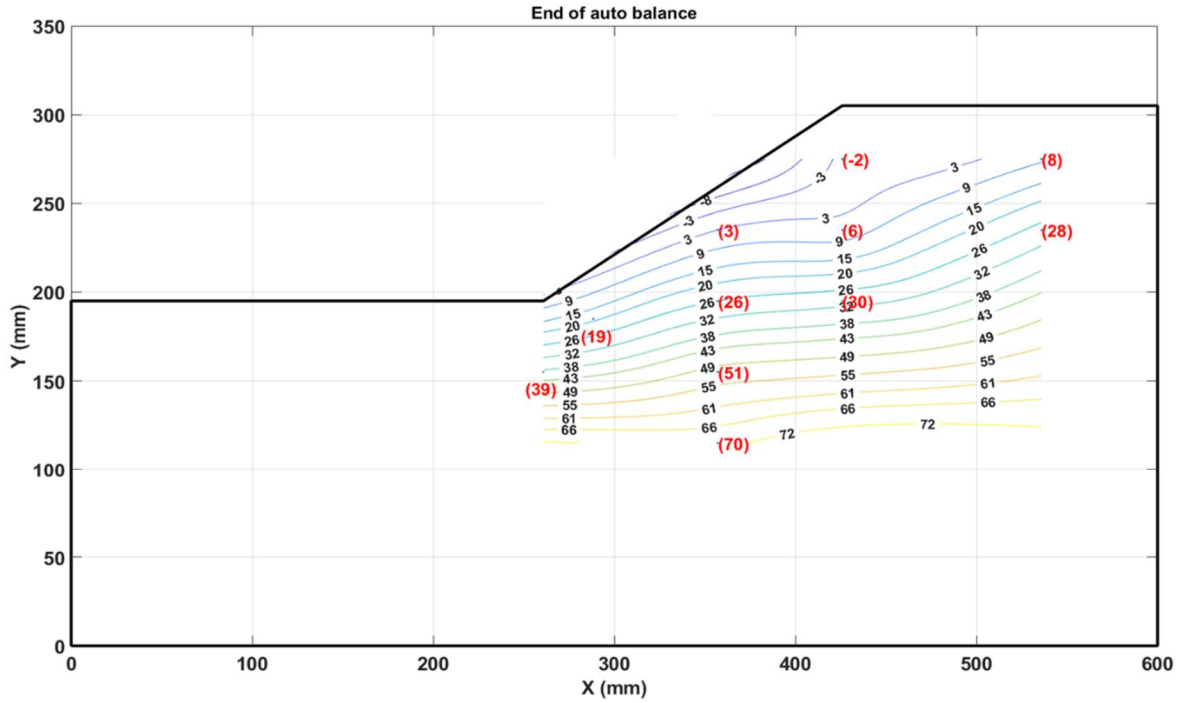


Figure 7-65 The contours of (PWP) during auto balance phase (M-T6r) test.

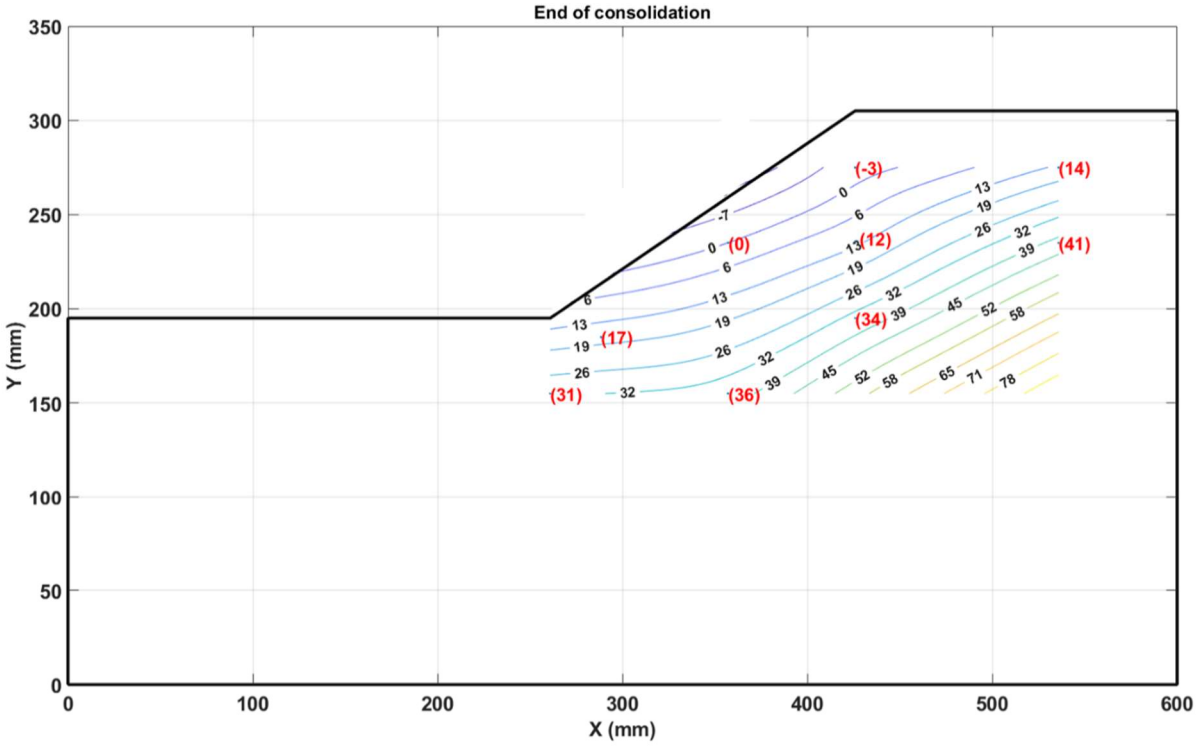


Figure 7-66 The contours of (PWP) during consolidation phase (M-T6r) test.

Figure 7-67 shows the PWP and RH data recorded during the first spin of the M-T6r test. The test was conducted with a redesigned slope geometry at 1:1.5 (33.7°) to recreate the conditions of the M-T6 test, which did not lead to slope failure. During the auto balance stage, everything proceeded as expected, with no observed issues. The g-level was maintained at 70 g to stabilise the model and ensure proper balance. PWP sensors showed slight initial adjustments, indicating the redistribution of pore pressure within the slope, with a piezometric line (PWP equal zero) exiting the toe of the slope due to the time spent off the centrifuge. RH stabilised during this stage as atmospheric conditions within the chamber reached equilibrium.

During Winter 1, alternating rainfall and drying cycles (1 week of rain, 1 week of no rain) resulted in noticeable cyclic fluctuations in PWP in some of the sensors. In the Summer 1 stage, the absence of rainfall caused PWP to gradually decrease across all sensors, reflecting drainage and drying effects. Sensors near the crest showed faster decreases, consistent with more efficient drainage and loss of moisture in the upper layers of the slope, while sensors near the toe exhibited slower responses due to water retention and slower drainage at deeper levels. Overall, the results from the first spin of the M-T6r test highlight consistent trends in PWP and RH behaviour, with cyclic responses to rainfall during winter and gradual drainage during summer. These observations set the baseline for further stages in the M-T6r test.

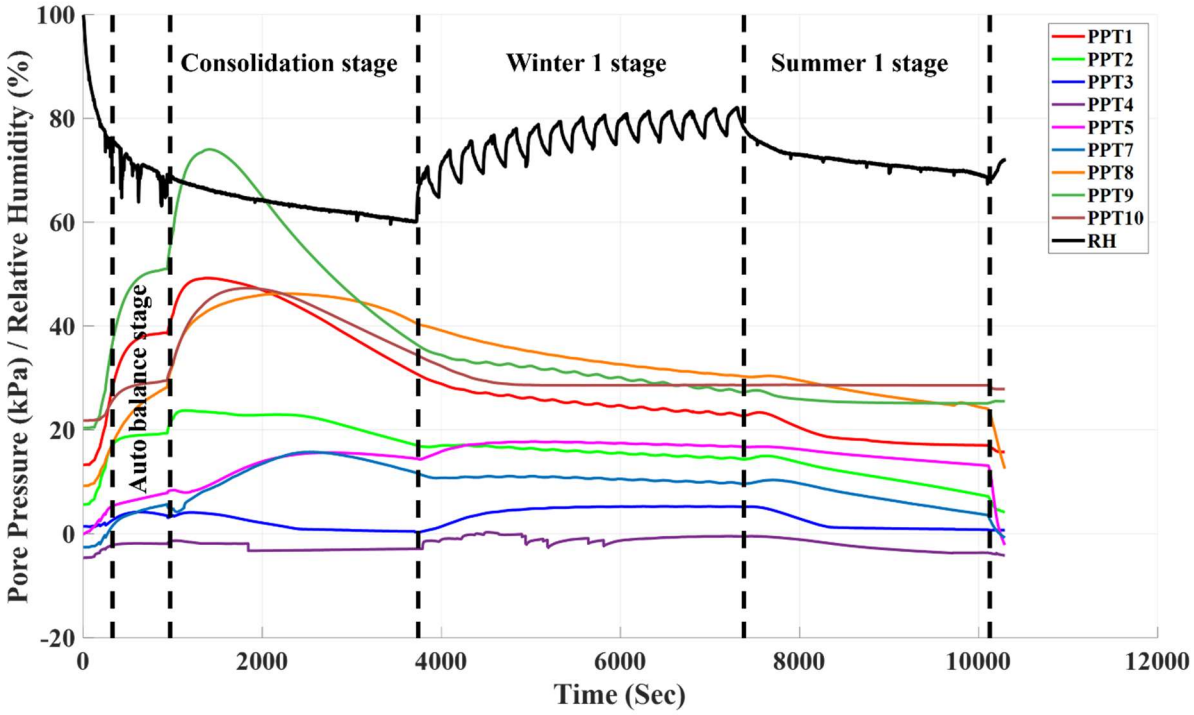


Figure 7-67 Pore Water Pressure (PWP) and Relative Humidity (RH) Variations During the First Spin of the M-T6r Test.

Figure 7-68 shows the PWP and RH data recorded during the second spin of the M-T6r test. This spin encompasses the Winter 2, Summer 2, and the Winter 3 stages. The test continued to simulate the cyclic effects of rainfall and drying on slope stability under redesigned slope geometry (1:1.5).

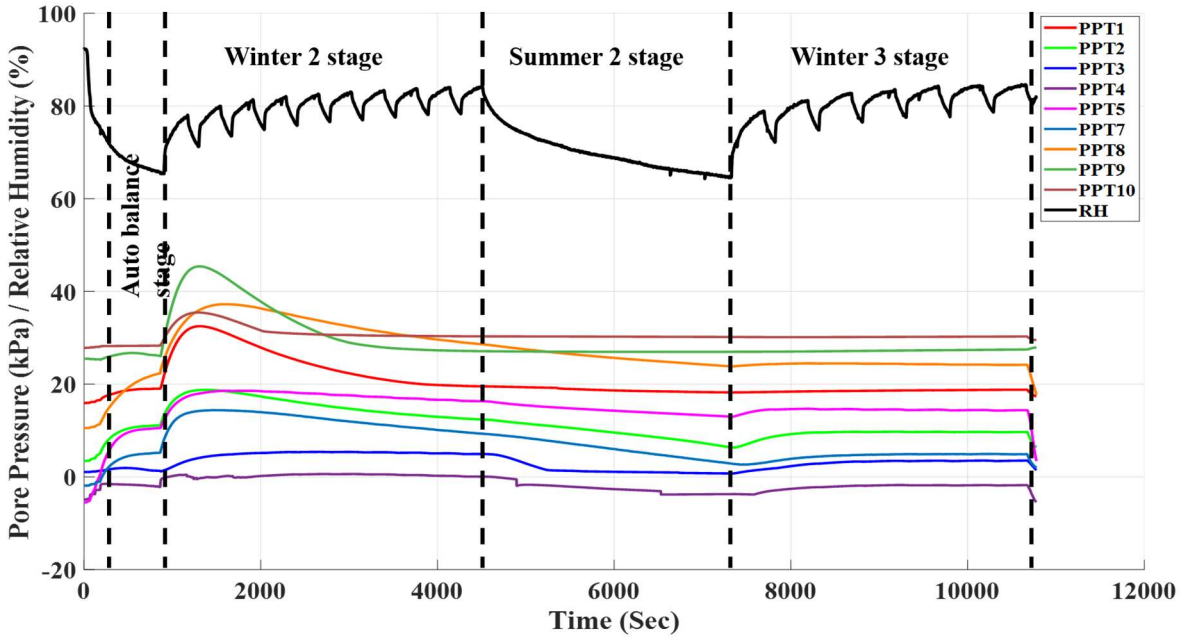


Figure 7-68 PWP and RH variations during the second spin of the M-T6r test.

In the Winter 2 stage, alternating rainfall and drying cycles (2 weeks of rain followed by 1 week of no rain) resulted in periodic fluctuations in PWP across the sensors. Sensors near the toe (e.g., PPT1 and PPT9) exhibited sharper cyclic changes due to their proximity to surface infiltration, while sensors near the crest (e.g., PPT5 and PPT7) responded more gradually, reflecting delayed water redistribution and accumulation. During the Summer 2 stage, the absence of rainfall caused a gradual decline in PWP across all sensors. Sensors near the surface of the soil showed faster decreases, consistent with more effective drainage in the upper layers of the slope. In contrast, sensors near the toe exhibited slower responses, likely due to residual moisture retention and slower drainage in the lower slope regions. The Winter 3 stage resumed the alternating rainfall and drying pattern. PWP sensors displayed cyclic variations similar to those observed in Winter 2, with higher magnitude fluctuations near the crest and dampened responses near the toe. RH followed the expected pattern, increasing during rainfall and stabilising during drying periods. The second spin demonstrated consistent behaviour, with the slope responding predictably to the applied climate scenario. The observed differences in PWP fluctuations across the slope highlight the impact of sensor location and depth on pore pressure redistribution.

Figure 7-69 shows the PWP and RH data recorded during the third spin in the next day of the M-T6r test, which aimed to apply the flood-drawdown scenario. Unfortunately, the test encountered significant challenges due to a suspected leak issue. During the initial phase, the model was spun at 70 g as per the planned procedure to stabilise the slope for the flood scenario. However, when attempting to create Flood 1, the water level rose slowly, indicating a potential issue. To address this, the g-level was reduced to 20 g to investigate the problem and facilitate water infiltration. Despite these efforts, the water level continued to rise very slowly. In an attempt to resolve the issue, the test was stopped, and the system was spun down to 1 g. The setup was inspected for leaks, and some bolts were re-tightened to address possible sources of leakage. After the adjustments, the test was resumed by starting rainfall at 20 g. Once rainfall commenced, the g-level was increased back to 70 g, but the issue persisted. The water level continued to rise too slowly, even when the g-level was reduced again to 20 g. Due to the recurring issue and the inability to achieve the desired flood scenario, the test was ultimately stopped. The suspected leak and subsequent operational difficulties prevented the successful completion of the flood-drawdown scenario during this spin.

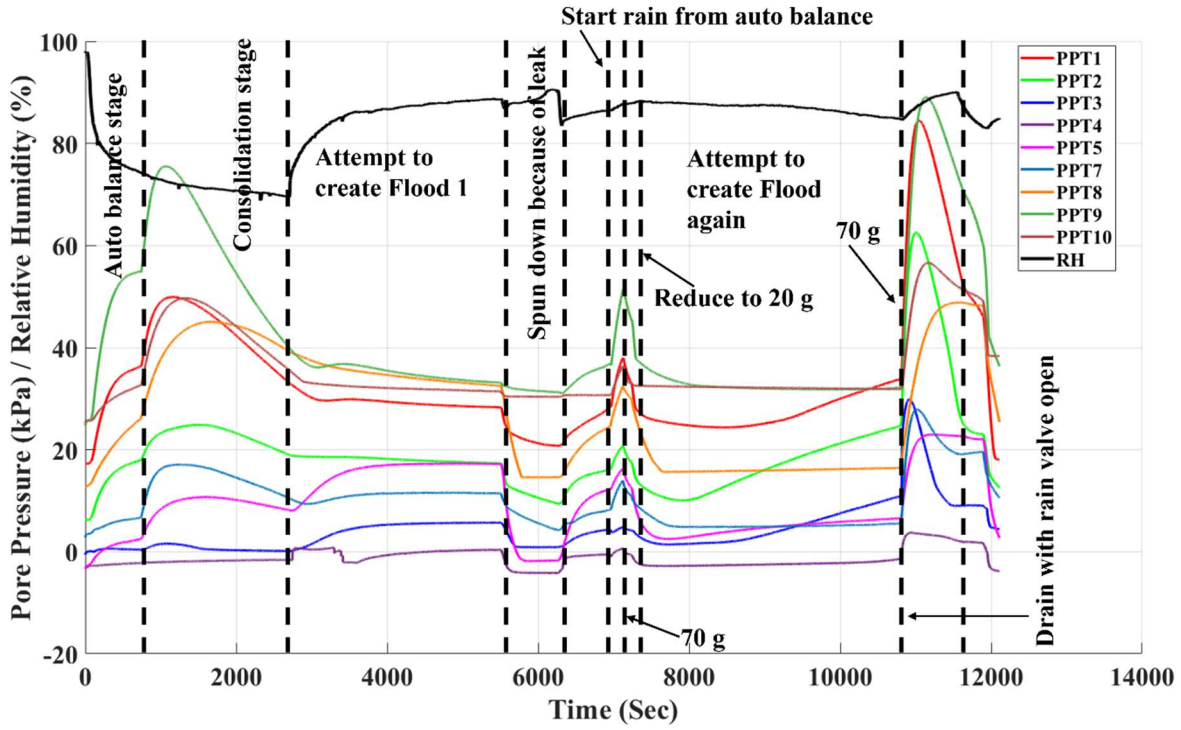


Figure 7-69 Pore water pressure (PWP) and relative humidity (RH) variations during the Third Spin of the M-T6r test with flood-drawdown attempt.

Figure 7-70 shows the PWP and RH data recorded during the final spin of the M-T6r test, focusing on the multiple flooding and drawdown scenarios. This spin was conducted after addressing the earlier operational challenges to further simulate flooding and rapid drawdown stages.

Flood 1: Rainfall began during the auto-balance stage to initiate Flood 1. However, the water level only reached the mid-slope and did not rise to the crest, indicating a leak issue at 70 g. To resolve this, the model was spun down, and the water level was increased at 1 g before spinning back up to 70 g. The model was then left spinning for approximately 27 minutes before initiating the drawdown. This approach might ensure sufficient infiltration and water redistribution before the drawdown stage.

Drawdown 1: The first drawdown phase followed Flood 1, resulting in a sharp and rapid decrease in PWP across all sensors, as seen in the graph. The drawdown behaviour was consistent with expectations, reflecting effective drainage mechanisms.

Floods 2, 3, and 4: For subsequent floods, rainfall was applied at 1 g to increase the water level, following a similar protocol to Flood 1. Once the desired water level was reached, the g-level was spun back up to 70 g, and the model was left spinning for shorter durations compared to Flood 1—approximately 12 minutes each time. Each flood stage resulted in sharp decreases in PWP across all sensors, as observed in the figure. This behaviour is consistent with the results from the ground-level M-T3 test. Sensors near the crest (e.g., PPT4 and PPT5) and mid-slope (e.g., PPT3 and PPT10) displayed the sharpest decreases due to the rapid infiltration and redistribution of water caused by the applied rainfall. Sensors near the toe (e.g., PPT1 and PPT2) exhibited similar sharp decreases, reflecting the uniform impact of the flooding event across the slope. This behaviour differs from typical flood-induced increases in PWP, suggesting rapid drainage at depth.

Drawdowns 2, 3, and 4: After each flooding phase, drawdown stages were initiated. Each drawdown phase showed steep decreases in PWP across all sensors. The drawdown took 3 minutes on the model scale to reach the surface of the toe. This final spin demonstrated consistent behaviour during the flood-drawdown scenarios. The protocol adjustments spinning down to 1 g to address infiltration limitations were effective in achieving the desired water levels for each flood stage, despite the initial challenges with Flood 1.

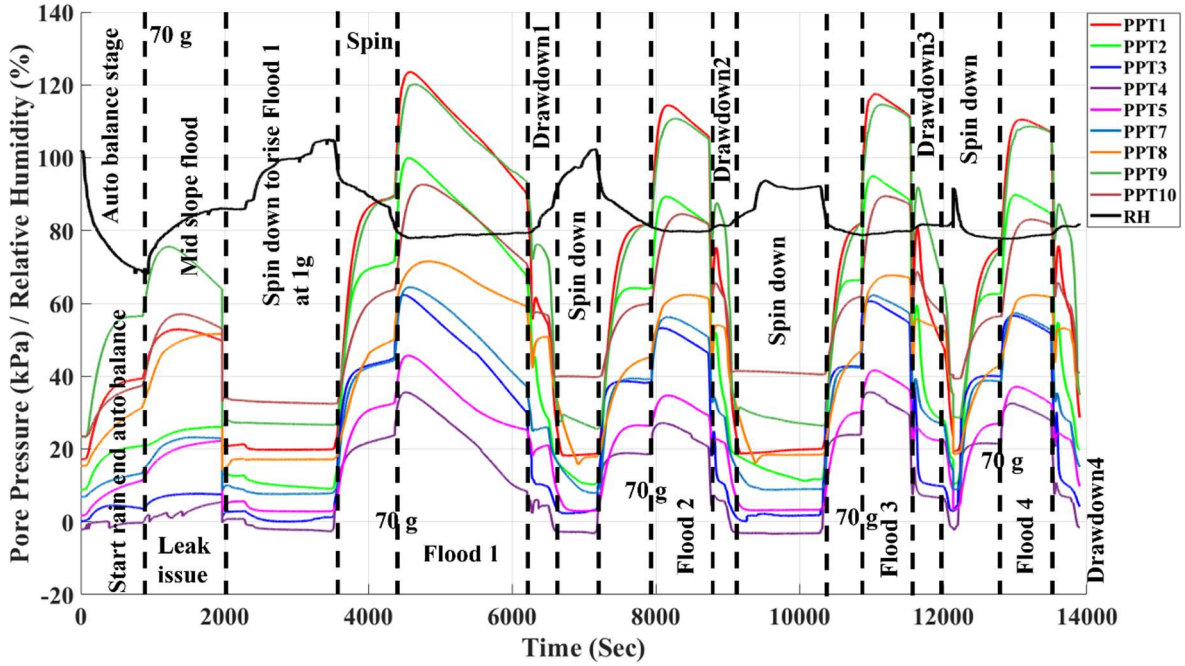


Figure 7-70 Pore water pressure (PWP) and relative humidity (RH) variations during multiple flood and drawdown stages in the final spin of the M-T6r test.

7.7.2 M-T6r: Auto balance and consolidation deformations

Similar to previous tests, these are detailed in Appendix A.4.2.

7.7.3 Seasonal cycle effect for M-T6r test.

At the end of both Winter 1 and both summer periods in the M-T6r test, no significant slope movement was observed, indicating that the model remained stable under cyclic seasonal wetting and drying conditions. The slope maintained structural integrity throughout, with minimal deformation. Detailed analysis for each stage is provided in Appendix A.4.2.

Slope movement at the end of Winter 2 / M-T6r.

At the end of the second winter in the M-T6r test as shown in Figure 7-71, localised shear was observed near the crest and upper slope due to extended rainfall, while the lower slope remained stable with minor compression. Displacement reached up to 0.4 mm near the crest, with shear strain exceeding 1% along two developing shear bands. Volumetric strain showed expansion near the upper slope from water infiltration and compression near the toe, indicating localized shallow failure but no large-scale instability.

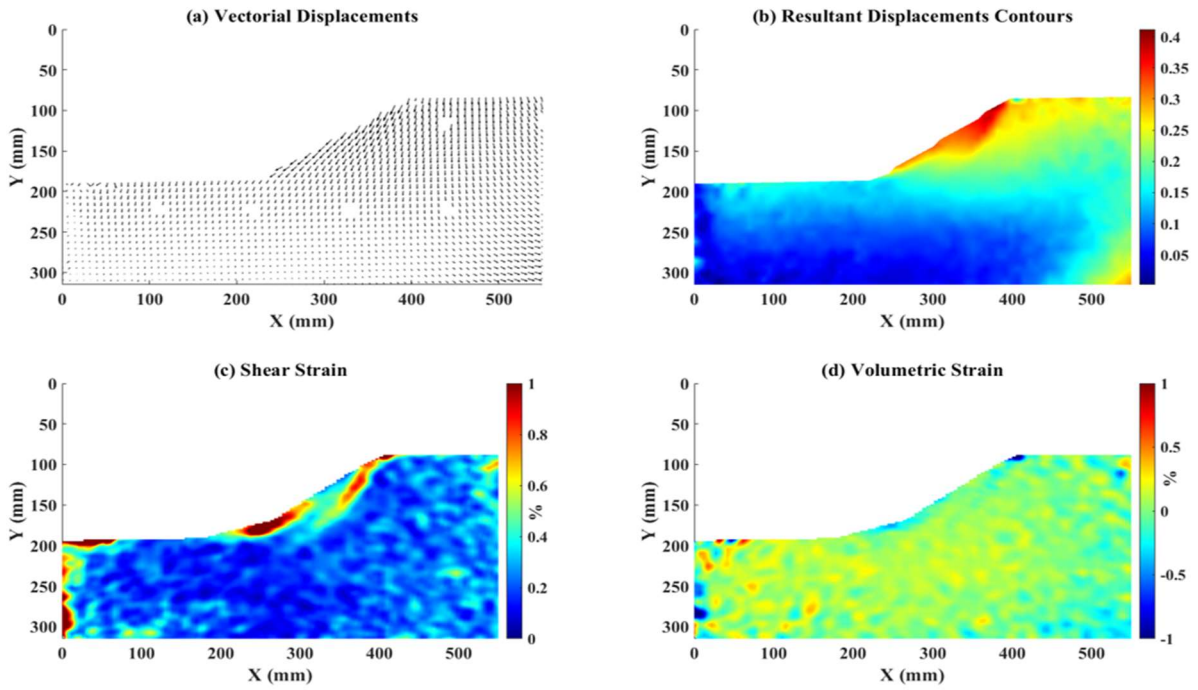


Figure 7-71 PIV analysis at the end of the second winter cycle for the M-T6r test.

Pore water pressure analysis at the end of second winter / M-T6r.

At the end of the second winter cycle in the M-T6r test as shown in

Figure 7-72, PWP remained low near the crest, indicating soil suction.

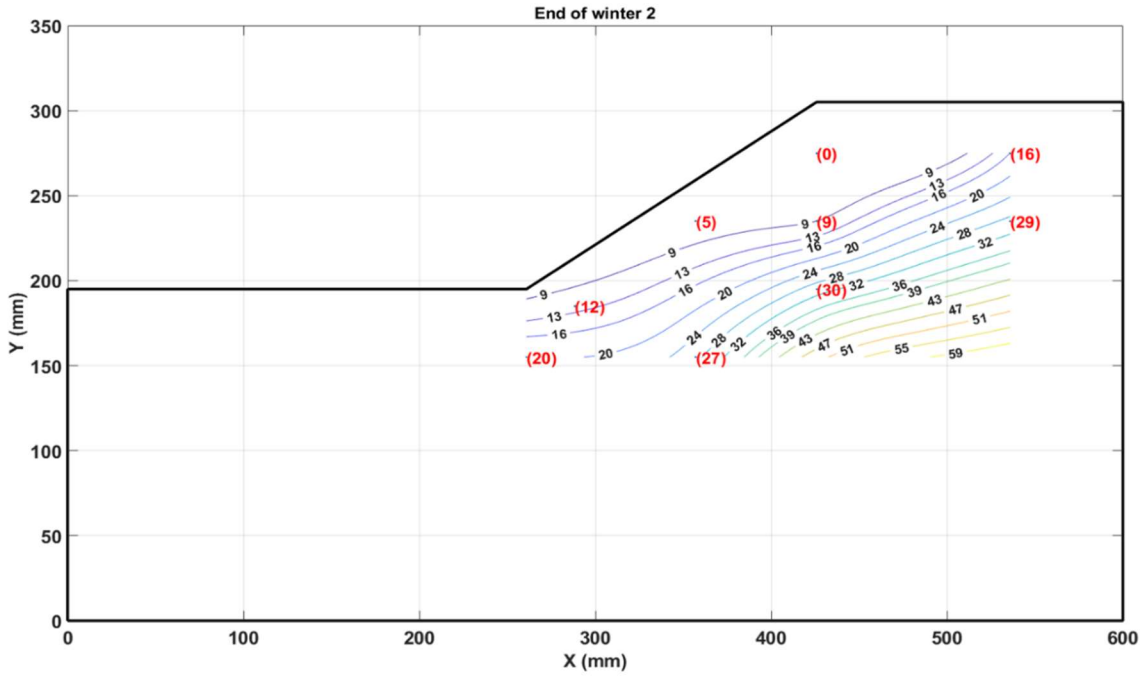


Figure 7-72 Pore water pressure distribution at the end of winter 2 in the M-T6r slope test.

Slope movement at the end of Winter 3 / M-T6r.

At the end of the third winter cycle in the M-T6r test as shown in Figure 7-73, moderate displacement and strain were observed, mainly near the crest and upper slope due to water infiltration. Displacement reached up to 1 mm, with shear strain peaking at 3%, indicating localized weakening. The lower slope experienced compression due to consolidation, while the upper slope showed expansion from swelling. Despite these localized deformations, overall slope stability was maintained without catastrophic failure.

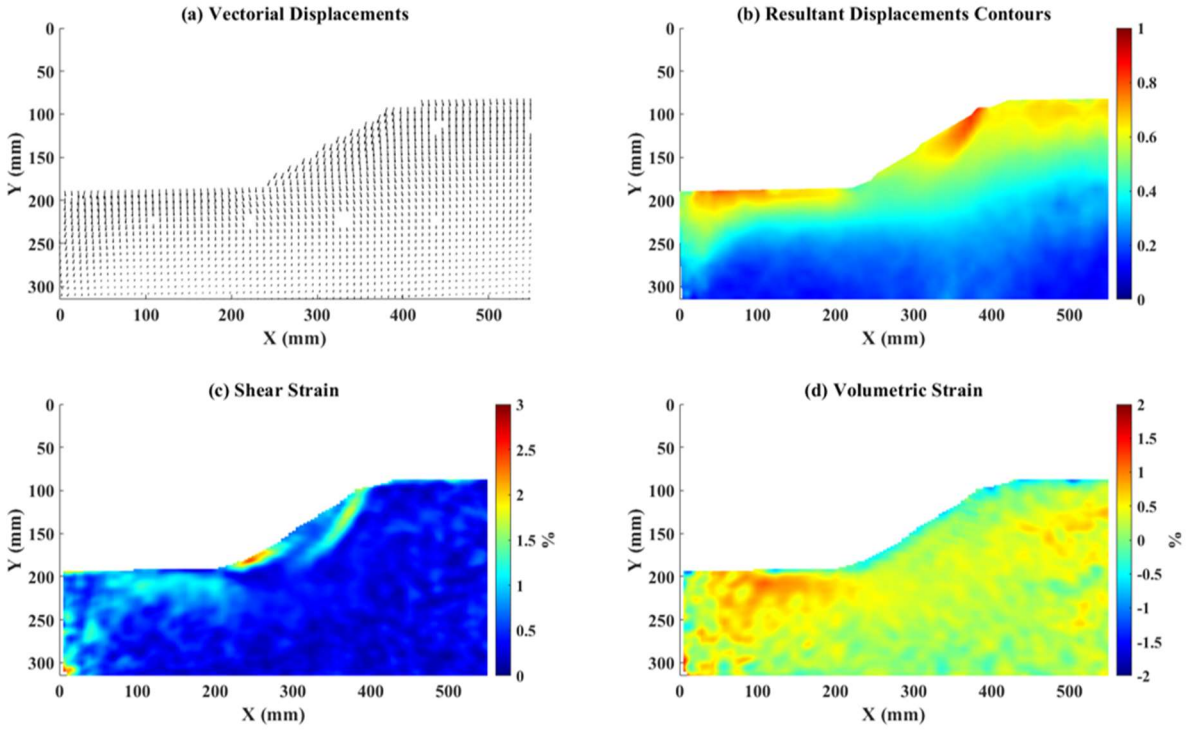


Figure 7-73 PIV analysis at the end of the third winter cycle for the M-T6r test.

Pore water pressure analysis at the end of third winter / M-T6r.

At the end of the third winter in the M-T6r test depicted in Figure 7-74, PWP remained low near the surface and crest, with slight negative values indicating suction effects from drying. PWP increased towards the base and toe, suggesting water retention and limited drainage in deeper regions. The comparison of PIV and PWP results indicates that while suction persists in the upper slope, rainfall infiltration is reducing it, contributing to potential destabilization.

.

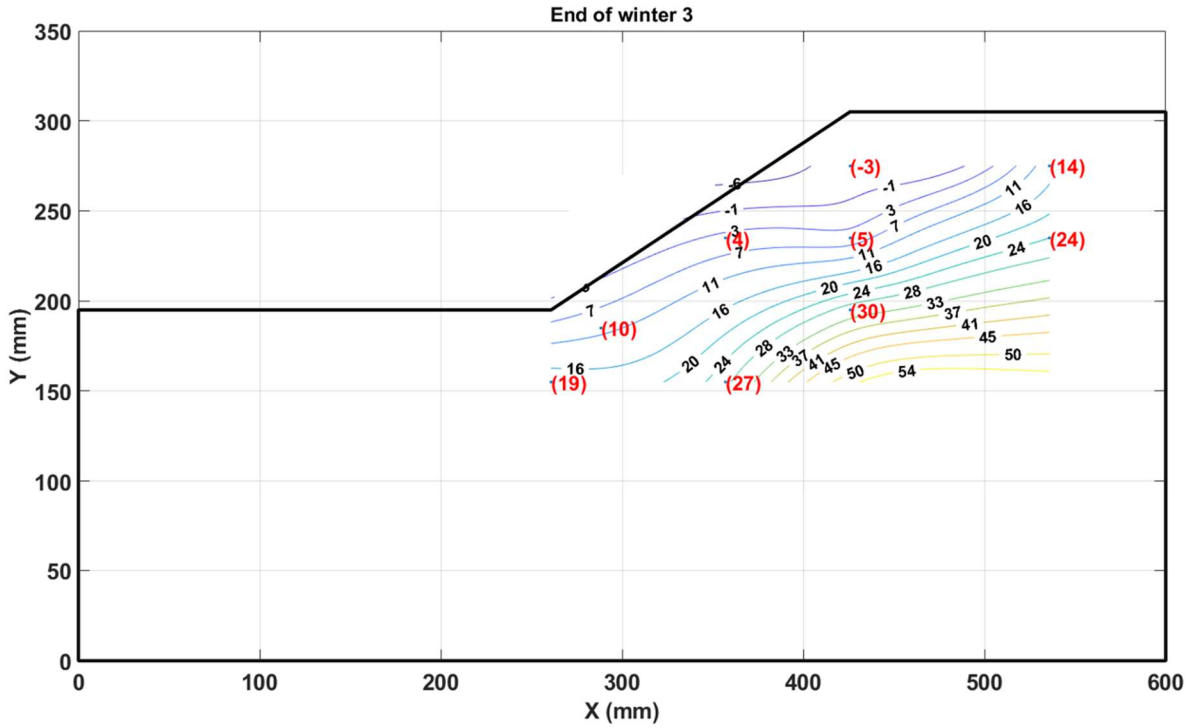


Figure 7-74 Pore water pressure distribution at the end of winter 3 in the M-T6e slope test.

Second consolidation - Slope movement / M-T6r.

The test was spun down and left for two days after Winter 3. During this time, it was not possible to monitor the strains. It was then spun up again, which caused reconsolidation to occur. PIV data shows that the slope remains stable with significant settlement. Detailed analysis is provided in Appendix A.4.2.

7.7.4 Flooding and the drawdown effect for M-T6r.

The flooding and drawdown effect introduces a dramatic shift in the stability of the slope, as rapid changes in pore water pressure due to water infiltration and subsequent drawdown lead to significant soil deformation. In the M-T6r test, two attempts were made to initiate the flood by applying continuous rainfall and reducing the g to auto balance (50 g) in order to open the valve. However, an issue arose with a leak from the box, leading to the decision to reduce the centrifuge to a fixed level.

Flood 1: Rainfall began during the auto-balance stage but only reached the mid-slope at 70 g due to a leak. The g-level was reduced to 20 g, then spun down to 1 g to raise the water level before spinning back up to 70 g. The flood lasted for 27 minutes before the drawdown began.

Drawdown 1: Following Flood 1, the drawdown lasted 3 minutes, resulting in sharp decreases in PWP across all sensors, indicating effective drainage.

Floods 2,3 and 4: These floods were conducted at 1 g due to persistent leak issues. After raising the water level to 1 g, the g-level was spun up to 70 g, with each flood lasting 12 minutes. Both floods showed sharp decreases in PWP across sensors. Flood 4 was chosen to be the case to set the PPT offsets as this was the longest duration and was most stable in outcome.

Drawdowns 2,3 and 4: Each drawdown lasted 3 minutes and showed steep decreases in PWP, with faster responses near the crest compared to the toe.

Slope movement at the end of the flood / M-T6r.

Across all four flood events in the M-T6r test, no significant slope deformation or instability was observed, indicating that the slope model maintained its structural integrity under repeated and prolonged flooding conditions. During the second flood, which simulated a 37-day prototype-scale flood over 11 minutes in model scale and involved 36 minutes of water infiltration (representing 4 months prototype time), the slope still exhibited stability. These findings confirm that the model withstood both isolated and cumulative flood effects without notable failure. Detailed analysis is provided in Appendix A.4.3.

Soil deformation at the end of first drawdown/M-T6r.

The flooding phase likely caused water infiltration into the slope, increasing the pore water pressure, particularly near the toe and mid-slope. However, the drawdown process, which took place over 10 days (at prototype scale), resulted in a rapid water level drop that redistributed the stresses within the slope. The PIV results indicate that the upper slope and crest are the most affected by the drawdown, with notable shear failure as shown in Figure 7-75. This suggests that the soil in these regions is more susceptible to deformation during rapid water level changes. Overall, the drawdown phase caused a lot of shear and volumetric strain in the upper slope and crest, which could mean that the structure could become completely unstable if the process happens again under the same conditions. The displacement was concentrated near the upper slope and crest, reaching up to 1 mm, while the lower slope remained stable. Shear strain exceeded 5%, forming a clear shear zone from crest to toe, indicating slope failure. Volumetric strain showed alternating expansion and compression along the shear zone, suggesting critical state shearing due to the rapid drop in water level.

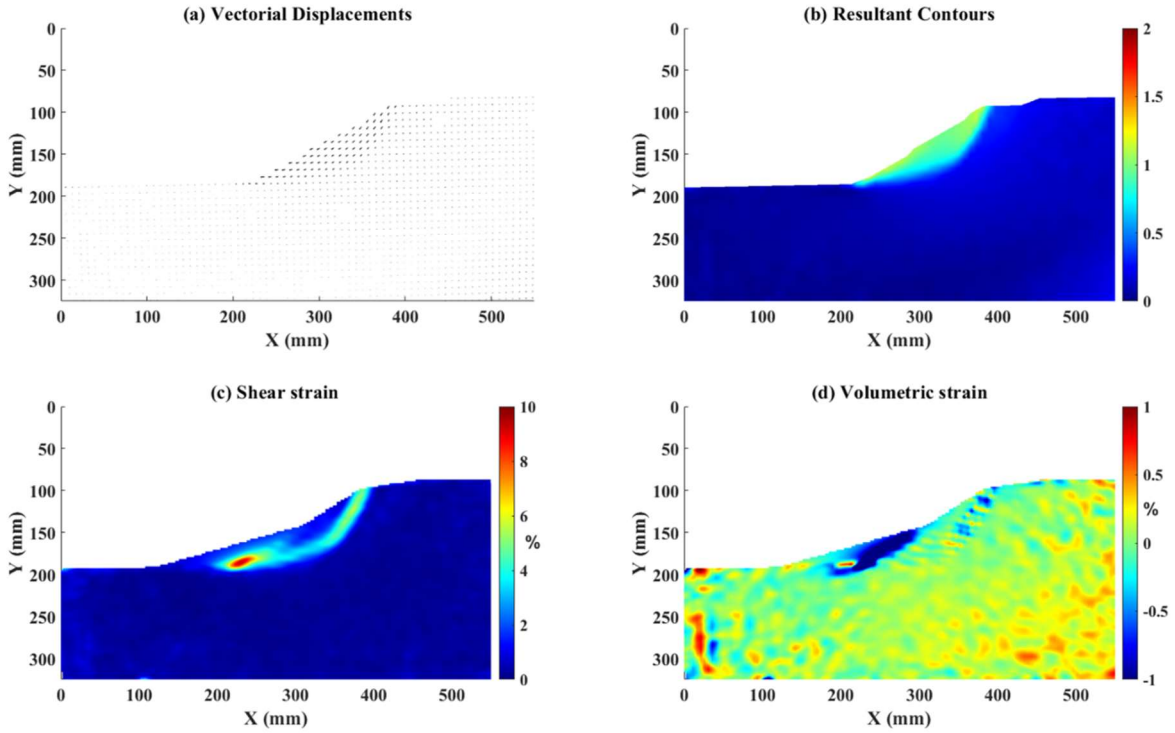


Figure 7-75 PIV analysis at the end of the first drawdown for the M-T6r test.

Pore water pressure distribution at the end of first drawdown event / M-T6r.

At the end of the first drawdown in the M-T6r test, pore water pressure (PWP) varied across the slope, with lower values at the crest (2–22 kPa) and significantly higher pressures in the midslope (19–51 kPa) and toe (up to 50 kPa) as shown in Figure 7-76. The base retained the highest PWP (6–86 kPa), indicating slow drainage. The drawdown triggered shallow slope failure, with ongoing PWP adjustments at the time of analysis.

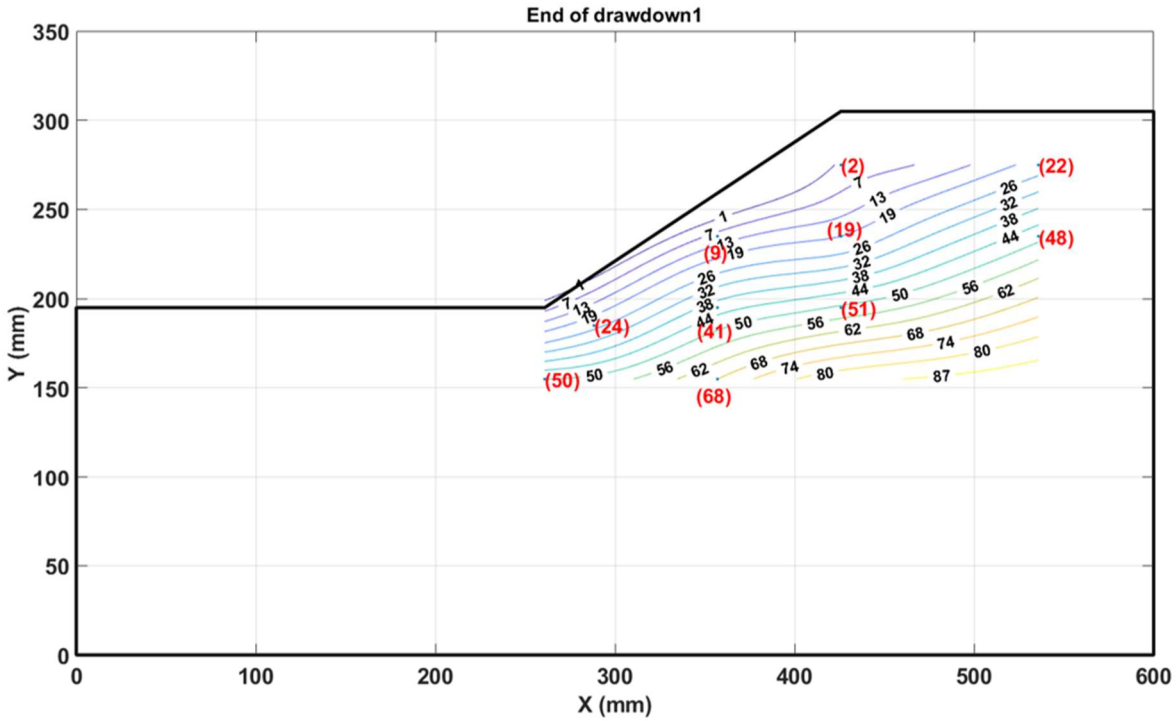


Figure 7-76 Pore water pressure distribution at the end of drawdown 1 in the M-T6r slope test.

Soil deformation at the end of the second drawdown/M-T6r.

The second drawdown had a substantial impact on the upper slope and crest, causing significant displacement and shear strain as displayed in Figure 7-77. This is typical behaviour as the rapid reduction in water levels removes support from the slope, leading to movement and instability, particularly in the upper parts. The drawdown took 10 days on the prototype scale to reach the surface of the toe. This duration highlights the drainage process from the slope, which had been subjected to significant water infiltration during the flood phase.

At the end of the second drawdown in the M-T6r test, significant displacement (up to 2 mm) was concentrated near the crest and upper slope, driven by the rapid drop in water levels and pore pressure changes. Shear strain exceeded 5% in the mid-to-upper slope, following the existing failure zone from previous drawdowns, with a new shear zone beginning to develop. Volumetric strain showed expansion and compression along the shear zone, indicating critical state shearing without significant overall volume change. The lower slope remained largely stable.

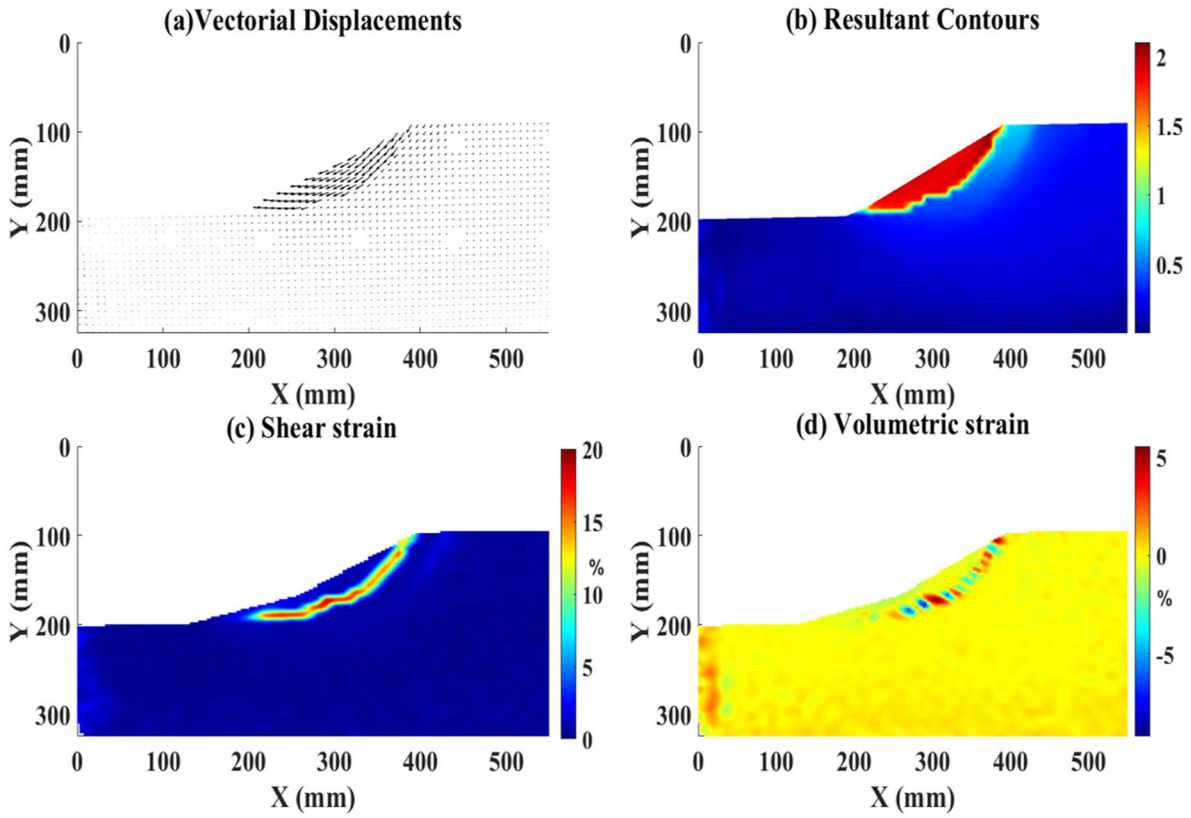


Figure 7-77 PIV analysis at the end of the second drawdown for the M-T6r test.

Pore water pressure distribution at the end of second drawdown event / M-T6r.

At the end of the second drawdown for the M-T6r test, the pore water pressure distribution shows a decreasing trend from the crest to the toe of the slope, as shown in Figure 7-78. The pore pressures are slightly elevated compared to the previous drawdown at the same time, but the flood level was also higher so this is not surprising. Clearly water is still leaving the slope at this point, leading to the destablisation of the slope.

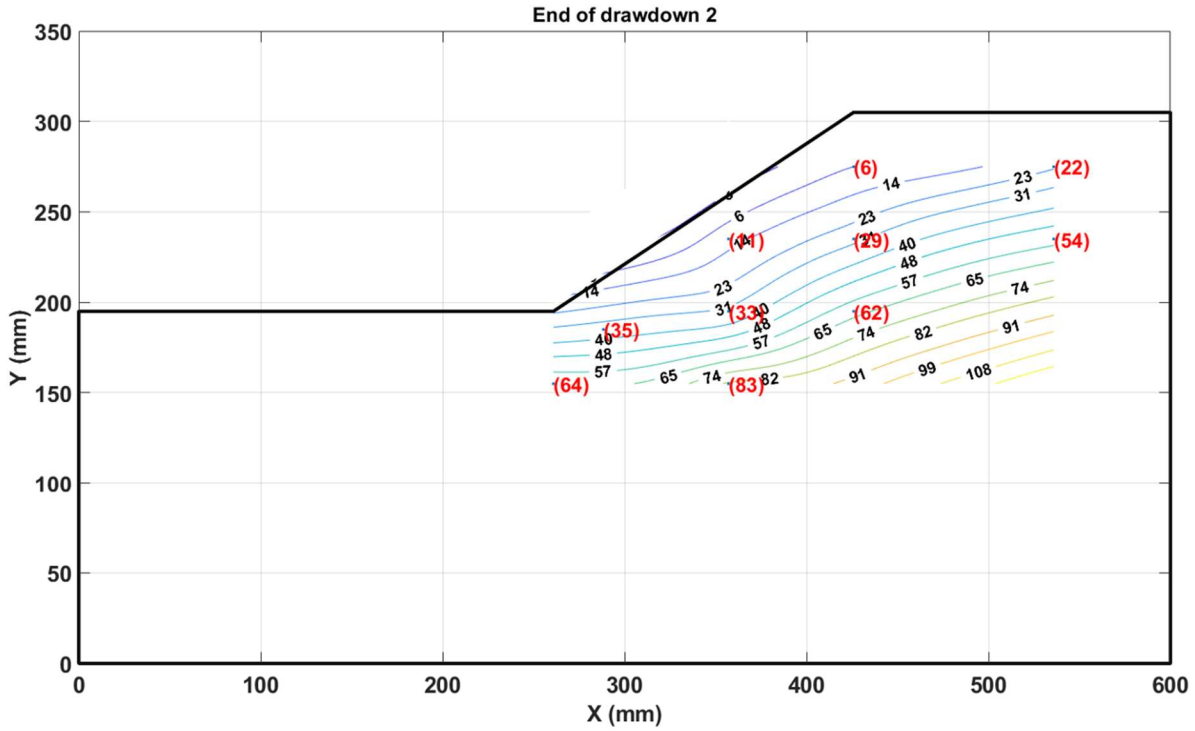


Figure 7-78 Pore water pressure distribution at the end of the second drawdown in the M-T6r test.

Soil deformation at the end of the third drawdown /M-T6r.

The large displacement and shear strain near the upper slope and crest, along with the volumetric expansion in these areas, suggest that the rapid drawdown caused continued slope failure from the crest to the toe. Figure 7-79 shows the PIV result at the end of the third drawdown during the M-T6r test. Significant slope instability was observed, with maximum displacement (2 mm) concentrated near the crest and upper slope. Shear strain reached up to 18% in the mid-slope, indicating severe deformation and ongoing failure along a fully developed shear zone. Volumetric strain patterns suggest critical state shearing, with no overall volume change, confirming continued slope instability due to rapid drawdown.

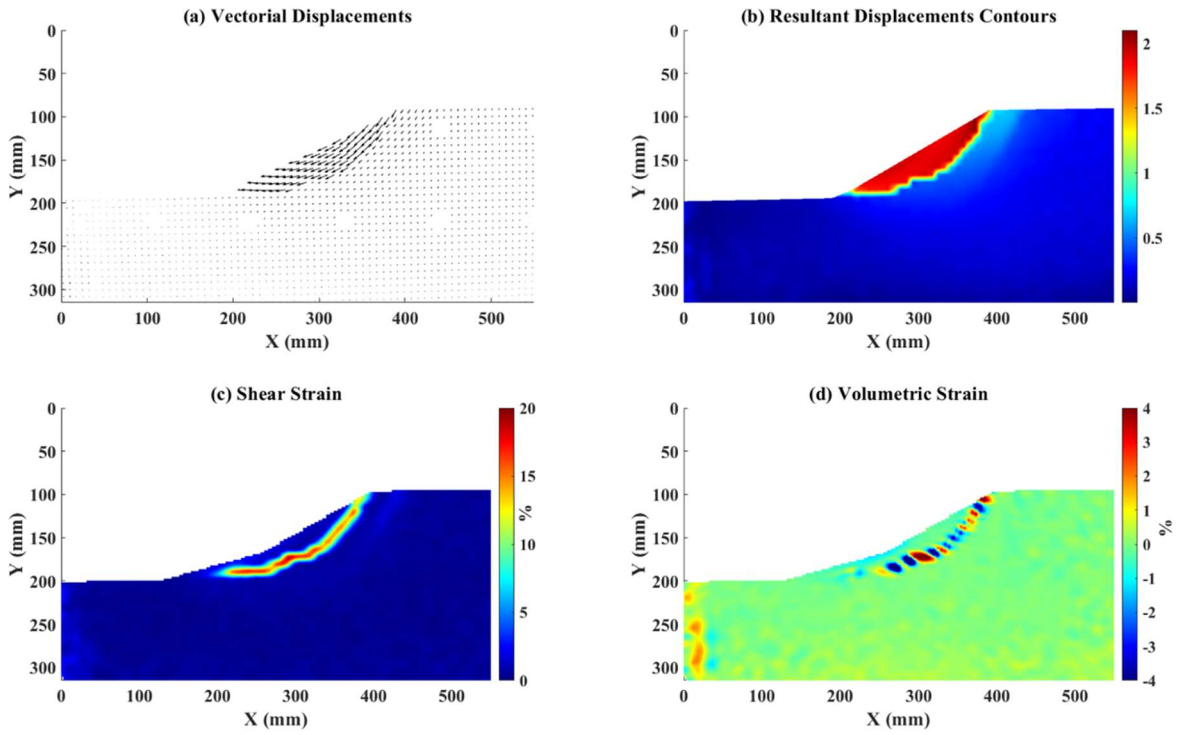


Figure 7-79 PIV analysis at the end of the third drawdown for the M-T6r test.

Pore water pressure distribution at the end of third drawdown event / M-T6r.

The pore water pressure (PWP) distribution at the end of drawdown 3 for the M-T6e test is shown in Figure 7-80. The drawdown process took 10 days on the prototype scale to reach the toe surface. Clearly water is still leaving the slope at this point, leading to the ongoing destablisation of the slope.

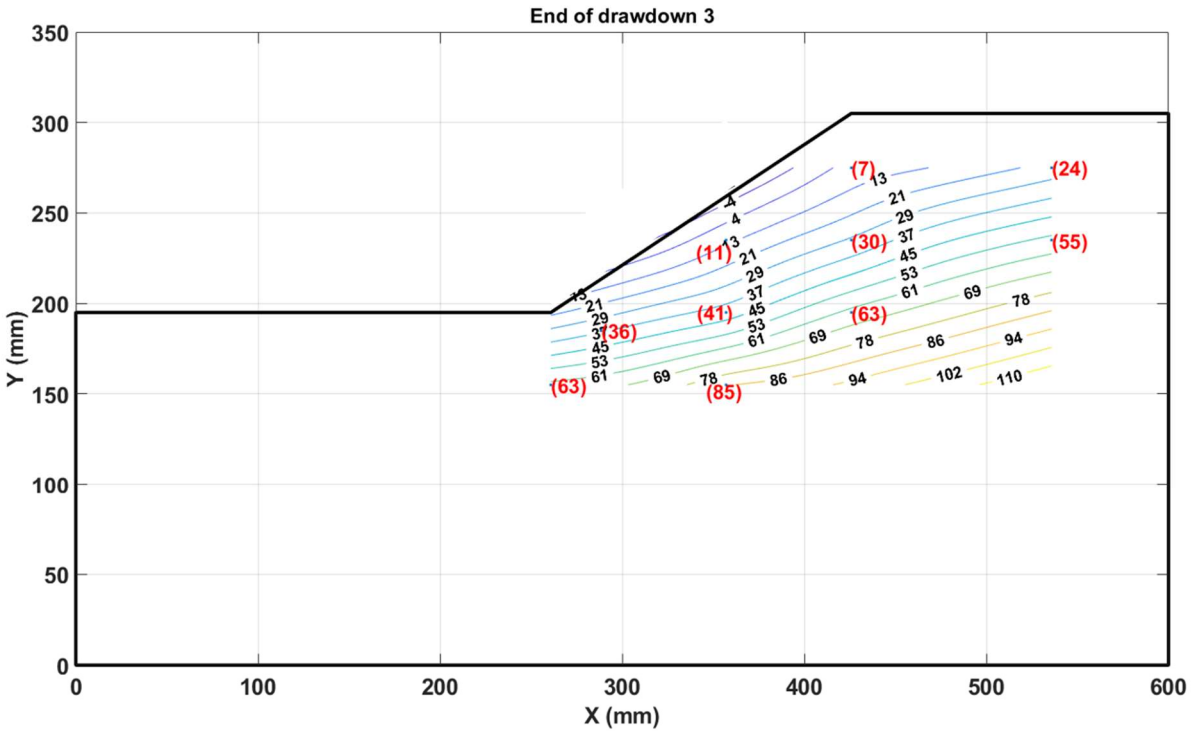


Figure 7-80 Pore water pressure distribution at the end of the third drawdown in the M-T6r test.

Soil deformation at the end of the fourth drawdown /M-T6r.

In this last case of drawdown, the effect was primarily concentrated near the crest and upper slope, where significant displacement, shear strain, and volumetric strain occurred. These areas experienced the most deformation due to the high hydraulic gradient leading to ongoing shear. The PIV result at the end of the fourth drawdown for the M-T6r test, as shown in Figure 7-81. Displacement reached up to 2 mm, with shear strain values peaking at 20–25% along the previously sheared zone, indicating continued failure. Volumetric strain confirmed critical state shearing along the main failure surface, with minimal changes elsewhere.

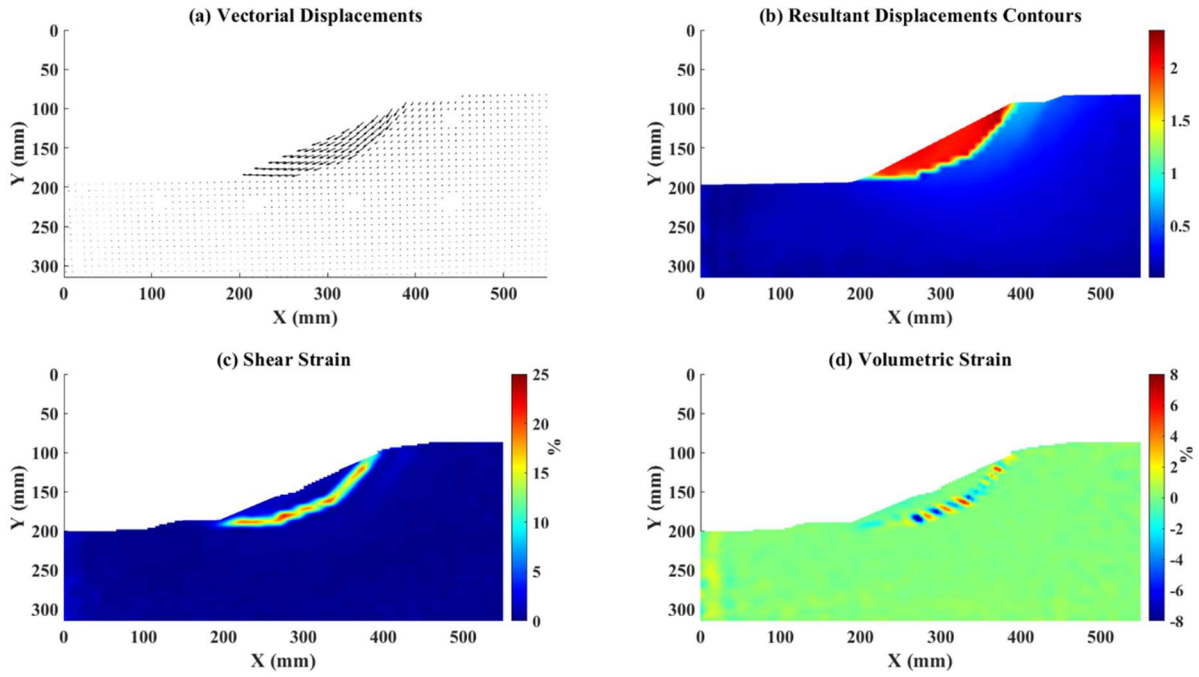


Figure 7-81 PIV analysis at the end of the fourth drawdown for the M-T6r test.

Pore water pressure distribution at the end of fourth drawdown event / M-T6r.

The pore water pressure (PWP) distribution at the end of the fourth drawdown for the M-T6r test, as shown in Figure 7-82, highlights that pore water pressures exhibit a gradual decrease towards the crest (to negative values), with higher PWP values remaining in the lower and mid-slope areas. The distribution indicates that the drawdown significantly reduced pore pressures at the crest and near the mid-slope, but the lower slope and toe still retain higher pressure values.

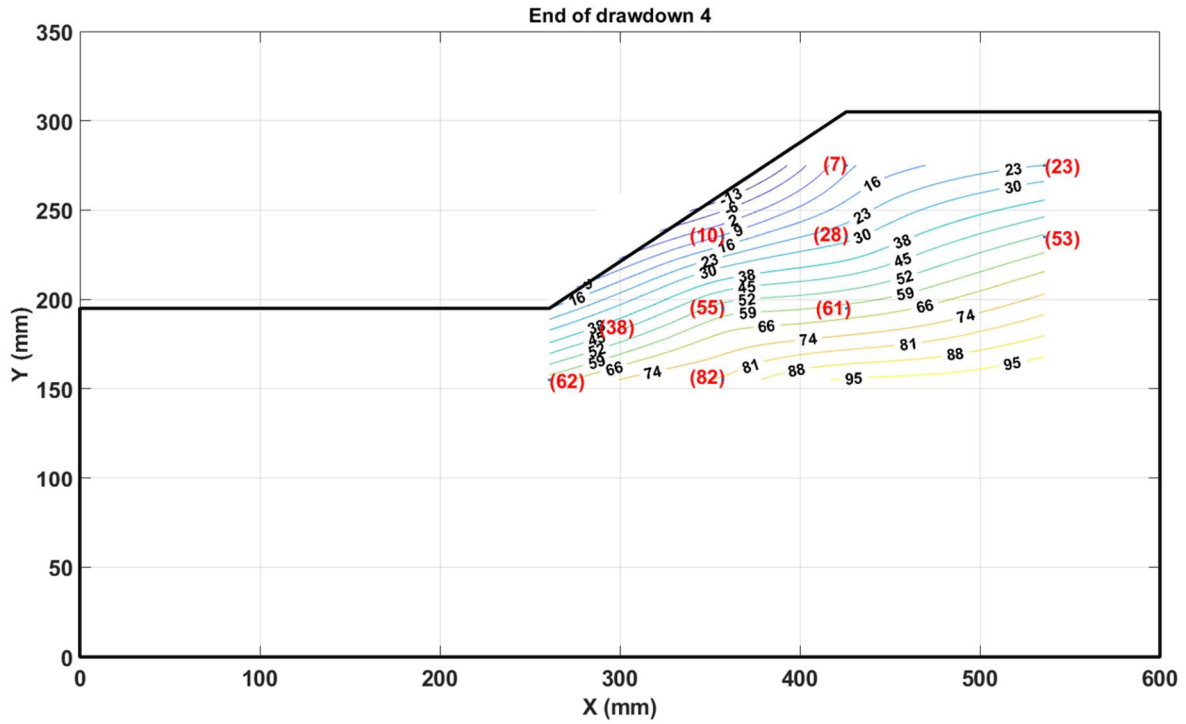


Figure 7-82 Pore water pressure distribution at the end of the fourth drawdown in the M-T6r test.

Slope failure after centrifuge M-T6r test.

Figure 7-83 depicts the slope failure observed at the end of the M-T6r test. The left side of the image shows a close-up of a crack that has developed on the slope, which appears to extend from the crest downwards. The crack formation likely occurred due to the drawdown and infiltration cycles applied to the slope. The crack length is indicative of localised slope instability at the crest, where water infiltration and subsequent drawdown caused differential settlement or movement within the slope material. The crest area would be more susceptible to these stresses, resulting in the observed failure.

On the right side of the image, the entire slope model is visible. The slope failure is clearly marked along the surface, showing the boundary where the slope has slid or shifted. The detachment of material near the crest suggests that the flood and subsequent drawdown cycles weakened the crest, with high hydraulic gradient during each drawdown event eventually leading to failure. The black line highlights the line of failure, indicating the extent of movement observed at the end of the test. In conclusion, the slope failure likely resulted from repeated cycles of water infiltration and drawdown during the M-T6r test, causing localised

instability and the formation of cracks at the crest. The failure mechanism appears to be a combination of shear failure and tensile cracking due to loss of soil strength under saturated conditions.

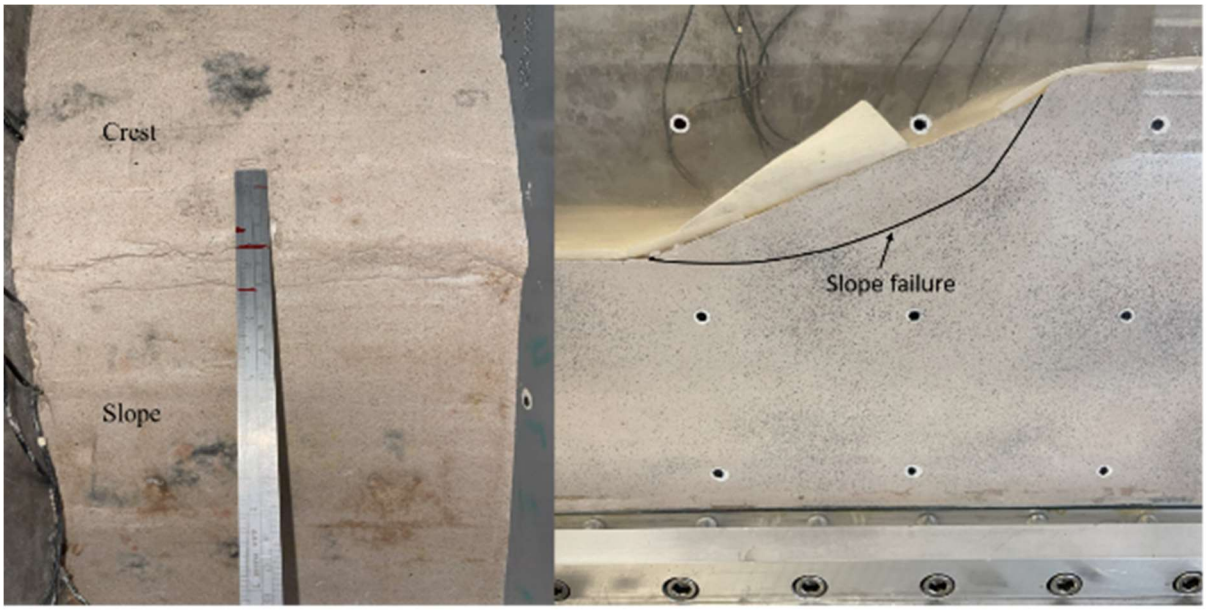


Figure 7-83 (a) Cracking at the crest of the slope after failure;(b) Slope failure at the end of the M-T6r test.

7.7.5 Failure mechanisms of the M-T6r test

The M-T6r test resulted in slope failure following drawdown, confirming that instability was triggered by pore pressure variations and effective stress reduction. A detailed analysis of pore pressure dissipation, effective stress redistribution, and observed failure patterns provides insight into the mechanisms governing failure in drawdown conditions.

1. **Pore pressure dynamics and effective stress reduction**

A key factor influencing the M-T6r slope failure was the variation in pore water pressure (PWP) dissipation rates. While most locations experienced a reduction in PWP, some regions exhibited delayed drainage and pore pressure retention, particularly at PPT1 and PPT2, which later became critical failure zones. The effective stress analysis confirms that PPT1 and PPT2 had the highest shear strength reductions, meaning these regions remained weaker than the rest of the slope. This behaviour aligns with the pore pressure lag theory proposed by Wright and

Duncan (1987), which states that delayed pore pressure dissipation can temporarily weaken the soil, making it more susceptible to failure during drawdown.

2. Effective stress and shear strength reduction

A key factor influencing the M-T6r slope failure was the variation in pore water pressure (PWP) dissipation rates. The calculated effective stress values before and after drawdown, along with the percentage of shear strength reduction, are summarised in Table 7-8.

Table 7-8 Shear strength reduction and stress variation at different depths at the end of drawdown.

PPT	Depth in Prototype (m)	Total Stress (kPa)	PWP Start Drawdown (kPa)	PWP End Drawdown (kPa)	Effective Stress Before (kPa)	Effective Stress After (kPa)	Shear Strength Reduction (%)
PPT1	10.85	195.3	105.25	83.21	130.69	98.05	33.29%
PPT2	12.95	233.1	78.39	59.7	193.31	153.85	25.65%
PPT3	16.45	296.1	51.02	23.63	277.52	249.93	11.04%
PPT4	19.25	346.5	27.32	6.19	324.92	313.14	3.76%
PPT5	19.45	346.5	30.54	25.78	311.19	304.81	2.09%
PPT7	7.75	296.1	52.17	35.34	235.71	216.95	8.22%
PPT8	6.25	195.3	55.72	48.65	252.62	248.32	1.73%
PPT9	11.85	233.1	103.81	85.69	102.58	84.41	21.53%
PPT10	8.75	144.9	78.34	67.67	155.21	137.93	13.08%

Interpretation for M-T6r discussion

1. Failure Initiation in weak zones

- The highest shear strength reductions occurred in PPT1 (~33.29%), PPT2 (~25.65%), and PPT9 (~21.53%), which suggests these were critical failure zones where pore pressure dissipation was insufficient.
- These zones likely lost shear resistance as effective stress decreased, leading to slope instability.

2. Localisd drainage effects

- PPT5 (~2.09%) and PPT4 (~3.76%) had minimal strength reduction, indicating better drainage efficiency in these areas.

- This suggests that not all regions contributed equally to the failure, reinforcing the role of differential pore pressure dissipation in triggering instability.

3. Drawdown failure mechanism confirmation

- The failure observed in M-T6r was controlled by areas with the highest shear strength reduction, supporting drawdown failure mechanisms Wright and Duncan (1987).
- Similarly, Miao et al. (2018) identified regions of high pore pressure as primary failure zones, further confirming this mechanism.
- The shear strain concentration detected in PIV analysis aligns with these findings, confirming that instability was initiated at mid-depths where shear strength loss was most pronounced. This suggests that the slope was experiencing progressive weakening before total failure occurred.

4. Seepage-Induced Instability (Terzaghi, 1943).

- Seepage forces generated by drawdown can act against the natural stability of a slope, increasing the potential for instability.
- The observed failure surface suggests that seepage forces contributed to shear failure initiation, especially in regions where PWP remained high.
- This theory is further reinforced by the volumetric strain patterns observed in PIV analysis, which indicate dilation and compression effects due to uneven pore pressure dissipation.
- Miao et al. (2018) highlight the impact of seepage forces on slope stability. In the M-T6r, the formation of high shear strain zones was detected in PIV analysis, particularly near the crest and mid-slope. This aligns closely with the findings of this study, where numerical models predicted that seepage forces contribute to increased instability during drawdown. However, a key difference is that in M-T6r, failure was more localised, whereas in this study, a deeper slip surface was observed. This could be due to:
    a) Differences in boundary conditions.
    b) Variability in soil permeability.
    c) Differences in drawdown rate.

7.8 Comparison of Failure Behaviour in M-T5, M-T6, and M-T6r.

7.8.1 Overview of Seasonal (Cyclic Weather) Response

While some minor instability occurred in the steeper slopes during rainfall (Winter) periods, failure in all tests was primarily triggered by gradual drawdown. M-T5 and M-T6r exhibited failure (both at 1:1.5 or 33.7°), but with distinct mechanisms. M-T5 showed a shallow rotational failure initiated after drawdown, while M-T6r experienced a progressive failure, likely due to the cumulative weakening from repeated wetting-drying cycles. The gradual reduction in water level after flooding led to increased seepage forces, reducing slope stability. Surface cracking was also observed. However, M-T6 (1:1.75 or 29.7°) remained stable throughout the test due to the slope being at a lower gradient, suggesting this is a stable configuration.

Surface cracking was observed before failure in M-T5 and M-T6r, indicating progressive weakening of the slope due to PWP fluctuations and soil saturation changes. A detailed comparison of failure type, triggering mechanisms, PWP response, and Factor of Safety trends across the three tests is presented in Table 7-9.

Table 7-9 Comparison of Failure Behaviour Due to Weather cycling in M-T5, M-T6, and M-T6r

Test	Failure Type	Triggering Mechanism	Deformation	Erosion & Cracking
M-T5 1:1.5	Shallow rotational failure	Failed during ½ season of 3 weeks of rain / 1 week no rain then continuous rain (Winter 3)	Incipient (?) failure at end of Winter 2; major failure at end Winter 3	Toe erosion and minor crest cracking
M-T6 1:1.75	No failure observed	None	Minimal (<1%)	Minimal erosion and no significant cracking
M-T6r 1:1.5 (recut)	Progressive slope failure	Failed during 2 weeks of rain and 1 week no rain (Winter 2)	Discontinuous shear failure progressive failure	Severe erosion at crest and mid-slope, deep-seated cracks

7.8.2 Seasonal (Cyclic Weather) Displacement and Strain Distribution Insights

The M-T5, M-T6, and M-T6r tests provide key insights into slope stability under gradual drawdown conditions. While M-T5 and M-T6r exhibited failure, M-T6 remained stable despite experiencing the same hydrological conditions.

Vectorial Displacement Behaviour

Figure 7-84Figure 7-84 illustrates vectorial displacement maps for M-T5, M-T6, and M-T6r captured at the end of the Drawdown 3 phase in each respective test. The timing of image capture was selected to represent the peak deformation stage during drawdown.

- M-T5: The vector field shows localised downslope movement concentrated at the crest and mid-slope, confirming a rotational failure mechanism.
- M-T6: The displacement vectors remain small and uniform, reinforcing the observation that no significant movement or failure occurred.
- M-T6r: The vectorial displacement field reveals progressive downslope movement extending deeper into the slope, consistent with a gradual failure mechanism.

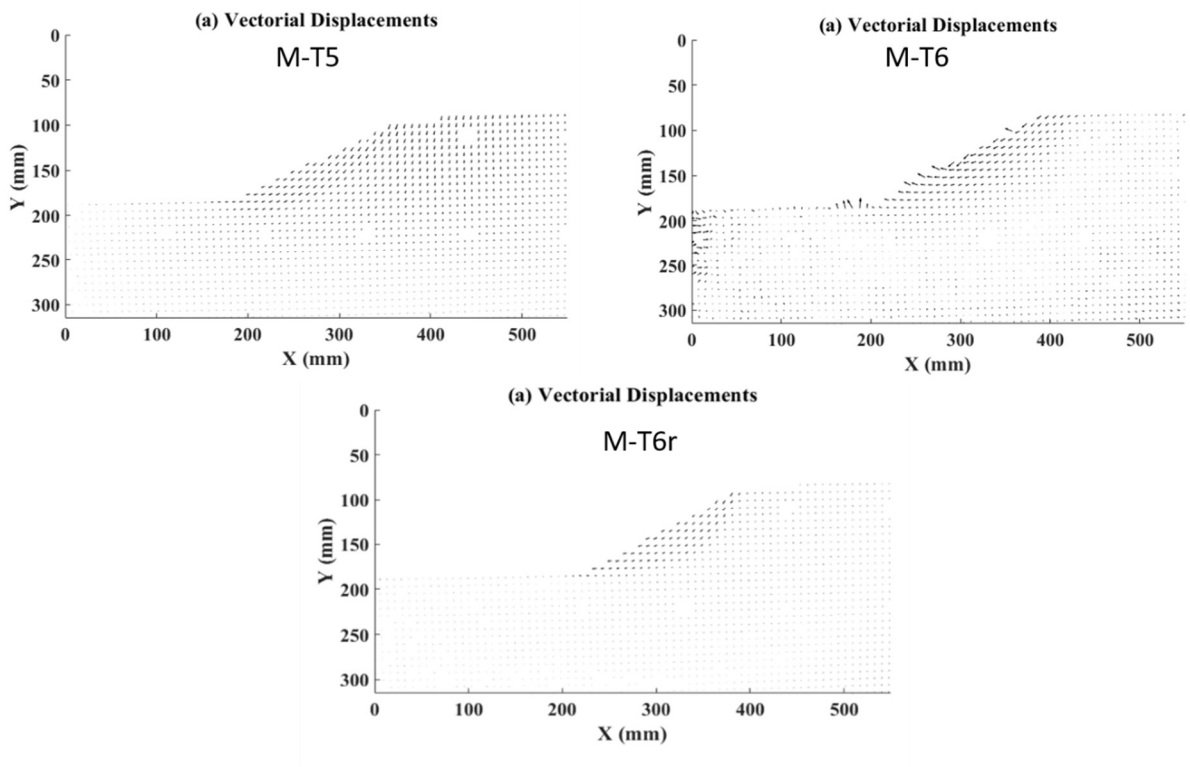


Figure 7-84 Comparison of vectorial displacements for M-T5, M-T6, and M-T6r at the end of Drawdown 3.

Shear Strain Patterns

Figure 7-85 presents shear strain maps across the three tests.

- M-T6r exhibited extensive shear strain localisation along a deep failure surface, confirming progressive failure.
- In M-T5, shear strain was concentrated at the crest and mid-slope, indicating a shallow rotational slip failure.
- M-T6 exhibited minimal shear strain, reinforcing that the slope remained stable throughout the test.

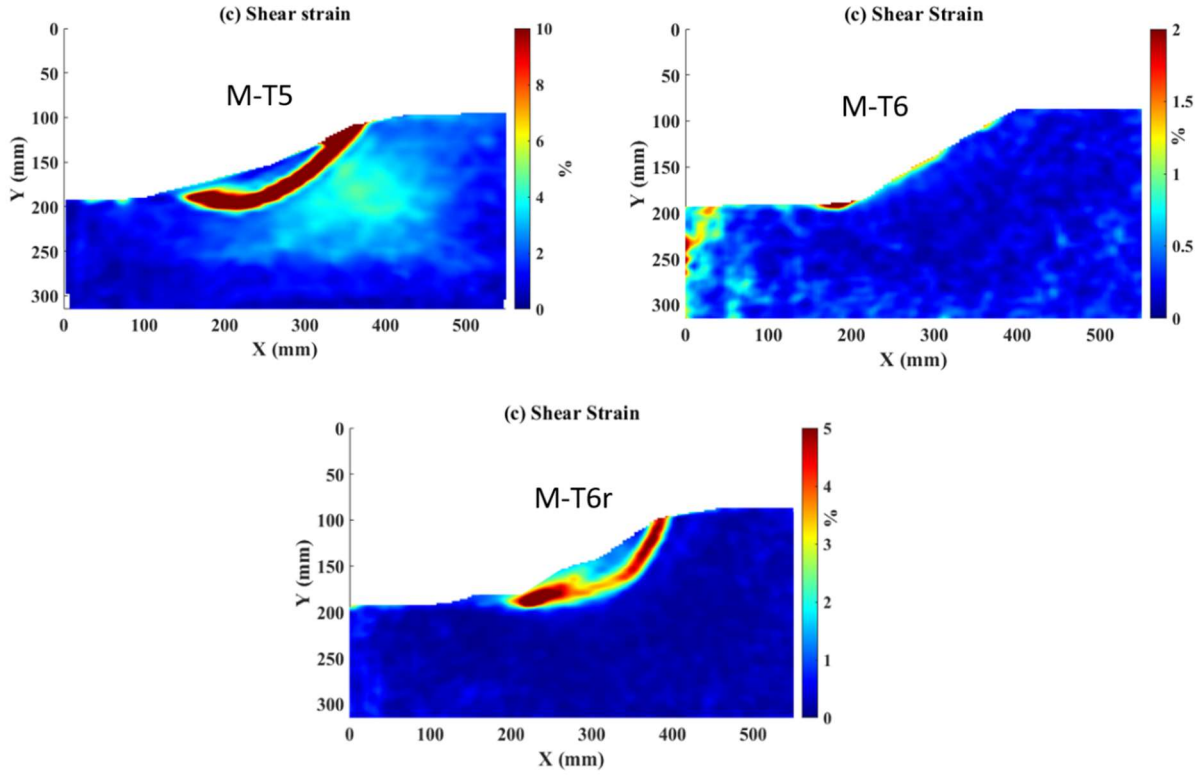


Figure 7-85 Comparison of shear strain for M-T5, M-T6, and M-T6r at the end of Drawdown 3.

7.8.3 Overview of Flooding and Drawdown Response

Error! Not a valid bookmark self-reference. summarises the key similarities and differences in failure mechanisms between the tests under flooding and drawdown, showing that M-T5 and M-T6r exhibited significant movement and strain accumulation under drawdown, whereas M-T6 remained stable with minimal deformation.

Table 7-10 Summary of Failure Behaviour at end of Drawdown 2 for M-T5 and Drawdown 3 across M-T6, and M-T6r.

Test	Failure Type	Vectorial Displacement	Shear Strain Distribution
M-T5	Shallow rotational failure	Movement concentrated at crest and mid-slope, vectors indicate sliding motion	High shear strain localized at crest
M-T6	No failure observed	Minimal movement, vectors show elastic recovery and some swelling near surface	Low and localised shear strain
M-T6r	Progressive failure	Distributed displacement along failure surface, vectors indicate progressive downslope	Shear strain more distributed, failure extended deeper than M-T5

		movement	

- M-T5 failed due to continuous rainfall and gradual drawdown, with instability developing near the toe.
- M-T6 remained stable, suggesting that its lower slope inclination (29.7°) and preparation from a consolidated soil block contributed to its resilience against drawdown-induced failure.
- M-T6r experienced progressive failure, emphasising the cumulative weakening effects of multiple flooding-drying cycles.

These findings highlight how drawdown-induced instability varies depending on drainage conditions, soil saturation levels, and prior climate exposure.

7.8.4 Influence of Boundary Conditions, Slope Inclination, and Soil Preparation on Failure Behaviour.

The results from M-T5, M-T6, and M-T6r demonstrate that failure was not guaranteed in all cases, highlighting the role of boundary conditions, slope inclination, and soil preparation methods in influencing slope stability. While M-T5 and M-T6r exhibited failure, M-T6 remained stable, despite experiencing the same gradual drawdown conditions. This suggests that factors beyond hydraulic forcing alone (drawdown) contributed to the slope response.

1. Influence of Slope Inclination on Stability

The key difference between the models was the slope angle:

- M-T5: 33.7° (steeper)
- M-T6: 29.7° (lower)
- M-T6r: 33.7° (steeper, reconstructed from M-T6)

The steeper slopes (M-T5 and M-T6r) experienced failure, whereas the shallower slope (M-T6) remained stable. A higher slope inclination increases gravitational driving forces acting downslope, making the model more susceptible to failure under drawdown conditions. In contrast, a lower slope inclination in M-T6 provided greater inherent stability, reducing the likelihood of failure.

2. Influence of Soil Preparation on Stability and Permeability

The preparation method of the soil block played a major role in determining the stability response:

- M-T5 was mechanically compacted, leading to higher density, lower permeability, and slower drainage.
- M-T6 was prepared from a consolidated soil block, meaning it experienced controlled preloading conditions, which may have improved homogeneity and drainage pathways.
- M-T6r was reconstructed from M-T6, but with a steeper slope (33.7°) and being allowed to swell at 1g (during period spun down), increasing its susceptibility to failure.

The higher density in M-T5 due to compaction compared to M-T6 (consolidated) might be expected to restrict water movement, resulting in higher retained pore water pressure (PWP) upon drawdown, which would delay dissipation and potentially contribute to instability. This is explored in Chapter 8.

3. Drawdown and PWP Distribution Effects on Failure

While gradual drawdown was the primary trigger for instability, the response varied depending on drainage conditions and PWP dissipation rates.

- M-T5 and M-T6r exhibited failure due to slow PWP dissipation, leading to progressive instability near the toe.
- M-T6 exhibited stable behaviour, probably due to the lower slope angle, preventing instability despite undergoing the same drawdown conditions.

The vectorial displacement data (

Figure 7-84) supports this, showing significant movement in M-T5 and M-T6r, while M-T6 displayed minimal displacement.

- M-T5 and M-T6r exhibited localized deformation, with failure zones concentrated at mid-slope and crest.
- M-T6 showed only minor elastic movement, confirming the influence of effective drainage and lower slope inclination on stability.

4. Failure Mechanisms and Soil Deformation Observations

- M-T5: Shallow rotational failure with large resultant displacement and high shear strain near the crest.
- M-T6: No failure, low shear strain, and negligible volumetric strain.
- M-T6r: Progressive failure with displacement extending from mid-slope to crest, leading to structural weakening over multiple cycles.

These findings emphasize that failure was not solely a result of drawdown rates, but was also influenced by slope inclination, soil preparation methods, and drainage conditions.

7.9 Rainfall intensity selection and expected failure behaviour

The selection of rainfall intensities in the centrifuge tests was based on scaling laws, ensuring physical consistency between the model and prototype conditions. Since rainfall in the centrifuge occurs under 70g acceleration, the model rainfall intensity was scaled up by a factor of N to maintain similitude with prototype conditions.

1. Choosing rainfall intensity

The rainfall intensities applied in the model tests were calculated to be equivalent to moderate rainfall events in the UK. Based on scaling calculations, the prototype rainfall intensity corresponding to the model rainfall intensity was approximately 1.14 mm/h, which aligns with moderate natural rainfall rates in the UK. This is comparable to observed rainfall intensities in moderate weather conditions rather than extreme storm events, ensuring that the tests simulated realistic climatic scenarios rather than artificially extreme conditions.

The applied rainfall intensities were chosen based on:

- Consistency with UK climate data – ensuring realistic simulation of wetting and drying cycles observed in infrastructure slopes.
- Preliminary calibration tests to validate nozzle performance and achieve uniform rainfall distribution.
- Previous literature on rainfall-induced slope failures to align with realistic rainfall scenarios observed in geotechnical studies (Take, 2003).

2. Failure Expectation

Failure was not a predetermined outcome of the tests but rather an observed response under different climate scenarios. The experiments aimed to simulate environmental loading conditions (e.g., prolonged wetting and drawdown) to evaluate if and when failure would occur.

7.9.1 Comparison of experimental results with existing literature.

Figure 7-86 presents the rainfall intensity-duration threshold plot, incorporating both global and local empirical thresholds as well as experimental data from this study. Additionally, threshold failure data from Ling et al. (2009) for 60° slopes is included to allow direct comparison. The objective of this analysis is to assess whether the experimental results from this study align with existing literature and to identify key differences in failure mechanisms for different slope geometries.

Slope Angle Differences (29.7° and 33.7° vs. 60°)

Ling et al. (2009) developed threshold failure curves for 60° slopes, which represent relatively steep terrain conditions, whereas this study examines a 29.7° and two 33° slopes. In general, steeper slopes tend to fail under shorter-duration rainfall because of faster infiltration, higher runoff, and reduced shear strength at critical depths. In contrast, shallower slopes in this study remained stable for prolonged durations before failure, suggesting that cumulative infiltration and progressive weakening played a more dominant role.

Rainfall Duration & Failure Mechanism

The experimental data points (red circles in Figure 7-86) from this study fall above most global thresholds but align more closely with Ling et al. (2009) in terms of general trend. However, a key distinction is the significantly longer failure durations observed in this study (168–504 hours) compared to the steeper 60° slopes in Ling et al. (2009), where failures typically occurred at shorter durations. This suggests that while intensity-driven failures were dominant in Ling et al. (2009), the failures observed in this study were driven by cumulative rainfall accumulation over extended periods.

Key learnings from this comparison

1. Effect of Slope Angle on Rainfall Thresholds

Ling et al. (2009) demonstrated that steeper slopes fail under shorter-duration rainfall due to faster infiltration, higher runoff, and shallower failure planes. In contrast, the 33.7° slopes in this study experienced delayed failure due to longer-duration rainfall exposure, indicating a shift toward failure dominated by cumulative infiltration rather than rapid surface-driven instability. The 29.7° slope did not experience failure, showing that there is a limit to the applicability of rainfall thresholds for shallow slopes.

2. Role of Cumulative Infiltration in Failure Onset

The prolonged failure durations observed in this study indicate that failure did not occur immediately after high-intensity rainfall but rather as a result of progressive saturation over multiple rainfall events. This suggests that short-duration rainfall thresholds may not be sufficient for assessing failure risk in lower-gradient slopes.

3. Implications for Slope Stability Assessments

These findings highlight the need to consider slope angle variations in rainfall-induced failure thresholds. Existing empirical models based on steep slopes may underestimate the risk of failure in lower-gradient slopes, where longer rainfall durations contribute significantly to instability. Future studies should refine threshold failure criteria by incorporating prolonged rainfall exposure effects, particularly for infrastructure built on moderate slopes.

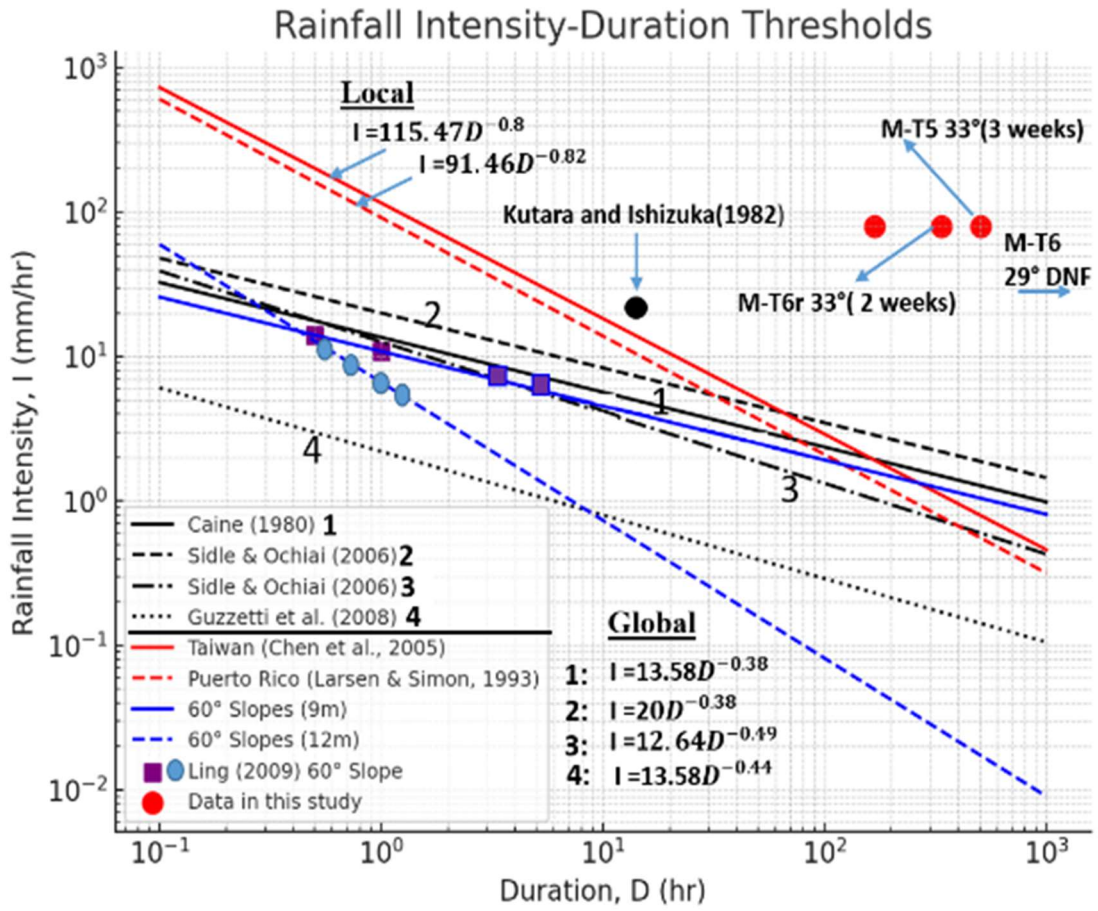


Figure 7-86 Comparison of Rainfall Intensity-Duration Thresholds with data from this thesis and length of rainfall at prototype (note that "DNF" denotes did not fail). Note: At first winter (1-week rain and 1-week dry) there is no failure in any test (M-T5, M-T6 and M-T6r).

M-T5 (1:1.5 slope): Subjected to Winter 2 (2 weeks rain/1 week dry) + Winter 3 (half season of 3 weeks rain / 1 week dry) followed by continuous rainfall (

Figure 7-87). M-T5 experienced slope failure, confirmed by high shear strain and visible displacement. The combination of steep geometry and prolonged rainfall exceeded the critical threshold for failure (

Figure 7-88).

M-T6 (1:1.75 slope): Despite undergoing similar rainfall scenarios, this test did not fail, largely due to the gentler slope angle (1:1.75). No significant movement was recorded in the PIV analysis.

M-T6r (1:1.5 slope) subjected to (winter 2 + winter3): Although this slope had the same geometry as M-T5, it was a re-cut slope and did not experience the additional continuous rainfall. However, failure occurred at the end of Winter 3, likely due to cumulative wetting, reduced shear strength from prior disturbance, and swelling effects during the rainfall cycles.

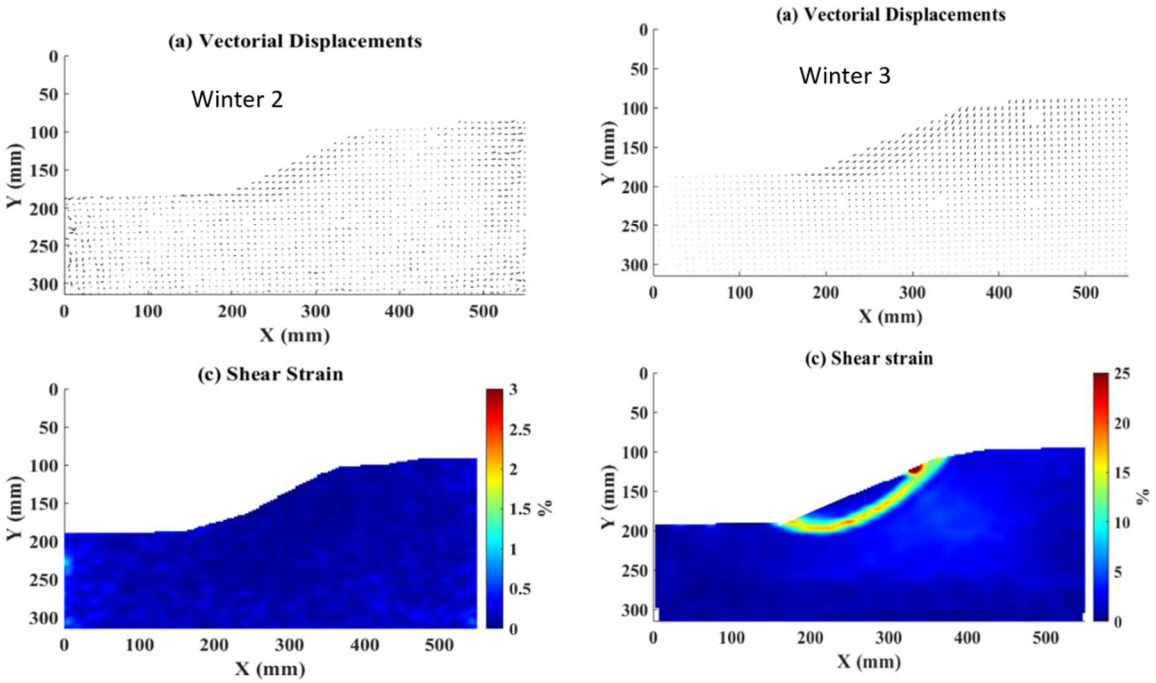


Figure 7-87 Comparison of vectorial displacements and shear strain distributions at the end of Winter 2 and Winter 3 for the M-T5 test.

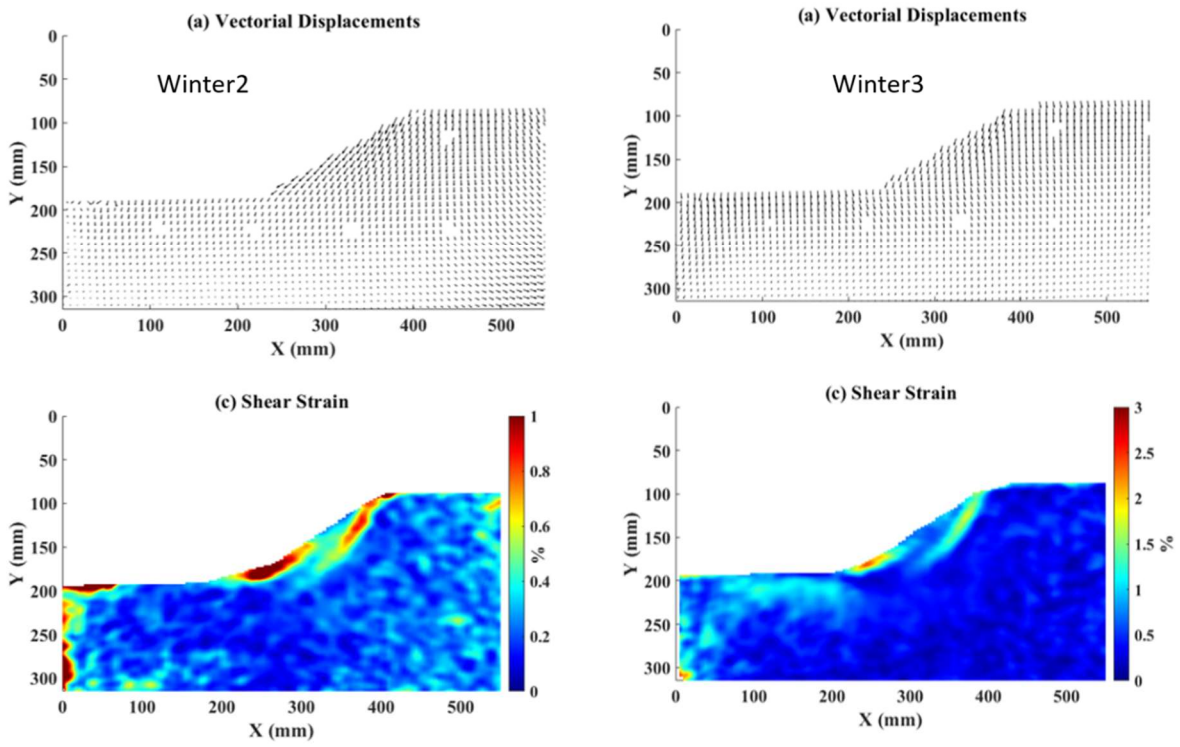


Figure 7-88 Comparison of vectorial displacements and shear strain distributions at the end of Winter 2 and Winter 3 for the M-T6r test.

7.10 Conclusions:

Chapter 7 presented a detailed investigation into the mechanical and hydraulic responses of a slope model subjected to climate-driven seasonal variations and controlled flooding events. This chapter aimed to replicate and understand the progressive effects of environmental stressors, such as winter rainfall and summer drying periods, on slope stability, with particular emphasis on pore water pressure (PWP) dynamics, displacement patterns, and strain distribution. Through systematic testing and monitoring, the chapter highlighted critical insights into the factors that govern slope behaviour under alternating wetting-drying conditions and transient flooding.

The experimental results demonstrated that sustained winter rainfall led to a gradual buildup of pore water pressure, especially concentrated near the slope toe and mid-slope regions. By

the end of each winter cycle, this pressure buildup from prolonged wetting contributed to visible soil degradation and localised erosion in the M-T4 test. Observations showed that the distribution of pore water pressure across the slope was non-uniform, with significant gradients between the lower and upper sections. This gradient was reflective of the gravitational influence on infiltrating water, which, due to gravity, naturally pooled towards the base of the slope. Over consecutive cycles, these areas experienced cumulative stress, making them more susceptible to deformation and structural weakening.

The introduction of flood events further emphasised the slope's sensitivity to sudden decreases in hydrostatic pressure. The PWP measurements during the flooding phase revealed a marked increase in pressure across the slope, with maximum values at the lower levels. The abrupt application and subsequent drawdown of water in these flooding scenarios created fluctuating pore water pressures, which in turn induced shear strain within the soil matrix. The drawdown phase, characterised by rapid water table reduction, posed a challenge by creating a pressure differential that led to high localised shear strain near the slope crest. These shear strains, lead to slope failure at shallow depth.

Chapter 7 illustrates that the interaction between seasonal wetting-drying cycles and periodic flooding significantly impacts slope integrity over time. The cyclic build-up and reduction of pore water pressures not only affect displacement and strain but also contribute to long-term slope instability through cumulative erosion and strain localization. This cyclic loading and unloading process was particularly evident in shallow slope regions, where localised shear strain and visible cracks pointed to areas of potential failure.

In summary, Chapter 7 underscores the critical role of environmental factors such as seasonal rainfall, prolonged saturation, and abrupt drawdown in influencing slope stability. The results of this study highlight the need for comprehensive monitoring of PWP and strain, especially in slopes subjected to cyclic climate variations and extreme weather events. Understanding these dynamics can contribute to better predictive models for slope stability, allowing for improved design and maintenance strategies for slopes in regions susceptible to seasonal wetting and drying as well as flood risks. This research reinforces the importance of integrating environmental variability into slope stability assessments. The long-term erosion and localised strain accumulation can lead to unexpected failure mechanisms over time.

Chapter 8

Numerical Analysis Using GeoStudio

8.1 Introduction

In this chapter, a numerical modelling approach is presented, to assess whether it is possible to replicate the behaviour observed in the experimental tests using very low plasticity clay with the GeoStudio software. The analysis aims to evaluate and interpret the effects of flooding and drawdown conditions on slope stability. The simulation was conducted on the M-T5, M-T6, and M-T6r tests. GeoStudio, specifically the SLOPE/W and SEEP/W modules, was utilised for the modelling. SLOPE/W allows for comprehensive slope stability limit equilibrium analysis by calculating the factor of safety (FoS) under various loading and boundary conditions. SEEP/W complements this by providing insights into water flow, pore-water pressure distributions, and how this influence slope stability, particularly during periods of flooding and drawdown. This approach is consistent with the methodology used (Kaczmarek and Leśniewska, 2010), where numerical modelling was applied to simulate the behaviour of flood embankments under varying water levels. The study by (Kaczmarek and Leśniewska, 2010) examines the stability and deformation of flood embankments under changing water level conditions by comparing physical model experiments with numerical simulations. Using the finite element method (FEM) in PLAXIS, the numerical model was validated against data obtained from physical tests analysed through the geoPIV program. The study found that minor fluctuations in groundwater levels can induce significant deformations within the embankment structure. Moreover, it highlighted the efficacy of numerical modelling, particularly FEM, in replicating the complex interactions between soil and water, with results aligning closely with empirical observations. This research emphasises the importance of using numerical analysis for predicting and mitigating embankment instability caused by varying water levels, providing a robust framework for designing and assessing flood infrastructure resilience (Kaczmarek and Leśniewska, 2010). This chapter's approach aligns with methodologies such as those demonstrated in the study on the Princeville levee by (Jadid et al., 2020), which investigated the effects of repeated rise and fall of water levels on seepage-induced deformation and stability. Using finite element analysis in Plaxis 2D, their research highlighted how cyclic water

level fluctuations lead to cumulative internal deformation, progressively increasing the risk of levee failure. While their work focused on storm cycles and their impact on levees, this chapter uses GeoStudio's SEEP/W and SLOPE/W modules to analyse similar hydraulic phenomena, particularly the effects of flooding and drawdown on slope stability. The inclusion of numerical analysis in both studies underscores its critical role in assessing internal mechanisms that may not be apparent through traditional observational methods.

8.2 Material properties

Soil properties determined in Chapter 3 were used as inputs to SLOPE/W as follows:

1. Effective Shear Strength Parameters (ø' and c'):

The effective angle of internal friction (ø') was determined to be (26.6°). The effective cohesion was measured as (5 kPa). These parameters were derived from consolidated, drained triaxial tests conducted on the consolidated sandy clay mixture used in the experimental slope models.

2. Soil Unit Weight:

The dry unit weight of the soil was determined to be 18.04 kN/m³, and the saturated unit weight was 20.0 kN/m^3. These values were measured using standard laboratory compaction tests.

3. Soil-Water Characteristic Curve (SWCC):

The SWCC, derived from the Dewpoint potentiometer, provided the relationship between matric suction and volumetric water content for the sandy kaolin mixture.

Air-entry value: 800 kPa

Residual suction: 100000kPa

Saturated volumetric water content: 0.2

4. Hydraulic Conductivity: The saturated hydraulic conductivity (Ks) was measured from falling head test as 9.8×10^{-10} m/s. The permeability function, derived from the SWCC, was used to define the variation of hydraulic conductivity with suction.

5. Soil Compressibility:

The compressibility of the soil was represented by its volumetric modulus, determined to be (0.0002) m^2/ kN, based on consolidation tests.

These properties were input into the SEEP/W module to simulate pore-water pressure distribution during flood and drawdown scenarios. The resulting pressure fields were then transferred to SLOPE/W for stability analysis, enabling the calculation of the factor of safety under varying hydraulic and stress conditions. This approach ensured that the numerical analysis was directly linked to the experimentally determined soil parameters, providing consistency and reliability in the results.

8.3 Analysis sequence

The numerical models in this chapter are calibrated to reflect the physical tests as accurately as possible. Each stage is analysed to understand its effect on slope stability, pore pressure distribution, and potential failure mechanisms, enabling a direct comparison with the results observed in the physical model tests.

It should be noted that the prototype model is reproduced without the centrifuge limitations including radial curvature and a variable g-field.

The prototype model is reproduced in the numerical analysis without the inherent limitations of the centrifuge model, such as radial curvature and a variable g-field. These differences are crucial to acknowledge, as the centrifuge model, while effective in simulating prototype stresses within a scaled environment, introduces unique conditions that are not present in real-world prototypes. Radial curvature in the centrifuge model can influence stress distributions, leading to variations in the mechanical response of the slope. Similarly, the artificially increased and variable gravitational field (g-field) in the centrifuge creates non-uniform stress conditions that differ from the consistent gravitational field experienced in a prototype. These factors mean that the centrifuge model and the numerical model are not directly comparable in all respects. Despite these differences, the centrifuge model provides valuable insights into slope behaviour under controlled conditions. The numerical model, on the other hand, offers a

closer representation of the prototype environment. This distinction is important for interpreting the results and understanding the implications of each approach.

Each SLOPE/W and SEEP/W analysis was conducted in three stages:

1. Steady-State During Flood:

This stage simulates the flooding conditions under steady-state seepage, where the slope experiences sustained high water levels. The flood state aims to establish an initial pore-water pressure distribution that reflects the pressure buildup in the slope.

2. Gradual Drawdown:

In this stage, a gradual reduction in the water level is simulated to replicate realistic drainage conditions, closest to the situation provided by the centrifuge analysis. This phase considers the influence of a slow, controlled reduction in water level and the corresponding changes in pore pressure within the slope. Gradual drawdown is particularly relevant for assessing potential slope deformations and the progressive reduction in stability.

Gradual drawdown timing comparison

The relationship between model time (t model) and prototype time (t prototype) in centrifuge modelling is given by following equation:

$$t_{model} = \frac{t_{prototype}}{N^2} \qquad 8\text{-}1$$

Where:

The gradual drawdown in the centrifuge model was measured as approximately 3 minutes

t_{model} = 3 minutes

Therefore:

$t_{prototype}$ = 3×70×/60×24 = 10 days

By using a scaling factor of N = 70, the drawdown timing in the centrifuge (3 minutes) corresponds directly to the 10-day prototype duration used in the numerical simulation. This consistency validates the numerical model's representation of the experimental conditions, ensuring reliability and comparability of the results.

For all tests (M-T5, M-T6, and M-T6r), the numerical model simulated the gradual drawdown over 10 days in the prototype scale, replicating the same conditions as derived from the centrifuge time scaling. This ensures that the numerical analysis corresponds to the prototype behaviour, maintaining consistency with the experimental data.

3. Rapid Drawdown:

This stage models a sudden drop in water level, simulating scenarios where drainage occurs quickly after prolonged flooding. Rapid drawdown is critical in slope stability analysis, as the dissipation of pore pressures may lag behind the receding water level, potentially triggering slope failure due to the loss of external support without sufficient internal pressure adjustment.

8.4 M-T5 Test

8.4.1 Steady-State Analysis for M-T5 Test.

The steady-state condition for the M-T5 test was modelled to simulate the effects of sustained flooding on the slope stability under constant water pressure. In the centrifuge model, the water level above the slope was set at 11.2 mm in model scale, which corresponds to 0.78 m in prototype scale at a scaling factor of 70g, creating a steady hydrostatic pressure within the slope. This initial condition serves as a baseline for assessing how variations in water pressure, such as those introduced during drawdown, affect the stability and potential failure mechanisms of the slope.

Water Pressure Distribution

In **Error! Reference source not found.**, the water pressure contours are displayed throughout the slope for the case of sustained flooding.

Gradual Increase in Pressure:

There is a gradual increase in water pressure down the slope, represented by different colour contours, reaching values over 200 kPa near the base of the slope.

Factor of Safety (FoS) Analysis

In Figure 8-2, the critical slip surface and the Factor of Safety (FoS) are presented:

Critical Slip Surface:

The assessment of the critical slip surface was performed using the Limit Equilibrium Method (LEM) in SLOPE/W, specifically selecting the Morgenstern-Price Method. This method satisfies both force and moment equilibrium. For the interslice force function, the Half-Sine Function was selected. By combining the Morgenstern-Price Method with the Half-Sine interslice force function and the Grid and Radius Search, the analysis provided a detailed and reliable evaluation of slope stability for the M-T5, M-T6, and M-T6r tests.

The red line indicates the critical slip surface, which represents the most likely failure plane under these conditions. This slip surface begins near the crest of the slope and extends to the midsection, indicating a potential shallow failure.

Factor of Safety: The calculated FoS for this steady-state condition is 1.015, which is very close to unity (1.0). This value indicates a marginally stable slope. The low FoS value is a significant finding, as it reflects just stable stress conditions under continuous flooding.

Conclusion.

The steady-state analysis of the M-T5 test under flood conditions shows that the slope is in a precarious state, with an FoS of 1.015 indicating marginal stability. In fact, according to the centrifuge test (Chapter 7), this slope had already failed at the end of the Winter 3 (continuous rainfall), but then appeared to be stable under the subsequent flood condition. Hence there is very good agreement with the observations from the centrifuge model. This stage provides a critical foundation for understanding the effects of flooding and sets the stage for analysing the impact of drawdown, where the slope is likely to experience further stress and potential failure.

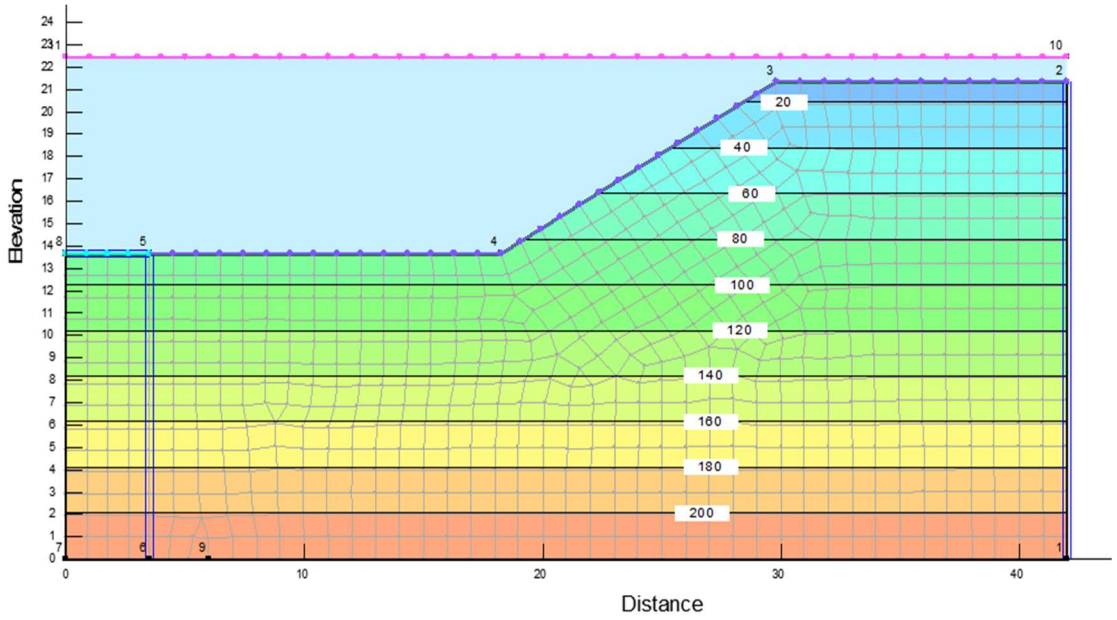


Figure 8-1 Steady state flooding condition for M-T5 test.

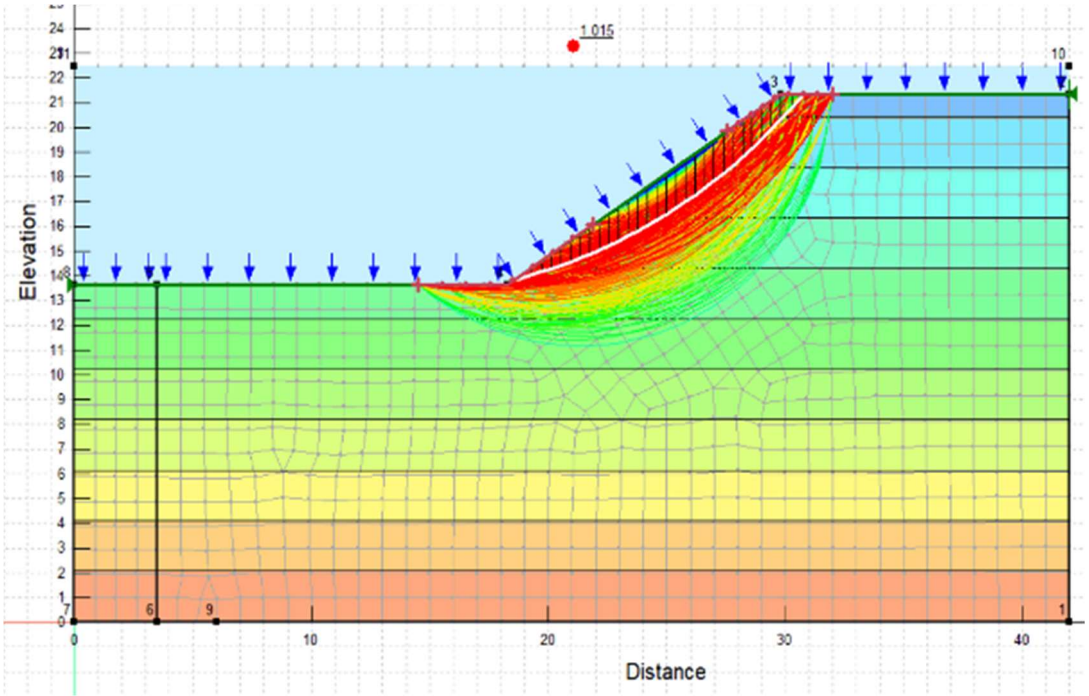


Figure 8-2 Critical slip surface and factor of safety of steady-state flooding condition for M-T5 test.

8.4.2 M-T5 Test: Gradual Drawdown Condition.

Figure 8-3 depicts the slope stability of the M-T5 model under gradual drawdown conditions. Gradual drawdown simulates a scenario where the water level is lowered relatively slowly, allowing for partial adjustment of pore pressures within the slope. Here, this scenario is closest to the case in the centrifuge as discussed in Section 8.3.

The water pressure distribution is shown in colour contours, and the critical slip surface is marked in red with a Factor of Safety (FoS) of 0.439. This low FoS suggests that the slope has completely failed, even though the water level was lowered gradually. The critical slip surface at the end of drawdown is located closer to the surface. This surface is indicative of a shallow rotational failure, a common failure mode in slopes experiencing reduced external support from gradual drawdown.

This suggests that even a gradual drawdown can induce instability in highly saturated slopes if pore pressure dissipation is insufficient. This scenario suggests that slopes in similar flood conditions may fail as water recedes, even when this is relatively slow.

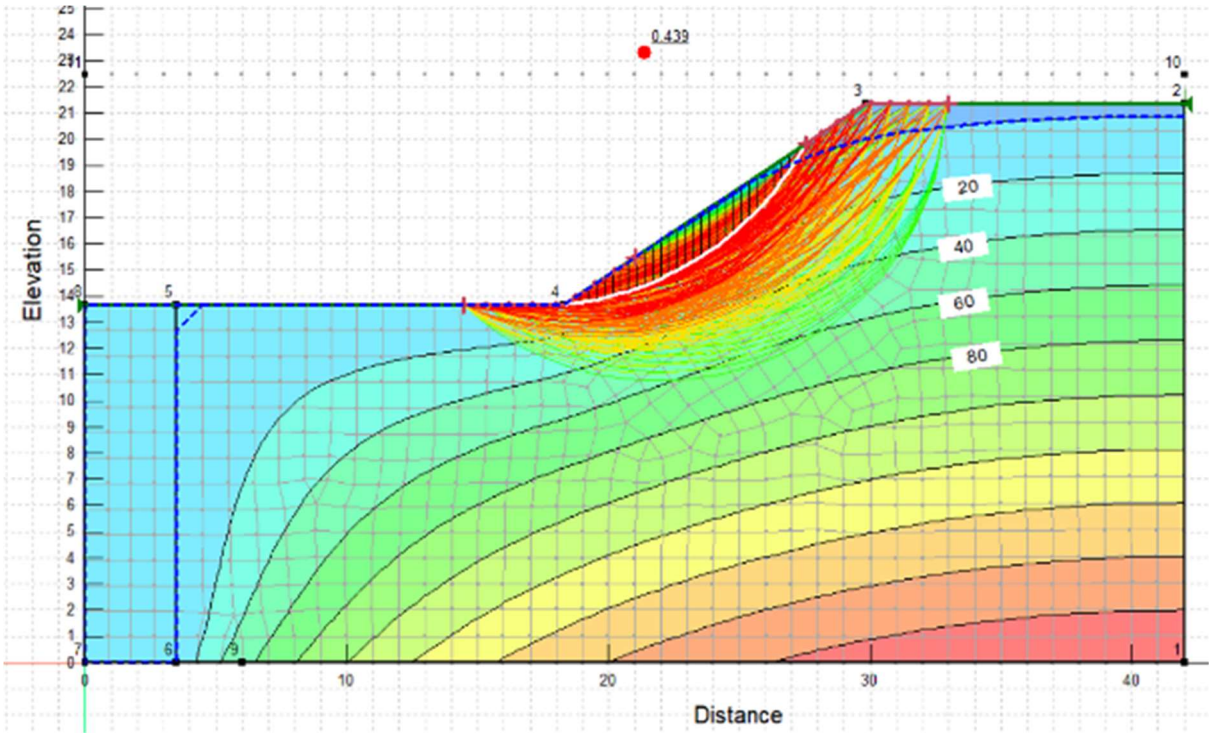


Figure 8-3 Gradual drawdown condition with critical slip surface and factor of safety for M-T5 test.

Analysis of factor of safety (FoS) during gradual drawdown (M-T5 Test).

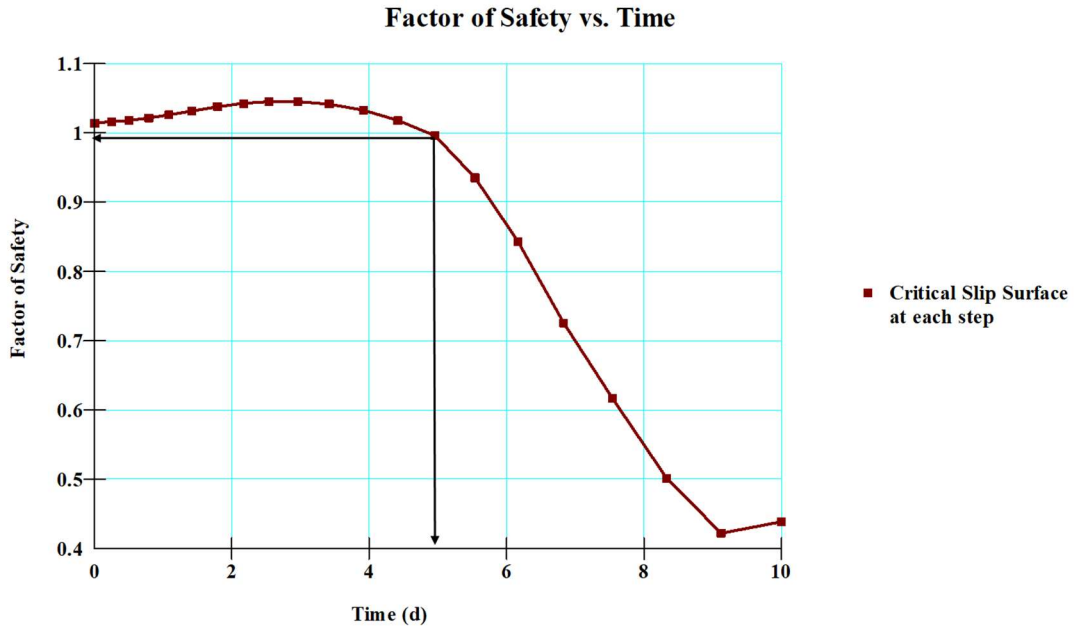


Figure 8-4Figure 8-4 shows the Factor of Safety (FoS) plotted against time (days) during the gradual drawdown condition for the M-T5 test. The FoS values were calculated over a period of 10 days. At the start of the drawdown process (Day 0), the FoS is approximately 1.015, indicating a just stable slope under initial steady-state flooding conditions. Over the first few days, the FoS initially increases then decreases slowly. By day 4, the FoS is around 1.03, which is still within a relatively safe range. This lack of decline in FoS in the early days suggests that the slope has some ability to adjust to the changing water pressures without immediately destabilising. After day 4, there is a noticeable acceleration in the decline of FoS, with the values dropping more sharply. After day 5, the FoS falls below 1.0, indicating an unstable condition. This period of accelerated decline corresponds to the deeper layers starting to release pore pressures. As internal pressures adjust more slowly than surface pressures, the overall stability of the slope is compromised, increasing the likelihood of failure. By day 9–10, the FoS reaches values close to 0.4. In reality the slope will have failed well before then.

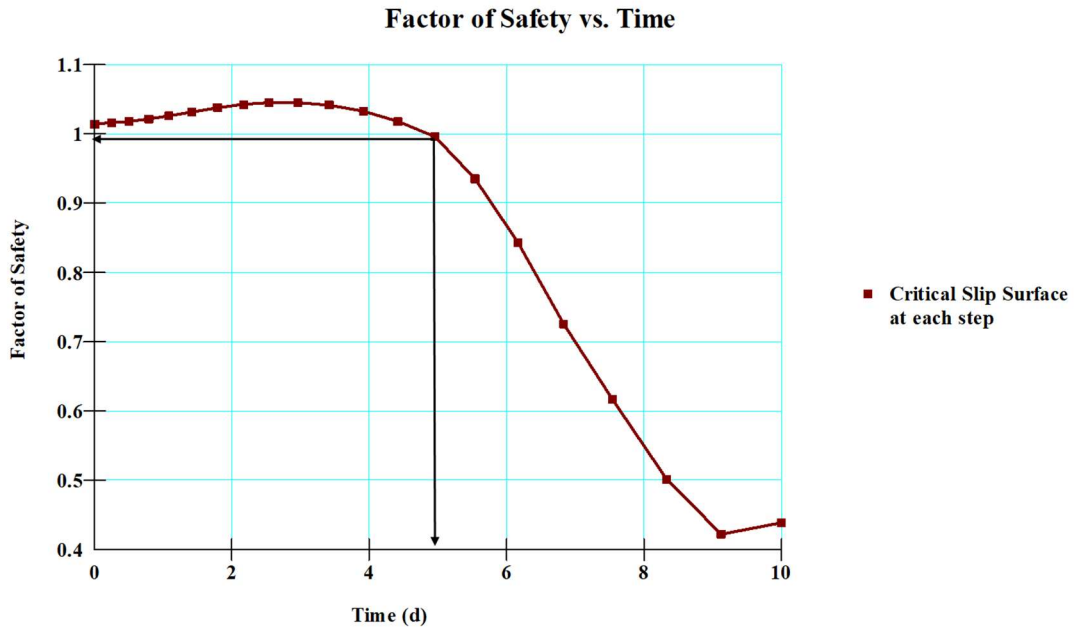


Figure 8-4 Factor of safety over time during gradual drawdown scenario for M-T5 test.

Pore water pressure at different heights over time

The selected PWP monitoring locations provide a comprehensive setup for analysing the effects of drawdown on slope stability in the M-T5 test. The arrangement along a vertical section under the mid slope allows tracking the delayed dissipation in deeper layers, essential for understanding internal stress changes and potential failure mechanisms. Figure 8-5 shows the chosen spots for checking the Pore-Water Pressure (PWP) in the mid slope model during the drawdown scenario of the M-T5 test. The blue points along the vertical section of the slope mark the positions where PWP data will be gathered.

Figure 8-6 shows pore water pressure changes over time at specific heights within the mid slope during the 10-day gradual drawdown process. Each curve represents a specific elevation, with different colours showing pressure variations over time. The higher elevations experience a quicker drop in pressure, reflecting the faster response to water level changes near the surface.

The gradual reduction in water pressure over time is evident, with pressures slowly decreasing as water is drawn out of the slope.

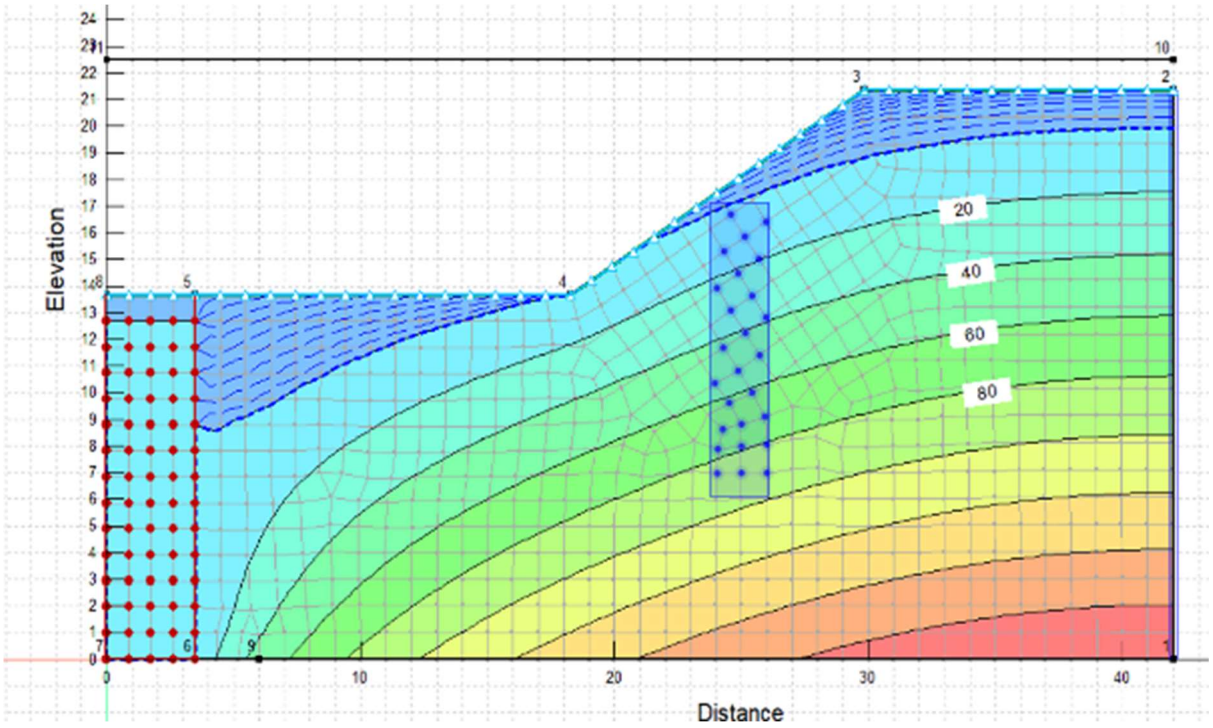


Figure 8-5 Pore water pressure monitoring locations in slope model during drawdown scenario for M-T5 test.

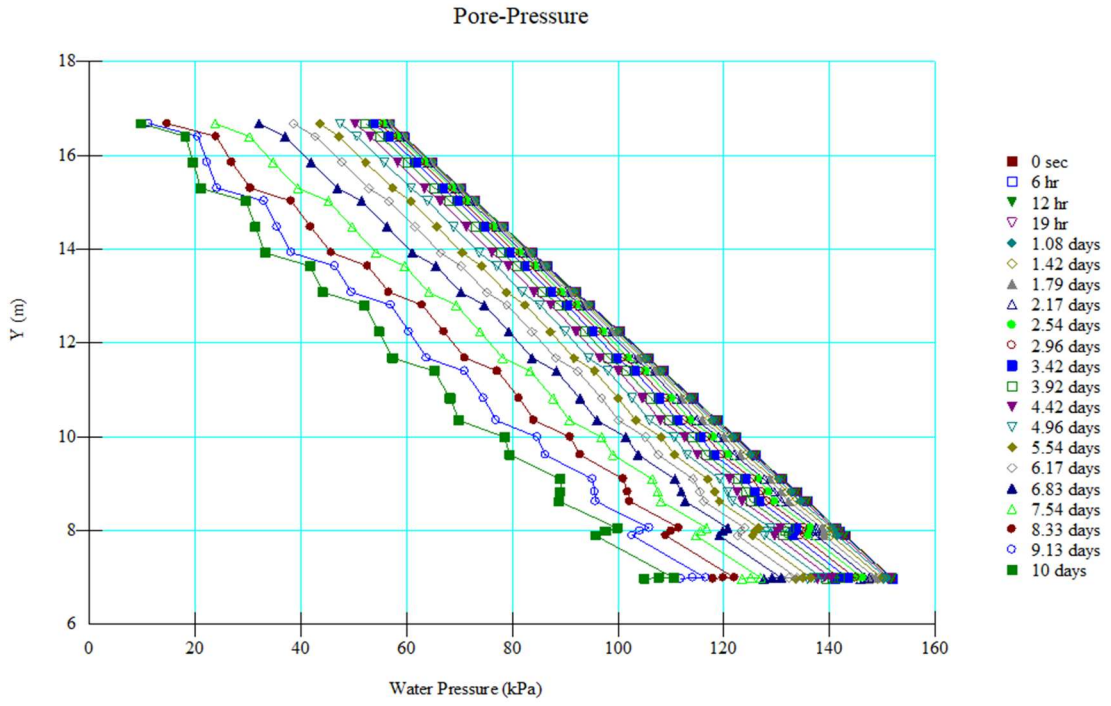
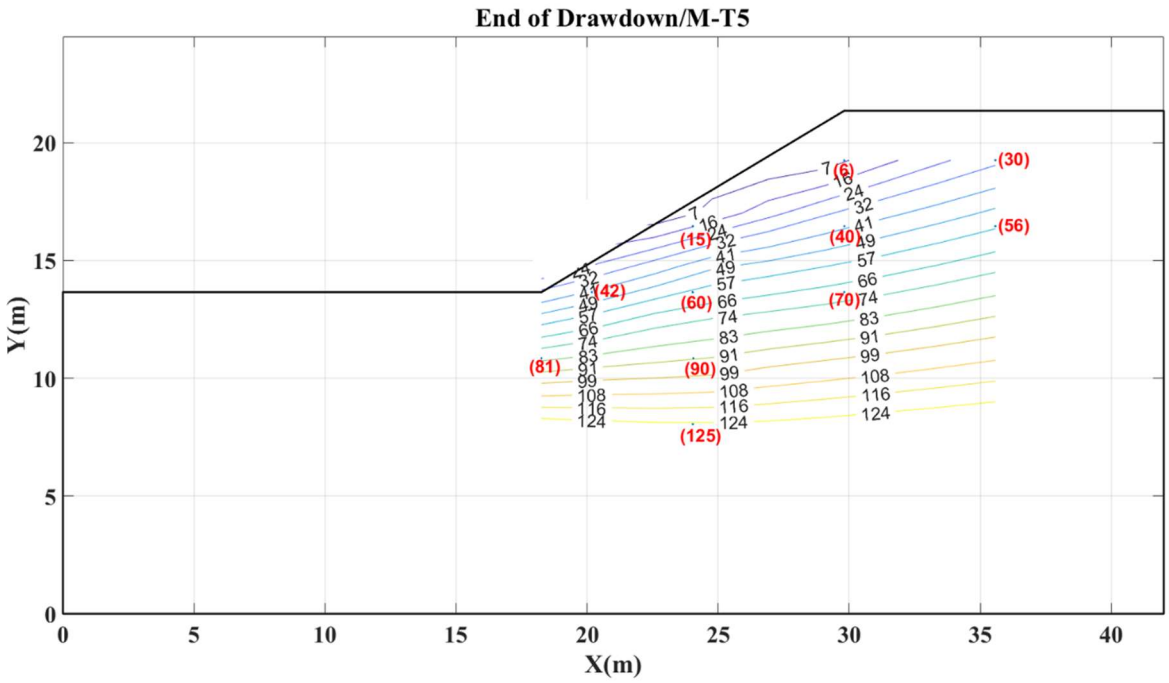


Figure 8-6 Pore water pressure dissipation at different heights in slope during gradual drawdown for the M-T5 test.

Validation of Pore Water Pressure Between Physical and Numerical Models:

Figure 8-7 compares the pore water pressure (PWP) distribution at the end of the drawdown in both the physical (centrifuge) and numerical (SEEP/W) models for the M-T5 test. The PPTs located along the slope profile, particularly in the lower and mid-slope zones, recorded high PWP values, reaching up to 125 kPa. This aligns closely with the SEEP/W numerical simulation, which shows a steep hydraulic gradient and similar pressure contours at those depths. The correlation in trend and magnitude between the measured and modelled PWP values provides strong validation of the numerical model's accuracy in simulating seepage behaviour during drawdown.



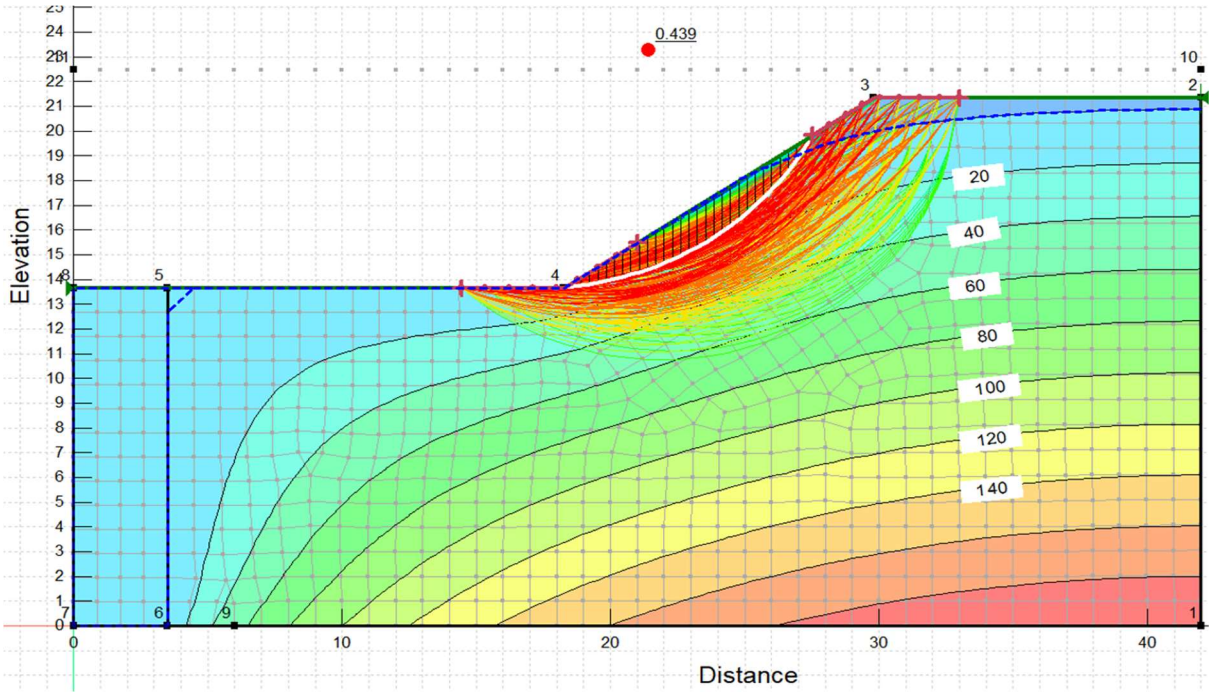


Figure 8-7 Comparison of Pore Water Pressure Distribution at the End of Drawdown between Centrifuge Test (PPT Readings) and SEEP/W Numerical Model for M-T5 (Prototype Scale).

8.4.3 Slope Stability Analysis for M-T5 Test: Rapid Drawdown Condition.

The rapid drawdown scenario represents an immediate lowering of the water level, simulating a situation where the slope loses its supporting water pressure very quickly (in fact infinitely quickly). In this condition, pore pressure remains high within the slope body due to the lack of time for dissipation. The critical slip surface typically appears close to the slope face, extending downward towards the toe, indicative of a surface-parallel failure mode.

As shown in Figure 8-8, the factor of safety (FoS) drops dramatically to below 0.2 almost immediately after the water level is rapidly lowered. This critically unstable condition reflects the immediate loss of stabilising water pressure on the slope face, which accelerates the potential for slope failure. Figure 8-9 further illustrates this, showing the rapid decline in FoS over time following the drawdown. The immediate nature of this response underscores that the rapid drawdown condition is significantly more critical compared to the gradual drawdown condition.

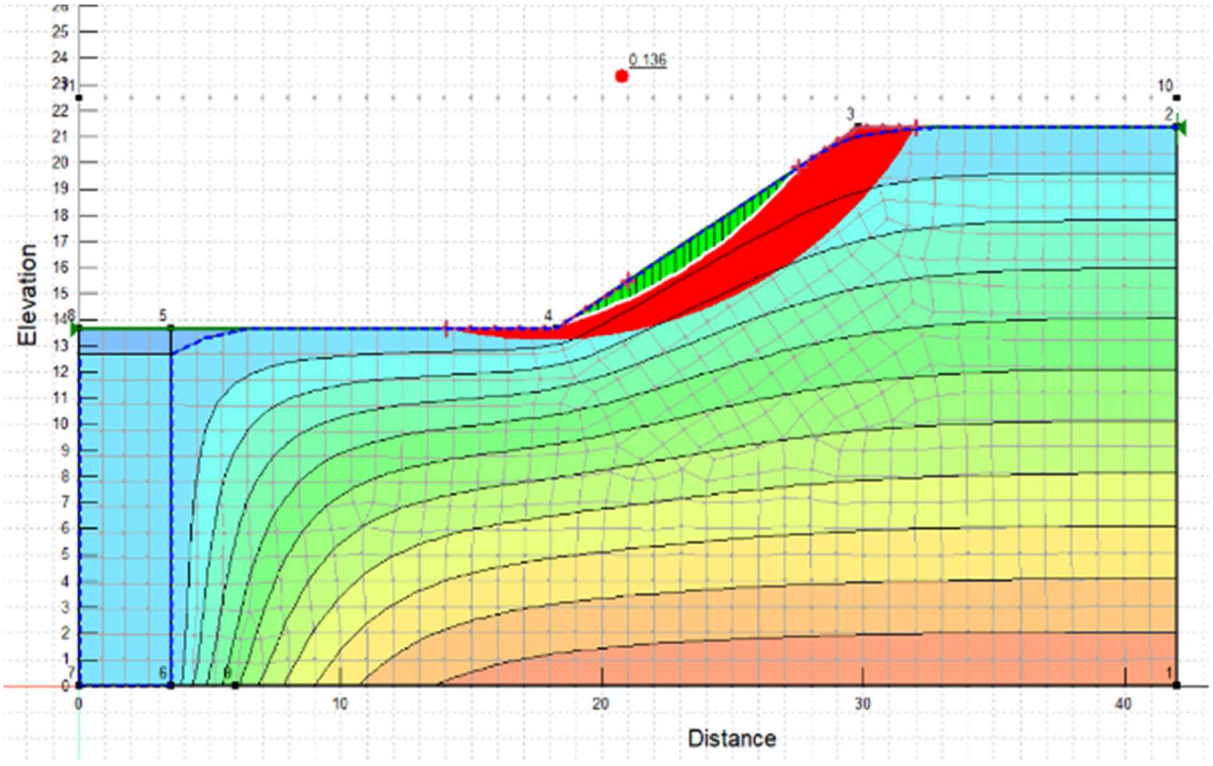


Figure 8-8 Pore pressure distribution and critical slip surface at 0.58 day during rapid drawdown.

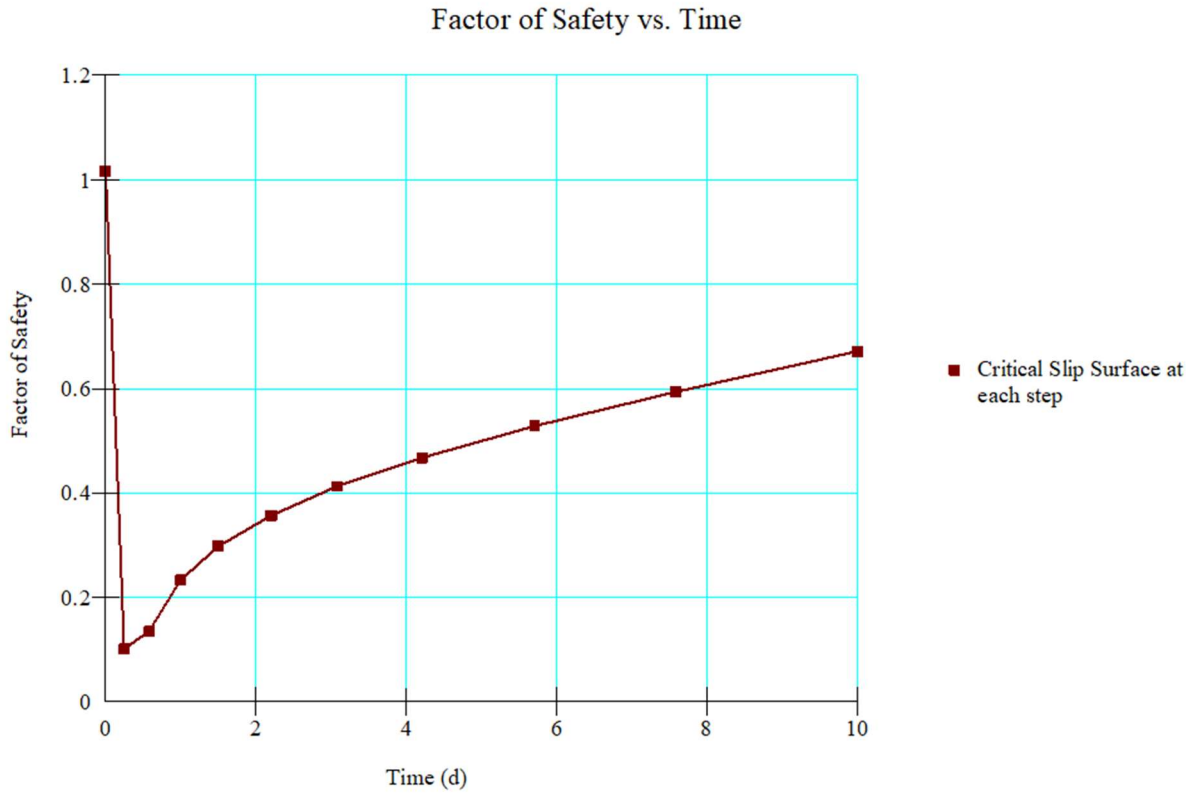


Figure 8-9 Factor of safety vs. time during rapid drawdown condition.

Pore water pressure at different heights over time

Figure 8-10 displays the time-dependent dissipation of pore-water pressure at different heights within the slope during the rapid drawdown condition for the M-T5 test. At the onset of rapid drawdown (0 seconds), pore-water pressures are relatively high throughout the slope due to the sustained flooding conditions that preceded drawdown. As the water level is quickly lowered, the surface layers respond immediately, with a noticeable reduction in pore-water pressure within the first few hours. This quick response reflects the rapid dissipation of pressure close to the exposed surface. It takes several days (up to 10 days) for the deeper layers to exhibit significant dissipation, highlighting the lag in pressure response with depth. This lag effect is typical in rapid drawdown scenarios, where deeper regions cannot equilibrate with the reduced surface water level as quickly, leading to potential stability concerns.

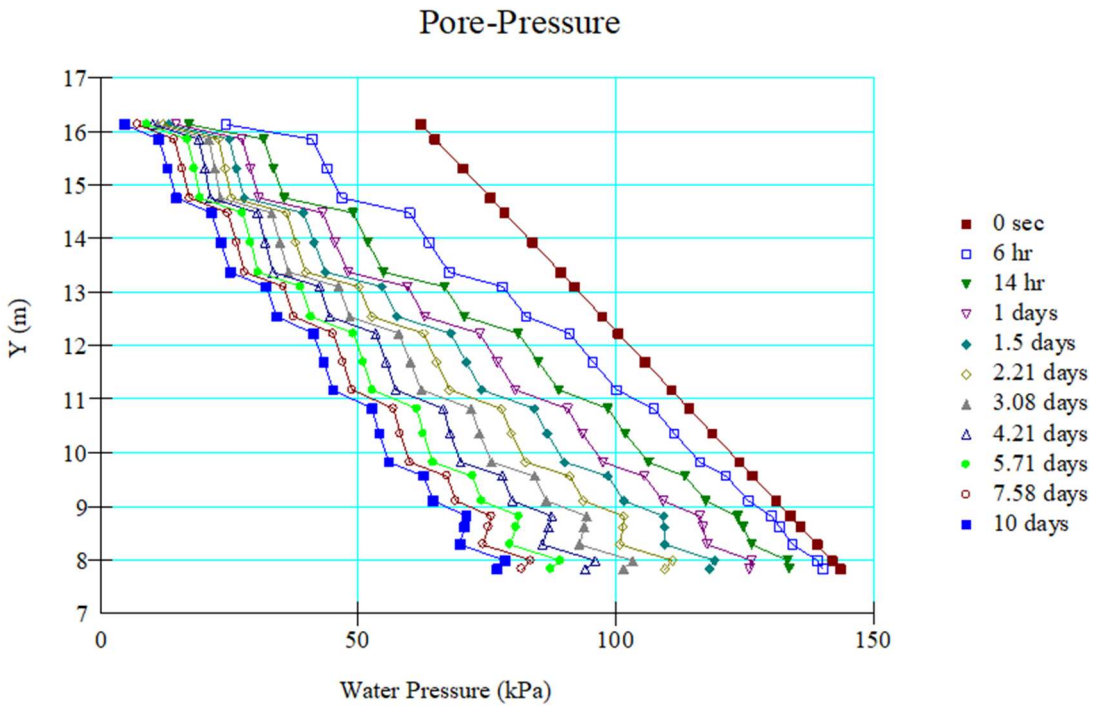


Figure 8-10 Pore water pressure during rapid drawdown (MT5 Test).

8.5 M-T6 Test

8.5.1 Steady-State Analysis for M-T6 Test using ϕ'=26.6°.

Figure 8-13 illustrates the steady-state condition for the M-T6 test, simulating the effects of sustained flooding on slope stability under constant water pressure. In this scenario, the slope is subjected to a steady water level, with pore-water pressures distributed throughout the slope profile. Compared to the M-T5 test, the water level above the crest in the M-T6 test is higher and equal to 31 mm which corresponding to 2.2 metres in prototype scale, increasing the overall hydraulic load on the slope. Using the critical state value of ϕ', the Factor of Safety (FoS) for this condition is approximately 1.147, indicating relatively high stability under these intense flooding conditions. The colour contours represent the pore-water pressure distribution across the slope, with higher pressures concentrated at the lower elevations. This steady-state condition provides an essential baseline before initiating drawdown, highlighting the initial stability status and internal pressure conditions. It establishes a reference for evaluating the subsequent effects of drawdown on slope stability in the M-T6 test.

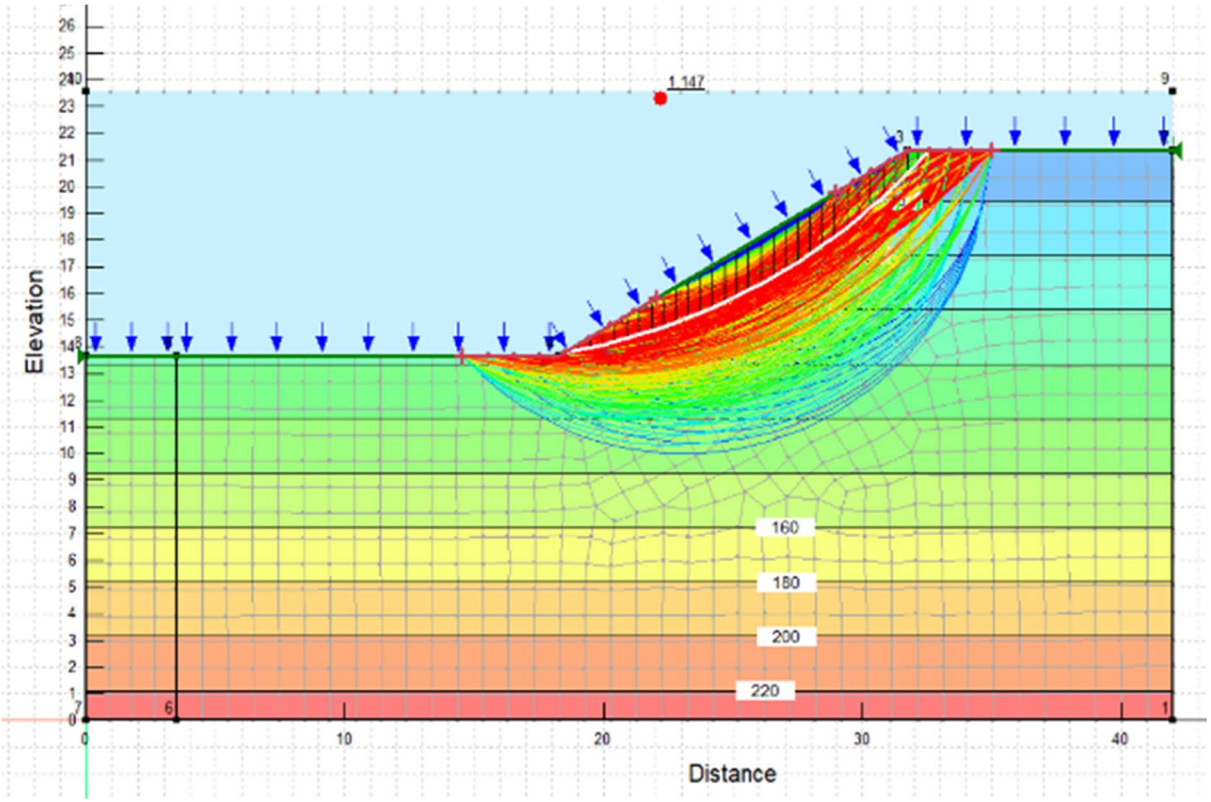


Figure 8-11 Steady-State Flooding Condition for M-T5 Test.

8.5.2 Stability Analysis for M-T6 Test: Gradual Drawdown Condition using ϕ'=26.6°.

Figure 8-14 illustrates the slope stability analysis for the M-T6 test under gradual drawdown conditions. In this scenario, the water level was reduced over a period of 10 days on a prototype scale, allowing for a controlled decrease in pore-water pressure across the slope. A critical slip surface is identified, shown in white, along with the Factor of Safety (FoS), which is approximately 0.473. This low FoS indicates that the slope has failed as drawdown progresses.

This is a different result in comparison to the centrifuge test which did not fail, even during drawdown. To examine the possible scenario that the shear strength was higher due to overconsolidation of the clay, an additional Slope/w analysis was conducted to examine what soil shear strength (i.e. friction angle) would be needed to just prevent drawdown failure. The iterated result is presented below.Figure 8-15

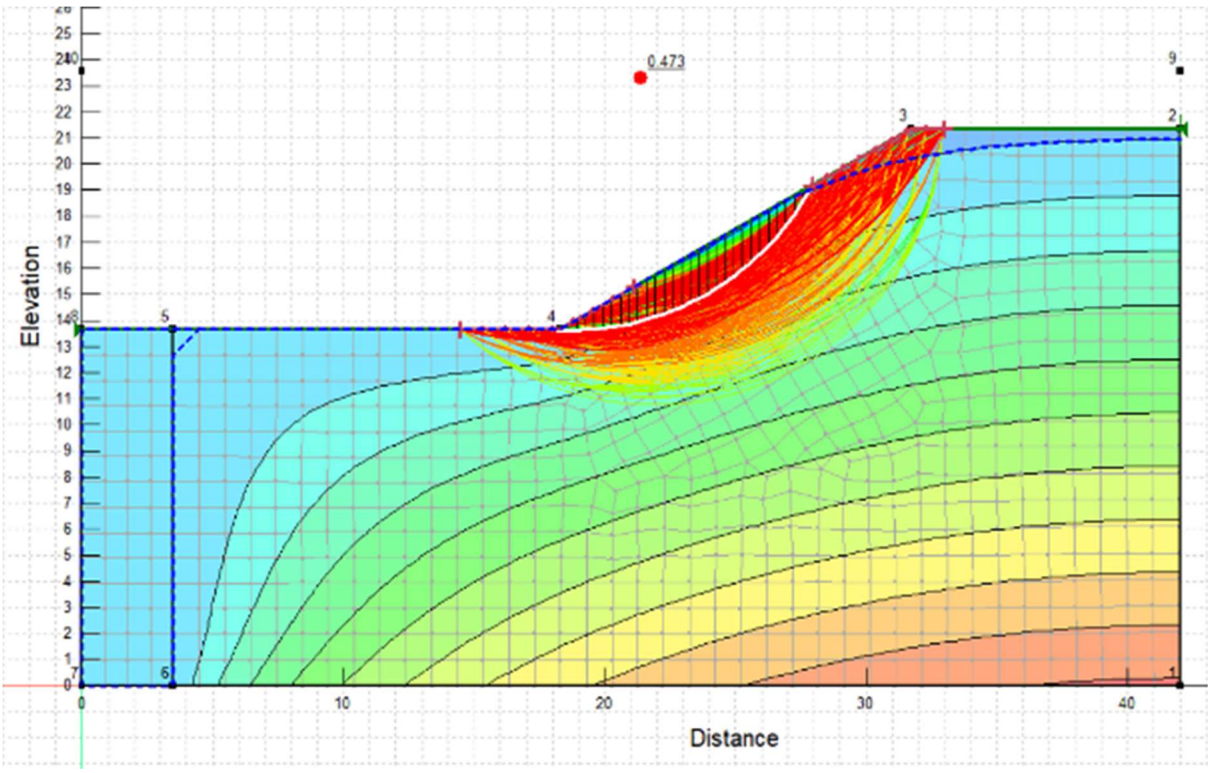


Figure 8-12 Gradual drawdown condition with critical slip surface and factor of safety for M-T6 test using ϕ'=26.6°.

8.5.3 Steady-State Analysis for M-T6 Test using ϕ'=31°.

Figure 8-13 illustrates the steady-state condition for the M-T6 test with ϕ'=31°, which is typical for an overconsolidated clay. In this scenario, the slope is subjected to a steady water level, with pore-water pressures distributed throughout the slope profile. As in the previous analysis, the water level above the crest in the M-T6 test is equal to 31 mm which corresponding to 2.2 metres in prototype scale. The Factor of Safety (FoS) for this condition is approximately 2.138, indicating relatively high stability under these intense flooding conditions. The colour contours represent the pore-water pressure distribution across the slope, with higher pressures concentrated at the lower elevations. This steady-state condition provides an essential baseline before initiating drawdown, highlighting the initial stability status and internal pressure conditions. It establishes a reference for evaluating the subsequent effects of drawdown on slope stability in the M-T6 test.

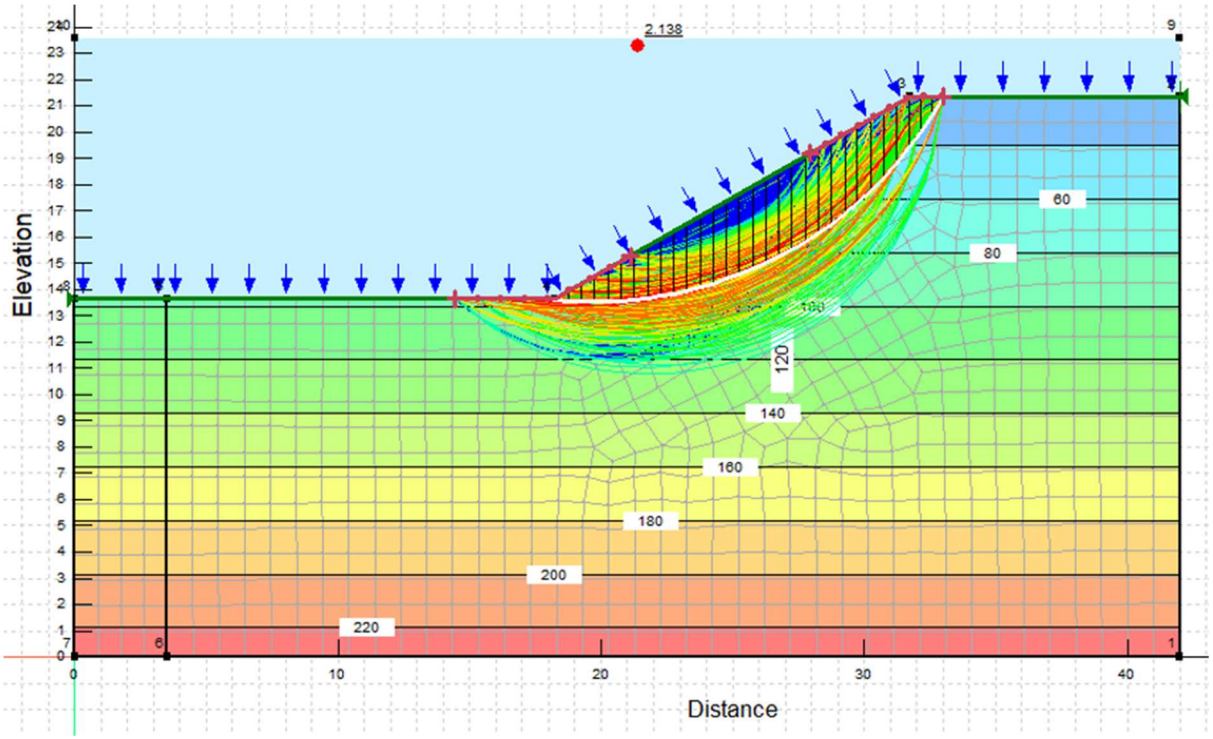


Figure 8-13 Steady-State Flooding Condition for M-T6 Test.

8.5.4 Stability Analysis for M-T6 Test: Gradual Drawdown Condition using ϕ'=31°.

Figure 8-14 illustrates the slope stability analysis for the M-T6 test under gradual drawdown conditions with a higher ϕ' of 31. In this scenario, the water level was reduced over a period of 10 days on a prototype scale. A critical slip surface is identified, shown in white, along with the Factor of Safety (FoS), which is approximately 1.02. This value suggests marginal stability during the drawdown process, which appears to be much closer to the centrifuge prototype condition. Figure 8-15Figure 8-15 shows the variation of the Factor of Safety (FoS) over time during the gradual drawdown scenario in the M-T6 test. Initially, the FoS remains stable at approximately 2.138, indicating a highly stable slope condition. However, as the water level begins to drop, the FoS gradually declines, reflecting the effect of pore-water pressure dissipation and changing hydraulic conditions within the slope. By Day 6, the FoS begins to decline more rapidly, dropping below 2.0 and continuing to fall until it reaches approximately 1.02 by Day 10. This significant reduction in FoS suggests a progressive reduction in slope stability, approaching marginal stability at the end of the drawdown period.

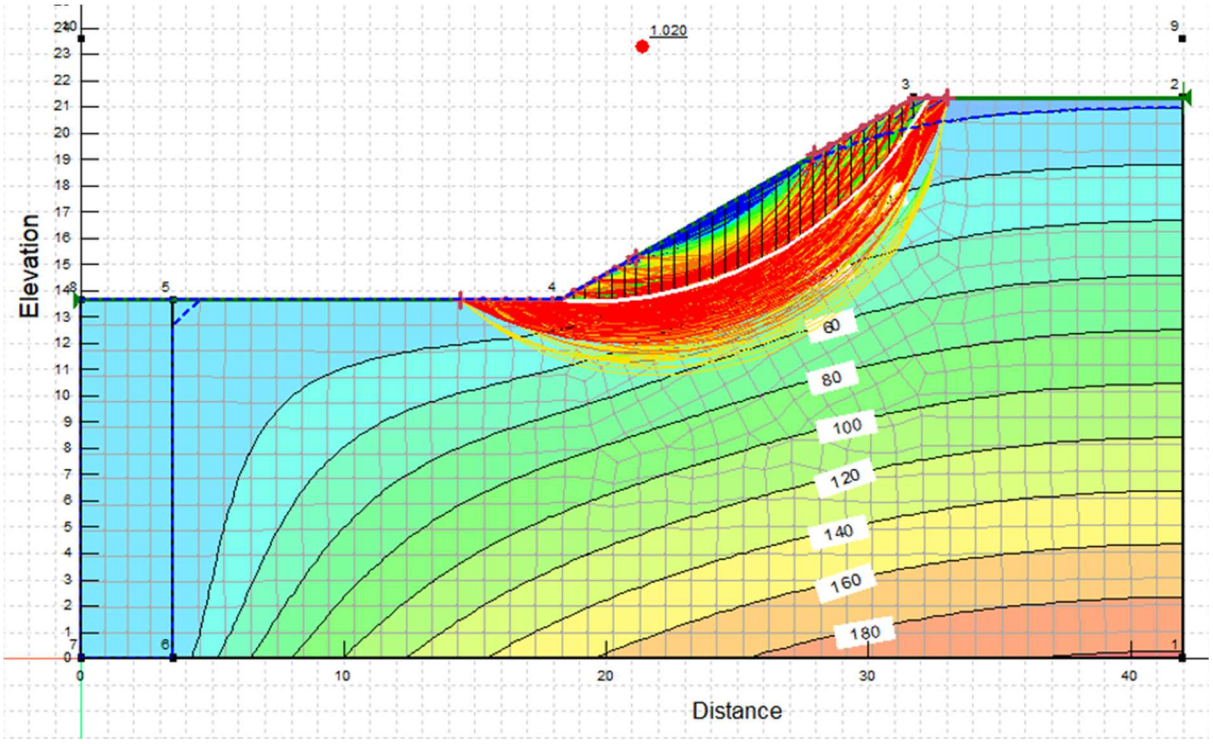


Figure 8-14 Gradual drawdown condition with critical slip surface and factor of safety for M-T6 test.

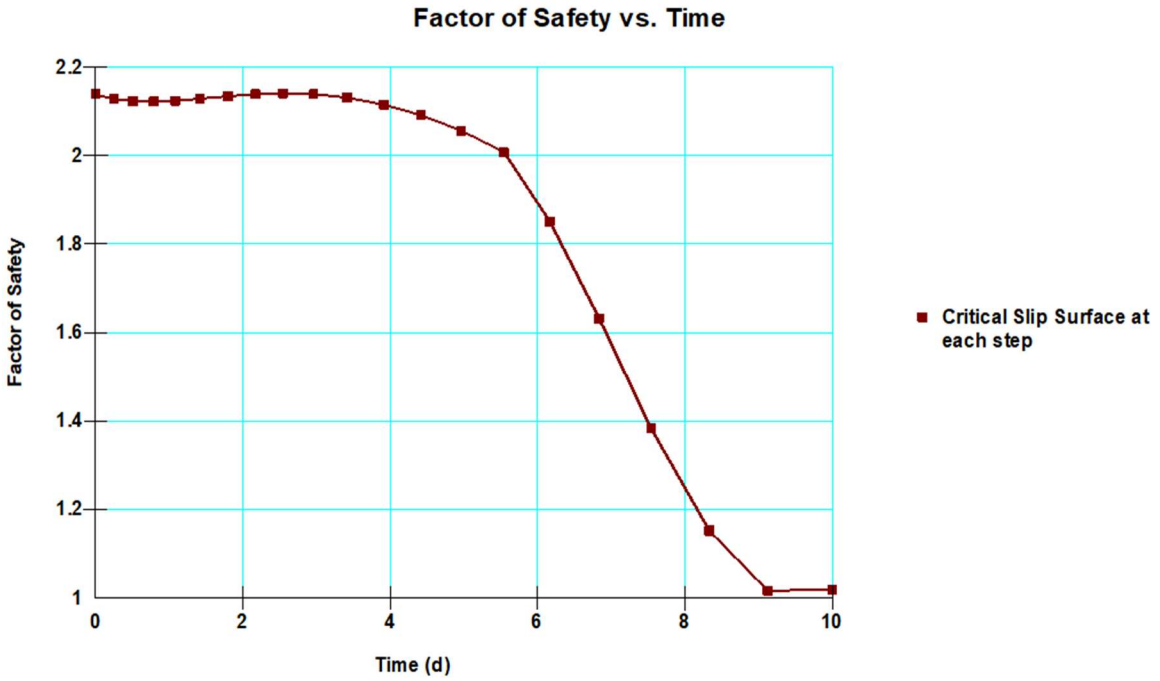


Figure 8-15 Factor of safety over time during gradual drawdown scenario for M-T6 test.

8.5.5 Pore water pressure at different heights over time

Figure 8-17 shows the changes in pore-water pressure at various heights under the mid slope during the gradual drawdown phase of the M-T6 test. This location is similar to the monitoring point used in the M-T5 test (Figure 8-16), providing a basis for comparison between the two tests. This pattern matches what was seen in the M-T5 test, proving that the same pore pressure dissipation trends happen during gradual drawdown, even when the water level rises above the crest.

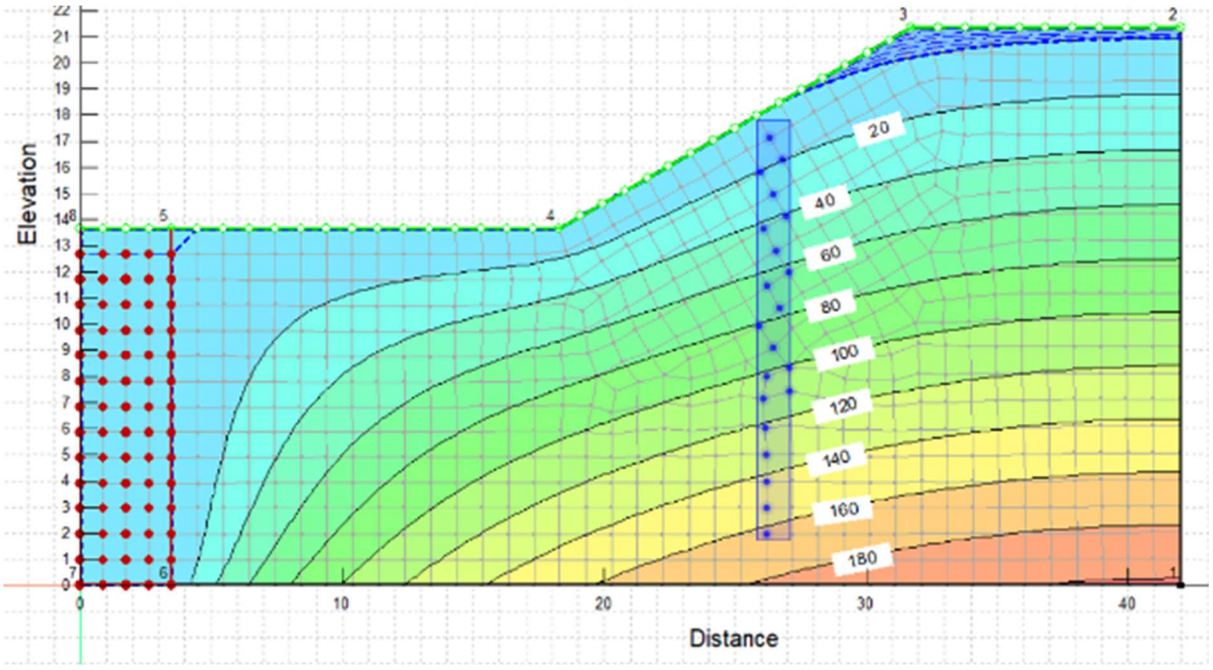


Figure 8-16 Pore water pressure monitoring locations in slope model during drawdown scenario for M-T6 test.

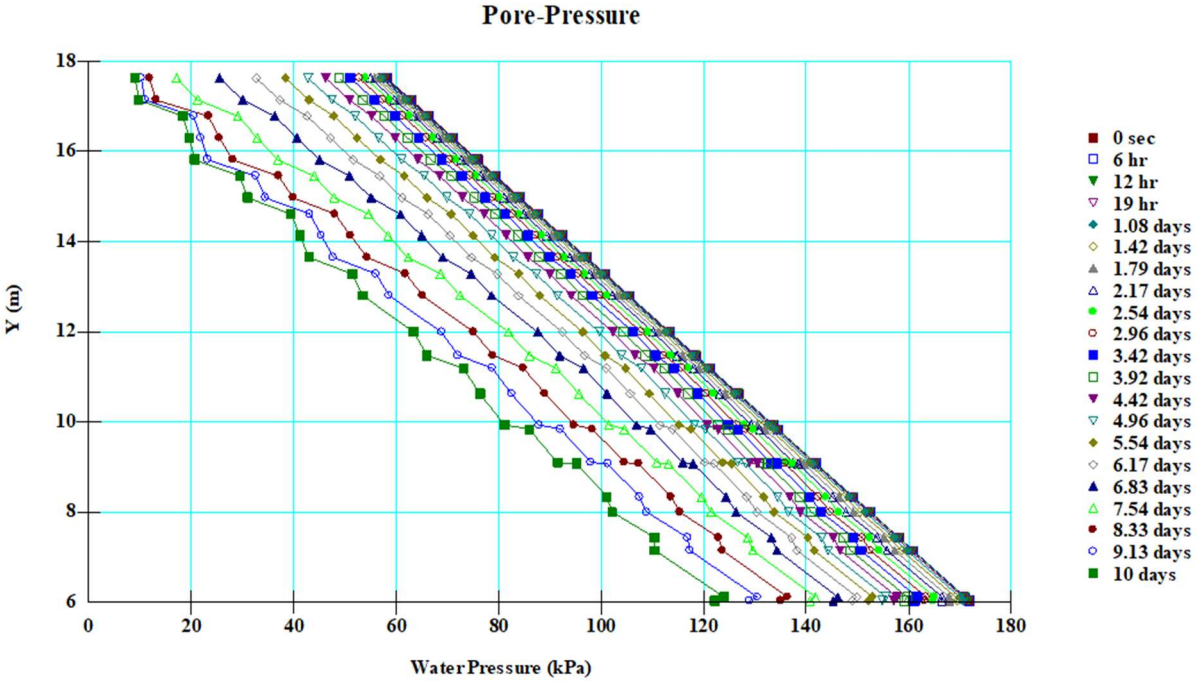
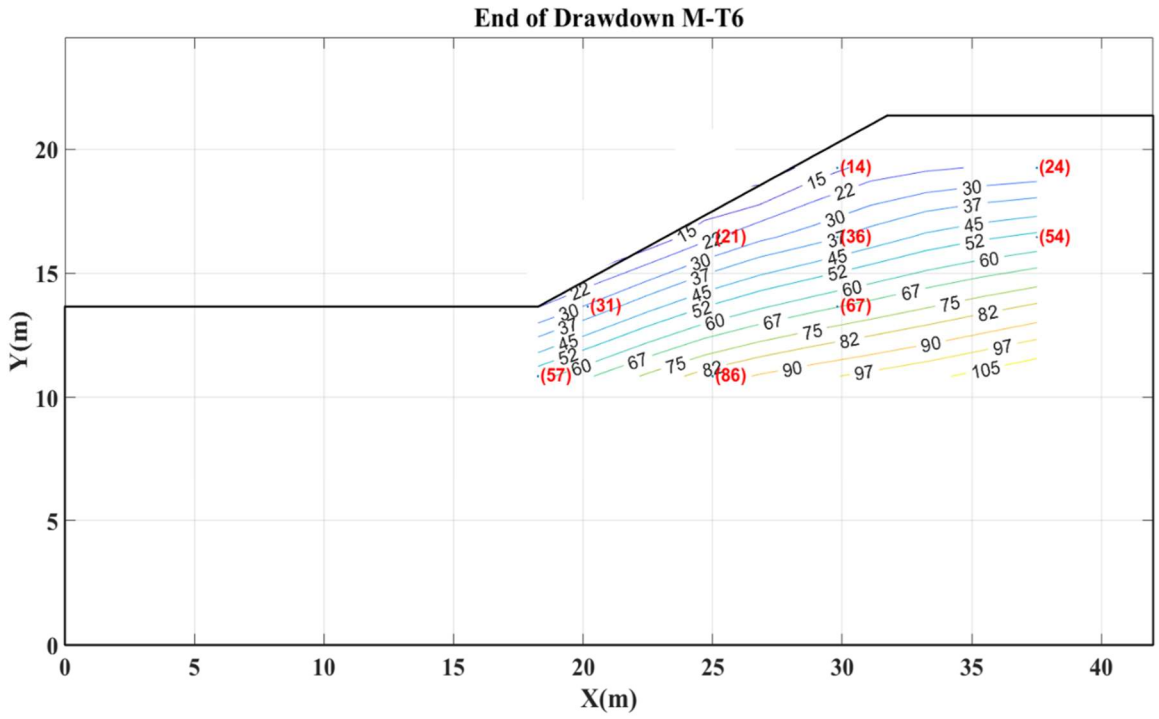


Figure 8-17 Pore water pressure dissipation at different heights in slope during gradual drawdown for the M-T6 test.

Validation of Pore Water Pressure Between Physical and Numerical Models for M-T6 test:

A comparison between pore water pressure (PWP) results from the centrifuge test (M-T6) and numerical simulations using SEEP/W (Figure 8-18) shows that the PWP readings in the physical model are generally higher than those predicted numerically. This discrepancy is largely due to the uncoupled nature of the SEEP/W analysis, which does not consider the coupling between hydraulic and mechanical behaviour in the soil. As explained by Pinyol et al. (2008) , rapid or semi-rapid drawdown is a complex phenomenon where the interplay between pore pressure dissipation, effective stress redistribution, and soil deformation must be accounted for. Uncoupled models, like SEEP/W, may underestimate PWP during drawdown due to the assumption of instantaneous pore pressure response, ignoring time-dependent consolidation and seepage lag. Additionally, the slope in M-T6 was formed from a pre-consolidated block, unlike the re-cut slope used in M-T6r, likely giving M-T6 a higher shear strength. To reflect this in the numerical model, the friction angle (φ) was adjusted from its original value to 31°, aligning better with the M-T6 slope. This higher strength may explain the absence of swelling and better resistance to instability under drawdown. The higher PWP observed in the centrifuge model also reflects the realistic retention capacity and stiffness of the slope material that may not be fully captured in numerical simulations.



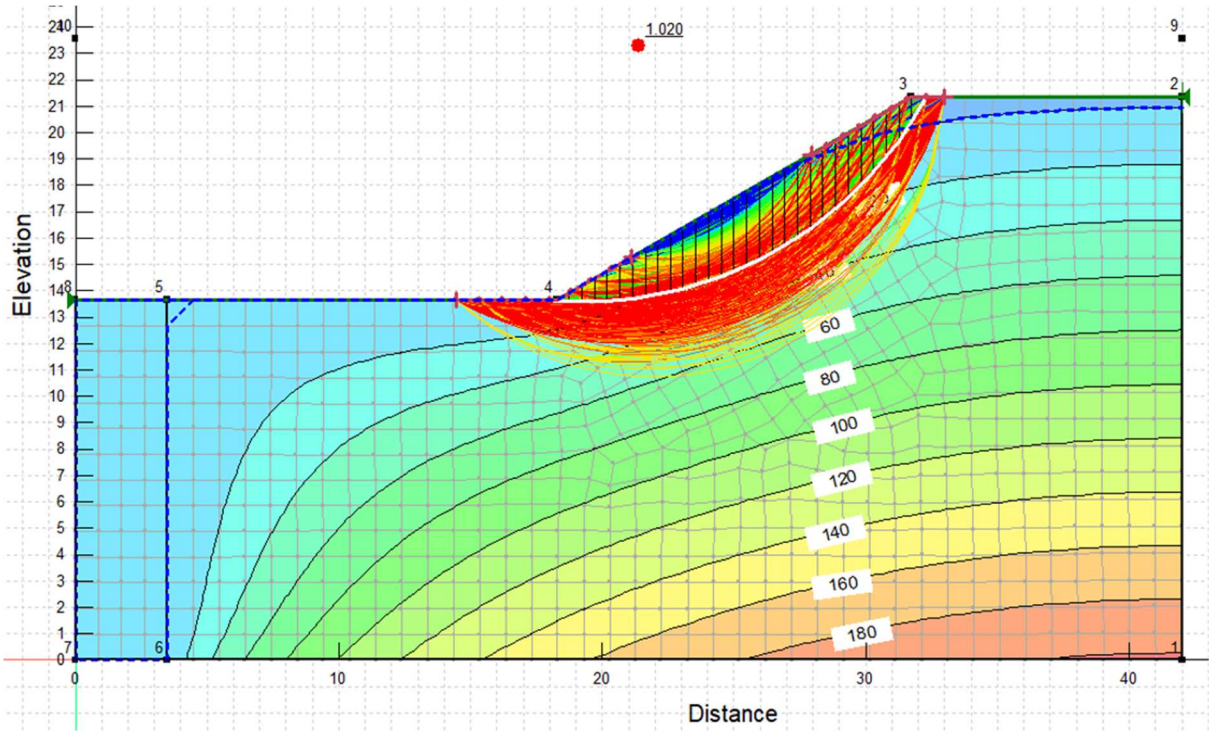


Figure 8-18 Comparison of Pore Water Pressure Distribution at the End of Drawdown between Centrifuge Test (PPT Readings) and SEEP/W Numerical Model for M-T5 (Prototype Scale).

8.6 M-T6r Test.

8.6.1 Steady-State Analysis for M-T6r Test.

Figure 8-19presents the steady-state water pressure distribution for the M-T6r test, showing the slope stability under sustained flooding conditions before any drawdown events. In this test scenario, the water level was positioned 3.45 m above the crest in prototype scale, creating significant hydrostatic pressure on the slope. The colour gradient illustrates the water pressure distribution within the soil, while the blue arrows indicate the direction of water flow. The white slip surface represents the potential failure plane under these conditions, with a factor of safety around 1.170, signifying marginal stability. The elevated water table exerts increased pore pressure, which can reduce the shear strength of the soil and overall stability. This steady-state condition serves as a baseline scenario, allowing for analysis of stability changes during subsequent drawdown phases in the M-T6r test.

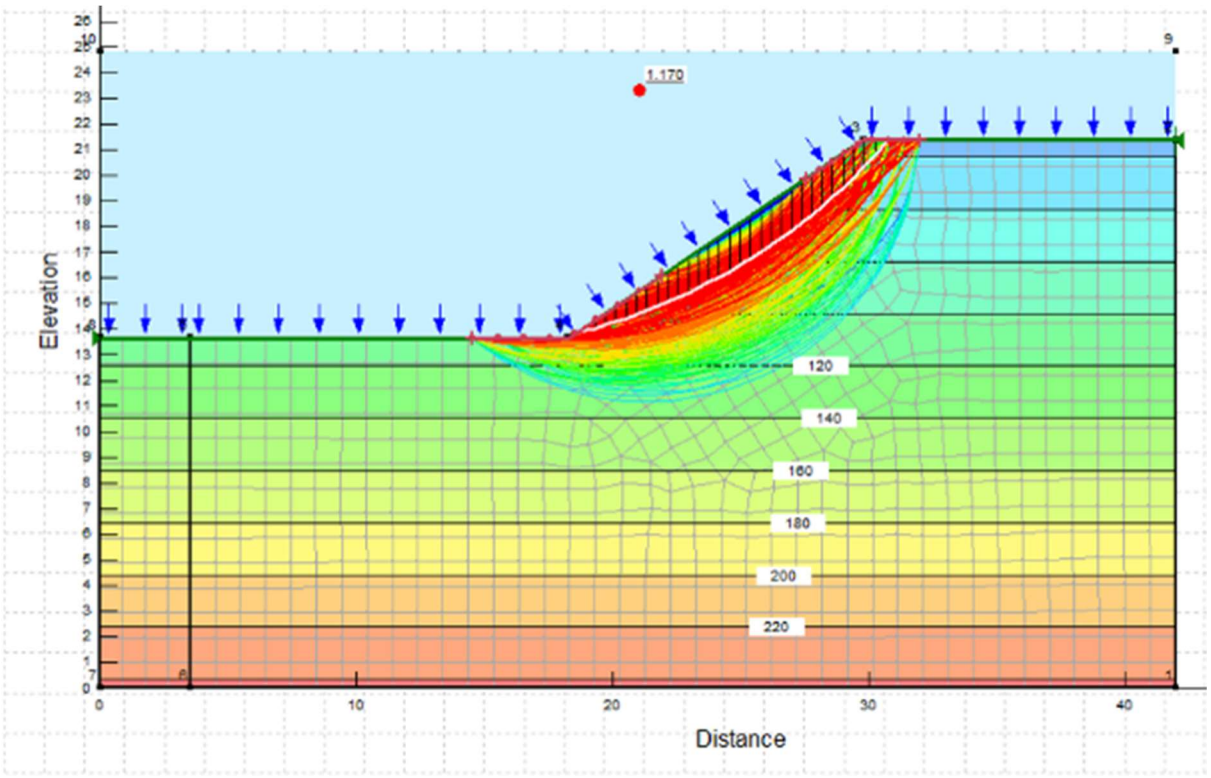


Figure 8-19 Steady state flooding condition for M-T6r.

8.6.2 Slope Stability Analysis for M-T6r Test: Gradual Drawdown Condition.

Figure 8-20 represents the slope stability analysis for the M-T6r test gradual drawdown condition. In this scenario, the gradual drawdown phase simulates a slow reduction in water level, allowing us to observe how the pore water pressure within the slope dissipates over time. The colour gradient displays the water pressure levels, while the contours show the resulting hydraulic gradients within the slope. The critical slip surface is highlighted in white, with a factor of safety around 0.398, indicating a heightened risk of slope instability as the drawdown progresses. This gradual reduction in water pressure leads to a decrease in stabilising forces as the internal pore pressure adjusts to the lowered water level, stressing the soil structure and reducing its overall shear strength.

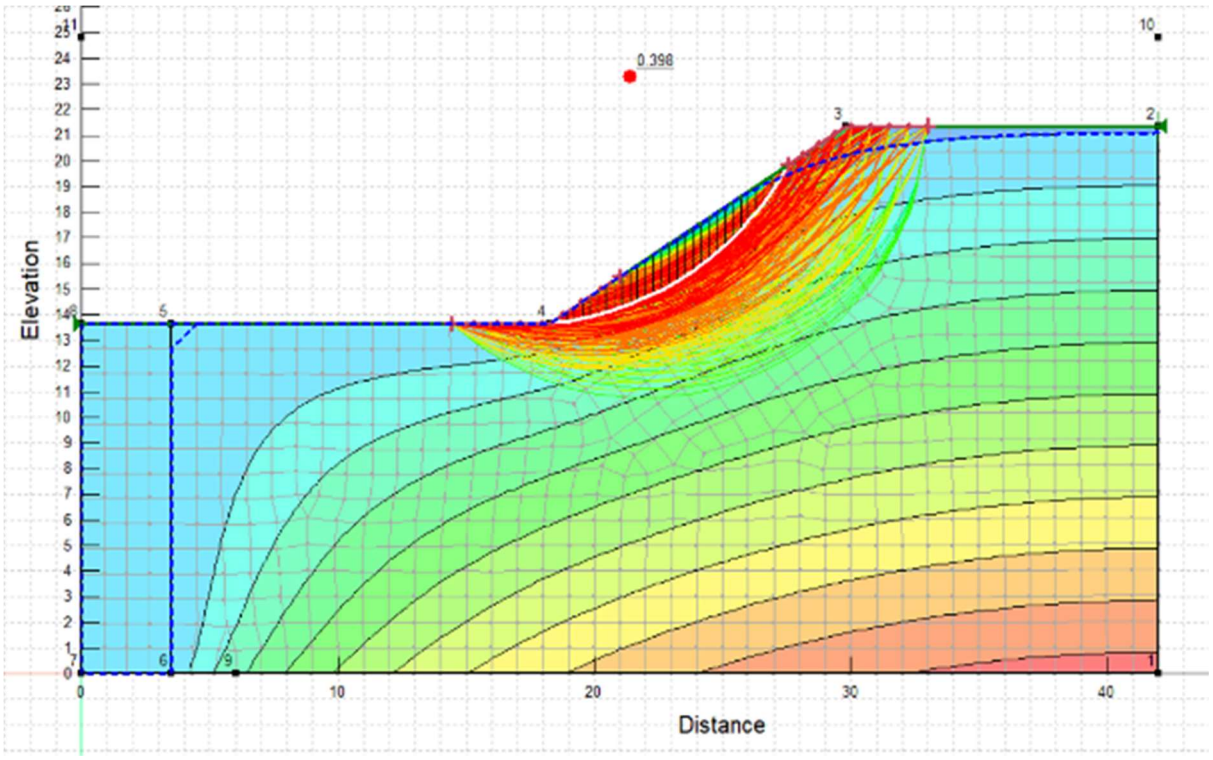


Figure 8-20 Gradual drawdown condition with critical slip surface and factor of safety for M-T6r test.

Figure 8-21 illustrates the evolution of the factor of safety (FoS) over the 10-day drawdown period. At the beginning of the drawdown, the FoS remains close to 1.17, but dips below 1.0 almost immediately, suggesting failure within half a day despite the slow drawdown. As the water level decreases, the pore pressures within the slope also adjust, leading to a progressive reduction in stability. The FoS declines gradually over the first 2-4 days but then begins to drop more sharply, reaching a low point below 0.4 near the end of the drawdown period. This trend means the slope is highly vulnerable even during long-term drawdown conditions.

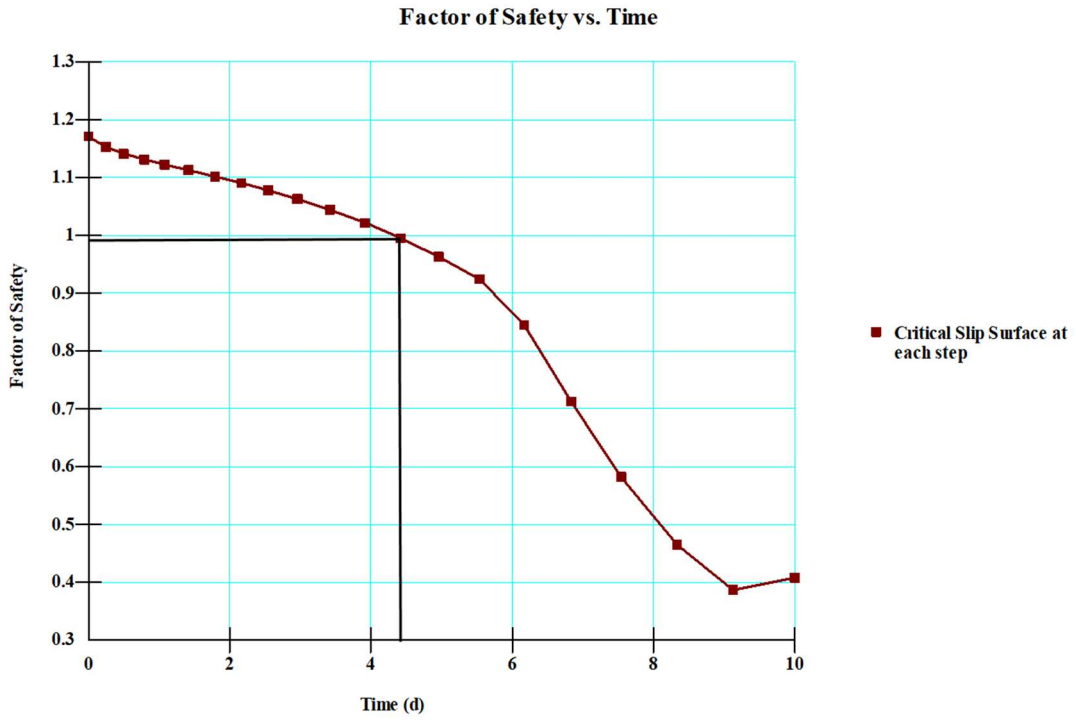


Figure 8-21 Factor of safety over time during gradual drawdown scenario for M-T6r test.

Pore water pressure at different heights over time

Figure 8-23 shows the variation in pore water pressure at various elevations within the slope over the course of the 10-day gradual drawdown period in the M-T6r test. The trends indicate that as the drawdown progresses, pore water pressures reduce progressively across different heights, reflecting the slope internal response to the falling external water level. This dissipation process is crucial in understanding how the slope stability is affected, as reduced pore pressure decreases buoyant forces within the soil mass, ultimately lowering the factor of safety and heightening the risk of slope failure. The pore water pressure measurement locations in the M-T6r test (Figure 8-22) are consistent with those used in the previous tests, M-T5 and M-T6. This consistency in measurement locations allows for direct comparison of pore pressure dissipation patterns across different tests. Additionally, offering insights into how differing situations, such as elevated water levels above the crest or varying drawdown rates, influence the internal stability of the slope.

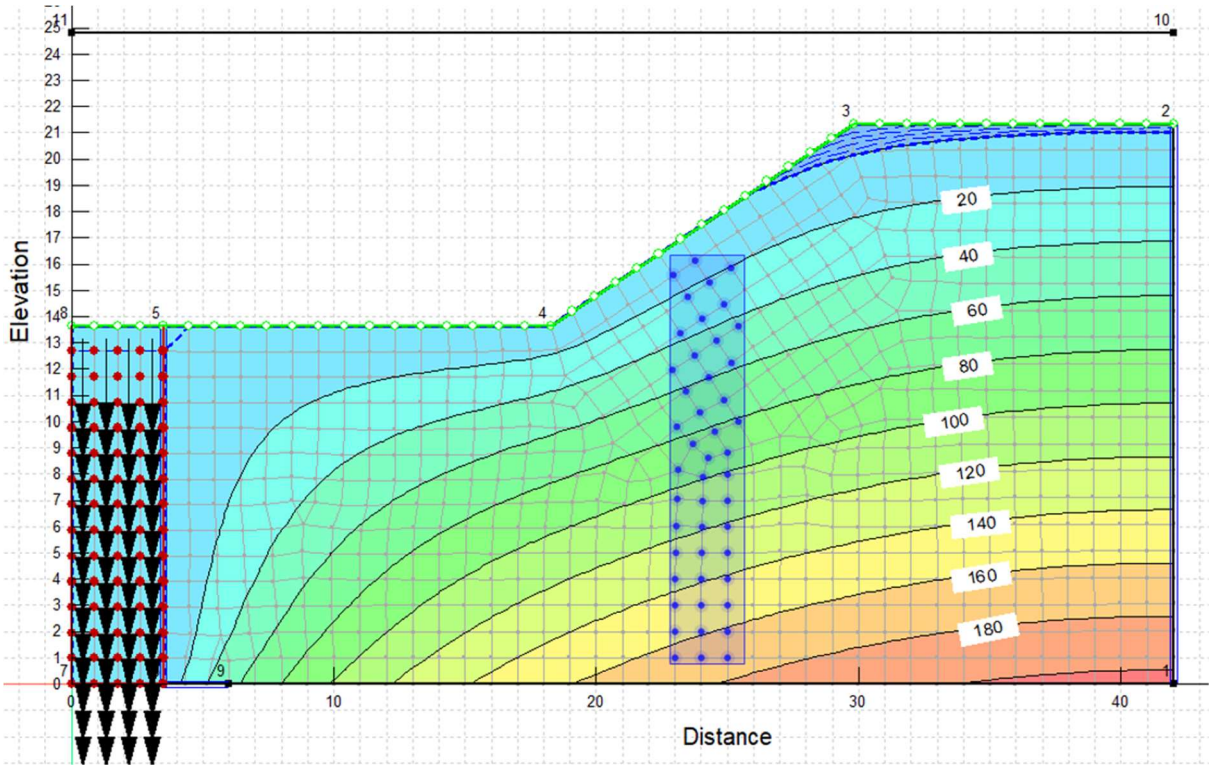


Figure 8-22 Pore water pressure monitoring locations in slope model during drawdown scenario for M-T6r test.

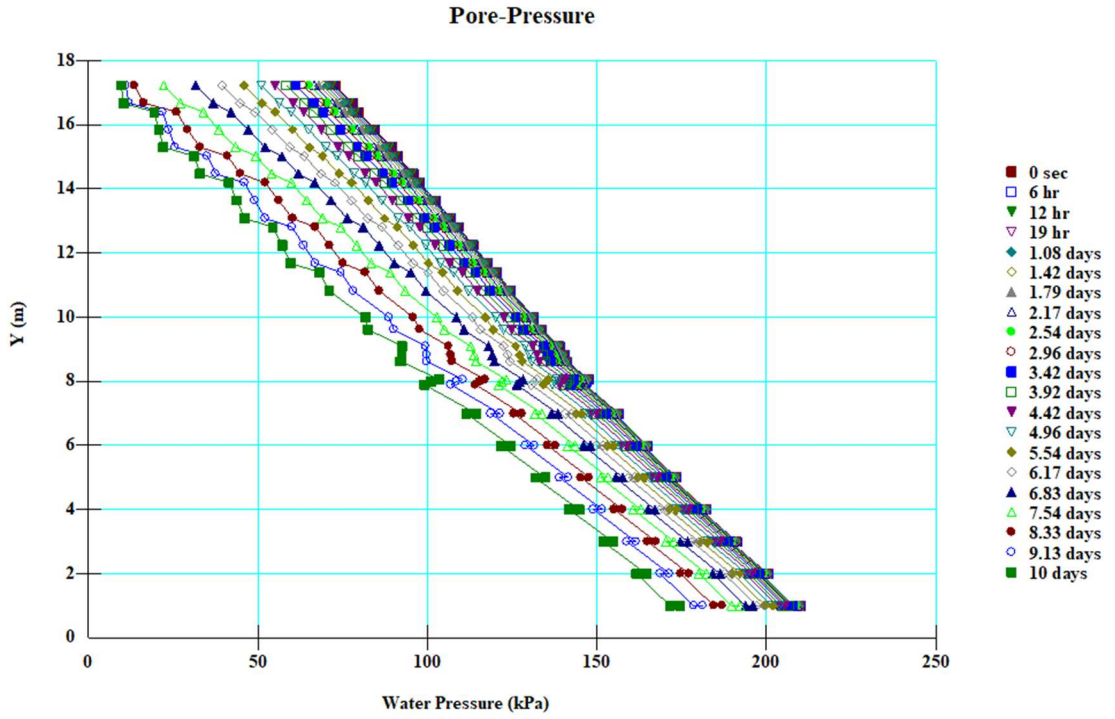


Figure 8-23 Pore water pressure dissipation at different heights in slope during gradual drawdown for the M-T6r test.

Validation of Pore Water Pressure Between Physical and Numerical Models for M-T6r test

Figure 8-24 presents the pore water pressure (PWP) distribution at the end of the drawdown phase for the M-T6r test, comparing numerical results from SEEP/W and experimental data from centrifuge PPT readings. While both approaches show a similar overall trend—with higher pore pressures near the toe and mid-slope and lower pressures near the crest—significant differences are evident in magnitude. The PPT readings from the physical model show consistently higher pore pressures than the numerical output.

This discrepancy can be attributed to several factors. Firstly, M-T6r underwent swelling during prior wetting and drying cycles, as it was a re-cut slope from the previously tested M-T6. Swelling tends to reduce the permeability of the soil, limiting drainage during drawdown and causing elevated PWP to persist, especially in the lower and mid-slope zones. In contrast, the numerical model assumes an uncoupled analysis, which does not account for the time-dependent effects of swelling or hydro-mechanical interactions. As noted by Pinyol et al. (2008), rapid and semi-rapid drawdown are complex phenomena that involve the interplay between hydraulic loading, soil structure, and mechanical strength. These effects are difficult to simulate accurately without fully coupled numerical models.

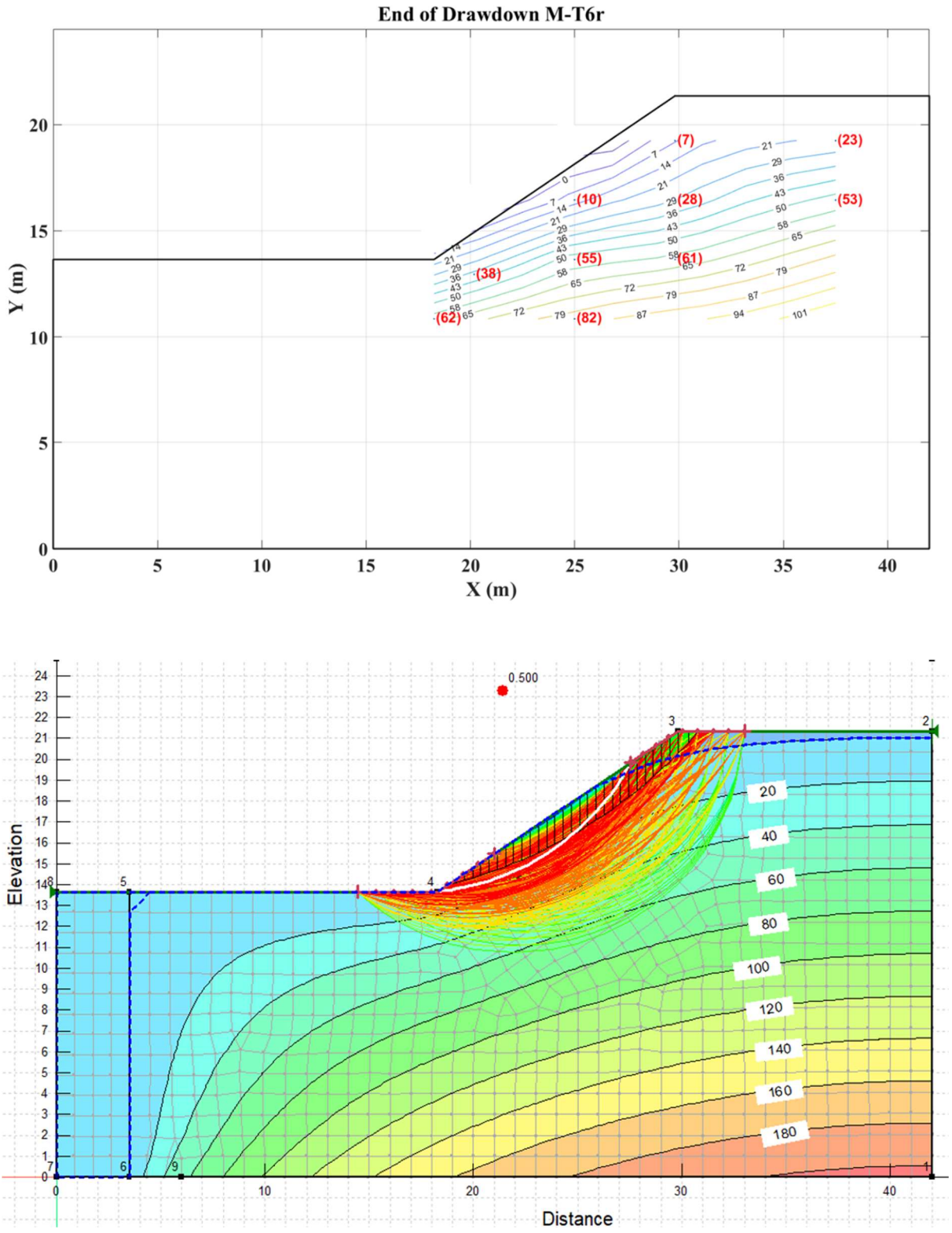


Figure 8-24 Comparison of Pore Water Pressure Distribution at the End of Drawdown between Centrifuge Test (PPT Readings) and SEEP/W Numerical Model for M-T6r (Prototype Scale).

8.6.3 Slope Stability Analysis for M-T6r Test: Rapid Drawdown Condition.

For the rapid drawdown analysis for the M-T6r test, similar to the M-T5 and M-T6 tests, slope failure is observed at approximately 0.58 days, highlighting the rapid onset of instability caused by the sudden reduction in external water pressure. FoS dropped to 0.119 for this relatively unrealistic scenario. Figures are similar to those for M-T5 and are omitted for brevity.

8.7 Comparison between numerical models and experiments

The comparison between numerical simulations and physical centrifuge tests for M-T5, M-T6, and M-T6r is presented in Figure 8-25 , illustrating both the critical slip surfaces from numerical modelling (left) and the corresponding shear strain distribution from PIV analysis (right). This side-by-side comparison provides a direct visual correlation between numerical predictions and experimental observations.

1. Key similarities between numerical and physical results
   - Failure Surface Alignment:
     In all three cases, the numerical models predict failure surfaces that closely correspond to regions of high shear strain observed in the centrifuge tests.
   - Factor of Safety (FoS) Trends:

a) M-T5 exhibits a near-critical condition (FoS = 0.998) using the critical angle of shearing resistance ϕ'=26.6° determined from triaxial testing, aligning with the observed instability in the physical test.

b) M-T6 shows a marginally stable scenario (FoS = 1.02) at the end of drawdown using a higher ϕ'=31°, which correlates with the experimental observations of limited displacement and low shear strain, as shown in the adjacent shear strain plot.

c) M-T6r predicts a progressive failure surface (FoS = 0.963) using ϕ'=26.6°, matching the distributed shear strain and gradual weakening seen in the experiment.

2. Differences between numerical and experimental results
   - Depth and Extent of Slip Surfaces:

a) The numerical slip surfaces tend to extend slightly deeper than the experimentally observed shear strain zones, possibly due to simplified soil behavior assumptions in the numerical model.

b) In M-T6r, the numerical model predicts a more progressive failure surface, whereas the experiment suggests a more localized shear concentration.

- Effect of Soil Heterogeneity:

  The numerical models assume a homogeneous soil profile, while the physical test results show localised variations in shear strain, likely influenced by material variability and small-scale heterogeneities.

- Influence of Boundary Conditions:

  The numerical models apply idealised boundary conditions, which may not fully capture the real effects of side-wall friction and model preparation differences in the centrifuge tests.

3. Interpretation of failure mechanisms

   - M-T5:

   Both numerical and experimental data confirm a shallow rotational failure mechanism, with slip surfaces initiating near the crest and propagating downslope.

   - M-T6:

The numerical model indicates a marginally stable condition (FoS = 1.02), with a less critical failure surface. This aligns with the experimental results, which show minimal displacement and low shear strain, suggesting that the slope remained stable but close to the threshold of instability during the drawdown phase.

   - M-T6r:

   The numerical model predicts a more progressive slip surface, aligning with the observed shear strain distribution, which suggests material weakening due to repeated wetting-drying cycles.

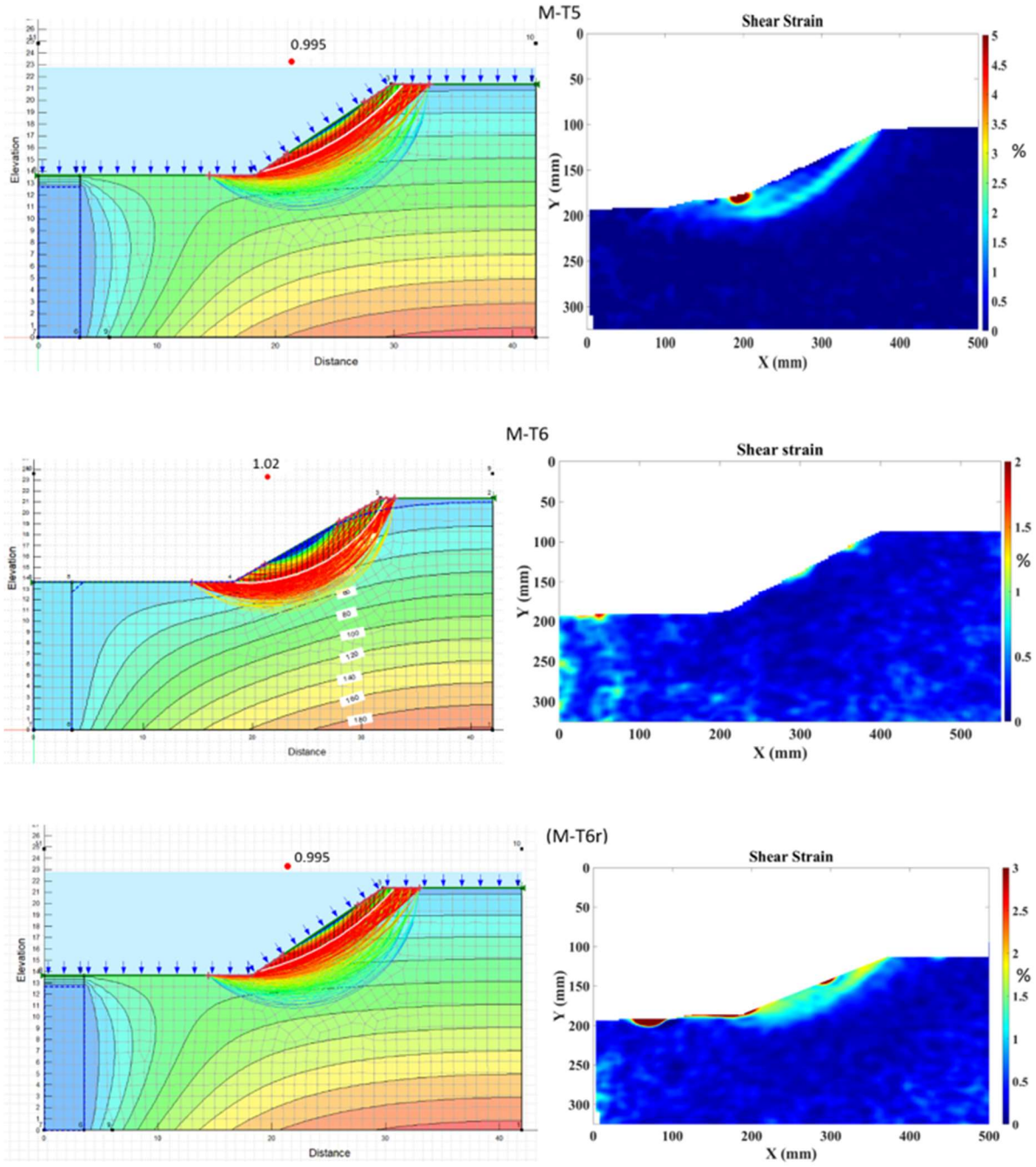


Figure 8-25 Comparison of numerical in the left and experimental shear strain patterns for M-T5, M-T6, and M-T6r right.

8.8 Summary:

This chapter presents the numerical modelling analysis conducted using GeoStudio to study the stability of slopes under flooding and drawdown scenarios. The numerical analysis aimed to validate the results obtained from centrifuge experiments by comparing the two approaches,

thus providing a more accurate assessment of failure mechanisms and slope stability under varying conditions. The numerical analysis aimed to validate the results obtained from centrifuge experiments by comparing the two approaches, thus providing a more accurate assessment of failure mechanisms and slope stability under varying conditions.

The analysis utilised the SEEP/W and SLOPE/W modules to evaluate pore-water pressure distributions and calculate the Factor of Safety (FoS) during flood and drawdown stages. The numerical results demonstrated significant agreement with the experimental findings:

No failure occurred during the flooding phase in both numerical and experimental tests, confirming slope stability under these conditions.

- Failure was evident during the drawdown phase, with the numerical models showing a reduction in the factor of safety consistent with the observed failure in the experimental tests.
- For tests M-T5 and M-T6r, which had the same slope angle, the slope stability showed agreement in both numerical and experimental analyses, demonstrating the accuracy of the numerical model in replicating real-world conditions.
- For test M-T6, an adjusted ϕ', allowing for peak strength behaviour which was likely for this test, resulted in good agreement between numerical and experimental analyses.
- The pore-water pressure values obtained from the numerical analysis closely matched those measured in the centrifuge experiments, indicating that the numerical model successfully captured the hydrological and mechanical behaviour of the slopes.

Conclusion

This thesis presents a comprehensive investigation into the stability of soil slopes subjected to varying climatic conditions, including rainfall, flooding, and drawdown events. By integrating experimental centrifuge testing and numerical modelling, the research provides significant insights into the mechanical response and deformation behaviours of soil under complex environmental loading. The findings enhance understanding of the key factors driving slope instability and failure, with implications for improved design and mitigation strategies in geotechnical engineering.

9.1 Key Contributions and Novel Aspects of the Study

This research fills critical knowledge gaps in slope stability analysis by addressing several limitations in past studies:

1. **Novel Experimental Approach for Drawdown-Induced Failures**

- Unlike most previous studies that relied primarily on numerical models or field observations, this research provides high-resolution centrifuge test data that quantifies real-time pore pressure dissipation, effective stress variations, and failure progression.
- The systematic testing program (M-T5, M-T6, and M-T6r) simulates complex hydro-mechanical loading conditions, enabling a detailed assessment of failure mechanisms under rapid and gradual drawdown scenarios.

2. **Integration of PIV Analysis and Pore Pressure Monitoring**

- The study uniquely combines high-resolution Particle Image Velocimetry (PIV) displacement tracking with detailed pore pressure transducer (PPT) measurements, capturing both external deformation and internal stress redistribution during failure evolution during seasonal weather and flooding and drawdown scenarios.
- The findings reveal that failure initiation correlates strongly with localised pore pressure peaks and shear strain concentration, confirming theoretical predictions but with new experimental validation.

3. Numerical Modelling and Validation

- This research bridges the gap between experimental observations and numerical modeling, demonstrating that while numerical models capture broad trends in slope failure, they may underestimate localized shear strain accumulation and delayed instability effects.
- Numerical analyses using GeoStudio's Slope/W and Seep/W modules successfully reproduce general trends in factor of safety (FoS) evolution, but experimental results highlight critical differences in slip surface locations and strain distribution as well as a sensitivity to strength parameters.

4. New Insights into Pore Pressure Lag and Shear Strength Reduction

- The results confirm that pore pressure dissipation does not occur uniformly during drawdown, leading to localised instability due to delayed stress recovery.
- The calculated shear strength reductions show that mid-depth layers exhibit the most significant reductions (~10–19%) in M-T5.
- The findings emphasise that failure may not occur immediately during drawdown but can be delayed due to stress redistribution, a phenomenon that has not been previously validated in controlled experimental conditions.
- The study demonstrates that pore pressure lag significantly influences slope instability during drawdown, validating the hypothesis proposed by Wright and Duncan (1987). Failure initiated approximately five days (at prototype) after the start of drawdown, indicating that retained excess pore pressure delayed effective stress recovery, reducing shear strength and leading to progressive failure before the drawdown process was completed.

9.2 Linking Findings to the Knowledge Gap

Chapter 2 identified three major knowledge gaps, which this study directly addresses:

1. **Lack of Experimental Validation for Drawdown Failures**

- Previous research primarily focused on rainfall-induced failures and seepage-driven instability, with limited studies on drawdown effects in centrifuge models.
- Prior research primarily relied on numerical models and case studies, lacking controlled laboratory data.
- This study provides new centrifuge-based physical data, allowing direct validation of theoretical predictions and improving numerical model calibration.
- A new method to interpolate between point measurements of pore pressure in the centrifuge tests was successfully used to develop contours of pore pressure that could be linked to numerical results.

2. **Limited Understanding of Soil Mixtures with Low Permeability**

- Previous studies focused on either pure sands or pure clays, whereas this study investigates gap-graded sand-kaolin mixtures, revealing unique infiltration and drainage behaviors that influence stability.
- Pore pressure lag contributes to shear strength reduction during drawdown, with failure occurring at fifth day of drawdown due to high seepage hydraulic gradients and localised excess pore pressure.

9.3 Main Results and Their Relation to Slope Failure Mechanisms

The experiments revealed that pore pressure fluctuation and corresponding deformation are key indicators of slope instability. Flooding and rainfall events caused pore pressure to rise, reducing effective stress and promoting slope deformation, while drying phases temporarily improved stability by lowering pore pressure. Notably, cyclic wetting and drying weakened soil cohesion over time, with M-T4 showing that sustained cycles lead to progressive erosion

and structural degradation. Tests M-T5 and M-T6r which showed slope failure under cyclic wetting and drying (i.e. seasonal influences) in the very low plasticity soil mixture tested did not fail catastrophically. While there was clear strain development along the failure surface, the slopes maintained their overall integrity. This has ramifications for flood embankments, which may have many years of drying and wetting before they are required to perform under flood conditions.

The drawdown phases in M-T5, M-T6, and M-T6r tests caused sharp reductions in external water support, creating significant hydraulic gradients at the slope toe and triggering internal movements along concentrated failure surfaces. These findings demonstrate that the timing and sequence of climatic events significantly influence the location and severity of slope failures.

The Particle Image Velocimetry (PIV) technique provided high-resolution measurements of displacement, validating the observed failure mechanisms. Careful camera calibration and reflection minimisation strategies improved measurement accuracy, allowing for detailed visualisation of strain localisation. Displacement fields revealed that failure typically initiated near mid-slope regions where pore pressures were highest and propagated toward the toe, highlighting the interplay between infiltration fronts, pore pressure accumulation, and mechanical degradation.

Numerical results using Seep/W and Slope/W (uncoupled seepage and limit equilibrium) generally agreed with drawdown failure outcomes for tests M-T5 and M-T6r which had the same slope angle and previously failed during weather cycling. However, M-T6 at a slightly shallower slope appeared to display greater resilience in the physical tests than the numerical model. This may be to do with the strength being at peak, rather than at critical state, as modelled, or may be due to the numerical analysis being uncoupled between fluid flow and deformation – i.e. overly simplistic.

9.4 Experimental Challenges and Data Interpretation

Ensuring uniform saturation of pore pressure transducers (PPTs) presented logistical challenges, as the cell configuration permitted only some PPTs to be saturated at a given time. The three-day saturation process, involving temporary disconnection and storage of PPTs in deaired water, introduced potential for slight unsaturation. To mitigate this, an offset correction method using hydrostatic pressure during flooding was applied. Despite these complexities,

the collected PWP data reliably captured the temporal and spatial variations crucial for understanding failure progression. Additionally, adopting the Gridfitdir method for pore pressure contour plotting enabled clearer visualisation of internal pressure distributions, further supporting the interpretation of failure.

9.5 Summary and Practical Implications

This research significantly advances knowledge on the stability of soil slopes under complex climatic scenarios. Key conclusions include:

- Cyclic wetting-drying cycles progressively weaken soil cohesion in gap graded sandy clay, promoting surface erosion and structural degradation over time.
- Rapid drawdown following flooding induces critical hydraulic gradients, particularly near the slope toe, leading to sudden and significant deformation.
- Gap-graded sand-kaolin mixtures exhibit complex infiltration behaviours, with faster pore pressure responses compared to pure kaolin, underscoring the importance of soil composition in slope stability assessments.
- The sequence and timing of climatic events play a crucial role in determining failure initiation points and deformation severity, with combined prolonged flooding and rapid drawdown producing the most critical conditions.
- Combined experimental and numerical approaches offer robust predictive capabilities, validating observed failure mechanisms and supporting safer slope design practices.

These findings highlight the necessity of considering the dynamic interplay between climatic loading conditions and soil mechanical behaviour when designing and maintaining slopes exposed to environmental fluctuations. Incorporating drawdown effects and cyclic loading into design criteria can improve resilience against climate-induced failure risks, particularly in flood-prone or reservoir-adjacent infrastructures.

9.6 **Recommendations and Future Work**

The following recommendations aim to improve the reliability of centrifuge tests, streamline the testing process, and enhance the quality of experimental data, thereby contributing to more accurate interpretations and validations.

1. Accurate Soil Characterisation: Before initiating centrifuge tests, it is crucial to perform precise characterisation of the soil mixture, especially when combining fine and coarse-grained soils. This will provide an initial evaluation of the soil's behaviour and its suitability for the intended testing conditions, ensuring reliable results.

2. Calibration of Measuring Instruments: Precise calibration of all equipment used during the tests, particularly pore pressure transducers (PPTs), is essential. PPTs should be fully saturated with deaired water prior to testing to ensure accurate data collection from the outset. This would help avoid the need for recalculating the hydrostatic pressure offset during flooding, saving time and improving data accuracy.

3. Camera Calibration for PIV Analysis: Proper calibration of the high-speed camera used for Particle Image Velocimetry (PIV) analysis is highly recommended. Selecting appropriate camera settings and properties that align with the test conditions and surrounding environment, such as lighting, is essential to ensure high-quality image capture and precise analysis of slope movements.

4. Addressing Solenoid Valve Efficiency at High g-Levels: A significant challenge encountered during testing was the inefficiency of the solenoid valve at 70 g. Efforts should be made to investigate the root cause of this limitation and develop a practical solution to improve the valve's performance under high g-levels. This could involve exploring alternative valve designs or testing configurations.

9.7 Future work

The following ideas may be explored in light of the findings of this thesis research.

a. Exploring Soil Mixtures:

1. Use different types of soils or reduce the percentage of kaolin in the mixture to assess the influence of fine-grained soils on slope stability under various climatic conditions.
2. Investigate the impact of higher-plasticity soils or soils with varying permeability characteristics to understand their behaviour under flooding and drawdown scenarios.

b. Enhancing Rainfall Simulations:

1. Improve the rainfall simulator to allow for the application of varying rainfall intensities and durations, replicating a wider range of real-world climatic events.
2. Develop the system to incorporate extreme rainfall events and seasonal rainfall patterns that align with UK weather conditions to evaluate their impacts on slope stability.

c. Advancing Seasonal Scenarios:

1. Create a system to raise the water table dynamically while applying seasonal scenarios to replicate field-scale hydrological responses more accurately.
2. Investigate how fluctuations in the water table during multi-seasonal cycles influence long-term slope deformation and stability.

d. Extreme Event Modelling:

1. Simulate extreme weather events, such as intense storms or prolonged flooding, to evaluate their immediate and long-term impacts on slope failure mechanisms.
2. Model and analyse potential mitigation techniques, such as drainage systems or slope reinforcement, to assess their effectiveness under extreme conditions.

e. Application to Field-Scale Studies:

1. Validate experimental and numerical results against field-scale observations to assess their applicability in real-world scenarios.

Investigate how existing infrastructure can be retrofitted or designed to withstand projected climatic changes, particularly for flood-prone areas.

References

(N.D.), U. 2017. History of the Lower Mississippi Levee System. U.S. Army Corps of Engineers.

AMJAD, M., ALI, S., IQBAL, M., QUDOOS, A. & SAROSH, A. Real Time Distress Monitoring of Soft Soil Highway Embankment. 2018 Singapore. Springer Singapore, 171-178.

ANDERSON, S. A. & SITAR, N. 1995. Analysis of rainfall-induced debris flows. *Journal of Geotechnical Engineering,* 121**,** 544-552.

ASKARINEJAD, A., BECK, A. & SPRINGMAN, S. M. 2015. Scaling law of static liquefaction mechanism in geocentrifuge and corresponding hydromechanical characterization of an unsaturated silty sand having a viscous pore fluid. *Canadian Geotechnical Journal,* 52**,** 708-720.

ASKARINEJAD, A., LAUE, J., ZWEIDLER, A., ITEN, M., BLEIKER, E., BUSCHOR, H. & SPRINGMAN, S. M. Physical modelling of rainfall induced landslides undercontrolled climatic conditions. Eurofuge 2012, Delft, Netherlands, 2012-04-23-2012-04-24, 2012.

BANG, H. N. & BURTON, N. C. 2021. Contemporary flood risk perceptions in England: Implications for flood risk management foresight. *Climate Risk Management,* 32**,** 100317.

BISHOP, A. W. 1959. The principle of effective stress. *Teknisk ukeblad,* 39**,** 859-863.

BISHOP, A. W., ALPAN, I., BLIGHT, G. & DONALD, I. 1960. Factors controlling the strength of partly saturated cohesive soils.

BRAČKO, T., ŽLENDER, B. & JELUŠIČ, P. 2022. Implementation of climate change effects on slope stability analysis. *Applied Sciences,* 12**,** 8171.

BRAND, E. W. Analysis and design in residual soils. Proc. ASCE Geotechnical Division Specialty Conference, Honolulu, Hawaii, 1982, 1982. 89-143.

BRUEN, M. & GEBRE, F. A. Worldwide public perception of flood risk in urban areas and its consequences for hydrological design in Ireland. Flood Risk Management Proc. Irish National Hydrology Seminar, Tullamore, 2001.

CAICEDO, B., TRISTANCHO, J. & THOREL, L. 2010. Centrifuge modeling of soil atmosphere interaction using a climatic chamber. *Physical Modelling in Geotechnics***,** 299-305.

CAICEDO, B., TRISTANCHO, J. & THOREL, L. 2015. Mathematical and physical modelling of rainfall in centrifuge. *International Journal of Physical Modelling in Geotechnics,* 15**,** 150-164.

CASCINI, L., CUOMO, S., PASTOR, M. & SORBINO, G. 2010. Modeling of rainfall-induced shallow landslides of the flow-type. *Journal of Geotechnical and Geoenvironmental Engineering,* 136**,** 85-98.

CHEN, Z., ZHANG, J.-M., HO, K. & WU, F.-Q. 2008. Analysis method for slope stability under rainfall action. *Landslides and Engineered Slopes. From the Past to the Future, Two Volumes+ CD-ROM.* CRC Press.

COLLINS, B. D. & ZNIDARCIC, D. 2004. Stability analyses of rainfall induced landslides. *Journal of geotechnical and geoenvironmental engineering,* 130**,** 362-372.

COTTAM, B. 2018. *Geo explainer: Why do we live on flood plains?* [Online]. Available: https://geographical.co.uk/science-environment/why-do-we-live-on-floodplains [Accessed].

D'ERRICO, J. R. 2006. Understanding gridfit. *Information available at: http://www. mathworks. com/matlabcentral/fileexchange/loadFile. do,* 55**,** 70-83.

DAS, B. M. & SIVAKUGAN, N. 2017. *Fundamentals of geotechnical engineering*, Cengage Learning.

DIXON, N. & BROOK, E. 2007. Impact of predicted climate change on landslide reactivation: case study of Mam Tor, UK. *Landslides,* 4**,** 137-147.

DIXON, N., DIJKSTRA, T., FORSTER, A., CONNELL, R., CULSHAW, M., REEVES, H., JEFFERSON, I. & SPINK, T. Climate change impact forecasting for slopes (CLIFFS) in the built environment. Engineering Geology for Tomorrow's Cities: Proceedings, 10th International Association of Engineering Geology Congress. Geological Society, London, 2006.

DUNCAN, J. M., WRIGHT, S. G. & BRANDON, T. L. 2014. *Soil strength and slope stability*, John Wiley & Sons.

DYER, M. Performance of flood embankments in England and Wales. Proceedings of the Institution of Civil Engineers-Water Management, 2004. Thomas Telford Ltd, 177-186.

FREDLUND, D., MORGENSTERN, N. R. & WIDGER, R. 1978. The shear strength of unsaturated soils. *Canadian geotechnical journal,* 15**,** 313-321.

FREDLUND, D. G. 2006. Unsaturated soil mechanics in engineering practice. *Journal of geotechnical and geoenvironmental engineering,* 132**,** 286-321.

FREDLUND, D. G. & RAHARDJO, H. 1993. *Soil mechanics for unsaturated soils*, John Wiley & Sons.

FREDLUND, D. G., RAHARDJO, H. & FREDLUND, M. D. 2012. *Unsaturated Soil Mechanics in Engineering Practice,* Newy York, UNITED STATES, John Wiley & Sons, Incorporated.

GARNIER, J., GAUDIN, C., SPRINGMAN, S. M., CULLIGAN, P., GOODINGS, D., KONIG, D., KUTTER, B., PHILLIPS, R., RANDOLPH, M. & THOREL, L. 2007. Catalogue of scaling laws and similitude questions in geotechnical centrifuge modelling. *International Journal of Physical Modelling in Geotechnics,* 7**,** 01-23.

GAZZINI, C. 2023. When the dams in Libya burst: A natural or preventable disaster? *International Crisis Group, October,* 2**,** 2023.

GERSCOVICH, D., VARGAS JR, E. & DE CAMPOS, T. 2006. On the evaluation of unsaturated flow in a natural slope in Rio de Janeiro, Brazil. *Engineering Geology,* 88**,** 23-40.

GREEN, W. H. & AMPT, G. 1911. Studies on Soil Phyics. *The Journal of Agricultural Science,* 4**,** 1-24.

HACKNEY, C. R., DARBY, S. E., PARSONS, D. R., LEYLAND, J., BEST, J. L., AALTO, R., NICHOLAS, A. P. & HOUSEAGO, R. C. 2020. River bank instability from unsustainable sand mining in the lower Mekong River. *Nature Sustainability,* 3**,** 217-225.

HARP, E. L., WELLS, W. G. & SARMIENTO, J. G. 1990. Pore pressure response during failure in soils. *Geological Society of America Bulletin,* 102**,** 428-438.

HUDACSEK, P., BRANSBY, M. F., HALLETT, P. D. & BENGOUGH, A. G. Centrifuge modelling of climatic effects on clay embankments. Proceedings of the Institution of Civil Engineers-Engineering Sustainability, 2009. Thomas Telford Ltd, 91-100.

IMRAN, J., NEMNEM, A., TANIM, A., KHAN, M. S., NAHIAN, A. & GOHARIAN, E. 2024. Rising Waters, Falling Dams: Deciphering the Derna Flood Disaster.

IVERSON, R. M. 2000. Landslide triggering by rain infiltration. *Water resources research,* 36**,** 1897-1910.

JADID, R., MONTOYA, B. M., BENNETT, V. & GABR, M. A. 2020. Effect of repeated rise and fall of water level on seepage-induced deformation and related stability analysis of Princeville levee. *Engineering Geology,* 266**,** 105458.

JAYAKODY, S. H. S., UZUOKA, R., UEDA, K. & XU, J. 2023. Unsaturated slopes behavior under antecedent intermittent rainfall patterns: centrifuge and numerical study. *Acta Geotechnica,* 18**,** 5773-5790.

JAZEERA, A. 2023. Disaster of epic proportions': Libya prosecutor probes deadly dam collapse.

KACZMAREK, J. & LEŚNIEWSKA, D. 2010. A flood embankment under changing water level conditions–a comparison of a physical and a numerical model. *Technical Sciences,* 13**,** 53-63.

KEMP, G. P., WILLSON, C. S., ROGERS, J. D., WESTPHAL, K. A. & BINSELAM, S. A. 2014. Adapting to change in the lowermost Mississippi River: Implications for navigation, flood control and restoration of the delta ecosystem. *Perspectives on the Restoration of the Mississippi Delta: The Once and Future Delta***,** 51-84.

KENDON, M., MCCARTHY, M., JEVREJEVA, S., MATTHEWS, A., SPARKS, T. & GARFORTH, J. 2021. State of the UK Climate 2020. *International Journal of Climatology,* 41**,** 1-76.

KHAN, I., AL-FERGANI, M. & BLACK, J. 2018. Development of a rainfall simulator for climate modelling. *Physical Modelling in Geotechnics, Volume 1.* CRC Press.

KIM, J., KIM, Y. & SATYANAGA, A. 2023. Instability of embankment slopes due to overflow and drawdown. *Water,* 15**,** 3402.

KIMURA, T. Failure of fills due to rain fall. Centrifuge, 1991. Balkema, 509-516.

KISCH, M. 1959. The theory of seepage from clay-blanketed reservoirs. *Geotechnique,* 9**,** 9-21.

KUMAR, G. V. 1996. *Some aspects of the mechanical behaviour of mixtures of kaolin and coarse sand*, University of Glasgow (United Kingdom).

LEE, Y., CHEUK, C. & BOLTON, M. 2008. Instability caused by a seepage impediment in layered fill slopes. *Canadian Geotechnical Journal,* 45**,** 1410-1425.

LEROUEIL, S. 2001. Natural slopes and cuts: movement and failure mechanisms. *Géotechnique,* 51**,** 197-243.

LEROUEIL, S., LOCAT, J., VAUNAT, J., PICARELLI, L. & LEE, H. Geotechnical characterization of slope movements. Landslides, 1996. 53-74.

LI, A., YUE, Z., THAM, L., LEE, C. & LAW, K. 2005. Field-monitored variations of soil moisture and matric suction in a saprolite slope. *Canadian Geotechnical Journal,* 42**,** 13-26.

LIKOS, W. J., SONG, X., XIAO, M., CERATO, A. & LU, N. 2019. Fundamental challenges in unsaturated soil mechanics. *Geotechnical fundamentals for addressing new world challenges.* Springer.

LING, H. I., WU, M.-H., LESHCHINSKY, D. & LESHCHINSKY, B. 2009. Centrifuge modeling of slope instability. *Journal of Geotechnical and Geoenvironmental Engineering,* 135**,** 758-767.

LIU, X. & WANG, Y. 2024. Quantifying impacts of precipitation scenarios projected under climate change on annual probability of rainfall-induced landslides at a specific slope. *Computers and Geotechnics,* 167**,** 106063.

LU, N. & LIKOS, W. 2004. Rate of capillary rise in soil. *Journal of geotechnical and Geoenvironmental engineering,* 130**,** 646-650.

LUMB, P. 1962. *Effect of rain storms on slope stability*, Local Property & Printing Company, Limited.

MAIR, R. J. 1979. Centrifuge modelling of tunnel construction in soft clay. *Ph. D Thesis, University of Cambridge*.

MARSH, T., KIRBY, C., MUCHAN, K., BARKER, L., HENDERSON, E. & HANNAFORD, J. 2016. *The winter floods of 2015/2016 in the UK-a review*, NERC/Centre for Ecology & Hydrology.

MATZIARIS, V. 2019. *Centrifuge modelling of rainfall-induced landslides in unsaturated soil slopes.* University of Nottingham.

MEIN, R. G. & LARSON, C. L. 1973. Modeling infiltration during a steady rain. *Water resources research,* 9**,** 384-394.

MIAO, F., WU, Y., LI, L., TANG, H. & LI, Y. 2018. Centrifuge model test on the retrogressive landslide subjected to reservoir water level fluctuation. *Engineering geology,* 245**,** 169-179.

MORIWAKI, H., INOKUCHI, T., HATTANJI, T., SASSA, K., OCHIAI, H. & WANG, G. 2004a. Failure processes in a full-scale landslide experiment using a rainfall simulator. *Landslides,* 1**,** 277-288.

MORIWAKI, H., INOKUCHI, T., HATTANJI, T., SASSA, K., OCHIAI, H. & WANG, G. 2004b. Failure processes in a full-scale landslide experiment using a rainfall simulator. *Landslides,* 1**,** 277-288.

NG, C. W. W. & SHI, Q. 1998. A numerical investigation of the stability of unsaturated soil slopes subjected to transient seepage. *Computers and geotechnics,* 22**,** 1-28.

OCHIAI, H., OKADA, Y., FURUYA, G., OKURA, Y., MATSUI, T., SAMMORI, T., TERAJIMA, T. & SASSA, K. 2004. A fluidized landslide on a natural slope by artificial rainfall. *Landslides,* 1**,** 211-219.

OFFICE, M. 2023. Hazard Manager user guide: Using the map and accessing the weather layers.

PASLEY, C. 1842. Report on the present state of the Swindon embankment', 14 Jan 1842. *Reports of the Railway Department***,** 91-92.

PENNING-ROWSELL, E. C. 2021. Comparing the scale of modelled and recorded current flood risk: Results from England. *Journal of Flood Risk Management,* 14**,** e12685.

PINYOL, N. M., ALONSO, E. E. & OLIVELLA, S. 2008. Rapid drawdown in slopes and embankments. *Water resources research,* 44.

POSTILL, H., DIXON, N., FOWMES, G., EL-HAMALAWI, A. & TAKE, W. A. 2020. Modelling seasonal ratcheting and progressive failure in clay slopes: a validation. *Canadian Geotechnical Journal,* 57**,** 1265-1279.

POWRIE, W. & SMETHURST, J. Climate and Vegetation Impacts on Infrastructure Cuttings and Embankments. 2019 Singapore. Springer Singapore, 128-144.

PSARROPOULOS, P. N., MAKRAKIS, N. & TSOMPANAKIS, Y. 2024. Climate Change Impact on the Stability of Soil Slopes from a Hydrological and Geotechnical Perspective. *GeoHazards,* 5**,** 1190-1206.

RAHARDJO, H., LEE, T., LEONG, E. C. & REZAUR, R. 2005. Response of a residual soil slope to rainfall. *Canadian Geotechnical Journal,* 42**,** 340-351.

RAHARDJO, H., LIM, T., CHANG, M. & FREDLUND, D. 1995. Shear-strength characteristics of a residual soil. *Canadian Geotechnical Journal,* 32**,** 60-77.

RAHARDJO, H., ONG, T., REZAUR, R. & LEONG, E. C. 2007. Factors controlling instability of homogeneous soil slopes under rainfall. *Journal of geotechnical and geoenvironmental engineering,* 133**,** 1532-1543.

RAIL, N. 2021. A review of earthworks management. Network Rail Milton Keynes, UK.

RICHARDS, L. 1931. Soil-water conduction of liquids in porous mediums. *Physics,* 1**,** 318-333.

RIDLEY, A. & BURLAND, J. 1993. A new instrument for the measurement of soil moisture suction. *Géotechnique,* 43**,** 321-324.

SCHOFIELD, A. N. 1980. Cambridge geotechnical centrifuge operations. *Geotechnique,* 30**,** 227-268.

SHENG, D., ZHOU, A. & FREDLUND, D. G. 2011. Shear strength criteria for unsaturated soils. *Geotechnical and Geological Engineering,* 29**,** 145-159.

SKEMPTON, A. 1954. The pore-pressure coefficients A and B. *Geotechnique,* 4**,** 143-147.

SOGA, K., EWAIS, A., FERN, J. & PARK, J. 2019. Advances in Geotechnical Sensors and Monitoring. *In:* LU, N. & MITCHELL, J. K. (eds.) *Geotechnical Fundamentals for Addressing New World Challenges.* Cham: Springer International Publishing.

SUN, H., WONG, H. & HO, K. Analysis of infiltration in unsaturated ground. Proceedings of the annual seminar on slope engineering in Hong Kong, 1998. 101-109.

TAKE, W. & BOLTON, M. 2003. Tensiometer saturation and the reliable measurement of soil suction. *Géotechnique,* 53**,** 159-172.

TAKE, W. & BOLTON, M. 2022. An atmospheric chamber for the investigation of the effect of seasonal moisture changes on clay slopes. *Physical Modelling in Geotechnics.* Routledge.

TAKE, W., BOLTON, M., WONG, P. & YEUNG, F. 2004a. Evaluation of landslide triggering mechanisms in model fill slopes. *Landslides,* 1**,** 173-184.

TAKE, W., BOLTON, M., WONG, P. & YEUNG, F. 2004b. Evaluation of landslide triggering mechanisms in model fill slopes. *Landslides,* 1**,** 173-184.

TAKE, W. A. 2003. *The influence of seasonal moisture cycles on clay slopes.* University of Cambridge.

TAMATE, S., SUEMASA, N. & KATADA, T. 2012. Simulation of precipitation on centrifuge models of slopes. *International Journal of Physical Modelling in Geotechnics,* 12**,** 89-101.

TAYLOR, R. E. 2018. *Geotechnical centrifuge technology*, CRC Press.

TAYLOR, R. N. 1994. *Geotechnical centrifuge technology*, CRC Press.

TERZAGHI, K. 1943. *Theoretical soil mechanics*.

TIDE, R. 1997. The Great Mississippi Flood of 1927 and How It Changed America. *Touchstone, New York*.

TULLER, M., OR, D. & HILLEL, D. 2004. Retention of water in soil and the soil water characteristic curve. *Encyclopedia of Soils in the Environment,* 4**,** 278-289.

VANAPALLI, S., FREDLUND, D., PUFAHL, D. & CLIFTON, A. 1996. Model for the prediction of shear strength with respect to soil suction. *Canadian geotechnical journal,* 33**,** 379-392.

VANAPALLI, S. K., FREDLUND, D. G. & PUFAHL, D. E. 1999. The influence of soil structure and stress history on the soil–water characteristics of a compacted till. *Géotechnique,* 49**,** 143-159.

VAUNAT, J., LEROUEIL, S. & FAURE, R. Slope movements: a geotechnical perspective. International congress International Association of Engineering Geology, 1994. 1637-1646.

WANG, G. & SASSA, K. 2001. Factors affecting rainfall-induced flowslides in laboratory flume tests. *Geotechnique,* 51**,** 587-599.

WANG, R., ZHANG, G. & ZHANG, J.-M. 2010. Centrifuge modelling of clay slope with montmorillonite weak layer under rainfall conditions. *Applied Clay Science,* 50**,** 386-394.

WHITE, D., TAKE, W. & BOLTON, M. 2003. Soil deformation measurement using particle image velocimetry (PIV) and photogrammetry. *Geotechnique,* 53**,** 619-631.

WILLIAMS, J. & SHAYKEWICH, C. 1970. The influence of soil water matric potential on the strength properties of unsaturated soil. *Soil Science Society of America Journal,* 34**,** 835-840.

WONG, J. L., LEE, M. L., TEO, F. Y. & LIEW, K. W. A Review of Impacts of Climate Change on Slope Stability. 2022 Singapore. Springer Singapore, 157-178.

WRIGHT, S. G. & DUNCAN, J. M. 1987. *An examination of slope stability computation procedures for sudden drawdown*, US Army Engineer Waterways Experiment Station.

ZHAN, T. L. & NG, C. W. 2004. Analytical analysis of rainfall infiltration mechanism in unsaturated soils. *International Journal of Geomechanics,* 4**,** 273-284.

ZHANG, M. 2005. *Centrifuge modelling of potentially liquefiable loose fill slopes with and without soil nails*, Hong Kong University of Science and Technology (Hong Kong).

ZHU, J.-H. & ANDERSON, S. 1998. Determination of shear strength of Hawaiian residual soil subjected to rainfall-induced landslides. *Géotechnique,* 48**,** 73-82.

Appendix A

A.1 Test M-T4

A.1.1 Deformations

Auto balance stage

During the auto balance phase, minimal soil movement was observed, with small vector displacements mainly near the slope base, indicating equilibrium adjustments as shown in Figure A-1. Resultant displacement contours showed localized movement near the toe (up to 4 mm), while the rest of the slope remained stable. Shear strain was concentrated at the toe (up to 5%), likely due to stress adjustments during initial loading. Volumetric strain revealed compression (-2%) in the lower left slope and slight expansion in upper regions, reflecting minor soil adjustments.

Consolidation stage

At the end of the consolidation stage, the slope remained stable with minimal displacement, shear, and volumetric strain Figure A-2. Vectorial displacements were negligible, indicating the soil had reached a balanced state. Resultant displacement contours showed displacements below 0.5 mm, confirming no significant deformation. Shear strain was low throughout, with slight increases near the bottom left corner. Volumetric strain showed minor compression (-3%) in localized areas, likely due to pore space adjustments during consolidation.

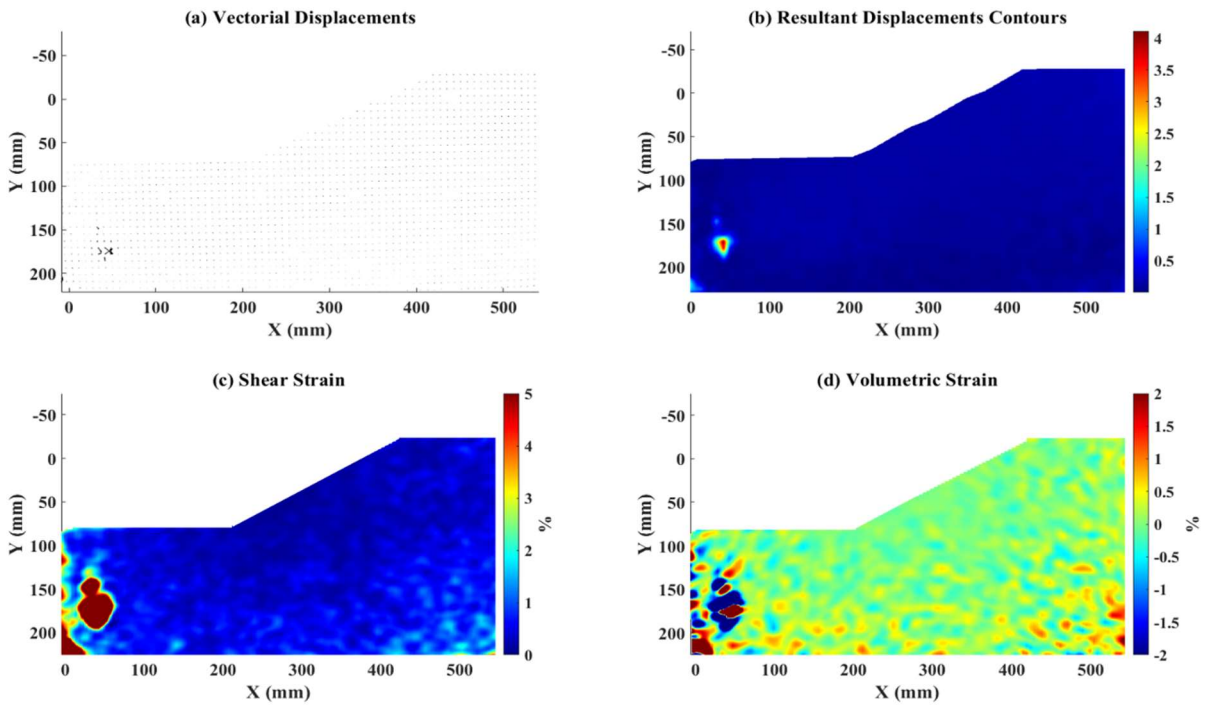


Figure A-1 Displacements and strain at the end of auto balance phase (M-T4) test.

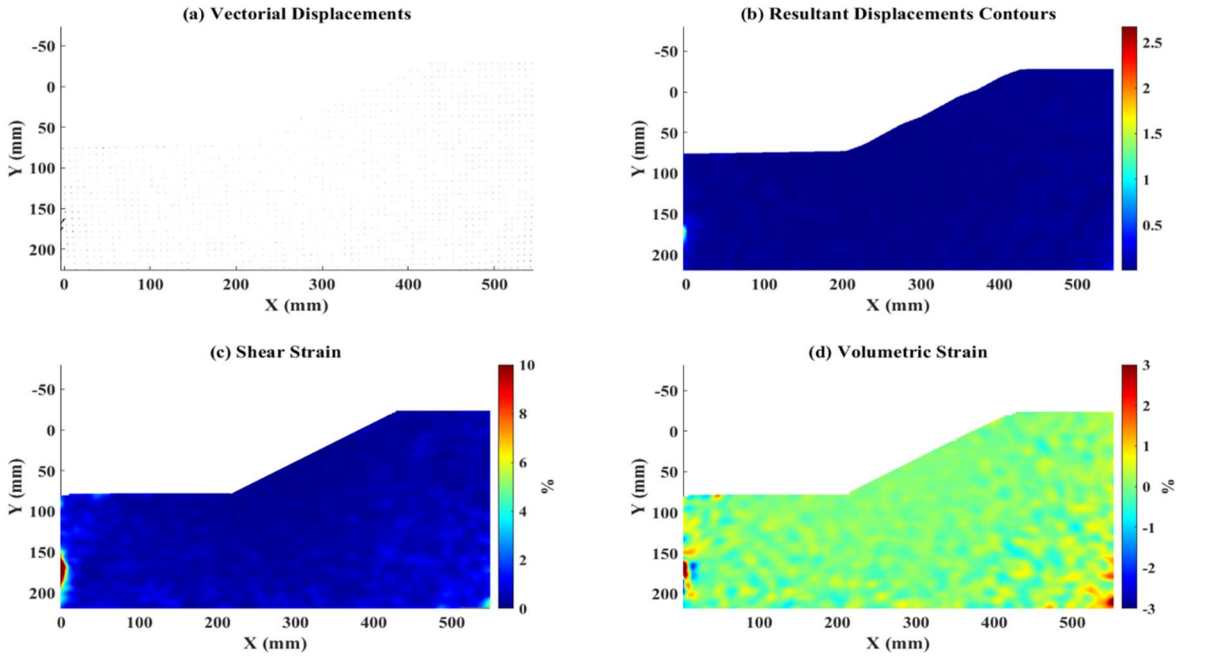


Figure A-2 Displacements and strain at the end of consolidation phase (M-T4) test.

A.1.2 Seasonal cycles effect.

Slope movement at the end of first summer / M-T4

At the end of the first summer in the M-T4 test, minimal soil movement was observed, indicating stabilization after wetting-drying cycles as shown in Figure A-3. Vectorial displacements were negligible, and resultant displacement contours showed uniform stability with displacements below 0.5 mm. Shear strain remained low, confirming no significant internal stress. Volumetric strain exhibited minor expansion and contraction, but no major internal changes, reinforcing the slope's stability under drying conditions.

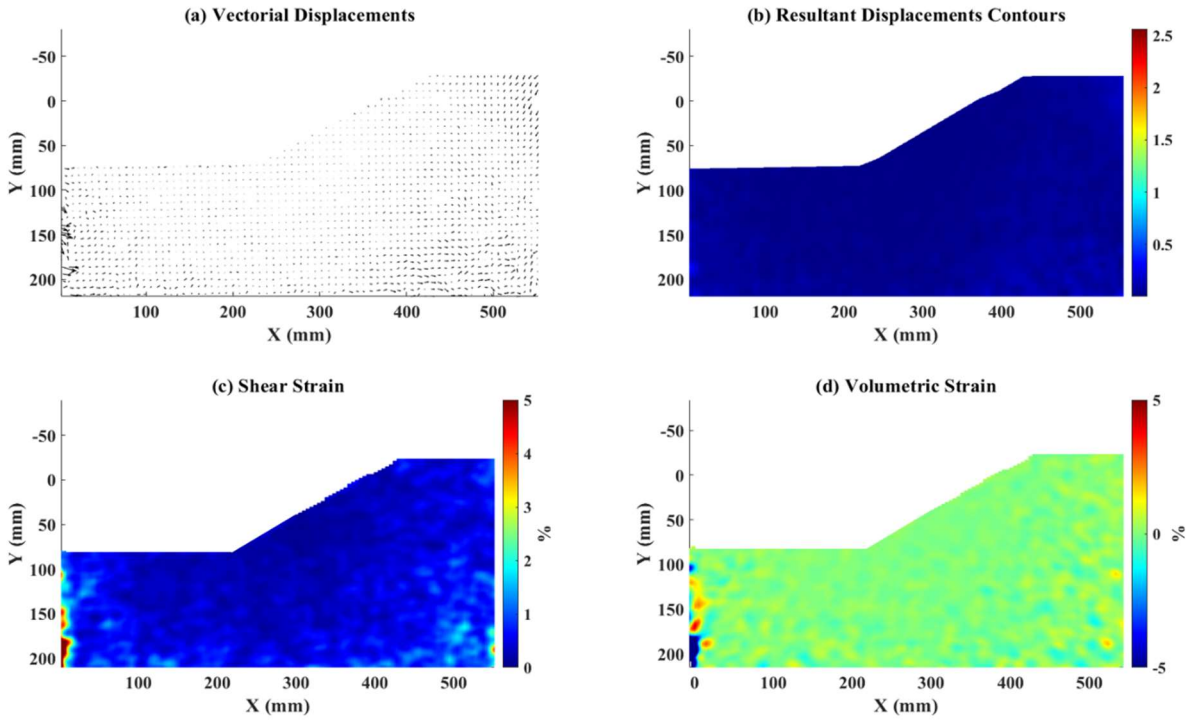


Figure A-3 Displacements and strain at the end of the first summer (M-T4) test.

Slope movement at the end of second summer/ M-T4.

At the end of the summer cycle in the M-T4 test as shown in Figure A-4, the slope remained stable, with minimal displacement and strain due to soil consolidation under drying conditions. However, visible erosion near the surface was noted, likely from repeated wetting-drying cycles. Vectorial displacements were limited, indicating no significant movement. Resultant

displacement contours showed slight displacements near the midslope (under 2 mm), reflecting soil resettlement. Shear strain reached 25% in localized midslope areas, suggesting erosion-induced weakening. Volumetric strain showed minor compression and dilation, but no signs of instability, confirming the slope's structural integrity.

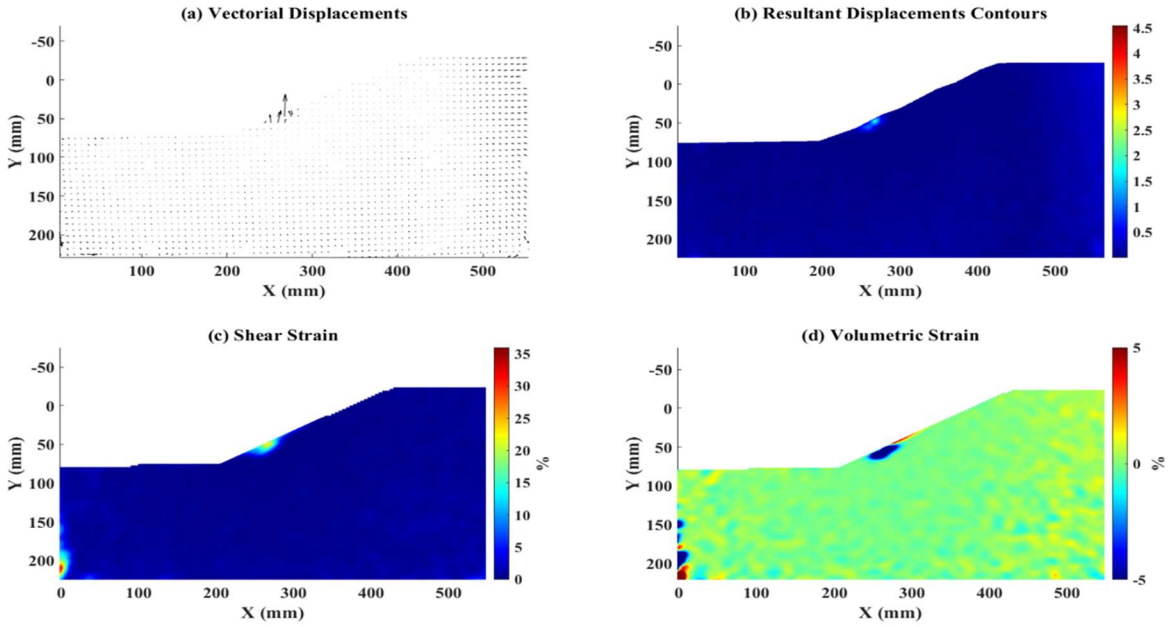


Figure A-4 Displacements and strain at the end of summer 2 phase (M-T4) test.

A.1.3 Flooding effect M-T4 test.

The PIV analysis in Figure A-5 indicates that the slope remained stable despite flooding, with minimal movement and low internal stresses. Vectorial displacements showed no significant shifts, and resultant displacement contours recorded low displacement (under 0.2 mm). Shear strain was localized near the toe (below 2%), reflecting minor soil adjustments due to increased pore pressure. Volumetric strain showed slight compression near the base, likely from flood-induced consolidation, but overall, soil volume and density remained unchanged.

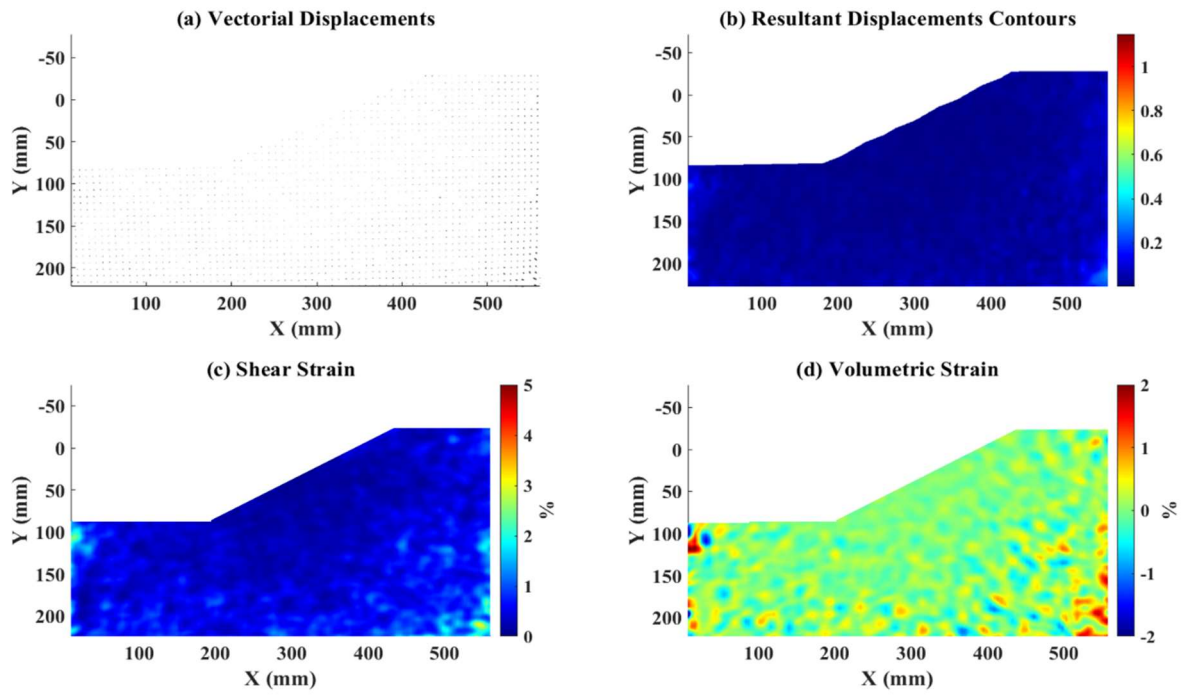


Figure A-5 Displacements and strain at the end of flood1 phase (M-T4) test.

A.2 Test M-T5

A.2.1 Seasonal cycles effect.

Slope movement at the end of first winter / M-T5

During the initial winter period in the M-T5 test (Figure A-6), PIV analysis showed minimal soil movement, indicating slope stability under wetting-drying cycles. Vectorial displacements were negligible, confirming structural integrity. Resultant displacement contours showed no significant internal or surface movements, implying no deformation. Shear strain remained very low, indicating no differential soil movement. Volumetric strain was uniform with minor changes, suggesting minimal soil-water interaction without significant expansion or contraction.

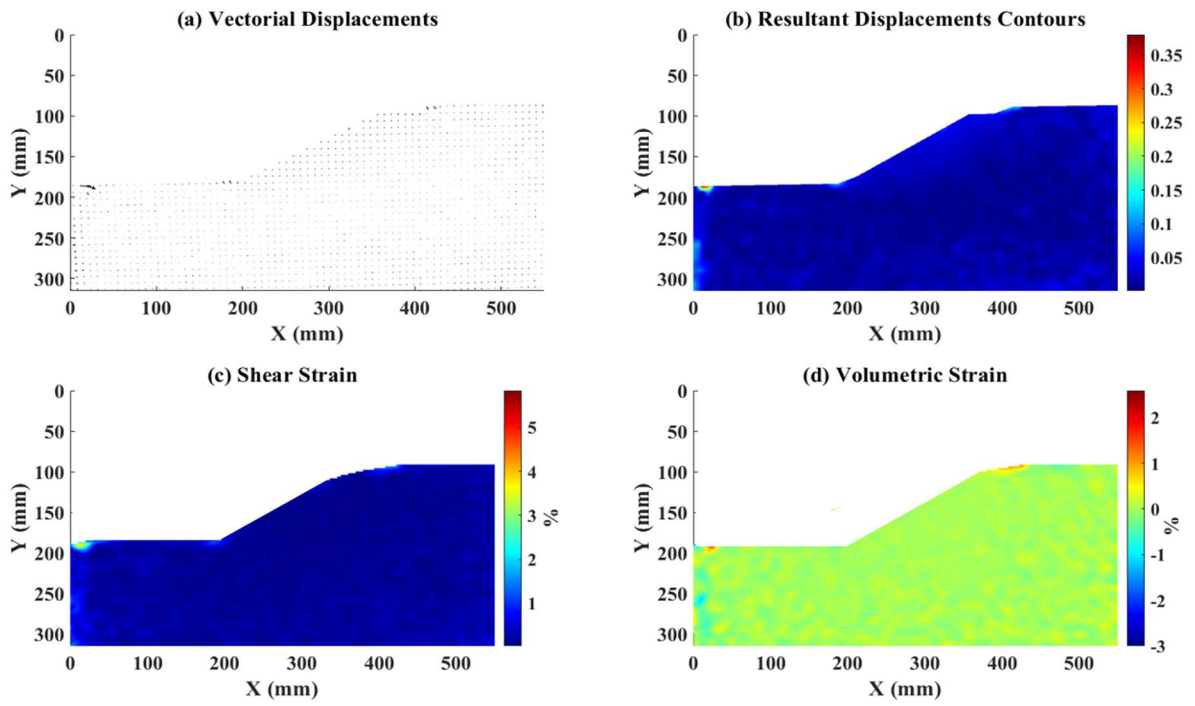


Figure A-6 End of the Winter 1 for M-T5 test.

Pore water pressure analysis

Figure A-7 presents the PWP distribution at the end of Winter 1, showing higher PWP near the toe and lower values towards the crest, indicating water accumulation in the lower slope. Denser contour lines at the toe suggest a steeper PWP gradient, while gradual spacing towards the crest reflects slower drainage. The rapid PWP stabilisation indicates the soil reached quasi-equilibrium quickly, balancing infiltration and drainage. The elevated PWP in lower areas highlights moisture accumulation and potential stability risks, whereas lower PWP at the crest suggests reduced moisture retention due to gravitational flow, a key factor in long-term slope stability.

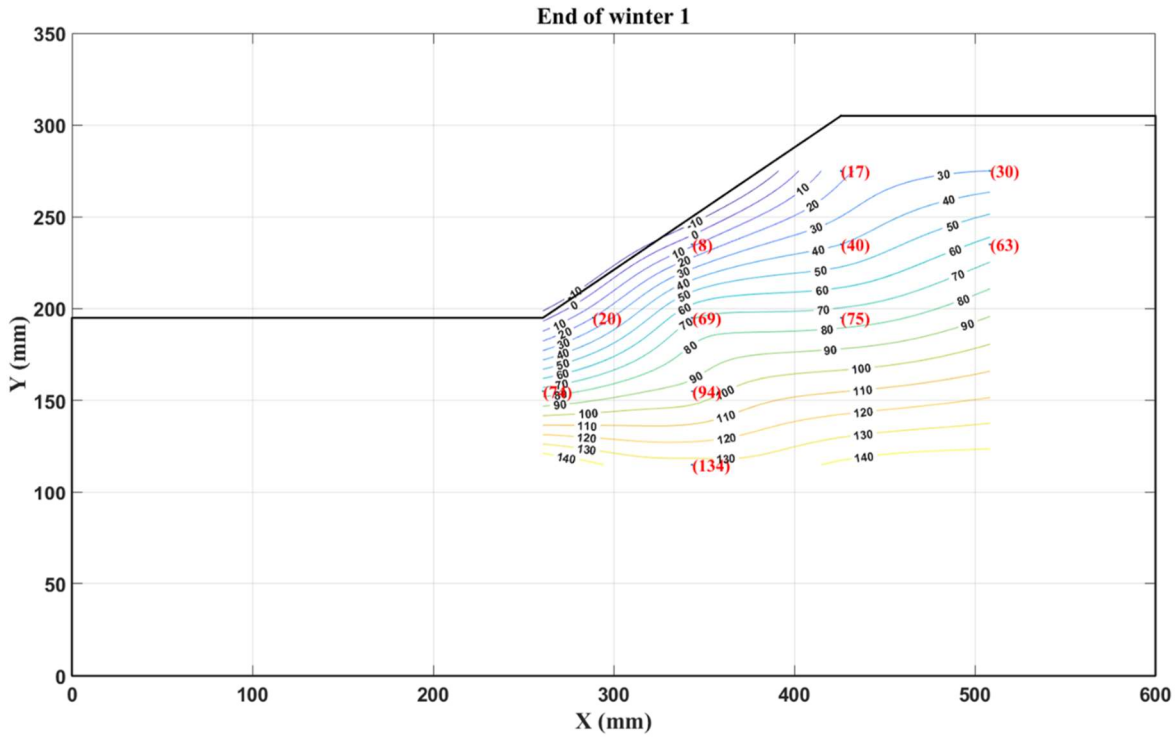


Figure A-7 Pore water pressure contours at the end of Winter 1.

Slope movement at the end of first summer / M-T5.

At the end of Summer 1 in the M-T5 test (Figure A-8), the slope remained stable, with low displacement, shear strain, and volumetric strain, indicating no critical deformation. Vectorial displacements were minimal, reflecting soil stabilization under dry conditions. Resultant displacement contours showed slightly higher values near the surface, likely due to minor settling during drying. Shear strain remained low, suggesting no internal stress buildup or instability. Volumetric strain exhibited minor contraction and expansion, reflecting moisture loss and soil adjustments, but without significant structural changes.

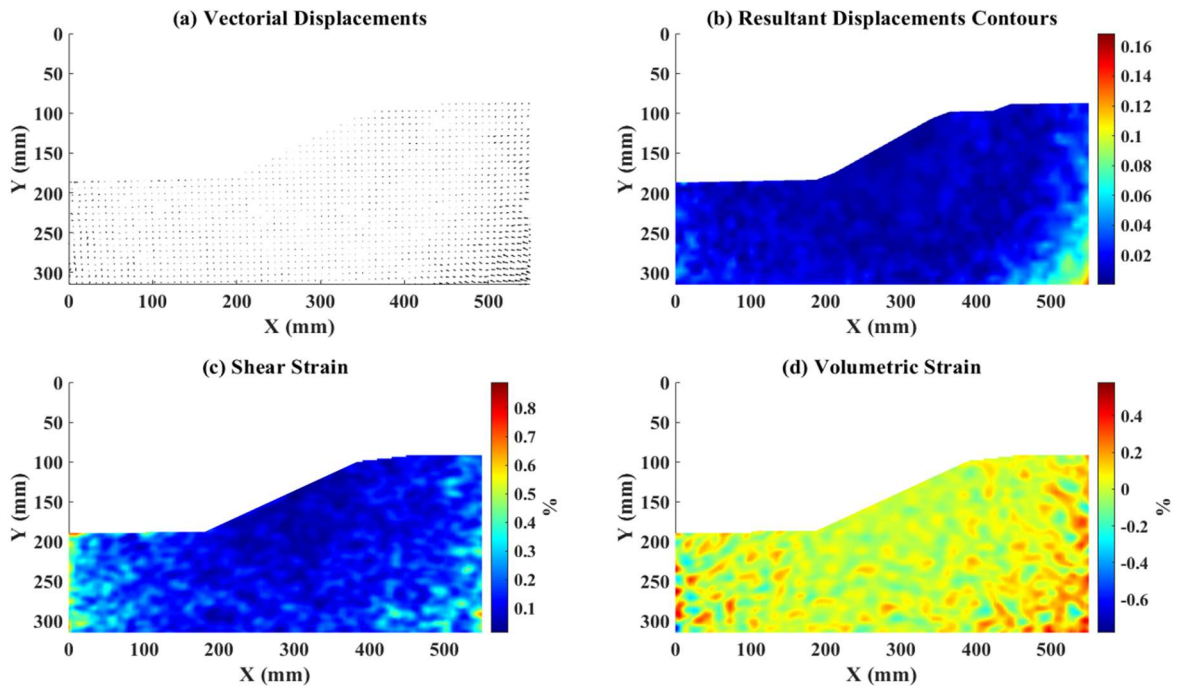


Figure A-8 PIV analysis at the end of summer 1 (M-T5) test.

Pore water pressure at the end of summer 1:

Figure A-9 depicts the distribution of pore water pressure (PWP) at the end of the first summer phase in the M-T5 test. The PWP values are generally higher in the lower regions of the slope and near the toe. The PWP values decrease gradually as we move towards the crest of the slope and are slightly negative at the surface, indicting a state of suction to -10 kPa or less. The contour lines indicate that the highest PWP values, reaching up to 117 kPa, are observed near the base of the slope. Significant PWP values are also recorded at the mid-height of the slope, around 71 kPa. The contour lines of PWP become denser near the slope toe.

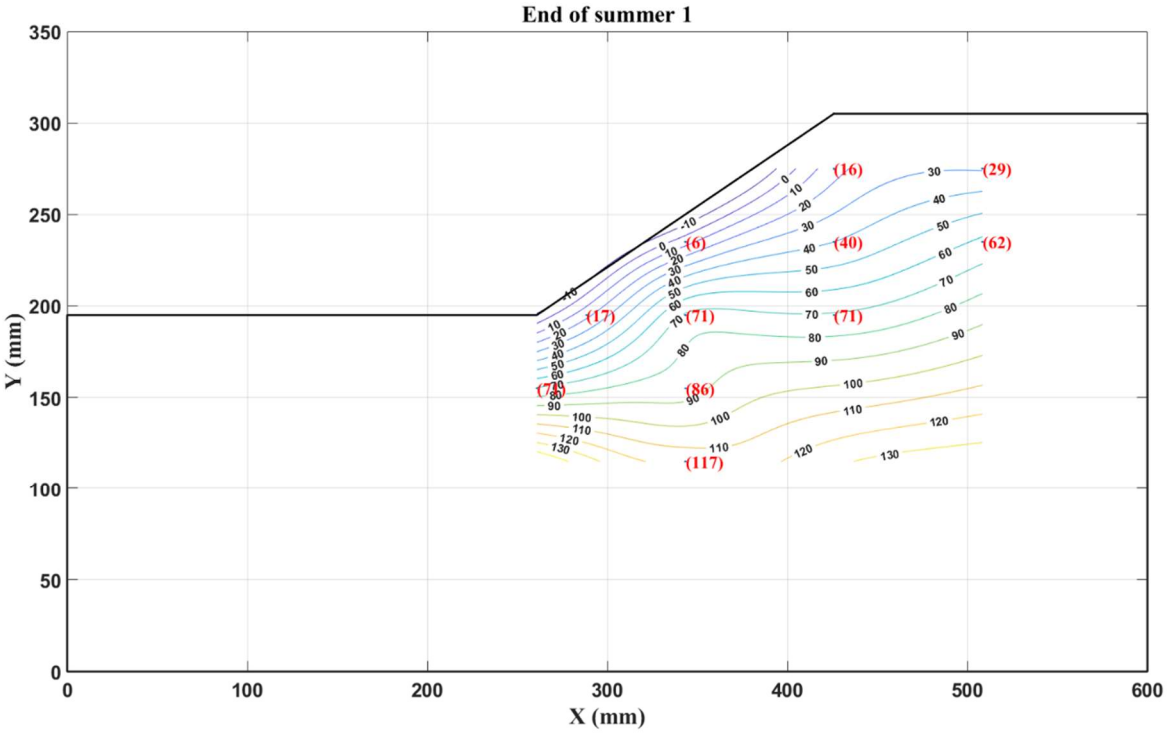


Figure A-9 Pore water pressure contours at the end of summer 1 for M-T5 test.

A.2.2 Flooding and drawdown effects M-T5 test.

Soil deformation during Flood 1

Figure A-10 shows that during the first flood event at 70g, the slope remained stable with minimal displacement and strain. Vectorial displacements were negligible, and minor irregularities are likely due to PIV artefacts such as reflections or camera vibrations. Resultant displacement contours show very low values, with no concentrated zones of movement. Shear strain is low, with minor values near the slope top and bottom, indicating no significant internal deformation. Volumetric strain ranges between -0.6% and 0.6%, but the distribution suggests noise rather than real compression or expansion, confirming the slope's stability during this flooding phase.

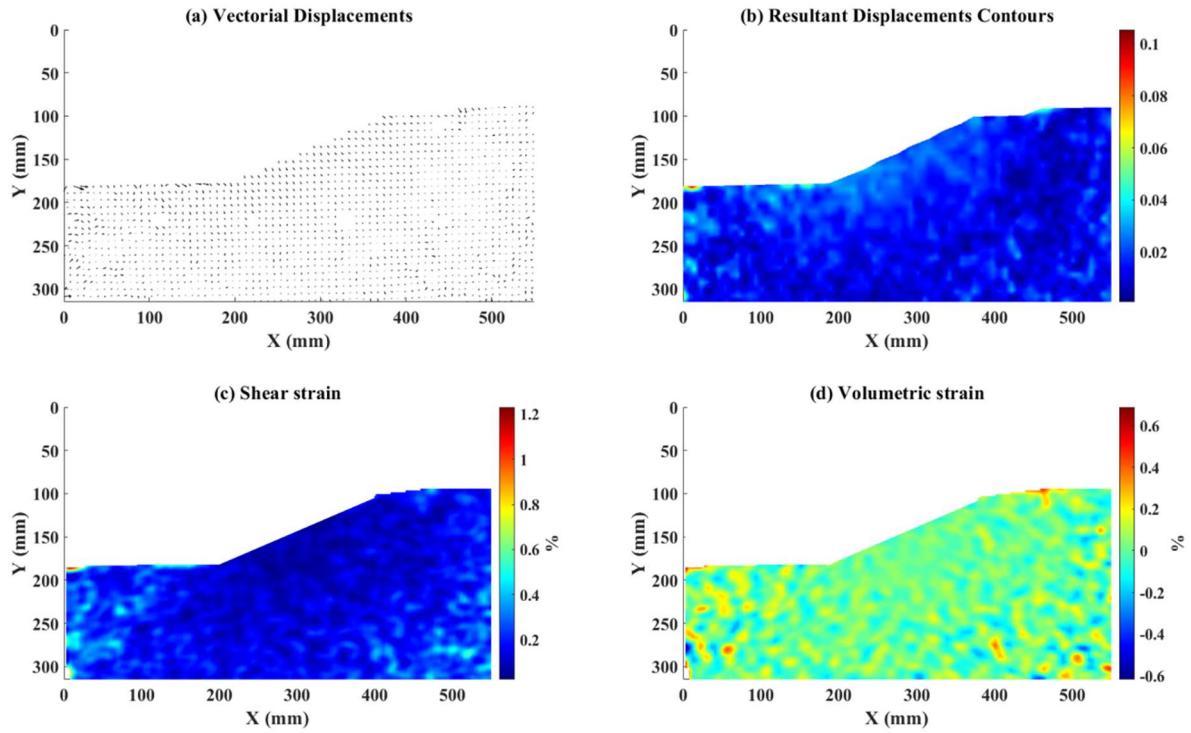


Figure A-10 Soil deformation during Flood 1.

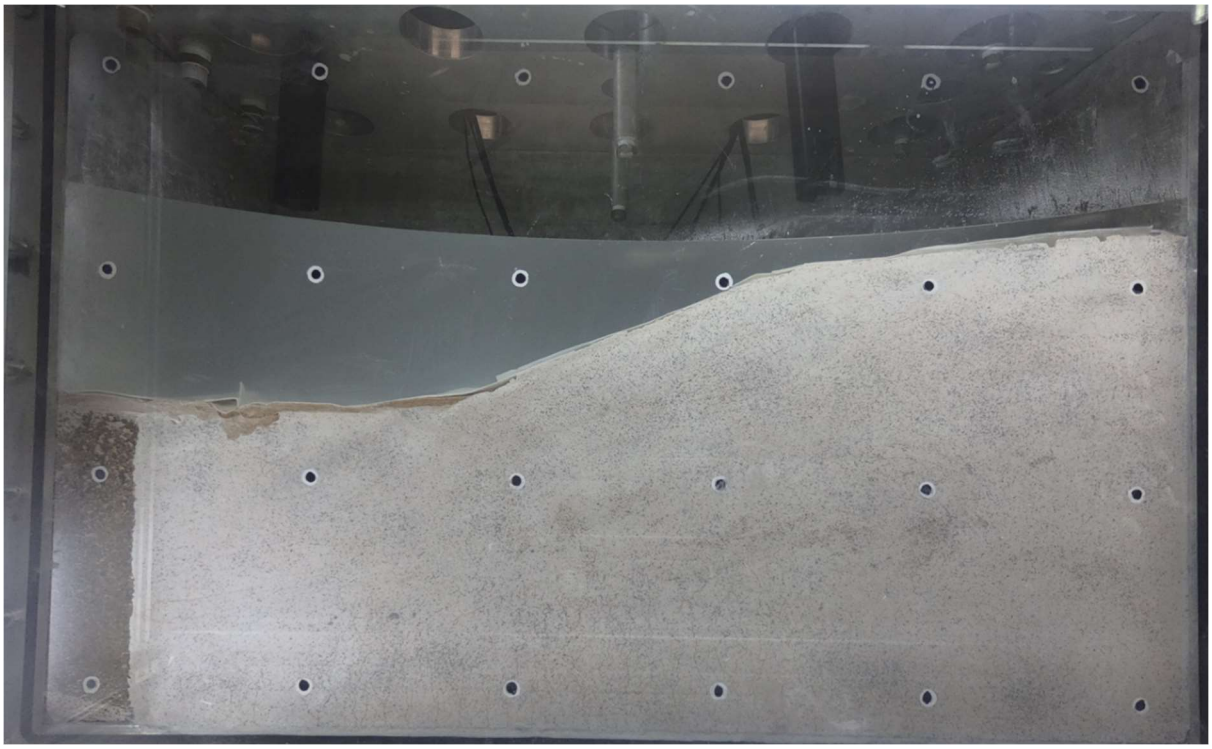


Figure A-11 Flood 1 phase of the M-T5 test in a centrifuge model.

Pore Water Pressure During Flood 1

Figure A-12 shows the pore water pressure (PWP) data during the first flood event. The higher pore water pressures observed towards the end of the flooding period reflect the hydrostatic pressure distribution within the slope model after the PPTs have been "corrected" to reflect theoretical values. That is, PPT positions and theorised PWP distribution were used to fix any errors in the pore pressure measurements.

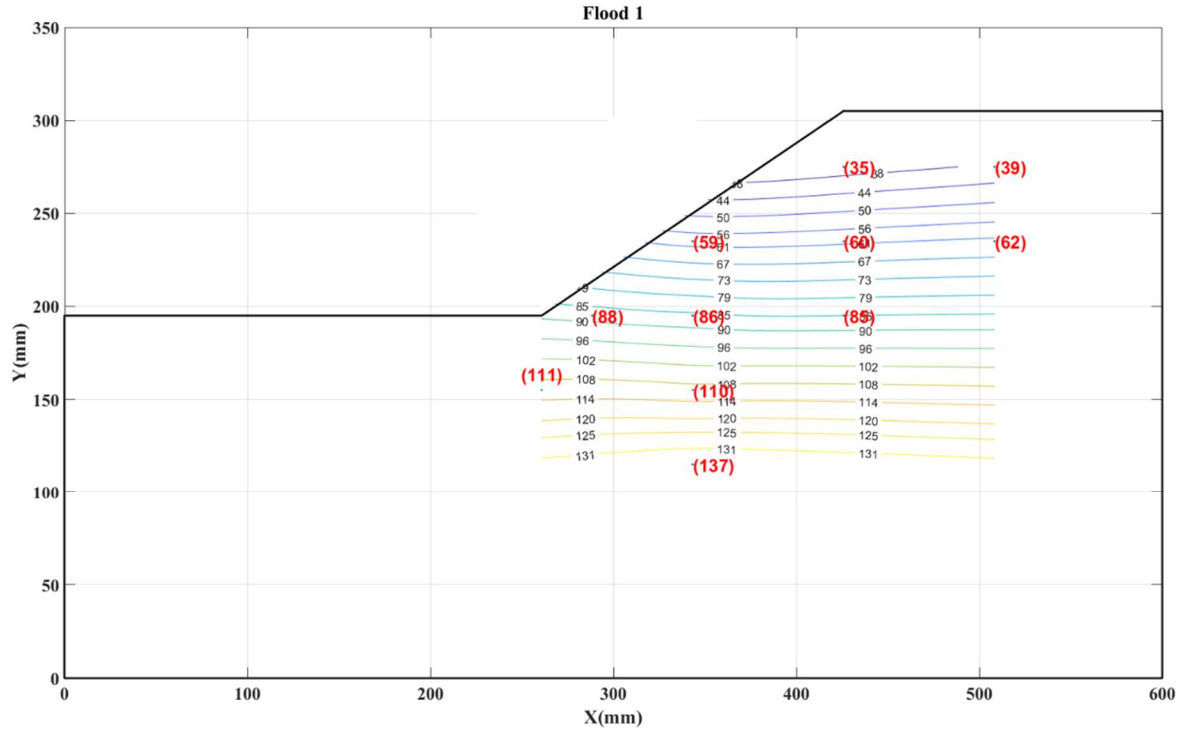


Figure A-12 Pore water pressure (adjusted to theory) during Flood 1 (M-T5 test)

Soil deformation during the second flood

Figure A-13 illustrates the soil deformation during the second flood event at 70g, showing localised movement and strain near the slope crest. Vectorial displacements indicate minimal overall movement, with slight activity at the crest suggesting soil softening. Resultant displacement contours show maximum displacements up to 9 mm near the crest, highlighting localised instability. Shear strain is concentrated at the crest, reaching around 5%, indicating surface deformation likely due to infiltration-induced softening. Volumetric strain reveals minor expansion and compression, with crest dilation suggesting swelling from water infiltration, which may contribute to strength reduction in that area.

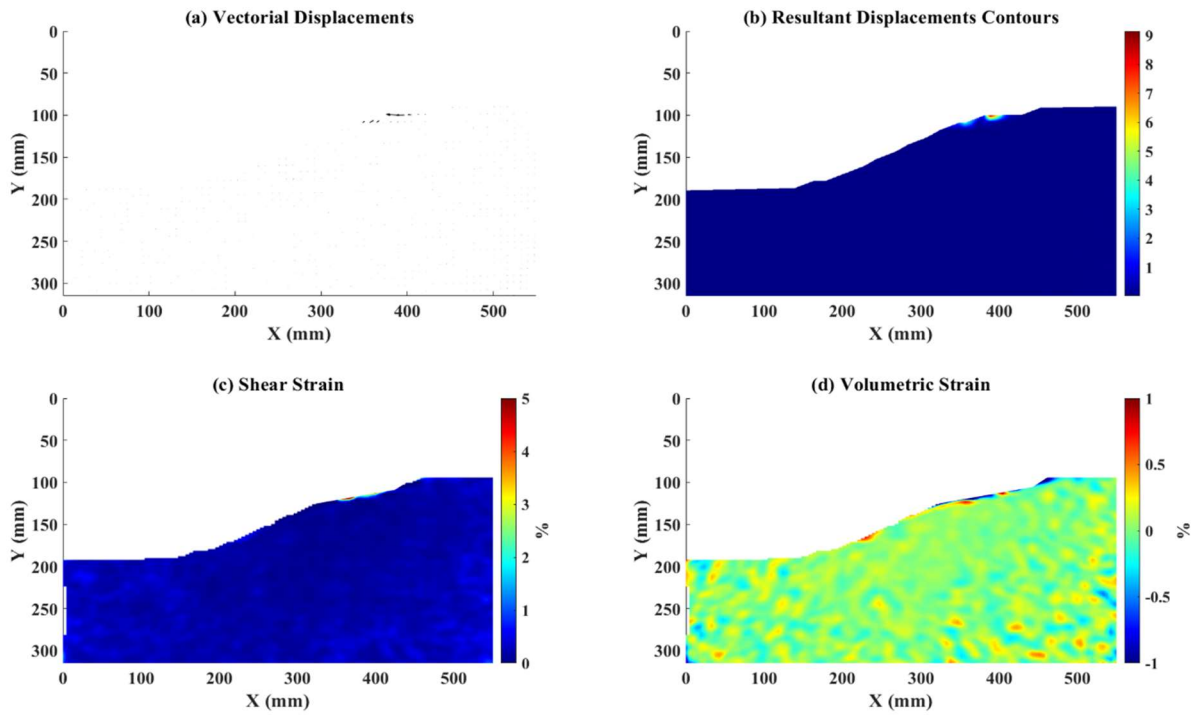


Figure A-13 Soil deformation during Flood 2.

Pore Water Pressure (PWP) Analysis (Flood 2)

The PWP ranges from 26 kPa to 134 kPa, with higher pressures concentrated at deeper levels and towards the slope toe as shown in Figure A-14. The contour lines suggest a gradient of decreasing pressure upwards – this is reflective of hydrostatic conditions in the curved g-field of the centrifuge. In this case, the PPTs have not been adjusted for the flood (they were adjusted only in Flood 1). The PPTs (pore pressure transducers) were adjusted for each subsequent flood, including Flood 2 and Flood 3, to ensure accurate and reliable data collection under changing water conditions.

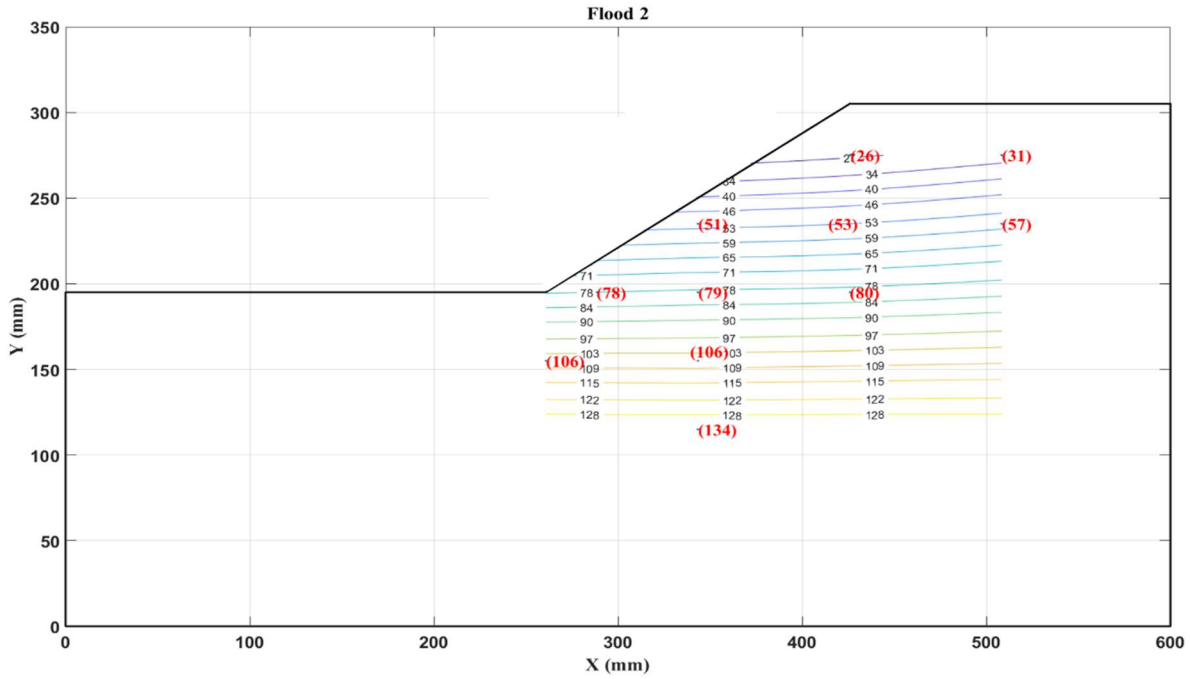


Figure A-14 Pore pressures at the end of Flood2.

A.3 Test M-T6

A.3.1 Hydrostatic calibration during flood stage in M-T6 centrifuge test

During the flood phase of test M-T6, a hydrostatic calibration was done to make sure that the pore pressure measurements were correct across the whole soil slope model (as for M-T5). It is required to perform the calibration procedure to correct any inaccuracies that may occur in the readings of the pore pressure transducers (PPTs). However, it is important to note that (PPTs) sensors may not have reached full saturation prior to testing for this test, potentially introducing discrepancies in the PWP readings otherwise. That is, inadequate saturation may result in lower pore pressures being recorded, which must be considered during result interpretation. During the flood stage, the water level was carefully controlled, and the pore water pressure (PWP) was measured at various locations within the slope. The recorded PWP values were then compared with theoretical hydrostatic pressure distributions, derived from the water head and the known properties of the soil. This comparison helped to identify discrepancies between the measured and expected pressures. Using this data, an offset was calculated for each PPT, accounting for variations in depth and local conditions within the

slope model. Table A-1 Hydrostatic pressure calibration during Flood 2 in the M-T6 test.provides the calculated offsets for each PPT sensor in test M-T6.

Table A-1 Hydrostatic pressure calibration during Flood 2 in the M-T6 test.

PPT	P1	P2	P3	P4	P5	P6	P7	P8	P9	P10	P11
Location (Y)model (m)	0.155	0.195	0.235	0.275	0.275	0.195	0.235	0.235	0.155	0.195	0.115
Ri (from Fug.center to PPT) (m)	1.795	1.755	1.715	1.675	1.675	1.755	1.715	1.715	1.795	1.755	1.835
Zi (from PPT to water surface)	0.156	0.114	0.073	0.034	0.043	0.113	0.074	0.083	0.153	0.114	0.193
u _flood	99.353	72.111	45.408	21.103	26.232	71.179	46.280	51.409	97.574	72.050	124.502
PWP(measured) from the test	96.64	67.945	50.814	26.726	27.986	33.666	65.569	35.845	95.967	66.441	127.097
Offset	2.713	4.166	-5.406	-5.623	-1.754	37.513	-19.289	15.564	1.607	5.609	-2.595

A.3.2 Deformations

Once the model reached 70g, it was allowed to equilibrate for 40 minutes before testing. Figure A-15 shows that between autobalance and the end of consolidation, the slope exhibited minimal displacement and strain, indicating stability. Vectorial displacements were small and uniformly distributed, confirming that the soil had settled and adjusted to the load. Resultant displacement contours showed very low values (0–0.25 mm), suggesting negligible movement. Shear strain remained below 0.2%, indicating stabilization of deep slope movement. Volumetric strain showed minor changes, likely within the noise range, reflecting final soil adjustments during consolidation.

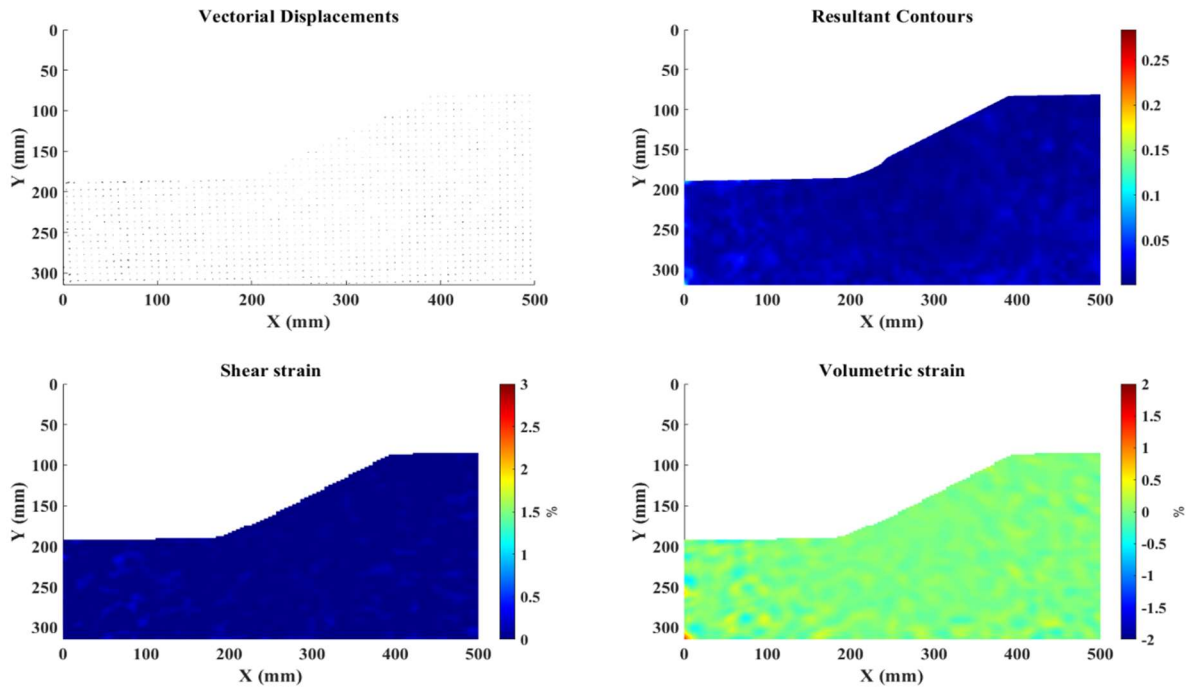


Figure A-15 Displacements and strain at the end of consolidation phase (M-T6) test.

A.3.3 Seasonal cycle effect for M-T6 test.

<u>Slope movement at the end of first winter / M-T6.</u>

During the simulated winter period in the M-T6 test, minor downward and lateral displacements were observed, with maximum movement near the lower slope (0.4 mm). Shear strain reached up to 2.5% in the upper slope, while volumetric strain ranged from +1% (expansion) near the crest to -1% (contraction) in the lower slope. These moisture-induced deformations could contribute to instability over successive wetting-drying cycles., as depicted in Figure A-16.

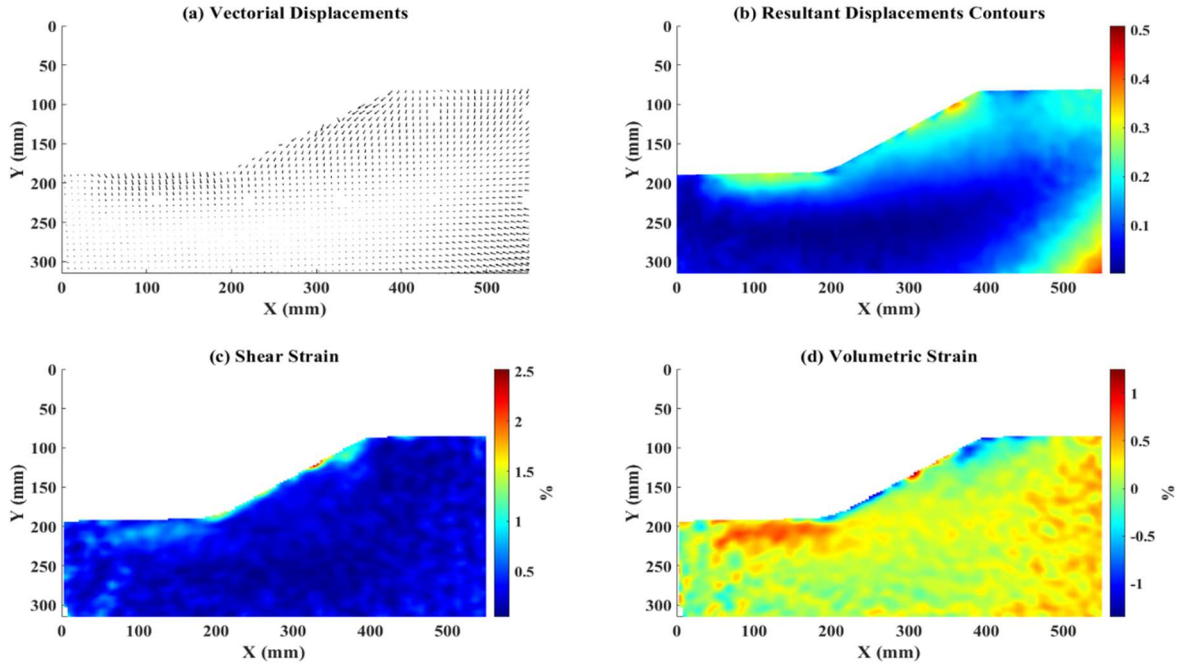


Figure A-16 PIV Analysis results for the M-T6 Slope model at the end of Winter 1.

Pore water pressure analysis at the end of first winter.

The pore water pressure (PWP) distribution at the end of winter is shown in

Figure A-17. The PWP results show a pattern of pressure accumulation, particularly in the surface regions of the slope.

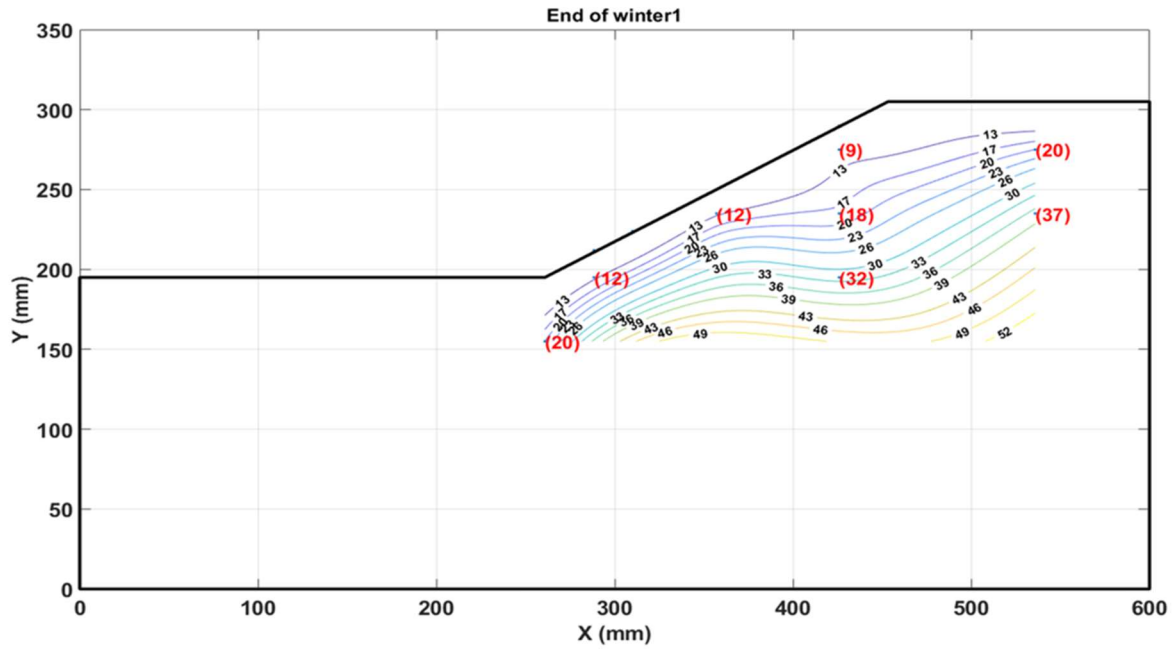


Figure A-17 Pore water pressure distribution at the end of winter 1 in the M-T6 slope test.

Slope movement at the end of first summer / M-T6

At the end of Summer 1, the M-T6 slope remained highly stable with minimal soil movement, deformation, and strain (Figure A-18). Vectorial displacements showed minor movement near the crest and slope face, while resultant displacement contours indicated displacements below 0.1 mm, confirming structural integrity. Shear strain remained low (<0.2%) with no significant deformation zones. Volumetric strain was near 0%, showing no notable shrinkage or swelling, reinforcing the slope's stability during the summer cycle.

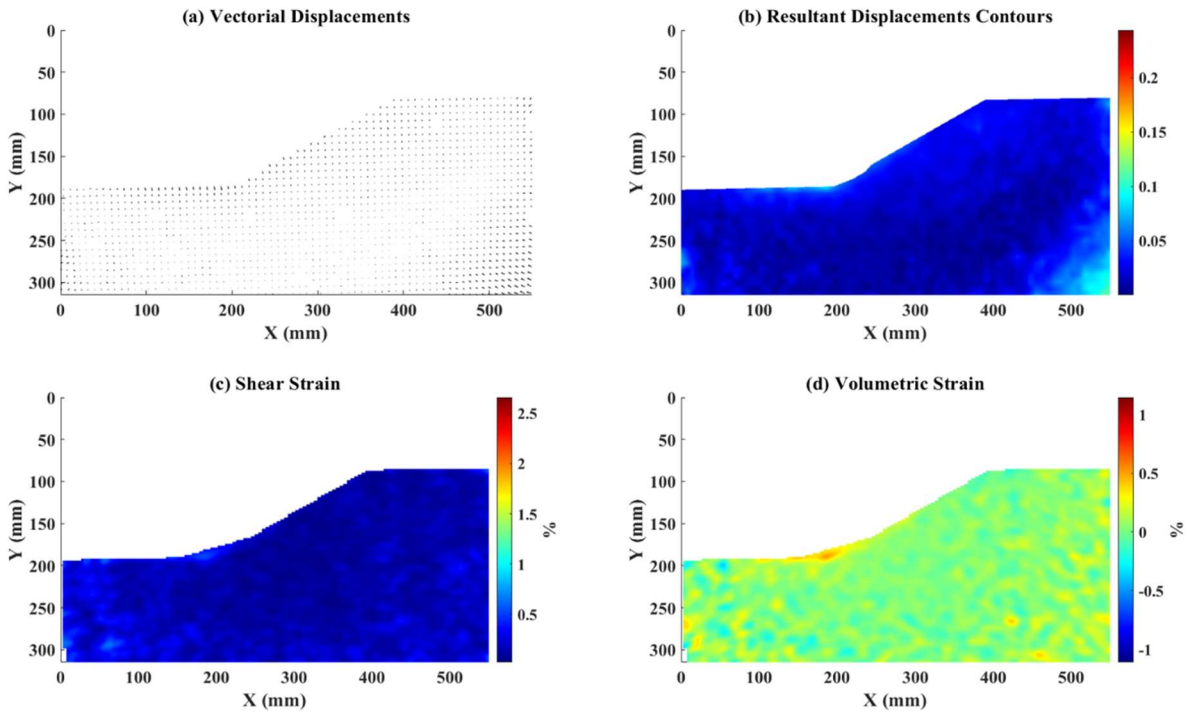


Figure A-18 Deformation and strain analysis of the slope at the end of summer 1 in M-T6 test.

Pore water pressure analysis at the end of Summer 1.

The pore water pressure (PWP) distribution at the end of Summer 1 in the M-T6 test shows a notable reduction in pressures compared to Winter 1 as shown in Figure A-19. This suggests that moisture has evaporated from the upper parts of the slope but is still retained at deeper layers below the crest. Overall, the contours follow the slope with a PWP of approximately zero at the surface.

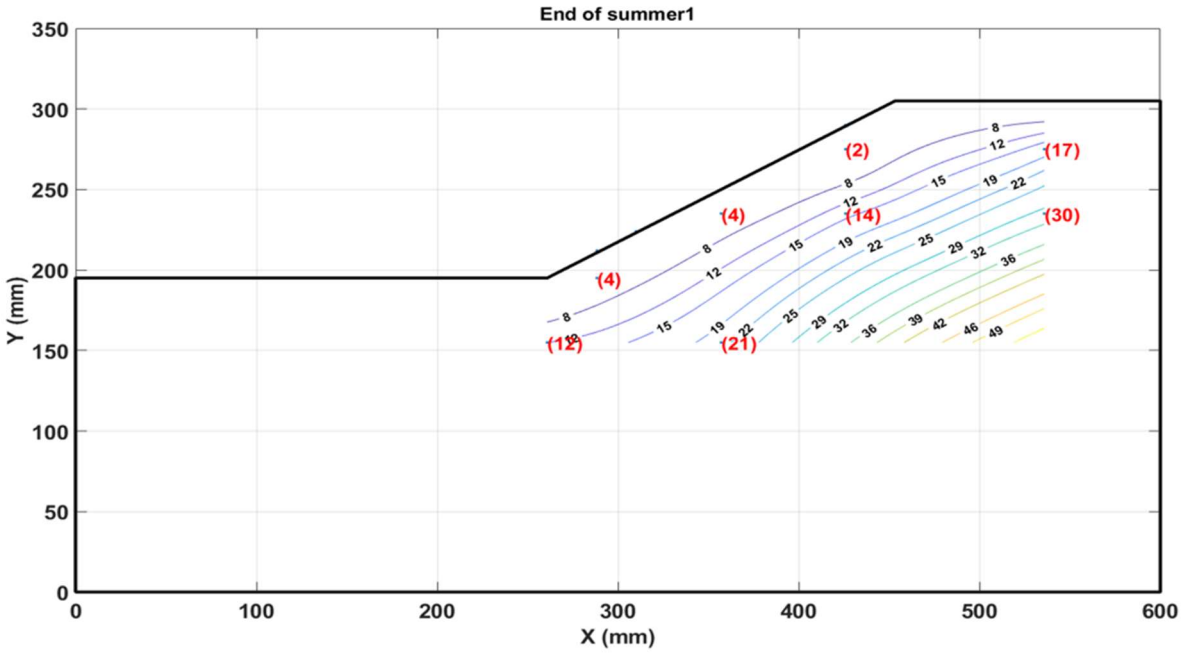


Figure A-19 Pore water pressure distribution at the end of summer 1 in M-T6 test.

Soil deformation at the end of the second winter /M-T6.

At the end of Winter 2, PIV analysis (Figure A-20) shows moderate soil deformation, mainly near the crest and upper slope. Vectorial displacements suggest lateral movement towards the crest, possibly due to moisture variations and weathering, while the lower slope remains stable. Resultant displacement contours show higher displacements near the crest (up to 0.3 mm), decreasing towards the base. Shear strain is moderate (up to 2%), indicating localized shear zones from repeated moisture fluctuations. Volumetric strain exhibits expansion near the crest (+1%) due to swelling and compression in deeper regions, suggesting differential settlement across the slope.

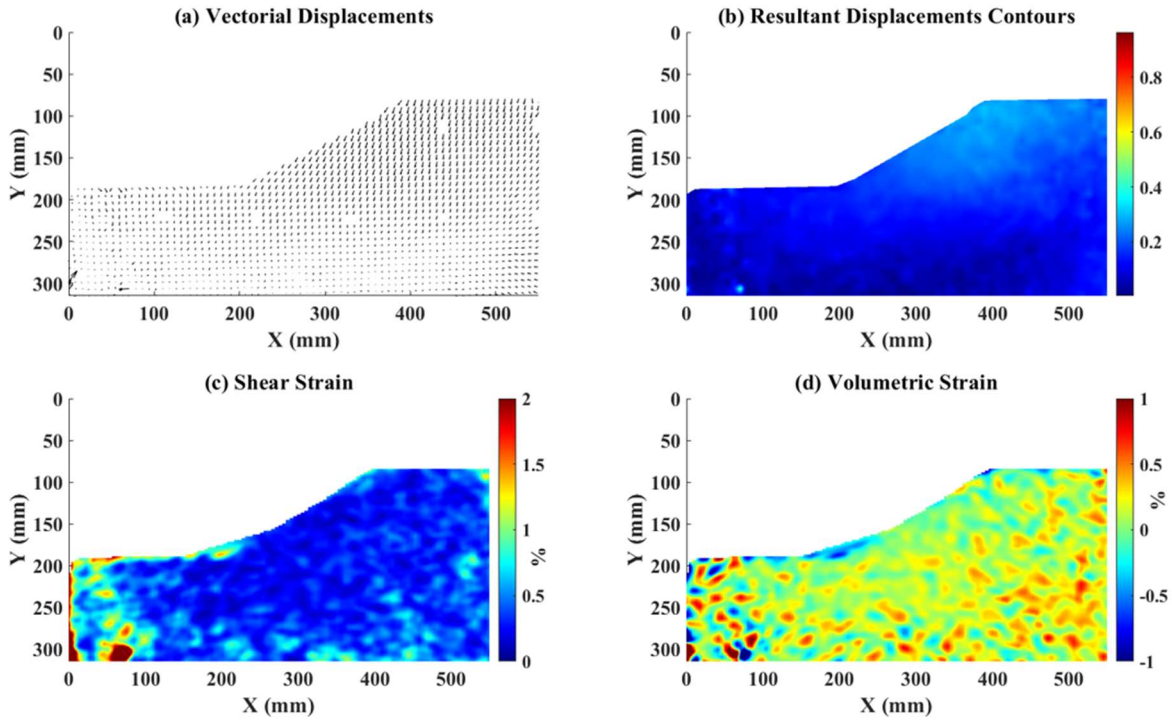


Figure A-20 Soil deformation analysis at the end of Winter 2 for M-T6 test.

Pore water pressure analysis at the end of Winter 2.

At the end of Winter 2, PWP distribution (Figure A-21) follows a slope-parallel pattern, with values increasing with depth, indicating a fully saturated slope. PIV analysis shows downslope and lateral movement, linked to high PWP at depth, which reduces effective stress and shear strength, leading to vertical settlements and lateral shifts. In the shallow mid-slope, where PWP is positive, volumetric strain contours indicate minor expansion, suggesting swelling in these areas.

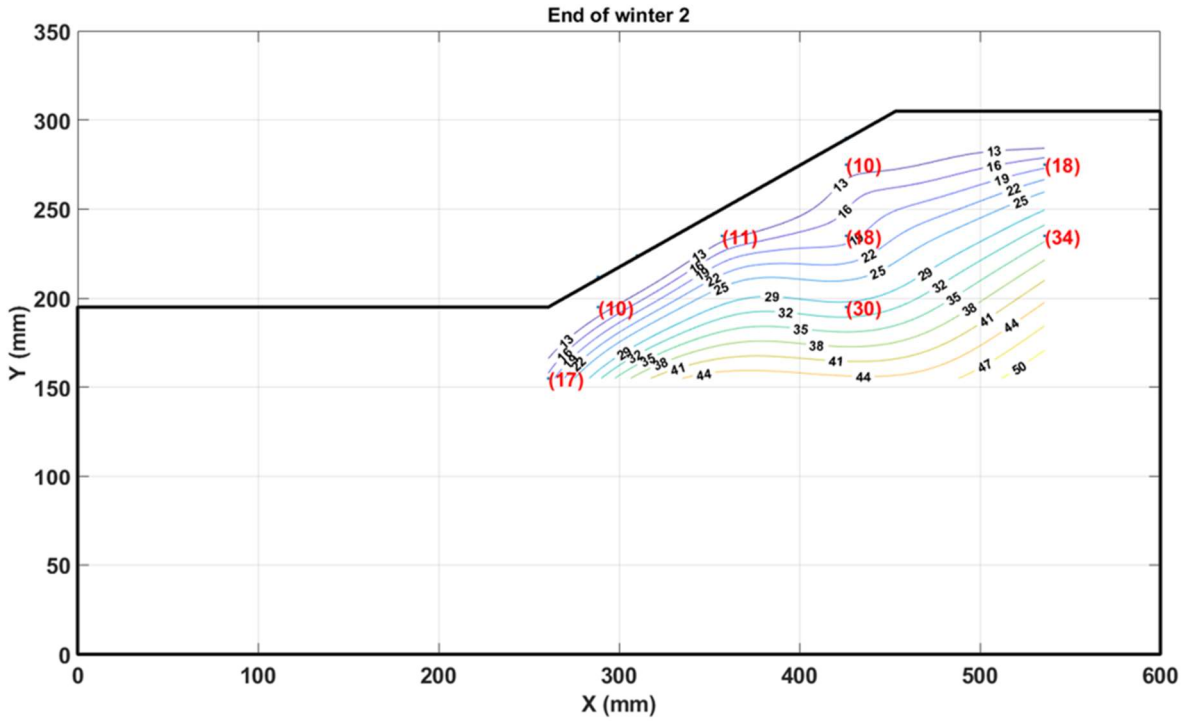


Figure A-21 Pore water pressure distribution at the end of winter 2 in M-T6 test.

Soil deformation at the end of second summer /M-T6.

At the end of the second summer (Figure A-22), minor deformation was observed, mainly near the crest and toe, but overall slope stability remained intact. Vectorial displacements showed slight upward movement towards the crest, indicating minor swelling from drying. Resultant displacement contours remained low (<0.25 mm), with slightly higher movement at the crest suggesting localized adjustments. Shear strain was isolated near the base and crest (up to 2%), reflecting minor stress concentrations but no failure. Volumetric strain exhibited both expansion and contraction, with surface swelling at the crest and minimal changes in deeper layers, consistent with seasonal drying effects.

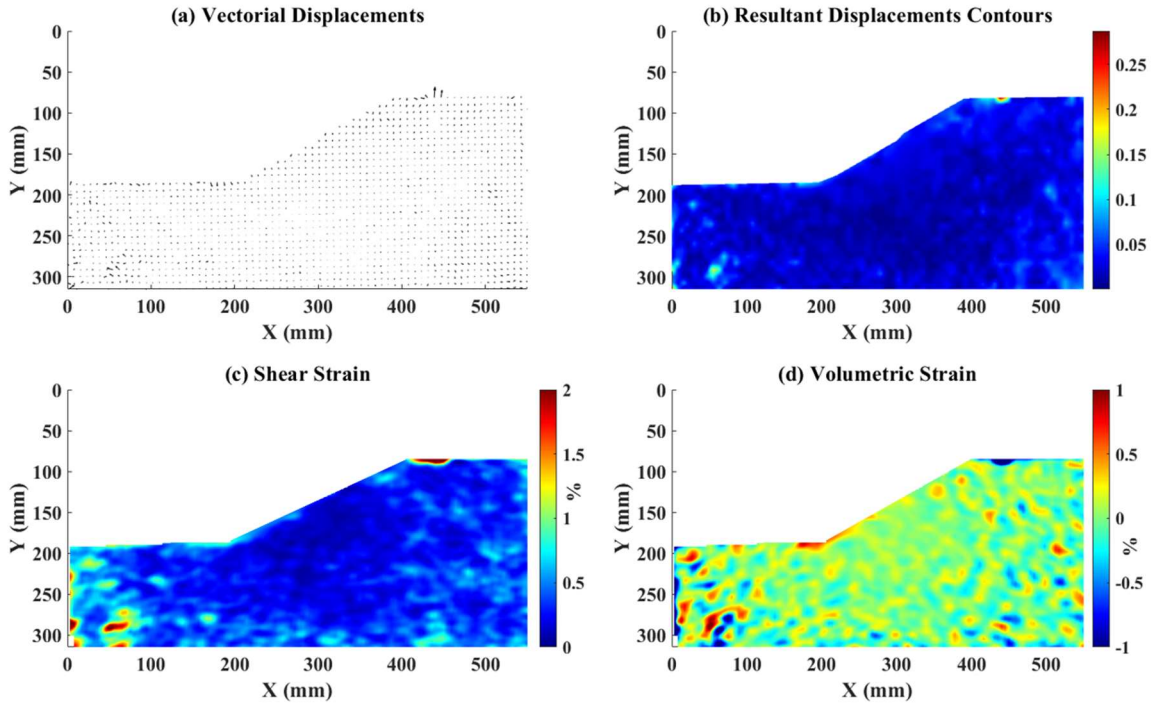


Figure A-22 Soil deformation analysis at the end of summer 2 for M-T6 test.

Pore water pressure analysis at the end of summer 2.

The PWP at the end of summer 2 reflects typical post-dry-season trends, with lower water pressures near the surface and higher pressures at depth, and contours of pressure parallel to the slope. These conditions suggest a stable slope with minor internal water retention, which could influence future movement or deformation during subsequent wetting phases. The pore water pressure (PWP) distribution at the end of Summer 2, shown in the Figure A-23, highlights the effects of moisture loss at the slope surface. Under the slope surface, where the pore pressure transducers (PPTs) are located, the PWP values show a gradual decrease compared to the winter periods, reflecting the seasonal drying effects.

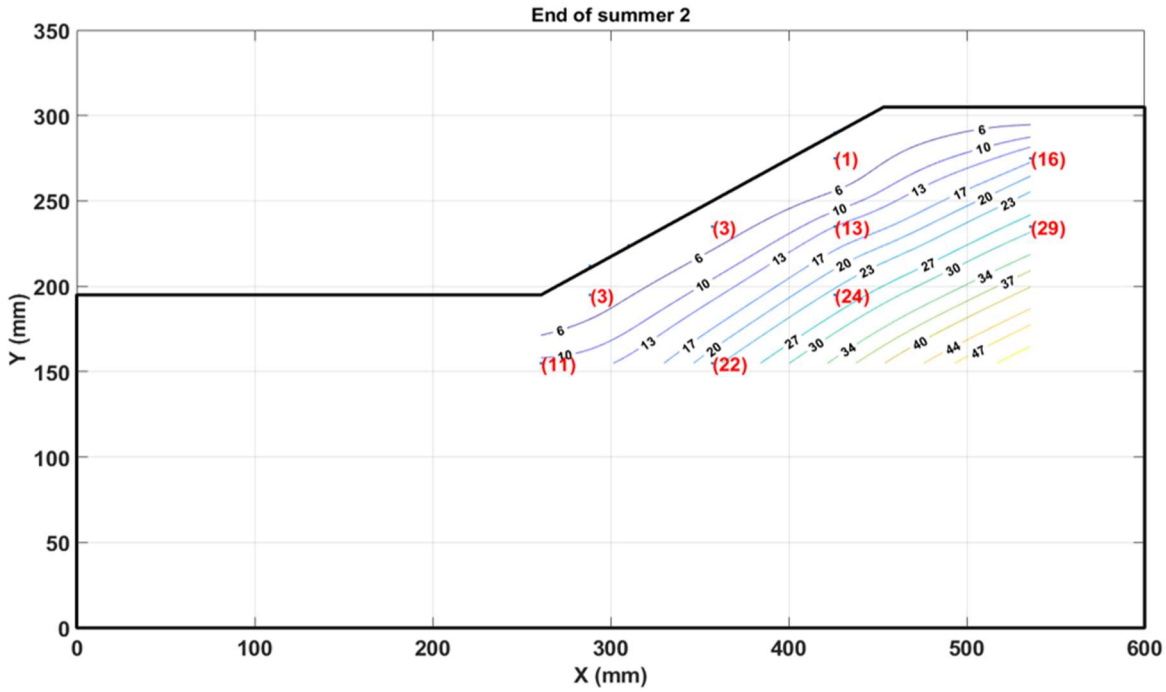


Figure A-23 Pore water pressure distribution at the end of summer 2 in M-T6 Test.

Soil deformation at the end of winter 3 for M-T6 test.

At the end of Winter 3 in the M-T6 test (Figure A-24), the slope remained stable with limited displacement and shear deformation. Vectorial displacements and resultant displacement contours showed minimal movement, indicating no large-scale failure. Shear strain reached up to 1% near the lower slope, suggesting minor localized stress. Volumetric strain displayed alternating zones of expansion and contraction, averaging near 0%, likely reflecting data noise rather than significant soil volume changes.

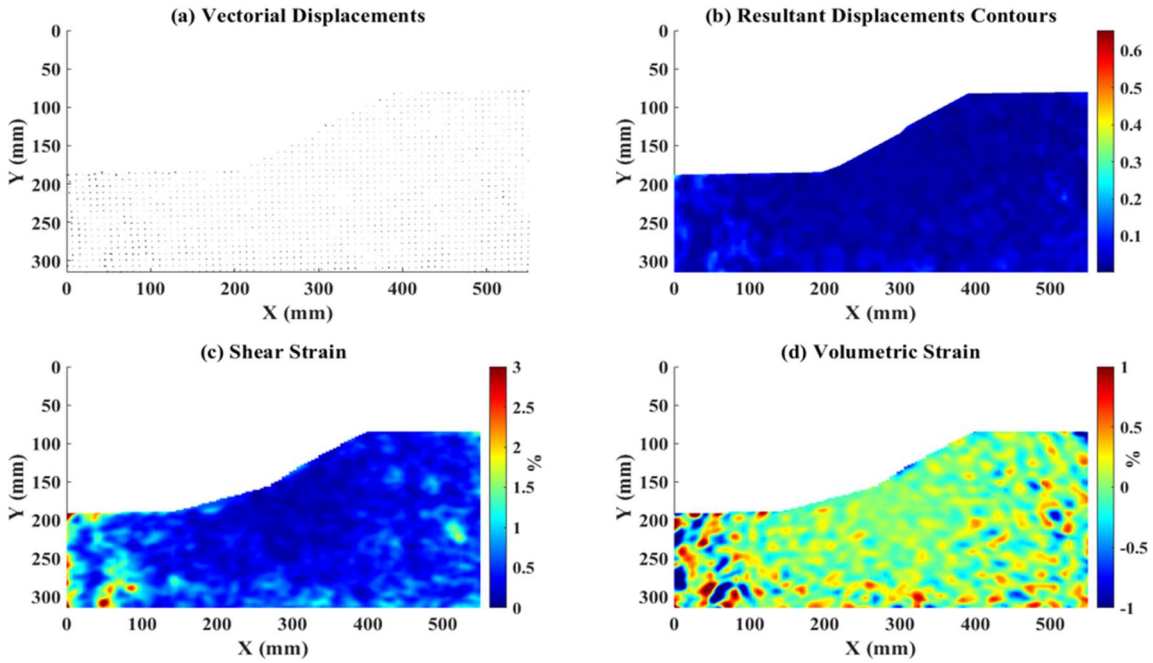


Figure A-24 Soil deformation analysis at the end of winter 3 for M-T6 test

Pore water pressure analysis at the end of winter 3.

At the end of the third winter cycle in the M-T6 test, a clear gradient can be observed, with increasing PWP values from the crest down towards the toe – again with slope parallel PWP contours and a positive pore pressure at the surface. The PIV analysis shows relatively low displacements across the slope, with little shear strain areas under the crest and toe of the slope. Overall there is little slope movement (Figure A-25).

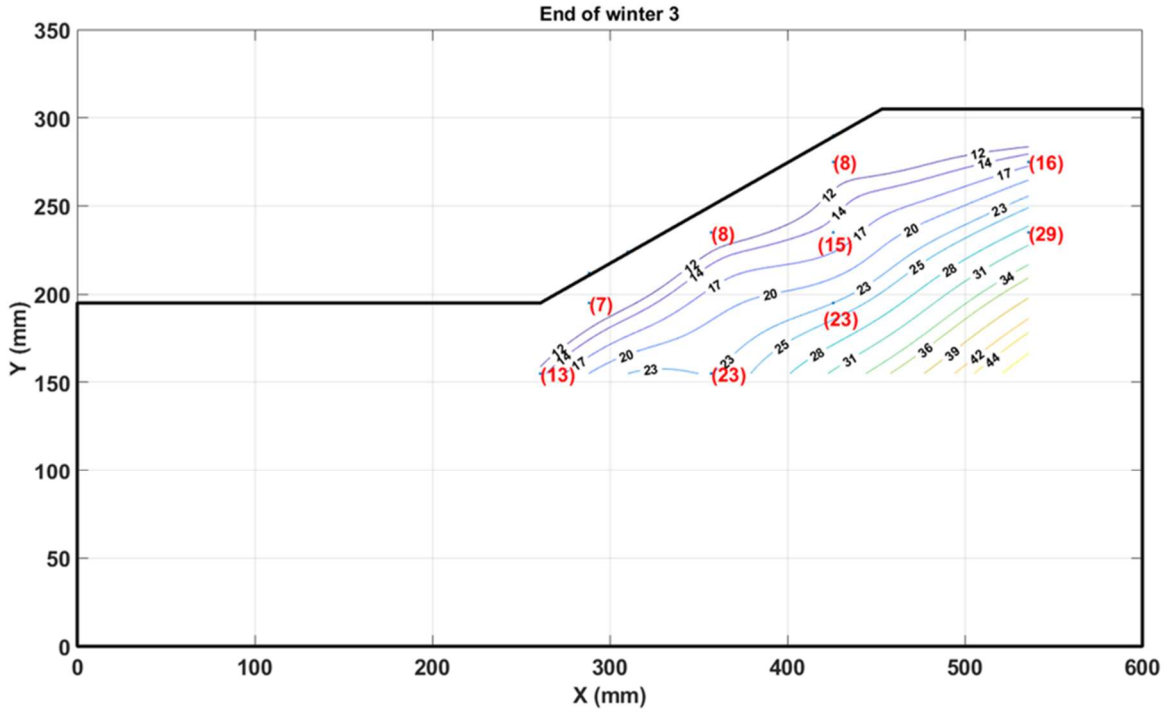


Figure A-25 Pore water pressure distribution at the end of winter 3 in M-T6 Test.

Swelling and second consolidation (reconsolidation)

After Winter 3, the test was spun down and left for 2 days before spinning up for the next stage of tests. The PWP data for the end of the reconsolidation period reflects high moisture retention and saturation in the lower slope and near the toe, with negative pore pressures at the crest as shown in Figure A-27. This suggests that water from the upper slope is likely to have flowed downwards and accumulated near the toe during the period at 1g. The piezometric surface (PWP of zero) is not parallel to the slope as for previous tests. The displacement contours are overwhelmingly vertical, suggestive of recompression after the 1g swelling period. The PIV analysis shows up to 1% compression, particularly in the mid area and around 0.5% shear strain as the soil seems to consolidate and shear slightly Figure A-26.

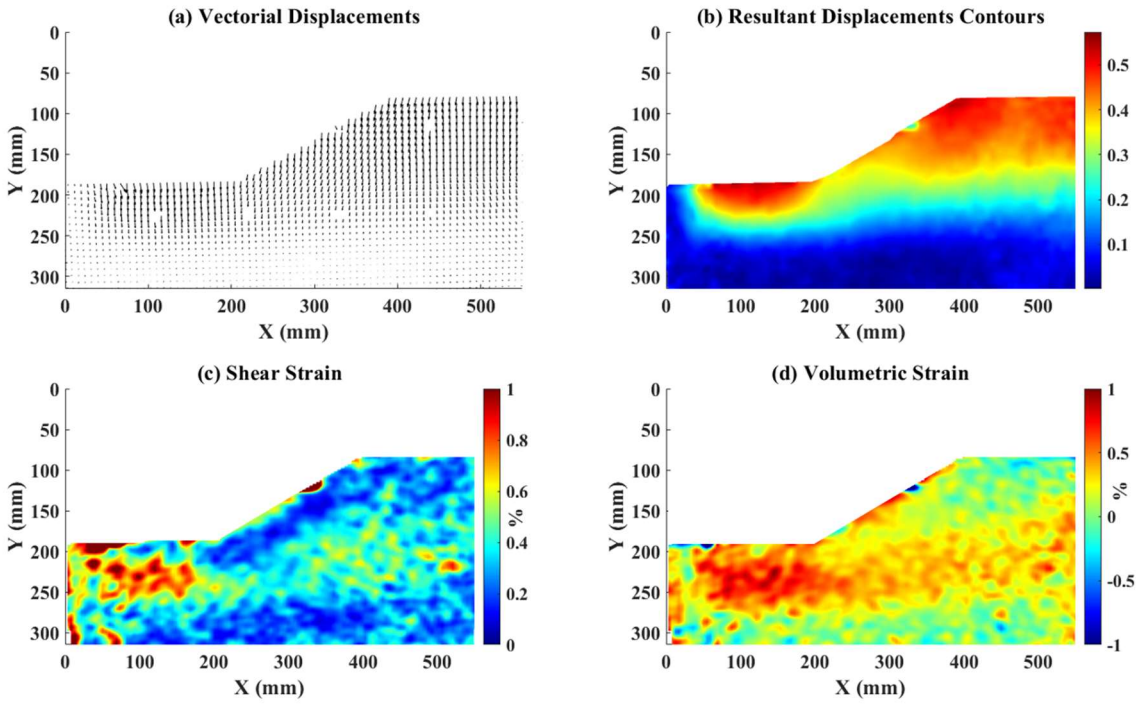


Figure A-26 Soil deformation analysis at the end of summer 3 for M-T6 test.

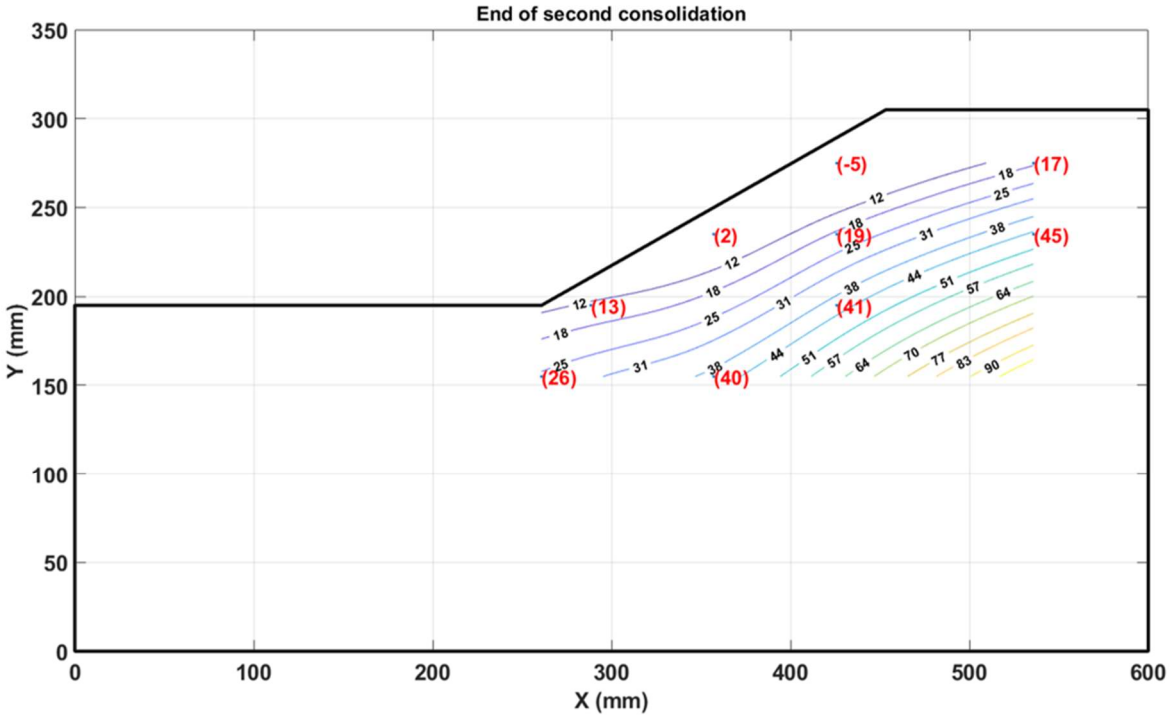


Figure A-27 Pore water pressure distribution at the end of second consolidation in M-T6 Test.

A.3.4 Flooding and drawdown effects M-T6.

Soil deformation during Flood 1

During Flood 1 of the M-T6 test (Figure A-28), the slope remained stable with minimal deformation. Vectorial displacements were negligible, indicating no significant surface movement. Resultant displacement contours showed low displacement, with slight movement near the crest. Shear strain reached up to 1.4%, localized at the slope top, possibly due to erosion artifacts. Volumetric strain revealed minor expansion and contraction, but no clear pattern, suggesting overall low volumetric response to the flooding.

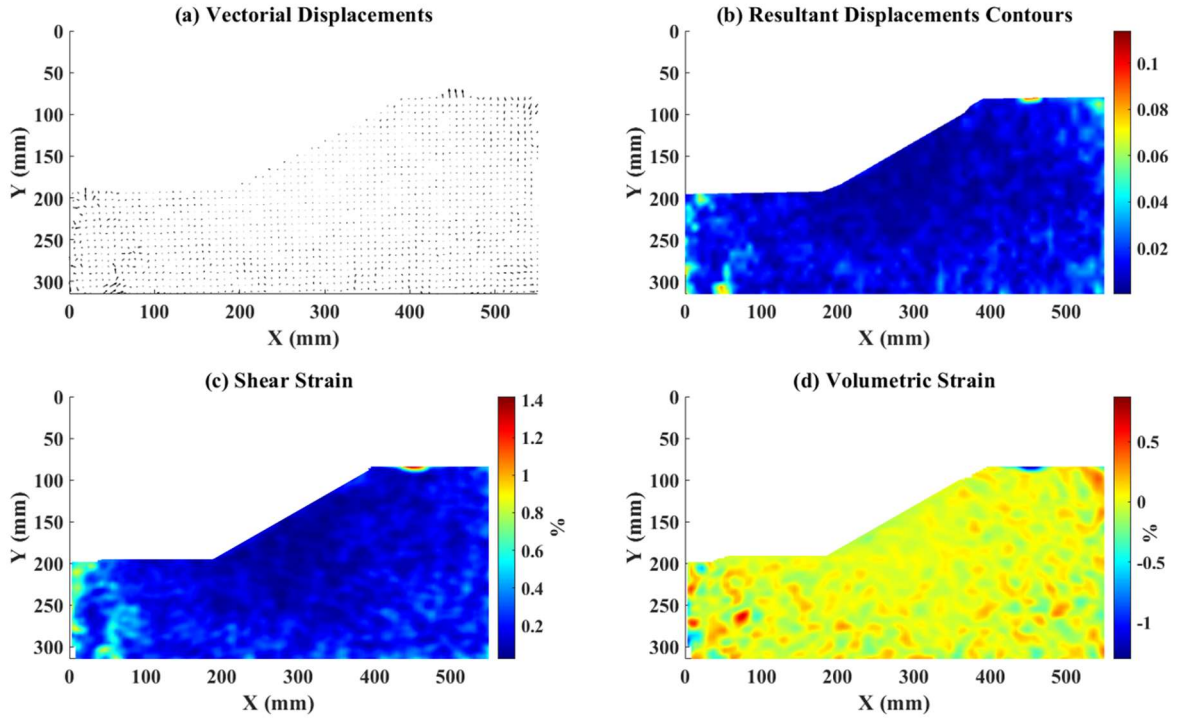


Figure A-28 Soil deformation analysis during flood 1 for M-T6 test.

Pore water pressure analysis during flood 1/M-T6.

During the Flood 1 stage, the PWP data shows significant increases in water pressure throughout the slope, as shown in Figure A-29. However, it should be noted that these data are modified by Flood 2 (i.e. with amended PPT offsets), which was used to effectively model the PWP response, allowing for variation in the radial g-field and curvature in the x direction due to the size of the centrifuge. This was done, as discussed in Chapter 6, in order to account for the offsets of the PPTs changing during spinning down between tests and test segments.

That said, the results conform to a typical hydrostatic response in the curved g-field, with Flood 1 being at a sightly lower height (although above the crest) than Flood 2.

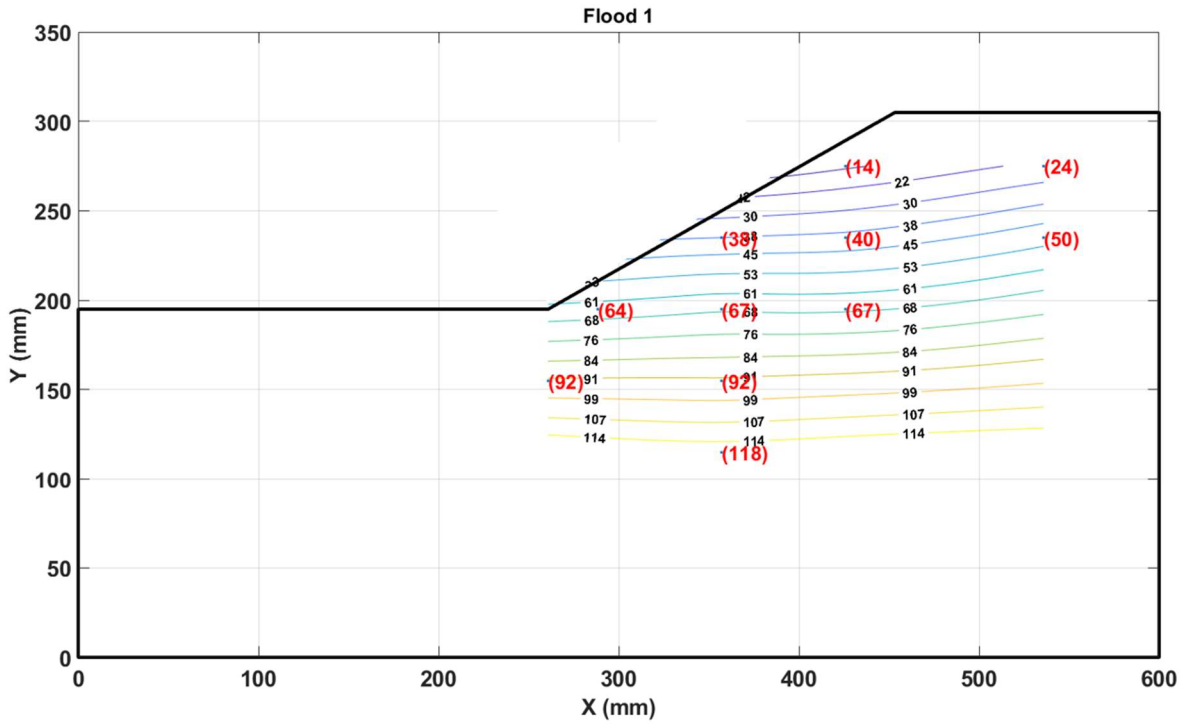


Figure A-29 Pore water pressure distribution during flood 1 in M-T6 Test.

Soil deformation at the end of first drawdown.

At the end of the first drawdown in the M-T6 test (Figure A-30), PIV analysis shows that the slope experienced downslope movement, primarily in the middle and lower sections. Vectorial displacements indicate downward and outward movement, with the crest remaining stable. Resultant displacement contours show maximum movement (0.1–0.25 mm) near the toe and lower slope, confirming localized deformation. Shear strain is concentrated in the lower and mid-slope regions (up to 1.5%), indicating significant stress, while the crest remains largely unaffected. Volumetric strain reveals contraction near the toe and some swelling in other areas, with little change deeper in the slope, reflecting typical drawdown effects.

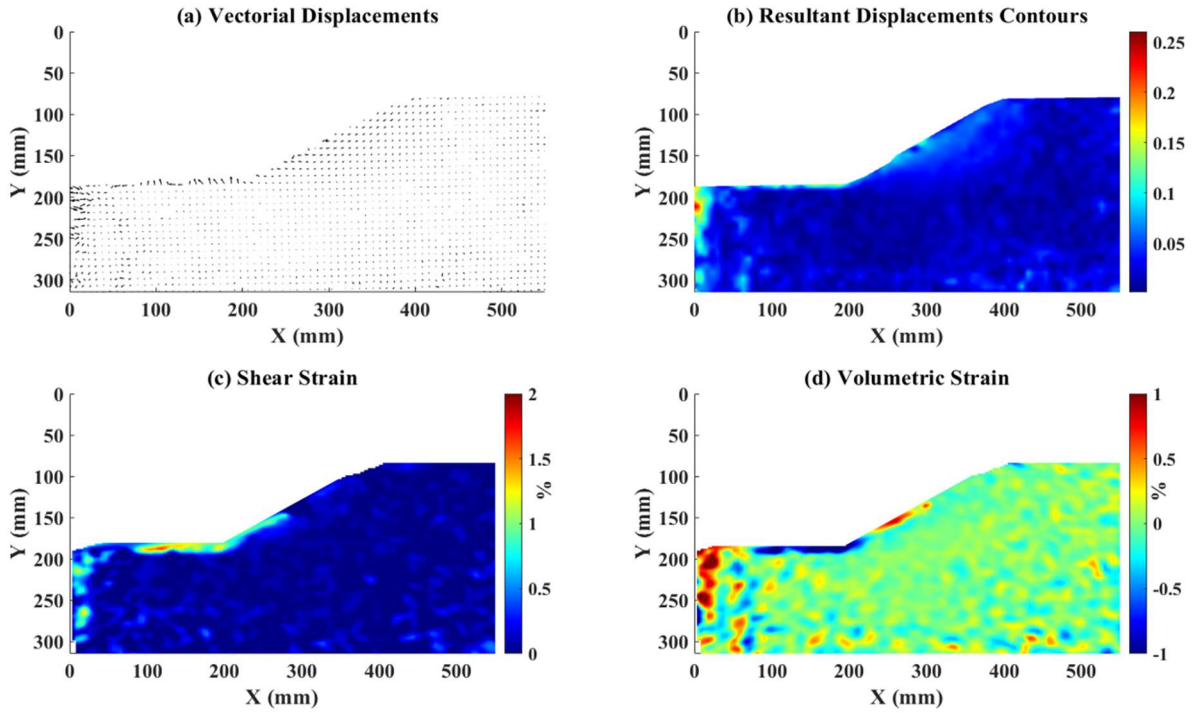


Figure A-30 Soil deformation analysis at the end of drawdown 1 for M-T6 test.

Pore water pressure analysis at the end of drawdown1.

The pore water pressure (PWP) data at the end of Drawdown 1 in the M-T6 test is presented in Figure A-31. The PWP values near the crest are relatively low, with readings around 8 kPa. This suggests that this part of the slope has experienced relatively effective drainage during the drawdown but with positive pore pressures apparently at the slope surface, that this drainage is still occurring (water is still leaving the slope face).

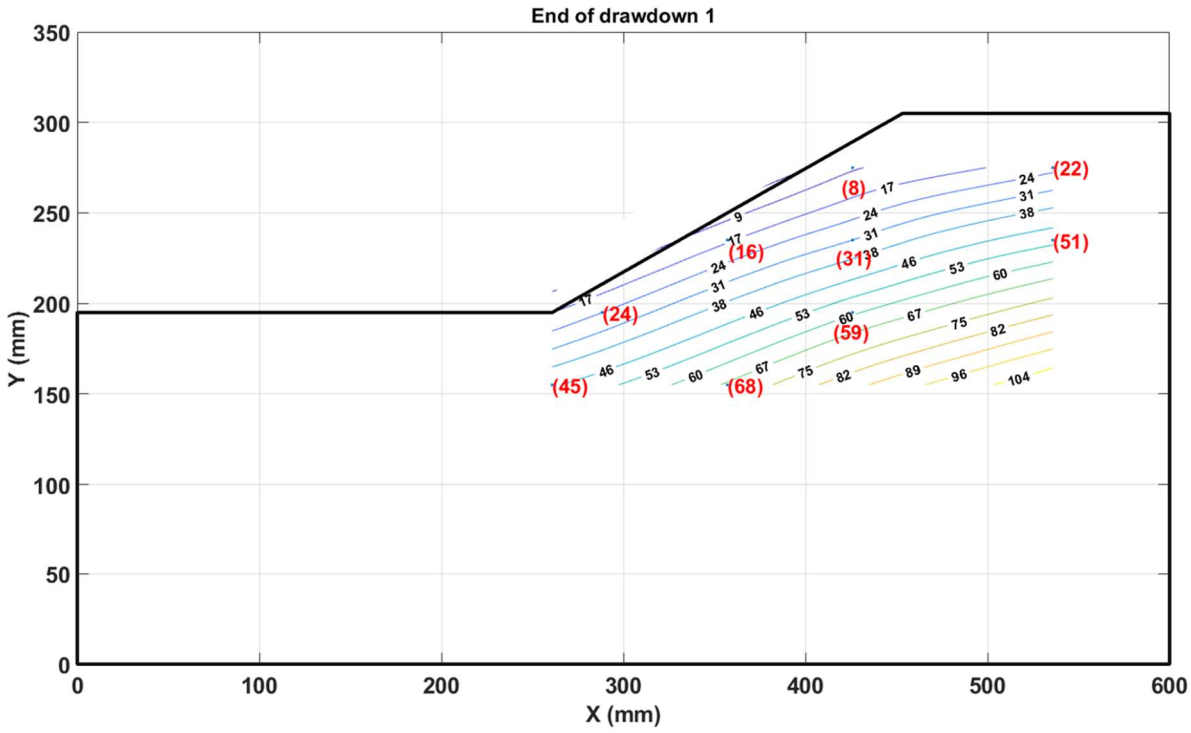


Figure A-31 Pore water pressure distribution at the end of drawdown 1 in M-T6 Test.

Soil deformation at the end of the second flood.

During Flood 2 of the M-T6 test (Figure A-32), PIV analysis indicates that the slope remained relatively stable, with minimal deformation. Vectorial displacements show apparent movement at the model's lower right edge, but this is attributed to lighting and calibration marker artifacts, not actual soil movement. Resultant displacement contours near the slope confirm low displacement, supporting the slope's stable condition. Shear strain and volumetric strain are both very low (shear < 0.5%), with no significant internal deformation, similar to the response in Flood 1.Figure A-33 shows a visual capture of the soil slope model during the M-T6 test, illustrating the current state of the slope during flood infiltration.

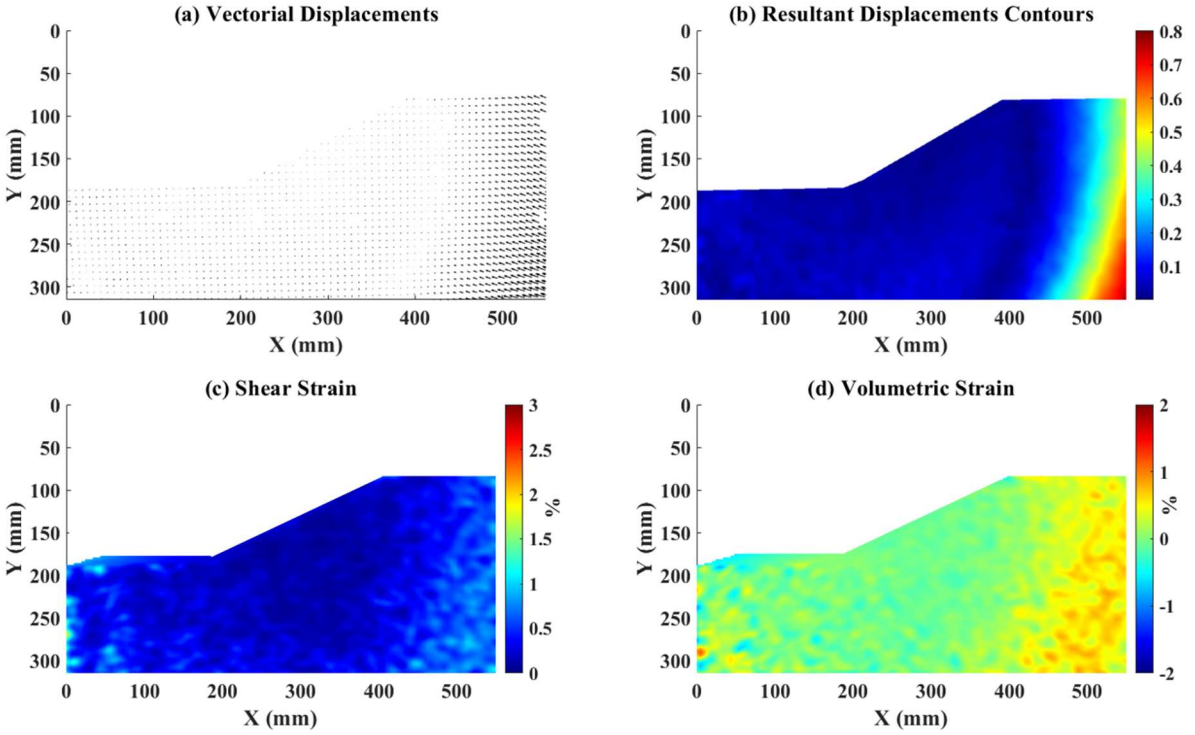


Figure A-32 Soil deformation analysis during second flood for M-T6 test.

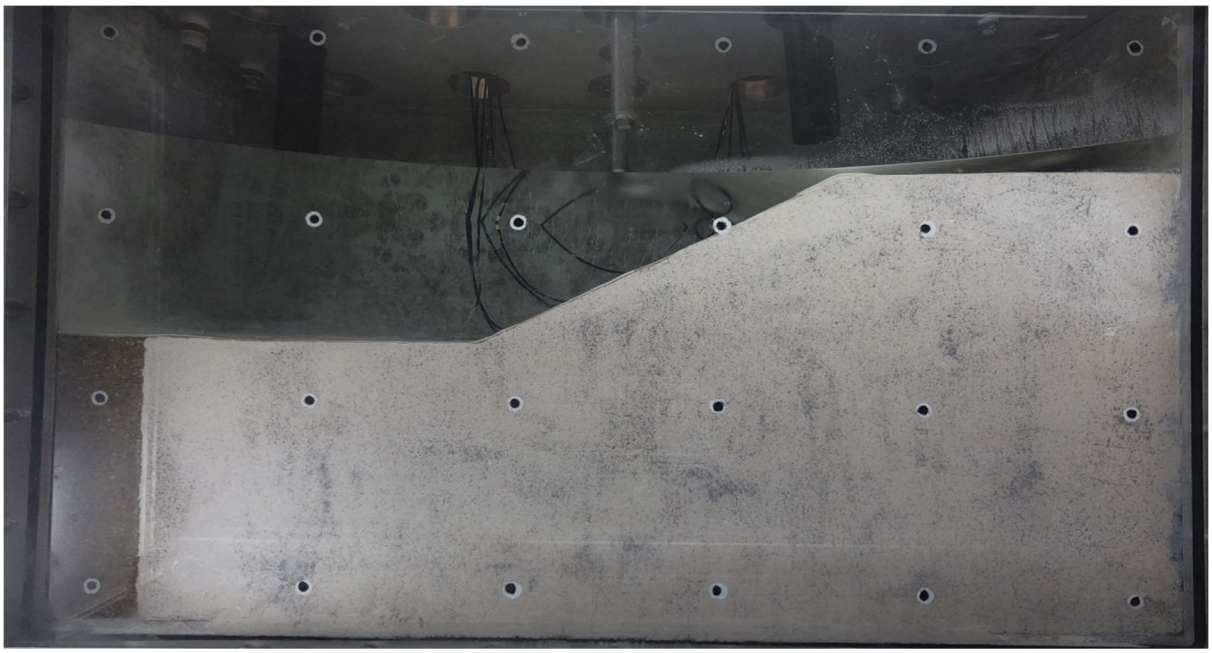


Figure A-33 Physical condition of soil slope model during second flood of M-T6 Test.

Pore water pressure analysis during flood 2.

During Flood 2 in the M-T6 test, the pore water pressure (PWP) data was amended to correct PPT offsets for the whole test (Figure A-34). Therefore, the values are reflective of theoretical PWP values for a centrifugal acceleration field with the given flood level.

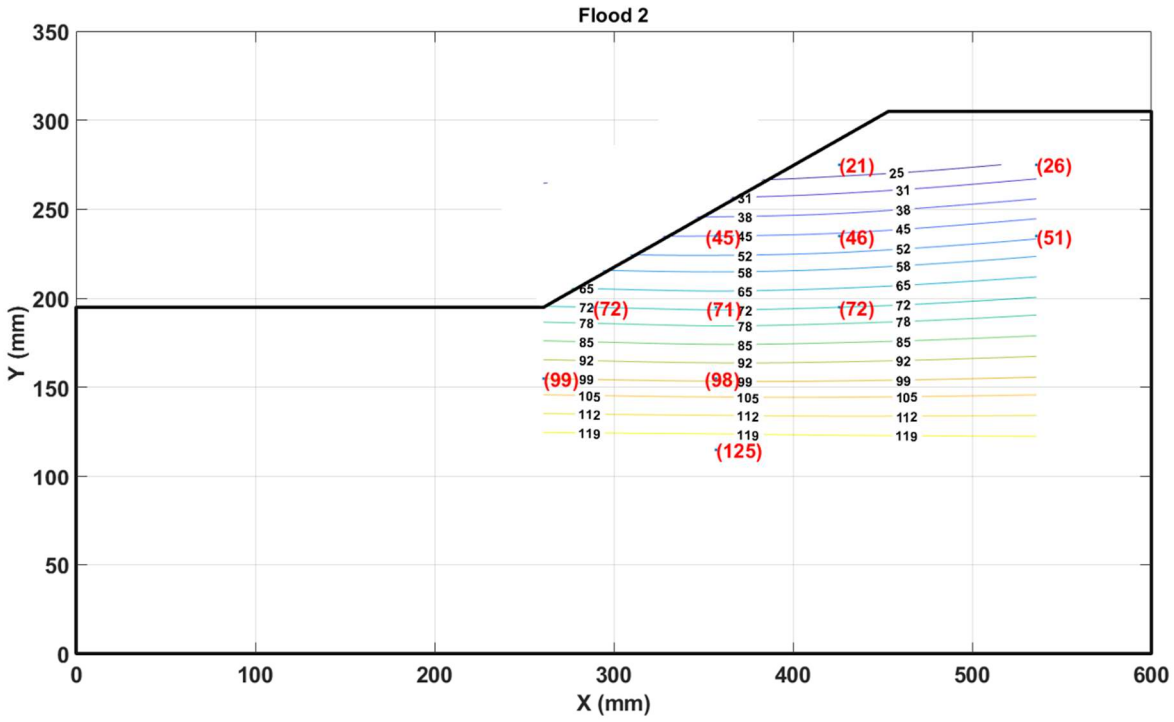


Figure A-34 Pore water pressure distribution during second flood in M-T6 Test.

Soil deformation at the end of the second drawdown.

At the end of the second drawdown in the M-T6 test (Figure A-35), PIV analysis indicates that the upper slope and crest experienced the most deformation. Vectorial displacements show downslope movement, with larger displacements near the crest. Resultant displacement contours reveal maximum movement (0.5–0.7 mm) in the upper slope, likely due to pore pressure reduction and loss of soil strength. Shear strain reaches 2% in the upper slope and crest, highlighting localised deformation. Volumetric strain suggests expansion in shallow regions, possibly due to water leaving the soil. This drawdown phase increased instability in the upper slope, with potential for further deformation over time.

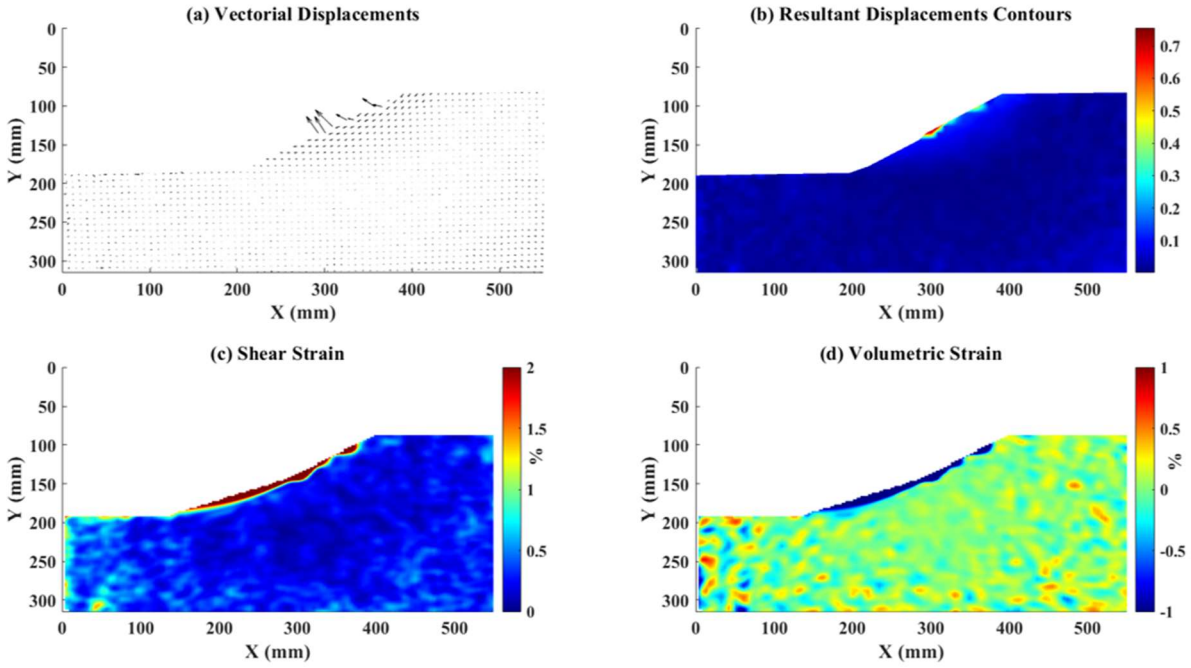


Figure A-35 Soil deformation analysis at the end of drawdown for M-T6 test.

Pore water pressure analysis at the end of second drawdown.

The pore water pressure (PWP) data at the end of the second drawdown stage is provided in Figure A-36. The pore water pressure at the crest is relatively low, with extrapolated contour values around 9 to 16 kPa leaving the slope face. This suggests that the drawdown process has caused water levels to drop significantly near the crest but that water is still leaving the front face at the time of recording. The PWP and PIV data show a clear correlation between the reduction of pore water pressure and the resulting soil deformations. The PIV analysis shows noticeable displacements near the crest where PWP values are lower, indicating that the loss of water from the soil and corresponding reduction in pore pressure have allowed the soil to shift downslope. The largest resultant displacements are observed near the crest (up to 0.7 mm), which correlates with the low PWP values in this region.

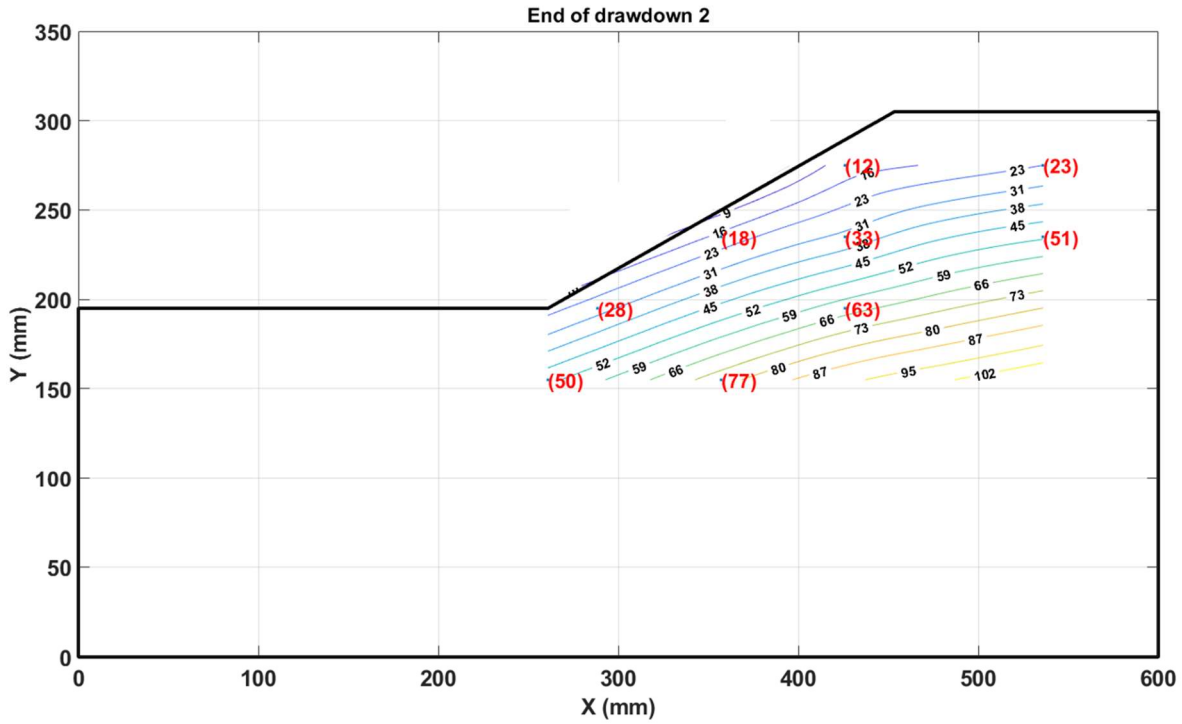


Figure A-36 Pore water pressure distribution at the end of second drawdown in M-T6 Test.

Soil deformation during the third flood of the M-T6 test.

During Flood 3 of the M-T6 test (Figure A-37), PIV analysis indicates that the slope remained stable with minimal deformation. Vectorial displacements were minimal, with some edge effects caused by calibration point issues. Resultant displacement contours near the slope show low movement, confirming overall stability. Shear strain was very low (up to 0.2%), and volumetric strain showed no significant changes—both consistent with previous flood event

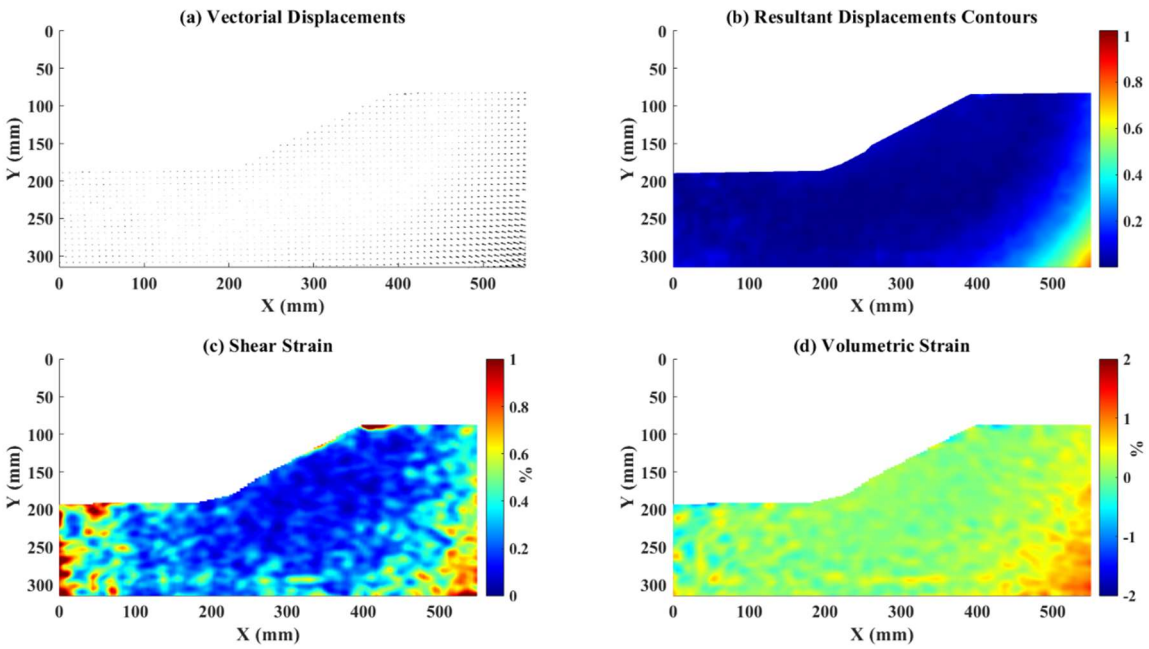


Figure A-37 Soil deformation analysis during flood 3 for M-T6 test.

Figure A-38 depicts the water level during the third Flood as it rises from the middle slope to the crest. The left side of the figure shows the water level reaching approximately halfway up the slope, indicating the middle stages of inundation. As the flood progresses, the right side of the figure demonstrates how the water rises further, approaching the crest of the slope.



(a) (b)

Figure A-38:The progression of water levels during Flood 3 as the water rises from the middle section of the slope (a) to the crest (b).

Pore water pressure analysis during the third flood of the M-T6 test.

The pore water pressure (PWP) data during Flood 3 of the M-T6 test is shown in Figure A-39. As for previous floods, the contours follow a modified hydrostatic field as expected (noting that this data is based on the modified PPT data from Flood 2), with pore pressures increasing near linearly with depth – with slightly curved contours.

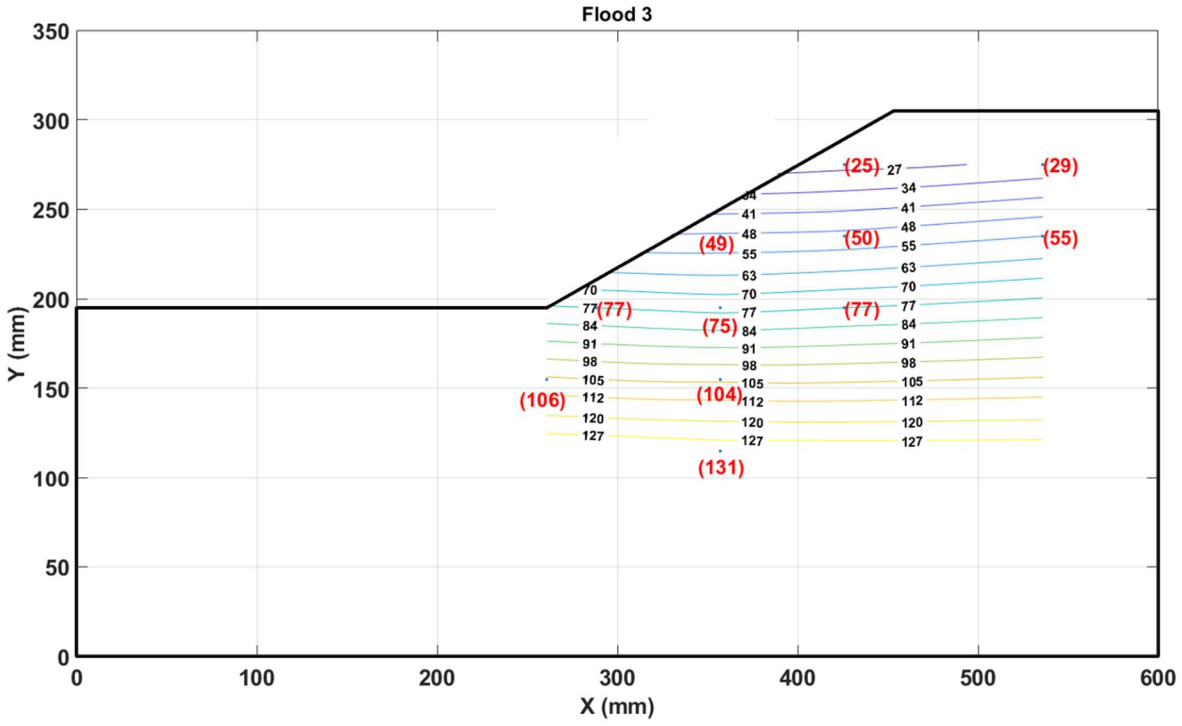


Figure A-39 Pore water pressure distribution during third flood in M-T6 Test.

A.4 Test M-T6r

A.4.1 Hydrostatic calibration during flood stage in M-T6r centrifuge test.

The M-T6r centrifuge test hydrostatic calibration during the flood stage closely follows the methodology used in the M-T6 test. Both involve key steps in ensuring the pore water pressure (PWP) within the soil model is calibrated correctly, considering that otherwise the PPT offsets may have shifted. Table A-2 shows multiple PPTs (P1 to P11) placed at different locations (Y-model), ranging from 0.115 m to 0.275 m. The PPTs were positioned at various radial distances from the centrifuge center (Ri) and with varying heights (Zi) from the PPT to the water surface. This closely follows the same layout principles in the M-T6 test.

The hydrostatic method calculates the theoretical pore water pressure (PWP) at each transducer based on the radial distance, the water height above the transducer, and the angular velocity of the centrifuge. This approach ensures that the measured pressures during flooding accurately replicate the expected values for a correctly simulated prototype scenario. The methodology aligns with the hydrostatic calibration techniques employed in M-T6, providing a consistent framework for validating pressure measurements. By maintaining this level of precision, the method ensures that the experimental results faithfully represent the hydraulic conditions of the prototype.

$$u = \rho\omega^2/2 \times (2 \times R \times Z - Z^2) \qquad A\text{-}1$$

Table A-2 shows a comparison of the calculated hydrostatic pressures and the measured PWP from the test during Flood 4 (the 4th flood applied to M-T6r), indicating slight differences (offset values). Such offsets are common and expected, often requiring adjustments or corrections in subsequent tests, just like in the M-T6. Figure A-40 shows the model in the centrifuge test with a labelled PPT1 and the water height (Zi). It clearly demonstrates the process of simulating a rising water level (flood stage). The soil slope is subject to inundation as water rises, similar to the M-T6 flood stage simulation. The water level, shown visually in the test setup, corresponds to the values listed in the table for Zi (distance from PPT to water surface), ensuring accurate representation of flood conditions.

Table A-2: Calculated offsets for PPT sensors during the Flood 4 stage in the M-T6r centrifuge test.

PPT	P1	P2	P3	P4	P5	P6	P7	P8	P9	P10	P11
Location (Y)model (m)	0.155	0.185	0.235	0.275	0.275	0.195	0.235	0.235	0.155	0.195	0.115
Ri (from Fug.center to PPT) (m)	1.795	1.765	1.715	1.675	1.675	1.755	1.715	1.715	1.795	1.755	1.835
Zi (from PPT to water surface)	0.174	0.143	0.091	0.052	0.061	0.131	0.092	0.101	0.171	0.132	0.211
u _flood	110	90	56	32	37	82	57	62	109	83	136
PWP(measured) from the test	113	92	65	47	49	49	89	53	119	100	139
Offset	-3	-2	-8	-15	-12	33	-32	10	-10	-17	-4

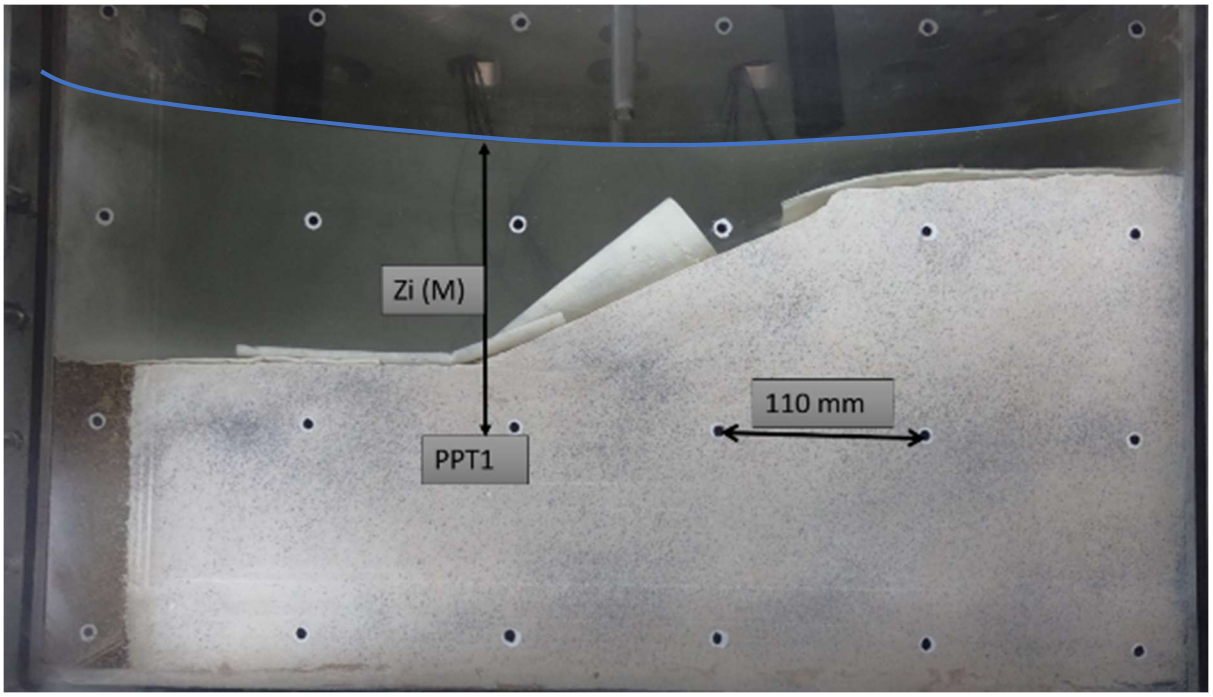


Figure A-40 Soil slope model with hydrostatic calibration during Flood 4 of M-T6r.

A.4.2 M-T6r: Autobalance and consolidation deformations

At the end of the auto balance and consolidation stages in the M-T6r test, the PIV results shown in Figure A-41 and Figure A-42 indicate the deformation behaviour of the soil slope. At the end of the auto balance and consolidation stages in the M-T6r test, deformation patterns

indicate increasing soil movement. During auto balance, displacement was concentrated near the crest (up to 2.5 mm), with lateral movement towards the slope face. Shear strain (up to 2.5%) was notable near the crest and toe, while volumetric strain showed minimal change. During consolidation, displacement increased, particularly near the upper slope (up to 2 mm), with a deep-seated shear zone developing. Shear strain exceeded 3%, and compression became more prominent near the toe, indicating ongoing settlement. During the consolidation stage of the M-T6r test, displacement increased, particularly near the crest and upper slope, indicating further settlement. Displacement contours reached 2 mm, with a deep-seated shear zone forming. Shear strain exceeded 3%, concentrated in the upper slope, while volumetric strain showed compression mainly near the lower slope and toe. The red dashed line in Figure A-43 highlights settlement magnitude, suggesting significant volumetric changes, though strain plots indicate that much of this is due to deep-seated slope shear or failure.

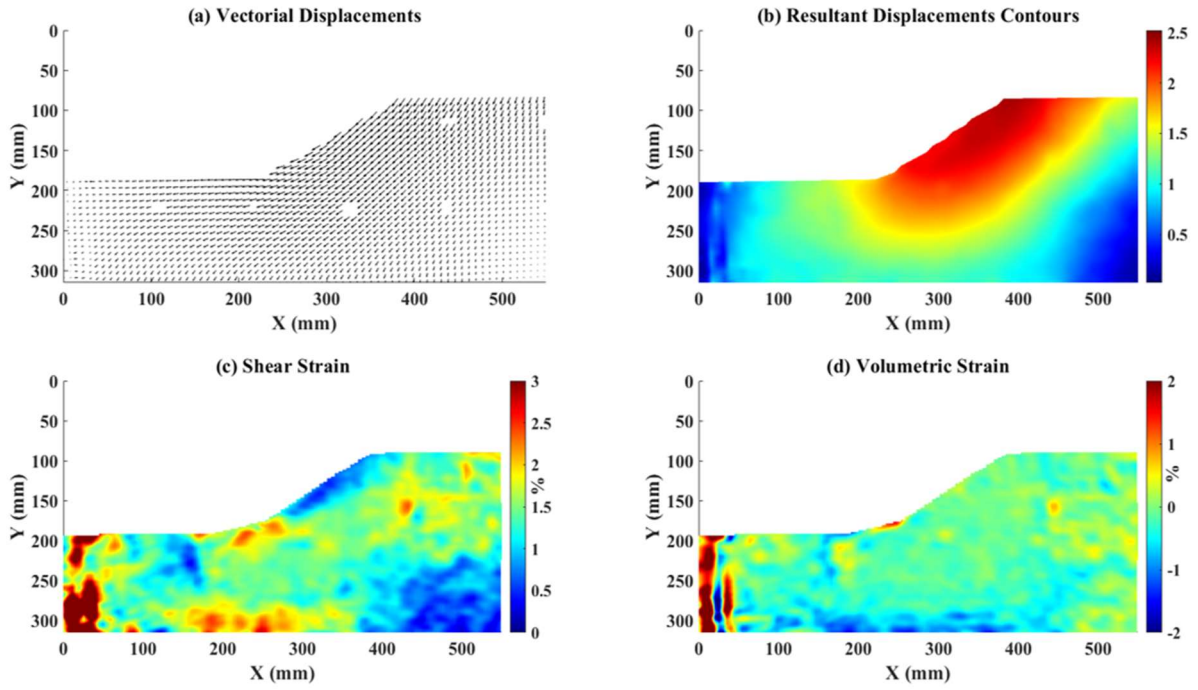


Figure A-41 Displacements and strain at the end of auto balance phase (M-T6r) test.

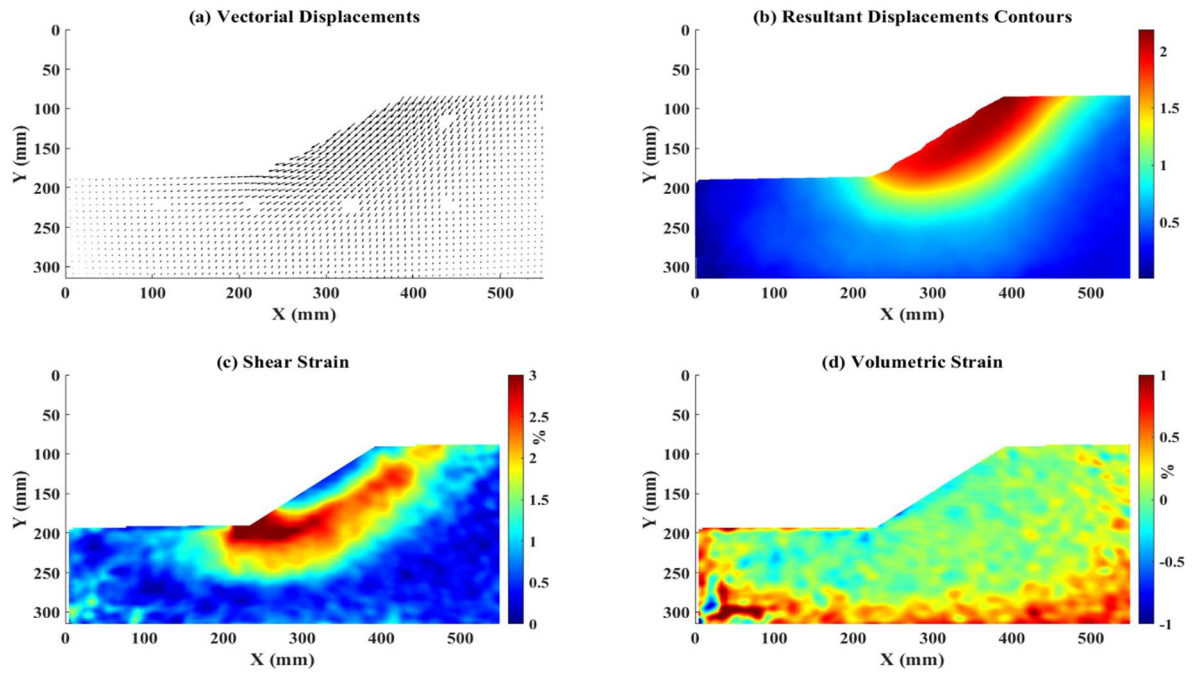


Figure A-42 Displacements and strain at the end of consolidation phase (M-T6r) test.

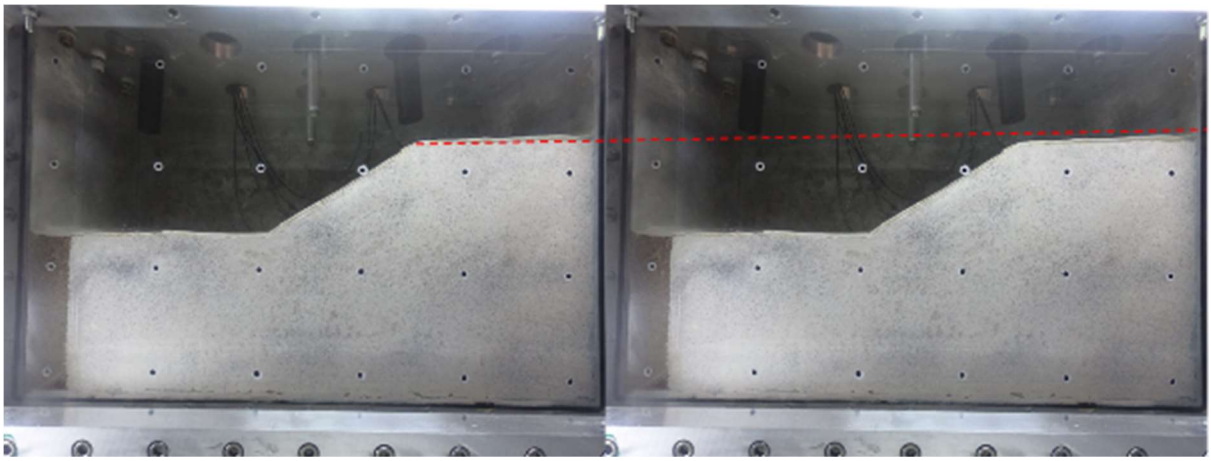


Figure A-43 Visualisation of settlement magnitude during the consolidation phase of the M-T6r Test.

A.4.3 Seasonal cycle effect for M-T6r test.

Slope movement at the end of first winter / M-T6r.

At the end of the first winter cycle in the M-T6r test (Figure A-44), PIV analysis shows minor deformations due to rainfall and drying cycles, but overall slope stability remained intact. Vectorial displacements were small and uniform, indicating no significant mass movement. Resultant displacement contours showed minimal surface movement, suggesting that seasonal

moisture variations had little impact. Shear strain remained low (<1%), with slight increases near the toe due to water infiltration and increased pore pressure, but no shear failure. Volumetric strain indicated minor compression (0.2%) in the lower slope due to drainage, and slight swelling (-0.5%) at the crest, likely from infiltration effects.

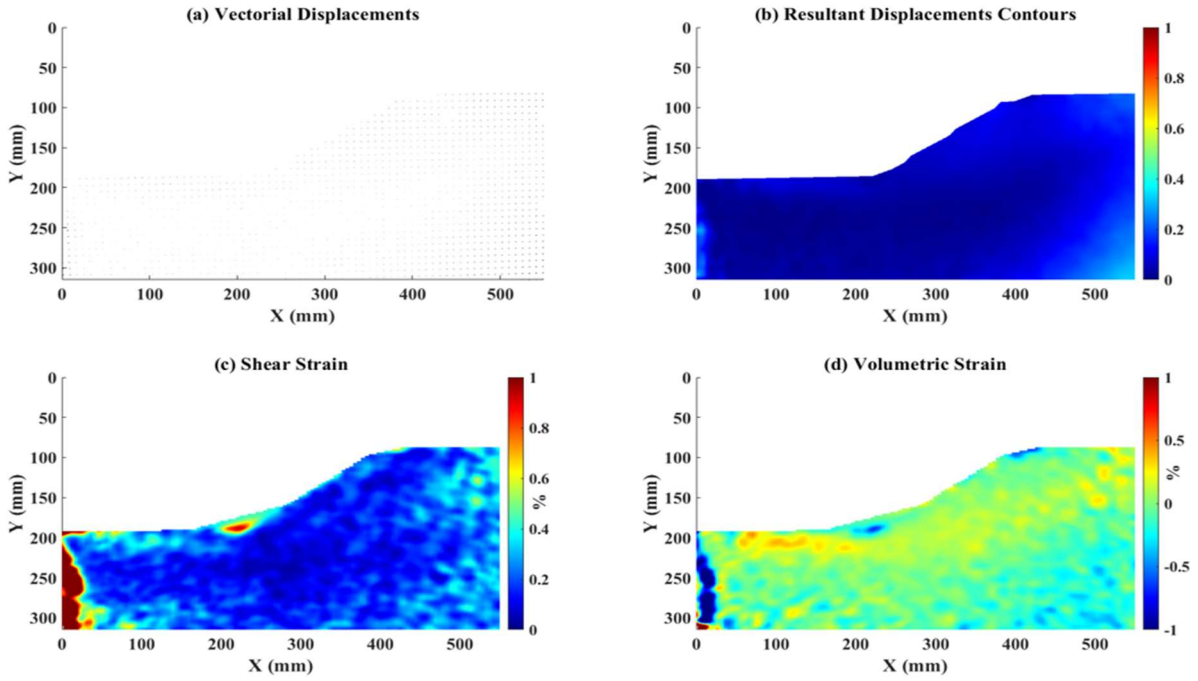


Figure A-44 PIV analysis at the end of the first winter cycle for the M-T6r test.

Pore water pressure analysis at the end of first winter.

The pore water pressure (PWP) distribution at the end of winter 1 for the M-T6r test indicates relatively low-pressure values over the slope. The largest pressures are localised towards the lower and mid-slope regions, as seen in Figure A-45, and range from 5 kPa to 30 kPa. The lower values towards the crest of the slope, nearing -1 kPa, suggest that the phreatic surface (u=0) is still quite low and no longer parallel to the slope so there is still suction near the crest and upper slope.

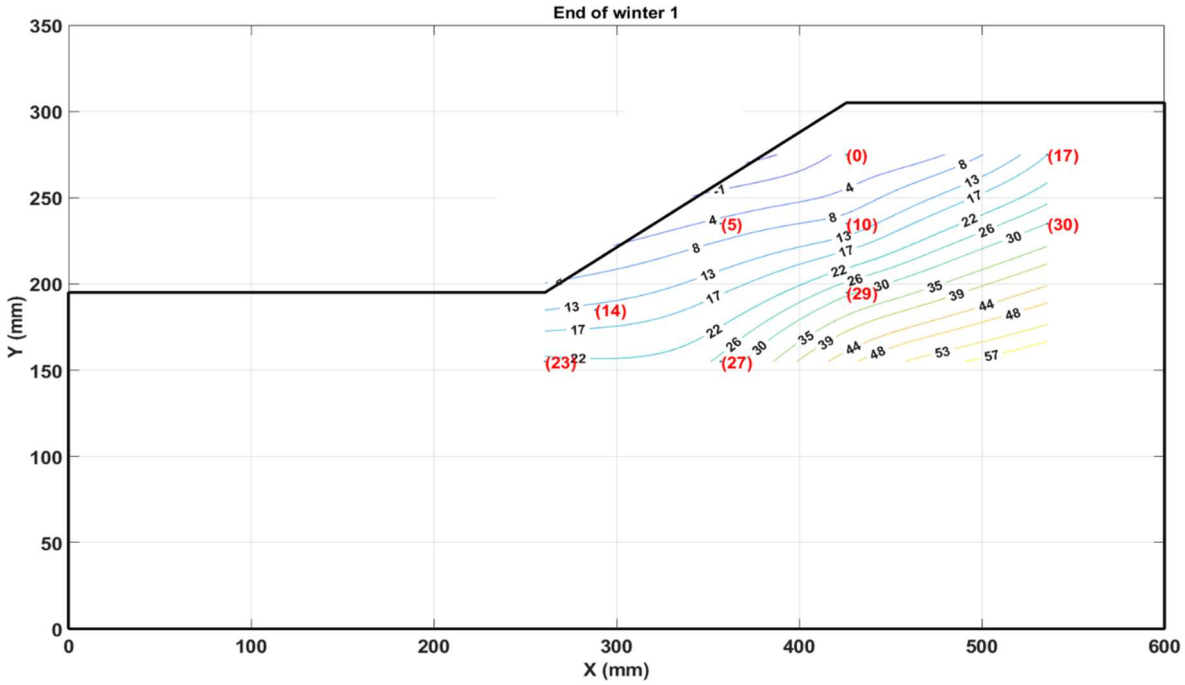


Figure A-45 Pore water pressure distribution at the end of winter 1 in the M-T6r slope test.

Slope movement at the end of first summer / M-T6r.

At the end of the first summer in the M-T6r test (Figure A-46), PIV analysis indicates localised displacements near the upper slope and crest, primarily due to drying and desiccation effects. Despite calibration issues affecting some displacement data, strain values remain reliable. Vectorial displacements show downward movement concentrated in the upper slope. Resultant displacement contours suggest moderate but stable deformation. Shear strain remains low (<2%), mainly near the crest, likely due to soil readjustment following moisture loss. Volumetric strain indicates minor compression (+1%) near the lower slope and toe, with slight expansion (-1%) elsewhere, reflecting adjustments due to summer drying. The slope remains stable, with no significant failure detected.

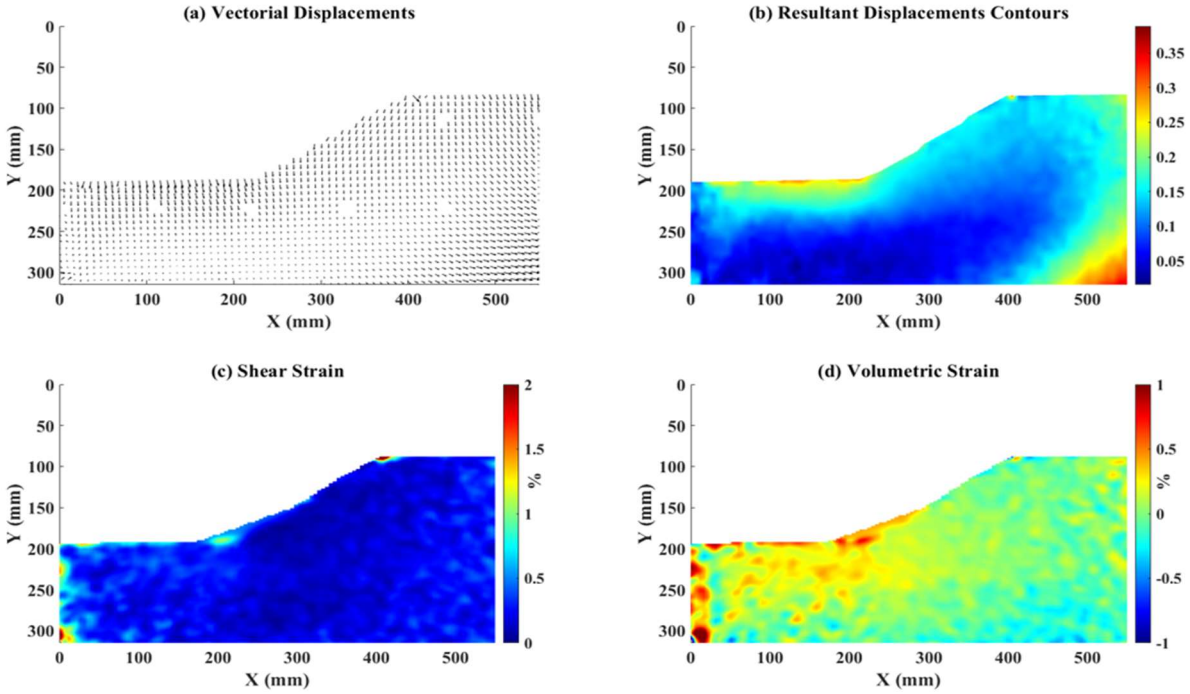


Figure A-46 PIV analysis at the end of the first summer cycle for the M-T6r test.

Pore water pressure analysis at the end of first summer/M-T6r

At the end of the first summer in the M-T6r test (Figure A-47), pore water pressure (PWP) distribution shows a clear moisture gradient along the slope. Near the crest, PWP is low or negative (-4 to 2 kPa), indicating drying due to evaporation. Mid-slope regions show moderate PWP (11–20 kPa), suggesting partial moisture retention or capillary effects. The highest PWP (~50 kPa) is at the lower slope, reflecting water accumulation and slower drainage in this area.

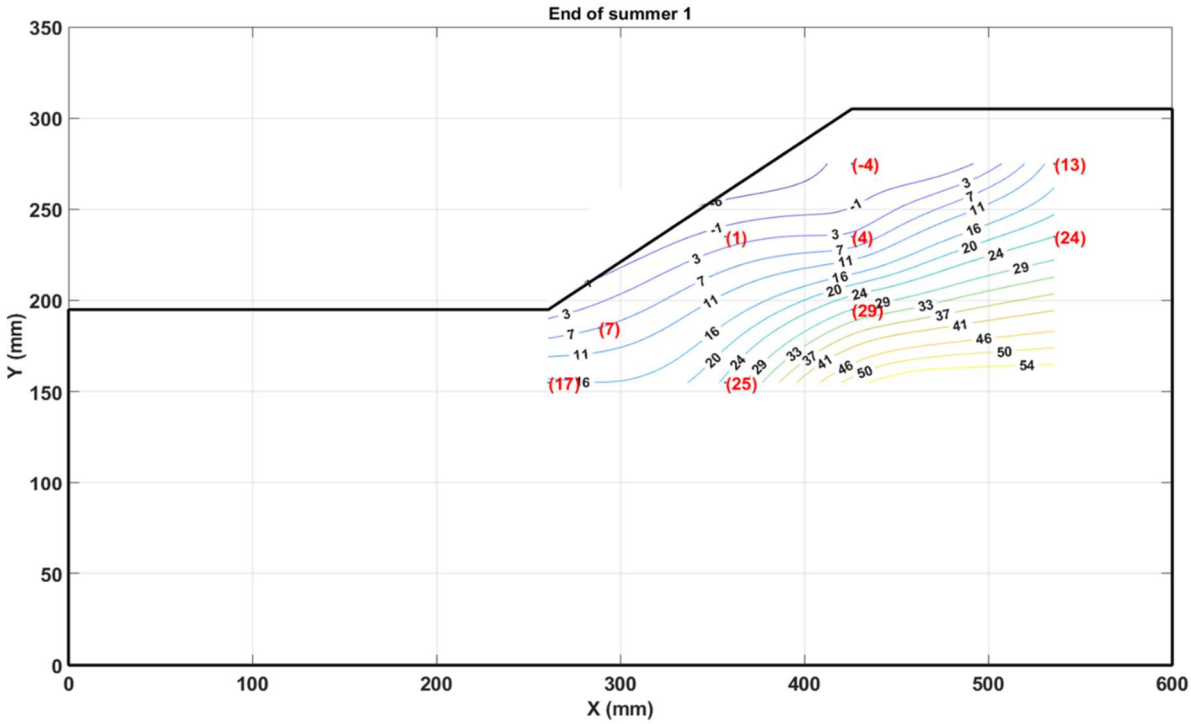


Figure A-47 Pore water pressure distribution at the end of summer 1 in the M-T6r slope test.

Slope movement at the end of second summer / M-T6r.

At the end of the second summer in the M-T6r test (Figure A-48), PIV analysis confirms that the slope remained highly stable, with minimal movement or internal strain. Vectorial displacements indicate no significant soil movement, while resultant displacement contours show uniform stability across the slope. Shear strain is extremely low, with only minor localized areas of strain, and volumetric strain remains negligible, indicating that the dry period did not induce notable deformation.

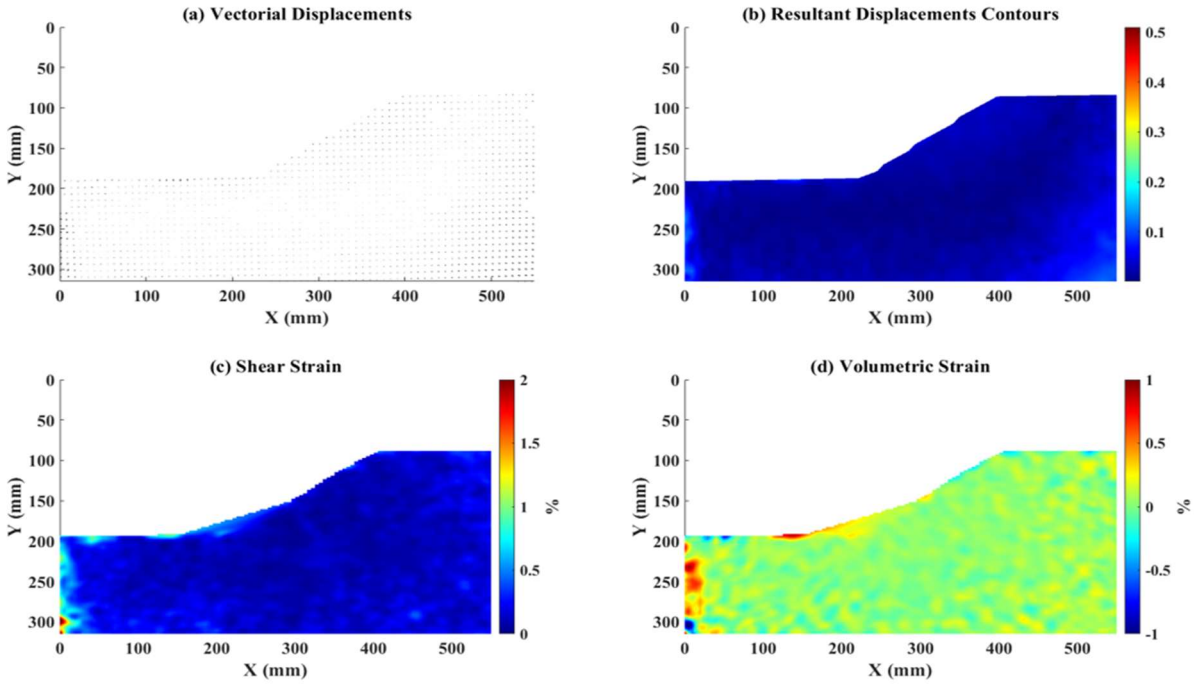


Figure A-48 PIV analysis at the end of the second summer cycle for the M-T6r test.

Pore water pressure analysis at the end of second summer / M-T6r.

The pore water pressure distribution at the end of summer 2, shown in Figure A-49, indicates a significant reduction in pore water pressure across the slope. The pressure measurements vary from slightly negative (-4 kPa) at the crest to around 56 kPa near the lower slope and 18 kPa at the toe. The negative pore water pressures near the upper part of the slope and crest suggest the drying effect during the summer period, where no rainfall was applied, causing the soil to desaturate and develop further suction. This correlates well to the PIV results which show virtually no strains developing.

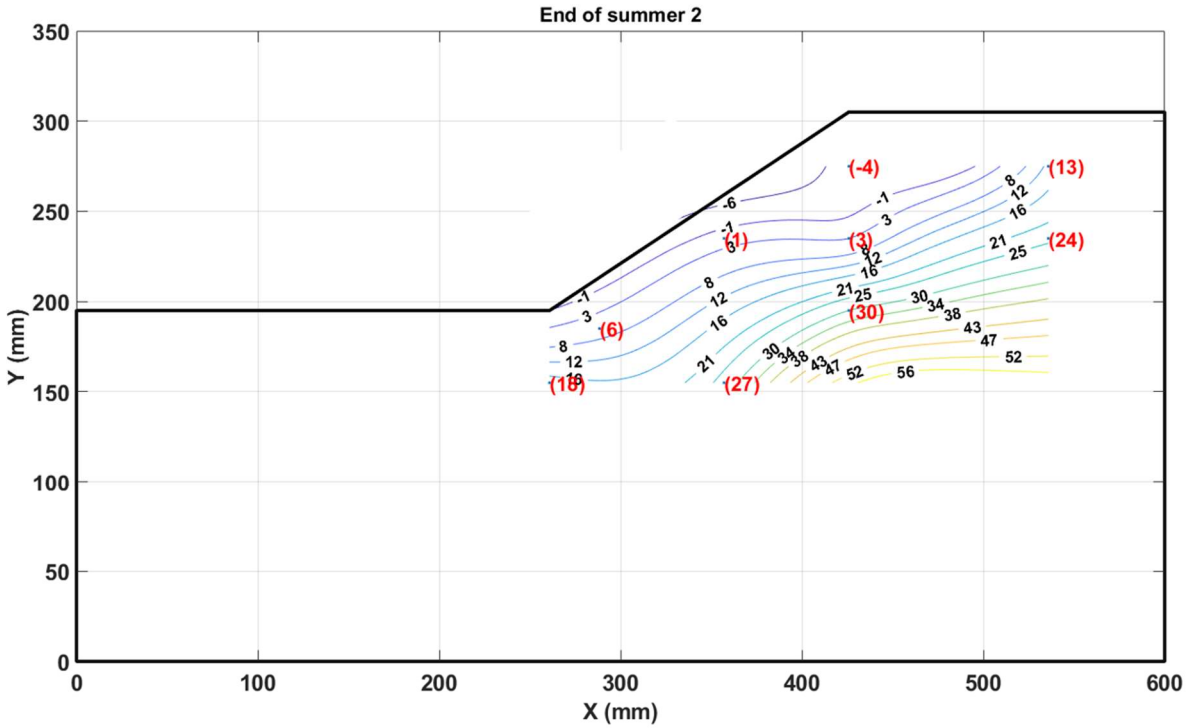


Figure A-49 Pore water pressure distribution at the end of summer 2 in the M-T6r slope test.

Second consolidation - Slope movement / M-T6r.

At the end of the second consolidation phase in the M-T6r test, the PIV results indicate minor slope movement primarily due to recompression after previous swelling at 1g. Figure A-50 shows that vectorial displacements are concentrated near the crest, while resultant displacement contours reach up to 0.5 mm in the upper slope. Shear strain remains low overall, with localized bands near the crest and mid-slope. Volumetric strain reveals compression below the toe, consistent with drainage and reconsolidation, while the rest of the slope shows minimal volume change.

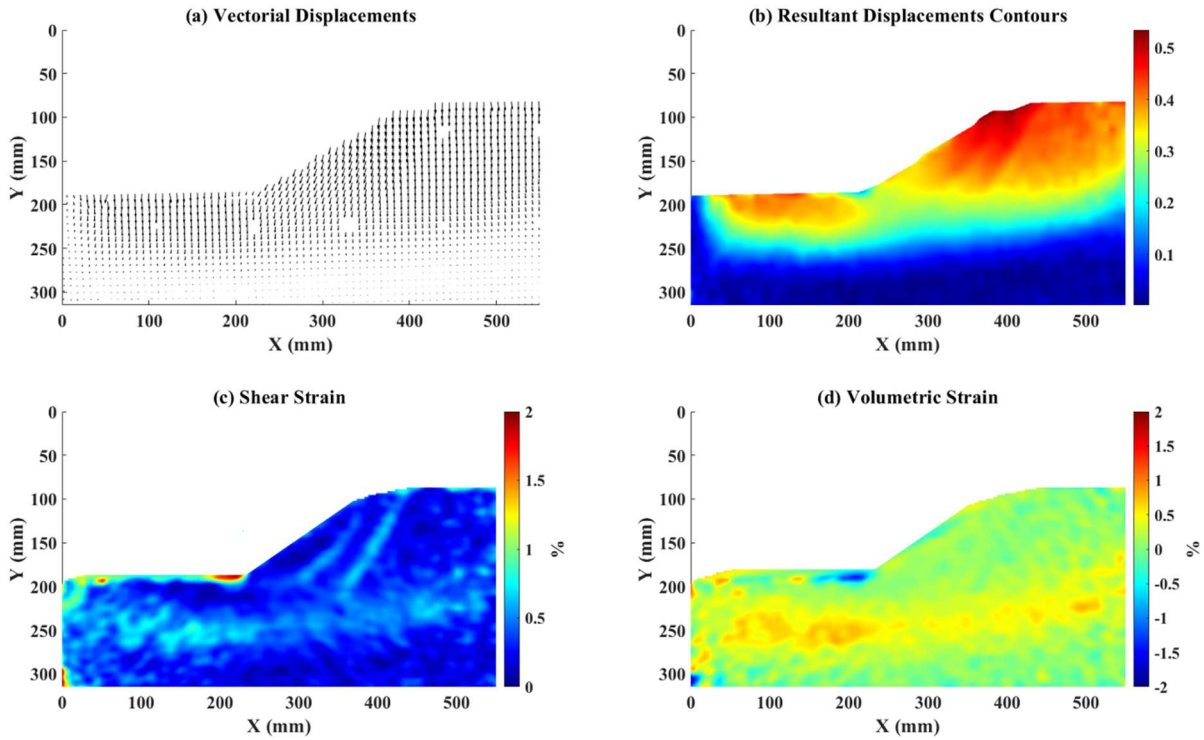


Figure A-50 PIV analysis at the end of the second consolidation for the M-T6r test.

Pore water pressure analysis at the end of second consolidation / M-T6r.

Key observations from Figure A-50are that the pore water pressure at the crest of the slope is negative, indicating suction effects. The values range from approximately (-9 kPa) to (-2 kPa). This suggests that the crest is experiencing the most drying, likely due to the absence of rainfall during the period at 1g and reconsolidation. The rest of the slope shows an increase in PWP with depth, as expected, with the phreatic line (u=0) possibly appearing around the toe. This is typical of long term slope conditions.

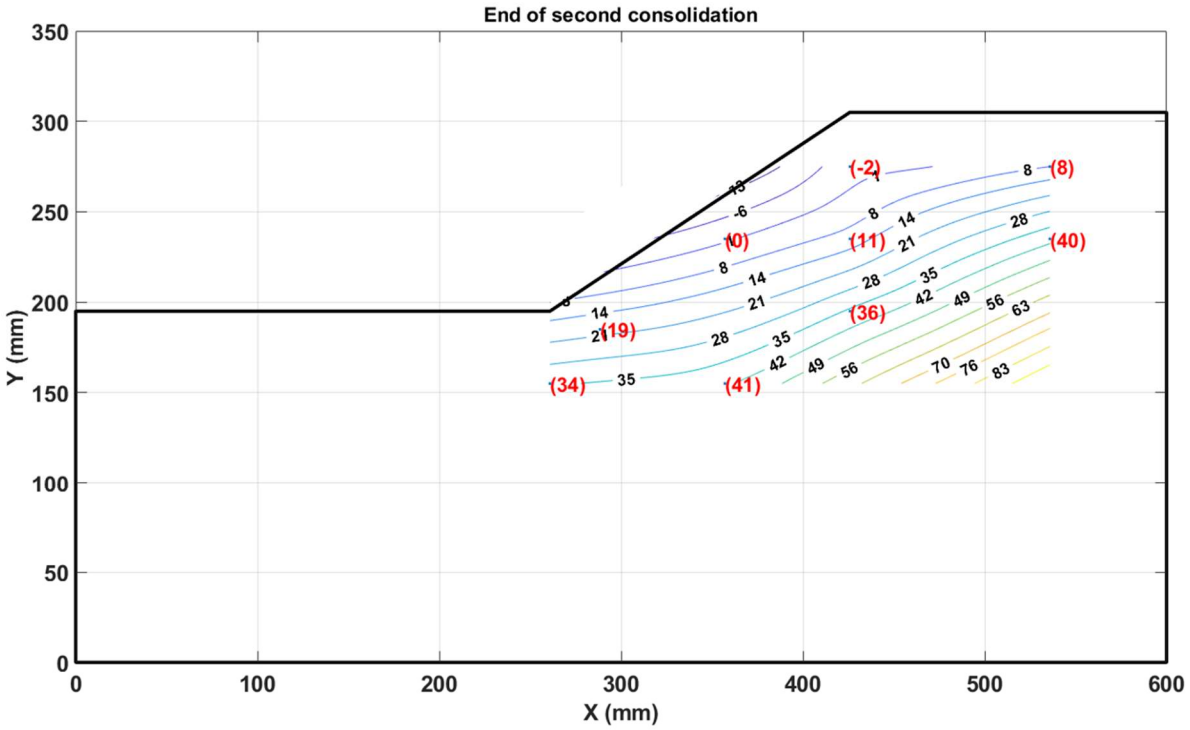


Figure A-51 Pore water pressure distribution at the end of summer 3 in the M-T6r slope test.

A.4.4 Flooding and the drawdown effect for M-T6r.

Slope movement at the end of the first flood / M-T6r.

At the end of the first flood in the M-T6r test, the slope remained largely stable, with minor displacements primarily near the crest due to water infiltration, as shown in Figure A-52. Compression was observed at the lower slope, which was fully submerged (Figure A-53), while shear strain remained minimal across the slope. Volumetric strain indicated slight compression near the toe and expansion near the crest, reflecting localised soil response to flooding without significant deformation.

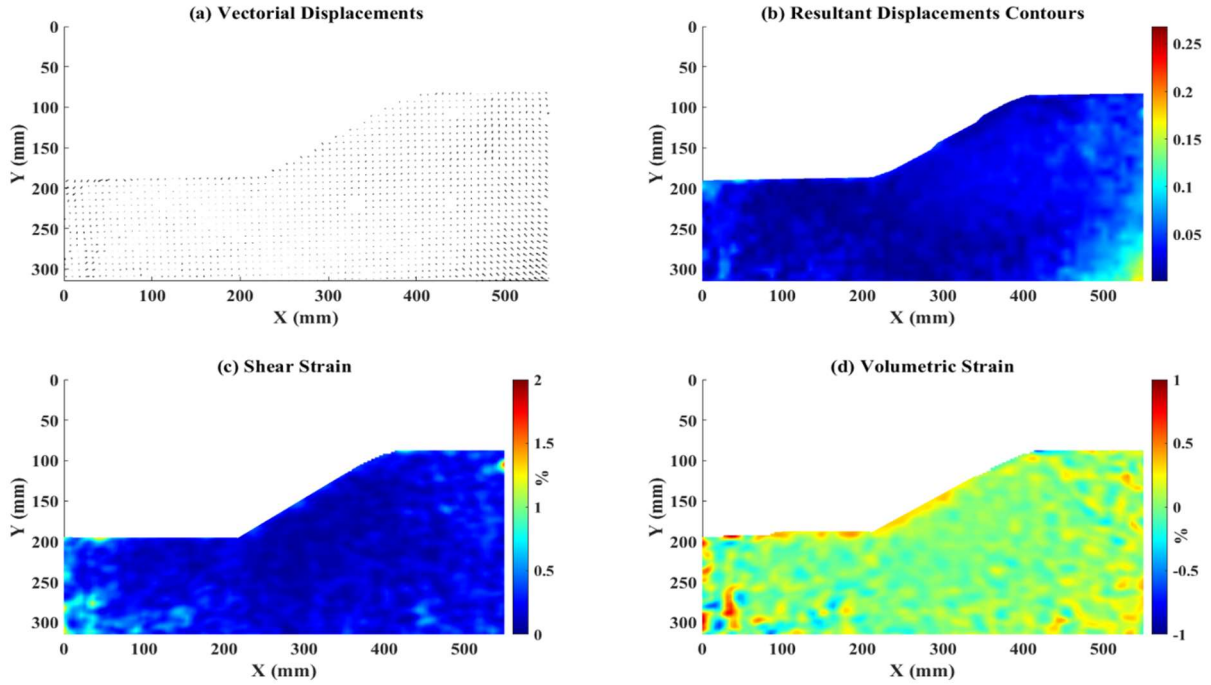


Figure A-52 PIV analysis at the end of the first flood for the M-T6r test.

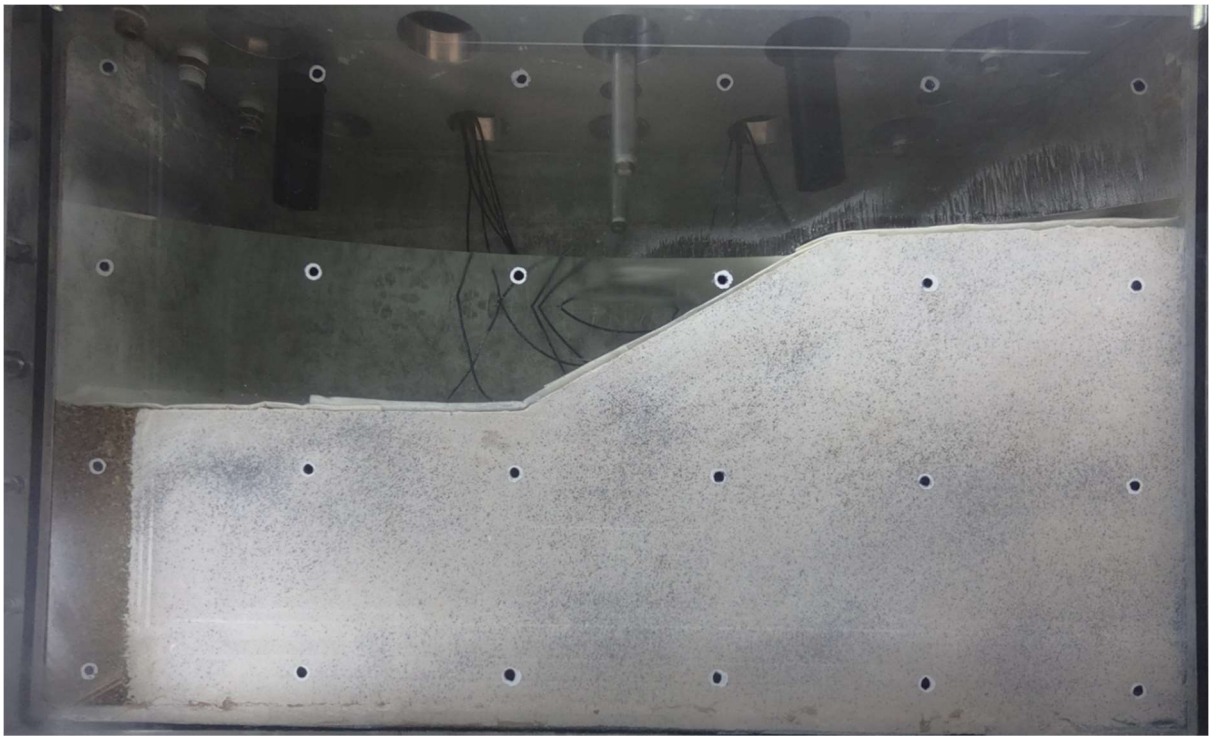


Figure A-53 First flooding event for the M-T6r Test.

Pore water pressure distribution at the end of first flood event / M-T6r.

During the flood phase, pore water pressure (PWP) varied significantly across the slope, as shown in Figure A-54. Low PWP values (3–9 kPa) were observed near the crest, reflecting limited flood reach. The mid-slope exhibited moderate PWP (20–33 kPa), with curved near-hydrostatic contours influenced by the centrifuge g-field. The highest PWP (59–89 kPa) occurred at the toe and lower slope, indicating substantial water accumulation in these regions.

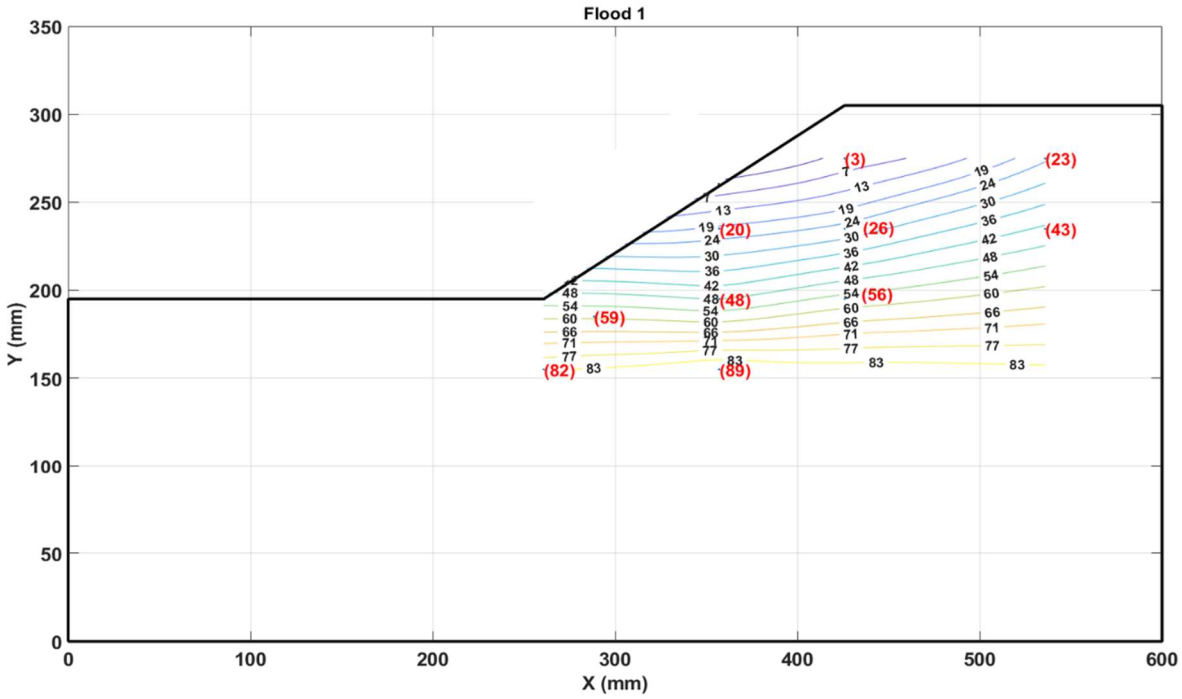


Figure A-54 Pore water pressure distribution at the end of flood 1 in the M-T6e slope test.

Soil deformation at the end of the second flood/M-T6r.

The PIV analysis for Flood 2 in the M-T6r test (Figure A-55 and Figure A-57) shows that the slope remained stable, with no significant displacement, strain, or deformation observed. The vectorial displacements and resultant displacement contours confirm minimal movement, while both shear strain and volumetric strain plots indicate negligible internal deformation, aside from edge calibration artifacts. This suggests that Flood 2 did not compromise slope integrity during this stage.

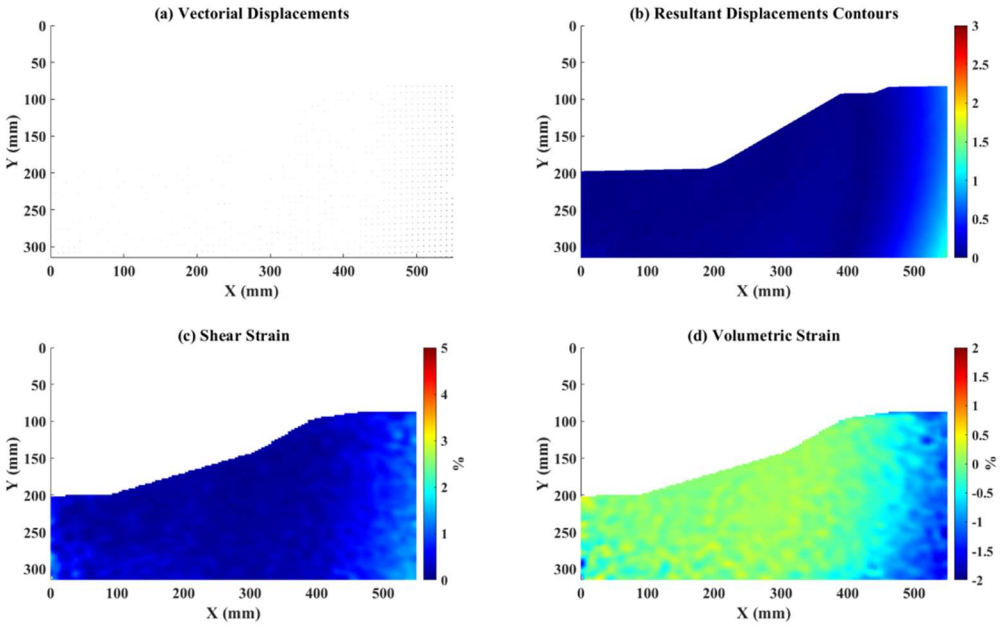


Figure A-55 PIV analysis at the end of the second flood for the M-T6r test.

Pore water pressure distribution at the end of second flood event / M-T6r.

The pore water pressure distribution at the end of Flood 2 reveals that the flood caused a notable increase in pore pressures, as shown in Figure A-56. The contours are typical of a hydrostatic distribution under a centrifugal g-field (i.e. the contours are slightly curved). Despite the full flood, the slope is clearly stable under the hydrostatic pressure – as seen in the strain data.

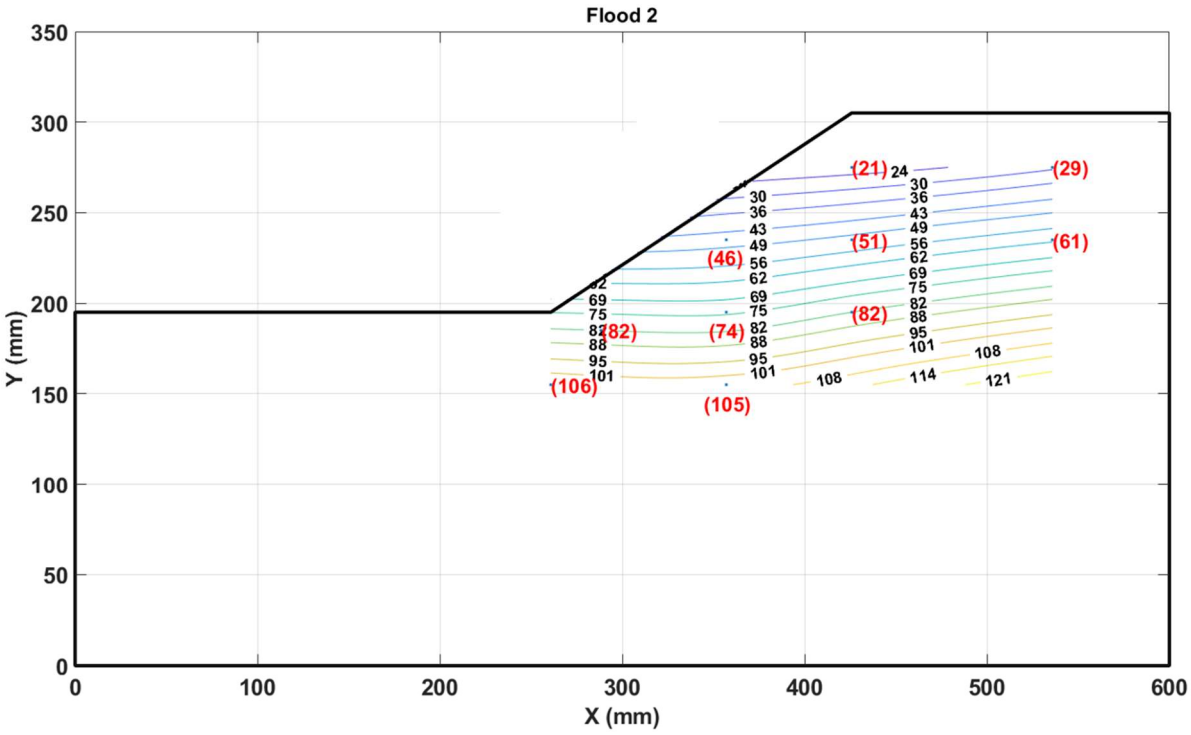


Figure A-56 Pore water pressure distribution at the end of the second flood in the M-T6e test.

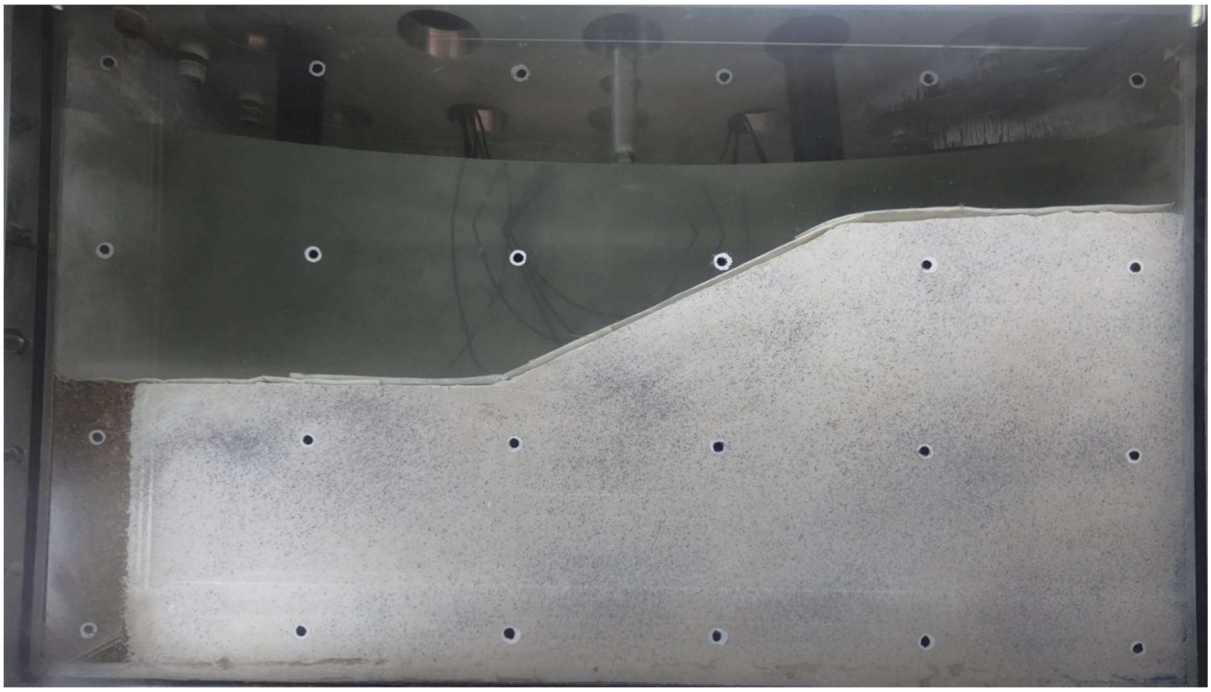


Figure A-57 Flooded slope model at the end of the second flood event (M-T6r Test).

Soil deformation at the end of the third flood/M-T6r.

At the end of the third flood in the M-T6r test, the PIV results (Figure A-58) show no significant soil deformation, though vectorial and displacement data appear compromised due to calibration issues. Despite this, both shear and volumetric strain plots remain consistent with previous floods, showing minimal internal deformation and suggesting the slope remained stable during this flooding phase.

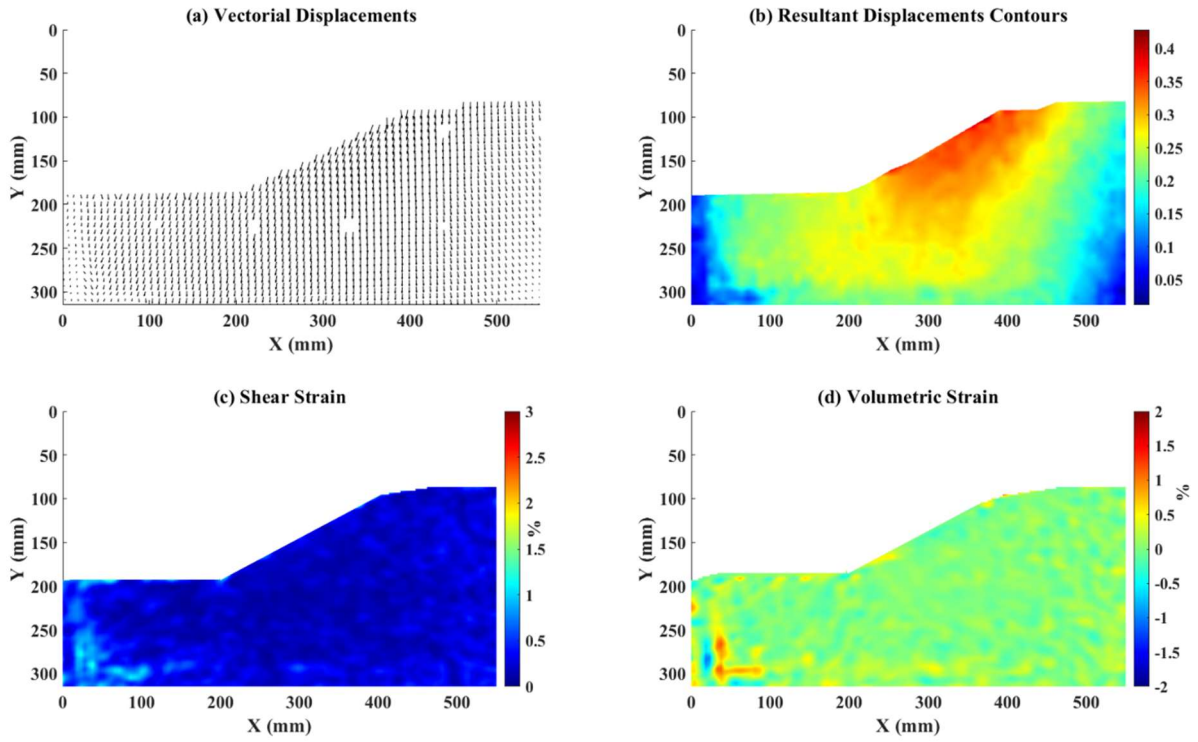


Figure A-58 PIV analysis at the end of the third flood for the M-T6r test.

Pore water pressure distribution at the end of third flood event / M-T6r.

From Figure A-59, which shows the pore water pressure distribution at the end of Flood 3 for the M-T6r test, it can be seen that the flood caused a notable increase in pore pressures. The contours are typical of a hydrostatic distribution under a centrifugal g-field (i.e. the contours are slightly curved). The slope remains relatively stable overall, with minimal strain or movement observed throughout despite high water pressures.

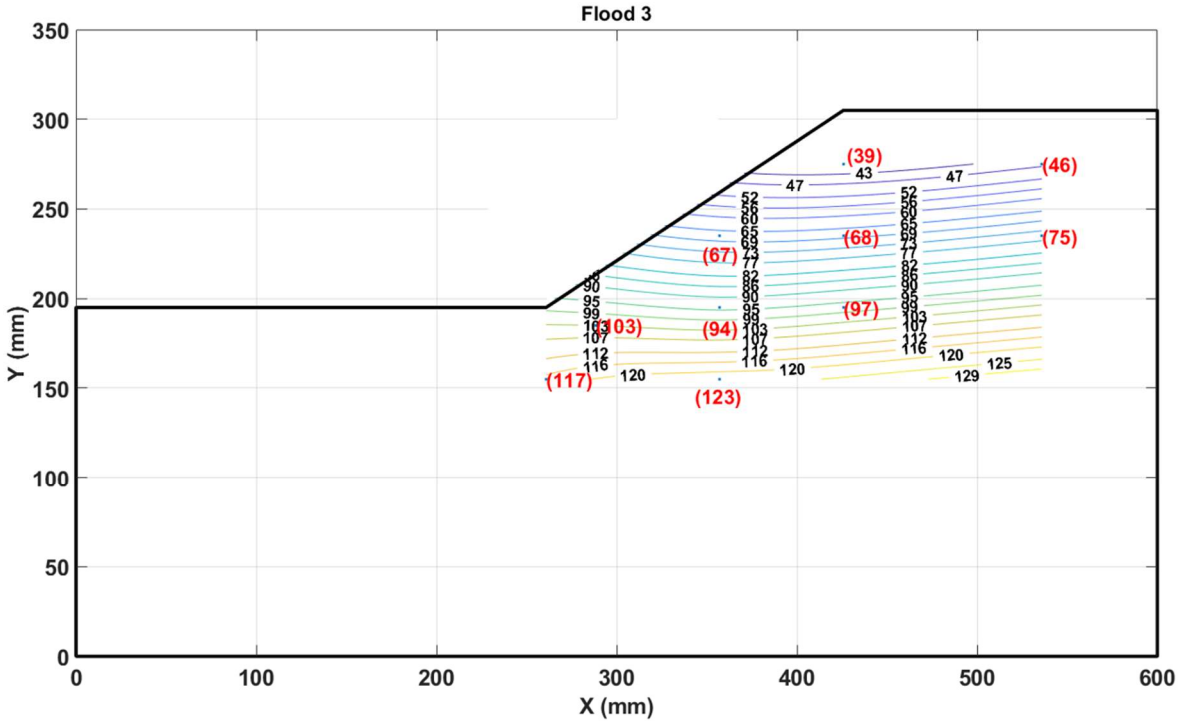


Figure A-59 Pore water pressure distribution at the end of the third flood in the M-T6r test.

Soil deformation at the end of the fourth flood /M-T6r.

At the end of the fourth flood in the M-T6r test, the PIV results (Figure A-60) indicate localised deformation near the crest, while the rest of the slope remains stable. Vectorial displacements show minimal movement except at the surface, possibly due to erosion. Displacement contours highlight movement up to 0.6 mm near the upper slope. Shear strain is concentrated near the crest (up to 6–7%), suggesting localised weakening from water infiltration. Volumetric strain is also limited to small compression near the crest, with negligible changes across the rest of the slope.

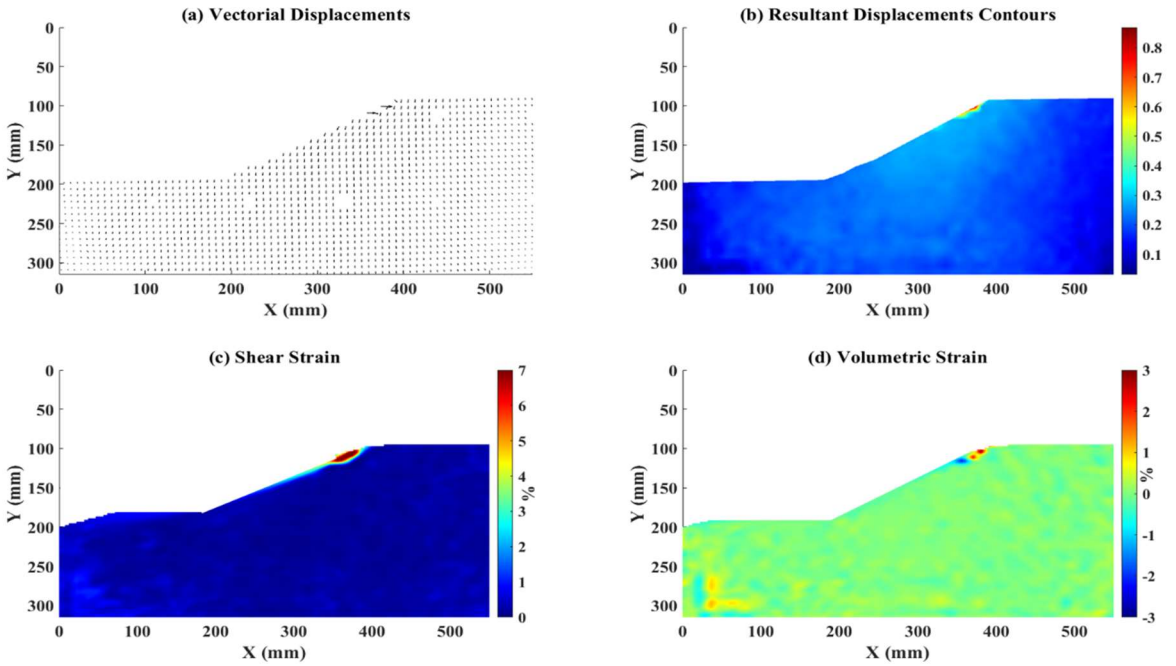


Figure A-60 PIV analysis at the end of the fourth flood for the M-T6r test.

Pore water pressure distribution at the end of fourth flood event / M-T6r.

The pore water pressure (PWP) distribution at the end of Flood 4 for the M-T6r test, as shown Figure A-61 in This flood was used to adjust the offsets to the expected distribution under the flood scenario, so it is reflective of the idealized hydrostatic case in the centrifuge g-field.

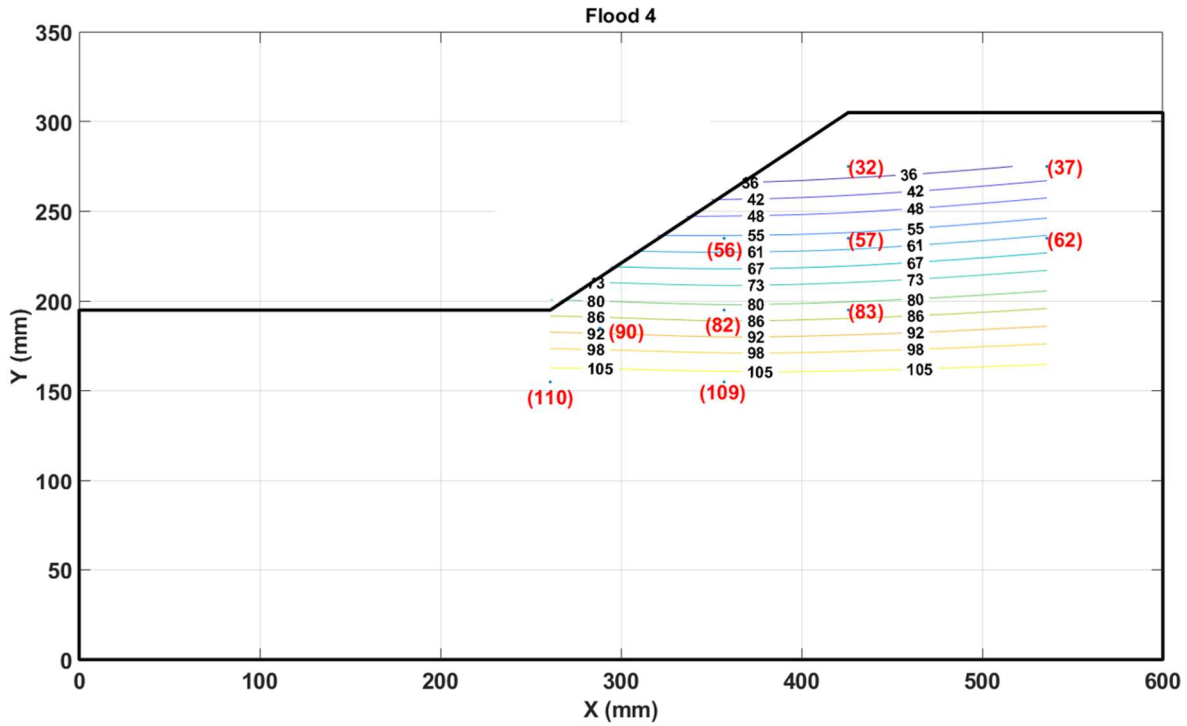


Figure A-61 Pore water pressure distribution at the end of the fourth flood in the M-T6r test.

A.5 Methodology for model M-T1 Test.

Introduction

The preliminary test M-T1 focused on the stability of slopes made from compacted kaolin with a primary objective of the M-T1 test to investigate the mechanical properties and failure mechanisms of the slope when subjected to high gravitational forces. The insights from this test were intended to:

- Evaluate the effectiveness of compacting the soil rather than consolidating to produce appropriate soil fabric to simulate constructed slopes.
- Assess the impact of water content on slope stability.
- Evaluate the function of the experimental rainfall nozzles and the impact of the centrifuge Coriolis effect.
- Establish baseline data for further comparative analysis in subsequent tests.

The M-T1 Preliminary Test was designed as an exploratory step in this research program, involving 100% kaolin slope model. The experiment utilised a scaled model approach, in which a kaolin slope was constructed to simulate a 3 m prototype in simulated situations. The kaolin slope had a height of 120 mm and a slope angle of 26°. The model was constructed within a centrifuge box, where the kaolin mixture was manually compacted into 50 mm using a 2.5 kg hammer. Prior to this, the kaolin was thoroughly mixed to achieve a uniform water content of 40% and left overnight for equalisation. This preparation process was intended to accurately replicate the physical and mechanical characteristics of manmade kaolin slopes as shown in the Figure A-62.



Figure A-62 Compaction procedure for M-T1

After compaction, the clay block was trimmed to achieve the desired slope profile. This was achieved using precisely shaped wood cutting templates in combination with a wire saw to ensure accuracy in shaping. During this process, careful attention was given to maintaining the slope's design integrity. To ensure uniform moisture content throughout the placed clay layers, the trimmings from the removed soil were examined. This step was critical in confirming the consistency of the clay. The model, after trimming, is shown in Figure A-63, which illustrates the slope profile.

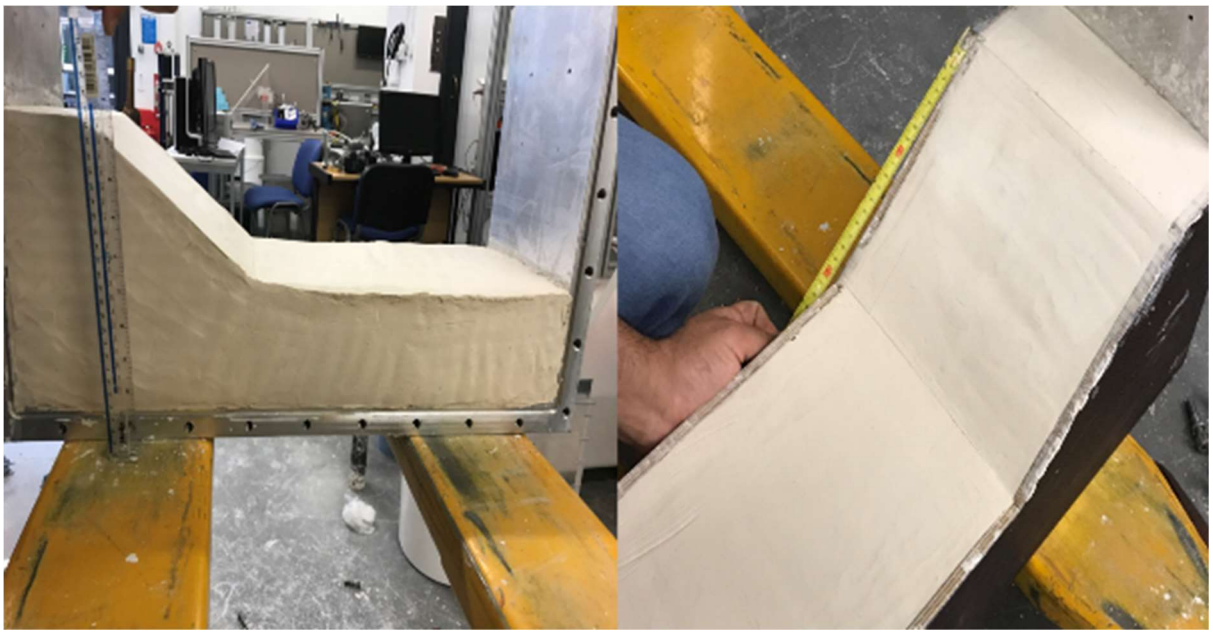


Figure A-63 Slope construction using wood template.

A validation test case was established using a plane strain model to examine the effects of rainfall. The configuration of this model facilitated the observation and analysis of the slope's profile by means of a transparent Perspex viewing window. To facilitate Digital Image Correlation (DIC) analysis, black seeds were uniformly distributed on the front surface of the kaolin slope model, as illustrated in Figure A-64. These seeds act as reference markers for tracking soil movement and deformation during testing. Their application ensures clear contrast and enables precise Particle Image Velocimetry (PIV) analysis, allowing for accurate displacement measurements. Additionally, the Perspex window was securely fixed onto the strongbox to provide an unobstructed view of internal deformations during the test.



Figure A-64 Setup of the M-T1 kaolin slope model in the Centrifuge Box and black seeds application.

Figure A-65 illustrates the final configuration for the M-T1 Preliminary Test, including the installation of a rainfall simulator using a single nozzle focused on the slope. The slope angle is clearly marked, and the PIV targets were positioned at a separation distance of 50 mm in order to monitor and subsequently analyse soil displacement and deformation. The nozzle is also indicated in the figure, which serves a critical function in controlling the water content and simulating rainfall or seepage conditions on the slope.

Due to the increased self-weight stresses caused by elevated gravity, an initial spin-up period of 30 minutes at 25g was allowed for the slope to settle. This ensured that any slope movement resulting from the imposed gravity occurred before the commencement of the rainfall stage. Furthermore, this also facilitated the establishment of equilibrium in internal pore water pressures, although it should be noted that these pressures were not monitored. After that, continuous rainfall was applied to induce slope movement initiation. After reaching initial equilibrium, the nozzle pressure was adjusted to 400 kPa to achieve a flow rate of 8.05×10^{-7} m^3/s for a duration of 20 minutes. This applied rainfall volume corresponds to an annual rainfall intensity of 2800 mm in the prototype, reflecting extreme rainfall scenarios forecasted in the United Kingdom.

Error! Reference source not found. Rainfall intensity in the prototype= 2800 mm/year.

Flow rate in the model = 8.05×10^{-7} m^3/s. Obtained from nozzle calibration.

Time duration in model scale 20 minutes which can be converted to second.

t = 20×60 = 1200 seconds

Total volume of water (V) that falls on the slope in the model scale can be calculated by multiplying the flow rate by time:

Total volume (V)= $8.05\times10^{-7}\times1200 = 9.66\times10^{-4}$ m^3.

Area in the model = 0.12 m^2.

To get The rainfall depth, divide the total volume by the area:

Rainfall depth = V/Area = 9.66×10^{-4} m^3 / 0.12 m^2 = 8.05×10^{-3} m = 8.05 mm.

The rainfall intensity in the model scale is 8.05 mm for 20 minutes. To express this as intensity per hour:

Rainfall intensity = (8.05mm/20min) × 60min/hour = 24.15 mm/hour.

Thus, the rainfall intensity in model scale is 24.15 mm/hour.

Centrifuge scaling factor (N) =70.

If the rainfall intensity in the prototype scale is 2800 mm/year, and the centrifuge g-level is 70g, then the rainfall intensity in the model scale can be calculated as below:

I_{model} = 2800mm/year ×70 = 196000 mm/year

To convert this to mm/hour:

I_{model} = 196000/8760 =22.37 mm/hour.

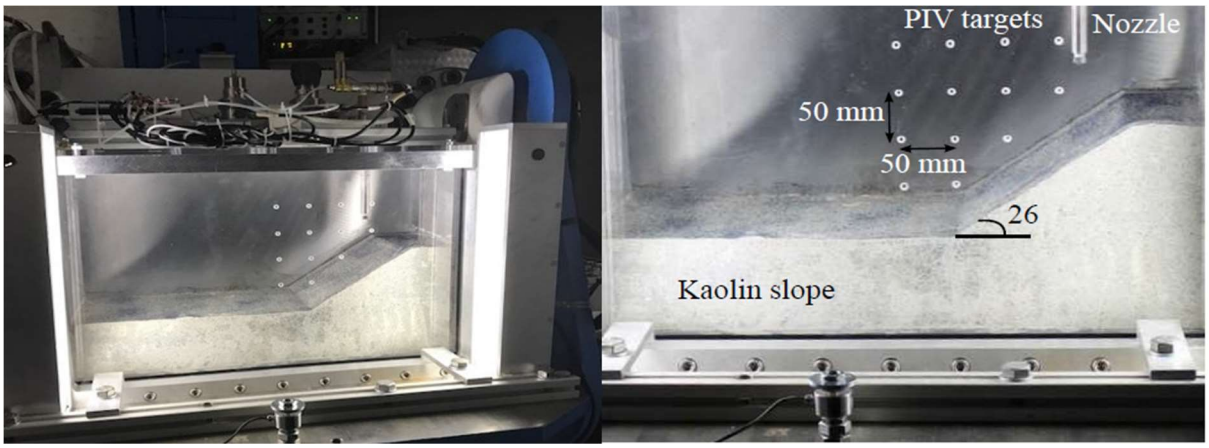


Figure A-65 Final adjustment and setup with rainfall simulator for M-T1test.

A.6 Methodology for model M-T2 test.

The following section provides an overview of the methodology used to generate slope models within the centrifuge strong box through the application of a compaction process. The experiment involves the use of a soil mix which includes 65% sand and 35% kaolin, mixed at the moisture content that has been determined to be optimal through previous compaction tests.

Soil Preparation

For the M-T2 test, a dry mixture of sand and kaolin was prepared and mixed with water to achieve the optimum moisture content of 12.3%. To ensure uniform moisture distribution throughout the mixture, the soil was placed into sealed containers and left undisturbed for over 24 hours. This step was crucial for equalizing the moisture content within the soil, ensuring consistent compaction and accurate simulation of field conditions.

Compaction Procedure

The prepared soil was then layered and compacted inside the centrifuge strong box. The compaction process involved placing the soil in 10 layers, each with a thickness of 30 mm, until the final height of the model reached 300 mm. Additionally, a base layer consisting of 100% compacted kaolin with a thickness of 50 mm (model scale) was placed under the slope to provide a stable foundation. This method of compaction is depicted in Figure A-66.

The slope angle was shaped to 26° using side-cutting templates and a wire saw to match the specified design parameters. This comprehensive preparation and compaction process for the M-T2 test provided valuable insights into experimental preparation, contributing to the development of the following tests.

Figure A-66 (a) shows the initial construction phase of the sandy kaolin slope model within the centrifuge strong box. The slope is being shaped and secured using side cutting templates to achieve the desired 26° angle. The visible compaction layers suggest a well-compacted. While specific density measurements were not recorded for this test, the compaction process was conducted systematically using layered deposition and tamping to ensure uniformity. Figure A-66 (b) illustrates the fully prepared and compacted sandy kaolin slope model, wrapped and equipped with pore pressure sensors for monitoring. Eight pore water pressure sensors were embedded within the model which were designed to capture pore pressure response. Unfortunately, however, due to issues with their saturation, the data cannot be relied upon, and they are not reported here.



(a) (b)

Figure A-66 (a) Initial construction phase and (b) Slope shaped and PPTs installation.

Final Adjustments and Loading on the Centrifuge Platform.

After constructing the slope model, filter paper sheets were placed over the soil surface to minimize erosion caused by simulated rainfall at 70g. Once these preparations were completed, the strong box containing the model and the rainfall simulator lid was weighed. This setup was then carefully mounted onto the centrifuge platform. The centrifuge counterweight was adjusted to match the total weight of the apparatus, ensuring balance during operation. All sensors were connected to a junction box, and their functionality was thoroughly tested using LabVIEW software. The precipitation distribution system was linked to the water supply through a 10 mm conduit that extended from the slip rings, allowing for controlled water flow during the test. For the M-T2 test, 10 nozzles were used to distribute rainfall, with a rainfall intensity of 2800 mm/year in the prototype scale. Figure A-67 depicts the final adjustments and setup of the slope model on the centrifuge beam, illustrating the essential connections required for the experiment.

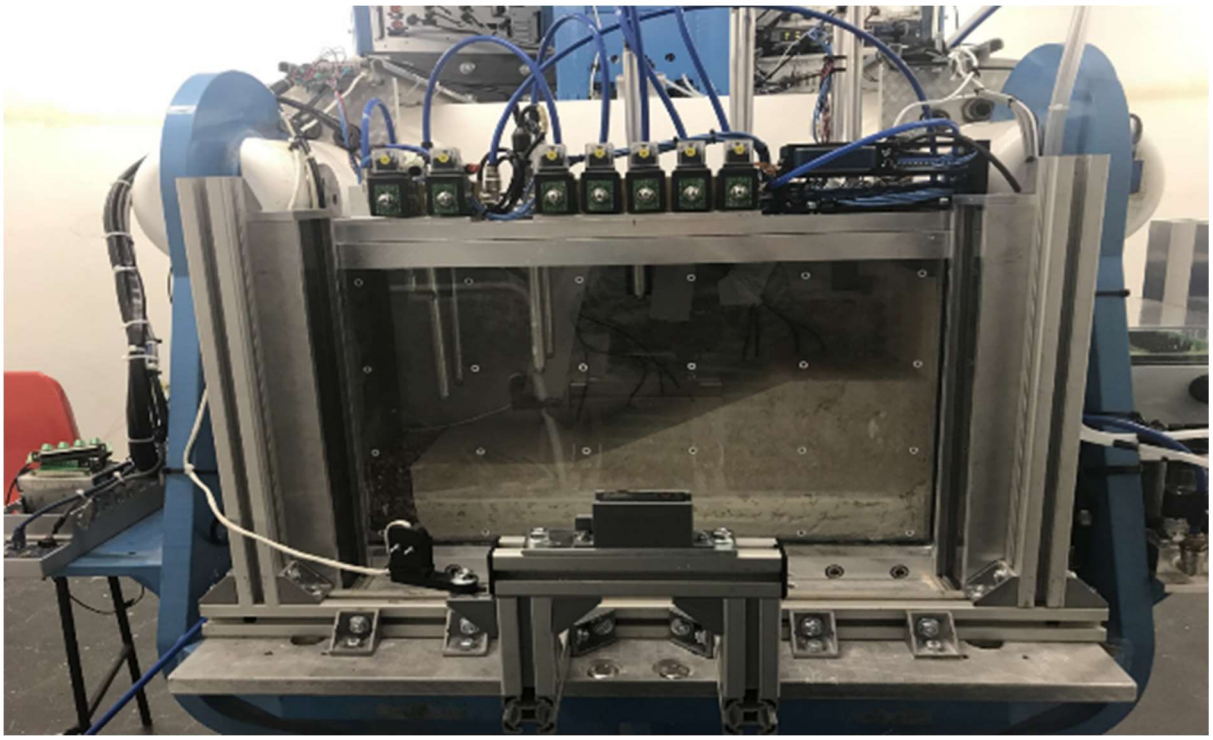


Figure A-67 The setup of centrifuge model and rainfall simulator for M-T2.

A.6.1 Testing procedure for M-T2

In the M-T2 test, the experimental protocol began by systematically increasing the centrifuge acceleration, initially reaching 50 g during an auto-balance phase that lasted approximately 25 minutes. Following this, the acceleration was elevated to the target level of 70 g. This consolidation phase lasted for 40 minutes, equivalent to 136 days at the prototype scale, allowing the system to achieve equilibrium. Unlike the later tests, the M-T2 test involved a distinct approach following the consolidation stage. After the initial stabilisation, the model was subjected to heavy and continuous rainfall. This phase did not follow the cyclic patterns of rainfall and dry periods seen in other scenarios. Instead, it maintained a relentless precipitation rate to examine its effects on slope stability and deformation under persistent wet conditions. The test was repeated twice to guarantee the accuracy and reproducibility of the reported effects, enabling an extensive investigation of the impact of continuous heavy rainfall on the beginning of slope failure.

Publications

5th ECPMG Delft · 2024

Proceedings of the 5th ECPMG 2024
5th European Conference on Physical Modelling in Geotechnics26/11/202412:24 PM
2-4 October 2024, Delft, the Netherlands
© 2024 the Authors

Centrifuge modelling of post failure behaviour of a compacted sandy clay slope induced by rainfall and flood

M.A. Alfergani, E.T. Bowman, T.A. Gaspar, T.A. Elmrom,
University of Sheffield, Sheffield, UK, malfergani1@sheffield.ac.uk, e.bowman@sheffield.ac.uk, t.a.gaspar@sheffield.ac.uk, telmrom@sheffield.ac.uk

ABSTRACT: Slope instability of engineered earthworks induced by rainfall can cause considerable damage to infrastructure, economic cost and loss of life. A small-scale physical model test was conducted using the 50gT beam centrifuge at the University of Sheffield in order to investigate the triggering and post-failure mechanisms of slope failure due to rainfall and flood events. The slope model was prepared from a sand-kaolin soil fill, compacted at optimum water content. Close range photogrammetric techniques were used to monitor slope movements and the volumetric changes of the ground during the cycles of wetting and drying as well as the changes in pore water pressure. This paper outlines the post-failure deformation of the slope and shows that movement thereafter can occur spontaneously during heavy rain, suggesting that the slope is in a metastable condition.

Keywords: Slope, Centrifuge, Post failure.

1 INTRODUCTION

Flood embankments, also known as levees or dykes, are a vital part of flood defences in low lying areas and it is therefore important to assess the stability of these structures against rainfall and flooding. The climatic condition, environment, vegetation, geology, and human activities are all considered as potential contributing factors to failure. Long and/or intense rainfall events cause serviceability problems, such as erosion, in earth structures. In addition, it is well known that the performance of earth structures such as clay embankments is influenced by climate, with wetter periods resulting in greater numbers of slope failures. Changing climate conditions affecting the UK are likely to consist of higher average temperatures, wetter winters and drier summers, with uncertain rainfall patterns and more extreme temperatures. It is increasingly evident that the performance of the UK's infrastructure slopes, such as flood embankments and railway embankments is deteriorating. For this reason, increased efforts are required to understand the likely impacts of changing climate conditions in order to establish effective asset management approaches to boost resilience.

While there are considerable efforts to unearth the answers to rainfall/climate induced slope failure in earth embankments via full scale monitoring and instrumentation, this process is protracted and may not yield effective understanding due to the isolation and variability of the test case. Conversely, centrifuge testing is an effective method to simulate movements in geotechnical phenomena and allows for careful control of boundary conditions and for multiple scenarios to be examined. The instability of slopes during rainfall has been linked to a number of parameters, including soil characteristics, rainfall intensity, the location of the initial water table, and slope geometry, according to previous studies on climate-induced slope instability (Kim et al., 2004; Yoshida et al., 1991).

Earthen dam failure is mostly caused by the cycle of rainfall and drought on unsaturated soil. Soil layers near the slope surface, which may be initially unsaturated during dry seasons, have negative pore-water pressure (i.e. matric suction), which contributes to the shear strength of soils and to the stability of soil slopes. During rainy seasons, rainfall infiltration into the soil raises the water content (particularly in cases where there is inadequate or no drainage), which lowers soil suction and thus the shear strength of soil which increases the possibility of slope movement (Fredlund and Rahardjo, 1993)..

Increased rainfall infiltration and more intense precipitation incidents have been found to be significant factors contributing to slope instabilities and gradual deterioration (Ling et al., 2009; Take, 2003). The loss of matric suction in unsaturated soils and the increase in pore water pressure, which in turn causes a decrease in shear strength owing to a decrease in the effective stress, are the main factors causing the collapse of earthen dams. The situation that occurred recently in Libya is a catastrophic example, as Hurricane Daniel caused the collapse of

the Derna dams, which resulted in the deaths of over 10,000 people and caused extremely large damage to infrastructure.

For flood embankments, during the lifetime of the structure, multiple flooding and drying events may occur during which the embankment is expected to remain stable. Given that there are over 35,000 miles of flood embankment in the UK (Dyer, 2004), inspection of each section may not be done regularly. As a result, hidden failures may occur which are not evident at the surface. This paper evaluates the failure patterns of a compacted slope under various rainfall patterns, flooding, and drawdown conditions in the 50g-tonne 2 m radius beam centrifuge at the University of Sheffield. The model flood embankme nt was subjected to failure (during spin up) and this paper is concerned with the post-failure response of the slope to ongoing rainfall and flooding events.

1.1 Physical Modelling of rainfall induced slope instability.

The relationships between rainfall patterns and slope instability are reported in the literature for a range of slope failure mechanisms e.g. shallow and deep-seated first-time slides and reactivated movements (Aleotti, 2004; Tan et al., 1987; Ng et al., 2001). Centrifuge modelling has proven to be a powerful tool for analysing long-term soil responses to climate change (Take et al., 2004), since various physical processes such as heat transfer, seepage, rainfall intensity and duration are accelerated. Various centrifuge tests have been carried out with rainfall simulators to investigate the stability of fills subjected to heavy rains for a general slope case (Kimura, 1991; Tamate et al., 2010).

This paper presents an experimental investigation, benefitting from the accelerated time scaling proved by centrifuge modelling, to observe the behaviour of sandy clay flood embankment structures over a period of several "years" at prototype scale. During the modelled period, various climatic conditions were considered including seasonal fluctuations in rainfall, flooding and drawdown events.

1.2 Centrifuge scaling laws

The modelling of geotechnical problems in a centrifuge allows recreation of prototype stress conditions in small scale models. To relate measurements in the centrifuge model to equivalent values at prototype scale, various scaling laws need to be utilised. **Error! Reference source not found.** contains important scaling laws that are particularly relevant to the modelling of rainfall in slopes (Askarinejad et al., 2015; Take, 2003) and include seepage, rainfall intensity, and rainfall duration.

Error! Reference source not found..Scaling laws used.

Term	Dimension	Model/Prototype
Length	L	1/N
Seepage velocity	L/T	1/N
Consolidation time	T	$1/N^2$
Rain duration	T	$1/N^2$
Rain intensity	L/T	N

2 EXPERMENTAL SETUP

2.1 Soil properties and slope preparation.

The model soil slope described here was formed by compaction, to provide realistic conditions with a slope angle of 1.5:1 (H: V), representative of typical prototype geometries and construction processes. The compaction was conducted into the centrifuge strong box payload in 30 mm thick layers and compacted equally using a steel plate attached to a vibrating machine , as shown in Figure 2-1.



Figure 2-1 Soil preparation and compaction.

The soil mixture (sand 65% / kaolin 35%) was selected on the basis that compacted gravel and chalk were typical embankment fill materials of early generation embankments (Skempton, 1964). A series of compaction tests were previously conducted on the mixture, where a maximum dry density of 1.8 g/cm^3 was obtained at an optimum water content of 12.3%. The specific gravity (Gs) of the soil mixture was measured to be 2.65. The liquid limit (27%) of the kaolin-sand mixtures was determined through Atterberg limit tests, following the specifications of BS 1377:1999. The plastic limit was not possible to precisely determine due to the crumbly nature of the soil. However, from this the soil should be characterised as having a very low plasticity. Via a falling head test as outlined in Head (2006) the saturated permeability coefficient, *k*, of the soil was

found to be 9×10^{-10} m/s. Via oedometer testing, the coefficient of consolidation, c_v, was found to be around 40 mm^2/min.

2.2 Geometry and model configuration

The model slope was created to replicate a common earthwork slope as might be found in UK flood embankments or railway embankments. Flood embankments range in height from around 2 m to 7 m. However, while railway embankments (which can be up to 18 m high) are not necessarily designed as flood embankments, it is estimated that around 35% of railway embankments are also prone to flooding across river, coastal and groundwater scenarios (Johnston et al., 2021). Therefore, a slope height was selected that was at the upper end of typical flood embankments and typical of railway embankments.

For the test described here, five individual bags of soil were prepared at the optimum moisture content and left overnight to enable even water distribution before use. From these, the soil block was compacted to 98% relative density – i.e. very dense. Using side cutting templates and a wire saw, the compacted soil block was then cut to the required shape, as shown in Figure 2-2. After two days to allow the water pressures in the block to equilibrate, the test was mounted for testing on the centrifuge.



Figure 2-2 Model construction – left: template positioned before cutting compacted slope; right: slope after cutting.

The test was conducted at 70g using a model slope height of 110 mm, representing a 7.8 m prototype and a slope angle of 33.7° or 1: 1.5. A 50 mm thick layer of saturated gravel was used as a free draining boundary at the toe of the slope.

In order to reduce friction and ensure plane strain conditions were met, a low friction Perspex sheet was provided on the back (non-window) side of the model while the Perspex window on the one face of the strong box enabled efficient observation and evaluation of soil deformations during testing. LED panel lights was applied to the top and right side of the window to ensure even lighting during the tests. Black seed texture was applied to the front face of the model slope during preparation in order to facilitate digital image correlation (DIC) analysis via GeoPIV-RG software (Stanier et al., 2016). Using a GoPro camera positioned in front of the Perspex window, soil displacements were tracked optically at 10-second intervals and at a resolution of around 10 pixels / mm. The model was observed in real time via a webcam that could be accessed from the control room. Overlapping strips of filter paper were positioned from the crest of the slope to the toe to reduce the possibility of erosion over the long seasonal moisture cycles.

2.2.1 Pore Pressure Instrumentation (PPT)

Constructing the model slope involved installation of eleven pore water pressure transducers (PPT) in the area of interest on the slope. The PPTs were inserted into the slope through the rear face of the model as indicated in Figure 2-3. All PPTs were capable of measuring both suction and positive pore water pressure, and were appropriately saturated and calibrated prior to testing.



Figure 2-3 Positions of PPTs used during construction.

2.2.2 Environmental and rainfall simulator

The strongbox used for this study has been modified to facilitate the controlled application of various rainfall conditions to the model while in-flight. The rain simulation in the centrifuge environment was achieved by using four nozzles that generate dispersed water droplets, similar to the method reported by Take (2003). Based on direct measurement, this led to a scaled rainfall rate of 1.14 mm/h. Two temperature and two humidity sensors were also connected to the lid of the strongbox. Note that the fluctuation of humidity and temperature were not independently controlled as the air passed through the test chamber. Instead, rainfall or flood conditions were applied and the temperature and relative humidity varied in response. As a result, the

maximum variation in temperature was from 21°C to 25°C and relative humidity from 56% to 92% which, for humidity, are typical extremes encountered in the UK. The experimental configuration, which includes the precipitation simulator and centrifuge model, is illustrated in Figure 2-4.

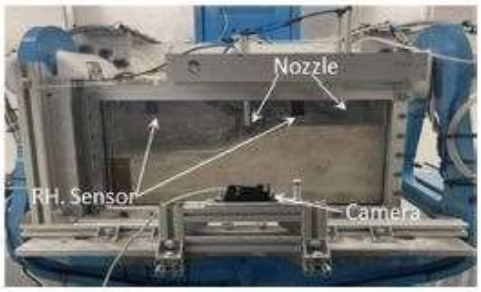


Figure 2-4 Experimental design of the centrifuge model and rainfall simulator.

2.3 Test procedure

The experiment was carried out with a step-wise increase in acceleration until it reached 50g for the auto-balance phase, which lasted approximately 25 minutes. Then, after reaching the targeted centrifugal acceleration of 70g, the model was left for 40 minutes (136 days at prototype scale) to equilibrate. Pore pressures developed steady readings in around one minute, which is in agreement with theory.

After this initial equilibration / summer phase, three "seasons" (winter, summer, winter) were applied to the slope model to observe the impact of rainfall duration on slope deformation and stability. The first "winter" lasted for 7 months at prototype scale, and consisted of alternating weeklong periods of rain and no rain respectively. During the "summer" period which lasted 5 months, no rainfall was applied. Finally, during the second (7 months long) winter, the rainfall period was increased to two weeks, separated by weeklong breaks of no rain. Following the above seasonal fluctuations, the model slope was subjected to a half-winter that lasted as three weeks of rain, followed by a dry week, where the other half-winter was continuous rain, with drainage allowed at the toe of the embankment. After this period, the drainage outlet at the toe of the embankment was closed to allow the applied rainfall to create a flooding scenario with the water level rising just above the embankment crest. Thereafter, the outlet valve was opened to facilitate a drawdown scenario. The flooding and drawdown conditions were applied twice before the model experienced a 310-day-long summer period with no rain. For all rainfall applications, a rainfall intensity of 1.14 mm/h (prototype) was used. In order to generate the precipitation patterns, the rainfall was manually activated and deactivated at predetermined time intervals.

3 EXPERIMENTAL RESULTS AND DISCUSSION

During the acceleration to 70g, the centrifuge at the University of Sheffield undergoes an auto-balance phase at around 50g. This phase caused small but discernible deep seated strains in the model (≤ 5%), as shown in Figure 3-1, which, using a GeoPIV-RG mesh size of 100×100 pixels with a 50 pixel overlap, illustrates the development of shear strain over a period of 10 seconds in model time. Additionally, a small crack in the crest was evident by the end of this auto-balance phase and has been labelled in Figure 3-1. This crack disappeared during the next few minute of auto-balance, possibly due to being infilled with fines (kaolin), and did not reappear subsequently. Similar slope movements were observed by Take (2003) during centrifuge spin up of pure kaolin models; he also noted that this did not appear to influence subsequent strain development. Once the model achieved a centrifugal acceleration of 70g, it was allowed to consolidate for 40 minutes in the absence of any precipitation events. During this period, visible movement was observed through DIC, where strain was occurred in the model, as depicted in Figure 3-2. The strains experienced during this period were approximately 4%.

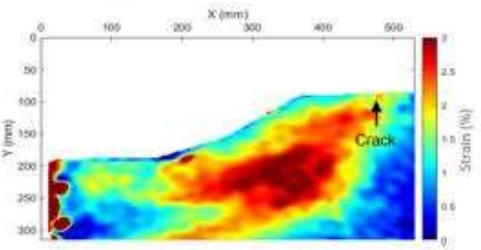


Figure 3-1 Shear strain developed during auto balance stage.

During the application of initial seasonal variations, no observable strains were detected. However, after the continuous application of rainfall for a period of the third winter, the greatest amount of strain (approximately 10%) during testing was observed, as illustrated in Figure 3-3. This occurred on a plane above the original slip surface.

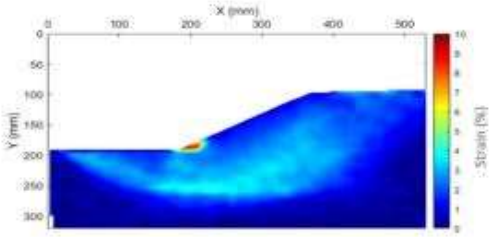


Figure 3-2 Shear strain developed during consolidation phase.

No movement was observed during the flood phase as shown in Figure 3-4. On the other hand, some movement occurred with the reduction of water level (drawdown phase) following the flood, as shown in Figure 3-5. While all the movements discussed above were clearly discernible from the DIC analyses, they were not accompanied by any abrupt changes in pore-water pressure. This is potentially indicative of drained instability; however, it cannot be ruled out that the sensors were simply not close enough to the shear zones to record changes in pore pressure associated with the movement.

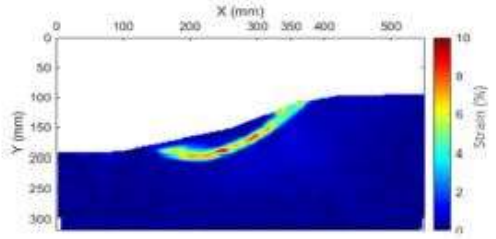


Figure 3-3 Shear strain accumulation: failure during continuous rainfall season.

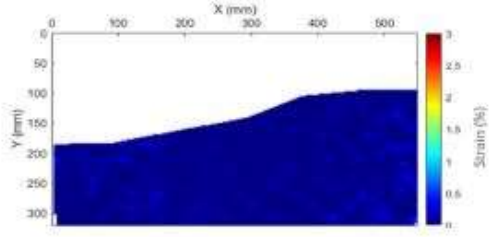


Figure 3-4 Shear strain developed during flood stage.

As illustrated by the DIC results presented, the application of various climatic scenarios resulted in significant slope deformations. Additionally, after testing it was observed that these slope movements were accompanied by surface erosion on the face of the slope near the crest.

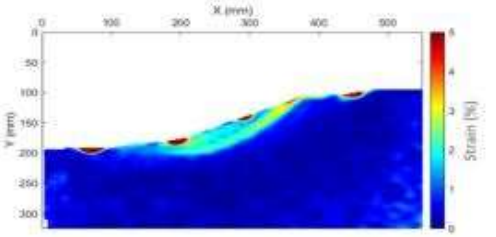


Figure 3-5 Shear strain accumulation: post-failure movement during flood drawdown.

Evidence of erosion was observed to a depth of approximately 10 mm as shown in Figure 3-6, indicating that the filter papers used to cover the soil surface did not adequately protect the slope during the extreme climatic conditions applied. Based on a post-test dissection however, it was deemed unlikely that this erosion led to the global failure of the slope.

The cumulative crest settlement following the auto-balance stage was 15mm, indicating possible slope instability under current climate conditions as presented in Figure 3-7.



Figure 3-6 The failure and erosion at the end of the test.



Figure 3-7 Crest settlement during auto balance phase.

4 CONCLUSIONS

This paper presents the results of a centrifuge test conducted to evaluate the response of a model slope

to extreme climatic conditions. With this procedure, a single, instrumented, and carefully controlled centrifuge test can be used to evaluate the performance of the slope over a number of years – under expected in-service loading to more extreme events. Although slope movement occurred during spin-up (auto-balance phase), there was no visible evidence of it on the model surface during subsequent testing. This suggests that the initial failure (even developing a crack that then "self-healed") did not cause any significant external damage or noticeable changes that could be later observed. This shows there is a possibility of slope deformations occurring as a result of the failure, which may only become evident when additional loading or stress is applied to the slope.

While there were the aforementioned initial deep seated strains during spin up and consolidation phases, no detectable strains were observed when the initial seasonal variations were applied. However, a relatively shallow shear plane (10% shear strain) developed during the third winter of continuous rainfall. This suggests that the lighter rainfall of the first two winters was insufficient to raise the pore pressure sufficiently to detablise the slope.

The subsequent flood phase did not cause any noticeable displacement or movement. However, there was some movement (approximately 2-3% additional shear strain) within the same shallow shear zone observed as the water levels decreased during the drawdown phase. There are various factors that could contribute to this phenomenon, including the settling or shifting of sediment, movement of groundwater, and other dynamic processes influenced by the decreasing water levels.

In summary, while this study only examined one soil type – namely a very low plasticity sandy clay – it has shown that a well-compacted embankment in such a material can experience significant long-term soil movements under current climatic conditions. These movements may not be easy to detect at the surface of the slope, resulting in difficulty in choosing to remediate such failures.

ACKNOWLEDGEMENTS

The first author would like to express her greatest appreciation to the University of Sheffield for valuable guidance and supporting this study. The study was completed with financial assistance from the Ministry of Science and Education in Libya. Additionally, the authors would like to express their gratitude to Mark Foster for his assistance with the experimental work.

5 REFERENCES

Aleotti, P. (2004). A warning system for rainfall-induced shallow failures. *Engineering Geology* 73(3-4): 247-265.

Askarinejad, A., Beck, A. & Springman, S. M. (2015). Scaling law of static liquefaction mechanism in geocentrifuge and corresponding hydromechanical characterization of an unsaturated silty sand having a viscous pore fluid. *Canadian Geotechnical Journal* 52(6): 708-720.

Dyer, M. (2004).Performance of flood embankments in England and Wales. In *Proceedings of the Institution of Civil Engineers-Water Management*, Vol. 157, 177-186: Thomas Telford Ltd.

Fredlund, D. G. & Rahardjo, H. (1993). *Soil mechanics for unsaturated soils*. John Wiley & Sons.

Head, K. H. (2006). *Manual of soil laboratory testing*. USA.

Johnston, I., Murphy, W. & Holden, J. (2021). A review of floodwater impacts on the stability of transportation embankments. *Earth-Science Reviews* 215: 103553.

Kim, J., Jeong, S., Park, S. & Sharma, J. (2004). Influence of rainfall-induced wetting on the stability of slopes in weathered soils. *Engineering Geology* 75(3-4): 251-262.

Kimura, T. (1991).Failure of fills due to rain fall. In *Centrifuge*, Vol. 91, 509-516: Balkema.

Ling, H. I., Wu, M.-H., Leshchinsky, D. & Leshchinsky, B. (2009). Centrifuge modeling of slope instability. *Journal of Geotechnical and Geoenvironmental Engineering* 135(6): 758-767.

Ng, C. W., Wang, B. & Tung, Y.-K. (2001). Three-dimensional numerical investigations of groundwater responses in an unsaturated slope subjected to various rainfall patterns. *Canadian Geotechnical Journal* 38(5): 1049-1062.

Skempton, A. (1964). Long-term stability of clay slopes. *Geotechnique* 14(2): 77-102.

Stanier, S. A., Blaber, J., Take, W. A. & White, D. (2016). Improved image-based deformation measurement for geotechnical applications. *Canadian Geotechnical Journal* 53(5): 727-739.

Take, W., Bolton, M., Wong, P. & Yeung, F. (2004). Evaluation of landslide triggering mechanisms in model fill slopes. *Landslides* 1: 173-184.

Take, W. A. (2003).The influence of seasonal moisture cycles on clay slopes. University of Cambridge.

Tamate, S., Suemasa, N. & Katada, T. (2010).Simulating shallow failure in slopes due to heavy precipitation. In *Physical Modelling in Geotechnics, Two Volume Set*, 1167-1174: CRC Press.

Tan, S., Lim, T., Tan, S. & Yang, K. (1987).Landslide problems and their control in Singapore. In *Southeast Asian geotechnical conference. 9*, 25-36.

Yoshida, Y., Kuwano, J. & Kuwano, R. (1991). Rain-induced slope failures caused by reduction in soil strength. *Soils and foundations* 31(4): 187-193.

Development of a rainfall simulator for climate modelling

I.U. Khan, M. Al-Fergani & J.A. Black
Department of Civil and Structural Engineering, Centre for Energy & Infrastructure Ground Research (CEIGR)
University of Sheffield, Sheffield, UK

ABSTRACT: This paper outlines the design and development of a rainfall simulator for the centrifuge for the purpose of evaluating infrastructure resilience in changing climate conditions. Pressure losses in the water supply system are evaluated and related to nozzle pressure and flow rate at both 1g and elevated gravity up to 100g. Coriolis effects are investigated and quantified with increasing gravity accounting for effects of air flow through the experimental package on the University of Sheffield 50gT beam centrifuge. The rainfall simulation capabilities are demonstrated on a slope boundary problem to validate the developed system. Slope deformation is captured using digital image correlation techniques which confirm triggering of slope movements with applied rainfall events.

1 INTRODUCTION

Simulating rainfall within the centrifuge is now a mainstream technique for the purpose of evaluating the impact of infiltration and cyclic pore pressures in engineered earth structures. The rain droplets are influenced by parameters such as coriolis force and artificial windage around the model (Caicedo & Thorel 2014, Hudacsek & Bransby 2008, Take & Bolton 2002). Due to the presence of these forces, it is difficult to ensure a uniform distribution of rainfall. Hence it is necessary to estimate the effect of parameters such as the centrifuge acceleration, nozzle position, injection pressure and wind velocity (Caicedo & Thorel 2014).

Considerable effort has been made to unearth the answers of rainfall/climate-induced slope failure via full-scale monitoring and instrumentation, however; this process is protracted and may not yield effective understanding due to the isolation of the test case (Brackley & Sanders 1992). Modelling this type of problem under controlled laboratory conditions, at full scale, is also not truly feasible owing to the magnitude and time taken to evaluate performance over many years (Ling et al. 2009). Small scale modelling at elevated gravity in a centrifuge is attractive, compared to 1g counterparts, as prototype self-weight body forces that drive downward slope movements are simulated.

Previous literature on slope instability triggered by climate conditions has identified various factors such as the soil properties, rainfall intensity, initial water table location, and slope geometry to contribute to the instability of slopes during rainfall (Kim et al. 2004, Yoshida et al. 1991). The aspect of rainfall simulation is further complicated owing to coriolis effects that affect the rainfall trajectory and how this advances to the model surface. To provide an adequate distribution over the soil surface, the coriolis effect and other properties previously highlighted should be calibrated.

To minimize the coriolis effect and to prevent surface erosion due to rainfall impact, the vertical distance between the surface of the model and spraying nozzles has to be carefully considered. Askarinejad et al. (2012) determined a stand-off distance between 70 to 100 mm was suitable to minimise coriolis effects, but noted this was dependant on the rainfall intensity and nozzle type. Caicedo et al. (2015) proposed a theoretical rainfall framework of coriolis incorporating factors such droplet size, initial velocity of droplet, wind velocity, rate of evaporation and relative velocity between air and droplet. Experimental observations validated the predictions.

In this paper, the aspect of rainfall generation and dispersion is evaluated for the University of Sheffield 50gT 2m radius beam centrifuge. This investigation supports ongoing work to develop an environmental climate chamber for modelling infrastructure resilience. The water supply system for the rainfall simulator is discussed in detail. The coriolis effect is studied based on the experimental tests at various g levels. A slope test has been conducted to analyze and validate the functionality of the developed system. The previous contributions identified, offer a brief summary of some of the major technical and scientific

contributions within centrifuge rainfall/climate simulation and form a valuable database to support the endeavours described in this paper.

2 SYSTEM DESCRIPTION

A schematic block diagram of water supply system to the centrifuge is shown in Figure 1. Two air supply lines pass to the centrifuge via a 4 port rotatory union interface from the external lab air ring main. One air supply line is connected to an air-water reservoir which provides the initial positive water pressure head to drive the rainfall system. Alternatively, this pressure head can originate by passing water directly over the central axis and allowing centrifugal force to generate water head at the package. The later method is suitable for longer test runs where fluid volume requirements exceed that of the local water reservoir.

The second air supply line is connected to a pneumatic regulator (ITV0050) that is used to step down and regulate the air pressure provided to a dome loaded valve (IR4001) to control the rainfall sprinkler nozzle. The pressure for both the air supply lines is set to 700 kPa. The pressurized water line from the reservoir is connected to the input of the dome loaded valve. The output of the dome loaded valve is connected to a solenoid valve and two pressure sensors, S_1 and S_2, monitoring the input and output pressures respectively. The output of the solenoid valve is connected to the rainfall nozzle and a further pressure sensor (S_4) measures the precise nozzle supply. The water pressure at the nozzle is controlled by regulating the output water pressure at the dome loaded valve. The dome loaded valve offers variable ratio of input to out pressure; however, in the current setup it is calibrated to yield 1 to 1 for air input to water output pressure. The air pressure input supply to the dome valve is regulated using a pneumatic regulator with a pressure sensor (S_3) and monitored using a Labview Virtual Instrument (VI) with integrated hardware USB-6211 data acquisition system. The air pressure is controlled via a PID (Proportional Integral Derivative) control loop with a continuous feedback from the pressure sensor (S_3). All the sensors are monitored online and the control signals are sent to the pneumatic regulator and solenoid valve using the user VI. Figure 2 shows the front and the top view of the experimental setup.

3 CENTRIFUGE WATER SUPPLY SYSTEM

It is very important to monitor the changes in the water pressure as this will affect the flow rate of the rainfall. These affects also vary with increasing gravity thus several calibration tests were conducted to understand the water pressure supply system and quantify head losses. The relationship between the flow rate and the applied pressure for the nozzle used is given by Equation (1):

Table 1: Centrifuge water pressure.

Gravity (m/s^2)	P_1(e) (kPa)	P_2(t) (kPa)	P_3(e) (kPa)	P_4(t) (kPa)	P_5(e) (kPa)
1g	697	2.25	697	0.39	0
25g	646	45.1	637	7.90	14
50g	590	101	571	17.9	32
75g	536	158	507	27.8	52
100g	489	214	447	37.7	80

$P_{1\to4}$ = water pressure

(e) = experimental, (t) = theoretical

$$Q = 4 \times 10^{-8}\, P_n{}^{0.5023} \tag{1}$$

where Q is the nozzle flow rate and P_n is nozzle pressure. Tests at four different gravity levels were considered, 25, 50, 75 and 100g. A time history trace of a tests at 100g, demonstrating the pressure response of the water supply system starting from stationary (0-3 min), spinning (3-29 min) and rainfall simulation (14-20 min) is presented in Figure 3.

The air pressure to the dome loaded valve is set to 300 kPa and the air pressure to the air-water interface is set to 700 kPa. At 1, 25, 50, 75 and 100g, the water pressure read by sensor S_1 at the input of the dome loaded valve is 697 kPa prior to spinning. At t = 3 min, the centrifuge starts spinning and after steady state, the water pressure at S_1 has reduced (Table 1. P_1(e)). The magnitude of pressure reduction increased with higher gravity levels up to a maximum of 489 kPa at 100g. The pressure loss due to a height difference between the water reservoir position (resting on the centrifuge platform at a radius of 2 m) and the rainfall system top plate on top of the centrifuge plane strain box which is at a radius of 1.56 m. The theoretical pressure loss is given by Equation (2):

$$P_{loss} = \rho N g h. \tag{2}$$

where ρ is the density of water, N is a multiple of earths gravity g and h is the height difference between the water reservoir and the top plate (0.23 m). The P_2(t) in Table 1 shows pressure loss calculated using Equation 2. It can be seen that the pressure drop at S_1 from the input pressure of 700 kPa (shown as P_1(e) in Table 1) and the pressure calculated in P_2(t) are similar in magnitude. This confirms that the location of the water reservoir is an important consideration in the pressure distribution system as the available head to drive the rainfall simulator can be significantly reduced.

Another interesting observation during the rainfall event that commenced at t = 14 min, for 6 minutes, was a constant reduction in supply pressure to the dome valve demonstrated in Table 1 (P_3(e)). This was due to the water column height reduction in the reservoir as rainfall continued. As expected the magnitude

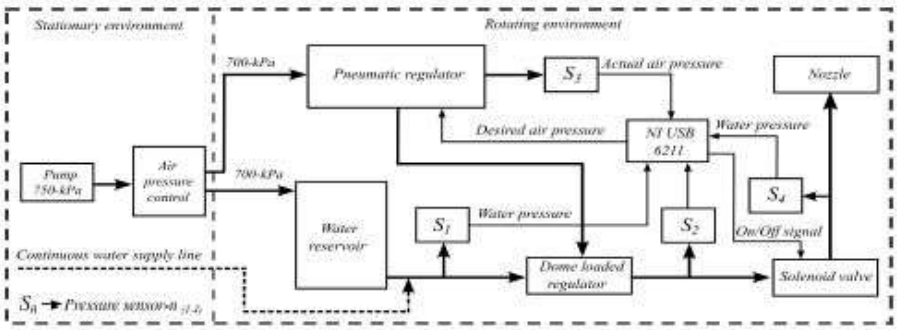
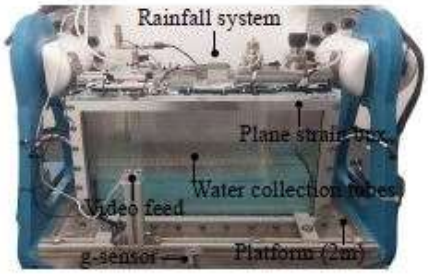
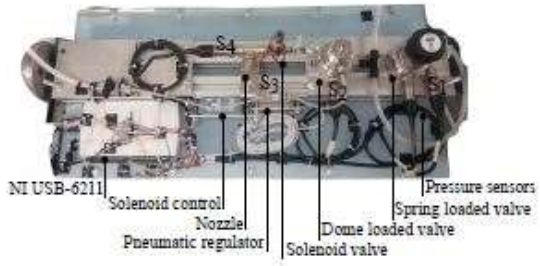


Figure 1: Centrifuge rainfall simulator block diagram.



(a) Setup



(b) Top plate

Figure 2: Experimental setup.

of the pressure reduction increased with increasing levels of applied gravity. Crucially, this reduction in system pressure also affected the water pressure supplied to the nozzle. $P_4(t)$ in Table 1, shows the calculated pressure loss due to the decreasing water column height (i.e. 0.041 m in this test case) which reflects the pressure loss observed during the rainfall event. While this supply pressure loss is unavoidable when supplying water via a closed reservoir system, a critical factor is whether these changes in pressure are sufficient to affect the characteristics of the rainfall produced and the discharge intensity. Hence, as demonstrated by Table 1, it would be necessary to refill the water reservoir in flight after each rainfall event to minimise the pressure losses and adverse effects on the nozzle pressure. To emphasise this aspect

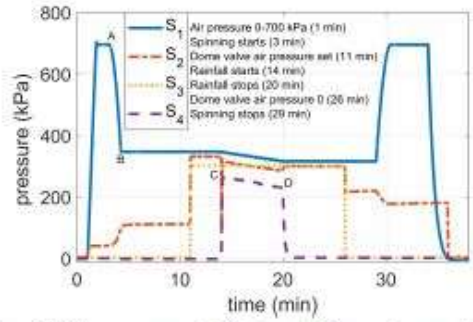


Figure 3: Water pressures at 100g in centrifuge water supply system starting from stationary (0-3 min), spinning (3-29 min) and rainfall simulation (14-20 min).

Figure 3 shows results of an additional test at 100g where the water reservoir was only half filled. The initial decrease in the water pressure (from point A to B) once 100g was achieved was 142 kPa greater than a previous 100g test shown in Table 1, in which the reservoir was full. In this test the nozzle pressure (S_4) at the start of the rainfall was 263 kPa (Point C) and dropped to 230 kPa (Point D) after the 6 minute rainfall event. Clearly this is not desirable as the supply pressure fell below that of the specified nozzle pressure of 300 kPa which affect the output flow rate.

The use of water reservoir in the centrifuge environment can create problems related to water pressure. An alternate to mitigate this problem would be the provision of a continuous water supply line. However, if the use of a water reservoir is unavoidable then it is recommended to be placed close to the nozzle position (i.e. as close to the top of the package) in order to minimise pressure losses associated with the height difference and reducing head. Another important observation from all the above mentioned results is an additional increase in the output water pressure of the dome loaded valve shown in Table 1 ($P_5(e)$) by S_2 at the steady state. This additional increase went up at higher g levels and is attributed to the internal mechanical spring assembly that controls the output orifice. Under elevated gravity, the spring compresses inside the valve due to increasing self-weight forces. However, once calibrated and the magnitude known,

this can be adjusted to ensure the desired pressure is achieve by reducing the control pressure by a known offset amount.

4 CORIOLIS EFFECT

Coriolis is one of the most important cited phenomena in the centrifuge when dealing with rainfall simulations. In order to study the coriolis effect different experimental tests have been performed at different gravity levels. In all the tests, nozzle pressure is regulated to 400 kPa using the pneumatic regulator. At this pressure, the nozzle flow rate is 8.05×10^{-7} m^3/s. The rainfall event lasts for 5 minutes. For the first three set of tests, the distance between the tip of the nozzle and the water collection tubes is set to 70 mm. In the fourth set of tests, this distance is increased to 140 mm. The centrifuge rotation is clockwise and the displacement of droplets in all the tests is measured with respect to the droplets position at 1g.

Figure 4 shows four different positions of the nozzle (i.e. n_1, n_2, n_3 and n_4). The first set of tests are performed (at 1, 25, 50 and 75g) with the top plate on to remove the air flow windage effects and the nozzle position at n_1. The results are shown in Figure 5. With each higher g level there is a 3 mm displacement in rainfall distribution towards the nozzle position. In the second set of tests, the top plate has been removed with the nozzle position at n_1 and the results are shown in Figure 6. At all the g levels a greater displacement of rainfall distribution was observed up to 19 mm from the original position. The coriolis effect is very small without air interference in the package. In the second set of tests, the air flow is generating increased drag force on the water droplets, resulting in greater translation of the distribution position. Note, it is observed that there is a non-symmetrical distribution from the nozzle. This was checked and is believed to be due to manufacturing tolerances.

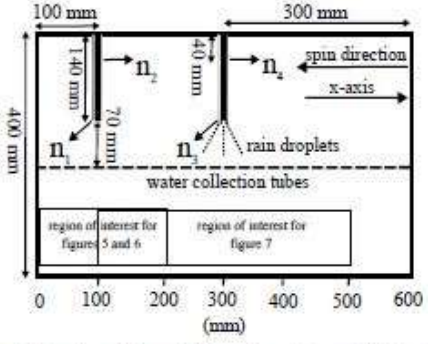


Figure 4: Nozzle positions in the package for coriolis tests.

In the third set of tests, to check the effect of the air on water droplets, the nozzle has been moved from position n_1 to n_2 without the top plate. At 75g with the nozzle at n_1, there is a displacement of 19 mm

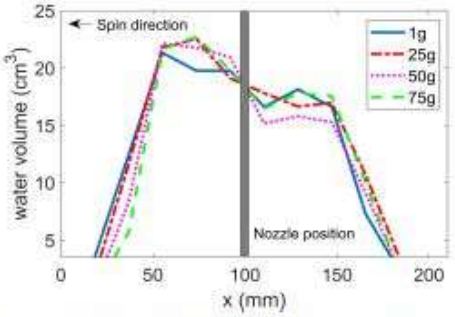


Figure 5: Water volume distribution at different g levels with top plate and nozzle position at n_1.

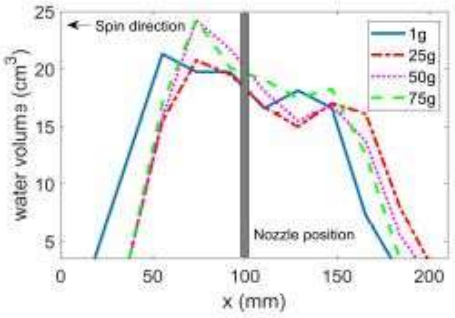


Figure 6: Water volume distribution at different g levels without top plate and nozzle position at n_1.

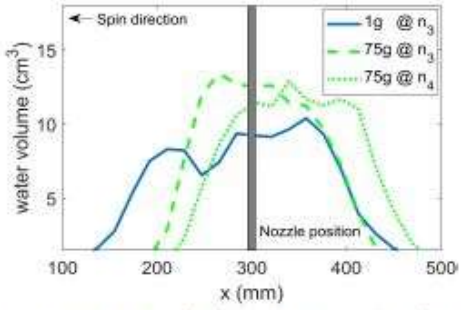
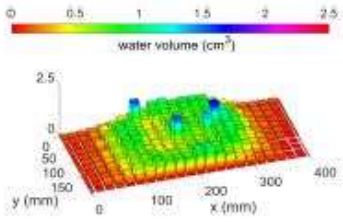
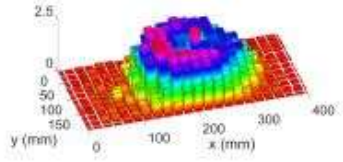


Figure 7: Water volume distribution at 1g & 75g without top plate and nozzle in the center of package.

along the x-axis. At 75g with the nozzle at n_2, there is a displacement of 22 mm along the same axis, which is not significant for the change in vertical position. In the fourth set of tests the nozzle position is moved between n_3 and n_4 without the top plate. The results are shown in Figure 7. At 75g with the nozzle at n_3 there is a displacement of 63 mm long x axis. At 75g with the nozzle at n_4, there is a displacement of 87 mm along the same axis. The effect of air is minimal at both n_1 and n_2 because of being very close to the package side wall. Therefore, the displacement of water droplets at n_1, n_2 is almost similar. However, the effect of air at n_3 and n_4 significantly influence the distribution position of the rainfall. Hence it is clear that windage substantially adds to the coriolis effect observed and this should be minimised. For



(a) 1g



(b) 75g

Figure 8: Water volume distribution at 1g and 75g without top plate and nozzle in the center of package (n_3).

both cases, the vertical nozzle position has some influence on the coriolis due to the increased free fall distance, although this is small in comparison to windage effects.

Figure 8 shows an increase in the water volume and a reduction in water collection area, with higher gravity levels (i.e. from 1g to 75g). This phenomenon is seen in all of the above tests. At 1g the water volume collected is 140×10^{-6} cm^3, whereas at 25g is 171×10^{-6} cm^3, at 50g is 183×10^{-6} cm^3 and at 75g is 191×10^{-6} cm^3. There is 30×10^{-6} cm^3 additional water volume collected at 25g with respect to 1g; however after 25g, at every higher gravity the additional water volume collected is 10×10^{-6} cm^3. There are two factors behind the increase of water volume, gravitational force and nozzle pressure. The nozzle pressure has increased at a fixed rate at each higher gravity level. The reason for this increase is spring compression inside the dome valve due to increasing self weight forces at every higher gravity level. The flow rate of the nozzle is dependant on the water pressure. This increase in the flow rate is adding 10×10^{-6} cm^3 at higher gravities. An additional increase of 20×10^{-6} cm^3 at 25g is because of the gravitational force. The increase in gravitational force is not allowing the water droplet to move further away from the nozzle, as the water loss at 1g was seen on the front and back wall of the package. Beyond 25g the effect of increased gravitational force reduces the water collection area.

5 SLOPE TEST

The previous sections outlined the initial development of a rainfall simulation system that will be incorporated within a climate control chamber to investigate infrastructure resilience. The impact of temporal changes in precipitation on the performance of engineered slopes and earthworks pose increased risk to linear infrastructure systems. To demonstrate the functionality of the rainfall system and the associated movements induced by rainfall, a trial validation case was considered for an engineered slope. A model slope of height 120 mm and slope angle of 26 degrees was tested at 25g, representative of a 3 m prototype (Figure 9). The slope was prepared from Kaolin clay, prepared at a moisture content of 40% and was compacted into the centrifuge payload in 50 mm thick layers using a 2.5 kg hammer. The clay block was trimmed to the desired slope profile with the aid of side cutting templates and a wire saw. Trimmings of the removed soil confirmed uniform moisture conditions of the placed clay layers. In order to observe the impact of precipitation, the validation test case was configured as a plane strain model whereby the side of the slope was exposed and visible through the Perspex viewing window. To enable Digital Image Correlation (DIC) analysis, texture was applied to the front face of the slope model during preparation.

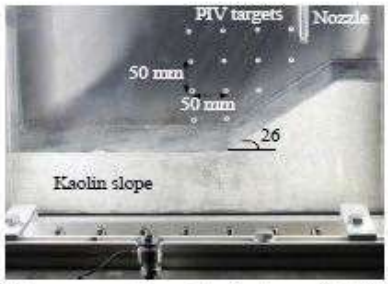
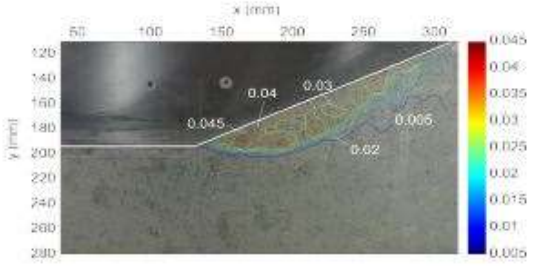


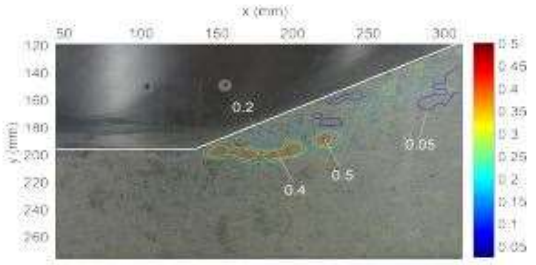
Figure 9: Slope prepared from Kaolin clay, with 40% of water content.

Due to the increase in self-weight stresses imposed by elevated gravity, an initial spin up time of 30 minutes was allowed at 25g for the slope to bed in. This ensured slope movement due to the imposed gravity during spin up occurred prior to commencing the rainfall stage. In addition this also allowed equilibrium of internal pore water pressures, although note these were not monitored. A continuous rainfall event was implemented in order to trigger the onset of slope movement. Note the ability for individual seasonal conditions (i.e. summer and winter) at various rainfall intensities has been incorporated into the control system development for future more complex rainfall conditions. The nozzle pressure was regulated to 400 kPa. After the initial equilibrium phase, rainfall was simulated for 20 minutes at a flow rate of 8.05×10^{-7} m^3/s. The volume of rainfall is equivalent to a prototype rainfall of 2800 mm per year, which corresponds to the most extreme rainfall predictions for the UK.

Figure 10(a) outlines the resultant displacements that occurred at the end of the 20 minute rainfall event



(a) Resultant displacement contour



(b) Shear strain contour

Figure 10: Contour plots for the slope test using Digital Image Correlation (DIC).

across the slope. The effect of the applied rainfall is clear whereby movement of the slope is observed parallel with the slope surface, commencing at the toe and propagating backwards to the crest. The maximum resultant displacement captured is 0.045 mm [0.001 m in prototype] at the interface of the slope and toe position, with displacements generally reducing with slope elevation. This location of maximum displacement also corresponds with the region of highest shear strain (Figure 10b) which can be seen extending from the toe into the slope. These observations confirm that the simulated rainfall event triggered the onset of slope movement. These observations are consistent with rainfall triggered movements in other tests reported by Take and Bolton (2002), corresponding to where the shear stresses and pore pressures are highest. Other positive aspects to be drawn from the preliminary trail test is that no preferential drainage paths along the clay-window boundary were observed, confirming that the application of silicone grease along this edge was sufficient to mitigate water ingress.

Furthermore, on completion of the test, no adverse surface erosion effects were observed, confirming that the selection of nozzle pressure, height and dispersion angle were suitable to model the rainfall event. After the test some surface cracking across the width of the slope between the front and back side walls was detected; which may offer some insight as to the deeper movement observed within the slope. At this stage it is not clear whether these cracks occurred during the initial spin up phase or as a consequence of rainfall induced movements; however, nevertheless they would have accelerated infiltration of water in the slope at increased depths which could give rise to the observed movements within the slope. Further discussion is beyond the scope of this paper and continued work relating to climate simulation is ongoing to reveal greater insight of infrastructure resilience in changing environments.

6 CONCLUSIONS

In this paper, characteristics of a rainfall simulator have been considered for the centrifuge environment. The water supply system for the rainfall simulator has been analyzed in detail. It has been concluded from the results that the use of a water reservoir in the centrifuge can pose problems related to water pressure losses. To avoid the pressure decrease during the rainfall events, a continuous water supply line should be used. The effect of coriolis has been evaluated, nozzle position and angular velocity are shown to influence the windage component for coriolis consideration. A slope test has been conducted to validate the developed system. Preliminary results indicated that the rainfall has induced slope instability. Further development of the system will allow the investigation of infrastructure resilience with more complex scenarios of the rainfall events.

REFERENCES

Askarinejad, A., J. Laue, A. Zweidler, M. Iten, E. Bleiker, H. Buschor, & S. Springman (2012). Physical modelling of rainfall induced landslides under controlled climatic conditions. *Proceedings of 2nd European Centrifuge Physical Modeling in Geotechnics*, 23–24.

Brackley, I. & P. Sanders (1992). In situ measurement of total natural horizontal stresses in an expansive clay. *Geotechnique 42*(3), 443–451.

Caicedo, B. & L. Thorel (2014). Centrifuge modelling of unsaturated soils. *Journal of Geo-Engineering Sciences* 2(1-2), 83–103.

Caicedo, B., J. Tristancho, & L. Thorel (2015). Mathematical and physical modelling of rainfall in centrifuge. *International Journal of Physical Modelling in Geotechnics 3*(15), 1–15.

Hudacsek, P. & M. Bransby (2008). Centrifuge modelling of embankments subject to seasonal moisture changes. In *Proc. Conf. Advances in Transportation Geotechnics*.

Kim, J., S. Jeong, S. Park, & J. Sharma (2004). Influence of rainfall-induced wetting on the stability of slopes in weathered soils. *Engineering Geology 75*(3), 251–262.

Ling, H. I., M.-H. Wu, D. Leshchinsky, & B. Leshchinsky (2009). Centrifuge modeling of slope instability. *Journal of Geotechnical and Geoenvironmental Engineering 135*(6), 758–767.

Take, W. & M. Bolton (2002). An atmospheric chamber for the investigation of the effect of seasonal moisture changes on clay slopes. In *Proc., Int. Conf. on Physical Modeling in Geotechnics*, pp. 765–770. Balkema Rotterdam, The Netherlands.

Yoshida, Y., J. Kuwano, & R. Kuwano (1991). Rain-induced slope failures caused by reduction in soil strength. *Soils and foundations 31*(4), 187–193.

Centrifuge modelling of slope stability failure

M.A.A. Alfergani
Department of Civil and Structural Engineering, the University of Sheffield, Sheffield S1 3JD, United Kingdom
abauthor@sheffield.ac.uk; cdauthor@sheffield.ac.uk

Primary Supervisor: Dr Jonathan A. Black – e-mail: j.a.black@sheffield.ac.uk
Secondary Supervisor: Dr Elizabeth Bowman – e-mail: e.bowman@sheffield.ac.uk

ABSTRACT. The simulation of realistic geotechnical design is often restricted to routine calculation based methods informed by simple element laboratory test data which fails to provide a holistic learning experience. Using the latest research techniques laboratory teaching can now offer the opportunity to test small-scale physical models representative of larger real world full-scale engineering problems. To provide greater connectivity between geotechnical theory and design, a small-scale 1.1m diameter educational teaching centrifuge has been developed at the University of Sheffield. This enables observation of the behaviour of small-scale models tested under increased gravity to be directly related to full scale field conditions. An example is summarised herein that outlines relevant theory, physical model experiment, assessment and impact for classical slope stability failure and comparisons are made with relevant theory.

KEYWORDS. Slope stability, Talyor stability number, centrifuge

INTRODUCTION

Laboratory based demonstrations are a valuable tool as they provide an opportunity to challenge and reinforce theoretical aspects. Typically demonstrations are limited to element tests used to assess soil properties or behaviour such as compressibility and strength. While beneficial to verify soil strength theory, these tests fail to provide observations of how actual real geotechnical structures perform in practice; for example, stability problems such as slopes, retaining structures and foundations. Commonly, design problems are routinely taught using simplistic analytical design methods for a given set of input soil parameters. These parameters are either fictitious or can be determined from complementary lab element test data and subsequent interpretation.

Physical models are widely adopted in engineering research, practice and education for this purpose. In geotechnical engineering it is exceedingly difficult to demonstrate design real world applications, such as slope stability, as the soil full scale stresses of self-weight cannot be reproduced in small bench scale models. The key limitation is that the stress dependent behaviour of soil is not properly accounted for in a 1g environment, thereby making it difficult for quantitative interpretations of the experimental data to be made (Dewoolkar et al. [3]). While reduced-scale, physical models at 1g can provide a basic overview of these problems; models tested at elevated accelerations can demonstrate the subtleties of soil behaviour, produce realistic failure mechanisms and provide simple data for back analysis (Newson et al. [8]).

Realistic self-weight induced stresses in a small-scale model can be achieved in a high gravitational acceleration field produced by a centrifuge and thus the stress and strain distributions in the model will be similar to that of a field situation. The geotechnical engineering centrifuge has become an important tool in research activities in many Universities and it

has led to significant breakthroughs in geotechnical engineering understanding in pile foundation, tunnelling and offshore foundation engineering.

Craig [3] was one of the first to formally discuss physical modelling for geotechnical engineering education using small-scale centrifuge facilities. He described a modelling initiative that began in the mid-1970s at the University of Manchester where experiments were performed using an inexpensive "teaching centrifuge". Mitchell [5], Collins et al. [2], Newson et al. [3] and Dewoolar et al. [4] also demonstrated the applicability of centrifuge modelling for instructional purposes to illustrate concepts of slope stability, retaining walls, foundations, tunnel stability, and lateral earth pressure theory (Wartman [7]). The most striking example is slope stability failure which otherwise would remain unseen in the laboratory. The purpose of this paper is to demonstrates the role of centrifuge modelling in demonstrating routine slope stability problem for the purpose of applying this to the undergraduate programme.

CENTRIFUGE FACILITY

A small-scale state-of-the-art beam centrifuge 1.0m in diameter was designed in-house and is capable of rotating a payload up to 20kg at 100 gravities (100g), referred to as UOS 2gT (Figure 2). The maximum sample size that can be tested is 160mm (L) x 100mm (H) x 80mm (W) which relates to full scale or "prototype" dimensions of 16m x 10m x 8m at 100g. This is sufficient to test a diverse range of reduced scale engineering structures such as failure mechanisms in slopes, retaining walls and foundations, while providing stress conditions that realistically duplicate prototype behaviour. The centrifuge is equipped with electrical power slip rings, dual port hydraulic rotating fluid union enabling the delivery of air and water in-flight, digital image capture, load/displacement measurement, signal acquisition, an onboard PC and real-time wireless data communication/transfer. Images are captured through the viewing window in the payload which enables observations of displacement and failure mechanisms. Detailed information about the centrifuge design and development is reported in Black et al. [1].

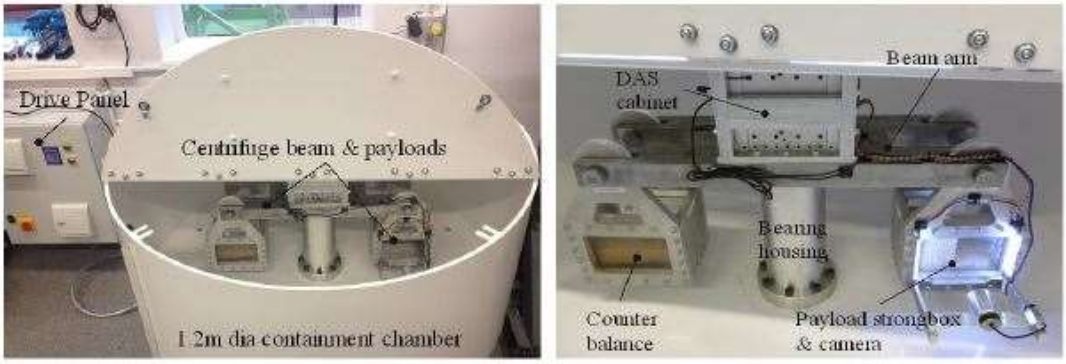


Figure 1: UoS2gT Centrifuge facility

SLOPE STABILITY DESIGN

Theory & Principal of centrifuge modelling

Consider the case of a saturated clay slope of height H having a slope angle α as shown in Figure 2a. The stability of the slope is dependent on the undrained shear strength of the soil, c_u, the slope height, H, and the unit weight $\gamma = \rho g$ and can be related to a dimensionless group referred to as the stability coefficient N_s. At failure, where the factor of safety is 1 the stability number, N_s is given by Equation 1. Reduced scale physical models for laboratory testing relate to prototype conditions by a linear scale factor, n. If the slope were at a scale n = 40 and tested at 1g (Figure 2b), it would be necessary to produce a model material having $c_u / \gamma = 1/40$. This is virtually impossible to achieve; however, similitude can be provided by testing the model slope in a centrifuge at n times the earth's gravitational field (Figure 2c) such that the slope stability number can be written as Equation 2 and 3. Equation 1 and 3 produce the same stability number hence it is evident that the model slope in a centrifuge will behave similar to that in the field.

$$FoS = \frac{c_u}{N_s \rho H} = \frac{c_u}{N_s \gamma g H} \quad [1]$$

$$N_s = \frac{c_u}{\gamma g H} \quad [2]$$

$$N_s = \frac{c_u}{\rho(ng)\frac{H}{n}} \quad [3]$$

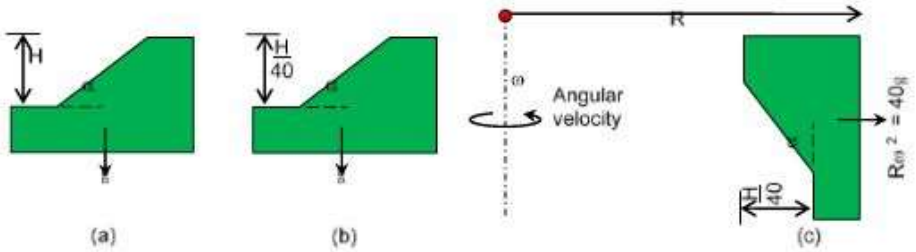


Figure 2: Slope modelling concept

Experimental methods – soil preparation and testing

The slope stability experiment is probably the most appealing among all centrifuge experiments because one can visually confirmation the development of a failure surface. Kaolin Clay samples for testing were prepared by consolidating kaolin slurry, prepared at 1.5 times the liquid limit, to a known vertical effective stress (700 kN/m²) to produce samples of uniform soil strength. Pressure increments were applied in stages of 25, 50, 100, 200, 400, and 700 kN/m². At the end of each consolidation stage the settlement readings were taken manually in four positions to obtain the average reduction of the sample height. Once the consolidation stages were finished, the loading procedure was reversed from 700 to 200 and 0 kN/m². The settlement and resulting consolidation curves are shown in Table 1 and Figure 3 respectively.

Pressure [kN/m²]	H1 [mm]	H2 [mm]	H3 [mm]	H4 [mm]	Average [mm]	Ho [mm]	Δh [mm]	Δe	e
1	6.8	6.9	7	7	6.93	15.56	0.00	0.000	2.650
13	8.6	8.4	8.5	8.2	8.43	14.06	1.50	0.026	2.624
26	10.1	10.2	10.3	10.2	10.20	12.29	3.28	0.058	2.592
55	10.8	10.7	10.8	10.9	10.80	11.69	3.88	0.068	2.582
110	11.3	11.4	11.5	11.4	11.40	11.09	4.48	0.079	2.571
220	12	12.2	12.3	12.1	12.15	10.34	5.23	0.092	2.558
440	12.7	12.8	12.9	12.8	12.80	9.69	5.88	0.103	2.547
700	13	13.2	13..2	13.2	13.13	9.35	6.21	0.109	2.541
440	13.1	13.2	13.2	13.2	13.18	9.31	6.25	0.110	2.540
1	12.5	12.5	12.7	12.6	12.58	9.91	5.65	0.099	2.551

Table 1: Consolidation data

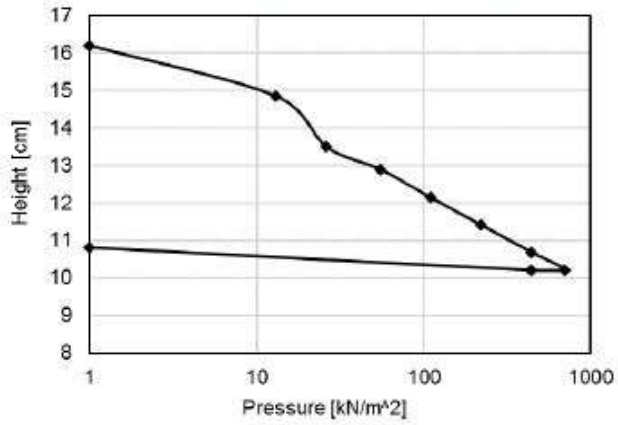


Figure 3: Sample consolidation

Several specimens were extracted for undrained strength assessment using unconsolidated undrained (UU) triaxial tests. The consolidated clay blocks had a target undrained strength (c_u) of approximately 30 kN/m². Liquid and plastic limit tests were also conducted and determined to be 70% and 34% respectively, yielding a Plasticity Index of 36%, such that the soil could be described as a high plasticity clay. The unit weight of the soft and firm soil was determined as 18 kN/m³.

Consolidated clay blocks were removed from the consolidation system in preparation for model construction. Side cutting templates and a wire saw where used to trim the block to the desired slope geometry, slope angles and height were input design variables. The side faces of the clay model were textured with 'flock' to provide sufficient contrast variation in colour to enable image correlation processes to be used for soil displacement tracking. It is very helpful to mark the slope to assist with visual identification of the failure.

The front and rear viewing windows were lightly greased to reduce interface friction and the sample was located into the strongbox with the rear side plate reattached. The mass of the counterweight was established and both the payload and counterweight were mounted into position on the beam. Once the internal safety related checks were complete the centrifuge containment lid was locked, data acquisition/image capture was started and the centrifuge was accelerated until slope failure occured. During gravity switch on the digital camera capture images of the progressive slope movement and failure mechanism where a distinctive slip plane is formed (Figure 4). The recorded images are used to assess the slope displacement and failure characteristics using image tracking methods developed for geotechnical applications.

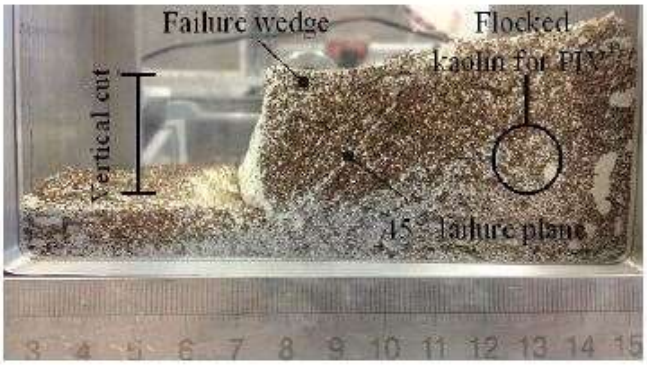


Figure 4: Slope stability failure observation.

Analytical & numerical modelling

The results of soil strength determined by unconfined compressive strength tests and in-situ vane shear tests are used in conjunction with relevant theory of stability numbers as described in Equation 1. In the slope test the failure g-level can be back calculated based on the undrained strength of the clay (using inverse relationships of Equation 1 & 2). These Class A predictions are compared with the actual test observations for the range of parameters investigated and collated data sets will be compared against routinely adopted slope stability design charts.

By way of example; a failed model slope was analysed. The model slope was 90 mm in height with a slope angle of 70°. The undrained cohesion determined by the laboratory vane test was 28 kN/m². The saturated unit weight of soil was determined to be 18 kN/m³ at earth's gravity. According to Taylor's stability chart, the stability coefficient (Ns) for this slope configuration is 0.21. The g-level (n) at which the model slope was expected to fail in the centrifuge is calculated using Eq 1 as follows:

$$0.21 = \frac{28\ kN/m2}{(\text{n x } 18\ \text{kN/m3})\ (0.090\ \text{m})} \Rightarrow n = 83g \quad [3]$$

Failure of the slope was observed at between 80 – 85g which is in good agreement with the Taylor stability analysis. Other tests in the series are shown below in Figure 5.

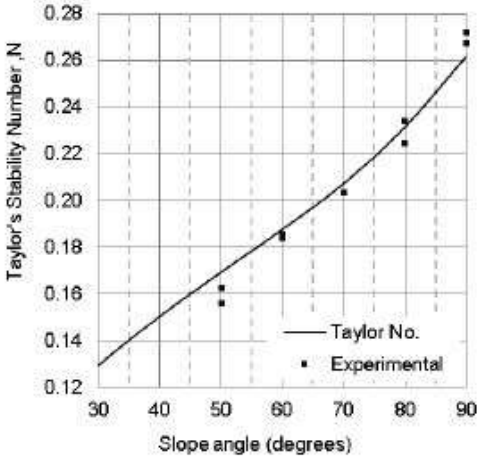


Figure 5: Slope stability failure compared to Taylor Stability Number.

CONCLUSIONS

This paper describes the development and operation of a small scale beam centrifuge in order to evaluate the performance of model slopes with theory. The centrifuge is 1.0 m in diameter and is capable of rotating a payload 20 kg at 100g. The mechanical arrangement, features and capability are summarisd. The relevant stability has been introduced and used to demonstrate the model test performance. The results confirm that the small-scale facility is capable of reveling realistic observations and quantifiable assessment of full scale field slopes.

References

[1] Black J.A.. Development of a small scale teaching centrifuge. (2014) ICPMG '14, University of Western Australia, Australia.
[2] Collins, B., Znidarcic, D., and Goddery, T. A New Instructional Geotechnical Centrifuge. Geotechnical News. (1997)
[3] Craig, W. H. The Use of a Centrifuge in Geotechnical Engineering Education. *ASTM, Geotechnical Testing Journal*, (1989) Vol. 12, No. 4, pp. 288–291.
[4] Dewoolkar, M.M., Goddery, T. and Znidarcic, D. Centrifuge Modeling for Undergraduate Geotechnical Engineering Instruction. *ASTM, Geotechnical Testing Journal*, (2003) Vol. 26, No. 2, pp. 201–209.
[5] Mitchell, R. J. Centrifuge Modeling as a Teaching Tool. *Geotechnical News*, (1994) Vol. 12, No. 3, September.
[6] Newson, T. A., Bransby, M. F., and Kainourgiaki, G.. The use of small centrifuges for geotechnical education." Proc., *Physical Modelling in Geotechnics*: (2002) ICPMG '02, St. Johns, Canada. pp. 215–220.
[7] Wartman, J. Geotechnical Physical Modelling for Education: Learning Theory Approach. (2006) *ASCE, Journal of Professional Issues in Engineering Education and Practice*. pp. 288-296.
[8] White, D.J. and Take, W.A. and Bolton, M.D. *Soil deformation measurement using particle image velocimetry (PIV) and photogrammetry*. (2003) *Géotechnique*, 53. pp. 619-632.